ANALYSIS OF CHEMICALLY-ACTIVATED PATHWAYS FOR MOLECULAR WEIGHT GROWTH

Anthony M. Dean
Exxon Research and Engineering Company
P. O. Box 998, Annandale, NJ 08801
and
Joseph W. Bozzelli
Department of Chemical Engineering and Chemistry
NJIT, Newark, NJ 07039

The unusually rapid rate of molecular weight growth in high temperature pyrolysis and oxidation of hydrocarbons has presented a substantial challenge to kineticists. Although there has been progress recently in characterization of the rapid rate of growth, attempts to accurately model the process have been only partially successful. For example, the extensive study of Frenklach et al[1] required rate constants for radical addition reactions which are several orders of magnitude larger than usually observed for these types of reactions.

There appear to be three possible pathways to rapid molecular growth:
    (1) Diels-Alder cycloadditions reactions
    (2) Ion-molecule reactions with their very large rate constants
    (3) Radical addition to unsaturates
A major difficulty with (1) is that the equilibrium constants for this type of reaction suggest that the cyclic product would tend to dissociate to the linear fragments at high temperatures where the fast growth is observed. Ionic mechanisms are suspect since rapid growth is observed under pyrolytic conditions where the ion concentration would be expected to be extremely low. By default, then, our attention (like Frenklach et al) have focussed upon radical addition reactions. Previously, we demonstrated[2] that new reaction channels could open up at higher temperatures in chemically-activated reactions like those involving radical addition to unsaturates.

The methane pyrolysis data of Back and Back[3] provided an opportunity to see if properly accounting for chemical activation might explain the observed sharp increase in rate of reaction at very low extents of conversion at temperatures near 1000K. It was possible to explain the observed acceleration[4] and to demonstrate that a critical feature of the mechanism was the very rapid production of cyclopentadiene via chemically-activated pathways. These chemically-activated adducts have enough internal energy to react unimolecularly before collisional stabilization can occur; this significantly increases the overall rate of production of heavier species because no time is required for collisional deactivation and subsequent activation to get to the same products.

This analysis also led to some useful generalizations about features of potential energy surfaces which can lead to rapid growth. Specifically, it was found that allyl addition to acetylene was critical, while the analogous addition to ethylene was not

important, even though ethylene was present in much larger concentrations. Fig. 1 compares the potential surfaces for these two reactions. Note the differences in the energetics. First the well for acetylene addition is deeper by 8 kcal/mole. Furthermore, the difference in energy between the linear and cyclic intermediates is greater in the acetylene case by about 9 kcal/mole. Much of this difference can be attributed the the relatively high energy vinyllic radical (C=CCC=C·). Even with respect to final products, the acetylene is overall exothermic while ethylene is endothermic. Each of these differences contribute to the enhancement for the acetylene reaction. The shallower well for ethylene addition will contribute to more stabilization since the barrier to cyclization is comparable to the entrance channel, while for acetylene the cyclization barrier is 11 kcal/mole lower. Similarly, the difference in energy between linear and cyclic intermediates means that the equilibrium constant for the cyclization involving C=CCC=C· is more favorable, i. e., by a factor of 60 at 1038K (the temperature of the Back and Back experiments), than for the cyclization of C=CCCC·. Thus we expect cyclization, whether it occurs via stabilized or energized adducts, to be much more favored for the case of C=CCC=C·; under the present conditions, this difference is enough to make contributions from allyl addition to ethylene unimportant. In general, the shallower wells in the ethylene system, coupled with the greater entropy of the reactants relative to the intermediates, favor redissociation of the adducts back to reactants, thus making this an inefficient channel for molecular weight growth.

These observations can be generalized to other addition reactions. The following factors should increase the probability that direct production of cyclic species can occur via an energized-complex mechanism:
(1) A deep well for the linear adduct—this will tend to make the barrier to cyclization lower than the entrance barrier, thus increasing its unimolecular rate.
(2) An increase in the exothermicity of the cyclization reaction—this is needed to offset the entropy loss upon cyclization.
(3) A final cyclic product with high stability—this will result in low energy exit channels relative to the entrance and will lead to faster unimolecular rates.

One such system where these factors are especially significant is the formation of benzene via the sequence:

$$1\text{-}C_4H_5 + C_2H_2 = 1\text{-}C_6H_7 = \text{cyclohexadienyl} = \text{benzene} + H. \qquad \textbf{(A)}$$

The potential energy diagram is shown in Fig. 2. Here the linear adduct is seen to gave a much deeper well than that resulting from the allylic addition shown in Fig. 1. Here the adding radical is vinyllic, as contrasted to the resonantly stabilized allyl; thus there is no loss of resonance upon addition as is the case with allyllic species. The cyclization is also much more favored in the benzene system since the combination of an unstable vinyllic linear radical and a very stable cyclic radical results in an exothermicity of 43 kcal/mole for the cyclization. Furthermore, note that the final exit channel for benzene production, due to its unusual stability as an aromatic molecule, is much lower than the entrance channel. As a result, this path to benzene can be very important. In fact, at 1 atm and 1200K, the rate of production of benzene via the direct reaction of the energized complex accounts for over 90% of the total reaction of the initially formed linear adduct. Here the overall exothermicity is sufficient to

1385

compensate for the loss in entropy upon cyclization. Such compensation is particularly important at high temperatures where the TΔS term plays a larger role.

Another interesting issue in molecular weight growth is the possibility of isomerization of methyl-cyclic C_5 compounds to cyclic C_6 compounds. Such isomerizations were considered in chlorobenzene pyrolysis to explain observed production of minor amounts of cyclopentadiene[5]. Given the prediction of cyclopentadiene production in methane pyrolysis, Fig. 3 suggests a possible route to benzene from cyclopentadiene. The recombination of the cyclopentadienyl radical with methyl is quite likely in these systems since both species are likely to build up to quite high concentrations, relative to other radicals, since the are no facile dissociation chaannels available. Note the production of methyl-cyclopentadienyl is only 8 kcal/mole endothermic. Once formed it can undergo beta-scission to form fulvalene. H-atom addition to the fulvalene (to the opposite end of the double bond) leads to the cyclopentadienylmethyl radical, which would be expected to quickly convert, over a series of low barriers, to benzene. This analysis would suggest that one really needs to consider formation of both 5 and 6 membered rings as the starting points for aromatics formation.

In an effort to better understand the detailed kinetics of molecular weight growth, we have used a molecular-beam sampling mass spectrometer (MBMS) to directly observe reactants, products, and reactive intermediates in hydrocarbon pyrolysis and oxidation[6]. A key component of this approach is use of photoionization at 10.5 ev., obtained by tripling the tripled (355 nm) out of a YAG laser. It is then possible to minimize fragmentation, substantially improving one's ability to observe free radicals that would otherwise be obscured by parent fragments. A schematic of the experimental set-up along with typical data from 1-butene pyrolysis is shown in Fig. 4. This system has been used to observe the production of both C_5 and C_6 species during pyrolysis and oxidation of C_4 molecules. In a typical experiment, the temperature is slowly increased at constant residence time and the molecular weight growth is monitored as one goes to higher conversions. A particularly interesting observation was that the allyl radical concentration was observed to decline at temperatures where C_5 and C_6 molecules were initially observed to be produced. We are now comparing these results with our detailed models of molecular weight growth.

An analysis of benzene production in low pressure flames[7] led to the identification of several radical addition reactions that might account for the observed production. One such path was that considered above in (A). This path was chosen by comparison of the measured concentrations C_4H_5 and C_2H_2 to the rate of benzene production. However, since C_4H_5 was measured with a mass spectrometer, it was not possible to distinguish 1-C_4H_5 from 2-C_4H_5. If these two isomers were equilibrated and if the secondary radical were much more stable, one would expect the majority of the measured C_4H_5 to be the secondary radical, which is not expected to rapidly form benzene, and this particular route would be unimportant. [However, it is important to note that the secondary radical can add to acetylene to form a fulvalene radical, and thus it might be converted to benzene in a second step, as discussed above.] Thus a critical issue, as yet not completely resolved, is the relative stability of these two isomers. At first glance, it might appear that the secondary radical would be much more stable, since the unpaired electron could be stabilized by the adjacent double bond. Indeed, The Sandia Thermodynamic database[8] indicates a normal resonance

stabilization (12 kcal/mole) in the secondary radical. However, the rotation required here would disrupt the conjugation in the system as well as result in the relatively high energy allenic structure (1,2 butadiene is 12.5 kcal/mole less stable that 1,3 butadiene[9]). Thus, it might appear that the normal resonance stabilization could be offset, and the energies of two isomers could be quite close. We feel this is an area which warrants further investigation. For the flame work considered here, benzene production occurs near 1500K. This implies that a difference in stability of 3 kcal/mole in the two isomeric forms would result in 42% of the C_4H_5 as the primary isomer, meaning that this could be a major route to benzene. However, a difference of 12 kcal/mole, i. e., a typical resonance stabilization energy, would mean that only 4% of the primary isomer would be present at equilibrium; thus ruling out this direct path to benzene in this flame.

(1)   Frenklach, M.; Clary, D. W.; Gardiner, W. C., Jr.; Stein, S. In *Twenty-first Symposium (International) on Combustion*; The Combustion Institute: 1986; pp 1067-1076.
(2)   Dean, A. M. *J. Phys. Chem.* **1985**, *89*, 4600.
(3)   Back, M. H.; Back, R. A. In *Pyrolysis: Theory and Industrial Practice*; L. F. Albright, B. L. Crynes and W. H. Corcoran, Ed.; Academic Press: New York, 1983; pp 1-24.
(4)   Dean, A. M. *J. Phys. Chem.* **1990**, *94*, 1432-39.
(5)   Ritter, E.; Dean, A. M.; Bozzelli, J. W. *J. Phys. Chem.* **1990**, *94*, 2493-2504.
(6)   Woodin, R. L.; Dean, A. M.; Kearsley, T., Paul, A.; Zhong, X.; Mancuso, J. In *Second International Conference on Chemical Kinetics*; Gaithersburg, MD, 1989.
(7)   Westmoreland, P. R.; Dean, A. M.; Howard, J. B.; Longwell, J. P. *J. Phys. Chem.* **1989**, *93*, 8171-80.
(8)   Kee, R. J.; Rupley, F. M.; Miller, J. A. "The Chemkin Thermodynamic Data Base," Sandia National Lab, 1990.
(9)   Pedley, J. B.; Naylor, R. O.; Kirby, S. P. *Thermodynamic Data of Organic Compounds*; Chapman and Hall: New York, 1987.
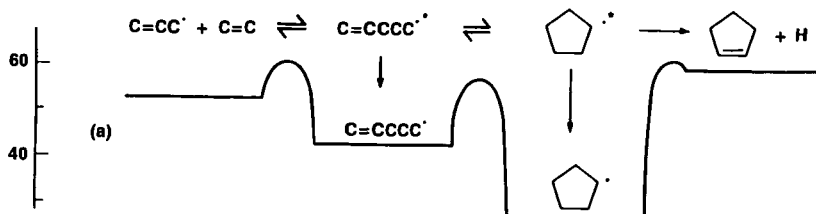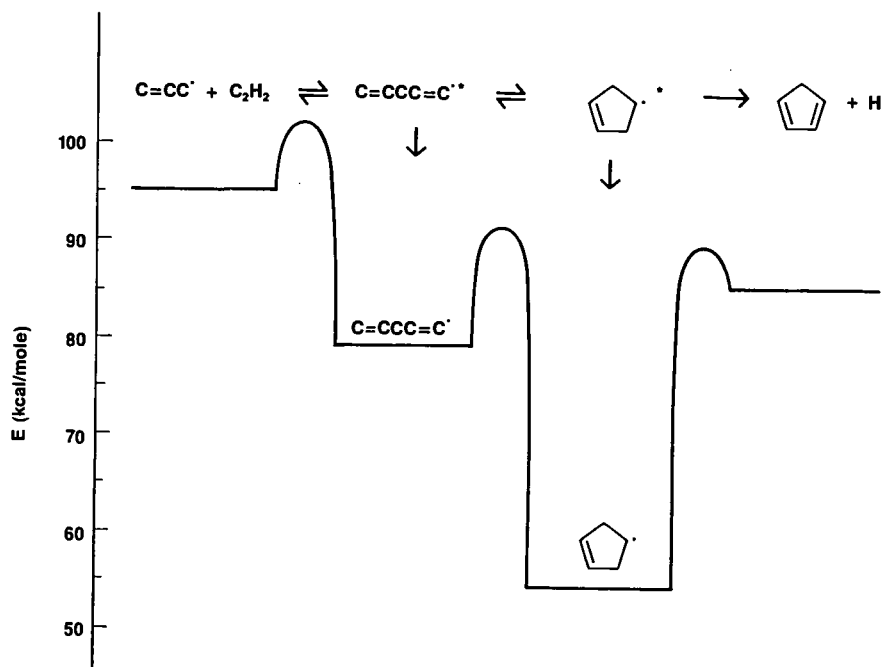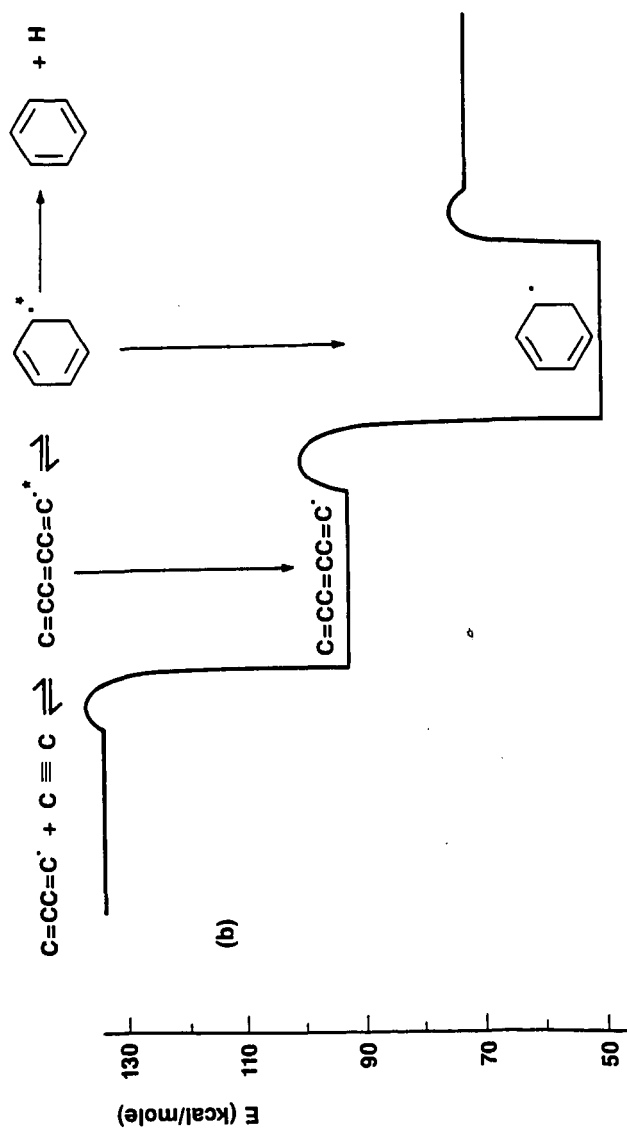
E (kcal/mole)

C=CC· + C₂H₂ ⇌ C=CCC=C·· ⇌ [cyclopentadienyl radical] · → [cyclopentadiene] + H

$C=CC^{\cdot} + C_2H_2 \rightleftharpoons C=CCC=C^{\cdot\cdot} \rightleftharpoons$

100

90

C=CCC=C·

80

70

60

50

C=CC· + C=C ⇌ C=CCCC·· ⇌ [pentadienyl] · → [cyclopentene] + H

60

(a)

C=CCCC·

40

Figure 1

1388

Figure 2

$C=CC=C^{\cdot} + C \equiv C \rightleftharpoons C=CC=CC=C^{\cdot}$

$C=CC=CC=C^{\cdot}$

$C=CC=CC=C^{\cdot}$
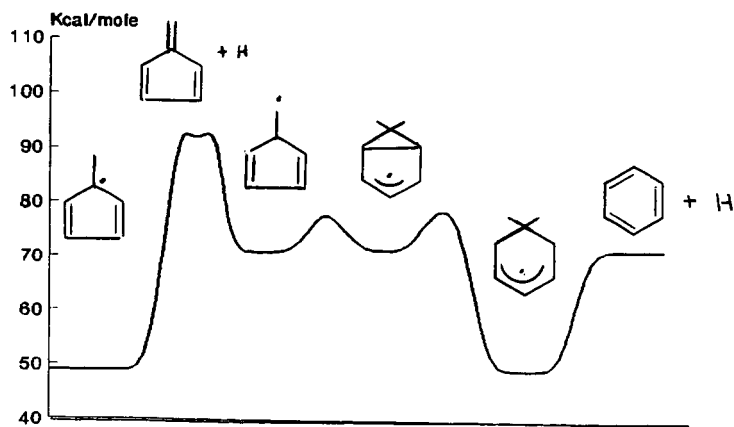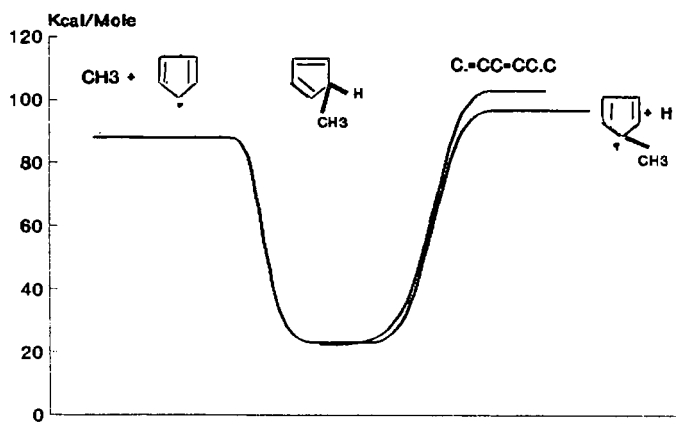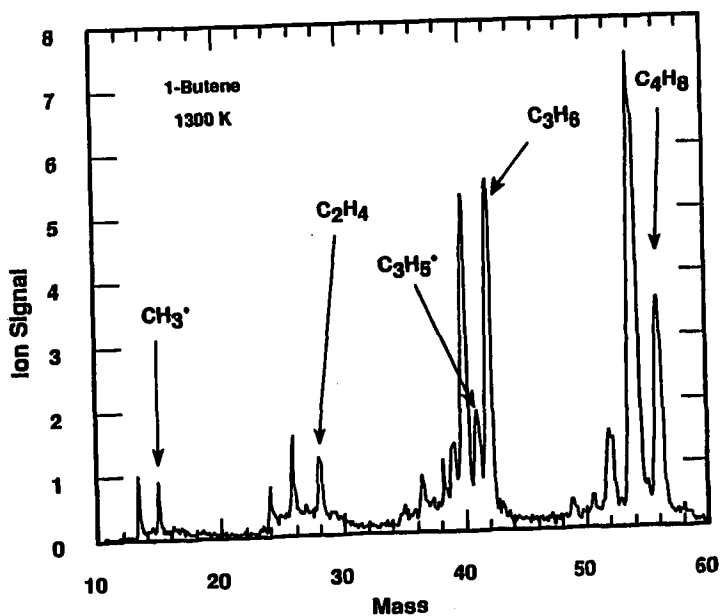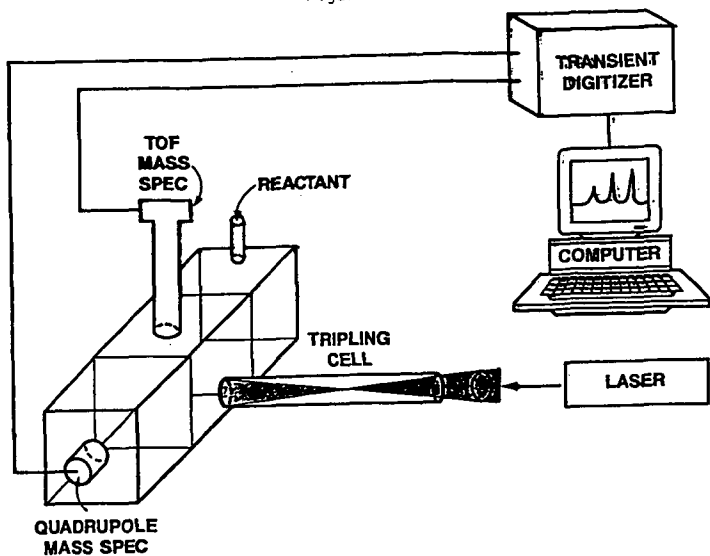
+ H

E (kcal/mole)

130
110
90
70
50

(b)

Figure 3

Figure 4

Studies on The Reactions: $C_2H+C_2H_2 \rightarrow C_4H_2+H$ **AND** $C_2H+H_2 \rightarrow C_2H_2+H$

K. Fukuda, M. Koshi, and H. Matsui*
Department of Reaction Chemistry, The University of Tokyo
7-3-1 Hongo, Bunkyo-ku, Tokyo 113, Japan

1. Introduction

Ethynyl radical (C_2H) has been recognized as an important precursor of soot formation in the pyrolysis of acetylene and is also believed to be important in the formation of intersteller molecules. The rate constants of the elementary reactions of C_2H with C_2H_2 and H_2 ,

$$C_2H_2 + C_2H \rightarrow C_4H_2 + H \qquad\qquad (1)$$

and

$$C_2H + H_2 \rightarrow C_2H_2 + H \qquad\qquad (2)$$

have been measured by several groups at room temperature, however, some disagreement among them were indicated [1]-[4], also no direct data are available at high temperature range except for those based on indirect measurement on the pyrolysis of C_2H_2[5], or from speculative simulation[6].

As the flash photolysis with intense excimer laser radiation combined with shock wave heating technique has enabled us to get direct information on the details of radical reactions at high temperature range, the processes (1) and (2) have been examined in this study. In addition, flash photolysis studies at room temperature with a mass spectrometer have been performed to ensure the temperature dependences on these reaction processes at wider temperature range. Thus, the kinetic informations derived in this work may be very useful both in the fundamentals of chemical kinetics as well as in the numerical simulations of practical combustion systems.

2. Experimental System

The details of the experimental systems were described in our previous publications[7],[8] Two independent experimental systems have been used in this study: an excimer laser photolysis behind shock waves was used to study these reaction processes at elevated temperatures (above 1000 K), where, hydrogen atoms produced in the reactions were monitored by using atomic resonance absorption spectroscopy (ARAS), and an electron impact ionization mass spectroscopy was used to measure the rate constants and examine the reaction products at room temperature.

For the high temperature experiment, a diaphragmless shock tube of 5 cm i.d. made of stainless-steel was used. Sample gases were irradiated by an ArF laser (Questek V-β, about 15 ns pulse duration) through a rectangular quartz window (4cmx1cm) located at the end plate after being heated by reflected shock waves. C_2H_2 was photodissociated by the UV laser radiation to form C_2H and H. In the high temperature experiment, time dependence of H atoms produced in the photolysis (in the range of 10^{11}-10^{12}

molecules/cm^3) were monitored by an atomic resonance spectroscopic system (ARAS) at 121.6 nm. Absolute concentration of H atoms were decided by using a calibration curve which was decided by conducting thermal decomposition experiment using H_2-N_2O-Ar mixtures. The main advantage of the diaphragmless type shock tube is its excellent reproducibility of the shock heated condition: signal averaging at a fixed shock condition, when required, and plotting first-order rate against the concentration of the reacting partner in deciding the bimolecular rate constant were performed in this study to improve the quality of the kinetic informations.

The 193 nm photolysis experiemnt at room temperature was conducted in a slowly flowing pylex tube of 1.5 cm i.d. Sample gases were directly introduced into the vacuum chamber through a pinhole of 100μm i.d. and continuously detected by an electron-impact ionization mass spectrometer (Anelva TE 600-S).The ion signals froma secondary electron multiplier operated under pulse-counting conditions were recorded with a gated counter following pulse amplification and discrimination. Time dependence of the individual mass peak was obtained by scanning the delay time of the gate with the fixed gate width of 50 or 100 μs. Signals were averaged over 10^4 laser shots for each run.

3. Experimental Results

Firstly, the reactions of C_2H produced by an ArF laser photolysis in the mixtures of C_2H_2 and C_2H_2+H_2 highly diluted in Ar were studied behind reflected shock waves.
Typical oscillogram traces for the ARAS experiment behind shock waves are shown in Fig.3. The absorption intensity at 121.6 nm incresed when shock waves passed through the observation section due to C_2H_2. With a proper delay time (typically 50 μs) after the shock wave passage, ArF laser was fired and the rapid increment of the absorption intensity was observed by the production of H atoms by the photolysis of C_2H_2: then, the intensity gradually increased to a steady state with a single-exponential profile.

The detailed mechanisms for the photodissociation of C_2H_2 by 193 nm laser has not been clarified yet. In this study, the rate of the incremnt of H atoms following the photolysis was not affected by the intensity of the ArF laser and, also the concentration of H atoms at steady state was always equal to about twice of that initially formed by the photolysis: moreover, the concentrations of the initial H atoms produced by the ArF laser photolysis was approximately proportional to the input laser energy, i.e., the ratio of (H) produced in the flash photolysis to the initial concentration of C_2H_2, (H)/(C_2H_2)$_\text{0}$ varied from about 0.15% to 1 % for the input laser powers of 10 to 60 mJ/cm^2 over the temperature range of 1000-2000 K. Thus, the multiphoton process that lead to the production of C_2+2H was concluded to be unimportant at this input energy range[9]. It was also confirmed that the rise rates of H atoms were proportional to both the initial concentration of C_2H_2 and that of added H_2, as are shown in Fig.4 and Fig.5.
Based on these experimental evidences, it was assumed that the

initial concentration of H atoms produced by the 193 nm photolysis was equal to that of $C_2H(X^2\Sigma^+)$ at the present experiment: the quenching rate of the possible electronically excited $C_2H(A^2\Pi)$ produced in the photolysis was supposed to be sufficiently fast in the time scale of the shock wave experiment. Thus, the informations on the time dependence of H atoms should be directly related to those for (1) or (2): the rate constants for these processes were evaluated from the slopes of the plot of the first order rate against initial concentrations of C_2H_2 and H_2 shown in Fig.4 and Fig.5, respectively.

The results are summarized as, $k_1 = (6.6\pm1.1)\times10^{-11}$ (cm^3 molecule^{-1} s^{-1}) over T = 1260-2487 K without appreciable temperature dependence, and $k_2 = (3.3\times10^{-10})$ exp(-13.8 kcal mol^{-1}/RT) (cm^3 molecule^{-1}s^{-1}) over T = 1565-2218 K. In order to check the sensitivity of the side reactions in these experimental conditions, numerical computations including 11 elementary reactions were performed at some typical experimental runs; no effective contribution from the side reactions was found in evaluating k_1 and k_2.

The reaction processes (1) and (2) were examined by the 193 nm photolysis also at room temperature, where the time dependent concentration of C_4H_2 was monitored by an electron-impact mass spectrometer with an electron energy of 20 eV.

For the experiment on C_2H_2-Ar mixtures, as is shown in Fig.6, when C_2H_2 was irradiated by 193 nm, the concentration of C_4H_2 (m/e =50) increased exponentially towards steady level, and the rise rate of it linearly depended on the initial concentration of C_2H_2. From the slope shown in this figure, the rate constant was decided as, $k_1 = 4.6\times10^{-11}$ (cm^3 molecule^{-1}s^{-1}) at 293 K. This value is consistent with that at high temperature range.

When sufficient amount of H_2 was added to the C_2H_2-Ar mixtures, the rise rate of C_4H_2 became too large to decide the rate constant for (2) accurately. However, the experimental conditions were chosen so that the effect of the side reactions except (1) and (2) could be neglected (as was already noted avobe), then the reaction rate constant for (2) could be decided by measuring the steady state concentration of C_4H_2, $(C_4H_2)_\infty$ with the following relation,

$$(C_2H)_0/(C_4H_2)_\infty = 1 + (k_2/k_1)(H_2)/(C_2H_2) \qquad (3)$$

where, $(C_2H)_0$ is the initial concentration of C_2H produced by the ArF photolysis. Fig.7 shows the validity of this relation. The experiment was conducted with 0.63 and 0.74 Torr partial pressure of C_2H_2 and the energy of 193 nm laser was fixed to 12 mJ/cm^2, where, the pressure of H_2 was varied from 0 to 310 mTorr: the rate constant for (2) estimated from the slope of this plot was, $k_2 = 4.83\times10^{-14}$ (cm^3 molecule^{-1}s^{-1}) at 293 K.

4. Discussion and Comparison with The Previous Results

The present results on k_1 together with the previous ones are summarized in Fig.8. The present results agree well with that by Frank and Just[5] at high temperature range and also with those by Lange and Wagner[2] and Laufer and Bass[3] at room temperature: it is not clear why only the rate constant measured by Stephens et

al.[1] who monitored the concentration of C_2H by color centered laser was about 5 times faster than the previous studies[2,3] or present result. They attributed this differnce of the rate constants to the formation of the intermediate species, however, more direct evidence may be required to support this mechanism.

The other important reaction in the initiation stage of C_2H_2 pyrolysis (2) has been studied by several groups but the rate constant of it shows substantial disagreement each other[1-4]: the reaction intermediate was discussed in order to explain the difference between the rate of reactant and products. As can be seen in Fig.9, the present result on k_2 at room temperature was smaller than the previous ones. This process is supposed to have substantial temperature dependence because of the energy barrier of the transition state.   No direct experimental data at high temperature are available, although some speculative rate constant has been used in the computer simulations[5]. The   rate constant suggested in the previous works has shown highly non-Arrhenius temperature dependence.   Our results at high temperature range has considarably large temperature dependence, thus, the extrapolation of them to the room temperature range gives much smaller rate constant than those directly measured. Such non-Arrhemius temperature dependence of the rate constant for (2) was discussed by Harding et al. based on transition state properties of C_2H estimated by ab initio calculation[10]. Although the observed activation energy in this study (13.8 kcal/mol) was much larger than that estimated in POL-CI calculation (4.0 kcal/mol), the TST theory seems consistent with the present experiment: it is suggested that the large temperature dependence of the rate constant for (2) was brought both by the temperature dependence of vibrational partition function of the transition state (high temperature range) and tunneling effect (low tempera-ture range).

References
1. J.W. Stephens, J.L. Hall, H. Solka, W.B. Yan, R.W. Curl, G.P. Glass, J. Chem. Phys., **91** 5740 (1987)
2. W. Lange and H.G. Wagner, Ber. Bunsenges. Phys. Chem., **79** 165 (1975)
3. A.H. Laufer and A.M. Bass, J. Phys. Chem., 83, 310 (1979)
4. A.M. Renlund, F. Shokoohi, H. Reisler, and C. Wittig, Chem. Phys. Lett., **84** 293 (1981)
5. P. Frank and Th. Just, Comb. Flame 38 231 (1980)
6. W. Tsang and R.F. Hampson, J. Phys. Chem. Ref. Data, 15 1087 (1986)
7. M. Koshi, M. Yoshimura, K. Fukuda, and H. Matsui, J. Chem. Phys., 93 8703 (1990)
8. M. Koshi, A. Miyoshi, and H. Matsui, Chem. Phys. Lett. (under submission)
9. T.A. Cool, P.M. Goodwin, and C.E. Otis, J. Chem. Phys., **93** 3714 (1990)
10. L.B. Harding, G.C. Schatz, and R.A. Chiles, J. Chem. Phys.,**76** 5172 (1982)
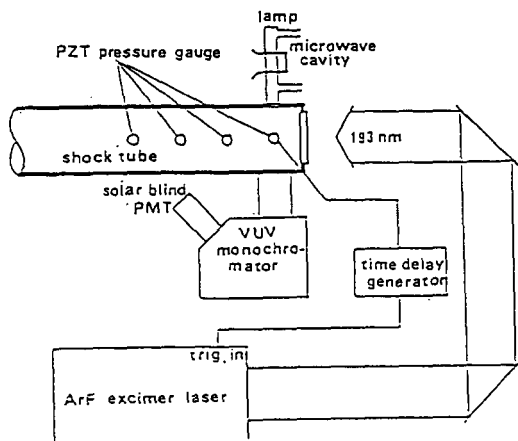
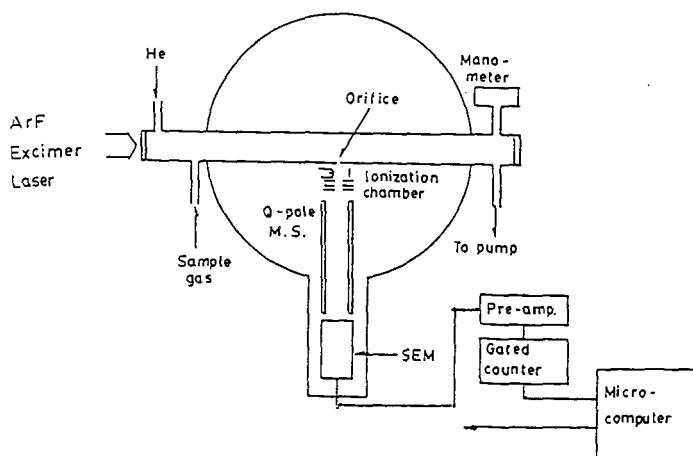Fig.1 A schematic of the shock tube – laser flash photolysis system used in the high temperature experiment

Fig.2 A schematic of the laser photolysis – mass specrometer system used in the room temperature experiment
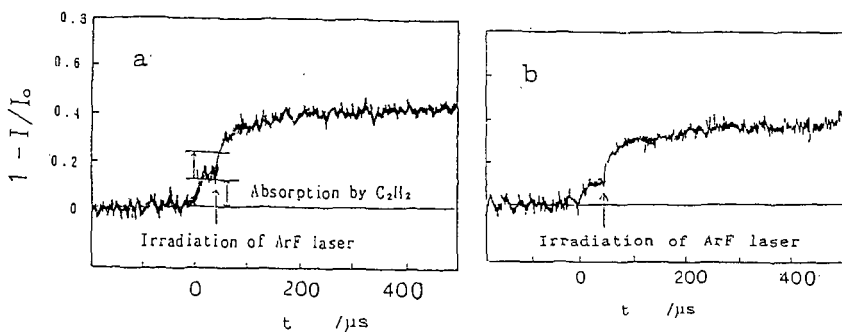
1396

Fig.3 Examples of oscillogram trace of 121.6 nm absorption
in ArF photolysis behind reflected shock waves
a: 86 ppm C_2H_2 in Ar, T = 1758 K, p = 1.92 atm.
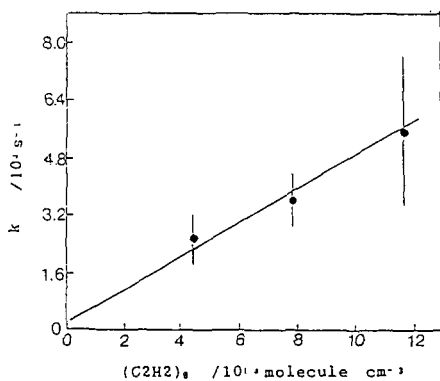b: 21 ppm C_2H_2 + 400 ppm H_2 in Ar, T = 1639 K, p = 1.33 atm.

Fig.4 Dependence of the rate
of increment of H atoms on the
initial concentration of C_2H_2
(T = 1640 ± 20 K, p_1 = 20 Torr,
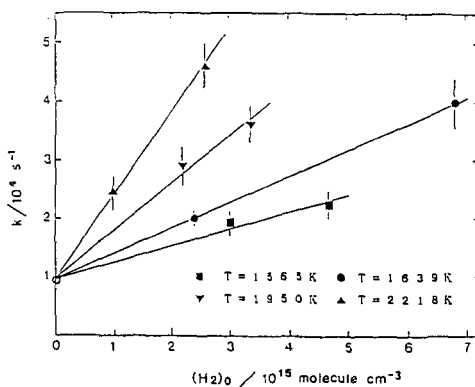30-150 ppm C_2H_2 diluted in Ar)

Fig.5 Dependence of the rate
of increment of H atoms on the
initial concentration of H_2
(21 ppm C_2H_2 +400-1100 ppm H_2
diluted in Ar, p_1 =20 Torr)

1397
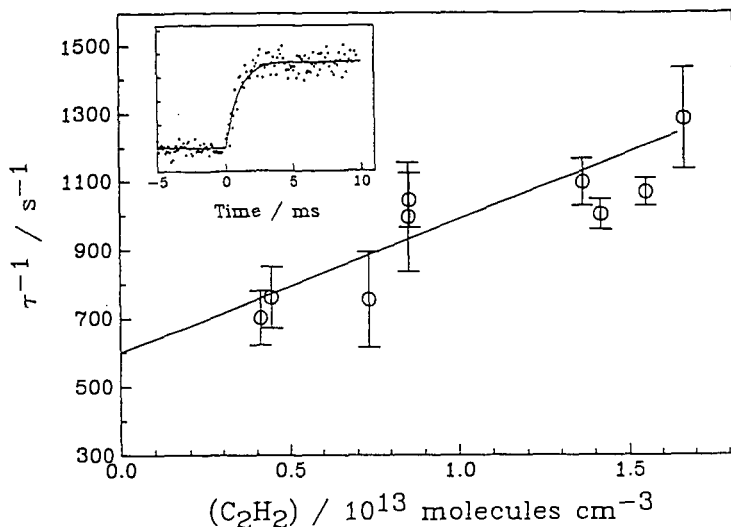
Fig.6 First order production rates of C_4H_2 as a function of C_2H_2 concentrations. A time profile shown in the figure was taken with $(C_2H_2)0=8.6 \times 10^{12}$ molecules/cm³.
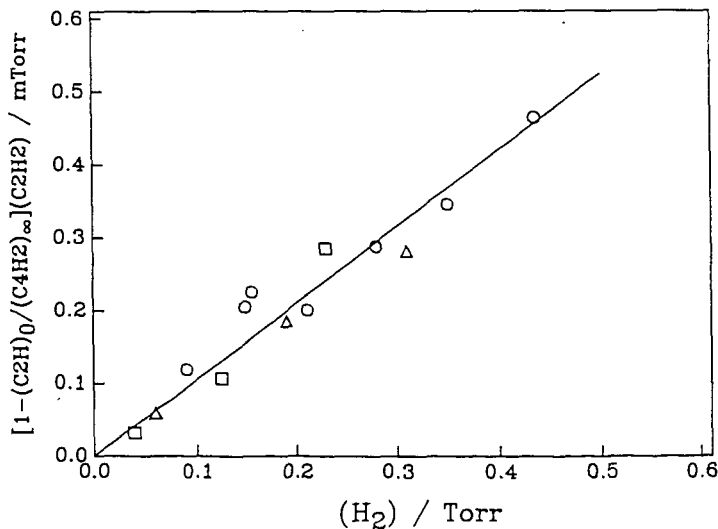
Fig.7 Plot of $[1-(C_2H)_0/(C_4H_2)_\infty](C_2H_2)$ vs (H_2). Slope of this plot is equal to k_2/k_1 (see Eq.(3)). O;$(C_2H_2)=0.24$ mTorr, □;$(C_2H_2)=0.63$ mTorr, △;$(C_2H_2)=0.74$ mTorr.
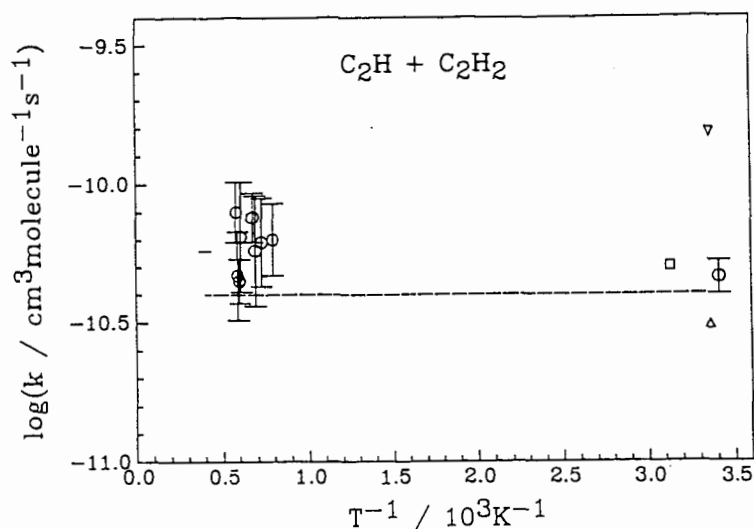
Fig.8 Arrhenius plot for the rate constant of the $C_2H+C_2H_2 \rightarrow C_4H_2+H$
reaction. Φ;This work, ∇;ref.1, $\square$;ref.2, $\triangle$;ref.3,
— ;ref.5,--;ref.6.

Fig.9 Arrhenius plot for the rate constant of the $C_2H+H_2 \rightarrow C_2H_2+H$
reaction. $\bigcirc$;This work, ∇;ref.1, $\square$;ref.2, $\triangle$;ref.3,
$\boxplus$;ref.4,--;ref.6. A solid curve is a result of TST
calculation with parameters given in ref.10.

1399

QUENCHING OF DIACETYLENE FORMATION DURING THE REACTION OF OXYGEN ATOMS WITH ACETYLENE AT 300 K
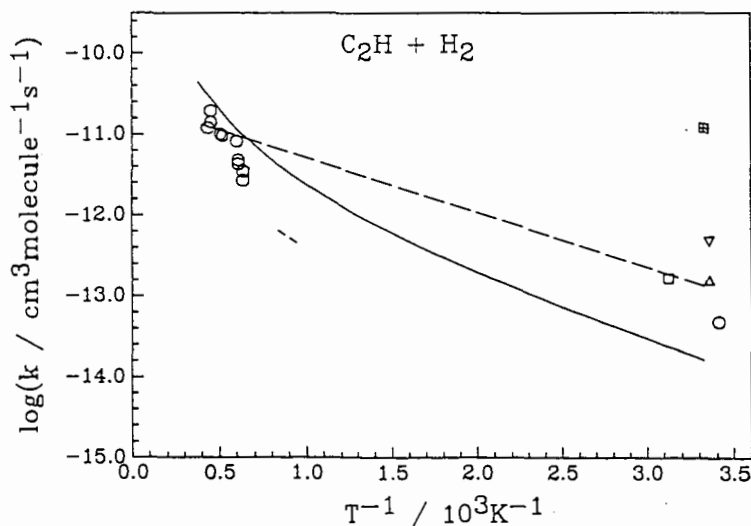
David E. Phippen and Kyle D. Bayes
Department of Chemistry and Biochemistry
University of California, Los Angeles, CA 90024-1569
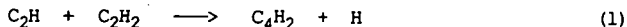
ABSTRACT

The production of diacetylene in the low pressure reaction of oxygen atoms with acetylene was monitored with a photoionization mass spectrometer. The addition of methane, nitrous oxide or molecular hydrogen quenched the formation of diacetylene. Stern-Volmer kinetics were observed, which implies that both acetylene and the quenching gas compete for a single reactive intermediate. This quenching appears to be closely connected with the quenching of chemi-ionization reported previously (*Chem. Phys. Lett.* **164**, 625(1989)). Quantitative comparisons of quenching rates with known rate constants suggest that $CH(X^2\pi)$ is the intermediate involved. Application of an electric field to this system had no affect on the diacetylene concentration, showing that chemi-ions are not involved in C_4H_2 formation.

INTRODUCTION

Diacetylene (C_4H_2) is an important intermediate in the combustion of acetylene and other hydrocarbons, especially for fuel-rich conditions [1-5]. As much as 35% of the acetylene consumed in a flame may pass through C_4H_2 [4]. It has been argued that diacetylene and heavier polyacetylenes are precursors of soot [1,4], although others do not support this proposal.

The atomic oxygen-acetylene system has been studied extensively and there is agreement that the mechanism of diacetylene formation is complex [6-8]. The initial rate of formation of C_4H_2 is proportional to the product of concentrations $[O][C_2H_2]$, and this rate can be accelerated by adding hydrogen atoms or inhibited by adding O_2 or H_2.

The reaction that forms diacetylene in flames has not been clearly established. The reaction usually proposed is,

$$C_2H \; + \; C_2H_2 \; \longrightarrow \; C_4H_2 \; + \; H \tag{1}$$

and this reaction is known to be fast [9]. However, a reasonable source of C_2H radicals in flames is not known. The direct abstraction, favored in the past,

$$O \; + \; C_2H_2 \; \longrightarrow \; C_2H \; + \; OH \tag{2}$$
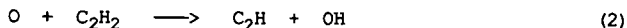
is now known to be endoergic by 30 kcal mol^{-1} [10], and thus can be ignored except for very high temperature combustion.

We have extended earlier quenching studies [11] in an attempt to clarify the mechanism by which diacetylene is formed during acetylene combustion.

EXPERIMENTS

Oxygen atoms were made by discharging a flowing mixture of 0.5% CO_2 in He in a microwave discharge (2450 MHz). Titration with NO_2 showed that the typical [O] was 3 mTorr. Acetylene, also diluted in He, and other quenching gases were added upstream of the pinhole to a photoionization mass spectrometer. The diacetylene was photoionized by Lyman α radiation (10.2 eV) and detected at mass 50. The total pressure was kept constant at 3 Torr as the quenching gases were added by varying the He flow. Further experimental details are given elsewhere [12].

RESULTS and DISCUSSION

We have observed that adding methane, nitrous oxide or molecular hydrogen to the O + C_2H_2 system quenches the formation of diacetylene. These quenching molecules are relatively inert to attack by oxygen atoms at 300 K for the short contact times (<15 ms) used in this study.

For methane and nitrous oxide the quenching followed a simple Stern-Volmer law, as can be seen in Figure 1. The quenching efficiency depends on the partial pressure of acetylene present. The original data are recorded elsewhere [12].

Simple Stern-Volmer plots suggest that both acetylene and the quencher molecule are competing for the same intermediate. If the intermediate, I, reacts with acetylene, a molecule of diacetylene is formed (not necessarily in a single step).

$$I \quad + \quad C_2H_2 \quad \longrightarrow \longrightarrow \quad C_4H_2 \qquad (3)$$

$$I \quad + \quad Q \quad \longrightarrow \quad \text{other products} \qquad (4)$$

$$I \quad \longrightarrow \quad \text{other products} \qquad (5)$$

Reaction between I and quencher molecule Q does not result in diacetylene formation. Reaction (5) is included to allow loss of I by other reactions, on the walls, etc.

If it is assumed that the addition of Q does not affect the rate of formation of I, then reactions 3, 4 and 5 lead to the steady state expression,

$$\frac{[C_4H_2]_o}{[C_4H_2]} \quad = \quad 1 \quad + \quad \frac{k_4[Q]}{k_3[C_2H_2] + k_5} \qquad (A)$$

where $[C_4H_2]_o$ refers to the diacetylene signal when no quencher gas is present. The quenching data for methane and nitrous oxide have been fit to Equation A using least squares.

If Equation A is valid, the inverse of the slopes of the Stern-Volmer plots should depend linearly on the acetylene concentration. A test of this relationship is shown in Figure 2. For this simple model, the slopes of the lines in Figure 2 then give the ratios for k_3/k_4 and the intercepts give k_5/k_4. Values for these k_3/k_4

1401

ratios are collected in Table I.

Molecular hydrogen was a less efficient quencher than methane or nitrous oxide and so more of it was necessary to give significant quenching. The resulting Stern-Volmer plots were slightly concave downward. It is not clear if this indicates that a more complex quenching mechanism is needed, or that some other effect resulting from the large concentrations of H_2 is involved. It is known that hydrogen atoms promote the formation of diacetylene [8], and it is possible that the large H_2 concentrations could result in hydrogen atoms being produced (e.g. by collisional dissociation of H_2 by $CO(a^3\pi)$, which is produced in this system [13], or by radical attack on H_2). The hydrogen quenching curves could be fit to equations of the form,

$$\frac{[C_4H_2]_0}{[C_4H_2]} = 1 + \beta[H_2] + \gamma[H_2]^2 \qquad (B)$$

By analogy to Eqn. A, the reciprocal of β was plotted against the acetylene concentration, and the resulting points are consistent with a straight line (Fig. 2). The slope of this line is entered in Table 1 under k_3/k_4 for hydrogen with the understanding that this assignment is tentative.

The second column of numbers in Table 1 gives the ratio of k_3/k_4 if the intermediate I is the ground state C_2H radical. According to the present study, the precursor to diacetylene reacts with methane only 2.7 times slower that it does with acetylene, while C_2H reacts 50 times slower. The tentative ratio for hydrogen is also not compatible with the intermediate being C_2H. Unfortunately, the rate constant for C_2H reacting with N_2O has not been measured yet. From the comparison of the first two columns of Table I, we conclude that the intermediate I is not the C_2H radical.

The CH radical has been proposed by Homann and Schweinfurth as one of the precursors leading to diacetylene [8]. The third column of Table I gives the ratios of k_3/k_4 for $CH(X^2\pi)$. In comparing the first and third columns of Table I, better agreement is seen, although the values for hydrogen still differ significantly.

A more impressive comparison can be made between the quenching of chemi-ionization reported previously for this system [11] and the quenching of diacetylene. The fraction of the chemi-ionization that can be quenched follows a Stern-Volmer law, and a plot of the reciprocal of the Stern-Volmer slopes vs. acetylene looks very similar to the present Figure 2. In particular, for methane quenching, the lines show identical slopes, i.e. identical values for k_3/k_4. Quenching by N_2O also agrees closely ($k_3/k_4 = 3.5$ for chemi-ionization quenching, compared to 4.8 in Table I). Since the quenching of the chemi-ionization almost certainly involves reaction with the $CH(X^2\pi)$ radical, this strengthens the case for CH being a precursor to diacetylene.

The similarity of quenching of chemi-ions and diacetylene raises the possibility that chemi-ions might be precursors to diacetylene. This possibility was tested in a radial electric field reactor, with a pinhole leading to the photoionization mass spectrometer. The diacetylene signals with and without an electric field (4.8 Townsend)

were carefully compared; no change in intensity could be observed (<5%). The smaller peak at mass 52 (C_4H_4) also did not change. Since this electric field will reduce the residence time of the chemi-ions by approximaetly a factor of 100, we must conclude that chemi-ions are not precursors to the observed diacetylene in this system.

In the Homann and Schweinfurth mechanism [8], the CH radical reacts with acetylene to form C_3H_2, which subsequently reacts with an oxygen atom to form C_2H. The diacetylene is then formed when C_2H reacts with another acetylene (Reaction 1). If this were the correct mechanism, then adding a quenching molecule that could react with both CH and C_2H should give Stern-Volmer plots that curve upward. The magnitude of this effect can be seen in Figure 3, where the solid curves show the expected behavior for methane quenching using known rate constants for C_2H and a linear term that fits the initial slope. The lack of curvature in the experimental points suggests that sequential quenching of two precursors is not important for this system.

If $CH(X^2\pi)$ is the radical that is being intercepted by the various quenching molecules, then it is very likely that the reaction,

$$CH(X^2\pi) \quad + \quad C_2H_2 \quad \longrightarrow \quad C_3H_2 \quad + \quad H \tag{6}$$
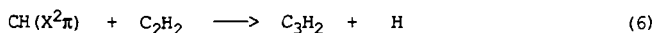
is the next step in forming diacetylene. Reaction 6 is sufficiently exoergic to form any one of the three isomers of C_3H_2. Direct sampling and trapping studies have shown evidence for C_3H_2 in flames [3,14]. However, very little is known about the kinetic behavior of any of these isomers. The mechanism leading from C_3H_2 to diacetylene can only be speculative at this time. However, it should be noted that any of the following intermediates that are known to be present in this system could donate a carbon atom to C_3H_2 to give diacetylene in an exoergic reaction: C; C_2O; CH; vinyledene; CH_2; HC_2O; or C_3H_2 itself.

CONCLUSIONS

The present quenching studies, especially the results with methane which are the most extensive, do not support C_2H as the precursor to diacetylene in the oxygen atom-acetylene system. Combining the present results with those from a previous chemi-ion quenching study suggests that $CH(X^2\pi)$ is the intermediate that is being quenched. Quenching by molecular hydrogen is anomalous and is not understood. Clearly chemi-ions do not participate in the formation of diacetylene. Kinetic studies need to be done on the C_3H_2 isomers to understand the next step in the formation of diacetylene in this system.

REFERENCES

[1] K. H. Homann and H. Gg. Wagner, *Ber. Bunsenges. Phys. Chemie* **69**, 20 (1965).
[2] J. Warnatz, H. Bockhorn, A. Moser and H. W. Wenz, *Symp. (Int.) on Combust. [Proc.], 19th,* 197 (1982).
[3] J. D. Bittner and J. B. Howard, *Symp. (Int.) on Combust. [Proc.], 19th,* 211 (1982).
[4] J. Warnatz, *Comb. Sci. Technol.* **26**, 203 (1982).
[5] H. G. Wagner and B. S. Haynes, *Prog. Energy Combust. Sci.,* **7**, 229 (1981).
[6] I. T. N. Jones and K. D. Bayes, *Symp. (Int.) on Combust. [Proc.], 14th,* 277 (1973).
[7] K. H. Homann, J. Warnatz and C. Wellmann, *Symp. (Int.) on Combust. [Proc.], 16th,* 853 (1977).
[8] K. H. Homann and H. Schweinfurth, *Ber. Bunsenges. Phys. Chemie* **85**, 569 (1981).
[9] J. W. Stephens, J. L. Hall, H. Solka, W. B. Yan, R. F. Curl and G. P. Glass, *J. Phys. Chem.* **91**, 5740 (1987).
[10] B. Ruscic and J. Berkowitz, *J. Chem. Phys.* **93**, 5586 (1990).
[11] D. E. Phippen and K. D. Bayes, *Chem. Phys. Lett.* **164**, 625 (1989).
[12] D. E. Phippen, Ph.D. thesis, University of California, Los Angeles, 1991.
[13] K. H. Becker and K. D. Bayes, *J. Chem. Phys.* **48**, 653 (1968).
[14] M. Hausmann and K. H. Homann, *Ber. Bunsenges. Phys. Chemie* **94**, 1308 (1990).

Table I: Comparison of Experimental Ratios of k_3/k_4 with Ratios of Known Rate Constants. Rate constants for C_2H were taken from [9] and from Lander *et al.* (*J. Phys. Chem.* **94**, 7759 (1990)). Rate constants for $CH(X^2\pi)$ were taken from the review by Sanders and Lim (*Chemical Kinetics of Small Organic Radicals*, Vol. 3, ed. Z. Alfassi, CRC Press, Boca Raton, 1986, p. 103). 95% confidence limits for k_3/k_4 are shown.

Quencher	Experimental k_3/k_4	If intermediate is	
		C_2H	$CH(X^2\pi)$
CH_4	2.7 ± 0.5	50	4.1
N_2O	4.8 ± 0.9	?	5.4
H_2	17 ± 7	340	>400
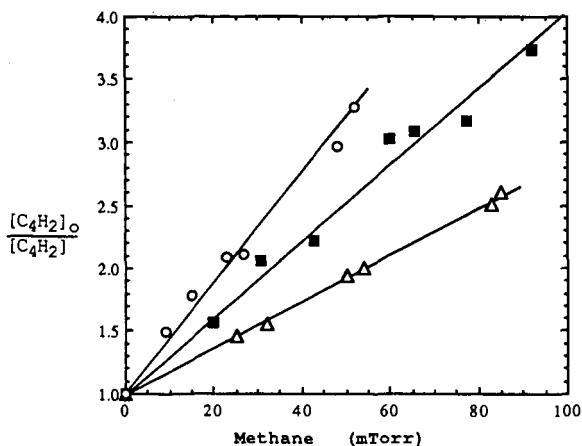
Figure 1: Stern-Volmer Plot of Diacetylene Quenching by Methane. The different symbols represent different partial pressures of acetylene: circles 3.9 mTorr; squares 8.4 mTorr; triangles 14 mTorr. All runs had [O] of 2.7 mTorr and 3 Torr total pressure. The least squares lines were forced through unity at zero methane.
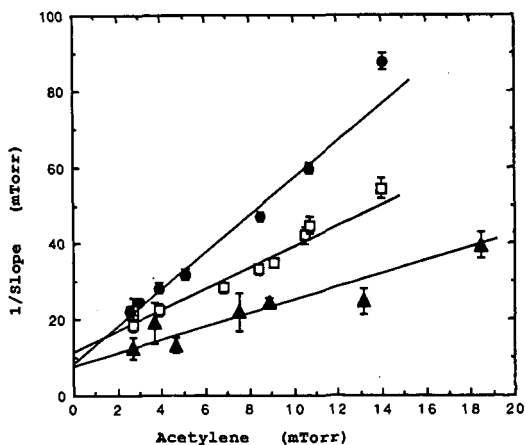
Figure 2: Reciprocal of the Stern-Volmer Slopes as a Function of Acetylene. The solid circles represent quenching by methane and the open squares quenching by nitrous oxide. For hydrogen the values of β^{-1} have been divided by 10 before being plotted. The straight lines represent weighted least squares calculations. The slopes of these lines are entered in the first column of Table I.

1405
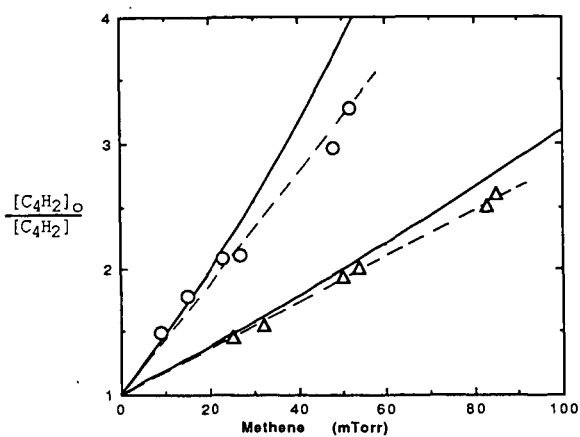
Figure 3: Comparison of Observed Quenching Data with Model
for Sequential Quenching. Data are the same as in Figure 1.

KINETICS AND THERMOCHEMISTRY OF THE OXIDATION OF UNSATURATED RADICALS: n-C$_4$H$_5$ + O$_2$

D. Gutman, I. R. Slagle, A. Bencsura, and S.-B. Xing
Department of Chemistry
Catholic University of America
Washington, DC 20064

Keywords: unsaturated radicals; C$_4$H$_5$ + O$_2$; C$_4$H$_5$ + C$_2$H$_2$

INTRODUCTION

The reactions of unsaturated free radicals (such as C$_3$H$_3$ and C$_4$H$_5$) either with themselves or with small unsaturated molecules 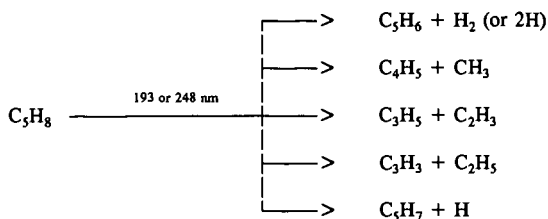have been proposed as pathways leading to the eventual formation of aromatic compounds and soot.[1] Little is known about the reactions of these intermediates. In particular, the chemistry of the butadienyl radical (C$_4$H$_5$) is almost completely unknown. In order to test the feasibility of this radical as a soot precursor, it is important to determine if molecular oxygen can compete as a radical sink for C$_4$H$_5$ in combustion systems, preventing the growth of [C$_4$H$_5$] to levels where reactions producing aromatic compounds can occur at a measurable rate. In this paper we report a direct experimental study of the kinetics and thermochemistry of the reaction of C$_4$H$_5$ with O$_2$ and use the results obtained to infer some general mechanistic pathways for the reactions of hydrogen-deficient free radicals with molecular oxygen.

EXPERIMENTAL

Apparatus and General Procedure Details of the experimental apparatus and procedures have been published elsewhere[2] and only those aspects of the method which are unique to the present study will be described in detail here. Pulsed, unfocused 193-nm or 248-nm radiation ($\approx$5 Hz) from a Lambda Physik EMG 201 MSC excimer laser was directed along the axis of a heatable, boric acid-coated quartz reactor (1.05-cm-i.d.). Gas flowing through the tube at $\approx$4 m s^{-1} contained the butadienyl radical precursor (trans-1,3-pentadiene) in small amounts, oxygen, and helium. The flowing gas was completely replaced between laser pulses. Gas was sampled through a hole (0.043-cm diameter) located at the end of a nozzle in the side of the reactor and formed into a beam by a conical skimmer before the gas entered the vacuum chamber containing the photoionization mass spectrometer (PIMS). As the gas beam traversed the ion source, a portion was photoionized using resonance lamps (10.2 and 8.9-9.1 eV) and mass selected. Temporal ion signal profiles of the reactant radical, products and the radical precursor were recorded on a multichannel scalar from a short time before each laser pulse up to 20 ms following the pulse. Data from 1000 to 45,000 repetitions of the experiment were accumulated before the data were analyzed.

Photolysis of Butadienyl Radical Precursors and the Nature of the C$_4$H$_5$ Radical A survey was conducted to determine the products of the photolysis of two possible C$_4$H$_5$ radical precursors: trans-1,3-pentadiene (expected to produce the 1-butadienyl radical) and 2-methyl-1,3-butadiene (expected to produce the 2-butadienyl radical). This survey was conducted at two photolysis wavelengths (193 and 248 nm) and two temperatures (298 and 650K). The mass spectrometric results were essentially the same at both wavelengths, with either precursor, and at either temperature. The largest ion signal detected after photolysis corresponded to the mass of C$_5$H$_6$, a stable product. Smaller signals of approximately equal amplitude were detected at the mass numbers corresponding to C$_4$H$_5$, C$_3$H$_5$, C$_3$H$_3$ and C$_5$H$_7$. These ion signals exhibited the temporal behavior of free radicals with the signals decaying in an exponential manner due to the presence of heterogeneous wall effects. Smaller amounts of CH$_3$, C$_2$H$_3$, C$_2$H$_5$, C$_3$H$_6$, and C$_4$H$_4$ were also detected. These results indicate that the important photolysis routes are

$$C_5H_8 \xrightarrow{\text{193 or 248 nm}} \begin{cases} \longrightarrow & C_5H_6 + H_2 \text{ (or 2H)} \\ \longrightarrow & C_4H_5 + CH_3 \\ \longrightarrow & C_3H_5 + C_2H_3 \\ \longrightarrow & C_3H_3 + C_2H_5 \\ \longrightarrow & C_5H_7 + H \end{cases}$$

While PIMS is a sensitive method for detecting small concentrations of free radicals (even in the presence of large concentrations of radical precursors), it cannot distinguish between structural isomers unless the ionization potentials of these isomers are extremely different. Such is not the case for the C_4H_5 isomers. However, it is likely that the initial photolysis occurs at different sites in the two C_5H_8 compounds studied here with the 1,3-pentadiene producing the 1-butadienyl radical,

$$CH_3\text{-}CH=CH\text{-}CH=CH_2 \longrightarrow \cdot CH=CH\text{-}CH=CH_2 + CH_3$$
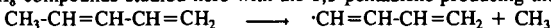
while the 2-methyl-1,3-butadiene produces the more stable 2-butadienyl radical.

$$CH_2=C(CH_3)\text{-}CH=CH_2 \longrightarrow CH_2=\dot{C}\text{-}CH=CH_2 + CH_3$$
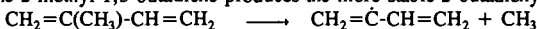
Although PIMS cannot distinguish between these two structural forms (or between a third form common to both precursors), a difference in observed reactivity can indicate the presence of two distinct isomers. At very low initial concentrations where radical-radical reactions are unimportant and in the absence of any other reactants, both possible C_4H_5 species react in a similar manner, displaying a simple exponential decay due to the presence of heterogeneous effects. However, when molecular oxygen is added to the system, there is a distinct difference in the temporal behavior of the two species. At room temperature in the presence of added oxygen the C_4H_5 produced from the pentadiene reacts slowly and decays in a purely exponential manner. On the other hand, the C_4H_5 from the methylbutadiene reacts much more rapidly with a temporal behavior that is bi-exponential (perhaps indicating the presence of two structural forms of C_4H_5 with very different reactivities). At higher temperatures in the presence of oxygen, the temporal ion signal profiles of both species exhibit bi-exponential behavior but with extremely different time constants, the C_4H_5 from the methylbutadiene always decaying much more rapidly than that from the pentadiene. On the basis of this difference in reactivity we conclude that the C_4H_5 produced from the 1,3-pentadiene is indeed the 1-butadienyl radical.

Measurement of $C_4H_5 + O_2$ Reaction Rate Parameters In the experiments reported here the 1-butadienyl radical was produced in presence of varying amounts of oxygen by the 193- or 248-nm photolysis of 1,3-pentadiene. Initial radical concentrations were chosen to be low enough to ensure that radical-radical recombination reactions, either of C_4H_5 with itself or with the other products of the photolysis, had negligible rates compared to the reaction of interest. The absence of radical-radical reactions was confirmed at each set of experimental conditions reported here by varying the initial pentadiene precursor concentration. These tests also confirmed that the reaction of C_4H_5 with C_5H_8 had a negligible rate under these conditions. Reaction rate parameters were also found to be independent of laser wavelength and intensity. These tests ensure that the 1-$C_4H_5 + O_2$ reaction was in fact isolated for direct study.

Search for Products of the $C_4H_5 + O_2$ Reaction The search for possible products of the $C_4H_5 + O_2$ reaction was hampered by the production of the additional C_5H_8 photolysis products, the low concentrations of C_4H_5 radicals necessary to avoid recombination reactions, and the high oxygen concentrations used in this study. The photolysis of pentadiene produces many radicals which are themselves possible products of the $C_4H_5 + O_2$ reaction or which react more rapidly with O_2 than C_4H_5 to produce the same possible products. For example, C_4H_4, a stable photolysis product, is also the product expected from either the direct abstraction of a hydrogen atom from C_4H_5 by O_2 or by the subsequent decomposition of a $C_4H_5O_2$ adduct. Another photolysis product, C_2H_3, reacts rapidly

1408

with O_2 to produce H_2CO while $C_3H_3 + O_2$ produces ketene at high temperatures. The $C_4H_5O_2$ adduct itself could not be detected. This was not unexpected since alkylperoxy radicals are not readily detected by PIMS. Another possible product, C_4H_4O, could not be detected because it lies at the same mass number as the precursor molecule. C_3H_4O, a product analogous to the ketene produced in the high-temperature $C_3H_3 + O_2$ reaction, was observed at 900K, but could not be confirmed as a product of the $C_4H_5 + O_2$ reaction since its temporal behavior did not mirror that of the C_4H_5 radical. There were no product signals detected that could be unambiguously assigned to the $C_4H_5 + O_2$ reaction. Since the mechanism for this reaction could not be established by direct methods, it will be assigned based on rate data and using analogies with what is known about the mechanisms of the reactions of similar unsaturated radicals.

RESULTS

From a preliminary set of experiments conducted over the temperature range of this study (295 - 900K), it was discovered that the 1-$C_4H_5 + O_2$ reaction has different mechanisms at low and high temperatures and that at intermediate temperatures (369 - 409K at the oxygen pressures used in these experiments) the equilibrium

$$C_4H_5 + O_2 (+M) \rightleftharpoons C_4H_5O_2 (+M) \tag{1}$$
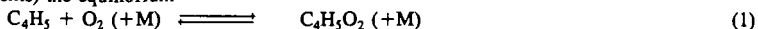
is clearly established.

The results obtained will be discussed separately for the three temperature ranges in which different kinetic behavior was observed. Rate constants were measured at three densities at room temperature and at two densities in the high temperature region. Equilibrium constants for reaction 1 were determined in the intermediate region. The conditions of all these experiments and the results obtained are given in Table I and plotted in Figures 1 and 2.

Room Temperature Reaction Near room temperature the $C_4H_5 + O_2$ reaction proceeds by simple addition

$$C_4H_5 + O_2 \longrightarrow C_4H_5O_2 \tag{1}$$
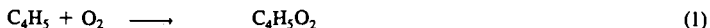
The temporal behavior of C_4H_5 in the presence of an excess of O_2 can be characterized by a simple first-order decay, with a decay constant (k') equal to the sum of $k_1[O_2]$ and k_2 where k_2 is the rate for the heterogeneous loss of C_4H_5.

$$C_4H_5 \longrightarrow \text{Heterogeneous loss} \tag{2}$$
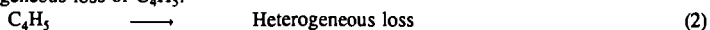
The bimolecular rate constant was obtained from the slope of the line fitted through the measured decay constants plotted against $[O_2]$. From the density dependence of this rate constant $(\Delta \log (k)/\Delta \log [M]) \approx 0.4$, it is apparent that the reaction is near the middle of the fall-off region at the densities used in this study (6-18×10^{16} molecule cm^{-3}). (See Figure 1.) The addition mechanism is inferred from this density dependence of the rate constant as well as the fact that the reaction is reversible at higher temperatures.

Intermediate Temperature Range Between 369 and 409K the loss of C_4H_5 in the presence of O_2 was not a simple exponential decay but was rather a rapid decay followed by a much slower one which is characteristic of the radical reaching an observable equilibrium with O_2, reaction 1. The second, slower decay is due to competing processes, such as the heterogeneous removal of C_4H_5 at the walls (reaction 2), other possible reactions of C_4H_5 with O_2, or other reactions of $C_4H_5O_2$ that produce products other than the original reactants. As can be seen in Table Ib, this second decay constant, m_2, increases with temperature while the wall loss rate (reaction 2) remains essentially constant. This observation indicates that a change in reaction mechanism is occurring in this temperature range. This conclusion is supported by the fact that an observable reaction of C_4H_5 with O_2 continues to occur at higher temperatures (see below), where normally equilibrium of C_4H_5 and $C_4H_5O_2$ would be established before measurable amounts of C_4H_5 had reacted with O_2.

The equilibrium constant, K_1, was obtained from the parameters of the double exponential function[3] which was fit to the experimental C_4H_5 ion signal profiles in this temperature range. The relationship between K_1 and these parameters is determined by the mechanism responsible for the temporal behavior of the C_4H_5. From the presence of a high temperature reaction and by analogy with reactions of other radicals, such as ethyl and propargyl, which exhibit similar behavior, we

conclude that the $C_4H_5 + O_2$ mechanism involves three steps: reversible addition (reaction 1), heterogeneous loss of C_4H_5 (reaction 2) and the unimolecular decomposition of the $C_4H_5O_2$ adduct.

$$C_4H_5O_2 \longrightarrow \text{Products} \tag{3}$$

Thermodynamic functions for reaction 1 were obtained from the temperature dependence of K_1^2. The values of ΔH°_{298} and ΔS°_{298} were determined from the slope and the intercept of the straight line fitted through the measured equilibrium constants on a modified van't Hoff plot (see Figure 2). They are

$$\Delta H^\circ_{298} = -18.7 \pm 0.8 \text{ kcal mol}^{-1}$$
$$\Delta S^\circ_{298} = -29.8 \pm 2.2 \text{ cal mol}^{-1} \text{ K}^{-1}$$

The correction to the ordinate variable, $\ln K_p$, on the modified van't Hoff plot (which converts $-\Delta G^\circ_T/RT$ to $-\Delta G^\circ_{298}/RT$) is small (0.7 to 2%) and is obtained from heat capacities estimated by using group-additivity rules.

High Temperature Reaction (600 - 900K) Above the temperature at which equilibrium can be observed, C_4H_5 continues to react with O_2. Radical decay profiles in this temperature region are again simple exponential functions and the decay constants (k') are proportional to $[O_2]$. The phenomenological bimolecular rate constants are independent of a factor of two in density (6 - 12×10^{16} molecule cm^{-3}) and increase with temperature in this regime (see Figure 1). The bimolecular rate constants for the overall reaction

$$C_4H_5 + O_2 \longrightarrow \text{Products} \tag{4}$$

were obtained in the same manner as for the low temperature reaction, i.e., from the slope of the line fitted through the measured first order decay constants plotted against $[O_2]$, and were fit to an Arrhenius expression

$$k_4 = 6.9\times10^{-14} \exp(-2.5 \text{ kcal mol}^{-1}/RT) \text{ cm}^3 \text{ molecule}^{-1} \text{ s}^{-1}$$

In the high temperature region the bimolecular rate constant increases with temperature and has no systematic density dependence. These observations indicate the importance of an irreversible C_4H_5 + O_2 reaction path at elevated temperatures which proceeds over an energy barrier.

$C_4H_5 + C_2H_2$ Reaction An attempt was made to observe a possible reaction of C_4H_5 with acetylene at 950K, a reaction indicated as potentially important in the formation of aromatic compounds.[1] There was no increase in the C_4H_5 decay rate over the heterogeneous loss rate when 3×10^{15} molecule cm^{-3} of acetylene was added to the system at a density of 1.2×10^{17} molecule cm^{-3}. Since an increase of a factor of two over the heterogeneous loss could have been observed with C_2H_2 present, an upper limit for the rate constant of the $C_4H_5 + C_2H_2$ reaction at 950K could be established. It is 2×10^{-14} cm^3 molecule^{-1} s^{-1}.

DISCUSSION

The simplest mechanism for the $C_4H_5 + O_2$ reaction which can account for the observations of this study and which is consistent with our current knowledge of the mechanisms of other unsaturated free radicals with molecular oxygen is one which involves the reversible addition of O_2 to the butadienyl radical and a second, irreversible decomposition path for the $C_4H_5O_2$ adduct.

Above 500K, C_4H_5 and O_2 establish and maintain equilibrium while the second, slower, irreversible decomposition reaction of $C_4H_5O_2$ takes place. These reaction pathways account for the observed high-temperature behavior of the $C_4H_5 + O_2$ reaction, including the exponential decay of C_4H_5 when O_2 is in excess, the proportionality of the C_4H_5 decay constants with $[O_2]$, and the lack of density dependence of the overall rate constant for the loss of C_4H_5. Under these conditions there is a relationship between the phenomenological rate constant k_4 and those of the elementary reactions responsible for the loss of C_4H_5, $k_4 = K_1 k_3^\circ/2$ (k_3° is the high pressure limit unimolecular rate constant for reaction 3). Using the measured values of K_1 and k_4 an Arrhenius expression for k_3° was determined, $k_3^\circ = 3\times10^{12} \exp(-21 \text{ kcal mol}^{-1}/RT) \text{ s}^{-1}$.

The rate constant derived for the decomposition of the adduct is very similar to that obtained for the decomposition of the $C_3H_3O_2$ adduct formed in the reaction of the propargyl radical with molecular oxygen.[3] Likewise, the R-O_2 bond strength when R is C_4H_5 is nearly identical with that when R is either C_3H_3 or C_3H_5 (see Table II). The mechanism proposed here for the $C_4H_5 + O_2$

reaction, i.e., reversible addition with a second, irreversible decomposition pathway for the RO_2 adduct, appears common to all $R + O_2$ reactions. The initial $R-O_2$ adducts are formed at rates expected for a simple combination process along an attractive potential. However, the $R-O_2$ bonds formed by the more stable unsaturated radicals are weaker (18 - 19 kcal mol^{-1}) than those formed between alkyl radicals and O_2 (32 - 38 kcal mol^{-1}). The overall reaction pathways observed and the nature of the final products are determined by the relative heights of the barriers to dissociation of the RO_2 adducts back to reactants and to rearrangement of the RO_2 adducts followed by dissociation into oxygenated products. If, as in the case of the allyl radical, the barrier to rearrangement is much greater than that to redissociation, no oxygenated products are observed and the $R + O_2$ reaction appears to "turn off" at high temperatures where the equilibrium favors the reactants. If, on the other hand, the barrier to rearrangement is only slightly higher than that to redissociation, the R/RO_2 equilibrium again favors reactants but small amounts of oxygenated products will be observed to be formed as the temperature increases. Such is the case in the C_3H_3 and C_4H_5 reactions. Finally, if the barrier to rearrangement is much less than to redissociation, the $R + O_2$ reaction appears to proceed directly to the oxygenated products as in the case of the i-C_4H_3 reaction.[4]

In conclusion, even at combustion temperatures, reactions of C_3H_3, C_3H_5, or C_4H_5 with molecular oxygen are not rapid. They do not effectively remove these intermediates from the pool of radicals. The loss mechanisms for these unsaturated radicals under combustion conditions must also include reactions with themselves to produce larger, unsaturated molecules, reactions with other free radicals (such as O and OH) and perhaps reactions with unsaturated molecules (such as acetylene or butadiene), reactions which could ultimately lead to the production of aromatic compounds.

ACKNOWLEDGEMENT

REFERENCES
1.   Westmoreland, P. R.; Dean, A. M.; Howard, J. B.; Longwell, J. P. *J. Phys. Chem.* **1989,** 93, 8171 and references therein.
2.   Slagle, I. R.; Ratajczak, E.; Heaven, M. C.; Gutman, D.; Wagner, A. F. *J. Am. Chem. Soc.* **1985,** 107, 1838.
3.   Slagle, I. R.; Gutman, D. *Twenty-First Symposium (International) on Combustion;* The Combustion Institute: Pittsburgh, PA, 1986; p 875.
4.   Slagle, I. R.; Bernhardt, J. R.; Gutman, D. *Twenty-Second Symposium (International) on Combustion*; The Combustion Institute: Pittsburgh, PA, 1988; p 953.

Table I: Conditions and Results of the Study of the $C_4H_5 + O_2$ Reaction

a) Experiments to Measure $C_4H_5 + O_2$ Rate Constants

T*, K	$10^{-16}[M]^b$, molec. cm^{-3}	$10^{-11}[C_5H_8]_o$, molec. cm^{-3}	$10^{-10}[C_4H_5]_o^c$, molec. cm^{-3}	$10^{-14}[O_2]$ Range, molec. cm^{-3}	k_2, s^{-1}	$10^{14}k_1^d$, cm^3 molec^{-1} s^{-1}
			Room Temperature Reaction			
296	6.00	7.11	3.20	1.93-13.4	37.8	23.
295	12.0	7.22	2.16	1.13-13.7	36.4	32.
299[e]	12.0	56.6	2.83	1.46-12.5	15.1	31.
296	18.0	2.69	2.64	1.10-9.52	35.9	38.
296	18.0	5.73	2.82	1.77-12.3	34.0	36.
299	18.0	1.27	1.16	1.22-9.34	31.5	38.
			High Temperature Reaction			
600[e]	6.02	7.82	3.46	60.7-216.	26.2	0.72
600[e]	12.0	28.5	11.0	17.7-172.	27.8	0.94
750[e]	6.02	50.1	8.94	29.7-188.	18.3	1.2
750[e]	12.0	20.0	9.00	60.7-215.	29.3	1.1
900[e]	6.07	18.0	7.65	12.8-256.	26.7	1.8
900[e]	12.1	6.55	11.1	54.7-237.	26.6	1.6

b) Experiments to Measure the Equilibrium Constant for the $C_4H_5 + O_2$ Reaction[f]

T*, K	$10^{-11}[C_5H_8]_o$, molec. cm^{-3}	10^5P_{O2}, atm^{-1}	k_2, s^{-1}	R_{12}	m_1, s^{-1}	m_2, s^{-1}	$10^{-3}K_{eq}^g$, atm^{-1}
369	7.81	5.54	23.5	1.58	309.	34.0	32.2
369	7.82	9.37	19.0	2.70	318.	29.9	31.9
374	6.78	7.73	27.0	1.97	345.	33.2	27.0
374	6.78	6.62	22.4	1.47	333.	34.9	25.4
379	7.85	10.1	21.7	1.47	374.	38.9	17.2
379	11.7	23.7	23.1	3.86	674.	41.9	17.5
384	14.5	25.2	29.9	2.63	679.	45.0	11.1
384	15.4	44.3	28.4	4.37	833.	43.8	10.3
389	7.95	26.2	31.0	3.15	847.	54.7	13.0
389	14.9	26.2	31.4	2.64	702.	41.1	10.5
389	14.7	45.7	34.2	4.86	1193.	52.5	11.0
394[e]	107.	46.0	22.8	2.43	1215.	57.5	5.74
394	13.6	53.4	21.3	3.27	1071.	54.0	6.65
399	9.96	30.5	30.8	1.65	674.	53.4	6.06
399	9.84	56.6	26.3	2.26	892.	53.0	4.37
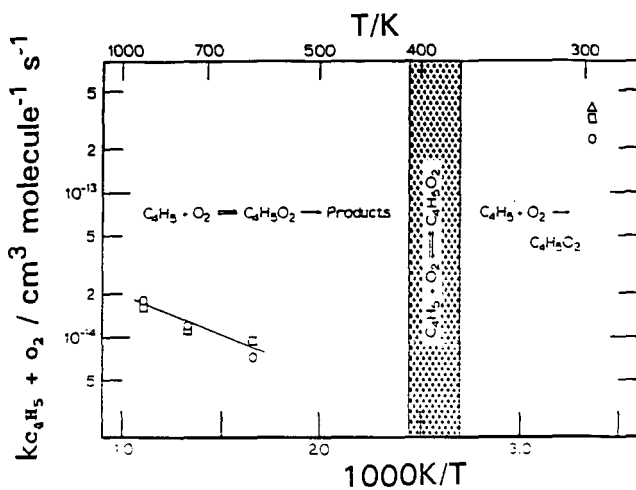
Figure 1. Arrhenius plot of measured second-order rate constants for the $C_4H_5 + O_2$ reaction. Shaded area indicates the temperature region where equilibrium was the dominant process observed. o indicates experiments conducted at a density of 6×10^{16}, □ at 1.2×10^{17}, and Δ at 1.8×10^{17} molecule cm^{-3}.
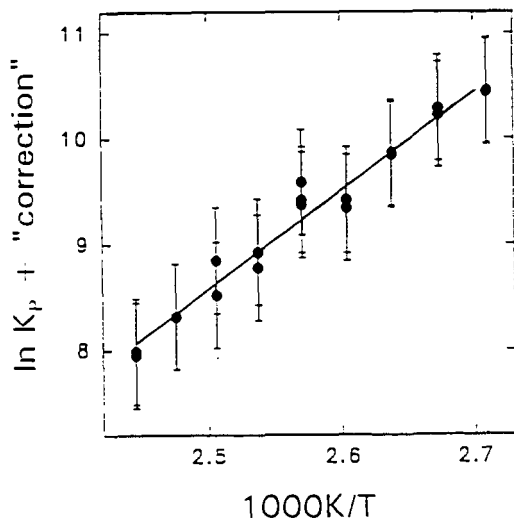

Figure 2. Modified van't Hoff plot of measured equilibrium constants for the $C_4H_5 + O_2$ reaction.

Table I (continued)

T^a, K	$10^{-11}[C_5H_8]_0$, molec. cm^{-3}	$10^5 P_{O2}$, atm^{-1}	k_2, s^{-1}	R_{12}	m_1, s^{-1}	m_2, s^{-1}	$10^{-3}K_{eq}{}^g$, atm^{-1}
404	20.2	45.6	37.8	1.39	921.	76.3	3.54
409	20.2	46.2	29.4	0.809	580.	69.3	2.42
409	12.6	57.9	29.8	1.23	1001.	74.5	2.51

[a]Temperature variations: 350-450±3K, 600±2K, 750±4K, 900±5K
[b]M = He + O_2
[c]Upper limit to $[C_4H_5]_0$ estimated assuming that one half of the precursor that decomposes produces C_4H_5.
[d]Estimated error limits are ±20% for room-temperature rate constants and ±30% for high temperature rate constants.
[e]248 nm photolysis light used in this experiment; 193 nm used in all other experiments.
[f]C_4H_5 ion signal, I(t), fit to expression $I(t) = A\exp(-m_1 t) + B\exp(-m_2 t)$. [M] = 1.2×10^{17} molecule cm^{-3}
[g]$K_p = (R_{12}/P_{O2})\{1 + [(R_{12} + 1)(m_2 - k_w)][R_{12}(m_1 - m_2)]\}^2$; R_{12} = A/B; estimated error limits: ±50%.

Table II: Comparison of Thermodynamic Variables for R + O_2 Reactions Involving Unsaturated Free Radicals

R	$\Delta H^o{}_{298}$, kcal mol^{-1}	$\Delta S^o{}_{298}$, cal mol^{-1} K^{-1}	Ref.
C_3H_3	-18.9±1.4	-31.3±2.9	3
C_3H_5	-18.2±0.5	-29.2±1.2	2
C_4H_5	-18.7±0.8	-29.2±2.2	Current Study

The Thermal Decomposition of 1,7 Octadiyne as
A Source of Propargyl Radicals

Wing Tsang and James A. Walker.
Chemical Kinetics and Thermodynamics Division
National Institute of Standards and Technology
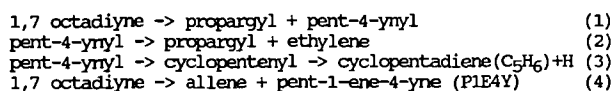Gaithersburg, Maryland 20899

ABSTRACT

Dilute concentrations of 1,7 octadiyne have been decomposed in single pulse shock tube experiments. At temperatures between 1000-1200K and pressures of 2-7 atm argon, the products are consistent with the main reaction involving the breaking of the propargylic carbon-carbon. The rate expression for bond breaking is $1.6 \times 10^{16} \exp(-35760/T)$ s^{-1}. The newly formed pent-4-ynyl radical can cyclize or decompose via beta bond cleavage to form another propargyl radical and ethylene. The ratio of rate constants for the two processes is $5.4 \times 10^{-4} \exp(6700/T)$. A parallel retroene reaction proceeds with the rate expression, $5.6 \times 10^{12} \exp(-27860/T)$ s^{-1}. The propargyl radicals recombine to form a large number of linear C_6 isomers. As the temperature is increased fulvene and benzene are among the main products. The use of 1,7 octadiyne as a thermal source of propargyl radicals for studying reactions with other reactive species will be discussed.

INTRODUCTION

Recent studies[1,2] have demonstrated the important role that propargyl radicals may play as a precursor for the formation of benzene and other C_6H_6 isomers in hydrocarbon combustion systems. Except for the work on Kern and coworkers[3] at very high temperatures, there have been no direct quantitative studies involving the reactions of propargyl radicals with other organic molecules under conditions that lead to results that can be used in combustion systems. A prerequisite for making such studies is a method for the generation of propargyl radicals in known quantities. This paper reports on the results of efforts in this direction and on the nature of the products from propargyl radical combination.

Stein et al[1] have confirmed[4] that one of the possible products of propargyl radical combination, 1,5 hexadiyne will easily rearrange through molecular processes to form fulvene and benzene. Alkemade and Homann[2] have generated propargyl radicals through reaction of propargyl bromide with sodium and reported on the formation of a variety of recombination products, 1,5 hexadiyne, 1,3 hexadien-5-yne, 1,2 hexadien-5-yne, 1,2,4,5-hexatetraene and benzene at temperatures between 623-673K. They distinguish between initial and secondary products with benzene and 1,3-hexadien-5-yne being in the latter category. To some degree these results are discordant with that of Stein et al, since one would have thought that with the low energy molecular decomposition channel for 1,5 hexadiyne, most of this compound would have been immediately converted upon recombination in the low pressure system used by Alkemade and Homann. In addition, they were not able to detect the well known characteristic products of 1,5 hexadiyne decomposition, bis-methylenecyclobutene and fulvene.

The focus of this study is 1,7 octadiyne decomposition. Previously, extensive studies[5] on the decomposition of the larger acetylenes have been carried out. The important reaction pathways were the breaking of the propargyl C-C bond and a molecular process (retro-ene reaction) leading to the production of allene and the appropriate olefin. On this basis it is expected that the mechanism for 1,7 octadiyne decomposition will be

$$1,7 \text{ octadiyne} \rightarrow \text{propargyl} + \text{pent-4-ynyl} \qquad (1)$$
$$\text{pent-4-ynyl} \rightarrow \text{propargyl} + \text{ethylene} \qquad (2)$$
$$\text{pent-4-ynyl} \rightarrow \text{cyclopentenyl} \rightarrow \text{cyclopentadiene}(C_5H_6)+H \quad (3)$$
$$1,7 \text{ octadiyne} \rightarrow \text{allene} + \text{pent-1-ene-4-yne (P1E4Y)} \qquad (4)$$

The desired reactions are (1) and (2) and it will be noted that every ethylene that is formed leads to the creation of two propargyl radicals. Reactions (3) and (4) are possible interfering processes. The consequence of (4) is not important since all that occurs is the release of two stable species into the system. Reaction (3) releases hydrogen atoms. This can lead to the formation of other radicals and to complications in the interpretation of the data. Such effects can be eliminated through the use of a chemical inhibitor. In addition, major contributions from this channel will mean that the 2 to 1 relation between propargyl and ethylene will be violated unless it is taken into consideration.

From another point of view the detection of cyclopentadiene is quite important since pent-4-ynyl is the result of the addition of propargyl to ethyene. Any products that are formed is indicative of ring closing becoming competitive with beta C-C bond cleavage leading to smaller molecular fragments. It is the competition between these two processes that is a key determinate of whether soot can be formed in any particular system.

In the course of this work experiments have also been carried out on the decomposition of 1,5 hexadiyne, 1-hexyne and 2,4 hexadiyne. All of these studies are aimed at providing confirmation for the surmise that a number of the gas chromatographic peaks that are observed arise from propargyl radical combination. This is necessary because it was not possible to identify specific compounds with these peaks.

Experiments are carried out in a single pulse shock tube. Such studies have unique capabilities for determining the stability characteristics (in the sense of unimolecular decompositions) of volatile organics at high temperatures. We have used the method for studying the thermal unimolecular decomposition processes of many organic compounds[6]. More recently, the mechanisms and rate constants for hydrogen-atom attack on unsaturated compounds[7] have been determined. For these studies, the hydrogen atoms were generated through the thermal decomposition of organic molecules in a manner similar to the generation of propargyl radicals in this study.

EXPERIMENTAL

The details of the single pulse shock tube and the experimental procedure[6] used in carrying out experiments on the thermal decomposition of organics have been described in earlier publications. Summarizing briefly, trace quantities of the organic in question, 100-1000 ppm, are decomposed by the reflected shock in the presence of large amounts of a thermally stable

chemical inhibitor such as mesitylene. Reactive radicals such as hydrogen atoms will attack the inhibitor leading to the formation of a less reactive, resonance stabilized species, 3,5 dimethylbenzyl radical. In the short time scale of shock tube experiments these can only recombine with itself and other long lived radicals and therefore can not play a role in the overall reaction. Analysis was by gas chromatography using flame ionization detection. The light gases were eluted isothermally using a 12 ft Poropak N^8 column while the heavier compounds, from C_4 on up, were eluted using a wide bore 30-meter dimethylsiloxane column in the programmed temperature mode. All products were identified on the basis of retention times of neat samples.

The experiments were carried out using the internal standard method. This eliminated the possibility of errors arising from uncertainties in the reaction temperature. The internal standard used in these experiments was the decomposition of 4-methylcyclohexene to form propene and butadiene. The rate expression for this reverse Diels-Alder reaction has previously been found to be

$$k(4\text{-methylcyclohexene->propene+butadiene})=2\times10^{15}\exp(-33400/T)\,s^{-1}$$

The use of the inhibitor makes impossible chain processes. Thus the only decomposition process must be the initial unimolecular reactions. It is expected that resonance stabilized radicals such as propargyl should not be particularly reactive with trimethylbenzene in the time scale of the experiments. Of course it can react with the benzylic type radicals that are generated in the course of the inhibition reactions. These are chain terminating processes.

DISCUSSION

The important products bearing on decomposition mechanisms for dilute quantities of 1,7 octadiyne in mesitylene and argon are listed in Table 1. It is clear that the dominating channels are the breaking of the propargylic C-H bond and the retroene reaction leading to the formation of allene and pent-1-ene-4-yne (P1E4Y). It can be seen that the concentration of the specific products formed; ethylene, cyclopentadiene, and P1E4Y is very close to the amount of the 1,7 octadiyne that is destroyed. Significant quantities of allene and propyne were also found. A large portion of the former is due to the retroene reaction. The excess quantities may be formed through a variety of other mechanisms. Note that as discussed subsequently, under certain conditions substantial quantities of propargyl radicals actually survive the heating period and it is possible that propargyl radical may undergo a variety of other unspecified reactions. Small quantities of meta-xylene was also found. This is evidence that hydrogen atoms are present in the system. Since the branching ratio for hydrogen atom attack on mesitylene have been determined, the total number of hydrogen atom released into the system can be placed on a quantitative basis. The concentrations found here are somewhat larger than that which can be accounted for by cyclopentadiene formation. However, any hydrogen atom in the system will in fact reveal its presence through the presence of meta-xylene.

In the time range where one expects C_6H_6 compounds to elute under the

present conditions a large number of peaks were detected. Unfortunately, it was not possible to obtain the neat samples that would lead directly to the identification of many of these compounds. Typical chromatograms in this elution region can be found in Figure 1. At low conversions (and temperatures) one sees the initial formation of a plethora of products. At high conversions and temperatures one notes increasingly the formation of fulvene and benzene as well as smaller quantities of other unidentified products.

An important question is whether these peaks can actually be attributed to the combination of propargyl radicals. The results of ancillary experiments with 1,5 hexadiyne, 1-hexyne and 2,4 hexadiyne are as follows. In the case of 1-hexyne, where the mechanism involve formation of the propargyl radical, many of the same peaks that were found in the decomposition of 1,7 octadiyne were also present. Unfortunately the parent hexyne-1 pick eluted at the same time as the fulvene peak. In the case of 1,5 hexadiyne the situation is similar to that found by Stein and coworkers, dimethylenecylobutene is first formed, followed by conversion into fulvene and benzene. Typical chromatograms can be found in Figure 2. It is interesting to note that in the studies with 1,7 octadiyne and 1-hexyne, 1,5 hexadiyne could barely be detected. Nevertheless the pattern of products, in these studies were very much similar to that found in the direct 1,5 hexadiyne decomposition. The obvious interepretation is that 1,5 hexadiyne is an important intermediate. The existence for this molecule of very low energy decomposition channels mean that at the high temperatures of these studies they are almost immediately converted into the stable decomposition products, fulvene and benzene. 2,4 Hexdiyne is a minor product. Its decomposition product was found to be chiefly benzene and a small quantity of fulvene. These results clearly establish that from the linear C_6H_6 isomers there must be a variety of pathways to form benzene. In the present instance benzene must be formed after various hydrogen shifts.

Quantitative results can give a better picture of the rate at which propargyl radicals are generated in this system. The analysis of this data and the determination of the appropriate rate constants and expressions follow from earlier publications. In the present case the propargyl C–C bond cleavage is monitored by the yield of ethylene and cyclopentadiene. The contribution from the molecular retro–ene reaction is determined from the yields of the pent-1-ene-4-yne (P1E4Y). The rate constants can be related to the measured yields on the basis of the following relations

$k(1) = \log(1-X*C_2H_4+cyclopentadiene/(1,7cyclooctadiyne)_i)/X*t$
$k(4) = k(1)*(P1E4Y)/C_2H_4+cyclopentadiene$

where $X = 1 + (P1E4Y)/C_2H_4+cyclopentadiene$, t is the total heating time of approximately 500 microsec. A plot of these results can be found in Figure 1. The rate expressions for the two initial processes are therefore

$$k(1)=1.6 \times 10^{16} \exp(-35760/T) \text{ s}^{-1}$$
$$\text{and} \quad k(4)=5.6 \times 10^{12} \exp(-27860/T) \text{ s}^{-1}$$

It should be noted that the reaction temperature is calculated on the basis of the propene yields from 4-methylcyclohexene decomposition and is derived from the relation $1/T = (\log k(4\text{-methylcyclohexene=propene+1,3butadiene})-$

LogA)/E, where the A and E are rate parameters for 4-methylcyclohexene decomposition decomposition given earlier.

It is interesting to compare these rate expressions with that for 1-hexyne decomposition. The rate expressions are

$$k(hexyne-1=propargy + n-propyl)=8 \times 10^{15} exp(-36300/T)s^{-1} \text{ and}$$
$$k(hexyne-1=allene+C_3H_6)=5 \times 10^{12} exp(-28400/T)s^{-1}.$$

At the reaction temperature the differences in rate constants are factors of 3.3 and 1.8 respectively. For the latter this is very close to the reaction pathway degeneracy. On the other hand for the bond breaking process the rate constant for 1,7 octadiyne decomposition is a factor of 1.7 higher than would be dictated by the two propargyl bond. From the rate expressions, it would appear that this is an activation energy effect, although this claim cannot be completely justified in terms of the uncertainties in deriving the rate expression. It appears that propargyl substitution in the beta position has a larger than expected effect on rate constants for bond cleavage. Studying octyne-1 decomposition will be very worthwhile.

The ratio of cyclopentadiene to ethylene yields a measure of the branching ratio for pent-4-ynyl decomposition. An Arrhenius plot of this ratio can be found in Figure 2. The rate expression is

$$k(3)/k(2)=5.4 \times 10^{-4} exp(6700/T)$$

In the temperature range of these experiments this is equivalent to 25% cyclization at the lowest temperatures and decreasing to 10% at the other extreme. Cyclization is thus favored at the lower temperatures and the activation energy for cyclization is about 50 kJ/mol smaller than that for beta C-C bond fission. This is a surprisingly large number since with an estimated activation energy for C-C bond fission of about 120 kJ/mol will lead to an activation energy for cyclization in the 80 kJ/mol range. It is also possible that this process is not kinetically controlled and that the ratio given above is a reflection of the equilibrium properties of the cyclic and linear radicals. Obviously further work is required. For the present purposes it is clear that optimum yields of propargyl radicals will be acheived at the highest temperatures. At 900 K cyclization and beta bond cleavage will be equally important.

With this data there is now sufficient information to deduce the temporal history of propargyl in the present system. Using a rate expression for propargyl combination similar to that for allyl[9], it was found that at lower concentrations, 200 ppm level and 2 atms pressure, a large portion of the radical remain unreacted during the entire heating period and much of the products are thus presumably formed at somewhat lower temperatures. On the other hand for the higher concentrations 1000 ppm and 7 atms. recombination is substantially completed in during the heating period. Despite this difference the chromatograms are substantially similar. In addition, recovery in the form of the C_6H_6 compounds is no more than 50% of all the propargyls that are released into the system. Here again the results appear to be independent of the concentration of radicals released into the system. The former may be a reflection of the low energy pathways available for decomposition and the formation of hot molecules from

propargyl recombination. Propargyl radicals can of course also be removed from the system by combination with 3,5 dimethylbenzyl and methyl radicals. These pathways cannot account for all the deficit.

The results are in general confirmatory of the observations of Stein et al regarding the nature of the decomposition products of 1,5 hexadiyne decomposition and that of Homann and Alkemade regarding the wide variety of linear C_6H_6 compounds that can be formed. Indeed the present results suggest many more peaks than the latter reported. It is difficult to account for the failure of Alkemade and Homann to find two of the decomposition products of 1,5 hexadiyne pyrolysis, dimethylenecyclobutene and fulvene. This is particularly serious for fulvene since it apparently is quite stable as the temperature is increased. It is possible from the reported retention times of Alkemade and Homann the 1,3 hexadiyne-5 and fulvene peaks may actually be coincident.

A system for the controlled release of propargyl radicals have now been described. The next step in this work must be studies where the propargyl radicals are allowed to react with other unsaturated compounds or radicals that may be present in high temperature reactive systems. A major problem in so far as single pulse shock tube studies are concerned is that the reaction time is very short and if truely quantitative results are to be obtained concentration of propargyl or reactants must be maintained at a sufficiently high level so that all the reactions occur during the heating period. With such a scenario, measurements of the concentration of one of the direct propargyl combination products, for example, benzene, and the product of addition or combination with another species can now be used as a means of determining relative rate constants. This can lead to a scale of propargyl reactivities and predictions regarding the quantity and distribution of the aromatic products formed in high temperature pyrolytic systems. Comparison with actual measurements will then lead to an assessment of the actual importance of propargyl radical in soot forming systems.

REFERENCES   •

1. Stein, S. E., Walker, J. A., Suryan, M. M. and Fahr, A. 23rd Symposium on Combustion, in press

2. Alkemade, U, and Homann, K. H., Zeit. Phys. Chemie Neue Folge. Bd 161, 19, 1989

3. Wu, C. H. and Kern, R. D., J. Phys. Chem., 91, 6291, 1987

4. Brown, R. F. C., "Pyrolytic Methods in Organic Chemistry",Academic Press, 1980 pg. 324

5. Tsang, W. Int. J. Chem. Kin., 10, 687, 1978

6. Tsang, W.,"Comparative Rate Single Pulse Shock Tube in the Thermal Stability of Polyatomic Molecules," Shock Tubes in Chemistry, A. Lifshitz ed., Marcel Dekker, pg. 59, 1981.

7. Cui, J. P., He, Y. Z., and Tsang, W., J. Phys. Chem, 93,724, 1989

8. Certain commercial materials and equipment are identified in this paper in order to specify adequately the experimental procedure. In no case does such identification imply recommendation of endorsement by the National Institute of Standards and Technology, nor does it imply that the material or equipment is necessarily the best available for the purpose.

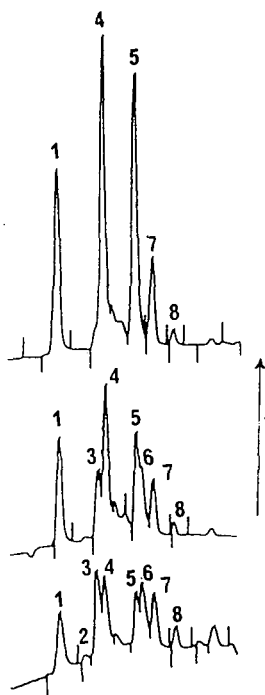9. Tulloch, J. M., MacPherson, M. T., Morgan, C. A., and Pilling, M. J., J. Phys. Chem., 86, 3812, 1982

Figure 1. Typical chromatograms in the C_6 region from 1,7 Octadiyne decomposition. Peaks 1,6-8 were not identified. (2)=1,5hexadiyne (3)= dimethylenecyclobutene (4)=fulvene (5)=benzene. Arrow points to higher temperature.
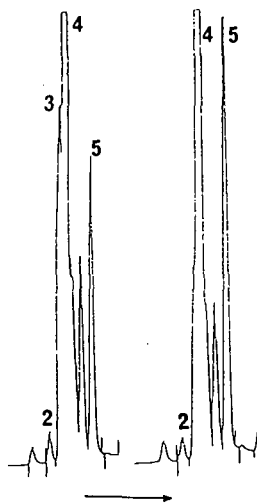
Figure 2. Typical chromatograms in the C_6 region from 1,5 hexadiyne decomposition (2)=1,5hexadiyne, (3)= dimethylenecyclobutene (4)= fulvene, (5)=benzene. Arrow points to higher temperature.

Figure 3. Arrhenius plots for the decomposition of 1,7 octadiyne. (○) propargyl C–C bond cleavage. (●) retroene reaction
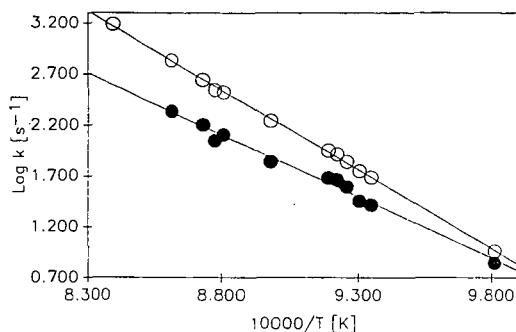

Figure 4. Arrhenius plot for the ratio of rate constants for cyclization vs beta bond cleavage during the decomposition of pent-4-ynyl
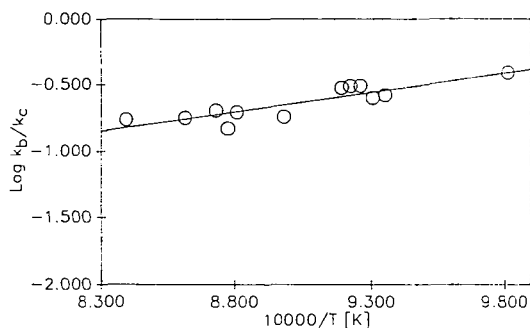
Table 1. Reactant and Product Distribution formed from 1,7 Octadiyne Decomposition in the Presence of Excesses of Mesitylene

Temp.	Pressure (atm)	C_2H_4	Allene	Propyne	P1E4Y	C_5H_6	1,7oct
				Compounds(%conversion)			

a. 200 ppm 1,7 octadiyne in 0.5% Mesitylene and Argon

Temp.	Pressure (atm)	C_2H_4	Allene	Propyne	P1E4Y	C_5H_6	1,7oct
1080	1.8	1.1	.9		.7	.2	100
1101	2.1	6.1	4.3	.6	4.1	1.5	87
1131	1.8	13.7	8.2	1.3	6.7	2.5	72
1150	1.9	21.9	11.1		10.1	4.9	52
1166	2.2	31.0	15.4	4.7	10.8	5.5	44

b. 1000 ppm 1,7 octadiyne and 1.0% Mesitylene and Argon

Temp.	Pressure (atm)	C_2H_4	Allene	Propyne	P1E4Y	C_5H_6	1,7oct
1034	1.8	.8	.8	.1	.8	.3	92
1101	2.1	6.1	4.3	.6	3.9	1.3	75
1141	6.2	17.7	10.5	3.0	8.8	3.7	65
1183	6.7	43.1	19.3	7.4	11.8	7.4	27

THE REACTIONS OF PROPARGYL CHLORIDE AND 1,5 HEXADIYNE
BEHIND REFLECTED SHOCK WAVES

R.D. Kern, K. Xie and H. Chen
Department of Chemistry
University of New Orleans
New Orleans, Louisiana 70148

INTRODUCTION

Several reports have appeared which describe the reactions of C_3H_3 and the subsequent formation of benzene. These investigations have been conducted using a variety of experimental techniques and precursor compounds to form propargyl radicals: allene,[1] 1,2 butadiene[2] (shock tube); 1,5 hexadiyne[3] (flow reactors); ethylacetylene[4] (microjet reactor); rich acetylene flames;[5,6] C_3H_3Cl or $C_3H_3Br + Na$[7] (flow reactor); allene and propyne[8] (shock tubes). Although there is general agreement that the reaction of 2 C_3H_3 ---> C_6H_6 is an efficient route to benzene, there are several C_6H_6 isomers such as bisallene, 3,4 dimethylenecyclobutene, and fulvene that have been proposed to participate in the sequence of reactions that precede benzene formation[9] and consensus is lacking on the details of the conversion.

Furthermore, reactions of C_3H_3 with allene and propyne have been proposed[1] as routes to benzene via the sequence $C_3H_3 + C_3H_4$ ---> C_6H_7 ---> $C_6H_6 + H$. The single pulse shock tube results of Hidaka et al. indicate that benzene yields are greater in the pyrolysis of allene compared to those recorded from a mixture containing an equivalent amount of propyne.[8]

There has been considerable effort expended on the allene ⇌ propyne isomerization by experimentalists and theoreticians which is described in a recent review.[10] The energetics of various intermediates involved in the isomerization such as trans-vinylmethylene, cyclopropene, and propenylidene have been calculated and the highest energy barrier, 65.8 kcal/mol, identified.[11]

The object of this work is to examine the reactions of two possible precursors for C_3H_3, propargyl chloride and 1,5 hexadiyne, and to study the reactions of C_3H_3 with itself and with allene (C_3H_4A) and propyne (C_3H_4P) with particular emphasis on the formation of benzene. This latter point is important since a correlation between benzene production and soot yield has been proposed.[12]

EXPERIMENTAL

A shock tube coupled to a time-of-flight (TOF) mass spectrometer is employed to analyze dynamically the reflected shock zone containing various mixtures of gases. The apparatus and experimental procedures have been described recently.[10] The mixture compositions and reaction conditions are listed in Table 1.

The sources of reactants are as follows: C_3H_3Cl (Aldrich, 98%); C_3H_4A (Matheson, 93%); C_3H_4P (Farchan); 1,5 C_6H_6 (Alpha); D_2 (Matheson, 99.5%); H_2 (Linde, 98.5%); Ne (Matheson, 99.999%). Ionization was achieved by 32 eV electron bombardment. The mass spectral range covers m/e 12 - 120. Peak heights were converted to concentrations using calibration plots obtained under no-reaction temperatures. The following mixtures diluted with neon were prepared for the calibration of the corresponding species: 3% C_3H_3Cl; 3% C_3H_4A; 3% C_3H_4P; 2% 1,5 C_6H_6; 3.2% C_2H_2; 2% HCl; 2% C_4H_2; 2% C_6H_6; and 3% CH_4. The mass spectral factor for C_6H_2 was obtained from previous work in which a carbon atom balance procedure was employed.[13]

RESULTS AND DISCUSSION

<u>Mixtures A, B, and C:</u> 3% C_3H_3Cl decomposes readily at temperatures above 1400 K. Major products are C_2H_2, HCl, and C_4H_2 which were observed to form at the same reaction time. The amount of HCl formed is equal to the amount of dissociation of propargyl chloride, indicating that Cl atom is balanced. However, carbon atom balance is only 60 - 80%. Concentration plots for 3% C_3H_3Cl pyrolysis at 1411 K are shown in Figures 1 - 4. Solid lines represent model calculations using the mechanism listed in Table 2. The C_3H_3Cl mass spectral cracking pattern displays a substantial peak at m/e 39 ($C_3H_3^+$). At late reaction times, m/e 39 disappears but m/e 74 remains, indicating the formation of C_6H_2.

Benzene was not recorded in the thermal decomposition of 3% C_3H_3Cl. However, upon addition of 5% H_2 (mixture B), benzene was detected. The major products distribution and the carbon balance are the same as in the decomposition of 3% C_3H_3Cl; Cl atoms are balanced. The results from 3%C_3H_3Cl - 5% D_2 (mixture D) are interesting. HCl and DCl are formed almost at the same time; the temporal HCL/DCl ratio is ~ 5. The following two parallel initation reactions are proposed to account for the experimental results:

$$C_3H_3Cl \quad \text{--->} \quad C_3H_3 + Cl \quad (17\%) \qquad (1)$$
$$\text{--->} \quad C_3H_2 + HCl \quad (83\%) \qquad (2)$$
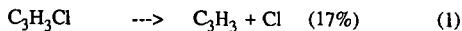
Mixtures D and E: Compared to the pyrolysis of 3% C_3H_3Cl, 1,5 hexadiyne decomposes at relatively higher temperatures. The major products are C_2H_2, C_4H_2, and C_6H_2. Carbon balance for 2% 1,5 C_6H_6 pyrolysis is 75 - 80% in the temperature range 1657 - 1800 K. Adding 5% H_2 does not change the product distribution but results in 100% carbon balance due to the increased amount of observable products. Benzene production was difficult to determine here due to the overlap of the parent molecule and benzene.

Mixtures F and G: The TOF results for a 4.3% allene mixture are published in ref. 1. We employed 3% allene or propyne mixtures here in order to maintain the same carbon atom concentrations as most other mixtures in Table 1 and to compare the respective benzene yields. 3% allene and 3% propyne mixtures were shocked at the same experimental conditions to determine if there are any kinetic differences as claimed in the single pulse shock tube work.[8] Benzene is formed in amounts of 2.3 - 3.2 x 10^{-9} mol/cm^3, about the same levels as in mixtures H and I. CH_4 is a minor product. The carbon atom balance is ~90%. The reaction profiles were modeled by the mechanism of ref. 1. Figures 5 - 8 show 3% propyne decomposition at 1770 K. Examining the C_3H_4 and the product concentrations, it is concluded that there are little or no observable differences between these two isomers at high temperatures which confirms that the isomerization reaction is faster than the decomposition.

Mixtures H and I: There are no significant differences in comparing the reaction profiles for these two mixtures. Benzene appears in amounts of 2.5 x 10^{-9} to 4.0 x 10^{-9} mol/cm^{-3} for the temperature range 1325 - 1735 K. Major products are C_2H_2, C_4H_2, HCl. Comparison of the respective profiles reveals that propargyl chloride decomposes much faster than allene or propyne. The C_3H_3Cl profile is obtained by Cl atom balancing, since its mass spectral sensitivity is low and interference from C_6H_2 at high temperatures is severe. The reaction profiles for mixtures H and I at 1458 and 1492 K are displayed in Figures 9 - 16.

The mechanism in Table 2 is composed of the previous allene mechanism[1] and reactions of propargyl chloride. Benzene appears at lower temperatures in H and I compared to F and G and is formed mainly from the overall net reaction

$$C_3H_2 + C_3H_4 \longrightarrow [2\ C_3H_3] \longrightarrow C_6H_6$$
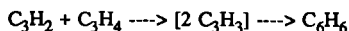
Benzene production predicted by the model is about 4 times higher than the experimental data as shown in Figures 12 and 16. The carbon atom balance for the two mixtures are about 70% at ~ 1450 K. This carbon deficiency is due to the formation of high molecular weight polyaromatic

hydrocarbons (PAH) and solid carbon; these steps are not included in our mechanism. The model describes reasonably well the observable species except for benzene. The overall reactions (3) and (4) are highly exothermic. It is likely that benzene or its isomers, some of which are highly reactive, are apparently consumed in a series of reactions leading to PAH and soot. The mechanism is tentative; extensive modeling of the experimental data is ongoing.

Mixtures J and K: C_2H_2, C_4H_2, and C_6H_2 are the detectable products. Reaction profiles and product distributions are the same as for mixtures J and K at similar reaction conditions. Carbon balance is around 70%. Information relevant to benzene formation is obscured due to the overlap of the parent peak.

CONCLUSIONS

The main decomposition channel for propargyl chloride pyrolysis is through the elimination of HCl to form C_3H_2. C_3H_2 plays an important role in producing benzene in reactions with allene or propyne. Benzene is not observed in the pyrolysis of C_3H_3Cl but it is formed readily in mixtures of C_3H_3Cl and allene or propyne.

References

1. Wu, C.H. and Kern, R.D., J. Phys. Chem., 91, (1987), 6291.
2. Kern, R.D., Singh, H.J. and Wu, C.H., Int. J. Chem. Kinet., 20, (1988), 731.
3. Stein, S.E., Walker, J.A., Suryan, M.M. and Fahr, A., 23rd Symp. (Int.) on Combustion, 1990, in press.
4. Boyle, J. and Pfefferle, L., J. Phys. Chem., 94, (1990), 3336.
5. Miller, J.A. and Melius, C.F., private communication.
6. Communal, F., Thomas, S.D. and Westmoreland, P.R., 23rd Symp. (Int.) on Combustion, 1990, poster paper P40.
7. Alkemade, V. and Homann, K.H., Z. Phys. Chem., 161, (1989), 19.
8. Hidaka, Y., Nakamura, T., Miyauchi, A., Shiraishi, T. and Kawano, H., Int. J. Chem. Kinet., 21, (1989), 643.
9. Brown, R.F.C., Pyrolytic Methods in Organic Chemistry, Vol. 41, p. 324, Academic Press, New York (1980).
10. Kern, R.D. and Xie, K., Prog. Energy Combust. Sci., 17, (1991), 191.

11. Yoshimine, M., Pacansky, J. and Honjou, N., J. Am. Chem. Soc., 111, (1989), 4198.
12. Kern, R.D., Wu, C.H., Yong, J.N., Pamidimukkala, K.M. and Singh, H.J., Energy & Fuels, 2, (1988), 454.
13. Wu, C.H., Singh, H.J. and Kern, R.D., Int. J. Chem. Kinet. 19, (1987), 975.

Table 1: Summary of Experimental Conditions

Mixture	Composition	T_5, K	P_5, atm
A	3% C_3H_3Cl	1411 - 1608	0.24 - 0.29
B	3% C_3H_3Cl - 5% H_2	1394 - 1633	0.24 - 0.31
C	3% C_3H_3Cl - 5% D_2	1364 - 1616	0.23 - 0.31
D	2% 1,5 C_6H_6	1530 - 1800	0.28 - 0.37
E	2% 1,5 C_6H_6 - 5% H_2	1367 - 1827	0.24 - 0.39
F	3% C_3H_4A	1564 - 2136	0.27 - 0.45
G	3% C_3H_4P	1549 - 2131	0.27 - 0.44
H	1.5% C_3H_3Cl - 1.5% C_3H_4A	1295 - 1698	0.20 - 0.32
I	1.5% C_3H_3Cl - 1.5% C_3H_4P	1304 - 1793	0.20 - 0.35
J	1.5% 1,5 C_6H_6 - 1.5% C_3H_4A	1316 - 1931	0.22 - 0.43
K	1.5% 1,5 C_6H_6 - 1.5% C_3H_4P	1438 - 1823	0.26 - 0.39

Table 2. Reaction Mechanism

	Reactions	A	E
1.	$C_3H_3Cl = C_3H_3 + Cl$	1.0E13	65.5
2.	$C_3H_3Cl = C_3H_2 + HCl$	5.0E13	65.5
3.	$C_3H_2 + C_3H_4A = C_6H_6$	4.0E11	0.0
4.	$C_3H_2 + C_3H_4P = C_6H_6$	4.0E11	0.0
5.	$C_3H_2 + C_3H_4A = 3\ C_2H_2$	1.7E13	15.0
6.	$C_3H_2 + C_3H_4P = 3\ C_2H_2$	1.7E13	15.0
7.	$2\ C_3H_2 = C_2H_2 + C_4H_2$	2.0E13	8.5
8.	$2\ C_3H_2 = C_6H_2 + H_2$	2.0E13	8.5
9.	$Cl + H_2 = HCl + H$	8.3E13	5.5
10.	$C_3H_4A = C_3H_4P$	2.0E13	62.0
11.	$C_3H_4A + M = C_3H_3 + H + M$	1.0E17	70.0
12.	$C_3H_4P + M = C_3H_3 + H + M$	1.0E17	70.0
13.	$C_3H_4A + H = C_2H_2 + CH_3$	2.0E13	2.4
14.	$C_3H_4P + H = C_2H_2 + CH_3$	2.0E13	2.4
15.	$C_3H_4P = C_2H + CH_3$	4.2E16	100
16.	$C_3H_4P + H = C_3H_3 + H_2$	1.0E12	1.5
17.	$C_3H_4A + H = C_3H_3 + H_2$	1.0E12	1.5
18.	$C_3H_4P + C_2H = C_3H_3 + C_2H_2$	1.0E13	0.0
19.	$C_3H_4A + C_2H = C_3H_3 + C_2H_2$	1.0E13	0.0
20.	$C_3H_4P + CH_3 = C_3H_3 + CH_4$	2.0E12	7.7
21.	$C_3H_4A + CH_3 = C_3H_3 + CH_4$	2.0E12	7.7
22.	$C_3H_3 + CH_3 = C_2H_5 + C_2H$	1.0E13	37.5
23.	$2\ CH_3 = C_2H_6$	2.0E13	0.0
24.	$C_3H_3 + CH_3 = C_4H_6$	5.0E12	0.0
25.	$C_3H_4A + C_3H_3 = C_6H_6 + H$	2.2E11	2.0
26.	$2\ C_3H_3 = C_6H_6(L)$	6.0E13	0.0
27.	$2\ C_3H_3 = C_6H_6$	3.0E11	0.0
28.	$2\ C_3H_3 = 3\ C_2H_2$	5.0E11	0.0

Units are: cm^3, mol, sec, kcal. Reactions 10 - 28 taken from ref. 1.

FIGURE 1

3% C$_3$H$_3$Cl   T = 1411 K
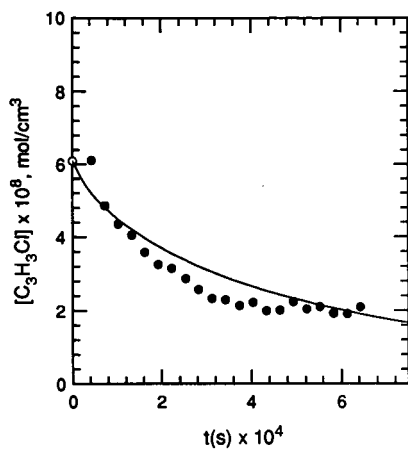
FIGURE 2

3% C$_3$H$_3$Cl   T = 1411 K
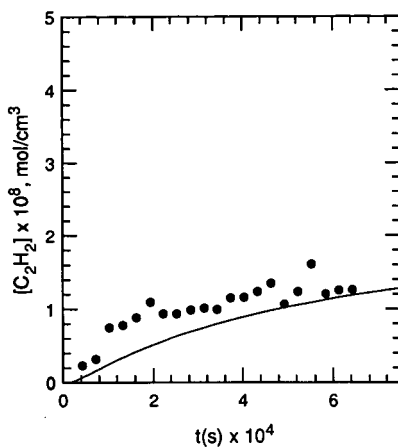
FIGURE 3

3% C$_3$H$_3$Cl   T = 1411 K
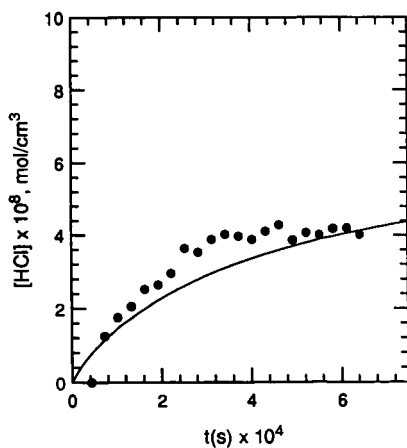
FIGURE 4

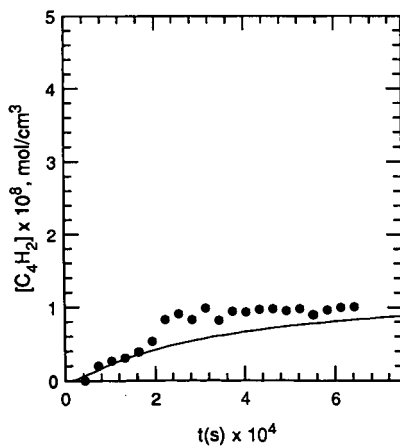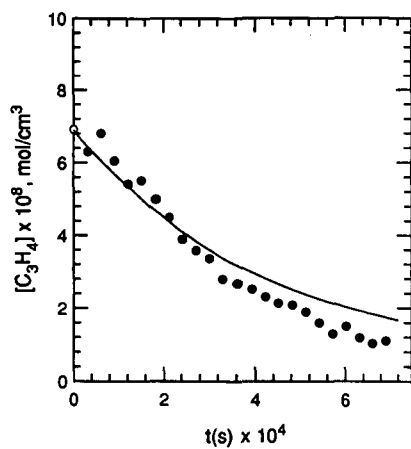3% C$_3$H$_3$Cl   T = 1411 K

1429

FIGURE 5

3% C_3H_4P T = 1770 K
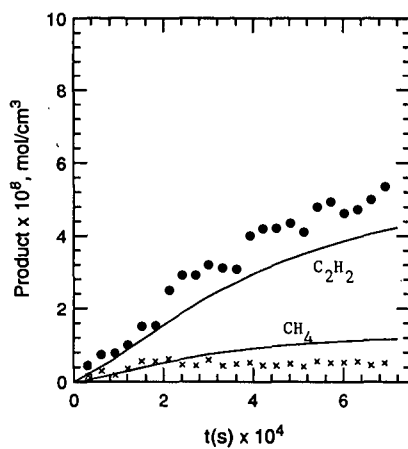

FIGURE 6

3% C_3H_4P T = 1770 K

FIGURE 7

3% C_3H_4P T = 1770 K
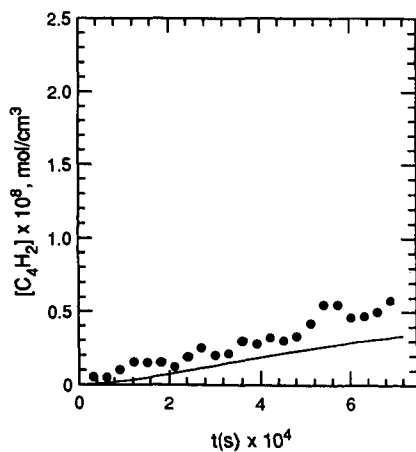
FIGURE 8

3% C_3H_4P T = 1770 K

1430
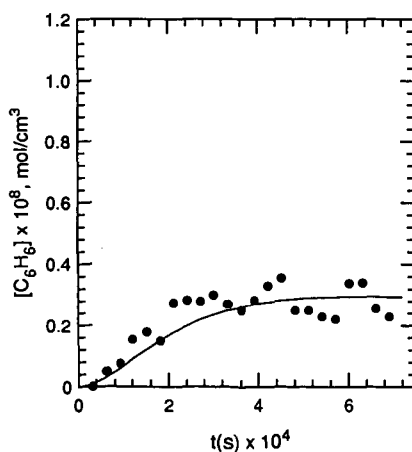
FIGURE 9

1.5% C$_3$H$_3$Cl - 1.5% C$_3$H$_3$A   T = 1458 K
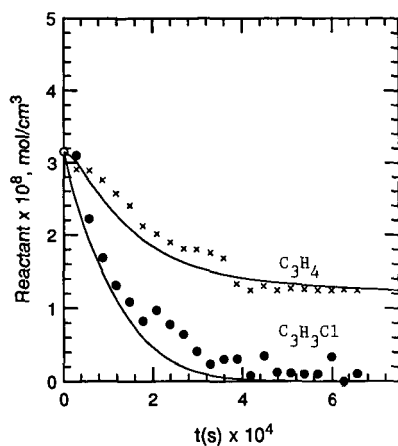
FIGURE 10

1.5% C$_3$H$_3$Cl - 1.5% C$_3$H$_4$A   T = 1458 K
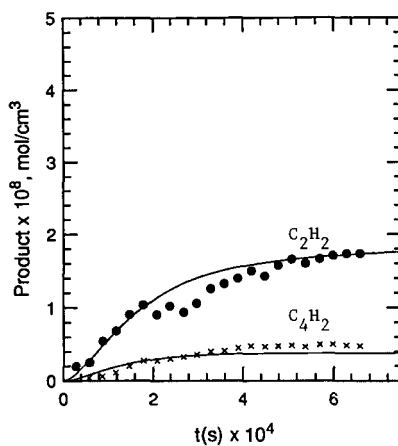
FIGURE 11

1.5% C$_3$H$_3$Cl - 1.5% C$_3$H$_4$A   T = 1458 K
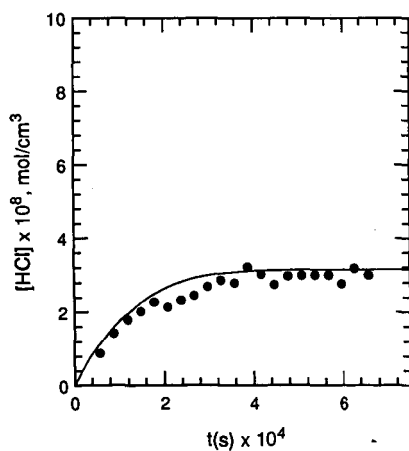
FIGURE 12

1.5% C$_3$H$_3$Cl - 1.5% C$_3$H$_4$A   T = 1458 K

1431
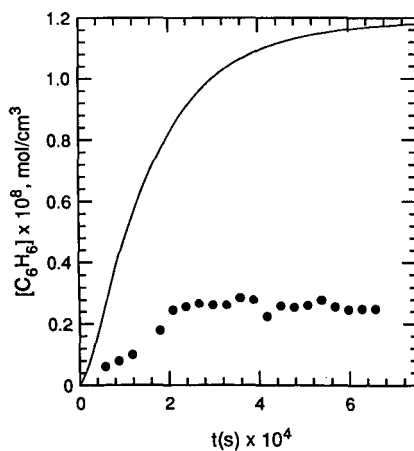
FIGURE 13

1.5% C_3H_3Cl - 1.5% C_3H_4P T = 1492 K
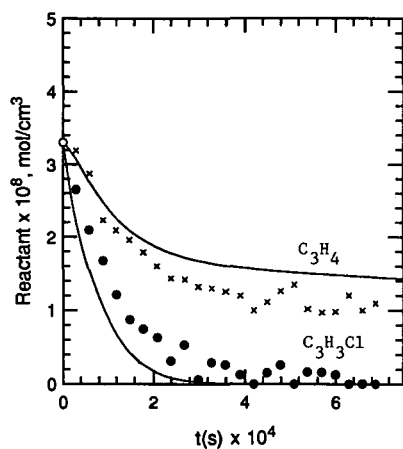
FIGURE 14

1.5% C_3H_3Cl - 1.5% C_3H_4P T = 1492 K
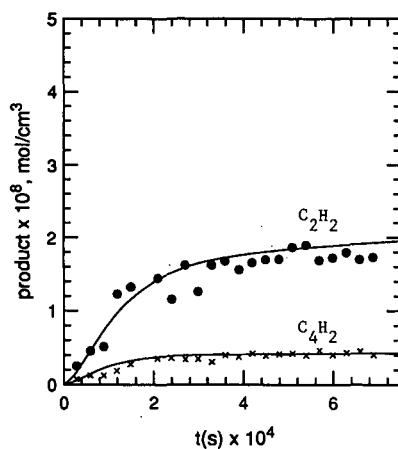
FIGURE 15

1.5% C_3H_3Cl - 1.5% C_3H_4P T = 1492 K
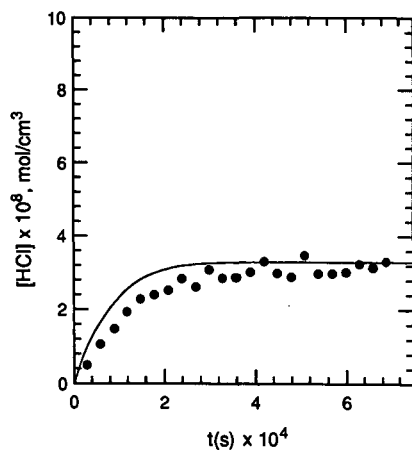
FIGURE 16

1.5% C_3H_3Cl - 1.5% C_3H_4P T = 1492 K

1432
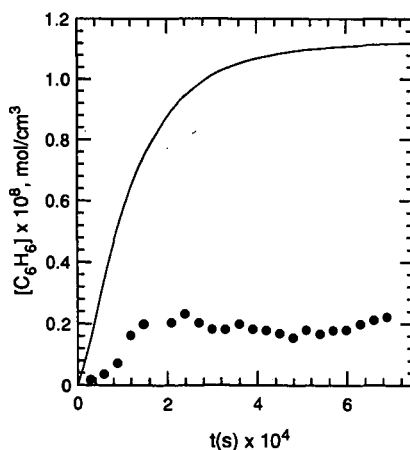
Benzene Formation during Allene Pyrolysis:
Possible Implications for Soot Formation

L. D. Pfefferle, J. Boyle, and G. Bermudez
Department of Chemical Engineering, Yale University
New Haven, CT 06520-2159YS

Introduction

Pyrolysis of allene in a microjet reactor at millisecond reaction times was used to study higher hydrocarbon growth processes from C3 hydrocarbon species. Species detection was carried out using VUV photoionization mass spectrometry. The first product observed as temperature was increased at a fixed mean residence time was mass 80 followed by smaller than parent mass pyrolysis products, mass 79 and a possible allene trimer at mass 120. A mechanism for higher hydrocarbon formation in the pyrolysis of allene is proposed . Allene dimerization to a dimethylenecyclobutane is proposed as the initial higher hydrocarbon production mechanism during allene pyrolysis and this route is examined for thermodynamic plausibility.

Background

It has become increasingly apparent in the past several years that C_3 routes for soot formation in flames can be important under some if not many conditions. In several recent studies of fuel pyrolysis and combustion where both stable and labile product measurements were made (1a,b,2), C_4/C_2 routes for benzene production were determined to be not fast enough to account for observed benzene production for some of the fuels used, especially those of C_2 and C_3 hydrocarbons. Westmoreland (1b) has recently made a reaction pathway study of C_3H_3 dimerization to benzene using a QRRK analysis and concluded that this route could in fact be fast enough to account for observed benzene production rates in several test flames including acetylene and ethylene.

Allene dimerization to dimethylenecyclobutane isomers has been observed at high conversion in several early flow reactor pyrolysis studies (e. g. 3,4). In one study (3), primarily the 1,2-dimetheyenecyclobutane isomer (1,2 DMCB) was produced at about 50% yield by passing allene over quartz chips at 800K with a 6s mean residence time. The reactor geometry used, however, did not preclude the possibility of significant surface effects on the rate of dimethylenecyclobutane production and a run with an empty tube reactor gave somewhat lower conversion but the same product distribution. In the current study, mass 80 was the first product detected and the detection of mass 120 (a possible allene trimer) at slightly higher temperatures is consistent with allene dimerization to dimethylenecyclobutane as the initial pathway for higher hydrocarbon formation. Although the DMCB isomers are likely the first mass 80 species formed, at higher temperatures (over 1300K) the predominant mass 80 component is likely hexadienes. The reaction pathways for formation of the various mass 80 isomers is the focus of our continuing modeling work. This study investigates the

1433

feasibility of the DMCB production through allene dimerization and how it can contribute to early higher hydrocarbon production during allene pyrolysis. It should be noted that from our previous work (2) methyl acetylene pyrolysis when carried out at temperatures and reaction times where isomerization to allene was not significant did not result in either significant mass 80 production or benzene production. This is consistent with mass 80 formation through allene dimerization.

Experimental Procedure

Allene pyrolysis was carried out in a microjet reactor source, described in detail earlier (5). This is a miniature fast-flow reactor coupled directly to a sonic nozzle with a volume of approximately 3.2×10^{-9} m^3. The reactor geometry consists of an alumina multibore thermocouple insulator tube inserted into a larger alumina tube with a sapphire nozzle (50-200 mm). The inner tube is positioned to leave a reaction chamber 1 mm in length. Reactants (pure allene or allene/Ar in this study) are introduced to the pyrolysis zone through the center-most hole in the inner alumina tube (0.4 mm ID) at rates varying from 0.1 - 1.0 sccm. The reaction zone is resistively heated and temperature within the reactor zone has been calibrated using thermocouples. Thermocouples were not used continuously during experiments due to the catalytic oxidation/pyrolysis observed on the platinum/rhodium wires.   Pressure within the microjet reactor was maintained at 600 ± 20 torr. Under the stated operating conditions, wall reactions were not observed to significantly affect product distributions. Significantly lowering the pressure (by a factor of >10), however, leads to greater aromatic abundance at lower temperatures.

A schematic of the VUV photoionization mass spectrometer (VUV-MS) and microjet reactor assembly is illustrated in Figure 1. The TOF-MS is equipped with Wiley-McLaren type acceleration for higher resolution and an ion reflectron to compensate for initial ion energy spread, to provide a longer effective flight length (1 meter) and to prevent the considerable quantities of neutral polymeric hydrocarbons produced from reaching the detector. Mass signals are displayed in real time and recorded directly onto a digital storage oscilloscope which is interfaced with a PC for data analysis. The mass resolution for the experiments described herein was measured as 325 at 78 amu.

VUV photons were generated by the non-linear optical mixing technique of third harmonic generation in Xe. A frequency tripled Nd:YAG laser (Quanta Ray DCR-11 system) operating at 10 Hz was focused into a Xenon cell with a 30 cm path length at 26 torr. The signal from $C_6H_6^+$ produced by single-photon ionization of C_6H_6 from a 300 K fixed flow microjet expansion was used to monitor relative UV to VUV conversion efficiency. Optimum efficiency was found at approximately 30 mJ of energy in a 8 ns pulse at 354.6 nm, corresponding to a peak power of approximately 3.75×10^6 W.

Ionization efficiencies at 118 nm are relatively constant (+/- 35%) and high for many five carbon hydrocarbons and larger, since these compounds have ionization potentials (IPs) of one to two eV below the photon energy (1182 Å =

10.49 eV). Therefore the simultaneously-obtained peak ratios are good approximations of relative concentration. However for smaller hydrocarbons with ionization potentials lying closer to the single photon energy, absorption cross sections and ionization efficiencies vary considerably. Consequently, these species must be calibrated individually. Detection efficiencies of the various molecular hydrocarbons must likewise be considered to obtain quantitative data. These calibration issues have been presented in an earlier publication (5) and are discussed in detail in the PhD thesis of J. Boyle (6).

In our detection scheme only the molecular masses are detected, and the identity of structural isomers can only be inferred from arguments of internal consistency or knowledge of kinetic mechanisms and rate constants.

Experimental Results and Discussion

An overview of the relative concentrations of higher than reactant mass hydrocarbons detected at 2ms mean reaction time is given in Table 1. As temperature was increased from 300K to 1200K at 2ms mean residence time, the first reaction product observed was mass 80 followed at slightly higher temperatures by reaction products smaller than the parent mass such as ethylene. Flow reactor results also indicate methane and hydrogen in significant quantities, although those products were not directly measured in this study due to their high ionization potentials (methane was indirectly measurable through its fragmentation product methyl radical). At 1320K mass 79 was detected above ppm levels and was observed to reach significant steady state concentrations prior to the appearance of mass 78. Benson and Shaw (7a,b) studied the pyrolysis of 1,3 and 1,4-hexadiene at low pressure and temperatures from 520 - 840K. These investigators found that while benzene production from1,4-hexadiene proceeds through molecular elimination of hydrogen, the mechanism for benzene formation from 1,3- hexadiene proceeds via a chain mechanism involving hydrogen atoms, hexadienyl radicals and cyclohexenyl-3 radicals. The rate constant data reported is consistent with our mass 79 and benzene formation rates assuming our experimentally measured mass 80 concentration at 1450K contains a significant component of 1,3-hexadiene. This analysis suggests that a possible pathway for early benzene production during allene pyrolysis involves conversion of 1,2 dimethylenecyclobutane formed through allene dimerization to 1,3-cyclohexadiene as temperature is increased followed by a higher activation energy, slower conversion of cyclohexadiene to benzene through the cyclohexadienyl radical.

As temperature was increased above 1450K a broad range of hydrocarbons with 6 or more carbons were detected including mass 78, with the largest contributions initially coming from masses 91/92, 94, 106, 116-118, 120, 144 and 158. Mass 120 was possibly formed through reaction of a DMCB component of mass 80 with allene as noted in early work on the thermal polymerization of allene. Note that the mass 120 abundance decraeses somewhat with temperature above 1515K. Mass 120 and 160, which are possible allene trimers and tetramers, were not seen in ethylacetylene pyrolysis but are present at significant levels in this study. At 1450K, mass 120 was observed in the next largest abundance to masses 80 and 79. This is another indication of allene dimer formation in this system. The mechanism

1435

illustrated below was reported for allene dimer and trimer formation by Weinstein et al. who identified the structural isomers using NMR.
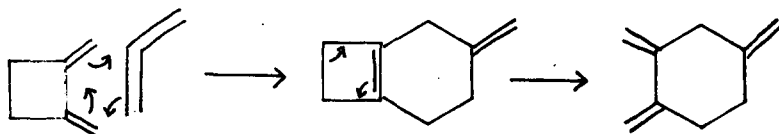
At higher temperatures and allene conversions, these species are converted through reactions with smaller hydrocarbons and hydrocarbon radicals such as C_2H. The early appearance of mass 144 suggests such a route.

Allene dimerization

Thermodynamic parameters for both 1,2 DMCB and 1,3 DMCB were estimated using the THERM program(9) and compared with experimental values where available. For 1,2 DMCB, the DH_{f298} = 47.3 kcal/mol (calculated) and 48 kcal/mol (measured) and for 1,3 DMCB, the DH_{f298} = 51 kcal/mol (calculated) and 53.3 kcal/mol (measured). These values are in good agreement (2-3kcal/mol lower) with the values calculated by Kovacevic and coworkers (10) using the maximum overlap method. These investigators also reported the experimental and calculated strain energy for 1,3 DMCB. From this data, equilibrium constants for the reactions

2Allene $\rightarrow$ 1,2 DMCB and 2Allene $\rightarrow$ 1,3 DMCB were calculated and are presented in Figure 2. The equilibrium constants for both reactions are greater than one at 1200 K. The rate of allene dimerization rate to 1,2-DMCB is pressure dependent and approximately 43.8 Kcal/mol exothermic.

Conclusion

A microjet reactor coupled to vacuum-UV photoionization was used to study the formation of higher hydrocarbons during the pyrolysis of allene. By use of this technique, a progression of intermediate species profiles including hydrocarbon radicals were obtained as a function of temperature at millisecond reaction times. Mass 80 was the first product species observed as temperature was increased which is consistent with early flow reactor studies of allene pyrolysis leading to the formation of predominantly the 1,2 isomer of dimethylenecyclobutane.

Our current work involves an analysis of a proposed mechanistic pathway for conversion allene to 1,2 dimethylenecyclobutane and subsequently to benzene and other higher hydrocarbons. A possible pathway for early benzene production during allene pyrolysis involves allene dimerization to 1,2 dimethylenecyclo-

butane followed by a multistep mechanism converting 1,2-DMCB to 1,3-hexadiene which goes through a higher activation energy, slower conversion mechanism to benzene through the cyclohexadienyl radical. A kinetic analysis using rate data for 1,3-cyclohexadiene to benzene conversion obtained by earlier investigators (7) shows that this route could account for the initial rate of mass 78 production observed experimentally. The higher hydrocarbon product distribution observed in particular the early formation of mass 120 supports the proposed allene dimerization to 1,2-DMCB. Future work will include resolution of mass 80 isomers to aid in the reaction pathway analysis. Data from earlier flow reactor studies can not be used to resolve these issues because of the intrusion of surface effects.

References

1a. Westmoreland, P. R., Dean, A. M., Howard, J. B., and Longwell, J. P., *J. Phys. Chem.* **1989**, 93, 8171-8180;   b) F. Communal, S.D. Thomas, and P.R. Westmoreland, "Kinetics of C_3 Routes to Aromatics Formation," Poster P40, 23rd International Symposium on Combustion, Orleans, July 22-27, 1990.

2. Boyle, J., and Pfefferle, L. D., "Methylacetylene and Allene Pyrolysis", presented AIChE Annual Meeting, Chicago Illinois, 12/90.

3. Blomquist, A. T., and Verdol, J. A., *J. Amer. Chem. Soc.*, **1956**, 78, 109-112.

4. Meinert, R.N., and Hurd, C. D., *J. Amer. Chem. Soc.*, **1930**, 52, 4540-4549.

5. Boyle, J., and Pfefferle, L. D., Lobue, J., and Colson, S., *Combust. Sci. and Tech.*, **1990**, 70:187-203.

6. Boyle, J. , PhD thesis, Studies of Pyrolysis and Oxidative Pyrolysis of Allene, Methyl Acetylene, Ethyl Acetylene and Butadiene using VUV Photoionization Mass spectrometry" Yale University, 1991.

7a. Benson, S. W., and Shaw R., *J. Amer. Chem. Soc.*, **1930**, 89:21,5351-4549.

8. Weinstein, B., and Fenselau, A. H., *J. Chem. Soc.* Section C:368-372 (1967).

9. Ritter, E., Bozzelli, J., THERM: Thermo Property Estimation for Radicals and Molecules, Dept. of Chemistry, New Jersey Institute of Technology.

10. Kovacevic, K., Eckert-Maksic, M., and Maksic, Z. B., *Croatica Chemica Acta*, **1974**, 46(4), 249-259.

Acknowledgements

Table 1

RELATIVE CONCENTRATIONS OF PRODUCT SPECIES DURING THE PYROLYSIS OF ALLENE 2ms, 600 Torr.

MOLECULAR WEIGHT	TEMPERATURE (K)					
	1280	1320	1450	1515	1545	1580
52	**	**	4.7	4.7	7	12
54	**	**	5.9	29	23	40
56	**	**	8.2	40	56	39
66	**	**	**	3.9	4.3	6
67	**	**	4.0	3.9	3.5	3.5
68	**	**	**	4.3	4.3	5
78		*	3.1	23	31	47.5
79		1.5	17	30	35	43.5
80	2.4	5	25	43	50.5	52
91			2.3	2	3.5	5.5
92			3.1	22	35	30
93			---	*	6	9.8
94			3.9	14	15	19.6
104			---	2.7	6.3	8.6
105				5.5	5.5	8.5
106			2.4	12.5	12	22
116				5.9	9.5	11.3
117			---	4.7	7.5	14
118				9.8	14	23
120			7.8	20.5	18	19
128					6.2	10
130					10.5	14
142				9	14.5	17
144			2.7	7	13	14.5
154					2	4
156				7	15	21
158			3.5	6.3	10.5	12
160				10	5	5
166					5	6
168						8.5
170					5	10
178					1	3
180					4.3	10

*   Species present in 0-1 unit
**   Species present in 1-2 units
Note: Only those hydrocarbon radical species with comparable concentration to the stable analog were included in this table.

Figure 1: Schematic of the VUV Photoionization Mass Spectrometer and
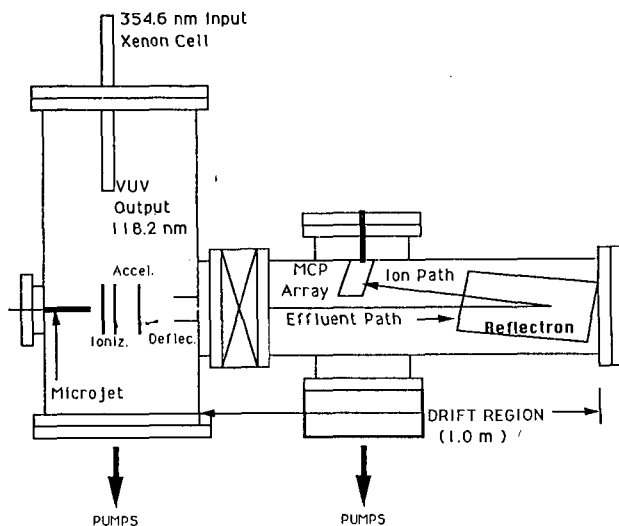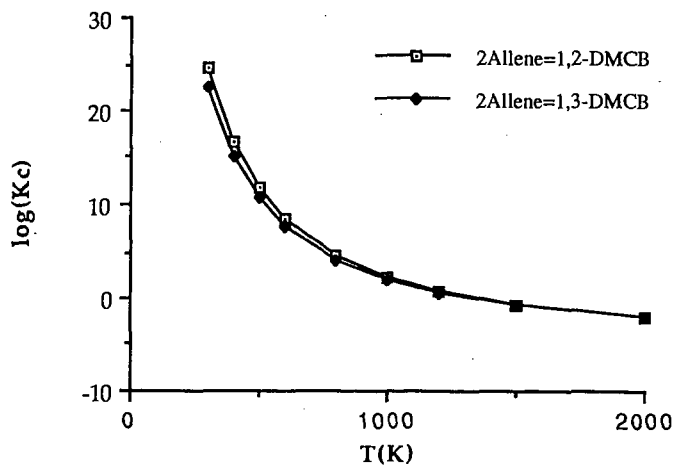Microjet Reactor Experiment

Figure 2: Equilibrium Constants for the Dimerization of Allene to the
1,2- and 1,3- Isomers of Dimethylenecyclobutane

THE FORMATION OF BENZENE
IN
FLAMES

James A. Miller and Carl F. Melius
Sandia National Laboratories
### Livermore, CA   94551-0969

Introduction

The mechanism by which aromatic compounds are formed in flames of aliphatic fuels is currently a "hot topic" in combustion. This interest stems from the importance of small aromatic compounds in the formation of PAH (polycyclic aromatic hydrocarbons) and soot (undesirable by-products) in combustion processes. The formation of the "first ring" is a key step in such processes and may well be rate limiting. The identification of the elementary reactions leading to the first aromatic compound consequently is of paramount importance.

Perhaps the two most cited reactions leading to cyclization (i.e., ring formation) are the reactions,

$$n - C_4H_5 + C_2H_2 \Leftrightarrow C_6H_6 + H$$
$$\text{and } n - C_4H_3 + C_2H_2 \Leftrightarrow C_6H_5,$$
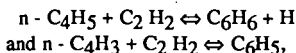
where C_6H_6 is benzene and C_6H_5 is phenyl. Unfortunately, both $n-C_4H_5$ and $n-C_4H_5$ have isomers, $i-C_4H_3$ and $i-C_4H_5$, that are more stable than they are, and distinguishing between the isomers on a mass spectrometer (the diagnostic tool in most flame experiments) is impossible. Consequently, to determine the extent to which these reactions occur in a flame requires a thorough understanding of the "pre-cyclization" chemistry. In fact, a thorough understanding of the pre-cyclization chemistry is essential in determining what the cyclization steps are in any event.

In the present paper, we review the mechanism we have proposed previously[1,2] for the formation of C_3 and C_4 hydrocarbons in rich acetylene flames. In doing this we compare the predictions of our kinetic model with the experimental results of Bastin, et al.[3] and Westmoreland,[4] in lightly sooting $C_2H_2/O_2/Ar$ flames. In addition, we discuss the implausibility of reactions (R191) and (R190) (reaction numbers refer to the table in Ref. 1) as primary cyclization steps in such flames. We show that the reaction between two propargyl radicals,

$$C_3H_3 + C_3H_3 \Leftrightarrow C_6H_5 + H \qquad \text{(RA)}$$
$$\text{or } C_3H_3 + C_3H_3 \Leftrightarrow C_6H_6, \qquad \text{(RB)}$$
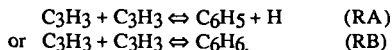
is a much better candidate for forming the first ring. This leads us to perform extensive BAC-MP4 calculations on this reation and to interpret the extensive amount of low-temperature pyrolysis data on non-aromatic C_6H_6 compounds in terms of this potential.

FLAME CALCULATIONS, CHEMICAL KINETICS, AND THERMODYNAMICS

The flame calculations discussed in this paper were performed in the same manner as described previously,[1,2] using the Sandia flame code.[5,6] Thermodynamic data come primarily from the Chemkin thermodynamic data base,[7] supplemented by BAC-MP4 results for some key

C_3 and C_4 species. These species have subsequently been added to the Chemkin data base. The reaction mechanism is the same as that described in Refs. 1 and 2. This mechanism utilizes the rate coefficient expressions given by Westmoreland for reactions (R190) and (R191).

THE FORMATION OF C_3 AND C_4 HYDROCARBONS

Even in sooting acetylene flames the dominant C_2H_2 removal step is the two - channel reaction,

$$C_2H_2 + O \Leftrightarrow HCCO + H \qquad (R100)$$
$$C_2H_2 + O \Leftrightarrow {}^3CH_2 + CO. \qquad (R99)$$
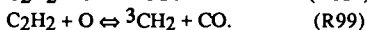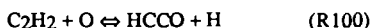
In rich flames, the ketyl formed in reaction (R100) reacts primarily with hydrogen atoms to form ${}^1CH_2$,

$$H + HCCO \Leftrightarrow {}^1CH2 + CO. \qquad (R126)$$
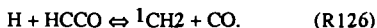
The presence of ${}^1CH_2$ in these flames has important consequences for the formation mechanism of C_3 and C_4 hydrocarbons.

Singlet methylene, ${}^1CH_2$, inserts rapidly into acetylene, forming propargyl and a hydrogen atom,

$$ {}^1CH_2 + C_2H_2 \Leftrightarrow C_3H_3 + H. \qquad (R143)$$

Reaction (R143) is the primary source of propargyl, which is principally consumed by reaction with H-atoms. Vinyl acetylene (C_4H_4) and C_4H_3 are formed by the reactions.

$$ {}^3CH_2 + C_3H_3 \Leftrightarrow C_4H_4 + H \qquad (R171)$$
$$ C_4H_4 + H \Leftrightarrow i - C_4H_3 + H_2 \qquad (184)$$
$$ \text{and } C_4H_4 + H \Leftrightarrow n - C_4H_3 + H_2 \qquad (R175)$$
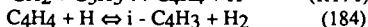
Diacetylene, C_4H_2, comes from

$$ i - C_4H_3 + H \Leftrightarrow C_4H_2 + H_2, \qquad (R182)$$

as well as the sequence

$$ OH + C_2H_2 \Leftrightarrow C_2H + H_2O \qquad (R111)$$
$$ C_2H + C_2H_2 \Leftrightarrow C_4H_2 + H. \qquad (R124)$$
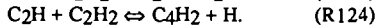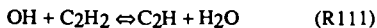
Butadiene and the butadienyl radical, C_4H_6 and C_4H_5, are formed from ${}^1CH2$ by circuitous routes through ethylene and vinyl,

$$ {}^1CH_2 + H_2O \Leftrightarrow CH_3 + OH \qquad (R141)$$
$$ \text{and } {}^1CH_2 + H_2 \Leftrightarrow CH_3 + H. \qquad (R140)$$
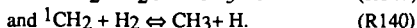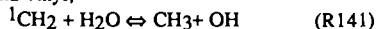
Reactions (R140) and (R141) are the most important sources of methyl in these flames. There then follows the reaction sequence leading to C_4H_6 and C_4H_5

$$ {}^3CH_2 + CH_3 \Leftrightarrow C_2H_4 + H \qquad (R95)$$
$$ C_2H_4 + H \Leftrightarrow C_2H_3 + H_2 \qquad (R92)$$
$$ C_2H_3 + C_2H_3 \Leftrightarrow i - C_4H_5 + H \qquad (R109)$$
$$ C_2H_3 + C_2H_4 \Leftrightarrow C_4H_6 + H \qquad (R208)$$
$$ \text{and } C_4H_6 + H \Leftrightarrow i - C_4H_5 + H_2 \qquad (R210)$$
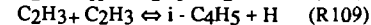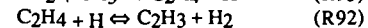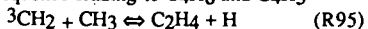
Figures 1 and 2 show comparisons of our model predictions with the experiments of Westmoreland for C_3H_3 and with those of Bastin et al. for C_4H_3 and C_4H_5. Many other comparisons are shown in Refs. 1 and 2.

FORMATION OF BENZENE

In the reaction mechanism of Ref. 1, there are only two ways to form benzene,

$$\text{n- } C_4H_3 + C_2H_2 \Leftrightarrow C_6H_5, \qquad \text{(R191)}$$

followed by phenyl either adding or abstracting a hydrogen atom, and

$$\text{n- } C_4H_5 + C_2H_2 \Leftrightarrow C_6H_6 + H. \qquad \text{(R190)}$$
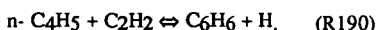
Because of the low levels of both isomers of C_4H_5 in the flame, neither (R190) nor its i-C_4H_5 counterpart is ever an effective route to benzene formation in our model. Consequently, all the benzene formed is through phenyl. In competition for phenyl with reactions that produce benzene are the oxidative paths.

$$C_6H_5 + O_2 \Leftrightarrow C_6H_5O + O \qquad \text{(R198)}$$
$$\text{and } C_6H_5 + OH \Leftrightarrow C_6H_5O + H \qquad \text{(R197)}$$

In order to be conservative about eliminating reactions as possible sources for benzene, we have in some cases added the C_6H_6 and C_6H_5O predictions to compare with the experimental benzene profiles

Figure 3 shows comparisons of model predictions with the experimental results for benzene from Bastin, et al.[3]. The basic model is unable to predict the benzene concentrations measured in the flame primarily because of the reactions,

$$\text{n - } C_4H_3 + H \Leftrightarrow \text{i - } C_4H_3 + H \qquad \text{(R177)}$$
$$\text{and } \text{n - } C_4H_5 + H \Leftrightarrow \text{i - } C_4H_5 + H \qquad \text{(R213)}$$
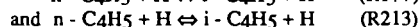
which render the n-isomers very small fractions the total radical concentrations in the flame. Even increasing k_{198} and k_{197} by a factor of ten (an unreasonable increase) does not result in sufficient benzene levels. Neither does including reactions of i - C_4H_3 and i - C_4H_5 with acetylene to form benzene. The fact that case (d) in Fig. 3 comes close to the experiment really implies that all the C_4H_3 would have to be the i-isomer to predict the benzene levels observed.

From Fig. 3 one can see that only the reactions,

$$C_3H_2 + C_3H_3 \Leftrightarrow C_6H_5$$
$$\text{and } C_3H_3 + C_3H_3 \Leftrightarrow C_6H_5 + H$$
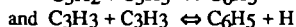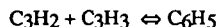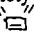
are capable of predicting the benzene levels observed in the flame. The first of these reactions, because of the high rate coefficient required and because our model overpredicts the C_3H_2 concentrations observed by Westmoreland (thus implying an even higher rate coefficient), is a less attractive candidate than the second. The second reaction, the recombination of two propargyl radicals, has been suggested as a source of benzene in shock tube experiments on the pyrolysis of allene and propyne by Kern and co-workers[8,9] and, independently and concurrently with our work, [1] has been suggested by Stein, et al. [10] as a possible source of benzene in acetylene flames.

1442

PROPARGYL RADICAL RECOMBINATION

In order to test the viability of forming an aromatic compound, i.e., either $C_6H_5 + H$ or C_6H_6, from the recombination of two propargyl radicals, we have performed an extensive set of BAC-MP4 electronic structure calculations. The results are presented in Figs.. 4 and 5. Propargyl is a resonantly stabilized radical with the two structures,
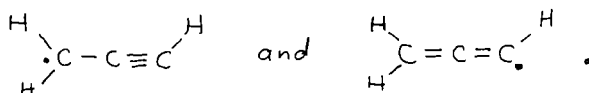
If we refer to the end of the radical with two hydrogens as the head and the end with one hydrogen as the tail, Fig. 4 shows the intermediate structures and potential energy barriers encountered in head-to-head or tail-to-tail recombination, and Fig. 5 shows those encountered in head-to-tail recombination.

Our potential is at least qualitatively consistent with a variety of low-temperature pyrolysis experiments[10] which show 3,4 - dimethylenecyclobutene and fulvene as primary products of both 1, 5 - hexadiyne ($\equiv$ $-$ $-$ $-$ $\equiv$) pyrolysis and 1,2,4,5 - hexatetraene ($=$ $=$ $-$ $=$ $=$) pyrolysis. Our one inconsistency with these experiments is the implication that there is a low energy path to benzene from 1,5 hexadiyne and 1,2,4,5 hexatetraene. We have not yet found one. The implication of these results we discussed in Ref. 1. However, we do find an energetically accessible path from $C_3H_3 + C_3H_3$ to benzene and to phenyl + H via head-to-tail recombination, as shown in Fig. 5. Thus, our calculations confirm the possibility of forming benzene in flames by a relatively fast reaction between two propargyl radicals. Such a result is also consistent with the experiments of Alkemade and Homann[11], which show a fast $C_3H_3 + C_3H_3$ rate coefficient and show benzene as a major product.

References

1. Miller, J. A. and Melius, C. F. : "Kinetic and Thermodynamic Issues in the Formation of Aromatic Compounds in Flames of Aliphatic Fuels," Combustion and Flame (submitted)

2. Miller, J. A., Volponi, J. V. , Durant, J. L., Goldsmith, J. E. M, and Kee, R. J.: "The Structure and Reaction Mechanism of Rich Non-Sooting $C_2H_2/O_2/Ar$ Flames", *Twenty-Third Symposium (International) on Combustion*, in press (1991)

3. Bastin, E., Delfau, J-L, Reuillon, M., Vovelle, C., and Warnatz, J.: *Twenty Second Symposium (International) on Combustion*, p. 313, The Combustion Institute (1989)

4. Westmoreland, P.R., Thesis Chem. Eng. Dept., M. I. T. 1986

   Westmoreland, P. R., Dean, A. M., Howard, J. B. and Longwell, J. P. : J. Phys. Chem. 93, 8171 (1989)

5. Kee, R. J., Grcar, J. F., Smooke, M. D., and Miller, J. A.: "A Fortran Program for Modeling Steady, Laminar, One-Dimensional, Premixed Flames," Sandia Technical Report SANDS85-8240, Sandia National Laboratories, Livermore, CA, December 1985

6. Grcar, J. F., Kee, R. J., Smooke, M. D., and Miller, J. A.: *Twenty-First Symposium (International) on Combustion*, p. 1773, The Combustion Institute (1987)

7. Kee, R. J., Rupley, F. M., and Miller, J. A.: "The Chemkin Thermodynamic Data Base", Sandia Technical Report SAND87-8215, Sandia National Laboratories, Livermore, CA, April 1987

8. Wu, C. H, and Kern, R. D.: J. Phys. Chem. 91, 6291, (1987)

9. Kern, R. D., Singh, H. J. and Wu, C. H.: Int. J. Chem. Kin. 20, 731 (1988)

10. Stein, S. E., Walker, J. R, Suryan, M. M., and Fahr, A.: "A New Path to Benzene in Flames," *Twenty-Third Symposium (International) on Combustion*, in press (1991) and references cited therein

11. Alkemade, U. and Homann, K. H.: J. Phys. Chem. Neue Folge 161, 19-34 (1989)
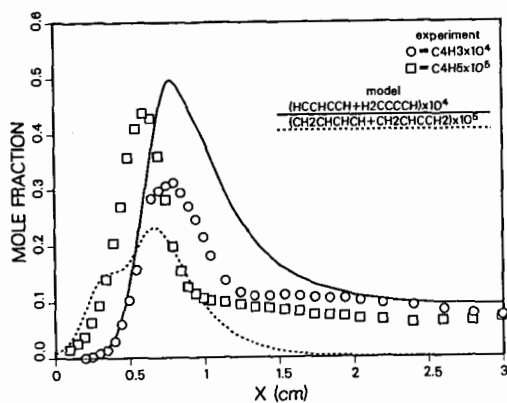
Figure 1. Comparison of model predictions with the experiments of Bastin, et al. for C_4H_3 and C_4H_5.
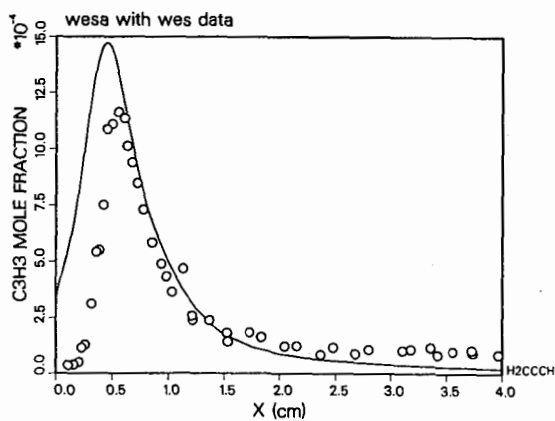
Figure 2. Comparison of model predictions with the experiments of Westmoreland for C_3H_3.
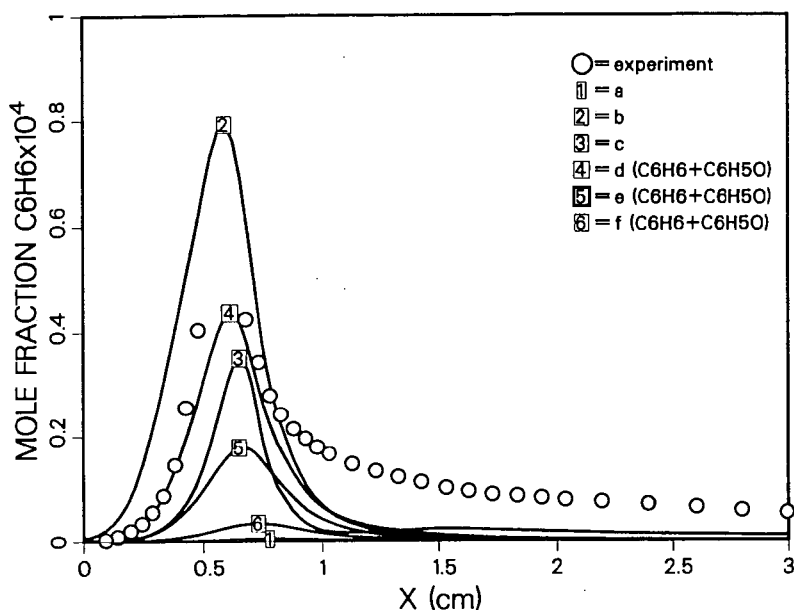
Figure 3   Comparison of model predictions with the experiments of Bastin, et al. for benzene (a) model of Ref. 1, (b) model of Ref. 1 with the addition of $C_3H_3 + C_3H_3 \Leftrightarrow C_6H_5 + H$ ($k = 1 \times 10^{13} cm^3/mole$ sec); (c) model of Ref. 1 with the addition of $C_3H_3 + C_3H_2 \Leftrightarrow C_6H_5$ ($k = 5 \times 10^{13} cm^3/mole\text{-}sec.$); (d) model of Ref. 1 with the addition of $i - C_4H_3 + C_2H_2 \Leftrightarrow C_6H_5$ and $i - C_4H_5 + C_2H_2 \Leftrightarrow C_6H_6 + H$ (same rate coefficients as for the analogous $n - C_4H_3$ and $n - C_4H_5$ reactions); (e) model of Ref. 1 with k_{190} and k_{191} increased by a factor of ten; (f) model of Ref. 1 with the heat of formation of $i - C_4H_3$ increased to 121.7 kcal/mole. In cases d, e, and f, the predictions are for the sum of C_6H_6 and C_6H_5O

Reaction of 2 C₃H₃ → Fulvene

$\Delta H(300)\,(\text{Kcal-mol}^{-1})$

2 CH₂CCH

?   ??

HC≡CCH₂CH₂C≡CH

CH₂=C=CHCH=C≡CH₂

CH₂=C=ĊH ⇌ H₂Ċ-C≡CH
Resonance Structures

Figure 4. Potential energy diagram for head-to-head or tail-to-tail recombination of two propargyl radicals.

Reaction of 2 C₃H₃ → C₆H₅ + H

$\Delta H(300)\,(\text{Kcal-mol}^{-1})$

2 CH₂CCH

CH₂=C=CHCH₂CH=C:

?   ?

+ H

CH₂=C=CHCH₂C≡CH

CH₂=CHCH=CHC≡CH

Figure 5. Potential energy diagram for head-to-tail recombination of two propargyl radicals.

C_3H_3 REACTION KINETICS IN FUEL-RICH COMBUSTION

S. D. Thomas, F. Communal, P. R. Westmoreland
Department of Chemical Engineering, University of Massachusetts
Amherst, MA 01003

Keywords: propargyl, chemical activation, benzene

ABSTRACT

At typical flame temperatures and pressures, we predict that direct propargyl (C_3H_3) combination forms the open-chain C_6H_6 species 1,5-hexadiyne, 1,2,4,5-hexatetraene, and 4,5-hexadienyne in preference to cyclic C_6H_6 species 3,4-dimethylenecyclobutene, fulvene, and benzene (, , and vs. , , and). These chemically activated reactions, analyzed by a new Q-formalism of Bimolecular Quantum-RRK, have rate constants and rates that are consistent with C_6H_6 data from a $C_2H_2/O_2/Ar$ flat flame. Cyclic C_6H_6's may then be generated by thermal isomerizations.

INTRODUCTION

Recently, C_3H_3 has been the subject of intense interest as a possible precursor to aromatics in flames.[1-8] In earlier work, Hurd and co-workers proposed in 1962 that aromatics might be formed by combination of trimethine (CHCHCH) [9], and Tsang had encouraged others to explore propargyl ($\cdot CH_2$-C≡CH or CH_2=C=CH$\cdot$) as an aromatics precursor based on his high soot yields from pyrolysis experiments.[10] Kern and co-workers provided the first experimental evidence and mechanism for C_6H_6 formation from C_3H_3,[1,2] stimulating much of the subsequent research.

In 1989 we proposed[4] a chemically activated pathway from C_3H_3 to benzene (Figure 1), similar to that of Kern, and presented preliminary calculations of its feasibility. The electron density of propargyl is best represented as propynyl[3] although it is a resonance structure of propynyl and propadienyl (CH≡C-CH$_2\cdot$ and $\cdot CH_2$=C=CH$_2$). Propynyls may combine to make chemically activated 1,5-hexadiyne ("hot" 1,5-hexadiyne). The hot adduct may isomerize by a Cope rearrangement to hot 1,2,4,5-hexatetraene, which may isomerize to make hot 3,4-dimethylenecyclobutene (DMCB) by a sigmatropic ring closure analogous to that of 1,3-butadiene forming cyclobutene. DMCB can isomerize to hot fulvene (methyl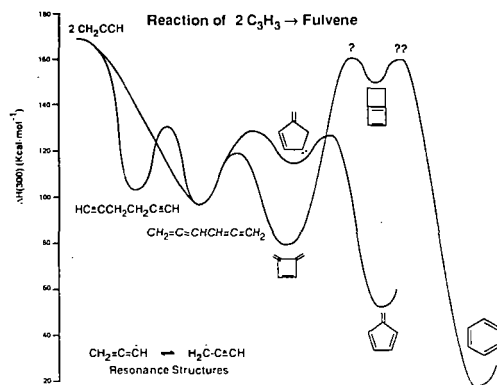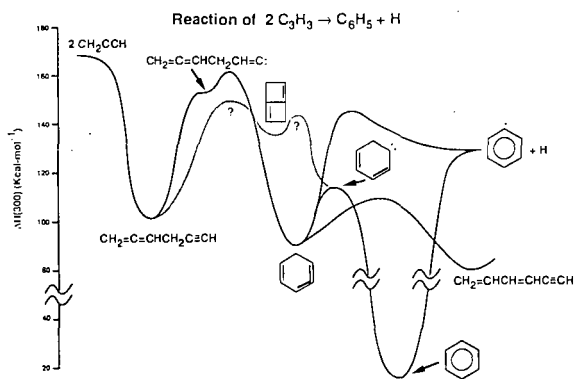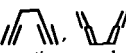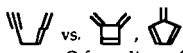enecyclopentadiene) which can isomerize to hot benzene. Because of chemical activation, the energy released into the first adduct by bond formation, each of these steps occurs above the intrinsic or thermal energy barriers. Each one of these chemically activated isomers may be stabilized by bimolecular collisions, or it may decompose or isomerize unimolecularly. This hypothesized route was based on thermal pyrolyses of 1,5-hexadiyne to DMCB, fulvene, and benzene;[11-15] pyrolysis of hexatetraene to the same products;[14] pyrolysis of DMCB to fulvene and benzene;[15] and pyrolysis of fulvene to benzene.[15,16] Compared to the route of Kern and coworkers,[2] this route could proceed without thermal intermediates and without diradicals.

Independently and at the same time, and Stein developed a route similar to that in Figure 1,[5] and Alkemade and Homann proposed a fourth, quite different route.[3] Stein pyrolyzed 1,2-hexadiyne at different temperatures in a VLPP reactor. At low temperatures, DMCB was formed, while at higher temperatures, fulvene and benzene were formed apparently from a DMCB intermediate; Stein proposed that parallel paths to the two products may occur. Alkemade and Homann have made the only direct experimental studies of C_3H_3 combination, finding a mixture of products including benzene. Their mechanism involved cyclopropenyl intermediates similar to those proposed as intermediates in propyne/propadiene isomerization.[17]

More recently, Miller and Melius[7] have proposed a fifth route via 4,5-hexadienyne, the head-to-tail combination product of propargyls. They suggest rearrangement of the acetylenic group to a vinylidene form, which would insert into an allenic C-H bond to form a 1,2,4-cyclohexatriene. Finally they suggest rapid rearrangement to benzene, apparently by a molecular 1,3 H-shift.

Most of these routes are energetically feasible, but there are energetic and entropic challenges to overcome en route. Direct closure to a six-membered ring requires a tight transition state with loss of internal rotation(s), and 1,2- or 1,3-H-shifts and cyclization to four- or five-membered rings is even tighter. The overall exothermicity in forming benzene is a strong driving force, but the intermediate steps must be successful as well. Calculations are presented here for the mechanism of Figure 1. The formation of thermal intermediates is predicted to play more of a role than in C_4H_3 and C_4H_5 additions to C_2H_2, where the low A-factors (entropic difficulty) are compensated for by low energy barriers to cyclization.

CALCULATIONAL METHODS

Multiple isomerizations require a new form of chemical-activation analysis, so we have developed[18] a "Q-formalism." Some discussion of the form and nomenclature serves to clarify the process of multiple chemically activated isomerization. The ith isomer can be designated either as being in a specific energy state, $I_i(E)$, or as being the thermal species I_i (species in a thermal distribution). High-energy states $I_i(E)$ may be collisionally stabilized by a third-body gas, or they may decompose or isomerize unimolecularly.

Consider Figure 1. Propynyl combination forms different quantum states $I_1(E)$ of 1,5-hexadiyne ($i=1$) with a rate constant $k_\infty f(E,T)$, where k_∞ is the high-pressure-limit rate constant for reactants forming the thermal adduct I_1 and $f(E,T)$ is the chemical-activation distribution function. With sufficient energy, $I_1(E)$ may:

(a) Be stabilized by a third-body gas M into a thermal distribution I_1 at a rate $\beta_i Z_i [M] \cdot [I_1(E)]$;
(b) Decompose to new products like H + ·≡---≡ at a rate $(k_{dec}(E))_{ij} \cdot [I_i(E)]$; where j is one of J(i) decomposition channels;
(c) Isomerize to $I_2(E)$ (1,2,4,5-hexatetraene) with a rate $(k_i(E))_i \cdot [I_i(E)]$; or
(d) Revert - just a decomposition channel for the first isomer, the adduct, but designated for generality as if it were a reverse isomerization with a rate of $(k_{-i}(E))_i \cdot [I_i(E)]$.

Likewise, $I_2(E)$ may isomerize in turn to $I_3(E)$ (3,4-dimethylenecyclobutene), $I_4(E)$ (fulvene), and $I_5(E)$ (benzene). Each $I_i(E)$ may be stabilized to I_i, decompose, isomerize to the next isomer, or revert to the previous isomer.

The rate constants have a compact form incorporating a recursive term Q_i. Here we show a Quantum-RRK form, where the energy variable, quantized relative to the bottom of the first energy well, is $n = E / h{<}v{>}$:

$$k(C_3H_3 + C_3H_3 \rightarrow I_i) = \sum_{n = E/h<v> = m_{-1}}^{\infty} \beta_i Z_i [M] \cdot \prod_{\iota=0}^{i} (Q_\iota(E)) \qquad [1]$$

$$k(C_3H_3 + C_3H_3 \rightarrow P_{ij} + P'_{ij}) = \sum_{n = m_{-1}}^{\infty} (k_{dec}(E))_{ij} \cdot \prod_{\iota=0}^{i} (Q_\iota(E)) \qquad [2]$$

$$Q_i(E) = \frac{k_{source}}{\beta_i Z_i [M] + \sum_{j=1}^{J(i)} (k_{dec}(E))_{ij} + (k_i(E))_i + (k_{-i}(E))_i - (k_{-i}(E))_{i+1} Q_{i+1}} \qquad [3]$$

where m_{-1} is the quantized barrier for reversion of I_1 to reactants;
$k_{source} = k_\infty f(E,T)$ for $i=1$ or $(k_i(E))_{i-1}$ for $i>1$; and
$(k_i(E))_i = 0$ and $(k_{-i}(E))_{i+1} Q_{i+1} = 0$ for $i=N$.

Energy-dependent rate constants $k(E)$ for the ith isomer are calculated relative to the bottom of the energy well for that isomer,[19] but the summations of Equation 1 and 2 are over the energies of the chemically activated adduct.

High-pressure-limit Arrhenius parameters of the different steps are the key input parameters for the calculations. Parameters in one direction are often available or may be estimated, but thermochemistry is necessary to obtain parameters in the opposite direction. Thermochemistry used here is summarized in Table I, and the resulting set of A-factors and activation energies is presented in Table II. Other parameters necessary for the calculations include mean frequency of the isomers (1010, 1240, 1176, 1209, and 1205 cm⁻¹ for $i=1$ to 5, respectively); molecular weight of 78.06; Lennard-Jones parameters $\sigma = 5.27$Å and $\varepsilon / \kappa = 440$ K; and molecular weight, Lennard-Jones parameters, and collisional step-down size for the third-body gas M.

RESULTS

At high pressure (1 atm, Figure 2a) and low pressure (600 Pa, Figure 3a), C_3H_3 combination as propynyls is predicted to form the thermal adduct as its dominant channel. This result is somewhat surprising, as there is

no intrinsic energy barrier to proceeding all the way to benzene or to phenyl and H. On the other hand, while the chemically activated adduct can go over the isomerization energy barrier, entropy loss in the tight transition state is a serious limitation, as manifested in the low A-factor. At its lowest energy level (the ground energy of the reactants), the hot adduct has 29 kcal/mol available for isomerization, but the A-factor, which limits $k(E)$, is only $3 \cdot 10^{11}$ and the energy gain in isomerization is only 1 kcal/mol. Stabilization of the adduct is then relatively easy. At higher energy levels, reached at higher temperatures, the A-factors favor reversion to reactants by a loose transition state. Phenyl contributes only slightly, and then only at 600 Pa and the highest temperatures; DMCB is the dominant thermal product, which may rapidly, thermally isomerize.[5]

Once 1,5-hexadiyne forms, it may isomerize thermally to benzene. Likewise, the next most important products, 1,2,4,5-hexatetraene and 3,4-dimethylcyclobutene may form benzene thermally.

Combination as propadienyls should be much less favorable. Radical density is greatest on the CH_2 group within C_3H_3, corresponding to propynyl, and C_3H_3 tends to react as propynyl.[3] If C_3H_3 had 10% propadienyl character, the probability of propadienyl+propadienyl combination would only be 1% of the total combination rate. Again, though, thermal isomerization of the products would be possible. Also, head-to-tail combination (propynyl + propadienyl) forms 4,5-hexadienyne, which may isomerize to benzene thermally.[29]

These results would agree with the experimental results of Alkemade and Homann[3] only if thermal isomerization contributed, but there is no conflict with the $C_2H_2/O_2/Ar$ flame data of Westmoreland et al.[30] The predicted rate constants would easily account for the rate of C_6H_6 production in that flame, as molecular-beam mass spectrometry does not resolve isomers of mass 78. Also in that work, a microprobe sample of the stable species was collected downstream of the region of high C_6H_6 production rate. GC/MS analysis using aDB-5 fused-silica column identified four isomers of mass 78 at concentrations of 6, 1.3, 20 (for benzene), and 0.4 ppmv in the flame. Future work in our laboratory will examine the isomer split throughout this flame.

Another possible cause of discrepancy is uncertainty in the input barriers. Stein inferred a rate constant of $8 \cdot 10^{12} \exp(-50.0/RT)$ for DMCB pyrolysis to fulvene and benzene.[5] Using these alternative parameters for DMCB $\rightarrow$ fulvene, little change in the largest rate constants is predicted at 1 atm. In contrast, direct formation of phenyl contributes much more significantly at 600 Pa and the highest temperatures, although the thermal path is also predicted to dominate at lower temperatures. Again, having no intrinsic barrier is helpful, but entropic limitations are also very important.

ACKNOWLEDGEMENTS

REFERENCES

1. Wu, C.H.; Kern, R. D. *J. Phys. Chem.* **1987**, *91*, 6291.
2. Kern, R. D.; Singh, H. J.; Wu, C.H. *Int. J. Chem. Kin.* **1988**, *20*, 731.
3. Alkemade, U., and Homann, K. H. *Z. Phys. Chem. N.F.* **1989**, *161*, 19.
4. Thomas, S. D.; Westmoreland, P.R. "Role of C_3H_3 in Aromatics and Soot Formation," Paper 130g, 1989 Annual Meeting of AIChE, San Francisco CA, November 5-10, 1989; F. Communal, S.D. Thomas, and P.R. Westmoreland, "Kinetics of C_3 Routes to Aromatics Formation," Poster P40, 23rd Symp. (Intl.) on Combustion, Orléans France, July 22-27, 1990.
5. Stein, S. E. *23rd Symp. (Intl.) on Combustion,* The Combustion Institute, Pittsburgh (in press).
6. Seshadri, K. *23rd Symp. (Intl.) on Combustion,* The Combustion Institute, Pittsburgh (in press).
7. Miller, J. A.; Melius, C. A. *Combustion and Flame* (in press); Miller, J. A.; Kee, R. J.; Westbrook, C. K. *Ann. Rev. Phys. Chem.* **1990**, *41*, 345.
8. Boyle, J.; Pfefferle, L. D. "Study of Higher Hydrocarbon Production During Methyl Acetylene and Allene Pyrolysis using Laser-Generated VUV Photoionization Detection," Paper 277f, 1990 Annual Meeting of AIChE, Chicago IL, November 11-16, 1990.
9. Hurd, C. D.; Macon, A. R.; Simon, J. I.; Levetan, R. V. *J. Am. Chem. Soc.* **1962**, *84*, 4509.
10. Tsang, W. , Personal communication (1984).
11. Huntsman, W. D.; Wristers, H. J. *J. Am. Chem. Soc.* **1967**, *89*, 342; Huntsman, W. D. *Intra-Science Chem. Rept.* **1972**, *6*, 151.
12. Heffernan, M. L.; Jones, A. J. *Chem. Commun.* **1966**, *4*, 120.
13. Kent, J. E.; Jones, A. J. *Aust. J. Chem.* **1970**, *23*, 1059.
14. Hopf, H. *Angew. Chem. Int. Ed.* **1970**, *9*, 732.
15. Henry, T. J.; Bergman, R. G. *J. Am. Chem. Soc.* **1972**, *94*, 5103.
16. Gaynor, B. J.; Gilbert, R. G.; King, K. D.; Harman, P. J. *Aust. J. Chem.* **1981**, *34*, 449.

17. Honjou, N.; Pacansky, J.; Yoshimine, M. *J. Am. Chem. Soc.* **1985**, *107*, 5332.
18. Communal, F. "Plasma Measurements and Gas-Phase Kinetics in Silicon Deposition by PECVD," M.S. thesis, Chemical Engineering, U. Massachusetts (1990); Westmoreland, P. R., "Thermochemistry and kinetics of $C_2H_3+O_2$ reactions" (submitted).
19. Westmoreland, P. R.; Howard, J. B.; Longwell, J. P.; Dean, A. M. *AIChE J.* **1986**, *32*, 1971.
20. McMillen, D. F.; Golden, D. M. *Ann. Rev. Phys. Chem.* **1982**, *33*, 493.
21. Rosenstock, H.M.; Dannacher, J.; Liebman, J.F. *Radiat. Phys. Chem.* **1982**, *20*, 7.
22. Roth, W. R.; Lennartz, H.-W.; Vogel, E.; Leiendecker, M.; Oda, M. *Chem. Ber.* **1986**, *19*, 837.
23. de Brouckère, G.; Berthier, G. *Mol. Phys.* **1982**, *47*, 209.
24. Roth, W.R., Personal communication (1984), cited in NIST Standard Reference Database 25: The NIST Structures and Properties Database and Estimation Program, Version 1.0 (1991).
25. Domaille, P. J.; Kent, J. E.; O'Dwyer, M. F. *Aust. J. Chem.* **1974**, *27*, 2463.
26. Benson, S. W. *Thermochemical Kinetics, 2nd Ed.*, New York: Wiley (1976).
27. Jasinski, J. M.; Frisoli, J. K.; Moore, C. B. *J. Chem. Phys.* **1983**, *79*, 1312.
28. Ackermann, L.; Hippler, H.; Pagsberg, P.; Reihs, C.; Troe, J. *J. Phys. Chem.* **1990**, *94*, 5247.
29. Hopf, H. *Chem. Ber.* **1971**, *104*, 1499.
30. Westmoreland, P. R.; Dean, A. M.; Howard, J. B.; Longwell, J. P. *J. Phys. Chem.* **1989**, *93*, 8171.

Table I: Thermodynamic properties of species used in the analysis (1 atm standard state).
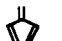
Species and structures	$\Delta H^o_{f\,298}$ (kcal/mol)	S^o_{298} (cal/mol K)	Source
Propargyl, C_3H_3	81.4	60.6	ΔH^o_f of McMillen and Golden (Ref. 20); S^o_{298} estimated.
1,5-hexadiyne	99.0	81.3	ΔH^o_f of Rosenstock et al. (Ref. 21), compared to 99.5 by group additivity; S^o_{298} by group additivity.
1,2,4,5-hexatetraene	98.0	78.6	ΔH^o_f of Rosenstock et al. (Ref. 21), compared to 94.5 by group additivity; S^o_{298} by group additivity.
Dimethylenecyclobutene	80.4	68.4	ΔH^o_f of Roth et al. (Ref. 22); S^o_{298} from statistical mechanics using literature moments (Ref. 23) and frequencies assigned by analogies with fulvene.
Fulvene	53.5	67.9	ΔH^o_f of Roth et al. (Ref. 22), compared to 45.4 by group additivity; S^o_{298} from statistical mechanics using literature frequencies (Ref. 24) and moments (Ref. 23).
Benzene	19.8	64.3	Benson (Ref. 25).
Phenyl	78.5	69.4	ΔH^o_f of McMillen and Golden (Ref. 20); S^o_{298} of Benson (Ref. 25).
H-atom	52.1	27.4	Benson (Ref. 25).

Table II: High-pressure-limit rate constants for steps in the $C_3H_3 + C_3H_3$ reaction set. A-factors are in cm^3, mol, s units; E_{act}'s are in kcal/mol.

Reaction	k_{fwd}		k_{rev}		Sources
	A_{fwd}	$E_{a,fwd}$	A_{rev}	$E_{a,rev}$	
[structure] → $2\,C_3H_3$	$6.6 \cdot 10^{17}$	63.2	$3.1 \cdot 10^{13}$	0.0	k_{rev} from $k(C_3H_3+C_3H_3)=3.4 \cdot 10^{13}$ by measurements of Alkemade and Homann (Ref. 3) assuming C_3H_3 had 90% propynyl character; k_{fwd} from K_c.
[structure] → [structure]	$3.0 \cdot 10^{11}$	34.4	$1.15 \cdot 10^{12}$	35.4	k_{fwd} from fit to data of Huntsman and Wristers (Ref. 11).
[structure] → $2\,C_3H_3$	$2.8 \cdot 10^{16}$	64.2	$3.4 \cdot 10^{11}$	0.0	k_{rev} from $k(C_3H_3+C_3H_3)=3.4 \cdot 10^{13}$ by measurements of Alkemade and Homann (Ref. 3) assuming C_3H_3 had 10% propadienyl character.
[structure] → [structure]	$3.4 \cdot 10^{11}$	15.9	$5.8 \cdot 10^{13}$	33.5	k_{rev} by analogy to k(cyclobutene → 1,3-butadiene) of Jasinski et al. (Ref. 27).
[structure] → [structure]	$3. \cdot 10^{13}$	66	$3.9 \cdot 10^{13}$	93.	k_{fwd} by analogy to$k$(fulvene → benzene); see text for comparison to $8 \cdot 10^{12}\exp(-50.0/RT)$ of Stein (Ref. 5).
[structure] → [structure]	$3. \cdot 10^{13}$	66	$1.8 \cdot 10^{14}$	100	k_{fwd} from midrange of Arrhenius parameters of Gaynor et al. (Ref. 16).
[structure] → H + Phenyl	$1.8 \cdot 10^{16}$	110.2	$2.2 \cdot 10^{14}$	0	k_{rev} from k_{300} of Ackermann et al. (Ref. 28).
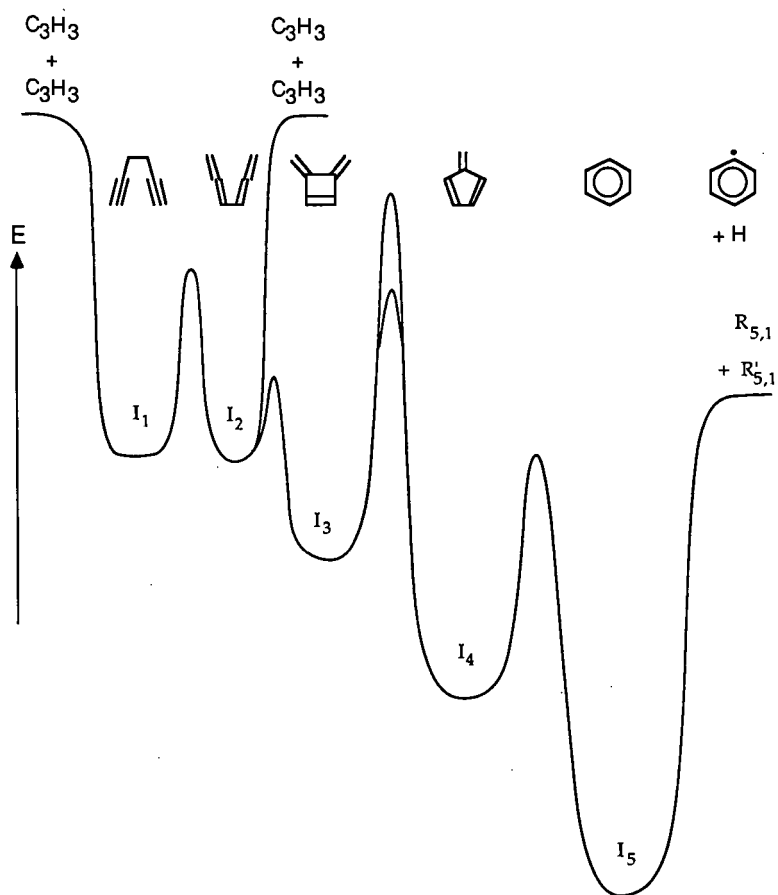
Figure 1. Energy diagram for propargyl combination, subsequent isomerizations, and decompositions.
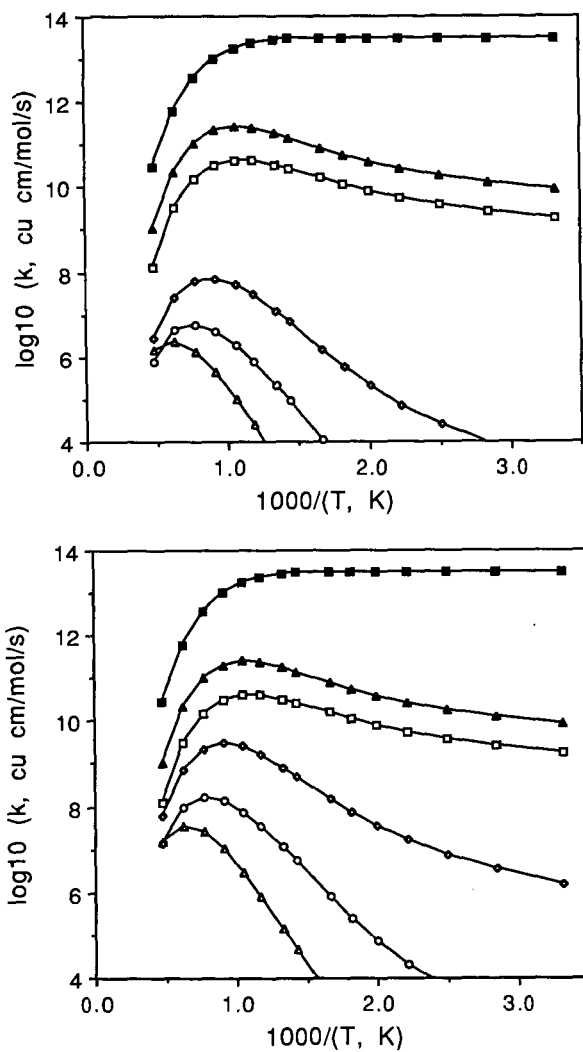
Figure 2. Arrhenius plot at 1 atm of predicted rate constants for $C_3H_3+C_3H_3$ combining as propynyls: (top) using 66 kcal/mol barrier for DMCB to fulvene, (bottom) using 50 kcal/mol barrier of Stein (Ref. 5). Product channels: 1,5-hexadiyne ■, 1,2,4,5-hexatetraene ▲, 3,4-dimethylenecyclobutene □, fulvene ◊, benzene O, H + phenyl △.
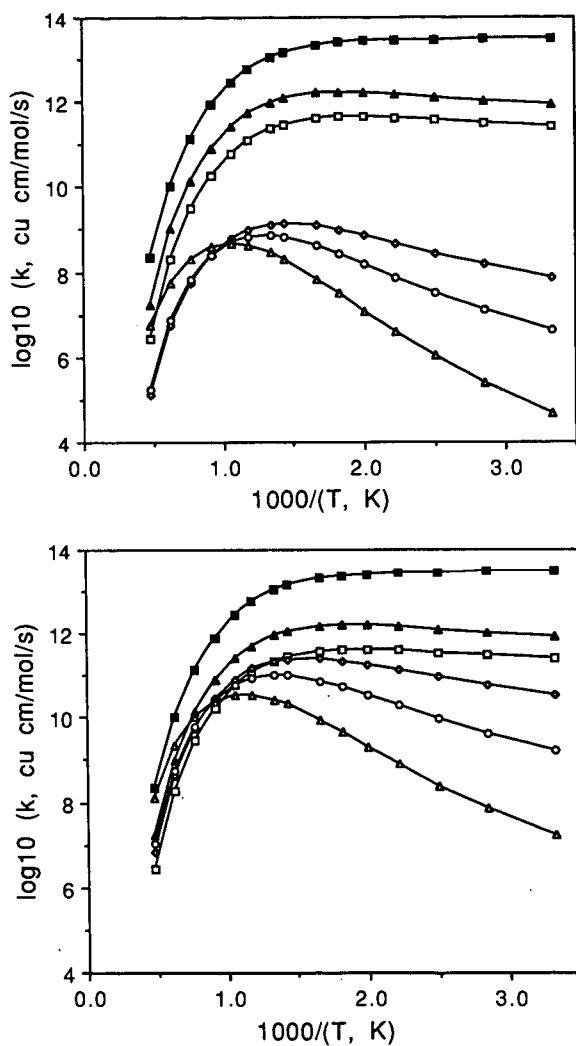
Figure 3. Arrhenius plot at 600 Pa of predicted rate constants for $C_3H_3+C_3H_3$ combining as propynyls: (top) using 66 kcal/mol barrier for DMCB to fulvene, (bottom) using 50 kcal/mol barrier of Stein (Ref. 5). Product channels: 1,5-hexadiyne ■, 1,2,4,5-hexatetraene ▲, 3,4-dimethylenecyclobutene □, fulvene ◊, benzene ○, H + phenyl △.

COMPARISON OF AROMATICS FORMATION IN DECANE AND KEROSENE FLAMES

Christian Vovelle, Jean-Louis Delfau
Marcelline Reuillon, Robert Akrich, Mohamed Bouhria, Oumar Sanogo.
Laboratoire de Combustion et Systèmes Réactifs (LCSR-CNRS)
1C Avenue de la Recherche Scientifique
45071 ORLEANS CEDEX 2, FRANCE

INTRODUCTION

Most studies on aromatics formation in flames have been concentrated on small fuel molecules[1-6]. On the other hand, practical combustion systems such as automotive or airplane engines burn hydrocarbon fuels containing seven to fourteen carbon atoms. Moreover, the few kinetic studies on the combustion of liquid fuels have been oriented towards knock phenomenon and have been conducted in a temperature range (lower than 1000K) where peroxides formation dominates[7,8]. Aromatics and soot are formed at higher temperature, and to improve knowledge on formation of these pollutants in practical systems, there is a need for experimental and modelling studies on flames of large fuel molecule.

A few years ago, we started both experimental and modelling studies on rich premixed kerosene flames. Since kerosene is a complex mixture with alkanes as major components, the structure of a near sooting decane flame (equivalence ratio 1.9) was studied first and we developped a kinetic model which predicted the mole fraction profiles of species involved in the formation of benzene with a good accuracy[9].

In this work we present the result of temperature and mole fraction measurements in sooting kerosene and decane flames. Results show that for all species except benzene there is a close similarity between the two flames so that the kinetic mechanism derived for decane is also valid for modelling kerosene combustion with only one change concerning benzene formation. A specific study was carried out to identify an additional source for aromatics formation in kerosene flames.

EXPERIMENTAL

The premixed sooting kerosene flame (8.0% kerosene, 56.4% oxygen, 35.6% argon) was stabilized on a flat flame burner at low pressure (6 kPa). If kerosene was decane, this corresponds to an equivalence ratio of 2.2. Gas velocity at burner exit was 24 cm/s. A decane-O_2-Ar flame with the same initial composition was stabilized and analyzed in identical conditions. Temperature and mole fraction profiles were measured along the symmetry axis. Molecular beam mass spectrometry technique was used for species analysis and Pt-Pt 10% Rh thermocouples for temperature measurements (wires diameter 50 μm). Coating with BeO/Y_2O_3 prevented catalytic effects, and heat losses due to radiation were compensated by electrical heating. Identification of species and calibration of the mass spectrometer have been described elsewere[10,11].

A Gilson pump manufactured for Liquid Chromatography was used to control the flow rate of kerosene. The fuel was first atomized by dragging through a small orifice by a high pressure argon jet and then

vaporized in a heated chamber. Adjustment of atomizer and vaporizer temperature was rather critical. Temperature had to be maintained between 170°C and 200°C to prevent fuel condensation or polymerization, respectively.

RESULTS

In a previous study on the modelling of acetylene flames, the formation of the first aromatic rings was described by acetylene addition to C_4 species :

$$C_4H_5 \quad + \quad C_2H_2 \quad ---> \quad C_6H_6 \quad + \quad H \qquad (1)$$
$$C_4H_3 \quad + \quad C_2H_2 \quad ---> \quad C_6H_5 \qquad\qquad (2)$$
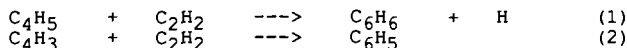
Kinetic parameters for these reactions were taken from Westmoreland[12]. The mechanism for rich decane flames was built upon addition to the acetylene mechanism of a few reactions for decane consumption[9]. The ability of the mechanism to predict aromatic formation depends strongly on the accuracy of the modelling of C_4 species and their precursors : C_2H_4 and C_2H_2. Maximum mole fraction measured for the major molecular and active species, and for the species involved in aromatics formation, in the kerosene and decane flames have been compared in Table I.

Slight differences are observed for some species. They were not considered as significant but rather due to a lower accuracy of the measurements in the kerosene flame where very low electron energies were used to prevent fragmentations of the fuel components. However the maximum mole fraction for benzene in the kerosene flame exceeds by one order of magnitude the maximum measured in the decane flame.

This point deserved attention and a specific comparative study on the formation of benzene and two others aromatic species : phenyl acetylene and vinyl benzene in decane and kerosene flames was undertaken. To check the possibility of a change in the mechanism for aromatics formation described above, acetylene was measured as well.

Aromatics formation in kerosene and decane flames

Detailed analysis of the structure of one flame is time-consuming and this study was limited to signal measurements. On the other hand, they were repeated for many flames with equivalence ratio in the range 1.0 - 2.5. Change in fuel composition have been done keeping constant both the overall and the argon flowrates. Gas velocity at the burner exit was 27.5 cm/s (at 298K and 6.0 kPa).

Figure 1 shows that the maximum mole fraction of acetylene in decane flames is slightly greater than in kerosene flames. In both flames, a linear increase is observed for equivalence ratios above 1.6.

Benzene measurements have been performed with an electron energy adjusted to 13 eV. For kerosene flames a second determination has been done with an electron energy of 11 eV to check the occurrence of fragmentations in the ionization source of the mass spectrometer. A similar result (linear variation of the maximum signal with the equivalence ratio) is obtained in both cases, so that we can conclude that measurements of the benzene signal are free from fragmentation

effects (Figure 2). Extrapolation of the signal gives a null value for an equivalence ratio equal to 0.8.

Measurements in the decane flame confirm that benzene is formed in lower concentration than in kerosene flames. The ratio is about 10 for an equivalence ratio of 2.0. A second difference with kerosene flames is observed for the variation of the maximum signal with the equivalence ratio, the exponent in a law $[C_6H_6] = f(\emptyset)$ being greater than 1.

The curves plotted in figure 2 show that benzene formation results from two different mechanism in decane and kerosene flames. In the former, benzene is formed by reactions (1) and (2) so that the signal is proportional to acetylene and either C_4H_3 or C_4H_5. Since in turn, C_4 species are formed from acetylene, benzene dependence with $[C_2H_2]^2$ must be observed. The dashed line in figure 2 corresponds to the variation with $\emptyset$ of the expression $k[C_2H_2]^2$ with the constant k adjusted so that the value calculated for $\emptyset = 2.4$ coincide with the signal measured for benzene. These two curves remains very close over the whole range of equivalence ratios. ($[C_2H_2]$ represents the maximum signal measured for acetylene).

In kerosene flames, the linear variation of the benzene signal with $(\emptyset - \emptyset_c)$ shows that the aromatics components of the fuel contribute directly to benzene formation. The procedure adopted to change the equivalence ratio of the flames (constant values of overall an argon flowrates) leads to the following relationship between decane flowrate and $\emptyset$:

$$F_d = (F_o - F_{Ar}) \frac{2(\emptyset - \emptyset_c)}{2(\emptyset - \emptyset_c) + 31}$$

(F_d, F_o, F_{Ar} represents respectively decane, overall and argon flowrates).

Since $2(\emptyset - \emptyset_c)$ is small compare to 31, this expression predicts a linear variation for F_d with $(\emptyset - \emptyset_c)$

Phenyl acetylene and vinyl benzene signals correspond as well to different sources for aromatics. In decane flames, these two species are not observed for equivalence ratios lower than 1.5, while a marked increase in the signal is observed for richer flames (Figure 3). Since these species are formed by addition of acetylene to benzene or phenyl radical we have plotted the variation of the expression $k[C_6H_6][C_2H_2]$ versus $\emptyset$. Here again, the value of the constant k was arbitrarily adjusted in order to match either the phenyl acetylene or the vinyl benzene signal at $\emptyset = 2.4$. The same comparison in kerosene flames leads to values derived from $[C_6H_6]$ and $[C_2H_2]$ lower than the experimental signal when $\emptyset$ is close to 1.0 (Figure 4). Expressions based on the product of the reactants signals give only an upper limit for the formation of a given species since consumption is not taken into account. Therefore, from the relative positions of the experimental points and the dashed curve, we can conclude that phenyl acetylene and vinyl benzene measured in .stoichiometric or slightly rich kerosene flames result from the aromatic components of the fuel.

Benzene formation in kerosene flames

1458

This comparative study clearly shows that consumption reactions of at least one aromatic species must be added to the decane mechanism to predict the structure of rich kerosene flames. Tri-methylbenzene is the main aromatic species in the kerosene that was used in this work. However, to simplify both the mechanism and the search for kinetic data, the aromatic part of kerosene was considered as toluene and the following reactions were considered to describe its consumption :

$$
\begin{array}{llllllll}
C_7H_8 & + H & \text{--->} & C_7H_7 & + H_2 & 1.24 \ 10^{14} & 0.0 & 35.10 & (3) \\
C_7H_7 & + H & \text{--->} & C_7H_8 & & 9.00 \ 10^{13} & 0.0 & 0.00 & (4) \\
C_7H_8 & + H & \text{--->} & C_6H_6 & + CH_3 & 3.50 \ 10^{13} & 0.0 & 15.50 & (5) \\
C_7H_8 & & \text{--->} & C_3H_3 & + C_4H_4 & 4.00 \ 10^{16} & 0.0 & 424.30 & (6) \\
C_7H_7 & + O_2 & \text{--->} & C_6H_6 & + Prod. & 1.00 \ 10^{13} & 0.0 & 0.00 & (7)
\end{array}
$$
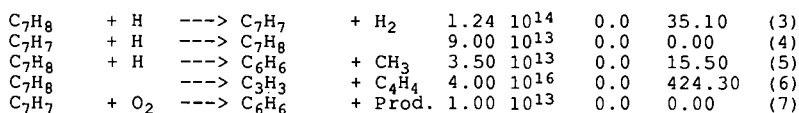
Kinetic data for these reactions have been taken from Rao and Skinner[13].

Modelling of kerosene flames

These five reactions have been added to the mechanism validated previously for decane combustion[9]. Simulation of the kerosene flame has been performed with a fuel composition of 10% toluene and 90% decane. Warnatz's computation code was used with the experimental temperature profile as input data, so that the energy equation was neglected. Temperature profiles were measured by moving the burner in the vertical direction. The thermocouple was kept at a fixed position, close to the quartz cone tip, in order to take into account flame perturbation by the cone. The measurements have been repeated for various distance (d) between the thermocouple bead and the cone tip (Figure 5). In the burned gases only a cooling effect is observed, while in the main reaction zone, flame attachment shifts the profiles towards larger distance from the burner surface. No one profile is representative of the gas sampling conditions in the whole flame : profiles with very small d correspond to the temperature evolution for sampling close to the burner surface, while profiles with large d give a better description of the temperature history for a gas sample taken far from the burner. In this work, the profile measured with d = 3 mm was chosen as the best compromise between these extreme situations.

The SANDIA thermodynamic data base[14] has been used for species involved in H_2, C_1 and C_2 submechanisms and Burcat's data[15] for decane and toluene combustion reactions.

Simulated mole fraction profiles are compared to the experimental ones for the reactants, the main products, and species involved in the formation of aromatics from the alkane part of the fuel (Fig. 6-9). In figure 10, prediction of the mole fraction profile is compared to experimental results for a decane and a kerosene flame. This figure shows that in the latter, benzene results mainly from the aromatic part of the fuel. This contribution can be modelled with a good accuracy by addition to the mechanism of a few reactions for the consumption of one aromatic.

CONCLUSION

This work was concerned with the formation of aromatics in kerosene flames. In previous studies we checked the possibility to substitute decane to kerosene to perform modelling in simpler conditions. Results showed that structure of decane and kerosene flames are similar except

for benzene that is formed in larger amount in kerosene flames. A specific study based on the systematic measurement of acetylene, benzene, phenyl acetylene and vinyl benzene in decane and kerosene flames was carried out. Variation of the maximum signal with the equivalence ratio leads to the conclusion that the aromatic part of kerosene is the main source of aromatics, while it is the addition of acetylene to C4 radicals in the decane flame. This difference was taken into account by addition of a few reactions for the consumption of toluene to the decane combustion mechanism used so far. This change leads to predictions in good agreement with the experimental mole fraction profiles in decane and kerosene flames.

REFERENCE

1. MILLER, J.A., MITCHELL, R.E., SMOOKE, M.D. and KEE, R.J., Nineteenth Symposium (International) on Combustion, p. 181, The Combustion Institute, (1988).
2. WESTBROOK, C.K. and DRYER, F.L., Progr. Energy Comb. Sci. 10, 1 (1984).
3. WARNATZ, J. Comb. Sci. Tech. 34, 177 (1983).
4. WESTMORELAND, P.R., HOWARD, J.B. and LONGWELL, J.P., Twenty First Symposium (International) on Combustion, p. 773, The Combustion Institute, (1988).
5. FRENKLACH, M. and WARNATZ, J., Comb. Sci. and Tech. 51, 265 (1987).
6. HARRIS, S.J., WEINER, A.M. and BLINT, R.J., Comb. and Flame, 72, 91, (1988).
7. AXELSSON, E., BREZINSKY, K., DRYER, F.L., PITZ, W.J. and WESTBROOK, C.K., Twenty First Symposium (International) on Combustion, p. 783, The Combustion Institute, (1986).
8. WESTBROOK, C.K., WARNATZ, J. and PITZ, W.J., Twenty Second Symposium (International) on Combustion, p.893, The Combustion Institute, (1988).
9. DELFAU, J.L., BOUHRIA, M., REUILLON; M., SANOGO, O., AKRICH, R. and VOVELLE, C., Twenty Third Symposium (International) on Combustion, The Combustion Institute, (1990).
10. BASTIN, E., DELFAU, J.L., REUILLON, M., VOVELLE, C. and WARNATZ, J., Twenty Second Symposium (International) on Combustion, p. 313, The Combustion Institute, (1988).
11. BASTIN, E., Thèse de Doctorat de l'Université Pierre et Marie Curie (Paris 6), Spécialité Cinétique Chimique Appliquée (1989).
12. WESTMORELAND, P.R., DEAN, A.M., HOWARD, J.B. and LONGWELL, J.P., J. Phys. Chem., 93, 8171 (1989).
13. RAO, V.S. and SKINNER, G.B., J. Phys. Chem., 88, 4362-4365, (1984).
14. KEE, R.J., RUPLEY, M. and MILLER, J.A., The Chemkin Thermodynamic Data base, SANDIA Report, SAND87-8215-UC-4 (1987).
15. BURCAT, A., Table of Coefficients Sets for NASA Polynomials, Appendix C, in Combustion Chemistry, (Gardiner, W.C. Jr. Ed.), Springler-Verlag, New York, (1984).

	Decane-O_2-Ar flame	Kerosene-O_2-Ar flame
CO	$3.4 \; 10^{-1}$	$2.9 \; 10^{-1}$
H_2O	$3.0 \; 10^{-1}$	$2.4 \; 10^{-1}$
H_2	$2.3 \; 10^{-1}$	$3.0 \; 10^{-1}$
CO_2	$6.0 \; 10^{-2}$	$7.0 \; 10^{-2}$
H	$8.9 \; 10^{-3}$	$1.2 \; 10^{-3}$
OH	$2.7 \; 10^{-4}$	$3.7 \; 10^{-4}$
C_2H_4	$5.3 \; 10^{-2}$	$1.7 \; 10^{-2}$
C_2H_2	$6.1 \; 10^{-2}$	$3.9 \; 10^{-2}$
C_4H_2	$1.4 \; 10^{-3}$	$1.8 \; 10^{-3}$
C_4H_4	$5.9 \; 10^{-4}$	$1.1 \; 10^{-3}$
C_4H_5	$3.3 \; 10^{-5}$	$1.0 \; 10^{-4}$
C_6H_6	$1.2 \; 10^{-4}$	$2.2 \; 10^{-3}$

Table I
Comparison of the maximum mole.fraction in decane and kerosene flames
(equivalence ratio : 2.2, pressure : 6 kPa).
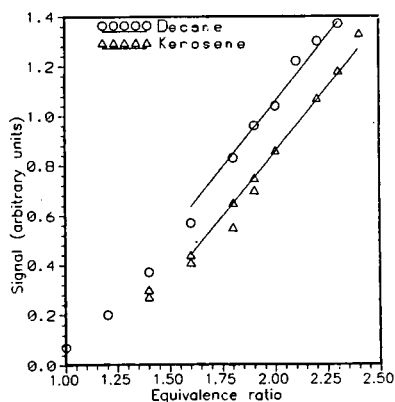
Figure 1
Evolution with
the equivalence ratio
of the maximum signal of C_2H_2
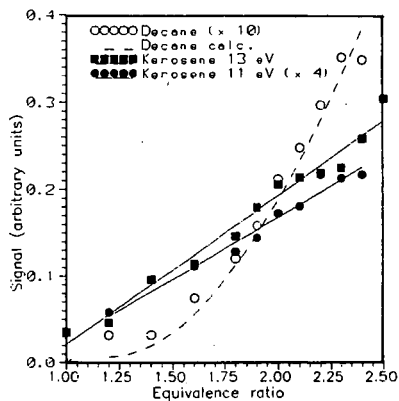
Figure 2
Evolution with
the equivalence ratio
of the maximum signal of C_6H_6
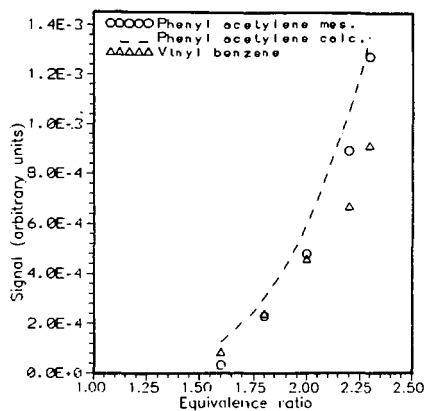
Figure 3
Decane flames
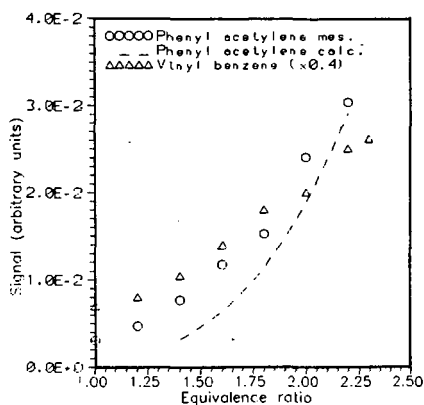
Figure 4
Kerosene flames
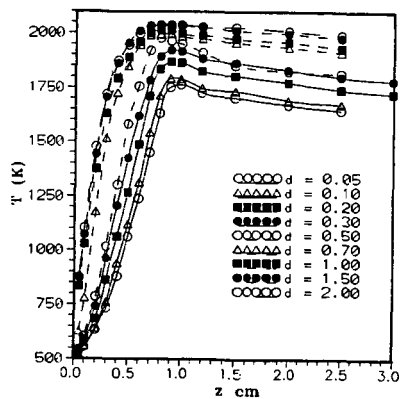
Figure 5
Temperature profiles
in a Ø = 2.2 Kerosene-O_2-Ar flame
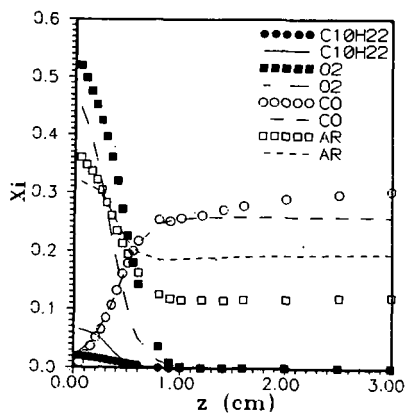
Figure 6
Comparison of experimental (points)
and simulated (curves)
mole fraction profiles
Ø = 2.2 Kerosene-O_2-Ar flame
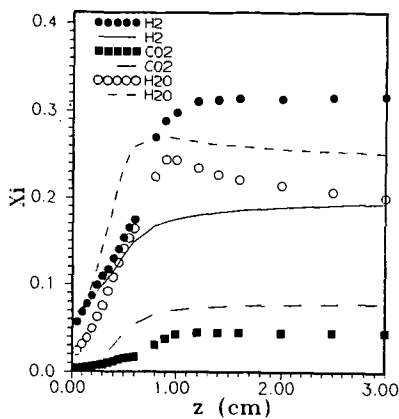
Figure 7
Comparison of experimental (points)
and simulated (curves)
mole fraction profiles
Ø = 2.2 Kerosene-O_2-Ar flame
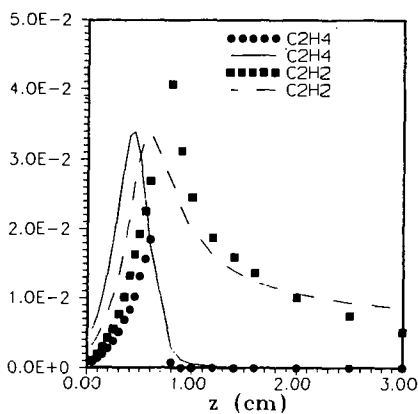
Figure 8
Comparison of experimental (points)
and simulated (curves)
mole fraction profiles
Ø = 2.2 Kerosene-O_2-Ar flame
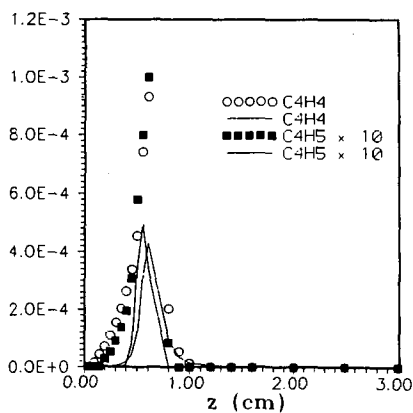
Figure 9
Comparison of experimental (points)
and simulated (curves)
mole fraction profiles
Ø = 2.2 Kerosene-O_2-Ar flame
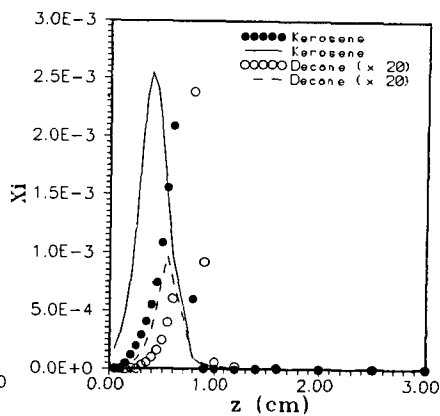
Figure 10
Comparison of experimental (points)
and simulated (curves)
mole fraction profiles
Ø = 2.2 Decane and Kerosene flames

REACTION RATES OF A FEW BENZYL TYPE RADICALS
WITH O_2, NO AND NO_2

J.F. Pauwels, L. El Maimouni, A. Goumri, P. Devolder, L.R. Sochet

Laboratoire de Cinétique et Chimie de la Combustion
URA CNRS 876
59655 VILLENEUVE D'ASCQ Cédex (France)

Introduction

Benzyl type radicals are important conjugated intermediates in the chemical mechanisms describing the oxidation of alkylbenzenes in reactive systems. In the atmosphere, they are formed during the first step (by OH abstraction) of the tropospheric oxidation of alkylbenzene derivatives (toluene, xylenes, trimethylbenzenes) : final oxidation are formed by subsequent competing reactions of the benzyl type radicals with O_2, NO and NO_2 (1) (2). In high temperature reactive systems, they can also play a role as intermediates in the mechanism of soot formation (3) (4) (5) (6). At last, with the allyl radical, the benzyl radical is a reference conjugated radical. With an absolute technique, the discharge flow/Laser Induced Fluorescence technique, we have measured the room temperature rate constants with O_2, NO and NO_2 of the following benzyl type radicals : m-fluorobenzyl, p-fluorobenzyl, o-methylbenzyl, m-methylbenzyl. Also, the rate constant with O_2 of the p-fluorobenzyl radical has been measured in the temperature range 297-433 K.

Experimental

A schematics of the experimental set up is presented figure 1. The radicals are formed by chlorine atom reaction with the parent molecule as a precursor. Chlorine atoms are prepared in the upstream part of the flow tube by the fast reaction of transfer (7) :

$$F + Cl_2 \longrightarrow FCl + Cl \qquad k = 1.6 \times 10^{-11} \text{ cm}^3 \text{ molec}^{-1} \text{ s}^{-1}$$
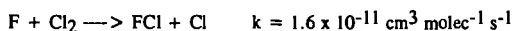
with F atoms first produced by a microwave discharge in F_2/He or CF_4/He. This method (chlorine abstraction) has been preferred to the more direct fluorine abstraction because (i) a significant fraction of fluorine atoms exhibit an addition on the aromatic ring (8) (9) (ii) chlorine abstraction is a very fast reaction ($k = 6 \times 10^{-10}$ cm^3 molec^{-1} s^{-1} (10)). The precursor and the reactant (O_2, NO or NO_2) are then successively added via a double movable injector. The benzyl type radicals are probed by Laser Induced Fluorescence via their visible absorption bands ($\lambda \sim 460$ nm) which have been characterized in gas phase either as absorption bands (13) or as fluorescence excitation bands (11) (12). The exciting wavelength ($\lambda \sim 460$ nm) is generated by a dye laser (Rhodamine 590) pumped by a Yag laser (both Quantel) and further blueshifted (generation of the first Anti-Stokes harmonics) via a Raman cell (14). The fluorescent light is filtered by an interference filter ($\lambda = (500 \pm 20)$ nm) and averaged by a boxcar (PAR 162/165).

For the room temperature measurements, both the flow tube and the injector are covered with a halocarbon, wax whereas for variable temperature measurements, all flow surfaces are simply washed with HF. Most experiments have been performed at a pressure of 1 torr with Helium as diluent gas. O_2 (Alphagaz N45, 99.995%) is used as received. NO_2 is purified as follows : to oxidize the other nitrogen oxides usually present

in NO_2 (bluish color at 77 K), liquid NO_2 is first placed under ultrapure oxygen during $\sim$ 24 hours and then submitted to extensive degassing at 77 K. Traces of NO_2 present in NO (Alphagaz N20, 99%) have been eliminated by flowing NO through a combination of charcoal filter and a filter packed with $FeSO_4$, $7H_2O$ (15).

<u>Results and discussion</u>

1) Rate constants of a few benzyl type radicals with O_2, NO and NO_2.

A few typical curves observed with the p-fluorobenzyl radical as an example are presented figure 2 : fig 2a represents a few logarithmic decay plots of radical concentration versus reaction distance ; fig 2b represents all the pseudo-first-order constants versus the reactant concentration. Our global results are presented table 1 together with the few other measurements available in the litterature for the benzyl radical itself ; the rate constant of the benzyl radical with O_2 has already been measured by flash photolysis (16), laser photolysis/Laser Induced Fluorescence (17) and mass spectrometry (18). Our results for the substituted benzyl radicals show that the reaction rate with O_2 is not very dependent upon the presence of a substituent ; the same conclusion has been observed in liquid phase (19) for a few benzyl radicals substituted in para position by a methyl group or a fluorine atom. Furthermore, since the reaction rate constants with O_2 and NO measured with the present technique (Pressure $\sim$ 1 torr) are very close to those measured by flash photolysis ($\sim$160 torr) (16), this suggests that these reactions have already reached their high pressure limiting values (k ∞) at pressures in the torr range.

2) Variable temperature measurements

The rate constant with O_2 of the p-fluorobenzyl radical, considered as a model for the benzyl radical, has been measured in the range 297-433 K. Preliminary measurements indicate a strong negative temperature coefficient, in agreement with the following Arrhenius expression :

$$k = 4 \times 10^{-15} \exp (1590/T) \, cm^3 \, molec^{-1} \, s^{-1}$$

This expression disagrees with the absence of any variation observed by Laser photolysis/Laser Induced Fluorescence (17) in the range 295-373 K ; however, it is in agreement with the lack of reactivity of benzyl with O_2 noticed by Troe et al (20) in their shock tube investigations ; furthermore, a few negative temperature coefficients have also been reported for the following (R° + O_2 ---> products) reaction rates : R° = neopentyl (21), R° = ethyl (at constant [M]) (22), R° = i - C_4H_3 (23).

REFERENCES

(1) R. Atkinson, Chem. Rev. 85 (1986) p. 69
(2) R. Atkinson, J. Phys. and Chemical Reference data, Monograph n° 1 (1989)
(3) K. Brozinski, G.T. Linderis, T.A. Litzinger and I. Glassman
21 st Symp. (int) on combustion (1986) p. 833
(4) R.R. Baldwin, M. Scott, R.W. Walker
21 st Symp. (int) on combustion (1986) p.991
(5) V.S. Rao, G.B. Skinner
21 st Symp. (int) on combustion (1986) p. 809
(6) W. Müller-Markgraf and J. Troe
21 st Symp. (int) on combustion (1986) p. 815
(7) J.J. Schwab and J.G. Anderson, J. Quant. Spectros.
Radiative transfer 27 (1982) 445
(8) M.A. Hoffbauer and J.W. Hudgens, J. Phys. Chem. 89 (1985) 5152

(9) J. Ebrecht, W. Hack, H. Gg. Wagner, Berichte Bunsenges Phys. Chem. 93 (1989) 619

(10) M. Bartels, J. Edelbüttel-Einhauss, K. Hoyerman, 22 sd Symp. (int) on combustion, Seattle (1988) 1041

(11) M. Fukushima, K. Obi, J. Chem. Phys. 93 (1990) 8488

(12) T.R. Charlton, B.A. Trush, Chem. Phys. lett. 125 (1986) 547

(13) T.F. Bindley, A.T. Watts, S. Walker, Trans. Faraday Soc. 60 (1964) 1

(14) U. Wilke, W. Schmidt, Opt. Comm. 19 (1976) 116

(15) G. Helas, M. Flanz, P. Warneck, Intern. J. Environ. Anal. Chem. 10 (1981) 155

(16) T. Ebata, K. Obi, I. Tanaka, Chem. Phys lett. 77 (1981) 480

(17) H.H. Nelson, J.R. Mc Donald, J. Phys. Chem. 86 (1982) 1242

(18) M. Bartels, J. Edelbuttel-Einhaus, K. Hoyermann
Proceedings of the 22 th Symposium on combustion (1988) 1041

(19) K. Tokumara, H. Nosaka, T. Ozaki, Chem. Phys. lett. 169 (1990) 321

(20) H. Hippler, J. Troe
23 rd (int) symposium on combustion, Orléans (1990) paper n° 55 p. 28

(21) Z. Xi, W-J Han, K.D. Bayes
J. Phys. Chem. 92 (1988) 3450

(22) A.F. Wagner, I.R. Slagle, D. Sarzynski, D. Gutman
J. Phys Chem. 94 (1990) 1854

(23) I.R. Slagle, J.R. Bernhardt, D. Gutman
22 nd (int) Symp. combustion (1988) p. 953

Radical	Reactant			Ref
	O_2	NO	NO_2	
benzyl	0.99	9.5		(16)
	1.5			(17)
	> 0.5			(18)
p-fluorobenzyl	0.82	10	49	this work
m-fluorobenzyl	0.6	9	48	this work
o-methylbenzyl	1.2	9.4	50	this work
o-methylbenzyl	1.2	8.6		(16)
m-methylbenzyl	1.1	13	60	this work

Table 1 : rate constants of benzyl and substituted benzyl radicals (in 10^{-12} cm^3 $molec^{-1}$ s^{-1})
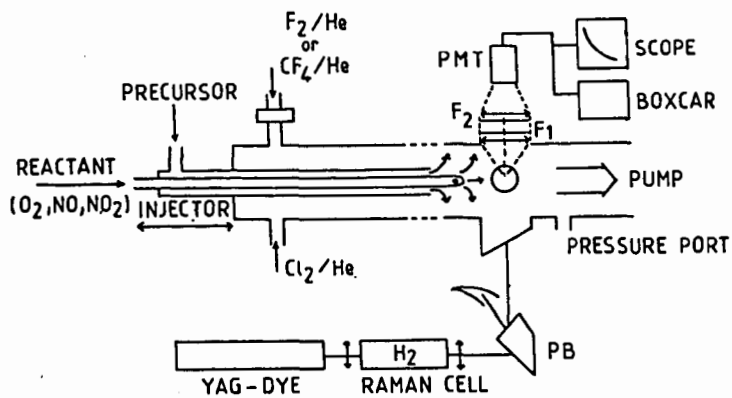
FIG.1

SCHEMATIC OF THE EXPERIMENTAL SET-UP
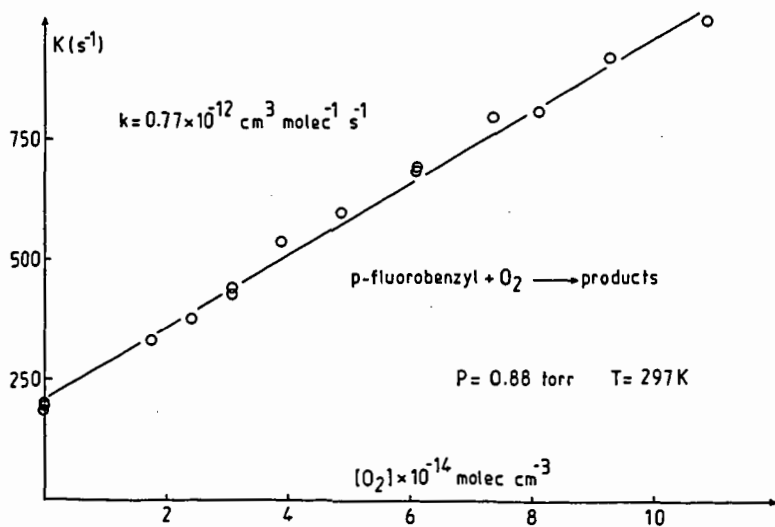
FIG.2b:PSEUDO-FIRST-ORDER RATE CONSTANTS($K(s^{-1})$)
VERSUS OXYGEN CONCENTRATION
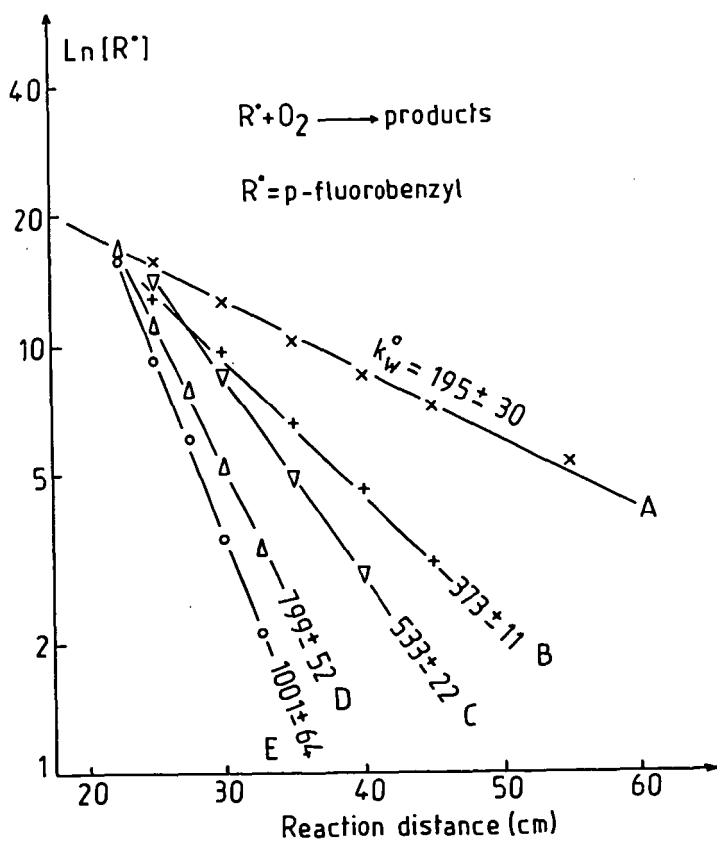
FIG 2a:RADICAL DECAY PLOTS VERSUS INJECTOR DISPLACEMENT
(REACTION DISTANCE)FOR VARIOUS OXYGEN CONCENTRATONS
(in 10^{+14} molec cm^{-3}):A(0),B(2.42),C(4.27),D(7.43)
E(10.9);THE CORRESPONDING SLOPES ARE IN s^{-1}

KINETICS OF REACTIONS OF PROTOTYPICAL AROMATIC HYDROCARBONS
WITH O (^{3}P) ATOMS AND CH$_2$ ($\tilde{X}$ ^{3}B$_1$) RADICALS: A COMPARATIVE STUDY

F. Temps and H. Gg. Wagner
Max-Planck-Institut für Strömungsforschung, Bunsenstrasse 10,
3400 Göttingen, Germany

Keywords: Aromatics, kinetics, methylene radicals, oxygen atoms.

INTRODUCTION

Mono- and polycyclic aromatic hydrocarbons constitute important intermediates and
by-products of technical combustion processes (see, e.g., [1]). Their build-up
and subsequent fate is well appreciated to be critically determined by reactions
with small, highly reactive O- or C-containing radicals. However, despite their
importance, the detailed mechanisms and kinetics of the distinctive elementary
reactions which can take place still present many questions. In the present pa-
per we consider reactions of selected aromatic hydrocarbons with two particularly
interesting free radicals, namely O (^{3}P) ($\equiv$ ^{3}O) and CH$_2$ ($\tilde{X}$ ^{3}B$_1$) ($\equiv$ ^{3}CH$_2$). While
O is an important oxidizing species, CH$_2$ as the most abundant highly reactive C-
-entered small radical in flames can contribute to the build-up of larger mole-
cules by adding reactive side groups to a substrate. Recent experimental results
for the kinetics of both species with prototypical unsubstituted mono- and poly-
cyclic aromatics as well as simple alkyl substituted derivatives are summarized.
Reactants include benzene, naphtalene, phenanthrene, toluene, ethylbenzene, and
cumene. The investigations were motivated by the desire to find some simple cor-
relations which would help to estimate rate parameters for ^{3}O or ^{3}CH$_2$ with other
reactants for which experiments cannot be performed easily. Thus, the focus is
on a critical comparison of the chemical reactivities of the two radicals, which
since they are isoelectronic are expected to exhibit parallel reactivities. Ana-
logies have been observed concerning addition reactions to the aromatics. On the
other hand, H atom abstraction from alkyl side chains could only be observed for
^{3}CH$_2$ but seems to play little role for ^{3}O. A difference with dramatic importance
to combustion processes arises as a consequence of the low singlet-triplet split-
ting between CH$_2$ ($\tilde{X}$) and CH$_2$ ($\tilde{a}$ ^{1}A$_1$) ($\equiv$ ^{1}CH$_2$), ΔH_0^0 = 37.7 kJ/mol [2].

EXPERIMENTAL

Experimental studies of reactions of ^{3}O and ^{3}CH$_2$ with aromatics A have been per-
formed using the discharge flow technique. Experimental set-ups have been de-
scribed [3a, 4]. Reactions of ^{3}O atoms were studied in the temperature range 300
K $\leq$ T $\leq$ 880 K under pseudo-first-order conditions with [O] $\gg$ [A]. Absolute O
concentrations were determined using the titration reaction N + NO. Concentrati-
on-versus-time profiles of O and A were followed by mass spectrometry. The reac-
tions of ^{3}O with benzene and toluene were also investigated using the shock tube
technique [3e-f]. Reactions of ^{3}CH$_2$ were studied in the temperature range 360 K
$\leq$ T $\leq$ 700 K under conditions [A] $\gg$ [^{3}CH$_2$] with Laser Magnetic Resonance (LMR) de-
tection of ^{3}CH$_2$. The reaction O + CH$_2$CO $\longrightarrow$ CH$_2$ + CO$_2$ served as the radical sour-
ce. Reaction product were determined by GC or GC-MS analysis after photolyzing
CH$_2$CO at either λ_1=366 or λ_2=312 nm in a static cell in the presence of reactants
A [5a]. CH$_2$CO photodissociation at these wavelengths yields practically only
^{3}CH$_2$ or ^{1}CH$_2$, respectively [6].

RESULTS AND DISCUSSION

The rate coefficients for the reactions of ^3O with reactants A can be determined
directly from the pseudo-first-order decay plots of [A] and the known O concen-
trations. Performing experiments under the condition $[O] \gg [A]$ has the advantage
that heterogeneous processes and consecutive reactions of the various products
can hardly affect the kinetic results. ^1O atoms play no role in thermal systems.

Data analysis for the reactions of $^3CH_2$ is somewhat more involved. Rate con-
stants obtained from pseudo-first-order decay plots of $[^3CH_2]$ in the absence and
presence of a large excess of [A] refer to the total depletion of $^3CH_2$ via all
possible pathways [7]. In the first place one has the reactive channels (T) of
$^3CH_2$ with the substrates. However, because of the small singlet-triplet split-
ting, partial thermal equilibration (E/D) with collision partners M between the
two CH_2 electronic states has to be taken into account as well. $^1CH_2$ undergoes
very fast consecutive reactions (S) with the reactants:

$^3CH_2 + A$	$\longrightarrow$	products	(T)
$^3CH_2 + M$	$\longrightarrow$	$^1CH_2 + M$	(E)
$^1CH_2 + M$	$\longrightarrow$	$^3CH_2 + M$	(D)
$^1CH_2 + A$	$\longrightarrow$	products.	(S)
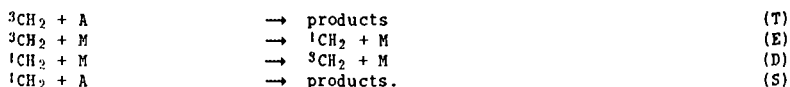
With the steady state assumption for $^1CH_2$, the rate coefficients for deactivation
and reaction of $^1CH_2$ taken from independent measurements [8] and the rate for
$^3CH_2$ excitation from the equilibrium constant for $^3CH_2 \rightleftharpoons {}^1CH_2$, the experimental,
directly measured effecctive rate constants can be separated to determine the
rate coefficients for the $^3CH_2$ reactive channels (T) [5d, 7].

REACTIONS OF ^3O WITH UNSUBSTITUTED AROMATICS: The rate constants for the reac-
tions of ^3O with the mono- and polycyclic unsubstituted aromatic hydrocarbons

^3O + benzene	$\longrightarrow$	products	(1)
^3O + naphtalene	$\longrightarrow$	products	(2)
^3O + phenanthrene	$\longrightarrow$	products	(3)
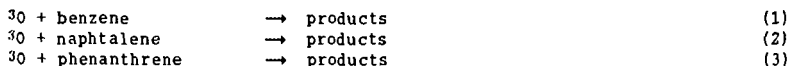
are shown as a function of temperature in Fig. 1. Data points are from [3a-e].
Results for reaction (1) obtained in other laboratories (for references see [3a])
are in good agreement. Table 1 summarizes the Arrhenius parameters. The reacti-
ons can be seen to exhibit moderate activation energies. In accordance with the-
oretical expectations [9] benzene is the least reactive molecule. Naphtalene and
phenanthrene behave very similarly. It is pointed out that the data for reacti-
ons (1) - (3) are in line with results for related molecules such as halogenben-
zenes and pyridine [3i-j], which are less reactive than benzene, and biphenyl
[3d], which reacts somewhat faster. Furthermore, in view of the different elec-
tron configurations the reaction with anthracene is expected to be significantly
faster than the one with phenanthrene.

The reactions of ^3O with these aromatics proceed via addition to the ring systems
yielding a triplet biradical as primary product. However, intersystem crossing
to the singlet state is likely to be fast, and different isomerization and frag-
mentation reactions can also take place. The most exothermic reaction channels
are those leading to phenols, which at high pressures can be collisionally stabi-
lized. Formation of a seven-membered ring containing the O atom or of correspon-
ding "epoxy" isomers are other possibilities. In the low pressure regime H eli-
mination to yield phenoxy type radicals has been observed, while elimination of
CO has been concluded to be of minor importance [1oa]. H atom abstraction by ^3O
from the aromatic ring is endothermic and has a high activation energy. Its role
under flame conditions can be estimated from an Evans-Polanyi plot.

1470

REACTIONS OF ^3O WITH ALKYL SUBSTITUTED AROMATICS: Compared to the unsubstituted aromatics discussed above, alkyl substituted derivatives stand out for their two reactive centers, the aromatic ring and the side chain. The measured activation energies and preexponential factors for the selected reactions

$$^3O + \text{toluene} \longrightarrow \text{products} \qquad (4)$$
$$^3O + \text{ethylbenzene} \longrightarrow \text{products} \qquad (5)$$
$$^3O + \text{cumene} \longrightarrow \text{products} \qquad (6)$$
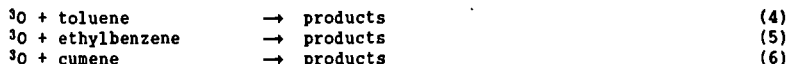
are given in Table 1. Experiments have been described in some detail in [3a, f, h]. Reaction (4) has also been studied in several laboratories (for references see [3a]), the different results being in good agreement with each other. The overall rate constants $k_4(T)$ - $k_6(T)$ and, for comparison, $k_1(T)$ are plotted in Figure 2. Considering the overall body of data it is apparent that the kinetics of the reactions of ^3O with benzene derivatives containing a single alkyl group are virtually identical under the conditions used. The reactions are somewhat faster than with benzene. However, there is little if any dependence on the nature of the alkyl chain (methyl vs. ethyl vs. isopropyl). Data for xylenes [3h] indicate that a second alkyl substituent leads to some further acceleration of the reaction.

Concerning the reaction mechanism, the question arises whether the main reaction channels involve attack by ^3O of the aromatic ring or of the alkyl group. Because of the weak benzylic C-H bonds (e.g., $\Delta H_{298}[\text{H-CH}_2\text{C}_6\text{H}_5]= 378$ kJ/mol [11]) H atom abstraction from these sites is exothermic. An Evans-Polanyi plot for reactions of ^3O with alkanes extrapolates to a very low value for the activation energy of H abstraction from toluene of ≈ 10 kJ/mol. Accordingly, H abstraction might be expected to constitute a main channel. In contrast, in a shock tube investigation of reaction (4) the OH channel has been determined to account for only 10 % at T $\approx$ 1100 - 1350 K. In a crossed molecular beam study of reaction (4) the addition-elimination products CH_3 + phenoxy and H + cresoxy were observed [10b]. Note also that the similarity of reactivities of toluene, ethylbenzene, and cumene despite of the significantly distinct benzylic C-H bond energies can be taken as evidence against H abstraction. However, an unambiguous answer cannot yet be given. Further experimental work is underway [12].

REACTIONS OF $^3CH_2$ WITH UNSUBSTITUTED AROMATICS: The rate parameters for the corresponding reactions of $^3CH_2$,

$$^3CH_2 + \text{benzene} \longrightarrow \text{products} \qquad (7)$$
$$^3CH_2 + \text{naphtalene} \longrightarrow \text{products} \qquad (8)$$
$$^3CH_2 + \text{phenanthrene} \longrightarrow \text{products}, \qquad (9)$$
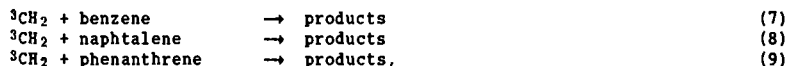
are listed in Table 1 [5b, e]. The different data points obtained from the LMR measurements and, for benzene, from an analysis of stable end products at room temperature are plotted in Arrhenius form in Fig. 1. Corrections for contributions from excitation to the singlet state and consecutive $^1CH_2$ reactions were applied as described [7]. In comparison to ^3O, $^3CH_2$ can be seen to be significantly less reactive. In particular, the reaction of $^3CH_2$ with benzene (7) exhibits almost twice as high an activation energy, its value being virtually equal to the CH_2 singlet-triplet splitting. Reactions (8) and (9) can be seen to be faster than (8), similar to the observations for ^3O, but still slower than ^3O + benzene.

Fig. 3 shows product histograms for $^3CH_2$ as well as $^1CH_2$ + benzene [5a]. $^3CH_2$ reacts via addition to the ring system. The product distributions under different conditions, including flame temperatures, can be rationalized with the help of unimolecular rate theory and the energy diagram of Fig. 4. At room temperature and pressures above a few mbars the reaction is in its high pressure limit

and cycloheptatriene is the main product. H abstraction by $^3CH_2$ from the aroma-
tic ring would have an activation energy far above the singlet-triplet separation
and thus cannot play a role in practical systems. The observed small yield of
toluene (see Fig. 3) is an unambiguous manifestation of the partial thermal equi-
libration between $^3CH_2$ and $^1CH_2$ taking place even at room temperature. $^1CH_2$ re-
acts with benzene either via addition to the aromatic ring, giving cycloheptatri-
ene as primary product, or via insertion into a C-H bond to yield toluene. Reac-
tion products of naphtalene and phenanthrene can be rationalized by analogy.

REACTIONS OF $^3CH_2$ WITH ALKYL SUBSTITUTED AROMATICS: The results for reactions of
$^3CH_2$ with a series of alkylbenzenes,

$$^3CH_2 + \text{toluene} \quad \longrightarrow \quad \text{products} \qquad (10)$$
$$^3CH_2 + \text{ethylbenzene} \quad \longrightarrow \quad \text{products} \qquad (11)$$
$$^3CH_2 + \text{cumene} \quad \longrightarrow \quad \text{products} \qquad (12)$$
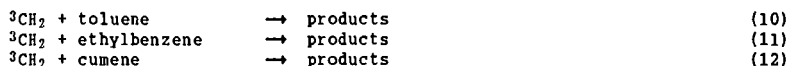
are given in Table 1 and illustrated in Fig. 2 [5c, d]. Reaction (11) has been
discussed in some detail before [5d]. However, with the data for the related mo-
lecules the overall picture becomes apparent. The reactions of $^3CH_2$ with alkyl-
benzenes have much higher activation energies than what has been measured for ^3O.
A most striking difference is the observation from Fig. 2 that the rate coeffici-
ents for (10) – (12) cannot be represented by single Arrhenius expressions. In-
stead, one has to distinguish two regimes. At high temperatures (> 450 K) the
different alkylbenzenes exhibit virtually identical kinetics, regardless of the
nature of the side group. "High temperature" activation energies for all three
molecules are close to the one for benzene, suggesting addition of the $^3CH_2$ to
the ring to account for the reaction. Similar behaviour has also been observed
for p-xylene [5c]. Product yields can be predicted using unimolecular rate theo-
ry [5d]. At temperatures below 450 K reaction channels with much lower activa-
tion energies and lower preexponential factors play a role, and the kinetics of
toluene, ethylbenzene, and cumene become distinct. Measured product distributi-
ons (see Fig. 3, [5a]) for reactions (10) and (12) indicate the importance of H
abstraction from the alkyl groups of these molecules under these conditions. The
observed high yields of ethylbenzene from (10) or n-propylbenzene and cumene from
(11) are produced via the subsequent cross recombination of the primary products
CH_3 and the respective "benzyl" radicals, e.g.

$$^3CH_2 + \text{toluene} \quad \longrightarrow \quad CH_3 + \text{benzyl}$$
$$CH_3 + \text{benzyl} + M \quad \longrightarrow \quad \text{ethylbenzene} + M.$$

The combination of addition and abstraction channels produces the apparent curva-
ture in the Arrhenius plots.

DISCUSSION: The general observation has been that $^3CH_2$ is a much less reactive
species than ^3O. However, interesting common trends as well as some differences
can be observed which shall be pointed out in the following.

From a study of H abstraction reactions from saturated hydrocarbons [7] the reac-
tivities of $^3CH_2$ are to vary with reactants in a manner parallel to the better
known trends for ^3O. Fig. 5 shows the respective correlation. The differences
in the activation energies for both species are of the order of only 5 kJ/mol.
However, the bond strength is higher in the product $H-CH_2$ than in $H-O$ (461 kJ/mol
vs. 428 kJ/mol). The preexponential factors for reactions of $^3CH_2$ had been found
to be lower by roughly an order of magnitude than for ^3O, reflecting the steric
requirements to form the transition states [7].

The reactions of ^3O and $^3CH_2$ with the aromatic hydrocarbons, as with other unsa-
turated reactants, are dominated by the electrophilic character of the radicals.

The correlations between activation energies for corresponding reactions are shown in Fig. 5. Different families of reactants (alkenes vs. alkines vs. unsubstituted aromatics vs. alkylaromatics) exhibit different trends. For ^3O the activation energies are known to correlate with the ionization potentials of the reactants [13, 3d]. Analogous trends can be observed for $^3CH_2$. Some theoretical support for such a correlation stems from recent ab initio quantum chemical computations of the potential energy surface for the reaction of $^3CH_2$ with C_2H_4 by Peyerimhoff and coworkers [14], who found the critical phase of the reaction to be accompanied by a charge transfer from the C_2H_4 moiety towards the methylene C. Loosely speaking, the energetics of the transition state regions might thus be expected to depend on the ease of charge transfer from the reactant, for which the ionization potential is a rough measure. Other factors, however, play a role as well. For instance, the activation energies for reaction of $^3CH_2$ with tetramethylethylene and cycloheptatriene have been observed to be much higher than expected from the simple correlations [5e]. For the first molecule hindrance by the methyl groups must be considered, whereas for the latter electronic effects due to the three conjugated π-bonds can play a role.

The preexponential factors for the addition reactions of ^3O and $^3CH_2$ to aromatics differ little. It is noted, however, that the $^3CH_2$ values depend on the correction for the pathway via excitation of $^3CH_2$ to the singlet state. Thus, they contain somewhat higher systematic uncertainties than the activation energies. In view of the spectroscopically known singlet-triplet couplings in CH_2, it is an interesting speculation, whether the chemical differences between "$^1CH_2$" and "$^3CH_2$" decrease towards high temperatures (high internal excitation). $^1CH_2$ is known to react with hydrocarbons with close to unit collision efficiency [8]. At room temperature, the observed distinct products of CH_2 in the two spin configurations indicate that both species do react independently. This picture is substantiated by the ab initio potential surface of Peyerimhoff [14], who showed the minimum energy pathways for the approach of CH_2 in both spin states to C_2H_4 to be entirely different, leaving little room for singlet-triplet conversion during the reaction. Instead, CH_2 singlet-triplet intersystem crossing seems to be governed by long-range processes [8, 15]. Little is known, however, about the reaction dynamics of $^3CH_2$ in vibrationally excited states, which would certainly be of importance under the conditions of combustion processes. In any case, for modeling combustion processes the distinct chemistry of $^1CH_2$ which has been well established now [8] but which cannot be discussed here in more detail has to be taken into account.

REFERENCES

[1] (a) K. H. Homann, 20th Symposium (International) on Combustion, p. 857 (1985); (b) B. S. Haynes, H. Gg. Wagner, Prog. Energy Comb. Sci. 7, 229 (1981); (c) I. Glassman, 22nd Symposium (International) on Combustion, p. 295 (1989).
[2] P. Jensen, P. R. Bunker, J. Chem. Phys. 89, 1327 (1988).
[3] (a) M Tappe, V. Schliephake, H. Gg. Wagner, Z. Phys. Chem. NF 162, 129 (1989); (b) H. Frerichs, R. Koch, M. Tappe, H. Gg. Wagner, Z. Naturforsch 44a, 1119 (1989); (c) H. Frerichs, M. Tappe, H. Gg. Wagner, Ber. Bunsenges. Phys. Chem. 94, 1404 (1990); (d) H. Frerichs, M. Tappe, H. Gg. Wagner, 23rd Symposium (International) on Combustion, p. 000 (1990); (e) H. I. Leidreiter, H. Gg. Wagner, Z. Phys. Chem. NF 165, 1 (1989); (f) A. Hoffmann, M. Klatt, H. Gg. Wagner, Z. Phys. Chem. NF 168, 1 (1990); (g) H. Frerichs, R. Koch, V. Schliephake, M. Tappe, H. Gg. Wagner, Z. Phys. Chem. NF 166, 145 (1990); (h) H. Frerichs, V. Schliephake, M. Tappe, H. Gg. Wagner, Z. Phys. Chem. NF 165, 9 (1989); (i) H. Frerichs, M. Tappe, H. Gg. Wagner, Z. Phys. Chem. NF 162, 147 (1989; (j) H. Frerichs, V. Schliephake, M. Tappe, H. Gg. Wagner, Z. Phys. Chem. NF 166, 157 (1990).
[4] T. Böhland, F. Temps, H. Gg. Wagner, Z. Phys. Chem. NF 142, 129 (1984).

[5] (a) K. Heberger, MPI f. Strömungsforschung, Report 4a/1988, Göttingen, 1988;
(b) T. Böhland, F. Temps, H. Gg. Wagner, Ber. Bunsenges. Phys. Chem. 93, 80
(1989); (c) S. Völker, Diplom Thesis, Göttingen, 1987; (d) K. Heberger, F.
Temps, S. Völker, W. Wolf, H. Gg. Wagner, 23rd Symposium (International) on
Combustion, p. 000, 1990; (e) H. Kraus, Diplom Thesis, Göttingen, 1991.
[6] C. C. Hayden, D. M. Neumark, K. Shobatake, R. K. Sparks, Y. T. Lee, J. Chem.
Phys. 76, 3607 (1982).
[7] (a) S. Dobe, T. Böhland, F. Temps, H. Gg. Wagner, Ber. Bunsenges. Phys.
Chem. 89, 432 (1985); (b) T. Böhland, S. Dobe, F. Temps, H. Gg. Wagner, Ber.
Bunsenges. Phys. Chem. 89, 1110 (1985); T. Böhland, S. Dobe, F. Temps, H.
Gg. Wagner, MPI f. Strömungsforschung, report 11/1985, Göttingen, 1985.
[8] (a) M. N. R. Ashfold, M. A. Fullstone, G. Hancock, G. W. Ketley, Chem. Phys.
55, 245 (1981); (b) A. O. Langford, H. Petek, C. B. Moore, J. Chem. Phys.
78, 6650 (1983); (c) T. Böhland, F. Temps, H. Gg. Wagner, Ber. Bunsenges.
Phys. Chem. 89, 1013 (1985); (d) W. Hack, M. Koch, H. Gg. Wagner, A. Wilms,
Ber. Bunsenges. Phys. Chem. 92, 674 (1988); (e) W. Hack, M. Koch, R. Wage-
ner, H. Gg. Wagner, Ber. Bunsenges. Phys. Chem. 93, 165 (1989); (f) R. Wa-
gener, Z. Naturforsch. 45a, 649 (1990).
[9] E. Clar, The Aromatic Sextett, Wiley, 1972.
[10] (a) S. J. Sibener, R. J. Buss, P. Casavecchia, T. Hirooka, Y. T. Lee, J.
Chem. Phys. 72, 4341 (1980); (b) R. J. Baseman, R. J. Buss, P. Casavecchia,
Y. T. Lee, J. Am. Chem. Soc. 106, 4108 (1984).
[11] H. Hippler, J. Troe, J. Phys. Chem. 94, 3803 (1990).
[12] W. Hack, H. Thiesemann, H. Gg. Wagner, unpublished results.
[13] R. E. Huie, J. T. Herron, Progr. React. Kinet. 8, 1 (1975).
[14] W. Reuter, B. Engels, S. D. Peyerimhoff, in press.
[15] (a) U. Bley, M. Koch, F. Temps, H. Gg. Wagner, Ber. Bunsenges. Phys. Chem.
93, 833 (1989); (b) U. Bley, F. Temps, 19th Informal Conference on Photoche-
mistry, Ann Arbor, 1990.

TABLE 1: Arrhenius parameters for reactions of ^3O and $^3CH_2$ with aromatics.

Reaction	A $[cm^3/mol \cdot s]$	E_a [kJ/mol]
^3O + benzene	$2.4 \cdot 10^{13}$	19.5
^3O + naphtalene	$1.4 \cdot 10^{13}$	7.5
^3O + phenanthrene	$1.9 \cdot 10^{13}$	7.7
^3O + toluene[a]	$2.2 \cdot 10^{13}$	15.6
^3O + ethylbenzene[a]	$2.2 \cdot 10^{13}$	15.9
^3O + cumene[a]	$2.0 \cdot 10^{13}$	15.3
$^3CH_2$ + benzene	$3.0 \cdot 10^{13}$	37.9
$^3CH_2$ + naphtalene	$1.3 \cdot 10^{13}$	27.9
$^3CH_2$ + phenanthrene	$2.2 \cdot 10^{13}$	28.3
$^3CH_2$ + toluene[b]	$6.0 \cdot 10^{13}$	36.8
$^3CH_2$ + toluene[c]	$2.0 \cdot 10^{11}$	19.0
$^3CH_2$ + ethylbenzene[b]	$6.0 \cdot 10^{13}$	36.8
$^3CH_2$ + ethylbenzene[c]	$1.6 \cdot 10^{11}$	13.6
$^3CH_2$ + cumene[b]	$6.0 \cdot 10^{13}$	36.8
$^3CH_2$ + cumene[c]	$3.0 \cdot 10^{11}$	13.6

[a] Presumably addition reaction, see text.
[b] Addition reaction to aromatic ring, see text.
[c] Estimated values, H atom abstraction from alkyl group, see text.
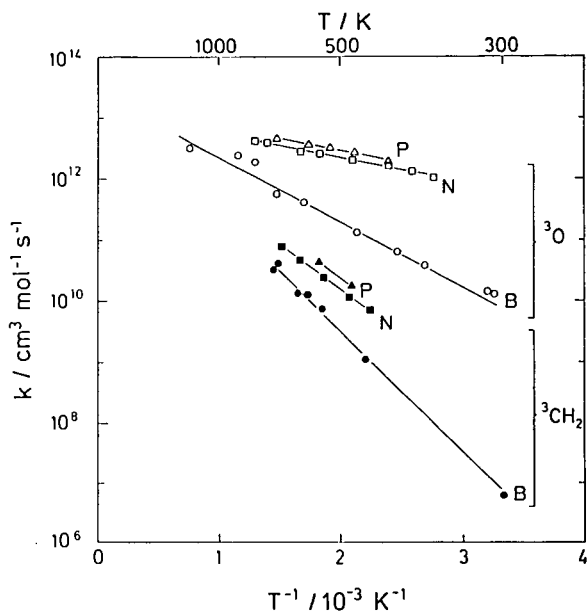
FIGURE 1: Arrhenius plot for the reactions of ^3O and $^3CH_2$ with benzene (B), naphtalene (N), and phenanthrene (P).
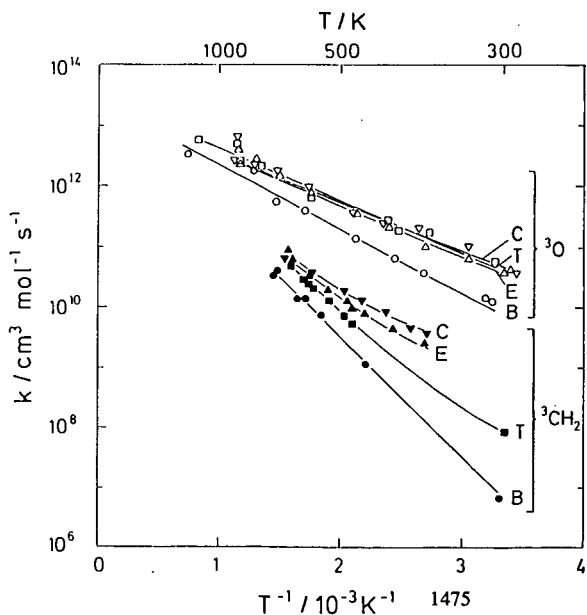
FIGURE 2: Arrhenius plot for the reactions of ^3O and $^3CH_2$ with benzene (B), toluene (T), ethylbenzene (E), and cumene (C).
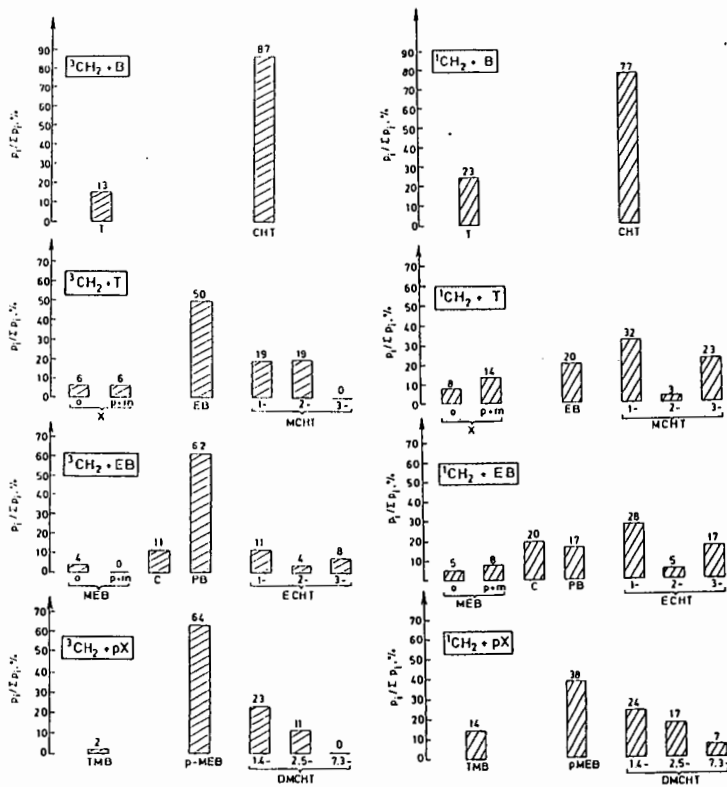
FIGURE 3: End product distributions for the reactions of $^3CH_2$ and $^1CH_2$ with ben-
zene, toluene, ethylbenzene, and p-xylene [5a]. B = benzene, T = toluene, CHT =
cycloheptatriene, X = xylene, EB = ethylbenzene, MCHT = methylcycloheptatriene,
MEB = methylethylbenzene, C = cumene, PB = n-propylbenzene, ECHT = ethylcyclo-
heptatriene, TMP = trimethylbenzene, MEB = methylethylbenzene, DMCHT = dimethyl-
cycloheptatriene.

Figure 4

(k/s⁻¹ , p(C₆H₆) = 60 mbar)

$(k/s^{-1}, p(C_6H_6) = 60 \text{ mbar})$

$\frac{6 \cdot 10^5}{4 \cdot 10^8}$ $\frac{10^4}{4 \cdot 10^8}$

100

0

-100

-200

-300

-400

$\Delta H_0^\circ / kJ\ mol^{-1}$

$<U_{500K}>$

$^1CH_2 \cdot$

$^3CH_2 \cdot$

$CH_3 \cdot$

$CH_2 \cdot H$

$C_2H_2 \cdot$

B CH
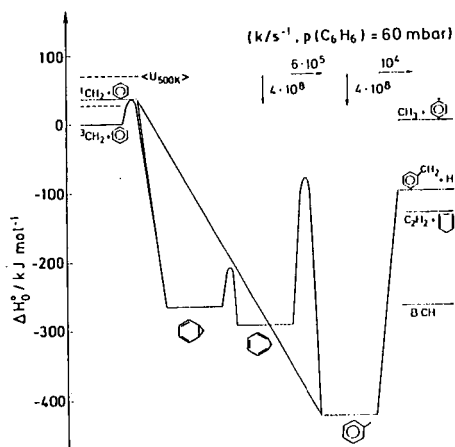
FIGURE 4: Energy diagram for the reactions of $^3CH_2$ and $^1CH_2$ with benzene [5b].

Figure 5

50

40

30

20

10

0

$E_A(CH_2\tilde{X})/kJ\ mol^{-1}$

-10   0   10   20   30   40   50

$E_A(O\ ^3P)/kJ\ mol^{-1}$

N P BP E T   B

C_2H_2

C_2H_4

C_4H_2

$1,3\cdot C_4H_6$

H_2CO

CH_3CHO $i\cdot C_4H_{10}$ $n\cdot C_6H_{14}$ C_3H_8 C_2H_6 CH_4
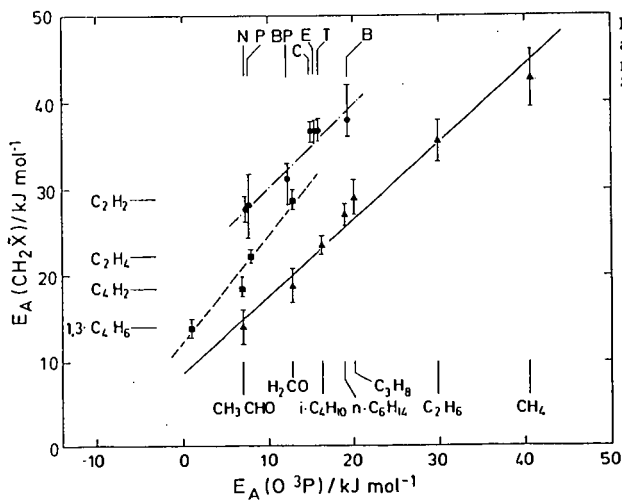
FIGURE 5: Correlation of activation energies for reactions of ^3O and $^3CH_2$.

1477

BENZENE/TOLUENE OXIDATION MODELS: STUDIES BASED ON FLOW-REACTOR AND
LAMINAR FLAME SPEED DATA

K. Brezinsky, F.N. Egolfopoulos, J.L. Emdee, C.K. Law and I. Glassman
Department of Mechanical and Aerospace Engineering
Princeton University
Princeton, N.J. 08544

Introduction

Aromatic hydrocarbons are expected to remain significant components of
gasolines and jet fuels because they offer many advantages such as a high
energy density (Goodger and Vere, 1985) and a high knock rating (ASTM Special
Technical Publication No. 225, 1958). In working towards a comprehensive
understanding of aromatic combustion, the high temperature oxidation mechanism
of toluene has been studied extensively at Princeton (Euchner, 1980, Venkat et
al., 1983, Brezinsky et al., 1984, Brezinsky, 1986, Litzinger, 1986, Brezinsky
et al., 1990). The mechanistic details that evolved in those studies have
indicated that at temperatures near 1000 K and 1 atmosphere pressure the early
time oxidation characteristics are dominated by side chain chemistry followed
by aromatics ring attack. The reactions of the small molecule fragments of the
aromatic ring, for the most part, occur later in the reaction sequence;
therefore a modest sized model, based largely on the mechanisms given by
Brezinsky (1986) for the oxidation of toluene near 1200 K. This model captures
the early time chemistry and the essential details of the later time small
molecule reactions for both toluene and benzene at flow reactor conditions.
The success of this model in predicting flow reactor species profiles, as will
be briefly described in the succeeding paragraphs, led to the application of
the model to the calculation of laminar flame speeds. The results of these
calculations will be described.

Experimental Data for Model Verification

The toluene oxidation data of Brezinsky et al. (1984) and the benzene
oxidation data of Lovell et al. (1989) were used to verify the toluene model
and its benzene sub-mechanism. These data were from Princeton flow reactor
experiments and include lean and rich equivalence ratios (ϕ) with initial
temperatures from 1100 K to 1190 K. The experimental details are described in
the individual papers.

Slight adjustments were made to the data presented in the above two
references to reflect recent calibration of the flow reactor rotameters and
velocity profile. The effect of these recent changes is to give reaction
times which are approximately 15-20% shorter than given in the original
papers. It should be noted that the velocity profile in the reactor tube is
still under investigation. Further details regarding the reduction of the
experimental data can be found in Emdee (1991).

Description and Analysis of the Model

The model consists of 68 reactions forming a benzene sub-model and 62
additional reactions for the toluene model. A complete description of the
model and associated thermodynamic properties of the chemical species is
available (Emdee et al., 1991; Emdee, 1991). Since benzene is a key
intermediate in the oxidation of toluene, the benzene sub-model results will
be considered before the toluene model is discussed.

Comparison of the Benzene Oxidation Model and Experimental Data

The flow reactor experiments approximate an adiabatic, constant

pressure, reaction system in which hydrodynamic and diffusional transport effects are small compared to changes brought about by chemical reaction. Thus, to make a comparison between the experimental data and the kinetic model, the reaction system was numerically treated as a time-dependent, adiabatic, constant pressure, homogenous mixture using CHEMKIN (Kee et al., 1980). Since mixing of the fuel and oxygen in the diffuser section of the flow reactor shortens the time for initial consumption of the fuel, the experimentally derived reaction time is only relative. Thus the comparison between experiment and model was made after shifting the experimental data in time so that the experimental fuel concentration at 50% of the measured consumption matched the model prediction. The time shift was constant for each experimental condition.

The experimental data and model results for benzene are compared in Fig. 1. Intermediate species profiles are shown for the $\phi = 0.91$ case only; further results for other conditions can be found in Emdee (1991).

The model prediction of the fuel decay was in good agreement with the experimental data for all three conditions considered. A fair match was achieved between the total C_4 and C_2 species. Lovell et al., did not make a distinction between the C_4's and the C_2's. However, they did indicate that the C_4's were vinyl acetylene (C_4H_4) and butadiene (C_4H_6) in about a 3:1 ratio, and the C_2's were "predominately acetylene and some ethylene". Because the present model can distinguish between species, the individual components of the C_4's and C_2's are also plotted in Fig. 1. The vinyl acetylene to butadiene ratio appears similar to the ratio indicated by Lovell et al., and the acetylene mole fraction is much larger than the ethylene mole fraction.

The mole fractions of phenoxy and cyclopentadienyl are included in the comparisons of phenol and cyclopentadiene because these species are resonantly stable and might be expected to build up to relatively high concentrations. If these radical species found a source of H in the sampling probe, they would have been detected as the stable parent species. Figure 1 shows that the inclusion of these radicals in the total phenol and cyclopentadiene profiles has a small effect on the former and a large effect on the latter.

Although good agreement between the predicted and experimental phenol profiles was achieved for the lean and near stoichiometric conditions, the model tended to underpredict the phenol mole fractions for rich conditions. The cyclopentadiene profiles were predicted with fair agreement by the total of the C_5H_6 and C_5H_5 concentrations for the lean and near stoichiometric conditions but was overpredicted by the rich condition. The overprediction of the cyclopentadiene coupled with the underprediction of the phenol for the rich case suggests that phenol is being consumed too quickly for this case. Carbon monoxide was underpredicted for all equivalence ratios considered which in part reflects the lack of a full sub-mechanism for small molecule chemistry.

Comparison of the Toluene Oxidation Model and the Experimental Data

The results of the calculations are shown in Figs. 2. The toluene model did very well at predicting the fuel consumption rate as well as the concentrations of many of the aromatic intermediates including benzene, benzaldehyde, ethylbenzene, benzyl alcohol and styrene for both lean and rich conditions. The concentrations of both phenol and cresol were however always underpredicted.

The figures show that the amounts of acetylene suggested by the model are at least a factor of two larger than the experimentally measured values.

All of the acetylene comes from the C_4 species which, although not shown, were underpredicted by the toluene model. Thus even though the C_2's and C_4's were predicted with fair agreement for the oxidation of benzene near 1100 K, the higher temperature (≈1190 K) oxidation model of toluene suggests that the decomposition rate of the C_4's to the C_2's may not have the correct temperature dependence.

In contrast to the benzene oxidation model in which CO was underpredicted, the CO concentrations predicted by the toluene model matched well with the experimental data. The better CO prediction by the toluene model can be partially attributed to the greater understanding of side chain chemistry which dominates the early oxidation of toluene as compared to the limited understanding of ring chemistry which was important in the oxidation of benzene.

Summary of Flow Reactor Modeling

By constructing a kinetic model for the oxidation of toluene based on mechanistic and kinetic information from the literature and from thermochemical estimates, it was possible to reasonably model flow reactor oxidation experiments of benzene and toluene. The consumption rate of toluene and benzene for both lean and rich oxidation conditions is predicted quite well by the model as are many of the intermediates. The predictive capability of the model is a significant improvement over previously reported results (Bittker, 1987,1988,1991; Fujii and Asaba, 1973; McLain et al., 1979).

The inhibitory effect of two major toluene consumption reactions

$$C_6H_5CH_3 + OH \rightarrow C_6H_5CH_2 + H_2O \qquad (1)$$
$$C_6H_5CH_3 + H \rightarrow C_6H_5CH_2 + H_2 \qquad (2)$$
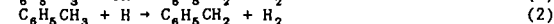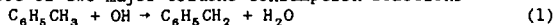
was clearly indicated by a linear sensitivity analysis. Furthermore, the high sensitivity of the model results to the abstraction reaction:

$$C_6H_5CH_3 + O_2 \rightarrow C_6H_5CH_2 + HO_2 \qquad (3)$$
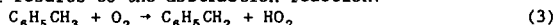
has allowed for an estimate of this reaction rate constant with reasonable confidence.

The major shortcomings of the model were found to be the over prediction of acetylene and the under-prediction of phenol compounds. The acetylene profiles were not predicted correctly for the higher temperature toluene oxidation even though the lower temperature benzene sub-model predicted reasonable levels. With regard to the phenol formation, the temperature dependence of the decomposition rate of phenoxy was expected to be the source of error since phenol was predicted reasonably well in the lower temperature benzene sub-model.

Flame Modelling

The modelling of measured laminar flame speeds, S_u, over a range of temperatures and pressures has been demonstrated to be an effective technique for developing and refining comprehensive chemical kinetic models (Egolfopoulos et al., 1991). For such modelling purposes, limited data from the measurement of laminar flame speeds of toluene and/or benzene are available in the literature (Garner et al., 1951, Gerstein et al., 1951, Wagner and Dugger, 1955, and Gibbs and Calcote, 1959). The encyclopedic work of Gibbs and Calcote (1959) contains flame speeds for benzene at atmospheric pressure over an equivalence ratio of 0.8 -1.3. These values were obtained using a bunsen burner conical flame and shadowgraphs for definition of the flame surface. Fristrom and Westenberg (1965) have pointed out the complications in defining the flame surface by shadowgraphy and these complications would affect the magnitude of the flame velocities reported by

Gibbs and Calcote. Similarly, Law (1988) has emphasized the role that flame stretch can play in the determination of flame speeds and pointed out the substantial variation in measured values that can result if the flame speeds are not evaluated in the limit of zero stretch (Egolfopoulos et al. 1989). All the aromatics flame speeds reported in the literature are affected by stretch. In the absence of stretch free flame speeds for aromatics, the flame speed values for benzene measured by Gibbs and Calcote were used for comparison with model predictions since their measurement technique tended to minimize stretch effects:

ϕ =	.8	.9	1.0	1.1	1.2	1.3	
S_u =	39.4	45.6	47.6	44.8	40.2	35.6	(cm/sec)

The data on the flame speeds of toluene are much more limited than for benzene. The value commonly found in textbooks for a stoichiometric, one atmosphere flame, 38.8 cm/sec, is attributable to Wagner and Dugger (1955). For comparison with the Gibbs and Calcote measured value, the stoichiometric, one atmosphere benzene flame speed measured by Wagner and Dugger was 44.6 cm/sec.

In order to model the reported flame speeds, the toluene model derived from flow reactor experiments was coupled to the PREMIX code (Kee et al., 1985). The calculated flame speeds for stoichiometric toluene/air and benzene/air mixtures were approximately 23 cm/sec - a value far beyond the range of error of the measured values. The low calculated flame speeds implied that the aromatics combustion process was not proceeding fast enough to the energy releasing, small molecule oxidation steps. The toluene model contained only a very basic sub-mechanism for the oxidation of species containing two or less carbon atoms in order to keep the number of reactions and species small. Therefore, the first attempt at altering the mechanism to obtain a higher flame speed consisted of replacing the abbreviated C_2 oxidation scheme with a more complete, validated one (Egolfopoulos et al., 1991). The substitution of this C_2 scheme led to a marginal increase of only 4 cm/sec.

A sensitivity analysis of the flame speed to each rate constant in the toluene model indicated that there was little sensitivity (less than 2%) to the alkyl side chain oxidation steps. Greater sensitivity (2% or more) was found for a subset of nine rate constants directly related to the oxidation of the aromatic ring and its fragments. The benzene flame calculations revealed a sensitivity to these same reactions. Of course, the greatest sensitivity of the flame speed was found to be for the CO + OH → CO_2 + H reaction (11%) and for H + O_2 → OH + H (21%). Since these latter two reactions have been extensively studied no further consideration was given to changing their rate constants. In view of the greater availability of benzene flame speed data and the sensitivity of both the toluene and benzene flame speeds to the same rate constants, the toluene mechanism was reduced, for ease of calculation and analysis, to a benzene mechanism by the removal of all the toluene related steps.

Among the rate constants having the most effect on the flame speed a number are uncertain either because they are estimated rather than measured, measured over a narrow range of temperature, or have been determined in only one set of experiments. Therefore, sequentially for each uncertain rate constant, the value of A in the three parameter representation of the rate constant, $k=AT^n exp(E_a/RT)$, was increased or decreased as indicated by the sensitivity analysis in order to "walk" the flame speed up into the 40 cm/sec range:

$C_6H_5O + H \rightarrow C_6H_5OH$; forward A decreased by 2.5 x; reverse increased 10x
$C_6H_5O \rightarrow C_5H_5 + CO$; forward A increased 10x
$C_6H_5 + O2 \rightarrow C_6H_5O + O$; forward A increased 10x
$C_6H_5 + OH \rightarrow C_5H_4OH + H$; forward A increased 10x

The result of the above changes was a calculated flame speed of 41.6 cm/sec. A sensitivity analysis of this calculated flame speed indicated that changes in the rate constants of the three reactions of C_5 species would have a significant effect (2% or more) on the flame speed. A ten fold increase in the forward and reverse A values of

$$C_5H_4O \rightarrow CO + 2C_2H_2$$
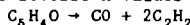
was sufficient to raise the stoichiometric flame speed to 43.8 cm/sec, a value lower than that measured by Gibbs and Calcote but within the range seemingly appropriate for benzene. The calculated flame speeds at other equivalence ratios were 31.2, 38.2, 48.7, and 50.1 cm/sec at $\phi = 0.8$, 0.9, 1.1 and 1.2 respectively.

Species profiles calculated with the altered model for flow reactor conditions were significantly changed from those described earlier in this article. The changes were not surprising since the altered rate constants were the same ones shown by sensitivity analysis of the benzene decay profile to be significant during the flow reactor modelling efforts. In particular, the altered rate constants led to an order of magnitude decrease in initial benzene concentration within 60 msec, maximization of the phenol concentration within 30 msec and, CO production and almost complete consumption within 120 msec. These latter observations suggest how the toluene/benzene model might be made more comprehensive in order to predict both flow reactor and flame speed results.

The altered model in its ability to approximately match the measured benzene flame speeds has required a much more rapid production and oxidation of the energy releasing, small molecule hydrocarbon fragments. However, the flow reactor profiles indicate that alteration of the rate constants in the above extent and manner is not fully justified. It appears that a subset of toluene/benzene reactions is needed that would not drastically affect the calculated species profiles at flow reactor temperatures but would lead to an accelerated production of small hydrocarbons at flame temperatures. This conclusion has two implications; the temperature dependent parameters of the above mentioned altered rate constants reactions may require re-adjustment in a way already suggested by some of the inadequacies revealed during flow reactor modelling and, the addition of high activation energy pyrolysis reactions, such as aromatic ring rupture steps, not currently in the toluene/benzene mechanism may be necessary in order to provide H atoms to drive the overall reaction progress. Both of these approaches to creating a comprehensive toluene/benzene model are currently being pursued.

References

ASTM Special Technical Publication No. 225; American Society of Testing Materials, Philadelphia, 1958.

Bittker, D. A., Detailed Mechanism of Benzene Oxidation; NASA Tech. Memo. 100202, 1987.

Bittker, D. A., Detailed Mechanism of Toluene Oxidation and Comparison with Benzene; NASA Tech. Memo. 100261, 1988.

Bittker, D. A., *Combust. Sci. Technol.* 1991, in press.

Brezinsky, K., Litzinger, T. A. and Glassman, I., *Int. J. Chem. Kinet.* 1984, 16, 1053.

Brezinsky, K., *Prog. Energy Combust. Sci.* 1986, 12, 1.

Brezinsky, K., Lovell, A. B. and Glassman, I., *Combust. Sci. Technol.* 1990, 70:1-3, 33.

Egolfopoulos, F.N., Cho, P. and Law, C.K., *Combust. Flame* 1989, 76, 375.

Egolfopoulos, F.N., Du, D.X. and Law, C.K., *Combust. Sci. Technol.* 1991, submitted.

Emdee, J. L., An Experimental and Modeling Study of the High Temperature Oxidation of the Xylenes; Ph.D. Thesis, Department of Mechanical and Aerospace Engineering, Princeton University, Princeton, NJ, 1991.

Emdee, J. L., Brezinsky K. and Glassman, I., *J. Phys. Chem.* 1991, submitted.

Euchner, J. A.: M.S.E. Thesis, Department of Mechanical and Aerospace Engineering, Princeton University, Princeton, NJ, 1980.

Fristrom, R.M. and Westenberg, A.A., *Flame Structure*, 1965, McGraw-Hill.

Fujii, N. and Asaba, T., *Fourteenth Symp. (Int.) Combust.*; The Combustion Institute, Pittsburgh, 1973, p.433.

Garner, F.H., Long, R. and Ashforth, G.K., *Fuel* 1951, 30, 17.

Gibbs, G.J. and Calcote, H.F., *J. Chem. Eng. Data*, 1959, 4, 226.

Goodger, E. and Vere, R., *Aviation Fuels Technology*; MacMillan Publishers Ltd.,   London, 1985.

Kee, R. J., Miller, J. A. and Jefferson, T. H., CHEMKIN: A General Purpose, Problem-Independent, Transportable, Fortran Chemical Kinetics Code Package; Sandia Nat. Lab. Report SAND80-8003, 1980.

Kee, R. J., Grcar, J. F., Smooke, M. D., and Miller, J. A. PREMIX; A Fortran Program for Modeling Steady Laminar One-Dimensional Premixed Flames; Sandia Report SAND 85-8240 UC4, 1985.

Kee, R. J., Rupley, F. M., and Miller, J. A. The Chemkin Thermodynamic Data Base; Sandia Nat. Lab. Report SAND87-8215, 1987.

Law, C.K., *Twenty-Second Symp. (Int.) Combust.*; The Combustion Institute, Pittsburgh, 1988, 1381.

Litzinger, T. A.: Ph.D. Thesis, Department of Mechanical and Aerospace Engineering, Princeton University, Princeton, NJ, 1986.

Litzinger, T. A., Brezinsky, K. and Glassman, I., *Combust. Flame* 1986, 63, 251.

Lovell, A. B., Brezinsky, K. and Glassman, I., *Twenty-Second Symp. (Int.) Combust.*; The Combustion Institute, Pittsburgh, 1989, p.1063.

McLain, A. G., Jachimowski, C. J. and Wilson, C. H., Chemical Kinetic Modeling of Benzene and Toluene Behind Shock Waves; NASA Tech. Paper 1472, 1979.

Wagner, P. and Dugger, G.L., *J. Am. Chem. Soc.* 1955, 77, 227.

Venkat, C., Brezinsky, K., and Glassman, I., *Nineteenth Symp. (Int.) Combust.*; The Combustion Institute, Pittsburgh, 1983, p.143.
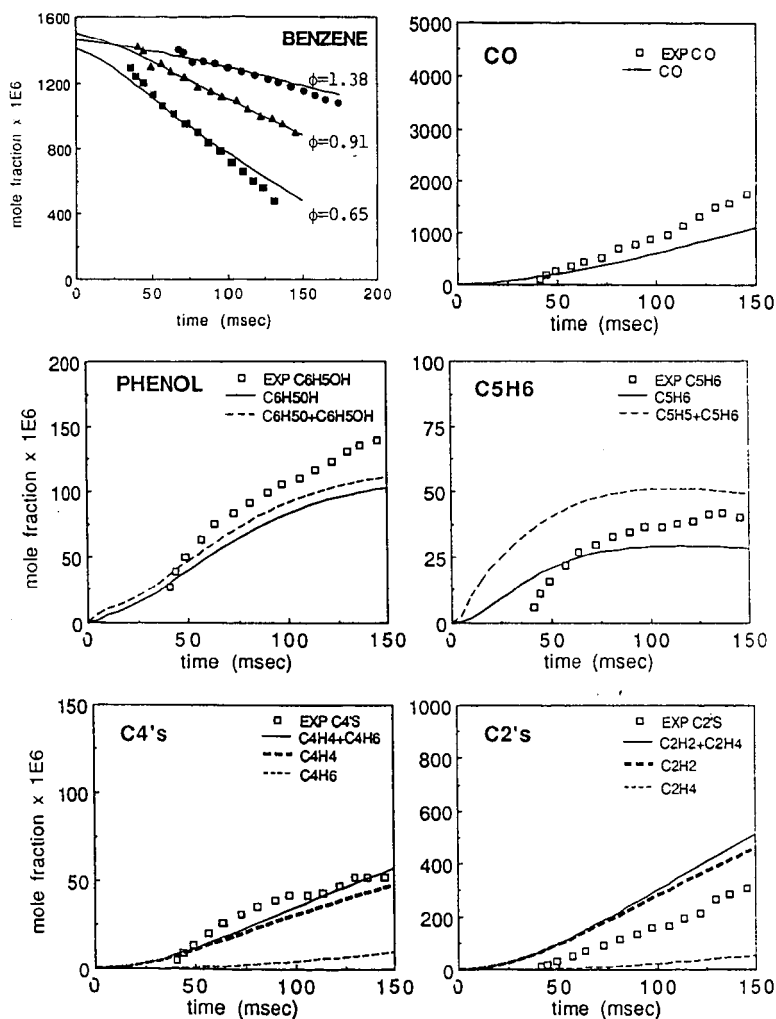
Fig. 1. Experimental (symbols) and model (lines) benzene decay profiles for three different equivalence ratios and, intermediates experimental and model profiles for a φ=0.91 oxidation of benzene.
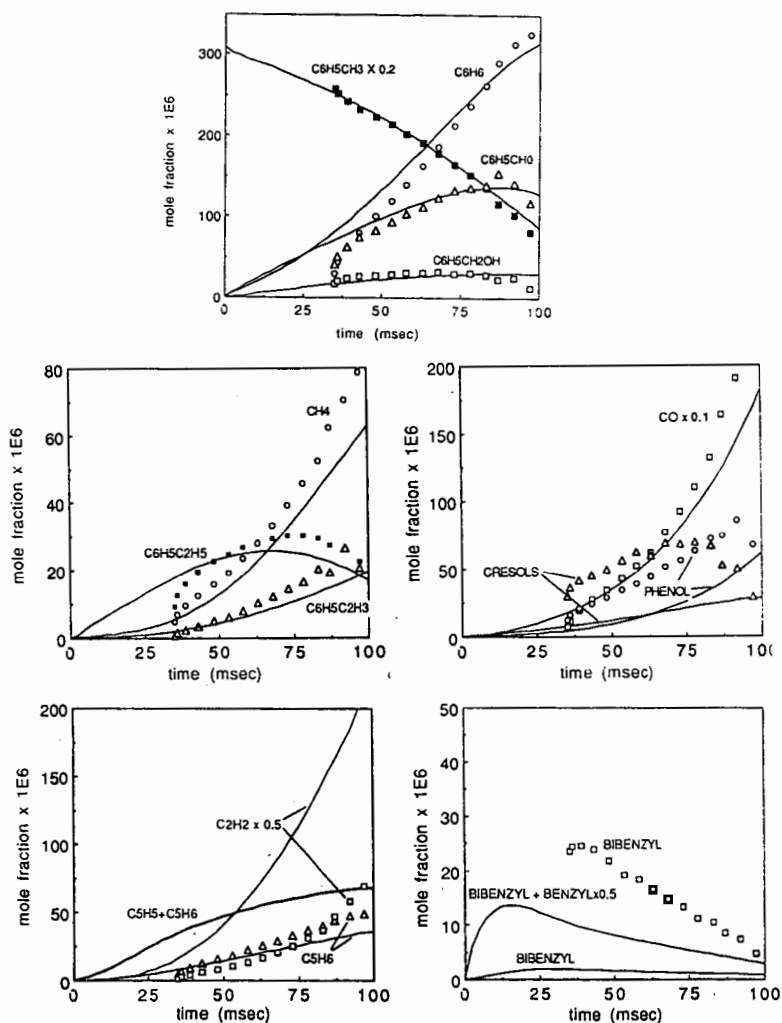
Fig. 2. Experimental (symbols) and model (lines) species profiles for a φ=0.69 oxidation of toluene.

A TENTATIVE DETAILED CHEMICAL SCHEME FOR THE OXIDATION OF BENZENE-AIR MIXTURES

Christophe Chevalier, Jürgen Warnatz
Institut für Technische Verbrennung, Universität Stuttgart
Pfaffenwaldring 12, 7000 Stuttgart 80, Germany

Keywords: Kinetics, numerical simulation, laminar flames and ignition of benzene.

INTRODUCTION

The increasing use of unleaded gasoline in western countries in the last 20 years has forced oil companies to find substitutes for the alkyl-lead compounds, in order to supply high-octane fuels. Among aromatic hydrocarbons, which are well known to have a high octane number, benzene is a preferred compound (up to 5% or more in liquid commercial fuels). Unfortunately, it has a pronounced propensity to form soot during its combustion (1). Nevertheless, a rather limited number of works on detailed chemical schemes has been published yet. Early studies considered the low temperature ignition of aromatic hydrocarbons in static reactors (2-9), where a major step is the addition of molecular oxygen to a phenyl radical, leading to a bridging peroxy radical which, according to Benson (10), is very unlikely to be formed at temperatures above 700 K. More recently shock tube (11) and flow reactor (12-15) experiments have pointed out the most important pathways at higher temperatures. It appears that a phenyl radical and O_2 react to form a phenoxy radical and an O atom. However, no detailed reaction mechanism for the oxidation of benzene in flames and for its auto-ignition over a wide range of conditions has been published yet. Based on a review of the rate coefficients proposed for each elementary reaction, a detailed chemical scheme is presented and discussed here. Numerical simulations of premixed laminar flames, and calculations of auto-ignition delay times are compared with experiments, in order to check the validity of the mechanism.

REACTION MECHANISM

The reaction mechanism presented here is based on a high temperature gas phase mechanism, which has been developed recently (16) for saturated and unsaturated hydrocarbons up to C_4. However, due to lack of space, this work (including several hundreds of literature references) cannot be presented here. Most of rate coefficients of the reactions involving C_6H_6 follow the recommendations of the CEC evaluation group (17). The reverse reaction rates have been calculated using the equilibrium constants (reactions characterized by "<-->"). Irreversible steps are denoted by "-->". Reactions directly related to the oxidation of benzene are discussed here, and summarized in table 1. The complete detailed mechanism contains 57 species and 475 elementary reactions.

1) Consumption of C_6H_6:
$$C_6H_6 \text{ <--> } C_6H_5 + H:$$
Due to the size of the benzene molecule, a fall-off behavior appears only for very low pressures; thus, at 1 bar, the high pressure rate coefficient may be used (18). This has been confirmed by RRKM calculations (Rice-Ramsberger-Kassel-Marcus theory).
$$C_6H_6 + H \text{ <--> } C_6H_7:$$
Measurements for this recombination reaction have only been carried out at low temperatures (T < 1000 K). The C_6H_7 radical may be one of the possible starting points for an opening of the cycle, but no rate coefficient is available for this step.
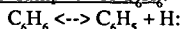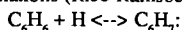
$C_6H_6 + H \longleftrightarrow C_6H_5 + H_2$:

Due to the scatter in the experimental data at high temperatures, it is difficult to evaluate the rate coefficient. Since this abstraction channel is necessary for a mechanism describing combustion in flames, the value of Fujii and Asaba has been taken (19).

$C_6H_6 + OH \longleftrightarrow C_6H_5 + H_2O$,

$C_6H_6 + OH \longrightarrow C_6H_5OH + H$:
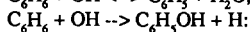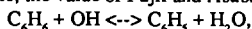
At high temperatures, the H-abstraction seems to be the dominant channel. The displacement reaction is probably not an elementary process (proceeding via a C_6H_6OH species), but cannot been neglected at high temperatures.

$C_6H_6 + O \longleftrightarrow C_6H_5 + OH$,

$C_6H_6 + O \longleftrightarrow C_6H_5OH$:
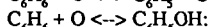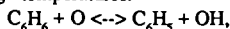
Experiments have been carried out up to 1000 K. Moreover, no clear separation between abstraction and addition was shown. We assumed the same reaction rate for both channels.

$C_6H_6 + O_2 \longleftrightarrow$ products:
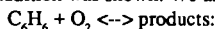
No data was found for this reaction, which may play an important role for the ignition.

2) Consumption of C_6H_5:

Most of the reactions concerning the phenyl radical have been studied in relation with the thermal decomposition. Thus, reactions with other radicals are not well known.

$C_6H_5 + H \longleftrightarrow C_6H_6$:
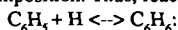
The reverse of this recombination reaction has been discussed above.

$C_6H_5 \longleftrightarrow l-C_6H_5$:
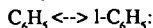
According to Braun-Unkhoff et al. (20), who monitored H atoms, the opening of the cycle is the only possible decomposition, the pathways leading to $C_4H_3 + C_2H_2$, $C_6H_4 + H$, $C_4H_2 + C_2H_3$, or $C_4H_4 + C_2H$ either have a too high reaction enthalpy, or produce not enough H atoms. The linear $l-C_6H_5$ radical may then decompose either to $C_4H_3 + C_2H_2$ or to $l-C_6H_4 + H$, both reactions being pressure dependent.

$C_6H_5 + O_2 \longrightarrow$ Products:
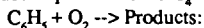
This major oxidation step is unfortunately not well known. Venkat et al. (13) propose the formation of a phenoxy radical $C_6H_5O + O$, but no rate coefficient for this reaction has been measured. Fujii and Asaba (19) suggest a complex reaction, leading to $C_4H_4 + H + 2CO$.

$C_6H_5 + C_6H_6 \longleftrightarrow C_{12}H_{10} + H$,

$C_6H_5 + CH_3 \longleftrightarrow C_6H_5CH_3$:
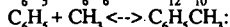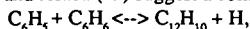
These reactions are not included in the mechanism at the moment, since they lead to biphenyl or toluene, which oxidation would require a much more complex mechanism.

3) Consumption of C_6H_5OH:

Phenol is formed in rather high amounts from benzene, by reaction with O and OH (see above), and its oxidation has to be included in the mechanism.

$C_6H_5OH + H \longleftrightarrow C_6H_5O + H_2$,

$C_6H_5OH + H \longleftrightarrow C_6H_6 + OH$:
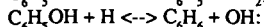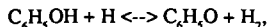
The only experiments available (21) show that the H-abstraction as well as the displacement reaction (the reverse one has been discussed earlier) both are possible at temperatures between 1000 and 1150 K.

$C_6H_5OH + OH \longleftrightarrow C_6H_5O + H_2O$,

$C_6H_5OH + OH \longleftrightarrow C_6H_4OH + H_2O$:
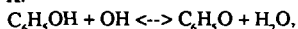
This reaction has also been investigated by He and others (21), who do not supply information about the branching ratios.

1487

4) <u>Consumption of C_6H_5O:</u>

    The only reaction reviewed by the CEC (17) has been proposed by Lin and Lin (22):

    $C_6H_5O \longleftrightarrow C_5H_5 + CO$,
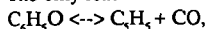
where the decomposition of the phenoxy leads to the formation of a cyclopentadienyl radical.

5) <u>Consumption of C_5H_5:</u>

    This species certainly reacts with radicals like O or OH, as suggested by Brezinsky (14), or with molecular oxygen (Venkat et al. (13)). However, the only pathway involving C_5H_5 for which a rate coefficient has been proposed (20) is reaction

    $C_5H_5 \longrightarrow l\text{-}C_5H_5$,
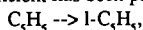
followed by the decomposition

    $l\text{-}C_5H_5 \longrightarrow C_3H_3 + C_2H_2$:
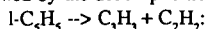
It seems that the lack of radical-radical routes for C_5H_5 is compensated by the semi-global reaction $C_6H_5 + O_2 \longrightarrow C_4H_4 + H + 2CO$, since the more detailed scheme proposed by Venkat (13) might be summarized as: $C_6H_5 + O_2 \longrightarrow C_6H_5O + O \longrightarrow C_5H_5 + CO + O \longrightarrow C_5H_5O + CO \longrightarrow C_4H_4 + H + 2CO$.

RESULTS AND DISCUSSION

    In order to check the mechanism, velocities of freely propagating premixed laminar flames as well as ignition delay times have been calculated, and compared with experiments, under non-sooting conditions (below the sooting limit: $\phi = 1.9$).

1) <u>Laminar flames:</u>

    The solid line in Fig. 1 shows the burning velocities of benzene-air mixtures at 298 K and 1 bar, computed for benzene contents from 1.9% to 3.8% (equivalence ratios $\phi = 0.7$ to 1.4). The figure also shows experimental data (23) available for comparison. The maximum computed burning velocity (47.6 cm/s) occurs in stoichiometric mixtures, in agreement with experimental results. For rich mixtures, the computed values lie slightly above the measurements, but in view of the uncertainties in the experiments and in the kinetic data (see above), this difference cannot be considered being significant.

    Fig. 2 shows the burning velocities of mixtures containing 1.5% to 5.0% benzene and 20.8% oxygen, diluted with nitrogen (equivalence ratios $\phi = 0.54$ to 1.80), P = 1 bar, $T_u = 298$ K, compared with experiments run under the same conditions (24). The maximum calculated speed (49.2 cm/s) is somewhat larger than the measured one (45.0 cm/s), and slightly shifted to lean mixtures ($\phi = 1.1$ instead of $\phi = 1.2$). Around stoichiometry, the computed velocities are found to be too fast (up to 9% discrepancy), but in rich mixtures, they are too slow (40% at most). Since the conditions of this experiment are very similar to those of the one presented first, this result is probably due to the reliability of the measuring techniques.

The pathways of the oxidation of C_6H_6 in a stoichiometric benzene/air flame and their relative importance are shown in Fig. 3. C_6H_6 is initially attacked by H, OH, and O radicals to form (i) benzyl radicals, which react with molecular oxygen as described above, (ii) phenol, which, after H-abstraction, leads to cyclopentadienyl radicals. Thus, it is clear that the mechanism leads to two parallel pathways, one being the phenyl route, the other the phenol route.

    The sensitivity analysis in Fig. 4 shows the rate limiting reactions, for lean, stoichiometric, and rich mixtures. The sensitivities are obtained by a systematic variation of the preexponential factors of the rate constants . For the ith reaction, the relative sensitivity $S_i = \Delta \ln v_u / \Delta \ln k_i$ denotes the change of the burning velocity with respect to a change of the preexponential factor.

The sensitivity analysis for the reactions of the H_2-CO-O_2 have been discussed earlier (25, 26). However, it is worth noting that the most sensitive reactions are (i) for all equivalence ratios the chain branching step

$$H + O_2 \quad \text{--> } O + OH, \qquad\qquad (R1)$$
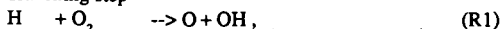
(ii) in lean and stoichiometric flames the heat-producing reaction

$$CO + OH \quad \text{--> } CO_2 + H. \qquad\qquad (R39)$$
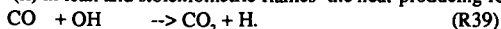
The reactions which are specific to the combustion of benzene are:

$$C_6H_5 \qquad\qquad \text{--> } l\text{-}C_6H_5 \qquad\qquad (R449)$$
$$C_6H_5 + O_2 \qquad \text{--> } C_4H_4 + H + 2CO \qquad (R453)$$
$$C_6H_5 + H \qquad \text{--> } C_6H_6 \qquad\qquad (R458)$$
$$C_6H_6 + O \qquad \text{--> } C_6H_5 + OH \qquad\qquad (R466)$$
$$C_6H_5OH + H \qquad \text{--> } C_6H_6 + OH \qquad\qquad (R472)$$
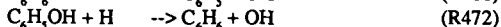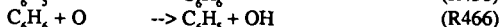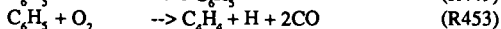
The decomposition of the linear l-C_6H_5 radical (produced in reaction R449) leads rapidly to the formation of H atoms; therefore, reaction R449 has a positive sensitivity in rich flames, where the molecular oxygen concentration is too low to oxidize all of the phenyl radicals through reaction R453. Reaction R453 directly produces H radicals, and has almost the same sensitivity under lean and as under rich conditions. The recombination reaction R458 deprives reaction R1 of H atoms and reactions R449 and R453 of phenyl radicals; its sensitivity is strongly negative. In lean flames, the branching reaction R466 shows a positive sensitivity. The H-consuming reaction R472 has a negative sensitivity, because it competes with reaction R1.

These results point out that a deep insight into the reaction between phenyl and molecular oxygen is fundamental, because the whole mechanism depends on the route chosen.

2) Ignition delay times:

Zero-dimensional simulations can be used to calculate ignition delay times of benzene-oxygen-argon mixtures in shock tubes. Fig. 5 shows calculated ignition delay times compared with experimental results of Burcat et al. (27), for stoichiometric mixtures containing 1.69% benzene, at pressures behind reflected shock between 2 and 3 bar, and at temperatures in the range 1286 to 1608 K. If a rather good agreement is observed at the highest temperatures (above 1450 K), an increasing discrepancy appears when decreasing the temperature.

Sensitivity tests with respect to the OH concentration (Fig. 6) show the rate limiting reactions during the induction period at the lowest investigated temperature (1286 K). The main rate-limiting process here is the chain branching reaction, too.

$$H + O_2 \quad \text{--> } O + OH \qquad\qquad (R1)$$
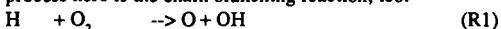
which competes with the recombination reaction

$$H + O_2 + M \text{ --> } O + OH + M. \qquad\qquad (R15)$$
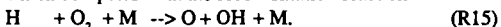
The H-atom producing reactions

$$C_6H_5 + O_2 \qquad \text{--> } C_4H_4 + H + 2CO \qquad (R453)$$
$$C_6H_6 \qquad\qquad \text{--> } C_6H_5 + H \qquad\qquad (R457)$$
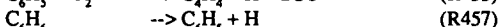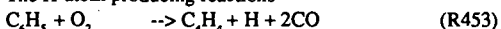
have also a pronounced positive sensitivity, in contrary to the H-consuming reaction

$$C_6H_6 + H \qquad \text{--> } C_6H_5 + H_2. \qquad\qquad (R461)$$
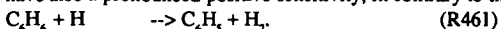
Furthermore, the chain branching reaction R466 has a very high positive sensitivity and competes with the termination reaction R468, which has of course a very strongly negative sensitivity:

$$C_6H_6 + O \qquad \text{--> } C_6H_5 + OH \qquad\qquad (R466)$$
$$C_6H_6 + O \qquad \text{--> } C_6H_5OH \qquad\qquad (R468)$$
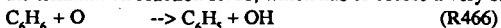
Further information about the relative importance of each channel is necessary to simulate correctly the ignition of benzene-oxygen mixtures.

CONCLUSIONS

1- A review of the elementary reactions for the high temperature oxidation of benzene has been carried out, in order to evaluate the current kinetic and thermodynamic knowledge in this field.

2- The calculation of premixed laminar flame velocities of benzene-air mixtures is in good agreement with experiments run at atmospheric pressure, over a wide range of equivalence ratios below the sooting limit. However, it would be helpful to get further data for some reactions (e.g. products, reaction rates):

$C_6H_5 + O_2$ --> products
$C_5H_5 + radical$ --> products
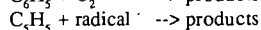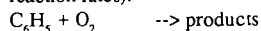
3- The computed ignition delay times of stoichiometric benzene-oxygen mixtures diluted in argon were 1.5 to 5 times too short compared with shock tube experiments, depending on the temperature. According to sensitivity analyses, these results could certainly be improved by a better knowledge of the following reactions:

$C_6H_5 + O_2$ --> products
$C_6H_6 + O$ --> $C_6H_5 + OH$
$C_6H_6 + O$ --> C_6H_5OH
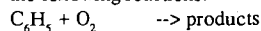
4- Based on these results, our preliminary mechanism will be improved in the near future. Calculated and measured species profiles in low pressure laminar flames will be compared, in order to obtain further information about the combustion processes in flames. Furthermore, ignition delay times at pressure ranging from 2 to 7 bar, in lean to rich mixtures will be computed in order to check the mechanism for auto-ignition.

ACKNOWLEDGEMENT

REFERENCES

(1) J.J. MacFarlane, F.H. Holderness, F.S.E. Witcher: Comb. & Flame 8, 215 (1964).
(2) R. Fort, C.N. Hinshelwood: Proc. Roy. Soc., A127, 218 (1930).
(3) D.W: Newitt, J.H. Burgoyne: Proc. Roy. Soc., A153, 448(1936).
(4) J.H. Burgoyne: Proc. Roy. Soc., A161, 48 (1937).
(5) J.H. Burgoyne: Proc. Roy. Soc., A171, 421 (1939).
(6) J.H. Burgoyne: T.L. Tang, C.M. Newitt, Proc. Roy. Soc., A174, 379 (1940).
(7) J.H. Burgoyne: Proc. Roy. Soc., A174, 395 (1940).
(8) J.H. Burgoyne: Proc. Roy. Soc., A175, 539 (1940).
(9) R.G.W. Norrish, G.W. Taylor: Proc. Roy. Soc., A234, 160 (1956).
(10) S.W. Benson: JACS 87, 972 (1965).
(11) C.R. Orr: 9th Symp. (Int.) Comb., 1034 (1963).
(12) R.J. Santoro, I. Glassman: Comb. Sci. Tech. 19, 161 (1979).

(13) C. Venkat, K. Brezinsky, I. Glassman: 19th Symp. (Int.) Comb., 143 (1982).

(14) K. Brenzinsky: Prog. Energy Combust. Sci., 12, 1 (1986).

(15) A.B. Lovell, K. Brenzinsky, I. Glassman: 22nd Symp. (Int.) Comb., 1063 (1988).

(16) C. Chevalier, J. Warnatz: to be published in Prog. Energy Combust. Sci.

(17) D.L. Baulch, T. Just, J.A. Kerr, M. Pilling, J. Troe, R.W. Walker, J. Warnatz: to be published in J. Phys. Chem. Ref. Data.

(18) J. Troe, private communication.

(19) N. Fujii, T. Asaba: J. Fac. of Eng. Univ. Tokyo (B) XXXIV, #1, 189 (1977).

(20) M. Braun-Unkhoff, P. Frank, Th. Just: 22nd Symp. (Int.) Comb, 1053 (1988).

(21) Y.Z. He, W.G. Mallard, W. Tsang: J. Phys. Chem. 92, 2196 (1988).

(22) C.Y. Lin, M.C. Lin: J. Phys. Chem. 90, 425 (1985).

(23) G.J. Gibbs, H.F. Calcote: J. Chem. and Eng. Data 4, 226 (1959).

(24) E.S. Goloniva, G.G. Fyodorov: 6th Symp. (Int.) Comb., 88 (1956).

(25) J. Warnatz: 18th Symp. (Int.) Comb., 369 (1981).

(26) U. Maas, J. Warnatz: Comb. & Flame 74, 53 (1988).

(27) A. Burcat, C. Snyder, T. Brabbs: NASA Technical Memorandum 87312 (1986).

Table 1

Benzene mechanism and rate constants in cm^3, mol, s, K, and kJ.

Reaction		A	ß	Ea	Ref.
414. C_5H_5	--> 1- C_5H_5	1.000e+14	0.0	188.0	20
415. 1- C_5H_5	--> C_3H_3 + C_2H_2	1.000e+14	0.0	71.1	20
449. C_6H_5	--> 1- C_6H_5	4.000e+13	0.0	305.0	17
450. 1- C_6H_5	--> C_4H_3 + C_2H_2	2.000e+62	-14.7	241.0	20
451. 1- C_6H_5	<--> 1- C_6H_4 + H	2.500e+58	-13.8	208.0	20
453. C_6H_5 + O_2	--> C_4H_4 + H + 2CO	1.000e+12	0.0	8.4	19
455. C_6H_5O	--> C_5H_5 + CO	2.500e+11	0.0	184.0	17
456. C_6H_4OH	--> C_5H_5 + CO	2.500e+11	0.0	184.0	17
457. C_6H_6	<--> C_6H_5 + H	4.410e+29	-3.9	489.9	18
459. C_6H_6	<--> C_4H_4 + C_2H_2	1.000e+15	0.0	450.0	17
461. C_6H_6 + H	<--> C_6H_5 + H_2	7.900e+13	0.0	41.8	19
463. C_6H_6 + OH	<--> C_6H_5 + H_2O	1.630e+08	1.4	6.1	17
465. C_6H_6 + OH	--> C_6H_5OH + H	1.320e+13	0.0	46.0	17
466. C_6H_6 + O	<--> C_6H_5 + OH	3.612e+01	3.7	4.5	17
468. C_6H_6 + O	<--> C_6H_5OH	3.612e+01	3.7	4.5	17
470. C_6H_5OH + H	<--> C_6H_5O + H_2	1.144e+14	0.0	51.9	17
472. C_6H_5OH + H	--> C_6H_6 + OH	2.230e+13	0.0	33.2	17
473. C_6H_5OH + OH	<--> C_6H_5O + H_2O	3.000e+12	0.0	0.0	17
475. C_6H_5OH + OH	<--> C_6H_4OH + H_2O	3.000e+12	0.0	0.0	17
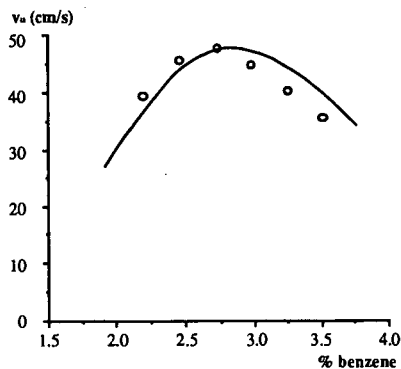
Fig. 1. Free flame velocities in benzene-air mixtures, P = 1 bar, T_a = 298 K. Points: measurements (23). Line: Calculation.
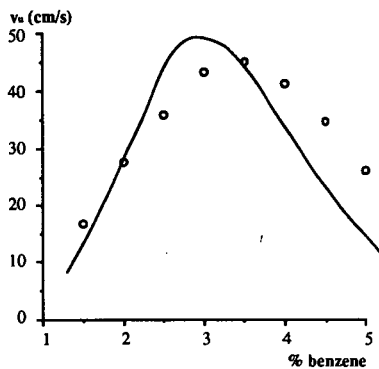
Fig. 2. Free flame velocities of benzene-20.8% oxygen-argon mixtures, P = 1 bar, T_a = 298 K. Points: measurements (24). Line: Calculation.
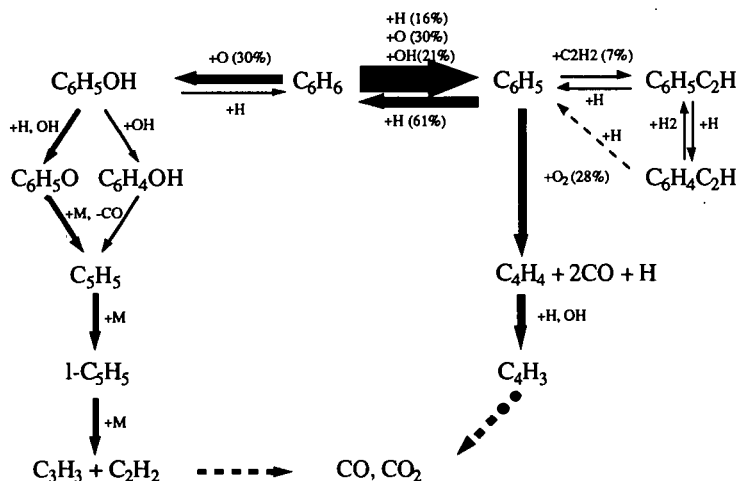
Fig. 3. Flow diagram for the oxidation of benzene in a stoichiometric flame, P = 1 bar, T_a = 298 K. The thickness of the arrows is proportional to the reaction rate integrated over the whole flame front

1492
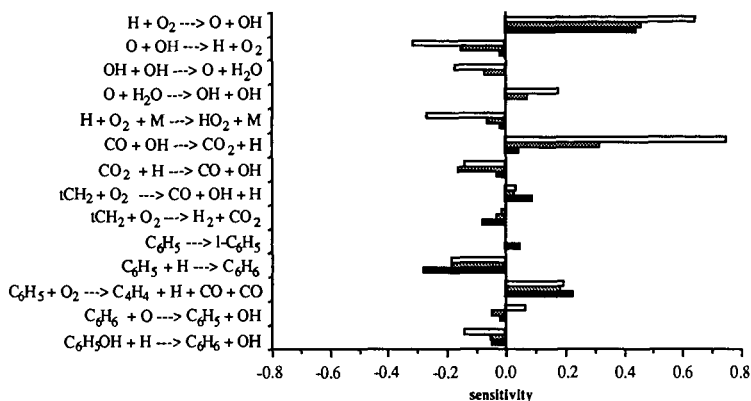
Fig. 4. Sensitivity analysis with respect to the laminar flame velocities in lean (white bars), stoichiometric (grey bars), and rich (black bars) benzene-air mixtures, P = 1 bar, T_u = 298 K.
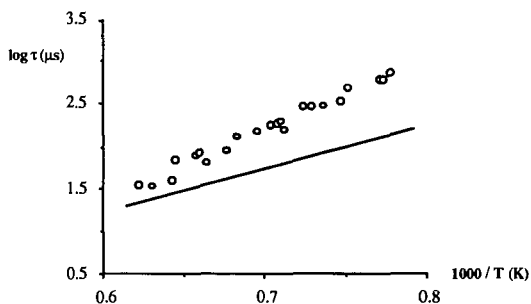
Fig. 5. Ignition delay times for stoichiometric benzene-oxygen-argon mixtures, P = 2 to 3 bar. Points: experimental values (27). Line: calculation.
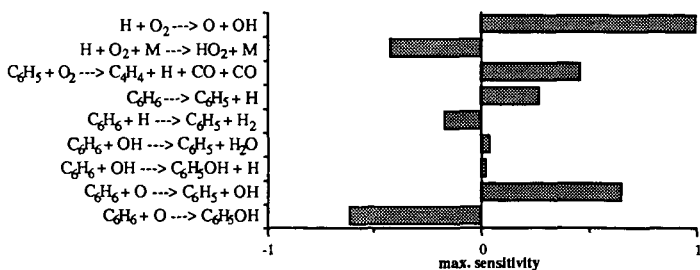
Fig. 6. Sensitivity test with respect to [OH] concentration of a stoichiometric 1.69% benzene-12.675% O_2 mixtures diluted with argon, at P = 2 bar, T_u = 1286 K, and at t = 30 μs (τ / 5).

1493

   CYCLOPENTADIENE   AND   CYCLOPENTADIENYL CONVERSION   DURING
BENZENE OXIDATION, THERMODYNAMIC AND MECHANISTIC CONSIDERATIONS.

Joseph W Bozzelli, Viral Desai, Edward R Ritter and Anthony M.
Dean[*]   Dept of Chemical Engineering and Chemistry,
New Jersey Inst. of Technology, Newark, NJ 07039,
[*]Exxon Research And Engineering, Annandale, NJ 08801

                         Abstract

There are a number of studies on benzene oxidation and pyrolysis,
yet we do not know of a detailed reaction mechanism based on
fundamental kinetic and thermodynamic principles that explains
published experimental observations. Benzene reacts by H trans-
fer (abstraction) forming phenyl radicals. Prior to unimolecular
decomposition, phenyl can react with O_2, O or HO_2 to form a
phenoxy radical. Phenoxy, the major channel for benzene loss, has
been shown to decompose to CO plus cyclopentadienyl radical. In
this study, we focus on the oxidation pathways to loss of cyclo-
pentadienyl species. We specifically consider thermodynamic and
kinetic analyses for reactions of cyclopentadiene and cyclopen-
tadienyl radical with O_2, O, H, OH and HO_2. Rate constants as
functions of pressure and temperature for the radical addition
and recombination reactions are calculated using bimolecular QRRK
theory. We compare predictions from our mechanism with phenoxy
and benzene reaction data.

INTRODUCTION
     Benzene reacts in the presence of oxygen (through phenyl or
cyclohexadienyl radical intermediates) to form phenyl and phenoxy
radicals in addition to stable phenol molecules. Phenyl radicals
in the presence of oxygen will undergo the rapid, exothermic,
chain branching reaction:

   $C_6H_5{}^{\cdot} + O_2 ---> C_6H_5O^{\cdot} + O^{\cdot}$
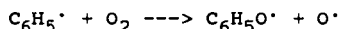
     The phenoxy and cyclohexadienyl radical intermediates are
resonantly stabilized and are usually present at higher concen-
trations than the more reactive phenyl or other non-stabilized
radicals. The phenoxy radical has been shown to unimolecularly
react to produce carbon monoxide and cyclopentadienyl (CyCpdj)
radical[1,2], while cyclohexadienyl radical produces methyl and
CyCpdj[3]. Cyclopentadienyl radical is highly resonantly stabi-
lized with references on its heat of formation ranging in value
from 57 to 45 Kcal/mole corresponding to a resonance stabiliza-
tion energy (RSE)[4,5] of ca. 18 to 30 Kcal/mole. This large RSE
essentially eliminates reaction of this radical with O_2 to form
a peroxy radical, which is favorable for normal alkyl radicals.
This occurs due to the very low, ca 11 Kcal/mole, well depth for

stabilizing the adduct with significant loss of entropy.

Our initial attempts to construct a mechanism comprised of elementary reactions to model benzene production and loss, for comparisons to our experiments on chlorobenzene and dichloroben-zene pyrolysis reaction in H_2[3,6], chlorobenzene oxidation[6] or the benzene oxidation data of Brezinsky[7], have produced relatively large concentrations of cyclopentadienyl radical (Cycpdj). Calculations, incorporating abstraction reactions for this radi-cal, indicate it would build up to concentrations equal to or larger than its cyclopentadiene parent and would clearly act as a bottle-neck to benzene loss. The reactions in our mechanisms included microscopic-reversibility and showed that the benzene, phenyl, cyclohexadienyl - phenoxy system would essentially remain at steady state.

Phenols and phenoxy species are known to be common interme-diates in oxidation of aromatic species and they are considered strong candidates as precursors in formation of dibenzofurans and dioxins. Knowledge of important reactions of phenoxy decomposi-tion products - Cycpdj and its parent is therefore critical to understanding possible formation of dibenzofurans and dioxins, through reverse reactions, as well as their destruction.

Aromatic species are also important in motor fuels, with small ring aromatics often used to increase octane rating in gasolines[7] since lead has been eliminated as a blending ingredi-ent. Understanding the fundamental reactions of these aromatic species will clearly benefit researchers who are working to understand preignition and engine knock. This understanding may also have implications for soot formation in diesels.

In formulating a detailed model of benzene destruction and/or formation in varied oxidation or pyrolysis environments, we need to consider the decomposition pathways for these reso-nantly stabilized cyclopentadienyl and phenoxy species. We currently do not know of any reaction mechanism for benzene oxidation comprised of elementary reactions, which are based upon fundamental thermochemical kinetic principles. Brezinsky[7] and Venkat et. al.[8] have published general reaction schemes, with no rate constants or thermodynamic properties. Bittker[9] published a mechanism which was based upon previously published reaction paths and presented rate constants which fit experimental data for ignition delay times and toluene loss profiles. Bittker, however, used a sensitivity code to determine the important reactions and then optimized the fit of the data by adjusting rate constants. No account for collisional fall-off of activated complexes formed by addition of atoms or radicals to unsaturated (olefinic or aromatic) bonds, or by combination of radical spe-cies was included. Published mechanisms for toluene and other aromatic pyrolysis sometimes include reactions where the Arrheni-us A Factor is reasonably close to the high pressure limit value, but the activation energy is significantly less than the known bond energy or energy barrier at the appropriate temperature. This serves to dramatically accelerate the reaction, instead of

slowing it down, as would occur if it were in the fall off region, and when Ea is less than $\triangle H_{rxn}$, it also appears to violate with thermodynamics. The exception, where one would expect to have a lower Ea is only if one were well away from the high-pressure limit, implying a much lower Arrhenius A factor. The unrealistic combinatiohn of a high A and low Ea serves to dramatically, but erronously, accelerate the reaction.

In this study we focus on thermodynamic and kinetic analysis for reaction paths of cyclopentadiene and cyclopentadienyl radical with O_2, O and H atoms, in addition to OH and HO_2 radical. These reaction paths are radical combination or addition to unsaturated bonds in the cyclopentadienyl ring which form energized complexes that can react back to reactants or to low energy products before being collisionally stabilized. We treat all of these reactions with the bimolecular Quantum Rice Ramsperger Kassel Theory (QRRK)[11]. We also treat dissociation of the complexes which become stabilized with unimolecular QRRK theory to account for collisional fall-off at temperatures of the experimental data we are modeling. Required thermodynamic properties for the radical intermediates were calculated using the THERM[12] computer code.

Metathesis reactions of cyclopentadiene with H, OH, HO_2, phenyl, phenoxy, and alkyl radicals all serve to abstract the weak allylic hydrogen and form the resonantly stabilized radical. These reactions are relatively fast at combustion temperatures and serve to form and maintain a relatively high concentration of Cycpdj, which remains in thermal equilibrium with the rest of the radical pool. Clearly when the Cycpdj builds up in concentration the reverse reactions become important. The abstraction reactions, therefore, serve to shuttle the H atoms back and forth between resonantly stabilized and other species with relative concentrations controlled more by thermodynamics (equilibrium) than by kinetics. We propose that radical addition and combination reactions involving these resonantly stabilized species play a major role in the oxidation loss processes of benzene.

Addition Reactions of H, OH, and O atoms to Cyclopentadiene

The addition of a radical such as OH or H to the parent Cycpd forms an energized adduct, which can decompose to lower energy, non-cyclic products by Beta Scission (B_{sc}) reactions, dissociate back to reactants or be collisionally stabilized. There are two sites that a radical can add to the CyCpd molecule, the 1 or the 2 position, where the 5 position is carbon with 2 hydrogens. If a radical or atom adds to the 1 position, a radical is formed at the 2 position, which can B_{sc} the allylic carbon – carbon bond, opening the 5 member ring and forming a stabilized radical. If an atom or radical adds to the 2 position a radical is formed at the 1 position, which B_{sc} a vinylic carbon–carbon bond opening the ring and forming a vinylic radical. The formation of a vinylic radical is less thermodynamically favored, but the vinylic radical, if formed, will rapidly decompose, unimolecularly, by a series of scission reactions to acetylene plus a

radical.

The example of H atom adding to the double bond of Cycpd at the 1 position is shown in Figure 1. Here the cyclic radical can decompose to a lower energy linear C_5 dienyl radical, which also has a large amount of resonance stabilization and is therefore not highly reactive. The addition of H atoms to the 2 position in the ring results in a non-resonantly stabilized cyclic radical, which can either dissociate back to reactants or undergo ring opening to form a 1,4-pentadiene-1-radical (vinylic) that will rapidly dissociate to acetylene and the relatively stable allyl radical. Thus the more energetic pathway, aalthough slower, serves, essentially, as an irreversible sink and is important.

The addition of OH to Cyclopentadiene (Fig 2) at the 2 position forms a radical at the 3 position (carbon adjacent to the CH_2 group). This radical will either dissociate back to initial reactants or B_{sc} a carbon-carbon bond to form a vinylic alcohol labeled C*CCOHC*C. (* denotes a double bond). This will either react back to the cyclic radical, beta scission to an endothermic channel forming acetylene and a resonantly stabilized primary alcohol radical of propenol as labeled in channel 3. An alternate reaction path of the linear C_5 vinyl radical, however, is a hydrogen shift from the alcohol to the vinyl group with the oxy radical then initiating the scission reaction to either vinyl + propene aldehyde or C*C(C*O)C*C + H. These carbonyl products will eventually react to CO + unsaturated C_2 and CH_3 hydrocarbons. OH adding to the 1 position will allow B_{sc} of an allylic C-C bond to form C.C*CC*COH which is equivalent to C*CC*CC.OH, and will beta scission to C*CC*CC*O + H. This linear unsaturated C_5H_6O will lose the carbonyl H atom (abstraction) and break down to acetylenes plus CO. Reactions of O atoms with CyCPD are also very important.

Reactions of Cyclopentadienyl Radical (CyCpdj)

CyCpdj + HO$_2$

In the benzene oxidation mechanism we have assembled, the reaction of CyCpdj + HO$_2$ is one of the most important chain branching reactions. These two radicals build up to relatively high concentrations at temperatures of the experiments we are modeling (ca 1000 - 1200 K), and this reaction is, therefore, important to reducing both radical concentrations. The potential energy level diagram illustrated in Figure 3 shows that combination of the two radicals can form a hot cyclopentadienyl hydroperoxide which will rapidly dissociate either back to reactants or to cyclopentadienyl-oxy (Cpd-oxy) radical + OH, with the products favored at these temperatures due to slightly lower exit barrier and the increased entropy. The OH product is also more reactive than HO$_2$, further accelerating the overall reaction via abstraction reactions.

The Cpd-oxy radical will undergo rapid unimolecular dissociation at these temperatures via two low energy pathways shown in Figure 4. One path forms a cyclopentadienyl ketone + H atom, and the second opens the ring to a vinylic pentadienyl aldehyde

radical. This will undergo rapid internal abstraction of the carbonylic hydrogen to form the resonantly stabilized complex shown in figure 4. The carbonyl radical formed will dissociate to CO plus a butadienyl radical which will further dissociate to acetylene + vinyl.

We note that the above Cpd-oxy radical (adduct) is also formed directly from the combination of O atoms with CyCpdj, but in this case, the adduct formed (initially) has 50 kcal/mole more energy than is needed to undergo B_{sc} reactions to the products in Fig. 4. This reaction is only limited by [O].

Several of the above reaction paths including O atom addition to either CyCpd or CyCpdj result in formation of cyclopentadien-one. This ketone can further react through addition of radical species to its unsaturated bonds, as shown in Fig. 5 for H atom addition. The initial adduct has enough energy to undergo ring opening forming a stabilized carbonyl radical, which will further decompose by unimolecular reaction to CO + butadienyl radical.

We have treated these reaction systems with the bimolecular QRRK formalism of Dean[11] to determine the apparent reaction rate constants to each channel including the stabilized adducts. Input parameters for the QRRK calculation are listed in below for reaction illustrated in Fig 5.

k	A	E_a (Kcal/mole)	Reference
k_1	3.98E13	2.6	A and Ea from H + C_2H_4, ref (11)
k_{-1}	1.53E14	47.74	Thermodynamics
k_2	7.83E14	18.22	Thermodynamics
k_{-2}	6.77E12	10.0	A TST, $\triangle S^{\#}$ = -4, Ea (Ring Strain + 5[13])
k_3	1.47E15	38.44	($\triangle HRxn + 5$[13])

(• denotes double bond, # denotes triple bond)

References
1. M. C. Lin and C. Y. Lin, J. Phys. Chem. 90, 425 (1986).
2. J. Manion and R. Louw, J. Phys. Chem., 93, 3563 (1989).
3. E. Ritter, J. Bozzelli and A. M. Dean, J. Phys. Chem 94, 2493. (1990), E. Ritter   Ph.D Thesis NJIT (1989).
4. D. McMillen and D. Golden, Ann. Rev. Phys. Chem.33, 493 (1982)
5. S. Stein and D. M. Golden, J Org. Chem, 42, p839 (1977)
6. E. Ritter and J. W. Bozzelli, Chemical Phys Process in Combustion Combustion Inet., Eastern Statee Section Albany, NY (1989).
7. K.Brezinsky Prog in Energy Combuet Science, 12, (1986).
8. C. Venkat, K. Brezinsky and I. Glassman, 19 Symp. Combustion, 143 (1982)
9. D. A. Bittker Central States Section, Combustion Institute Symposium, Indianapolis, In, May 1988.
10. L. D. Brouwer, W. M. Margraf and J. Troe, J Phys. Chem. 92, 4905 (1988).
11. A. M. Dean, J. Phys. Chem. 89, 4600, (1985).
12 THERM Thermodynamic Property Estimation of Radicals and Moleculee, E. Ritter and J. W. Bozzelli, Int. J. Chem Kinetics (1991).
13 S. Stein and A Fahr, Proceedings of 22nd Comb. Inst. Symp, 1023 (1988).
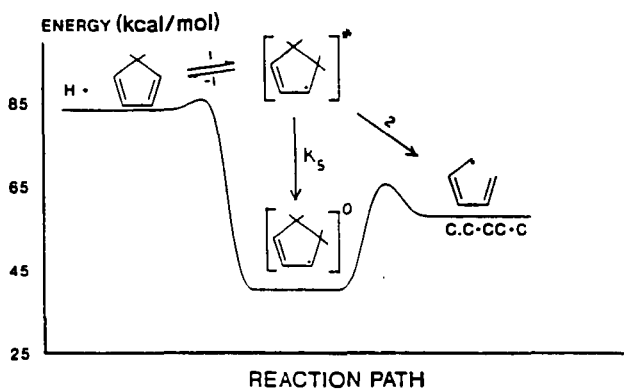
FIGURE 1. CYCLOPENTADIENE + H --> PRODUCTS
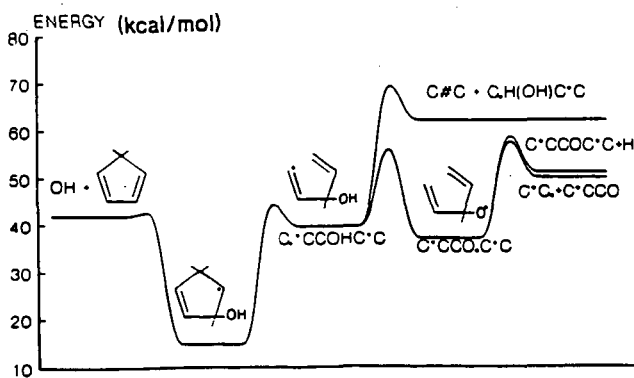
FIGURE 2. CYCLOPENTADIENE + OH --> PRODUCTS

1499
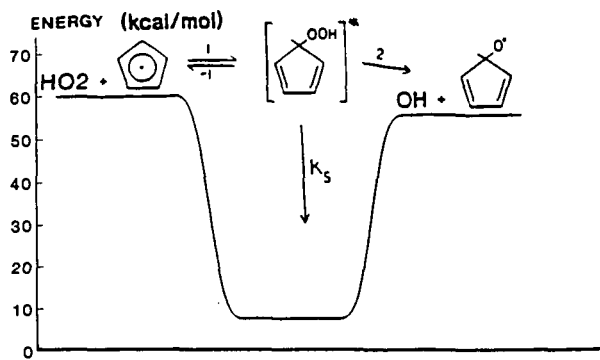
FIGURE 3. HO2 + CYCLOPENTADIENYL RADICAL
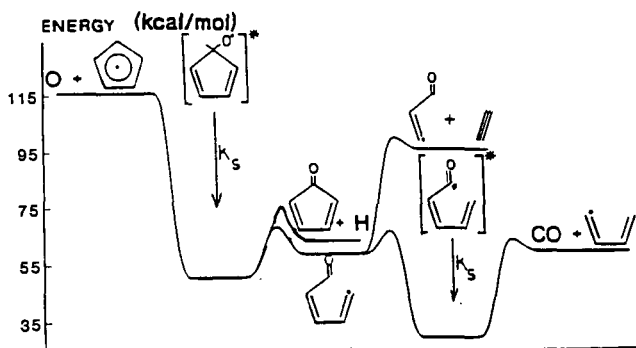
FIGURE 4. O + CYCLOPENTADIENYL RADICAL
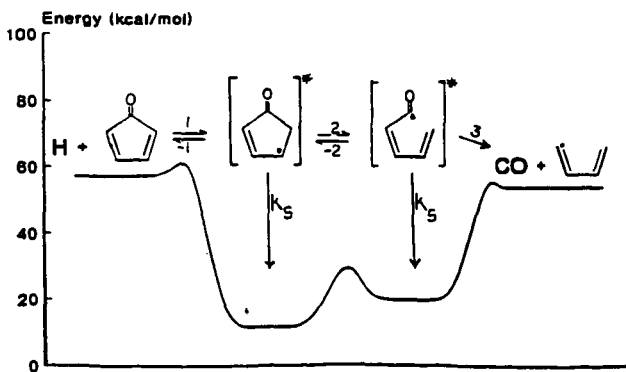
FIGURE 5. H + CYCLOPENTADIEN-ONE

SOOT DEPOSITION FROM ETHYLENE/AIR FLAMES AND THE ROLE OF AROMATIC
INTERMEDIATES. Joanne M. Smedley and Alan Williams. Department of Fuel
and Energy, Leeds University, Leeds, LS2 9JT, UK.

ABSTRACT

The formation of soot is of interest as a pollutant but also because it forms
deposits in combustion chambers. In this work a McKenna flat flame, water-
cooled, premixed burner was used to study soot deposition from two rich
ethylene/air flames (ϕ = 2.52, ϕ = 2.76). Rates of soot deposition for both
cooled copper and uncooled stainless steel surfaces were investigated. Soot
samples from these experiments were analysed for PAH by solvent extraction.
Temperature profiles were taken using Pt/Pt 13% Rh thermocouples. A quartz
microprobe sampling system was used in conjunction with a gas chromatograph to
determine the concentration profiles of aromatic and polyaromatic species in the
deposition region. Experimental results indicate that soot deposition occurs by
a thermophoretic mechanism when cooled surfaces are used and that soot deposition
rates increase as samples are taken further in the flame zone. If uncooled
surfaces are used then direct surface deposition takes place. The chemical
mechanisms involved are discussed.

INTRODUCTION

The formation and deposition of soot in any combustion system is undesirable.
Soot deposits can have adverse effects on heat transfer characteristics or
combustion behaviour which can cause performance or failure problems in a range
of systems from rocket engines to diesels. The emission of soot particles from
combustion chambers into the atmosphere is also of environmental concern due to
the fact that soot particles can contain significant concentrations of PAH.
There is thus a need to accurately predict under what conditions soot formation
will occur and to quantify the amount of soot deposited in any part of a
combustion system.

Over recent years more progress has been made in understanding the chemical route
of soot formation but work in this area is difficult due to the complex
interaction of aromatic species in sooting flames (1-5). Harris et al (1) have
attempted to model single ring aromatic species but have only succeeded in
modelling benzene because of the complexity of the subsequent growth steps. They
encountered the problem that most of the rate constant data must be estimated
since absolute values are not available. Minor species such as C_2H_2 have been
accurately modelled by Miller et al (2) and Harris et al (3) as more reliable
data are available for these species. Even though these models exist, many gaps
remain in the mechanism of the subsequent steps leading to soot formation.
Whilst acetylene is recognised as a major growth species there is uncertainty
about the level of participation of the PAH species. Soot deposition onto a
cooled surface has been recently investigated by Makel and Kennedy (4) using a
laser diagnostic technique to measure soot deposit thickness and free stream soot
concentrations. A numerical model to make predictions of soot deposition rate
was also developed by them.

EXPERIMENTAL METHODS

Two rich ethylene/air flames (ϕ = 2.52 and ϕ = 2.76) were studied using a flat
flame, water-cooled, premixed burner (McKenna Industries). The gas flows in
litres/minute for the ϕ = 2.52 flame were O_2 = 2.22, N_2 = 8.36, C_2H_4 = 1.79 and
the flows for the ϕ = 2.76 flame were O_2 = 2.36, N_2 = 8.90, C_2H_4 = 2.09. To
investigate soot deposition rates an uncooled stainless steel plate and a cooled
copper plate were used to support stainless steel and copper sample squares
respectively within the flame. The sample plate dimensions were approximately

10 mm x 10 mm x 2 mm. Four flame heights were of interest, these were 5, 10, 15 and 20 mm above the burner surface. At each height weighed sample plates were inserted into the flame for intervals of 15 seconds (from 15 to 75 seconds) and were reweighed after to give the weight of soot produced.

The PAH content of some of the soot collected was determined using a solvent extraction process. Deposited soot from the metal plate and free steam soot which was collected on a Whatman glass microfilter GF/C paper from both flames was analysed using a pyrolysis chromatography. A Perkin Elmer 8320 gas chromatograph fitted with a Quadrax 007' series fused silica capillary column was coupled with a CDS Pyroprobe to desorb hydrocarbons from the soot. Approximately 2.5 mg of soot is heated at a rate of 0.1°C per millisecond up to 600°C. A quartz microprobe with a 6 mm outside diameter similar to that used by Harris et al (3) was used to obtain gas samples at various heights above the burner surface and a syringe method was used to transfer samples into a gas chromatograph (Perkin Elmer 8700 gas chromatograph fitted with a J & W megabore GS-Q column).

RESULTS AND DISCUSSION

Soot Deposition

Figures 1 and 2 give typical experimental data for the rate of soot deposition for the uncooled and cooled plates. In these each line represents different sampling heights above the burner. As expected the deposition rate of soot increases on an uncooled stainless steel plate as the plate is moved vertically away from the burner surface. However the deposition rate of soot at 20 mm above the burner surface is less than the deposition rate at 15 mm above the burner surface when the water cooled copper plate is used. This was found to occur in both flames (ϕ = 2.52 and ϕ = 2.76). It has been observed that the ultimate soot load on sample squares is approximately 0.7 mg regardless which plate is used. For the uncooled plate a 0.7 mg soot load occurs at 20 mm but when using the water cooled plate a soot loading of 0.7 mg is achieved at 15 mm when both had 75 seconds exposure in the flame. It is thought that above 0.7 mg the soot load is too great and the soot breaks off and is dispersed back into the flame. This is why a reduced soot deposition rate is seen for the 20 mm height samples when using the water-cooled plate. In general, for both plates the soot deposition rates are greater for the ϕ = 2.76 flame at all heights than for the ϕ = 2.52 flame. The exception for the metal plate is at 20 mm. Similar rates are experienced for both flames at this height and this again suggests that there is a limit to the amount of soot that can be deposited under these conditions.

When comparing the results from the uncooled plate and water cooled plate for ϕ = 2.52 flame it can be seen the soot deposition rate at 10 mm above the burner surface for the uncooled plate is much less than the soot deposition at the same height for the cooled plate. For example, at 75 seconds a soot load of under 0.1 mg is recorded for the uncooled plate. Whereas on the water cooled plate a soot load of approximately 0.4 mg is recorded at 75 seconds. The same is noticed at 15 mm above the burner surface at 75 seconds. The uncooled plate has a soot load of 0.4 mg while the cooled plate has a soot load of 0.55 mg. This is consistent with the thermophoretic transport of soot particles. From the results it also seems that thermophoresis is more prominent at lower regions in the flame. This may be because the soot particles are smaller earlier in the flame and as they become larger later thermophoresis has less influence on the movement of the soot particles. Makel and Kennedy (4) assumed that thermophoresis was the primary transport process for soot particles (~10 - 100 nm in diameter) although no allowance was made for variation in particle size. He also experienced the process of resuspension when the soot load increases to a certain limit. This was incorporated into his model to try and determine the final soot loading.

1502

The soot mass flux to the surface can be expressed (4) as

$$J''_{tot} = \rho_s \, V_d \, \phi_{s\ell} \qquad\qquad (1)$$

where ρ_s is the particle density (1900 kg/m^3), $\phi_{s\ell}$ is the soot volume fraction at the edge of the diffusion sublayer and the deposit velocity, V_d, is equal to the thermophoretic drift velocity, V_t, given by

$$V_t = -0.55 \, \nu \, d \, (\ell nT)/dy \qquad\qquad (2)$$

where ν is the viscosity and which is largely determined by the temperature gradient.

Experimental deposition rates were found to be 1×10^{-2} mg/cm^2 s at 15 mm above the burner using the water-cooled plate and 0.75×10^{-2} mg/cm^2 s using the uncooled metal plate. This is consistent with Makel and Kennedy's experimental data although they used a water-cooled cylinder to collect their samples. The calculated deposition value for our experiments using their theory is 1.2×10^{-2} mg/cm^2 s for the water-cooled plate and 0.6×10^{-2} mg/cm^2 s for the uncooled plates. The agreement is excellent.

PAH Content of the Soots

Deposited soot samples at 20 mm above the burner were collected from both flames after 75 seconds exposure within the flame. These soot samples were analysed in the Pyroprobe apparatus. Some results from this experiment are shown in Figures 3 and 4. Most of the peaks in the chromatograph were identified using a standard PAH mixture or by using retention indices (5-7). The major peaks are identified in Fig. 3. The gas chromatograph results for both the flames studied were very similar. Generally each PAH component was found in greater quantities in the richer ϕ = 2.76 flame. The ϕ = 2.52 flame contained much more volatile material which is expelled from the soot very early and is the first peak. The ϕ = 2.52 also contained more amounts of the larger components such as benzopyrenes and other 5-ring compounds which occur in the latter part of the chromatogram. Larger ring compounds also exist in both flames.

Free stream soot samples were collected on to Whatman glass microfibre filters were also analysed using the Pyroprobe system. Results from the ϕ = 2.76 flame are shown in Figure 4a. The collecting conditions for the free stream soot are identical to those quoted above for the deposited soot samples. When comparing the results from the free stream soot and the results for the soot deposited on the uncooled plate (Figure 4b) it is noted that the free stream soot always contains greater amounts of the 2 and 3 ring compounds such as acenaphthylene and the deposited soot always contains larger amounts of the 4 and 5 ring compounds like pyrene and also 6 and 7-ring compounds. This may be because the filter paper collection is at a lower temperature which favours the absorption of the smaller volatile gas phase material. If this is not the case there are important implications to the ability of soot to have varying compositions depending on whether it is in the gas phase or deposited on a surface.

Soot Formation Steps

Figure 5 shows the gas composition profiles obtained using the quartz probe sampling system. The reaction zone (based on O_2 decay) is quite extended. Figure 6 shows profiles of some aromatic species and their precursors. The results show that as combustion takes place C_2H_4 and O_2 are depleted. In Fig. 6 it can be seen that C_2H_2 peaks at about 5 mm above the burner after which it levels off to a fairly constant value between 10 and 20 mm. C_6H_6 rises gradually at about 6 mm and begins to fall at 12 mm. Initially there was more C_6H_6 in the ϕ = 2.52 flame but at 20 mm there was more in the ϕ = 2.76 flame. Laser beam

attenuation studies at 670 nm indicated that soot formation began at 6 mm above the burner. From the results it can be seen that as C_2H_2 is consumed C_6H_6 is produced as well as soot; this is consistent with the fact that C_2H_2 is involved in C_6H_6 formation and it is generally considered that C_2H_2 is an important precursor to soot formation. C_2H_2 and C_6H_6 fall as soot is formed and other larger hydrocarbons are produced in the flame. In Fig. 5 both CO and H_2 increase gradually as the probe is moved away from the burner surface. It was found that H_2 was in greater concentration in the $\phi = 2.52$ flame and CO was in a higher concentration initially. O_2 was only found in small amounts in the $\phi = 2.52$ flame. These increase as combustion takes place and are products of oxidation reactions. These trends were seen by Harris (3) et al but they only probed to about 3 mm above burner so they did not observe the fall in C_2H_2 and C_6H_6 in the later part of the flame. Miller (2) et al however undertook experiments up to 22.5 mm and also found similar profiles for CO, O_2 and H_2.

The mechanism of soot formation from an ethylene flame involves the formation of acetylene and its polymerisation to single and then multi-ring species. The subsequent growth of the initial soot particles involves surface growth involving acetylene and polyaromatic species the relative extent of them being subject to different interpretation (eg. 5, 8 and 9). In the free stream soot samples taken here the product involves soot particles, surface adsorbed PAH and gas phase PAH. However the deposited samples can only contain PAH associated with the soot particles as adsorbed or growth species. The deposited samples are significantly different to the free stream soot in that the dominant PAH species are the 4+ ring species and smaller species are present in lower concentrations.

The suggestion must be implicit in these findings that the acetylene grows on the soot surface generating multi-ring compounds there which ultimately become part of the soot particle. During pyrolysis gc these compounds are desorbed as shown in the experimental results.

CONCLUSIONS

1. The deposition rate of soot increases with height above the burner surface (up to 20 mm) and sampling time (up to 75 seconds). More soot is deposited as ϕ is increased, but there seems to be a limit in the amount of soot that can be deposited regardless of the method of deposition because of soot break off at relatively low loadings.

2. There is evidence that thermophoresis is involved in soot deposition on to a cooled plate and that it is more dominant earlier in the flame when soot particles are smaller. The measured rates are consistent with the values calculated using the model proposed by Makel and Kennedy.

3. Soot samples from the uncooled metal plate contain large aromatic compounds with 4 and 5 and larger rings. The $\phi = 2.52$ had a higher concentration of some of these compounds.

4. Free stream soot samples contain a higher concentration of 2 and 3 ring aromatics than deposited soot. Higher concentrations of 4 and 5 ring aromatics were found in the deposited soot for the same conditions. This implies that these compounds are implicated in the soot growth mechanism.

ACKNOWLEDGEMENTS

REFERENCES

1. Harris, S.J., Weiner, A.M. and Blint, R.J. Combustion and Flame 72, 91-109 (1988).

2. Miller, J.A., Volponi, J.V., Durant, Jr. J.L., Goldsmith, J.E.M., Fisk, G.A. and Kee, R.J. Twenty-third Symposium (International) on Combustion, The Combustion Institute (1990).

3. Harris, S.J., Weiner, A.M. and Blint, R.J. Twenty-first Symposium (International) on Combustion, The Combustion Institute, pp 1033-1045 (1986).

4. Makel, D.B and Kennedy, I.M. Twenty-third Symposium (International) on Combustion, The Combustion Institute (1990).

5. Lam, F.W., Howard, J.B. and Longwell, J.P. Twenty-second Symposium (International) on Combustion, The Combustion Institute, pp 323-331 (1988).

6. Bartle, K.D. Handbook of Polycyclic Aromatic Hydrocarbons, Vol. 2, p 193 (edit. Bjorscth and Randahl) (1985).

7. Rostad, C.E. and Pereira, W.E. J. of High Resolution Chromatography and Chromatography Communicators, p 328 (1986).

8. Frenklach, M., Clary, D.W., Gardiner, Jr. W.C. and Stein, S.E. Twentieth Symposium (International) on Combustion, The Combustion Institute, pp 887-896 (1984).

9. Harris, S.J. and Weiner, A.M. Twenty-second Symposium (International) on Combustion, The Combustion Institute, pp 333-339 (1988).

Fig. 2. Plot of soot deposition against time for uncooled metal plate, $\phi = 2.76$.

Fig. 1. Plot of soot deposition against time for water-cooled plate, $\phi = 2.52$.
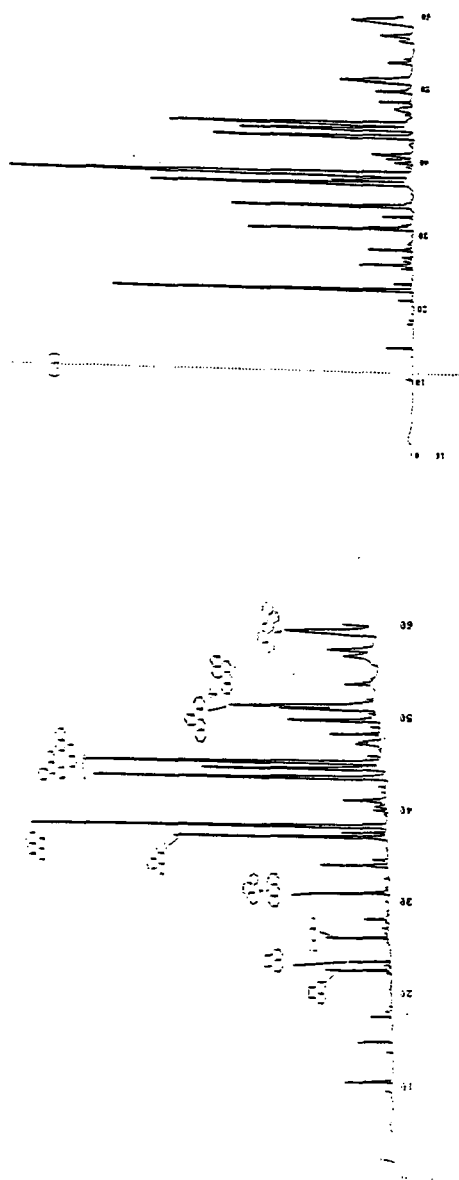
Fig. 3. Gas chromatogram with major peaks labelled sample for uncooled metal plate, $\phi = 2.76$.
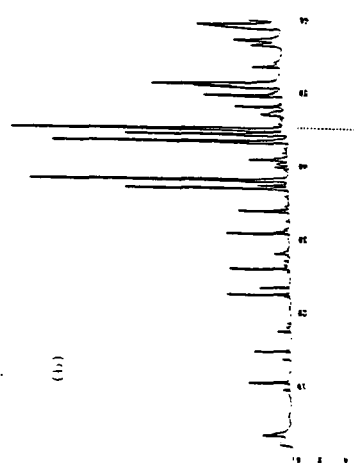
Fig. 4 (a) Gas chromatograph of free stream soot at 15 mm above burner, $\phi = 2.76$.
(b) Gas chromatograph of deposited soot at same conditions.

Fig. 6. Hydrocarbon species profiles for
ϕ = 2.76 flame (arbitrary concentration
scales) and ϕ = 2.52 flame (mol fraction).
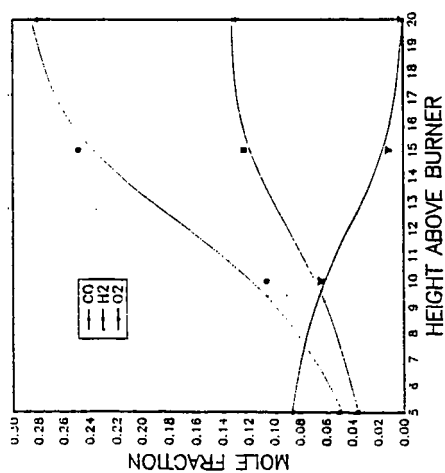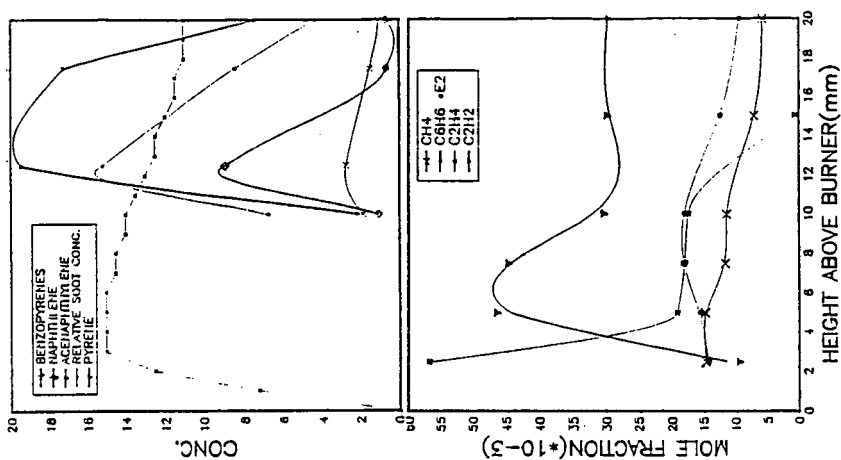
Fig. 5. Small molecule species profiles for
ϕ = 2.76 flame (mol fraction).

AROMATICS GROWTH BEYOND THE FIRST RING AND THE NUCLEATION OF SOOT PARTICLES

Michael Frenklach and Hai Wang

Fuel Science Program
Department of Materials Science and Engineering
The Pennsylvania State University
University Park, PA 16802

INTRODUCTION

In this manuscript, we discuss the the reaction mechanism responsible for the formation and growth of polycyclic aromatic hydrocarbons (PAHs) and subsequent nucleation and growth of soot particles in combustion of hydrocarbon fuels. The discussion is based on the results of a detailed chemical kinetic study,[1] and we refer the reader to this reference for the computational details. Here, we focus on the principal reaction pathways and mechanistic features identified in the analysis.

OVERALL PROCESS

The overall model of soot formation can be thought of as consisting of four major processes: *initial PAH formation*, which includes the formation of the first aromatic ring in an aliphatic system; *planar PAH growth*, comprised of replicating-type growth; *particle nucleation*, consisting of coalescence of PAHs into three-dimensional clusters; and *particle growth* by coagulation and surface reactions of the forming clusters and particles. Our primary attention in this discussion is on the last three processes, although some comments are pertinent concerning the formation of the first aromatic ring.

Formation of the First Aromatic Ring

The formation of the first aromatic ring in flames of nonaromatic fuels begins usually with vinyl addition to acetylene. At high temperatures, it forms vinylacetylene followed by acetylene addition to n-C_4H_3 radical formed by the H-abstraction from the vinylacetylene (Fig. 1). At low temperatures, the addition of acetylene to vinyl results in n-C_4H_5, which upon addition of acetylene produces benzene. Benzene and phenyl are converted to one another by the H-abstraction reaction and its reverse.
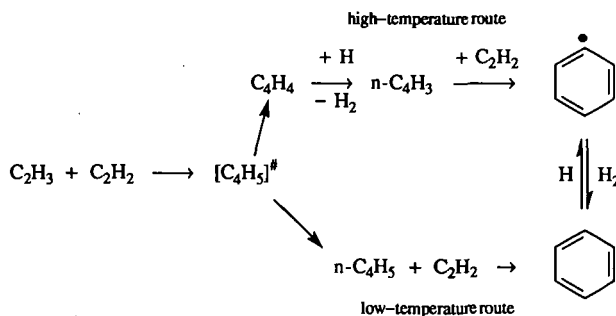
Figure 1. Formation of the first aromatic ring

In a recent review article on chemical kinetics and combustion modeling, Miller, Kee and Westbrook[2] suggested that the above cyclization reactions cannot be responsible for the formation of the first aromatic ring because the concentrations of n–C_4H_3 and n–C_4H_5 radicals should be low since the reactions

$$H + n\text{–}C_4H_3 \rightleftharpoons H + i\text{–}C_4H_3 \tag{1}$$

$$H + n\text{–}C_4H_3 \rightleftharpoons H + i\text{–}C_4H_3 \tag{2}$$

deplete the concentrations of the n–isomers required for the cyclizations. Reactions (1) and (2) were not included in our model. Our computational results indicated that the n– and i–isomers are already equilibrated by several other reactions in the system. Nonetheless, to test the Miller et al.'s suggestion, we performed additional simulations of the three laminar premixed flames we analyzed previously.[1,3] The reactions (1) and (2) were now included in the simulations assuming rate coefficients 1×10^{14} mol $cm^{-3}s^{-1}$ for the exothermic directions. The results of these simulations for all the three flames tested in Refs. 3 indicated that the inclusion of reactions (1) and (2) — even with upper-limit rate coefficient values — does not make a difference on the computed profile of benzene.

As an alternative, Miller et al.[2] suggested that benzene is formed by combination of propargyl radicals producing benzene or phenyl. A similar proposal was made by Stein et al.[4] Figures 2 and 3 show the results of flame simulations with reaction

$$C_3H_3 + C_3H_3 \rightleftharpoons \quad \text{(benzene ring structure)} \tag{3}$$
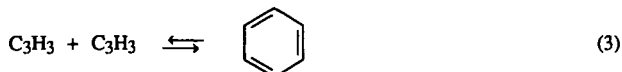
included with the rate coefficient of 5×10^{12} mol $cm^{-3}s^{-1}$ suggested by Stein et al.[4] Analysis of these results indicate that the inclusion of cyclization channel (3) does not *always* increase the production rate of benzene, as clearly shown in Fig. 2 for the flame conditions of Harris and co-workers.[5] For the conditions of the Westmoreland's flame,[6] the inclusion of reaction (3) significantly overpredicts the amount of benzene determined experimentally (Fig. 3). This is clearly a challenging issue, as the reaction chemistry of C_3H_x species is not well known.
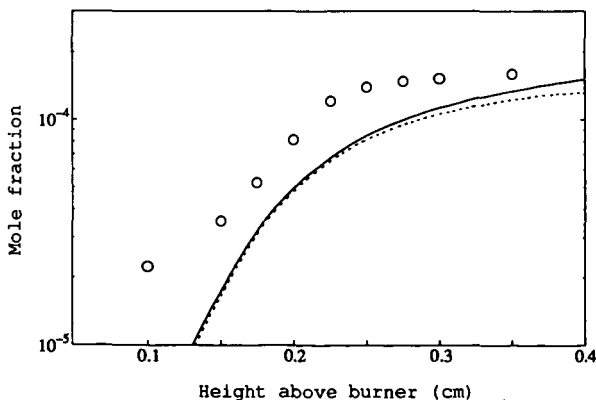
Figure 2. Benzene mole fraction: circles — experimental data,[5] solid line — computed with the mechanism used in Refs. 1 and 3, dotted line — computed with reaction (3) included
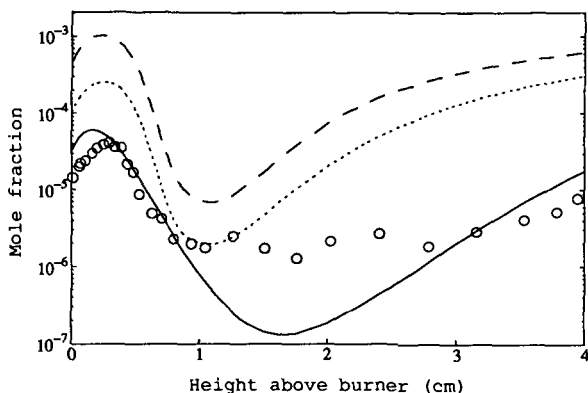
Figure 3. Benzene mole fraction: circles — experimental data;[6] solid line — computed with the mechanism used in Refs. 1 and 3; dashed and dotted lines — computed with reaction (3) included, dotted line represents the result computed with the mechanism tuned to fit the experimental C_3H_3 profile

Growth of the Aromatic Rings

Once formed, aromatic rings grow by a sequential two-step process: H-abstraction which activates the aromatic molecules, and acetylene addition which propagates molecular growth and cyclization of PAHs (Fig. 4).
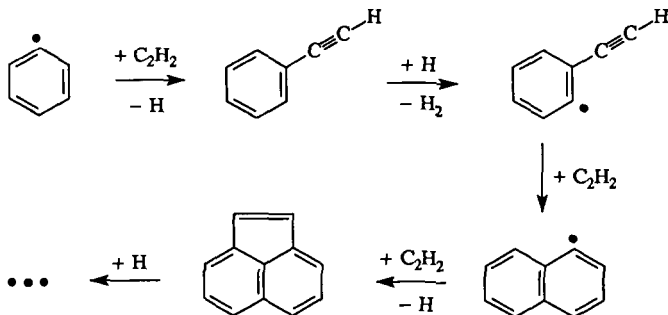
Figure 4. H-abstraction–C_2H_2-addition reaction pathway of PAH growth

Starting with an aromatic fuel, a "direct" condensation of intact aromatic rings becomes important. For example, in the case of high-temperature pyrolysis of benzene the reactions shown in Fig. 5 were found to dominate the initial stages of PAH growth.[7]

1511
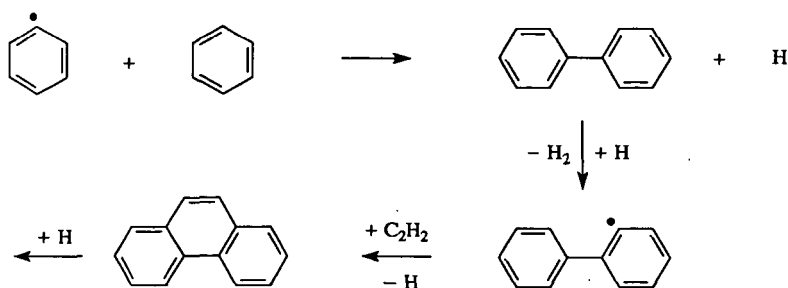
Figure 5. PAH growth initiated by aromatics "condensation"

However, as the reaction progresses, the initial benzene molecules decompose, primarily forming acetylene. As the concentration of acetylene approaches that of benzene, which occurs shortly after the initial period, the PAH growth switches to the acetylene-addition mechanism discussed above for nonaromatic fuels. In other words, the reaction system *relaxes* to the acetylene-addition pathway. The relaxation is faster in oxidation[8] as compared to pyrolysis and in mixtures of hydrocarbons[9] as compared to individual fuels.

Some of the acetylene addition reactions in the PAH growth sequence form particularly stable aromatic molecules, like pyrene, coronene, etc. The change of the free energy in these reactions is so large that the reactions become practically irreversible. This, in turn, has an effect of "pulling" the reaction sequence forward, towards formation of larger PAH molecules. Other acetylene addition steps are highly reversible, i.e., the rate of the forward reaction is nearly balanced by the rate of the reverse reaction. These steps with tightly balanced reaction fluxes create a thermodynamic barrier to PAH growth. It is this thermodynamic "resistance" which is responsible for the appearance of most stable, condensed aromatic structures, as opposite to open shell carbon clusters leading to fullerenes.[10] For instance, due to small differences in reaction enthalpies, the reaction flux from phenanthrene to benzo[ghi]perylene shown on the left of Fig. 6 was computed[11] to be faster by an order of magnitude than the one on the right hand side of Fig. 6.

The main kinetic features of PAH growth after a certain PAH size, i_0, can be schematically represented by the following set of reactions[12]

$$A_i + H \rightleftharpoons A_i\bullet + H_2 \tag{4}$$

$$A_i\bullet + C_2H_2 \rightleftharpoons A_iC_2H_2\bullet \tag{5}$$

$$A_iC_2H_2\bullet + C_2H_2 \longrightarrow A_{i+1} + H , \tag{6}$$
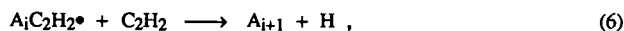
where A_i denotes an aromatic molecule containing i fused aromatic rings ($i = i_0, i_0+1, ..., \infty$), $A_i\bullet$ is an aromatic radical formed by the abstraction of an H atom from A_i, and $A_iC_2H_2\bullet$ is a radical formed by the addition of C_2H_2 to $A_i\bullet$. It is assumed that reactions (5) and (6) are reversible and reaction step (6) is irreversible. The rate of PAH mass accumulation is proportional to

$$Rate = \frac{K_4\frac{[H]}{[H_2]}}{\frac{1}{K_5k_6[C_2H_2]^2} + \frac{1}{k_5[C_2H_2]} + \frac{1}{k_{-4}[H_2]}} \int r_0 dt , \tag{7}$$

where t is the reaction time, r_0 is the rate of irreversible formation of A_{i_0} by initiation reactions, k_j is the rate coefficient of the j th reaction, and $K_j = k_j/k_{-j}$ is the equilibrium constant of the j th reaction.

In this equation, term $\int r_0 dt$ represents the contribution of the initiation reactions, i.e., those leading to the formation of first few PAHs. Term $K_4 \frac{[H]}{[H_2]}$ accounts for the "equilibrium position" or, in more rigorous terms, reaction affinity of reaction (1); it represents the superequilibrium of H atoms — the first kinetic factor responsible for PAH growth. Term $k_6[C_2H_2]$ is the effective rate constant of the irreversible addition of acetylene, reaction (6), forming particular stable PAH molecules — the second kinetic factor responsible for PAH growth. Terms $k_5[C_2H_2]$ and $K_5[C_2H_2]$ specify kinetic and thermodynamic factors, respectively, of the reversible addition of acetylene, reaction (5); the latter expresses the thermodynamic resistance to PAH growth. And finally, term $k_{-4}[H_2]$ accounts for the effective rate constant of the H-abstraction, reaction (4); to illustrate it, consider the limit of $k_{-4}[H_2] \rightarrow 0$ under which condition the ratio in Eq. (7) reduces to $k_4[H]$. At high pressures, reaction

$$A_i\bullet + H \longrightarrow A_i \qquad (8)$$

should contribute to the overall balance of the $A_i\bullet$ radical, and at a high concentration of hydrogen atoms, such that $k_8[H] \gg k_{-4}[H_2]$, we obtain an interesting limit of the PAH growth rate being independent of the H concentration.
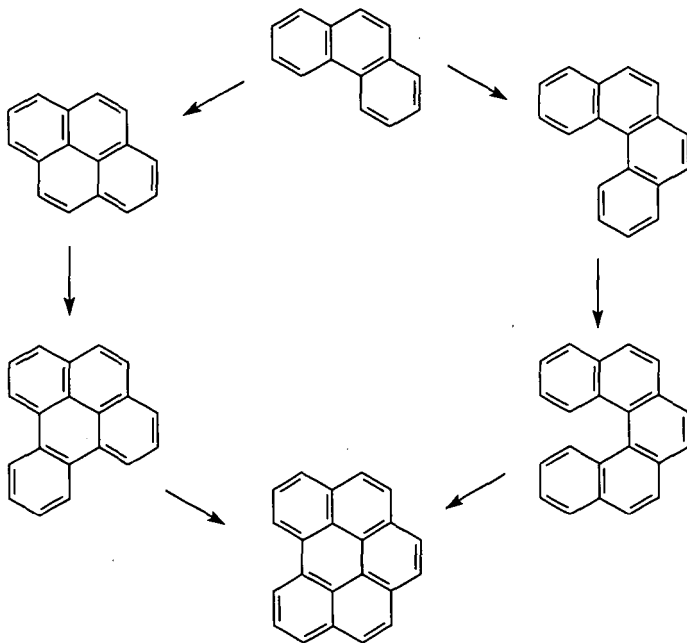
Figure 6. Comparison of two pathways of PAH growth.

An additional kinetic factor, $k_9[O_2]$, where k_9 is the rate coefficient of oxidation reaction

$$\text{Aryl} \bullet + O_2 \longrightarrow \text{products}, \tag{9}$$

is introduced in oxidative environments. Although many oxidative reaction channels are possible, it appeared, as a result of our kinetic analysis of shock-tube oxidation[8] and flame[13] environments, that PAH removal by oxidation occurs predominantly via molecular oxygen attack on aromatic radicals. Also, due to similar reactions of O_2 with C_2H_3 and C_4H_3 radicals (and of OH with C_2H_2, *etc.*), the concentrations of these critical intermediates are decreased, which in turn reduces the formation rate of the first aromatic ring. At the same time, the presence of O_2 in the mixture has a promoting effect on aromatics formation because of the accelerated chain branching leading to enhanced fuel pyrolysis and thus increased production of critical intermediates and hydrogen atoms. The balance of all of these factors determines the net effect of oxygen addition.

Nucleation and Growth of Soot Particles

We have developed a detailed kinetic model of soot particle formation and growth in the following manner. The formed PAH species were allowed to *coagulate*, that is, all the A_i's $(i = 4, 5, ..., \infty)$ collide with each other forming dimers; the dimers, in turn, collide with A_i forming trimers or with other dimers forming tetramers; and so on. The coalescence reactions were treated as irreversible having sticking coefficients of unity. As the focus of this work is on very young, small particles, it was assumed that the coagulation dynamics is in the free-molecular regime.

Beginning with the dimers, the forming clusters were assumed to be "solid phase" and allowed to add and lose mass by surface reactions

$$C_{soot}\text{-H} + H \rightleftharpoons C_{soot}\bullet + H_2 \tag{10}$$

$$C_{soot}\bullet + H \longrightarrow C_{soot}\text{-H} \tag{11}$$

$$C_{soot}\bullet + C_2H_2 \longrightarrow C_{soot}\text{-H} + H \tag{12}$$

$$C_{soot}\bullet + O_2 \longrightarrow \text{products} \tag{14}$$

$$C_{soot}\text{-H} + OH \longrightarrow \text{products}, \tag{15}$$
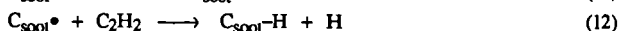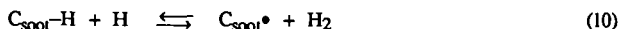
where C_{soot}-H represents an arm-chair site on the soot particle surface and $C_{soot}\bullet$ the corresponding radical. This mechanism is adopted based on the postulate[1,14] that the H-abstraction/C_2H_2-addition reaction sequence above is responsible for high-temperature growth of all forms of carbonaceous materials. Following this postulate, the rate coefficients of the heterogeneous reactions (10)–(15) were estimated based on analogous gas-phase reactions of one-ring aromatics, benzene and phenyl. In doing so, it was assumed that collision efficiencies on a per-site basis are the same for both gas-phase and gas-solid reactions. The particle dynamics — the evolution of soot particles undergoing simultaneous nucleation, coagulation and surface reactions described above — was modeled by a method of moments which does not require the assumption of a particle size distribution function.

The model predictions were found[1] in relatively close agreement with experiment for such properties as soot particle number density, specific surface area, average soot particle diameter, and laser-light scattering moments for the initial, particle inception part of several simulated laminar premixed flames. The reliability of the model was further supported by the facts that the computed net surface growth rate is in close agreement with that determined by Harris and Weiner[15] and that the predicted rate of soot oxidation by O_2 agrees well with the expression of Nagle and Strickland-Constable.[16]

Some major results of this modeling study[1] are summarized below:

(i) The computed rate of nucleation is balanced by the rate of coagulation throughout the particle inception zone, however, the nucleation rate decays more slowly with flame height than is usually deduced from experiment;

(ii) Particle inception is primarily determined by PAH coagulation, initiated and controlled by PAH coalescence into dimers. For instance, excluding all surface processes results in a substantial decrease of the particle mass but does not really change the order of magnitude of the particle size. In other words, the particle size is essentially determined by coagulation;

(iii) While the average soot particle is computed to contain 10^3-10^5 carbon atoms, the corresponding average PAH size is only 20 to 50 carbon atoms. This indicates that the crystallites comprising incipient soot particles should be on the order of 7 to 12 Å, in agreement with experiment[17] and against the proposal that soot is formed via spheroidal, polyhedral carbon clusters;

(iv) The oxidation by OH and O_2 is quite insignificant in the post-flame zone;

(v) The surface growth of soot mass is primarily determined by two processes: acetylene addition via the H-abstraction/C_2H_2-addition reaction sequence, and PAH condensation on the particle surface. The relative contribution of each of these processes appears to change with experimental conditions. Thus, while the acetylene addition dominates surface growth in an atmospheric ethylene flame of Harris et al.,[5] PAH condensation prevails in a low-pressure acetylene flame of Bockhorn and co-workers.[18] The main contribution of the PAH condensation occurs at the early stages of PAH coagulation;

(vi) The model predicts the classical structure of soot particles: a less dense particle core, composed of randomly oriented PAH oligomers, and a more dense concentrically-arranged particle shell;

(vii) Surface processes can be understood in terms of elementary chemical reactions of surface active sites. The number density of these sites is determined by the chemical environment.

ACKNOWLEDGEMENTS

REFERENCES

1. Frenklach, M. and Wang, H., "Detailed Modeling of Soot Particle Formation and Growth,"*Twenty-Third Symposium (International) on Combustion,* in press.

2. Miller, J. A., Kee, R. J. and Westbrook, C. K., *Annu. Rev. Phys. Chem.* 41, 345 (1990).

3. Wang, H. and Frenklach, M., "Modeling of PAH Profiles in Premixed Flames," Fall Technical Meeting of the Eastern States Section of the Combustion Institute, Albany, New York, October 1989.

4. Stein, S. E., Walker, J. A., Suryan, M. M., and Fahr, A., "A New Path to Benzene in Flames," *Twenty-Third Symposium (International) on Combustion,* in press.

5. Harris, S. J., Weiner, A. M., Blint, R. J., and Goldsmith, J. E. M., *Twenty-First Symposium (International) on Combustion*, The Combustion Institute, Pittsburgh, 1988, p.1033; Harris, S.J., Weiner, A.M., and Blint, R.J., *Combust. Flame* **72**, 91 (1988).

6. Westmoreland, P. R., "Experimental and Theoretical Analysis of the Oxidation and Growth Chemistry in a Fuel-Rich Acetylene Flame," Ph.D. thesis, MIT, 1986.

7. Frenklach, M., Clary, D. W., Gardiner, W. C., Jr., and Stein, S. E., *Twenty-First Symposium (International) on Combuistion*, The Combustion Institute, Pittsburgh, 1988, p. 1067.

8. Frenklach, M., Clary, D. W., Yuan, T., Gardiner, W. C., Jr., and Stein, S. E., *Combust. Sci. Technol.* **50**, 79 (1986).

9. Frenklach, M., Yuan, T., and Ramachandra, M. K., *Energy & Fuels* **2**, 462 (1988).

10. Frenklach, M. and Ebert, L.B., *J. Phys. Chem.* **92**, 561 (1988).

11. Frenklach, M., Clary, D.W., Gardiner, W.C., Jr., and Stein, S.E., *Twentieth Symposium (International) on Combustion*, The Combustion Institute, 1985, p. 887.

12. Frenklach, M., *Twenty-Second Symposium (International) on Combuistion*, The Combustion Institute, Pittsburgh, 1989, p. 1075.

13. Frenklach, M. and Warnatz, J., *Combust. Sci. Technol.* **51**, 265 (1987).

14. Frenklach, M., "A Unifying Picture of Gas-Phase Formation and Growth of PAH, Soot, Diamond and Graphite," in *Carbon in the Galaxy: Studies from Earth and Space*, J. Tarter, S. Chang, and D. J. DeFrees, Eds., NASA CP 3061, 1990, p. 259.

15. Harris, S.J. and Weiner, A.M., *Combust. Sci. Technol.* **32**, 267 (1983).

16. Nagle, J. and Strickland-Constable, R.F., *Proceedings of the Fifth Conference on Carbon*, Pergamon, London, 1962, p. 154.

17. Ebert, L.B., Scanlon, J.C. and Clausen, C.A., *Energy & Fuels* **2**, 438 (1988).

18. Wieschnowsky, U., Bockhorn, H. and Fetting, F., *Twenty-Second Symposium (International) on Combustion*, The Combustion Institute, 1989, p. 343.

MODELLING THE GROWTH OF POLYNUCLEAR AROMATIC HYDROCARBONS IN DIFFUSION FLAMES

J. Houston Miller
Department of Chemistry
George Washington University
Washington, DC 20052

Damon R. Honnery and John H. Kent
Department of Mechanical Engineering
University of Sydney
NSW 2006, Australia

Abstract

It has been noted for some years that the concentrations of many species in laminar hydrocarbon diffusion flames correlate with mixture fraction, or alternatively, local equivalence ratio. Therefore, once the spatial profile for the mixture fraction is established, it is possible to approximate both the concentration and net chemical rate profiles for a great many flame species. However, some species exhibit concentration gradients along contours of constant mixture fraction in a flame. The results of our past work show that most of the species along the chemical pathway leading to soot particle formation in diffusion flames, including all of the Polynuclear Aromatic Hydrocarbons, exhibit this type of behaviour. For these species, it is necessary to consider not only the chemistry of the growth environment, which may be adequately described by the mixture fraction, but also the residence time within the growth region. This paper will describe how such a model could be expressed, and present some initial comparisons with laboratory flame data.

Introduction

The earliest mathematical treatment of diffusion flame structure was that of Burke and Schumann [1]. Although incremental improvements to the Burke-Schumann model have been made over the years, it was not until recently that a new and more realistic approach to thinking about diffusion flame structure could be formulated. This can be traced to two improvements: the evolution of powerful computers and the development of the conserved scalar description of flame structure. The former has provided the capacity for the calculation of the two-dimensional structure, including up to C_2 chemistry, for laminar diffusion flames. The latter provides a framework for the development of simplification schemes for flame structure calculations.

In general, to compute the structure of a laminar diffusion flame requires the simultaneous solution of the energy, momentum, and species conservation equations. The latter can be written in the Shvab-Zeldovich form as [2]:

$$L(Y_i) \equiv \rho u_k \cdot \left(\frac{\partial Y_i}{\partial x_k}\right) - \frac{\partial\left(\rho D_i \cdot \left(\frac{\partial Y_i}{\partial x_k}\right)\right)}{\partial x_k} - w_i \qquad (1)$$

where Y_i is the mass fraction of species i, w_i is its chemical production rate of species i, ρ is the gas density and u_k is the component of velocity in the x_k coordinate.

Chemical elements (such as C, H, and O) are conserved during chemical reaction ($L(Z_1) = 0$) and linear combinations of elemental abundances, such as the mixture fraction, ξ, will also be conserved [3].

It has been noted that the concentrations of many flame species are only a function of mixture fraction, $Y_i = f(\xi)$ [2]. For these species, since

$$\rho u_k \cdot \left(\frac{\partial \xi}{\partial x_k}\right) - \frac{\partial\left(\rho D \cdot \left(\frac{\partial \xi}{\partial x_k}\right)\right)}{\partial x_k} - 0 \qquad (2)$$

it follows that the chemical rate is given by

$$w_i - -\left(\frac{1}{2}\right) \cdot \rho \chi \cdot \left(\frac{d^2 Y_i}{d\xi^2}\right) \qquad (3)$$

with the instantaneous scalar dissipation rate, χ, defined as:

$$\chi - 2D \cdot \left(\frac{\partial \xi}{\partial x_k}\right)^2 \qquad (4)$$

What if a species concentration is not a function of only mixture fraction? In particular, what if the chemistry is slow enough that transport might occur before a reaction proceeds? This is the case for the species along the chemical pathway leading to soot particle formation in diffusion flames, including all of the Polynuclear Aromatic Hydrocarbons, which exhibit concentration gradients along lines of constant mixture fraction [4]. For these species, it is necessary to consider not only the chemistry of the growth environment, which might be adequately described by the mixture fraction, but also the residence time within the growth region.

If this residence time dependence is included, a more complicated version of Eq. 3 can be derived which has two simple limits. The first would be if the time dependence was zero. In that case the equation would reduce to the result of Eq. 3. The other limit would hold if the diffusion coefficient for the species under consideration were zero, or at least small enough that terms which include it were small with respect to the residence time dependent terms. This would be almost exactly true for soot particles. Even small aromatics have diffusive velocities which are small with

respect to their convective velocities [4]. In this latter limit, the change in a species concentration would be simply given by integration over the residence time. We adopt this simple view in formulating the model presented in the next section.

A Model for PAH Chemistry in Laminar Diffusion Flames

We describe below a model which describes the physical and chemical processes that affect PAH and soot concentrations along a stream line in a laminar methane/air diffusion flame. The development is similar in spirit to that presented in a recent paper by Kennedy et al. [5]. In both models, soot processes are divided into three broad categories: inception, chemical growth, physical growth (agglomeration), and oxidation. Both assume that the rate of the soot processes depends on local temperature and the concentrations of major species, and these are fully determined by mixture fraction. In our model, we attempt to rationalize the choice of rates based on a knowledge of the fundamental chemical processes which are occurring in the flame combined with detailed measurements of species concentrations.

Growth
The growth chemistry in our model is based on the work of Frenklach et al. who proposed a model for ring growth based on the successive addition of acetylene to a growing aromatic radical core [6]. This model, in various forms, has been applied to studies of PAH and soot formation in shock tubes and premixed flames [6-10]. Frenklach developed a simplified version of his model to identify key parameters controlling PAH growth in combustion environments [10]. We used this simplification to demonstrate the important role of agglomeration in PAH growth [11].

In Frenklach's simplified mechanism parent PAH, A_i, are converted into a phenyl-like radical, A_i-, by hydrogen abstraction. The resulting radical reacts with acetylene to form a radical addition product $A_iC_2H_2$-. A subsequent acetylene addition irreversibly forms the next largest parent PAH. This reaction sequence is illustrated as:

$$A_i + H\cdot \rightleftharpoons A_i\text{-} + H_2 \qquad (R1)$$
$$A_i\text{-} + C_2H_2 \rightleftharpoons A_iC_2H_2\text{-} \qquad (R2)$$
$$A_iC_2H\text{-} + C_2H_2 \rightarrow A_{i+1}\text{-} . \qquad (R3)$$

In this reaction scheme, steady-state estimates for the concentrations of A_i- and $A_iC_2H_2$- can be derived. The rate of formation of the A_{i+1} PAH can therefore be written as

$$\frac{d[A_{i+1}]}{dt} \sim k_{eff}\cdot [A_i] , \qquad (5)$$

where k_{eff} is dependent upon the concentrations of C_2H_2, H_2, and H·.

In our prior work, we found that agglomeration only becomes important when the reduced mass of the colliding pair is suitably large: greater than 400 amu. Following the lead of this earlier work, we here assume that an agglomeration reaction can be written as

$$A_i + A_j \rightarrow A_{i+j} \qquad (R4)$$

where the rate constant of this process will be 0 for collisions of lighter PAH and close to the gas kinetic limit for collisions among the heavier PAH.

Inception
As seen above the aromatic growth is treated as an irreversible sequence of acetylenic addition steps to a growing aromatic core whose source is benzene, A_1. There are a number of

1519

models for the chemistry of the formation process of benzene which involve either reactions of C_2 with C_4 species [6] or the reaction of two C_3 species [15]. It is conceivable that a simplified expression for this process using steady state arguments (analogous to Frenklach's approach for ring growth) might be derived. If successful, such an approach would be expected to result in an expression for the A_1 inception rate which depends only on mixture fraction. However, given the current active debate on the mechanisms for the formation of benzene in flames, such a simplification may be premature.

Fortunately, there may be another approach to deriving an inception rate. Over the past few years we have collected an extensive data base for species concentrations and temperature in a laminar methane/air diffusion flame. This data has included measurements of the concentration of stable species such as acetylene and molecular hydrogen [12] and has been recently extended to include profile measurements of radicals species [13,14]. With this data base, we have demonstrated how the overall rates for a species chemistry may be calculated [13]. For the initial work presented here, we will assume that the benzene formation rate dependence on mixture fraction is given by our previous results for the Wolfhard-Parker diffusion flame [13].

Oxidation

In his dissertation work, McKinnon developed a comprehensive soot model which explicitly included a soot oxidation step [9]. Based on the work of Brezinsky [17], McKinnon assumed that successive reaction of carbons on the PAH or soot with hydroxyl radical results in a decrease of one ring number for the PAH and the formation of carbon monoxide. McKinnon found that inclusion of the Nagle and Strickland-Constable expression for soot oxidation by molecular oxygen overpredicted the soot oxidation rate, and he omitted this pathway from his final model. In the initial steps of the current research, we will also only include oxidation of PAH and soot by hydroxyl radical.

If it is assumed that (1) the concentrations of C_2H_2, H_2, $H\cdot$, and $OH\cdot$ are only functions of mixture fraction (i.e. their concentrations will not be affected by the aromatic growth chemistry) and (2) aromatic species will not diffuse then the progress of aromatic growth may be followed by integrating aromatic concentrations along a stream line using mixture fraction correlation data from our data base. The derivation of this flame field is discussed in the next section.

Flame Field Calculations

We have modelled the structure of a methane/air diffusion flame which has been studied by Santoro et al. [18]. Velocity, density, and mixture fraction fields throughout the flame are obtained using a computer code which has been described previously [19-21]. In this model, it is assumed that (a) major species concentrations are only a function of mixture fraction (and their concentrations can be found upon solution of the transport equation for mixture fraction, Eq. 2), (b) the rates of chemical reactions that determine major species concentrations are large with respect to transport rates, and (c) all species diffusivities are the same.

The transport equations for mixture fraction and momentum are solved for axisymmetric flow using a streamline coordinate transformation. The flow is parabolic and the boundary layer assumptions are made that the transverse pressure gradient and longitudinal diffusion fluxes are negligible. Buoyancy forces are included in the momentum equation. Diffusivity and viscosity were calculated from the local temperature using the Sandia transport property data [22]. The temperature vs. mixture fraction correlation was obtained from our analysis of a methane/air diffusion flame

1520

supported on a Wolfhard-Parker burner [12]. The predicted mixture fraction field and streamlines are shown in Figure 1.
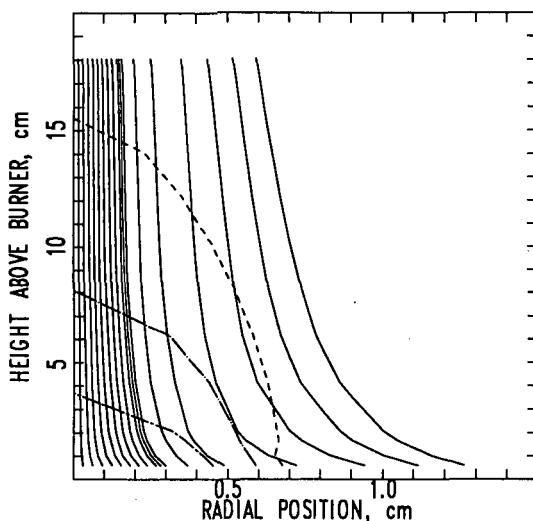
Figure 1 Streamlines and contours of mixture fraction in calculated axisymmetric methane/air diffusion flame. The stoichiometric contour ($\xi = 0.055$), and two fuel-rich contours ($\xi = 0.1$ and 0.2)

Results and Discussion

The concentrations of polynuclear aromatic hydrocarbons have been calculated along a series of streamlines in the flame shown in Figure 1. The model was first run using the expression for the effective rate constant for chemical growth derived form local temperature, and the concentrations of C_2H_2, H_2, and H· correlated against mixture fraction from the Wolfhard-Parker flame data. It should be noted that a H-atom plays a critical role in this chemistry: abstraction of ring hydrogens from the PAH is responsible for "activating" the surface for further growth. Unfortunately, in the

flame region that growth is likely to occur, there are no reliable measurements of H-atom concentration [14]. In these flame regions we have calculated [H·] assuming total local equilibrium. There has been much written about the importance of super-equilibrium concentrations of radicals in combustion processes in general [19] and aromatic growth in particular [10]. Although it is well known that super-equilibrium exists near the high temperature reaction zone of hydrocarbon diffusion flames [13], calculations also suggest that super-equilibrium extends well into the fuel rich flame regions where growth may occur [19]. Therefore, assumption of total equilibrium may grossly underpredict the concentration of hydrogen atoms and, consequently, the rate of ring growth. Our model calculations bear this out: unless an enhancement factor for chemical growth was included, no appreciable build-up of PAH occurs. To reach a volume fraction of soot approaching that which has been observed experimentally [18], this factor must be on the order of 500, which implies hydrogen atom concentrations in the growth region on the order of a few hundred parts per million. With current measurement strategies for hydrogen atom, this is a value near the detection limit in fuel rich regions of a diffusion flame [23].
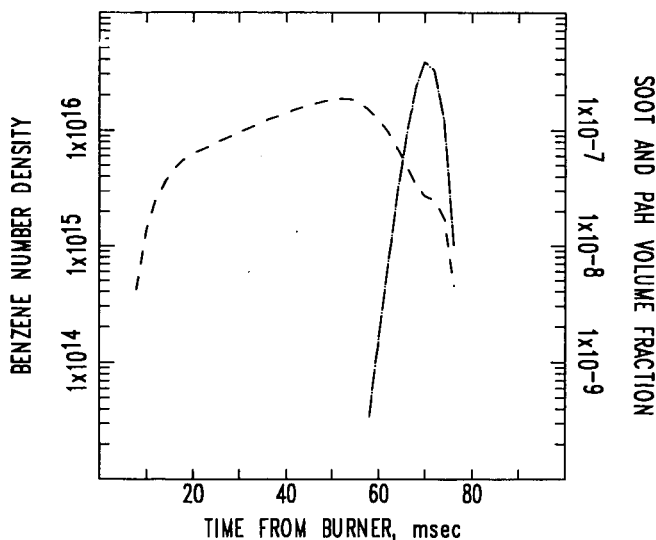
Figure 2 Concentrations of benzene (---) and heavy PAH and soot (-·-) as a function of time from burner surface for the streamline of peak soot loading (the fifth from the right streamline in Figure 1).

Figure 2 shows the concentrations of benzene and the soot volume fraction along a streamline which exhibited maximum PAH growth rates. Soot volume fraction is defined as the volume occupied by all species larger than coronene (A_7) in the model assuming that they all have the same density as soot. As expected, large concentrations of benzene precede the formation of larger PAHs in the

flame and that the volume fractions in this flame are small enough that total oxidation of the PAH occurs near the flame tip. (The oxidation of larger PAH leads to the shoulder on the benzene profile at 70 msec.)

Figure 3 shows a contour plot for soot concentrations in the flame calculated with the factor of 500 used for the enhancement of chemical growth rates. This picture looks qualitatively similar to comparable pictures derived from laser light scattering and extinction measurements [18] and to other model calculations of soot formation and oxidation in diffusion flames [5].
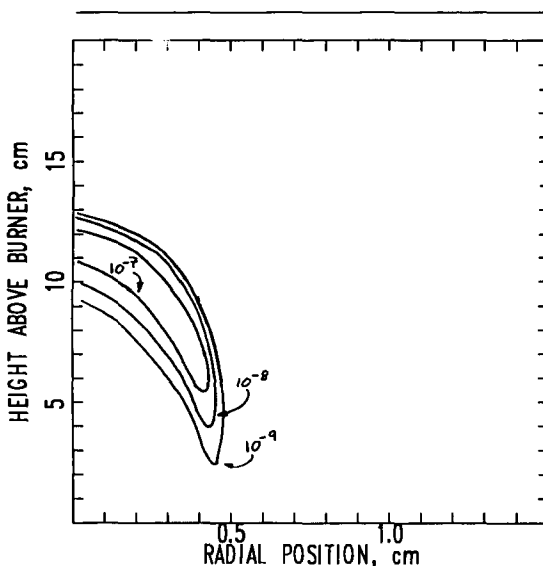
Figure 3 Contours of soot volume fraction in methane/air diffusion flame.

Conclusions

These model calculations provide an initial attempt to combine simplified aromatic growth chemistry with the conserved scalar description of diffusion flame structure. Although preliminary, the results suggest the important role that super-equilibrium hydrogen atom concentrations play in the growth chemistry. Future model improvement will hinge on the development of a more quantitative understanding of this factor.

1523

References

1. Burke, S.P., and Schumann, T.E.W., *Industr. Engng. Chem. 20*, 998 (1928).
2. Bilger, R.W., *Combust. Flame 30*, 277 (1977).
3. Bilger, R.W., *Ann. Rev. Fluid Mech. 21*, 101 (1989).
4. Hamins, A., Anderson, D. and Miller, J.H., *Combust. Sci. Technol. 71*, 175 (1990).
5. Kennedy, I.M., Kollmann, W. and Chen, J.-Y., *Combust. and Flame 81*, 73 (1990).
6. Frenklach, M., Clary, D.W., Gardiner W.C., Jr. and Stein, S.E., *Twenty-First Symposium (International) on Combustion*, p. 1067, The Combustion Institute, 1986.
7. Frenklach, M. and Warnatz, J., *Combust. Sci. and Tech. 51*, 265 (1987).
8. Harris, S.J., Weiner, A.M. and Blint, R.J., *Combust. and Flame 72*, 91 (1988).
9. McKinnon, J.T., Jr., Ph.D. Dissertation, Massachusetts Institute of Technology, 1989.
10. Frenklach, M., *Twenty-Second Symposium (International) on Combustion*, p. 1075, The Combustion Institute, 1989.
11. Miller, J.H., *Twenty-Third Symposium (International) on Combustion*, The Combustion Institute, in press.
12. Smyth, K.C., Miller, J.H., Dorfman, R.C., Mallard, W.G. and Santoro, R.J., *Combust. Flame 62*, 157 (1985).
13. Smyth, K.C., Tjossem, P.J.H., Hamins, A. and Miller, J.H., *Combust. and Flame 79*, 366 (1990).
14. Smyth, K.C. and Tjossem, P.J.H., *Twenty-Third Symposium (International) on Combustion*, The Combustion Institute, in press.
15. Stein, S.E., Walker, J.A., Suryan, M.M. and Fahr, A., *Twenty-Third Symposium (International) on Combustion*, The Combustion Institute, in press.
16. Miller, J.H., Mallard, W.G., and Smyth, K.C., *Twenty-First Symposium (International) on Combustion*, p. 1057, The Combustion Institute, 1986.

17. Brezinsky, K., *Prog. Energy Combust. Sci. 12*, 1 (1986).
18. Santoro, R.J., Yeh, T.T., Horvath, J.J. and Semerjian, H.G., *Combust. Sci. and Tech. 53*, 89 (1987).
19. Bilger R.W. and Stårner, S.H., *Combust. and Flame 51*, 155 (1983).
20. Honnery, D.R. and Kent, J.H., *Combust. and Flame 82*, 426 (1990).
21. Kent, J.H. and Honnery, D.R., *Combust. Sci. and Tech. 54*, 383 (1987).
22. Kee, R.J., Miller, J.A. and Jefferson, T.A., *Sandia National Labs. Report SAND80-8003*, (1980).
23. Smyth, K.C., personal communication.

MOLECULAR-BEAM STUDIES OF CARBONACEOUS CLUSTERS*

Thomas J. Butenhoff and Eric A. Rohlfing
Combustion Research Facility
Sandia National Laboratories
Livermore, CA 94551

INTRODUCTION

Carbon clusters ranging in size from a few to a few hundred atoms are currently a topic of intense theoretical and experimental study. Recent advances have made it possible to synthesize C_{60}, buckminsterfullerene, and other even-numbered carbon clusters ("fullerenes") in macroscopic quantities so that these spherical clusters, and their chemical derivatives, have made the leap from laboratory curiosities to potentially important materials. This has lead to an explosion of research in fullerene characterization and chemistry. Fullerenes are ubiquitous to a variety of growth environments that abound in species with elements other than carbon and are implicated in environments ranging from sooting flames to interstellar space. Fullerene ions can be observed as the dominant mass spectral features when a variety of substrates, including polycyclic aromatics,[1] polymers,[2] and soot particles,[3] are vaporized by a laser *in vacuo*. They are also observed in sooting flames in the region where soot particles first form.[4,5]

No matter what the conditions of growth, it now seems clear that the fullerenes and carbon (or soot) particles are intimately connected. At question is the model for particle growth proposed by Kroto[6,7] and Smalley[8] that has been postulated to account for the molecular beam results and has been extended to explain soot formation in combustion. Simply put, this model assumes that the nucleus of the growing particle is an incomplete spherical shell that accumulates primarily graphitic carbon on its reactive edges. A fullerene is formed in the rare event that a shell closes, thereby becoming inert with respect to further growth. This model has been the subject of much debate[9] between its proponents and those who favor the more traditional mechanism for soot formation. The traditional view[10-12] explains the rapid growth of soot at its inception by reactions between large polycyclic aromatics that are found in abundance in sooting flames. Subsequent addition of mass then proceeds via surface growth reactions between the soot particle and smaller gas phase reactants. The observation of fullerenes in sooting flames by Homann et al.[4,5] has been taken by some as evidence for the spiraling shell model. However, Homann et al. interpret their results within the traditional mechanism and hypothesize that the fullerenes are formed from nascent soot particles by an evaporative process.

We have begun a program to study the reactions of large carbon clusters and their hydrogenated analogs, which we shall call carbonaceous clusters, and attempt to make the connection between the molecular beam/flow reactor environment and a sooting flame. Smalley and co-workers have previously examined the reactivities of small (n<20) and large (n>40) carbon clusters in molecular beam work with the laser vaporization clusters source. In one study, Heath et al.[13] looked at the C_n and C_nH_m ions produced by the multiphoton ionization of neutrals created by the addition of various hydrogen-containing reactants to the carrier gas upstream of the laser-induced plasma. In another study, Zhang et al.[8] examined the reactivities of the large neutral clusters in a fast flow reactor located downstream of the vaporization region; they used single-photon ionization to probe the neutral cluster distributions. These experiments showed the unique inertness of the fullerenes to chemical attack by a variety of reactants. In both these studies, the authors used a linear time-of-flight mass spectrometer (TOF MS) with moderate mass resolution. In particular, the mass resolution in the fullerene study was insufficient to observe the products of the facile reactions between the injected reactant and the

odd-numbered clusters (which cannot achieve closed shells). These products appeared as an unresolved background from which the fullerene peaks stood out.

In this paper, we summarize results from experiments in which the formation of clusters is modified by addition of hydrogen to the carrier gas that flows over the graphite in the laser-vaporization source.[14] The resulting carbon and carbonaceous clusters (for $n \geq 20$) are gently single-photon ionized by a vacuum ultraviolet laser (F_2 158 nm) in order to probe the neutral cluster distribution without extensive perturbation from ionization efficiency or multiphoton fragmentation. The cluster ions are subsequently mass analyzed in a high resolution reflectron TOF MS. The resolution of this instrument at high mass ($M/\Delta M \sim 1700$ at 720 amu) allows us to completely resolve mass peaks separated by 1 amu, i.e. each value of m in C_nH_m. By adjusting the growth conditions in the cluster source through combinations of carrier gas density and residence times, we can produce carbon cluster distributions that exhibit wide variations in their degree of local maxima, or magic numbers. For example, we find low-growth conditions in which the abundances of odd clusters are nearly equal to those of the fullerenes. Alternatively, we can create very "magic" distributions in which the fullerenes, especially C_{60}, dominate the neighboring odd clusters. The carbonaceous cluster distributions produced by the addition of hydrogen to the carrier gas always show a dramatic preference for the formation of C_nH_m clusters with odd n. Remarkably, the clusters with even n appear predominantly as pure C_n, i.e. the fullerenes. We quantify these qualitative trends through a hydrogenation analysis that determines the fraction of each cluster that is hydrogenated and the distribution of hydrogens among the C_nH_m. The quantitative results (hydrogenation fraction, hydrogenation distribution, C/H ratio, etc.) show vivid evidence for the formation of long polyacetylenes, C_nH_2, for even n up to n=44. In addition, they reveal a dramatic change in hydrogenation behavior at about n=40 that provides more indirect evidence in support of the fullerene structural hypothesis. Finally, we discuss the implications of our results with respect to incomplete spherical shells and the corresponding model for particle growth.

EXPERIMENTAL TECHNIQUE

Carbon clusters are created by laser vaporization of graphite (3.2-mm-diameter rod, Pure Tech, 99.99%) into the helium flow following a piezoelectrically actuated pulsed valve that operates with 10-100 psig backing pressure and a 1-mm-diameter orifice. The vaporization laser is the second harmonic of a Nd:YAG laser (Spectra Physics DCR-11) at 532 nm with a pulse length of 6-7 ns and energy of 17 mJ. The flow channel is 2.5 mm in diameter at the target rod and for 22 mm downstream; the last 12 mm of the channel forms a 30° conical nozzle from which the flow expands into a vacuum chamber pumped by an unbaffled diffusion pump (Varian VHS-10). The cluster/helium expansion is skimmed once in the source chamber (5-mm-diameter skimmer, Beam Dynamics) at 35 cm downstream of the source. The resulting molecular beam enters a second vacuum chamber pumped by a 500 l/s turbomolecular pump (Balzers TPU 510) and is further collimated by a second 5-mm skimmer (98 cm downstream) before entering the ionization chamber of the reflectron TOF MS, which is located 109 cm downstream of the source. Carbonaceous clusters, of the generic formula C_nH_m, are formed in the same manner as C_n except that the helium carrier gas is replaced by a mixture of H_2 in helium. Vacuum ultraviolet photoionization using the light from an excimer laser (Questek 2820) operated on the F_2 line at 158 nm (7.89 eV) creates cluster ions in the ion source of the reflectron TOF MS. Typical laser pulse length and fluence are ~17 ns and 0.1 mJ/cm^2, respectively. The timing for these experiments is controlled by two digital delay generators (SRS DG535) under computer control.

The reflectron TOF MS is a modified version of a commercially available instrument (R. M. Jordan Co.) and is arranged such that the initial ion-beam axis is collinear with the neutral cluster beam. The repeller-extractor and extractor-ground plate spacings are 1.9 cm and 0.95 cm, respectively; the repeller and extractor voltages are 1800 V and 1000 V, respectively. The ion beam (nominal energy 1400 eV) is accelerated out of the ionization source along the neutral beam for 0.5 cm before entering a static deflection field of 37 V/cm that extends for 3.8 cm. This field deflects the ions over a total angle of 7.2°. After passing the first flight region (97.7 cm), the ions are deccelerated and re-accelerated in a two-stage reflector. The first stage is defined by two grided plates separated by 1.2 cm and has a 1000 V potential increase. The second stage is

9.7 cm long and consists of 11 guard rings with elliptical openings terminated by the reflector plate. Final temporal focusing of the ions is achieved by fine adjustments of the electric field in the second stage by changing the voltage applied to the reflector plate (nominally 1620 V). Ions emerging from the reflector traverse the second field-free flight region of 64.2 cm in length before striking a 40-mm-diameter dual microchannel plate detector (R. M. Jordan Co.). The ion time-of-flight signals are amplified (Comlinear CLC 100) and digitized by a 400 MHz digital oscilloscope (LeCroy 9450). The TOF mass spectrum is acquired as separate summation averages (typically 1000 laser shots) in 50-μs increments and is transferred from the digital oscilloscope to a host computer for analysis.

RESULTS
A. Mass Spectra
In Fig. 1 we display an example of the TOF mass spectrum of C_nH_m ions for n=16-160 obtained under moderate-growth source conditions with a 0.5% H_2/He mixture. We have taken many other C_n and C_nH_m mass spectra under low-growth and high-growth source conditions.[14] Our definitions of the growth characteristics in the cluster source are predicated on the nature of the carbon-cluster mass spectrum taken under identical detection conditions. We define "low-growth" conditions as those under which the odd-numbered C_n are roughly as abundant as the even-numbered clusters in the region near n=60 . A distribution near n=60 in which the even clusters, and particularly C_{60}, have considerably more intensity than the odd clusters defines "moderate growth" (see Fig. 1). For our cluster source with the flow channel described above, moderate growth is the norm, i.e. 100 psig backing pressure, full driving voltage applied to the valve, and vaporization timed to occur in the center of the gas pulse. Low growth can be achieved in several different ways: lowering the backing pressure to 10 psig, lowering the driving voltage on the piezoelectric valve, or by firing the vaporization laser early in the gas pulse. All of these approaches lower the effective density of the carrier gas over the target when the vaporization laser fires. We can also achieve high-growth conditions, in which C_{60} completely dominates the C_n distribution at 50≤n≤70, by running under nominal conditions and increasing the length of the flow channel by 27 mm. The observation of enhanced even/odd alternation with increasing carrier gas in the source is consistent with the model proposed by Smalley and Kroto in which the fullerenes are the survivors of the cluster-growth process that ultimately leads to carbon particles. Increasing the carrier gas density provides greater containment of the carbon vapor in the laser-induced plasma and thus provides a higher density of growth species and leads to more rapid condensation.

The moderate-growth mass spectrum produced with a 0.5% H_2/He mixture in Fig. 1 shows hydrogenated clusters, C_nH_m, that appear both with n even and odd up to about n=40. At this point the odd clusters continue to appear predominantly as hydrogenated species while substantial intensities of even C_n appear above this hydrocarbon "soup". Figure 2 displays the comparison of the C_n and C_nH_m moderate-growth mass spectra for n=21-24 and n=58-62. For a given n, the signal for each mass peak in the C_nH_m spectrum has contributions from the ^{13}C isotopic variants of C_n and from the C_nH_m species and their ^{13}C isotopic variants. This convolution, which increases in severity with increasing n because the ^{13}C distribution widens, makes it impossible to determine the distribution of hydrogenated species directly from the mass spectrum. Note the propensity for the formation of C_nH_2 for the even-numbered clusters in the n=21-24 range. The C_nH_m spectrum for n=58-62 in Fig. 2 shows hydrogenation of both even and odd clusters near n=60. However, the extent of the hydrogenation is clearly much greater for the odd clusters; substantial amounts of the even clusters appear as bare carbon clusters. In the low growth case, the addition of hydrogen enhances the appearance of the even C_n, and especially C_{60}, with respect to the hydrocarbon background. Remarkably, this occurs even when the even clusters do not appear as "special" in the corresponding C_n spectrum.

B. Hydrogenation Analysis
To quantify the extent of hydrogenation and the distribution of hydrogen atoms for C_nH_m at a given n, we have developed a procedure in which the effects of the ^{13}C isotopic distribution are deconvoluted from the hydrogenation distribution. Ref. 14 describes this procedure in detail.

It is applicable to situations in which the hydrogenation distribution for cluster n ends before the one for cluster n+1 begins, i.e. m≤11. For the data presented here, we can apply the deconvolution to the moderate-growth spectrum over the entire range of n in which sufficient mass resolution is maintained (typically n≤100). From the analysis we extract the hydrogenation fraction, x_h, and the fractional abundance for each m, g_m.

One of the more dramatic effects, discussed qualitatively above, that we observe in the carbonaceous cluster distributions is the tendency for the even clusters above n=40 to appear as bare C_n while the odd clusters are hydrogenated. This effect is shown vividly in Fig. 3 in which we plot the hydrogenation fraction, x_h, versus cluster size, n, for the moderate-growth experiment. At low n both odd and even clusters show hydrogenation fractions that are high, 75-90%. At about n=40 there is a sharp drop in x_h for the even clusters while the hydrogenation fraction for the odd clusters stays high, never dropping much below 80%. The hydrogenation fraction is lowest for the even clusters in the n=50-70 range with a sharp minimum at n=60. The dramatic odd/even alternation near n=60 is shown quite nicely in the mass spectrum (Fig. 2); only 34% of the n=60 peak corresponds to $C_{60}H_m$ while 85% of the neighboring n=61 peak is due to hydrogenated species. Above n=70 the hydrogenation fraction gradually increases for even n and decreases for odd n, with the two curves apparently heading toward a common asymptote. This trend cannot be confirmed in this data because of the loss of mass resolution at n>100.

We can quantify the tendency for even C_nH_m to appear with m=2 by examining the ratio of the fractional abundances for m=2 and m=1, g_2/g_1. Fig. 3 displays a plot of g_2/g_1 versus n for the moderate-growth data. For the odd clusters this ratio stays constant at or near unity until around n=70. By contrast, g_2/g_1 is much larger for the even clusters until it drops quickly near n=40 so that for n≥46 the ratio is nearly identical for both odd and even clusters. This data demonstrates that with small amounts of hydrogen present in the source clusters as large as n=44 have a decided preference to appear as C_nH_2; odd clusters show no such preference. Near n=60, both even and odd clusters show a hydrogenation distribution that decreases monotonically with m and thus $g_2/g_1<1$. As n increases above about 70, the distributions widen and develop maxima at m>1 so that the ratio g_2/g_1 gradually rises to values larger than unity.

DISCUSSION AND CONCLUSIONS

The mass spectra of C_nH_m ions for 8≤n≤20, produced by multiphoton ionization of neutrals made by addition of various reactants to the carrier gas, have been discussed by Heath et al.[13] They also observe the tendency for even clusters to form C_nH_2 species while the odd numbered clusters generally are found to have no distinctive hydrogenation pattern. The formation of C_nH_2 species is a strong signature of linear polyacetylenes of the form H-C≡C-(C≡C-)$_m$C≡C-H. Heath et al. postulate that these form by the addition of two hydrogens to the terminal carbons of linear carbon chains that are triplet diradicals, •C≡C-(C≡C-)$_m$C≡C•. Our data extends the results of Heath et al. to larger clusters. Interestingly, we observe a preference for C_nH_2 formation for even clusters up to n=44. This preference demonstrates that at least some of the C_nH_m species formed in our experiments are very long polyacetylenes. For n≥10 theoretical calculations for bare carbon clusters agree that monocyclic rings are more stable than linear chains. However, for reasons we now explore, it seems highly unlikely that long polyacetylenes are formed by hydrogenation of existing monocyclic rings.

In this type of experiment, where H_2 is added to the carrier gas upstream of the laser-induced plasma, we interpret the results in terms of a modification of the cluster growth that occurs without the reactant gas. The most important hydrogenation reactions are probably facile radical-radical reactions, i.e. reactions between H atoms and carbon or carbonaceous radicals. The results of Heath et al. support the assertion that H-atom reactions are important; they observe similar C_nH_m products for a variety of hydrogen-containing reactants.[8] Under our experimental conditions the carbon density in the vaporization plume is in great excess of the H-atom concentration and carbon-cluster growth via reactions with small growth species (C, C_2, and C_3) will proceed largely as if there was no reactant gas. The important difference is that hydrogen atom attack on a radical center might now render a cluster relatively inert with respect to further growth or hydrogenation. For even clusters with less than about 44 atoms this is observed as the formation of long polyacetylenes, the first non-radical species that can be formed

for a linear geometry. It is important to note that H-atom attack on a radical center might occur at any point in the cluster growth, not just at the end. For example, a linear C_{10} might be terminated at one end but continue to grow via carbon addition at the other, reactive end until it also encounters an H atom and is terminated.

The same picture of the modification of cluster (and ultimately particle) growth can be used to interpret our results for the larger carbonaceous clusters ($n \geq 40$). The results of our hydrogenation analysis of the data taken under moderate-growth conditions show dramatically the change in nature of the carbon and carbonaceous clusters near n=40. The plots of hydrogenation fraction and the ratio g_2/g_1 versus cluster size (Fig. 3) are particularly vivid in this regard. This pronounced change in behavior must be associated with a global change in geometric structure. Near n=40 the evidence for linear polyacetylenes disappears and the even clusters become inert relative to their odd neighbors. Clearly, even-numbered can adopt structures that do not have reactive, radical centers, i.e. closed shell fullerenes. By contrast, the odd clusters always appear hydrogenated, since they can only eliminate dangling bonds by hydrogenation.

As with the smaller clusters, the addition of hydrogen to the source in our experiments produces a relatively small perturbation in the overall growth of clusters and particles. One possible effect is that the H atoms in the cluster-growth region might decrease the likelihood of shell closure by tying up the radical sites at the edges of spiraling shells. However, the addition of hydrogen always accentuates the appearance of the fullerenes through the preferential hydrogenation of the neighboring odd clusters. This effect is especially pronounced in the low-growth spectra. On the basis of the low-growth C_n distribution alone, one might infer that both even and odd clusters are unclosed, reactive isomers, i.e. the even clusters have not yet found their way to closure. Yet, the addition of hydrogen under low-growth conditions clearly shows that some of the even clusters have already closed and become unreactive.

The implication of these results is that cluster growth and cluster hydrogenation are at least partially separable processes, with growth preceding hydrogenation. As noted above, it is dangerous to interpret our experiments entirely in this manner since hydrogen is present at all times in the course of cluster growth. However, such behavior can be rationalized both on fluid dynamic and thermodynamic grounds. Large clusters, and even particles, grow rapidly in the vaporization plume where the concentration of growth species in the carbon vapor is high relative to the hydrogen reactant. Significant hydrogenation may not take place until the vaporization plume is mixed by turbulence with the reactant/carrier gas mixture at points downstream. Also, in the high-temperature vapor plume the graphitic, spiraling shells are thermodynamically favored over their hydrogentated analogs. As the temperature drops during the flow through the source, irreversible hydrogenation of reactive sites can produce carbonaceous clusters. The even clusters can adopt closed structures under high-temperature pyrolytic conditions and thus become inert to subsequent hydrogenation at lower temperatures. By increasing the carrier gas density to our moderate-growth conditions, we drive the condensation process harder by increasing the carbon density in the high-temperature region, thereby allowing more even clusters to become fullerenes. Addition of small amounts of hydrogen under these conditions effectively "titrates" the odd clusters by hydrogenation but the unreactive even clusters emerge largely unscathed (see Fig. 2).

The conditions in our experiments are intentionally adjusted in order to avoid extensive hydrogenation. The relatively small amount of hydrogenation is thus insufficient to tie up all the reactive sites in a growing cluster and substantially slow further growth toward particles. The C/H ratio for the C_nH_m species that we produce in the moderate-growth experiment increases monotonically from ~6 at n=20 to ~18 at n=100. These values are much higher than what one would expect for spiraling shells whose reactive edges were completely saturated with hydrogens. As an upper bound on the C/H ratio of such species, consider the series of D_{6h} polycyclic aromatics of the form $C_{6j2}H_{6j}$, i.e. C_6H_6, $C_{24}H_{12}$, $C_{54}H_{18}$, $C_{96}H_{24}$, etc. The C/H ratio in these planar species is simply j; the C/H ratio is 3 at n=54 and 4 at n=96. Generally, a partially closed shell will have fewer possibilities for C-H bonds than these species. A reasonable estimate might be a shell with half as many reactive sites; this gives a C/H ratio of 6-8 for n=54-96. We observe a C/H ratio of 15-20 in this size range in our moderate growth

experiment. This indicates that the hydrogenation distributions are still in the kinetically limited regime and do not represent saturation of all reactive sites. Finally, we note that our carbonaceous clusters are more carbon-rich than soot particles formed in combustion processes. Typically, nascent soot particles have a C/H ratio of 2-3 that may increase to 8-10 as the soot dehydrogenates at later stages in the flame.[10]

Our results, in which we study the formation of carbon and carbonaceous clusters in a laser-vaporization source with controlled addition of hydrogen, are quite similar to those obtained in a variety of other *in vacuo* laser vaporization studies[1-3] and in the flame studies of Homann et al.[4,5] In all these cases, the large, even carbon clusters appear as the dominant mass spectral feature under conditions where there are substantial quantities of elements, especially hydrogen, other than carbon in the growth region. In our controlled hydrogenation studies we create conditions in which the neighboring odd clusters form a hydrocarbon background against which the fullerenes appear. We suspect that in some of the other vaporization studies and flame investigations the fullerenes stand out from a similar, unresolved hydrocarbon background, although the hydrogenation may be more extensive and thus spread the cluster distribution over a wider mass range. The idea that rapid carbon-cluster growth, and occasional fullerene shell closure, occurs in high-temperature regions where hydrogenation, or oxidation, is not favored must also apply to these environments. In the laser vaporization experiments, the high-temperature region is the laser-induced, high density plasma formed above the substrate, whether it be soot[3] or various polymers.[2] In the flame studies, the fullerenes are found in the region where the temperature is near it maximum (T~2100 K) and soot particles first begin to form.[4,5] The exciting and unanswered question in these experiments is whether the fullerenes are created during soot formation, as proposed by Smalley and Kroto, or as the result of vaporization from the surface of a soot particle, as hypothesized by Homann et al.[5]

One of the great difficulties in elucidating the mechanism of soot inception is that the species one observes in a sooting flame, whether they be polycyclic aromatics or fullerenes, are the by-products of the process. The keys to any chemical mechanism are to be found in the radical species that control the kinetic pathway. Unfortunately in the case of soot formation, these radicals wind up buried in the soot particles; the manner in which they arrived there is but a distant memory. Analysis of the particles, while informative, cannot provide the data necessary to differentiate between hypothetical formation pathways.

In the future, we shall investigate the role of large carbonaceous clusters in soot inception and growth by concentrating on reaction studies of the reactive clusters. These may be the odd clusters, which can never completely close, or the reactive isomers of the even clusters. The cluster beam source provides an ideal forum for studies of reactive intermediates because these species can be frozen out in the free jet expansion. We shall perform more studies, such as those presented here, in which reactants are added upstream of the vaporization. Of particular interest is the formation of carbonaceous clusters under conditions that emulate those in a sooting flame, i.e. oxidative, not just pyrolytic. In addition, we shall pursue more controlled chemical reactions using the fast-flow reactor techniques that have been used so successfully in the study of metal cluster chemistry. Zhang et al. have performed some initial work in this area on the large carbon clusters.[8] However, their study was aimed principally at the unique, unreactive nature of the fullerenes; the products of reactions with odd clusters were observed only as unresolved background. We intend to use the high resolution of the reflectron to sort out the products of reactions such as $C_nH_m + C_2H_2$, which represents a model for the growth of a soot particle through the addition of acetylene. Again, the emphasis will be on arresting the growth process in order to examine clusters that are reactive intermediates and not on the stable by-products, such as the fullerenes.

References
1. D. N. Lineman, K. V. Somayajula, A. G. Sharkey, and D. M. Hercules, J. Phys. Chem. **93** (1989) 5025.
2. W. R. Creasy and J. T. Brenna, J. Chem. Phys. **92** (1990) 2269; W. R. Creasy and J. T. Brenna, Chem. Phys. **126** (1988) 453.
3. H. Y. So and C. L. Wilkins, J. Phys. Chem. **93** (1989) 1184.

4. Ph. Gerhardt, S. Löffler, and K. H. Homann, Chem. Phys. Lett. **137**, 306 (1987).
5. Ph. Gerhardt, S. Löffler, and K. H. Homann, *Twenty-Second Symposium (International) on Combustion*, p. 395 (The Combustion Institute, 1989).
6. H. W. Kroto, Nature **329**, 529 (1987).
7. H. W. Kroto and K. McKay, Nature **331**, 328 (1988).
8. Q. L. Zhang, S. C. O'Brien, J. R. Heath, Y. Liu, R. F. Curl, H. W. Kroto, and R. E. Smalley, J. Phys. Chem. **90**, 525 (1986).
9. R. M. Baum, "Ideas on Soot Formation Spark Controversy," Chem. and Eng. News, February 5, 1990, p. 30.
10. S. J. Harris and A. M. Weiner, Ann. Rev. Phys. Chem. **36**, 31 (1985).
11. K. H. Homann, *Twentieth Symposium (International) on Combustion*, p. 857 (The Combustion Institute, 1984).
12. H. GG. Wagner, *Seventeenth Symposium (International) on Combustion*, p. 3 (The Combustion Institute, 1979).
13. J. R. Heath, Q. Zhang, S. C. O'Brien, R. F. Curl, H. W. Kroto, and R. E. Smalley, J. Am. Chem. Soc. **109**, 359 (1987).
14. E. A. Rohlfing, J. Chem. Phys. **93**, 7851 (1990).
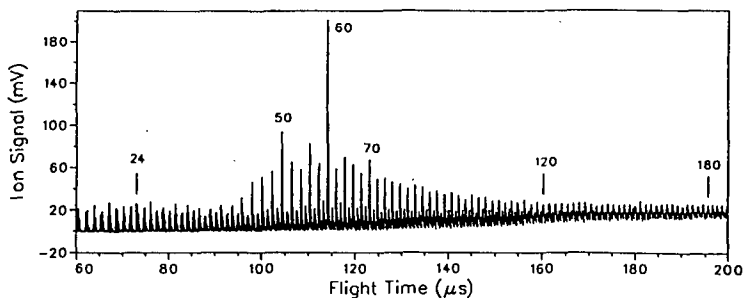
FIG 1. Reflectron TOF mass spectrum of carbonaceous clusters, C_nH_m, produced with a 0.5% H_2/He mixture as the carrier gas under moderate-growth conditions in the cluster source.
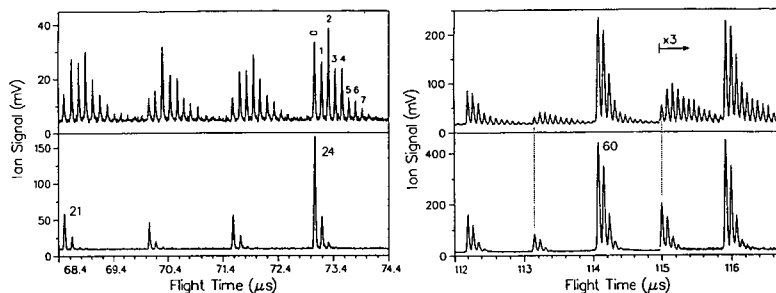
FIG. 2. Close-up views (n=21-24 and n=58-62) of the C_n and $C_n H_m$ mass spectra taken under moderate-growth conditions. Top panels: spectra of C_n taken with He carrier gas; bottom panels: spectra of $C_n H_m$ taken with 0.5% H_2/He carrier gas.
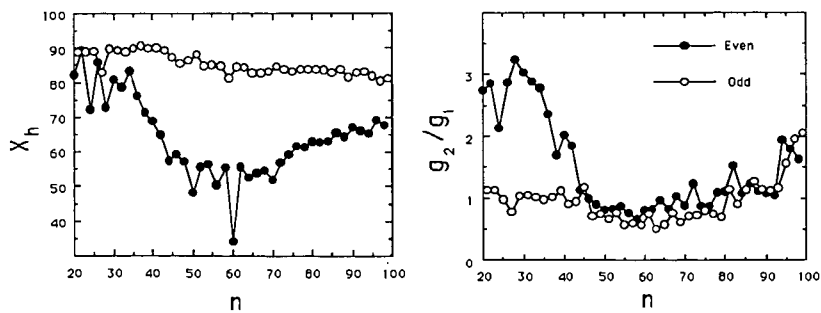
FIG. 3. Results of hydrogenation analysis for moderate-growth $C_n H_m$ mass spectrum (Fig. 1) as a function of cluster size, n. Left: the fraction of hydrogenated species. Right: the ratio of fractional abundances of for m=1 and m=2.

1532

Polycyclic Aromatics, Fullerenes and Soot Particles
as Charged Species in Flames

Th. Baum, S. Löffler, P. Weilmünster and K. H. Homann
Institut für Physikalische Chemie, Technische Hochschule Darmstadt
Petersenstr.20, D-6100 Darmstadt

1. INTRODUCTION AND EXPERIMENTAL

The ionic structure of fuel-rich hydrocarbon flames resembles the
profiles of the larger neutral intermediates much more than those of
initial reactants and main products. This applies in particular to
polycyclic aromatic hydrocarbons (PAH). They have low and rather
similar ionization potentials and relatively large proton affinities.
The pattern of reactions of positive ions, condensation and cycli-
zation reactions, shows many similarities with the behavior of their
neutral counterparts. Apart from the predominance of some PAH$^+$ with
an odd number of C atoms, which would be radicals in the neutral
state, the occurrence of PAH$^+$ is an indication of the existence of
the respective neutral compounds. Thus, large flame ions, their
composition, reactions and equilibria at high temperature are not
only of interest for themselves, but also reflect the existence and
behavior of large neutral PAH. The discussion of fullerenes in flames
has still to be based solely on their ions.

The experimental procedure of sampling 26.6-mbar flat premixed flames
via a two-stage nozzle/molecular beam sampling system and analyzing
the ions by a time-of-flight MS has been reported [1, 2]. Recently,
the MS was modified by adding a Mamyrin-type ion reflector, thereby
increasing the mass resolution $(m/\Delta m)_{50\%}$ to about 1500. The
flight time was determined by a multi-stop time-to-digital converter.
Ion signals from about 20.000 extraction pulses were summed up to
give the mass spectrum. Details will be published elsewhere [3].

2. POLYCYCLIC AROMATIC HYDROCARBON IONS (PAH$^+$)

The main formation of the PAH$^+$ in sooting flames takes place in the
oxidation zone where their concentrations go through maxima (Fig. 1)
[2]. The decrease of the PAH$^+$ with $m \lesssim 325$ u after their
maxima is due to thermal decomposition, probably initiated by
oxidative attack. It takes place almost simultaneously for these
lower-mass PAH$^+$. The larger PAH$^+$ with $m \gtrsim 325$ u continue to
grow as shown by the shift of their maxima to greater heights with
increasing mass. The largest PAH$^+$ in acetylene flames reach masses
of about $2.5 * 10^3$ u.

PAH$^+$ occur with any number of C atoms and those with a certain car-
bon content contain a varying number of hydrogen atoms (Fig. 2). The
number of H atoms points to certain structures. Other arguments in
this respect are the thermal stability, the relation to identified
neutral PAH and the occurrence of certain side chains, the prevalance
of peri-condensation and the possibility of protonation and deproto-
nation as a function of temperature.

The relatively large concentration of $C_{13}H_9^+$ in C_2H_2
flames, an indication of little reactivity, is a strong argument for
the stable fully condensed phenalenylium (I):

(I)   (II)

1533

Other isomers such as (II) would be less stable. The far less ther-
mally stable dihydro-compound, $C_{13}H_{11}^+$, occurs in extremely low
concentration. At higher temperature, $C_{13}H_7^+$ is formed, an ion
that cannot be formulated as a tricyclus without assuming a benzyne
bond which was never observed in flame components. A more probable
structure, compatible with structural elements normally found in PAH,
would be:

It could be formed by thermal decomposi-
tion from phenalenylium via retro-inser-
tion out of a six-membered ring followed
by H_2 elimination from the resulting
side chain. Structures with side chains
containing triple bonds are suggested for the relatively hydrogen-
poor PAH^+ with $m \lesssim 300$ u. It is known from butadiyne pyrolysis
that such side chains are split off from PAH at temperatures $\gtrsim 1400$ K
[4]. This would fit the finding that the lower-mass PAH^+
decompose thermally in a flame zone where polyyne ions are formed.

A $C_xH_{y+2}^+$, being present in appreciable concentration compared to
a main PAH^+ $C_xH_y^+$, indicates a change in the carbon skeleton
rather than hydrogenation. For $C_{15}H_9^+$ probable structures are

or

while $C_{15}H_{11}^+$ is rather a tricyclus with a CH_2 group

or
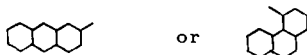
Protonation enlarges the variation in the number of H atoms of even-
numbered PAH^+ without change in the carbon skeleton (Fig. 2). An-
other example is the C_{16}-PAH which is present as $C_{16}H_{11}^+$
(protonated pyrene or less probable fluoranthene, closed-shell ions)
and $C_{16}H_{10}^+$ (ionized pyrene, radical ion). At lower temperature
the protonated PAH is formed, but at higher temperature the latter
attains even larger concentrations. $C_{16}H_9^+$ which is assumed to be
a butadiynyl-acenaphtylene ion is also formed at high temperature.

For larger PAH, the number of H atoms depends on the arrangement of
rings. Divergence from a more circular system to an elongated or
ribbon-like PAH increases the number of hydrogen atoms by 2 or a
larger even number, for example

$C_{48}H_{18}$ $C_{48}H_{18}$ $C_{48}H_{20}$ $C_{48}H_{22}$

On the other hand

$C_{48}H_{16}$ $C_{48}H_{14}$
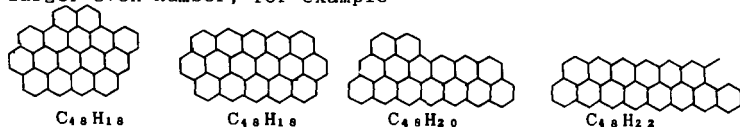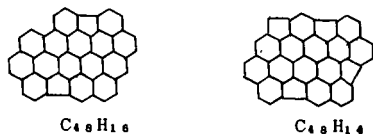
Formation of 5-rings condensed with the 6-rings diminishes the number
of H atoms by 2 or a multiple thereof. This possibility of forming
relatively hydrogen-poor PAH+ is held more probable for high-mass
ions.

Of the many possible variations in the number of H atoms for a fixed
number of C atoms only a few, seldom more than 3 for odd-numbered and
4 for even-numbered PAH+, are realized, even in the case of large
PAH+. Although there are shifts in the abundance of H-rich and
H-poor PAH+ with temperature, there is always one certain C-H-com-
position that dominates in a group of ions with the same number of C
atoms. This is always compatible with a highly condensed arrangement
of 6-rings with one or no 5-ring. However, in the case of large
PAH+ these predominant C-H-compositions would also fit to elongated
or ribbon-like ring arrangements with an increased number of 5-rings.
This option would be in favor of fullerene formation, see below.

Oxo-PAH+, such as $C_{12}H_9O^+$, $C_{16}H_{11}O^+$ and $C_{18}H_{11}O^+$ up to
$C_{34}H_{13}O^+$, are intermediates in fuel rich benzene flames. They
occur together with PAH+ [5]. Probably, the positive charge is
located on an O atom outside the ring system, for example:

or
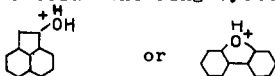
This structure is more stable than

Oxo-PAH+ are thermally less stable than PAH+ with the same number
of C atoms. A primary decomposition step of oxo-PAH+ probably is
the elimination of CO, for example:
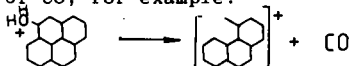
This mechanism of PAH+ formation is not taking place in acetylene
flames, since no oxo-PAH+ are formed from this fuel. Many PAH+ in
benzene flames contain two more H atoms and probably have structures
different from those with the same number of C atoms in acetylene
flames. $C_{13}H_9^+$ is missing in benzene flames since there is no
easy mechanism by which it could be formed through CO elimination
from $C_{14}H_9O^+$. High-resolution mass spectrometry will show
whether such differences in H content do also occur in larger PAH+.
This might have to do with the stop of PAH+ growth at 900 to 1000 u
and the absence of charged soot particles in benzene flames up to a
C/O = 0.93.

Oxo-PAH- which are only formed in flames of aromatic fuel also
decompose within the oxidation zone by elimination of CO giving
PAH-, for example:
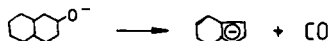
The resulting PAH- with their comparatively stable cyclopentadienyl
anion structure, also unique in benzene flames, do not show further
growth. That the negative charge of oxo-PAH- is located on the O
atom is supported by the fact, that they are able to grow by conden-
sation reactions with lower unsaturated hydrocarbons.

3. POSITIVELY CHARGED SOOT PARTICLES

PAH$^+$ with $m \gtrsim 350$ u grow continuously until their average mass
reaches about 800 to 1400 u in sooting acetylene flames. Then a new
broad distribution of masses ranging from about 2.5 to 7 $*$ 10^3 u
appears. It has a flat maximum at about 4 $*$ 10^3 u (Fig. 3, 11mm).
This is due to the first charged soot particles. About 0.3 ms later
(12 mm), it has increased in intensity, peaks at 5 $*$ 10^3 u and
extends to 10^4 u. Meanwhile, the large PAH$^+$ have disappeared to a
large degree. Instead of a continuous shift of the PAH$^+$ distribu-
tion into the range of the beginning charged soot, there remains a
minimum at about 2 $*$ 10^3 u. This behaviour is interpreted as a
switch from a mainly two-dimensional growth of the PAH$^+$ to a three-
dimensional growth of soot particles, initiated by sticky collisions
of large PAH$^+$ with neutral PAH of the same mass range. The total
ion concentratiom stays almost constant between 11 and 12 mm [1].

From 14 mm on, the number density of charged soot particles increases
strongly because of the onset of thermal ionization. The further
development of the particle mass distributions is shown on Fig. 4,
obtained from measurements using a combination Wien-filter/energy
discriminator for mass analysis [6].

At the start of soot formation in acetylene flames, the fraction of
positively charged soot is very low, of the order of 1 % . It increa-
ses to 30 - 40 % (depending on the burning conditions) when the sin-
gle particles have reached their final size [7]. Thus, the largest
part of positively charged soot is formed by thermal ionization from
neutral soot and not as a consequence of growth of PAH$^+$. Most of
the charged particles carry a single charge. With increasing flame
temperature the fraction of doubly charged particles increases up to
about 10 %. There is also negatively charged soot. It is formed some-
what later and its amount does not reach that of the positively char-
ged soot (15 to 25 %). The percentage decreases with increasing flame
temperature. As pointed out, PAH$^-$ do not grow. Therefore, there is
no connection between PAH$^-$ and the first negatively charged soot
which most probably is formed by electron attachment to neutral
particles.

In benzene flames (for C/O < 0.93) the growth of PAH$^+$ stops at
about 1 $*$ 10^3 u and only neutral soot is formed thereafter. The
reason for this behavior of PAH$^+$ is not quite clear. The lower con-
centration of acetylene and polyynes, the higher temperature together
with the partly different structure of PAH$^+$ in benzene flames might
be the reason. The lack of thermal ionization of soot is caused by
the smallness and the slow growth of the first particles in low-pres-
sure benzene flames which is also correlated with the lower concen-
tration of highly unsaturated aliphatics.

4. FULLERENE IONS

Fullerene ions of both sign cover a much larger mass range than PAH
ions. The smallest positive ion detected in benzene flames is
C_{32}^+ (384 u). The largest one in sooting acetylene flames exceeds
C_{500}^+ (6000 u) as shown by the mass spectrum in Fig. 5. General-
ly, there are a few outstanding peaks (C_{50}, C_{60}, C_{70}, C_{74},
C_{82}, C_{84}) and a much larger number of quasi-continuously distri-
buted species [5]. A mass spectrum of negative fullerene ions from

the burned gas of a benzene flame in Fig. 6 shows the same general
appearance. It differs, however, in some details such as the forma-
tion of very small fullerenes like C_{36}^- (smallest in acetylene
flames is C_{44}^-) and the occurrence of odd-numbered fullerenes
containing 1 to 2 H atoms centered around C_{50}^- and (to a less
degree) around C_{70}^-. There are further differences in the ion
abundances depending on the height in the flame, the sign and the
burning conditions.

The largest difference in the nature of fullerene ions is caused by
the onset of soot formation. Fig. 7a demonstrates the change in the
fullerene mass spectrum from the soot-free oxidation zone to the soot
forming zone in the burned gas of the same benzene flame. A princi-
pally similar result was obtained with mass spectra from the burned gas
of acetylene flames below and above the critical C/O for soot forma-
tion, see Fig. 7b. In both cases the overall abundance of the ions
increases and the quasi-continuous distribution of the heavier fulle-
renes appears when soot is formed. There are mainly some of the
outstanding peaks where the fuel-rich flames are free of soot.

In acetylene flames, where the oxidation and the soot-forming zone is
clearly separated, the concentration of fullerenes drops to very low
values where the temperature is near its maximum and the O_2 is not
yet completely consumed. This minimum is specially marked for nega-
tive fullerene ions. It is interpreted as burning of the lower-mass
fullerenes. A decrease in the total negative ion concentration may
contribute to this effect [1]. In benzene flames where these two
zones overlap the intermediary decrease is weak for negative fulle-
renes and not expressed in the positive ion profiles. Formation of
fullerenes in the oxidation zone can be suppressed by increasing the
temperature.

In the secondary reaction zone of the flame, where O_2 is not yet
completely consumed, large fullerene ions of vastly different mass
are formed almost simultaneously in the presence of soot. The pro-
files do not indicate a growth of fullerenes. They reach a second
maximum in the burned gas and also decrease simultaneously, probably
by charge recombination. The formation of the "prominent" fullerene
ions (C_{50}, C_{60}, C_{70}) in this zone is more or less retarded,
depending on the burning conditions. In particular, C_{60}^- increa-
ses steadily in the burned gas where large negative fullerenes
decrease.

While the formation of large PAH may in principle be explained by the
growth of lower mass species through reaction with unsaturated C_2-,
C_3- and C_4-hydrocarbons and/or the respective radicals, this is
not so for the fullerenes. C_{60}^+ is always the first to be obser-
ved without being preceded by lower-mass fullerenes. It lies between
the C_{58}- and C_{59}-PAH$^+$ in the mass spectrum. But these species
contain between 18 and 20 H atoms and therefore have quite a diffe-
rent structure. The question is, how might closed-cage molecules (or
ions) with 12 five-membered rings be formed in a homogeneous reaction
without going through intermediates with too much ring tension.

If the mass spectrum of PAH$^+$ is searched for possible "pieces" of
C_{60}^+, the free valencies of which being saturated by H, there are
mainly smaller mass PAH$^+$ up to 250 u, the C skeletons of which are
structural elements of C_{60}. Mass 250 ($C_{20}H_{10}$) could represent a
PAH consisting of five 6-rings surrounding one 5-ring. $C_{30}H_{12,13}$
with mass 372 and 373 u which would be the molecular formula for one

"half" of a C_{60} occurs only in very minor concentration. A formation of C_{60} by reactive collision of two half-shells would be too slow because of the low concentrations of the reactants. There is an ion with composition $C_{30}H_6^+$ in very low abundance, which does not fit any C_{60}^+ fragment. The fact that large PAH$^+$ with very low hydrogen content could not be detected, indicates that the loss of hydrogen and the formation of most of the 5-rings takes place simultaneously in late stages before completion of the ball. A possible mechanism along these lines might be the following: If two 6-rings at the poles of C_{60} are removed, there remains a closed ribbon of 48 C atoms that unwrapped has the structure
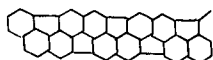
This would correspond to $C_{48}H_{18}$ which is the main C_{48}-PAH$^+$. It contains the structural elements of acenaphthylene and benzo-[ghi]perylene which are quite common among the PAH. As the number of 5-membered rings is relatively low for the size of the ring system and they are condensed only with four 6-rings, there is no serious ring tension. The molecule bends almost by itself towards closing of the ribbon, see Fig. 8. Most of the C_{48}-PAH$^+$ will have flat structures given in section 2, but a few percent might be ribbon-shaped. Addition of two benzene molecules and a rapid stepwise formation of C-C bonds by an intramolecular condensation with simultaneous splitting off of H_2, while double bonds are regenerated, could finally give C_{60}. This accumulates because of its chemical inertness. The fact that fullerene concentration may be up to ten times larger in benzene flames than in acetylene flames might be an indication that reactions with benzene are important steps. A similar mechanism could be possible for C_{70}. However, there is still no indication how the large fullerenes could be formed, other than probably by heterogeneous reaction which involves very small soot particles.

References

[1] Ph. Gerhardt, K.H. Homann, Combust.Flame 81, 289 (1990)
[2] Ph. Gerhardt, K.H. Homann, J. Phys. Chem. 94, 5381 (1990)
[3] Th. Baum, P. Weilmünster, K. H. Homann, Ber. Bunsenges. Phys. Chem. to be published
[4] K.H. Homann, U.v.Pidoll, Ber. Bunsenges. Phys. Chem. 90, 847 (1986)
[5] S. Löffler, K.H. Homann, 23rd Sypm. Internat. on Combust., The Combustion Institute, Pittsburgh, 1991, in press
[6] K. H. Homann, J. Traube, Ber. Bunsenges. Phys. Chem. 91, 828 (1987)
[7] K. H. Homann, H. Wolf, 21st Symp. Internat. on Combust., p. 1013, The Combustion Institute, Pittsburgh 1986
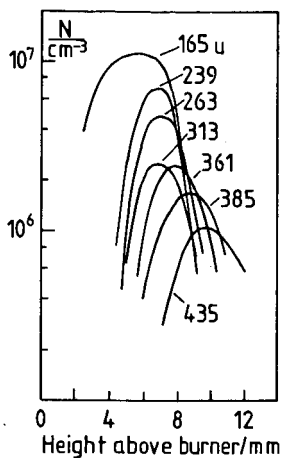
Fig. 1 PAH⁺ profiles in a sooting C_2H_2/O_2
flame; C/O $\approx$ 1.12; p = 26.6 mbar
v_u = 42 cm/s
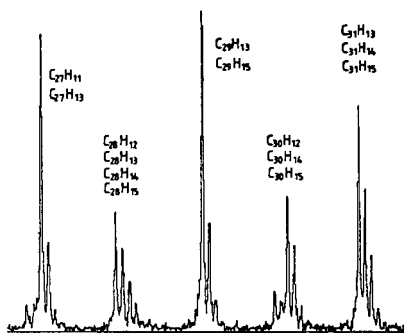
Fig. 2 PAH⁺ with the same number of C
occur with different numbers of H;
C_2H_2/O_2 = 1.0; p = 26.6 mbar
$v_u \approx$ 42 cm/s; h = 12 mm
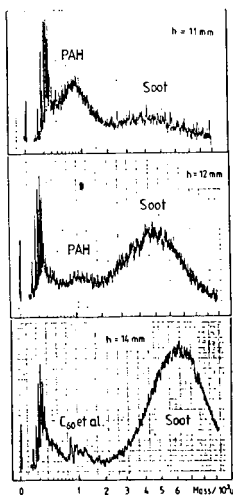
Fig. 3 Mass distributions at
the transition from
PAH⁺ to charged soot
particles;
C_2H_2/O_2 = 1.12
p = 26.6 mbar; v_u = 42 cm/s
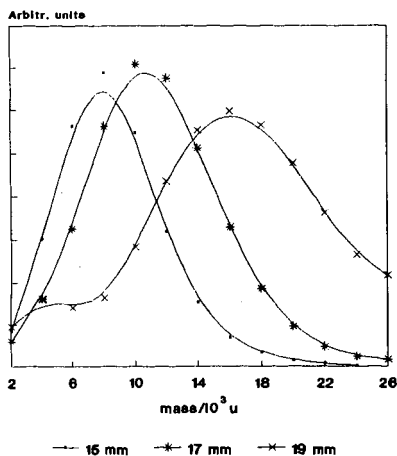
Fig. 4 Mass distribution of charged
soot particles in a C_2H_2/O_2
flame;
C/O = 1.06; p = 26.6 mbar;
v_u = 50 cm/s

1539
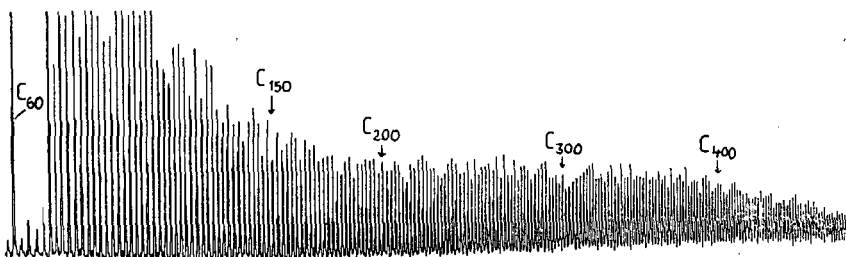
Fig. 5 Mass spectrum of positive fullerene ions from a sooting
C_2H_2/O_2 flame; C/O = 1.0, h = 20 mm, p = 26.6 mbar,
v_u = 42 cm/s. The peaks to C_{104} are truncated.

Fig. 7a Negative fullerene ions in the
soot-free oxidation zone (7 mm) and in
the sooting zone (9 mm) of a C_6H_6/O_2
flame; C/O = 0.76, v_u = 42 cm/s;
7b: The same ions in the burned gas of
a non-sooting (below, C/O = 0.84) and
a sooting (C/O = 0.90) acetylene/O_2
flame; h = 28 mm, v_u = 42 cm/s

Fig. 6 Mass spectrum of
negative fullerene ions from
a benzene/oxygen flame;
C/O = 0.76, h = 12 mm,
p = 26.6 mbar, v_u = 42 cm/s

Fig. 8 Tentative mechanism of C_{60}
formation from a bent ribbon-shaped
PAH $C_{48}H_{18}$ and two benzene
molecules. The dots mark C atoms
which carry H atoms while the hidden
ones are not marked.

1540
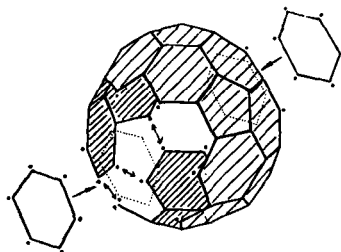
FLUXES AND NET REACTION RATES OF
FLAME SPECIES PERTINENT TO FULLERENES

Christopher J. Pope and Jack B. Howard
Department of Chemical Engineering
Massachusetts Institute of Technology
Cambridge, MA 02139

ABSTRACT

Signal intensities of 200+ amu material previously obtained by molecular beam mass spectrometric (MBMS) probing of a low-pressure premixed near-sooting benzene-oxygen flame were analyzed so as to determine mole fractions, fluxes and net reaction rates for 50-amu fractions of high molecular weight flame species. The results show trends indicative of preferential accumulation of mass in the 700-750 amu fraction. The pertinence of these results to Buckminsterfullerene (C_{60}) will be considered, and the observed concentrations will be compared with literature values for C_{60} ions in similar flames. Mechanistic implication of the presence of fullerenes in a non-sooting flame will be discussed.

INTRODUCTION

Understanding the behavior of molecular weight growth products in flames in the mass range of roughly 300 to 2000 amu has been limited by the scarcity of data for these species. The concentration profiles of chemical species in flames have been measured for compounds as large as $C_{16}H_{10}$ (MW=202) by molecular beam/mass spectroscopic (MBMS) sampling[1], and $C_{24}H_{12}$ (MW=300) by gas chromatography (GC)[2]. Homann and coworkers, using MBMS with time-of-flight (TOF) mass spectrometry, have observed in the above mass range both positively- and negatively-charged ions, suspected to be fullerenes[3,4] and their precursors[5].

Bittner's MBMS data for a near-sooting (equivalence ratio ϕ=1.8) benzene-oxygen-30% argon 20-torr flat flame also include high-mass signal profiles for all species with masses greater than a given cutoff value; this cutoff mass was incremented by 50 amu in the range of 200 to 750 amu, inclusive. Howard and Bittner[6] analyzed these high mass data for the near-sooting flame and similar data from a sooting (ϕ=2.0) benzene flame, reaching tentative conclusions about the formation and destruction of the high molecular weight material (HMWM) and about its possible role in soot formation. Their analysis of the near-sooting data also gave evidence of the development of a bimodal distribution of the masses of the HMWM with increasing height above burner (HAB). The earlier work was done without detailed flux and rate information, which was later generated by Pope[7], and with only an approximate treatment of the diffusion of the HMWM.

In the present work, the high-mass signals of Bittner's near-sooting flame are analysed. The earlier analysis of these data by

Howard and Bittner is extended by treating each 50-amu interval as an individual species and by calculating fluxes and net reaction rates for each interval. Approaches used to overcome limitations of the earlier work are discussed. Preliminary analysis of the results gives information on the prevalence and behavior of soot precursors. The results also give evidence consistent with the existence of C_{60} in a non-sooting flame.

TRANSPORT PROPERTIES OF HIGH MOLECULAR-WEIGHT MATERIAL

In flat flames, knowledge of the transport properties of the individual species is essential in obtaining kinetic information from concentration data. Flat flames can be described as one-dimensional plug flow reactors with strong axial diffusion. Due to strong diffusional effects, concentration profiles reflect both transport processes and chemical reaction. Kinetics or rate information is obtained from individual species concentration data by application of the one-dimensional flame equations of Fristrom and Westenberg[8]. The concentration data (as a function of location) are combined with the diffusion equation to obtain molar fluxes of each species at each location; the derivative of the molar flux with respect to distance yields the net reaction rate of the individual species.

The mixture diffusion coefficients used in the calculation are obtained from the binary diffusion coefficients using the relation of Wilke[9]; binary diffusion coefficients are calculated from the Lennard-Jones (12,6) potential. Since the mixture diffusion coefficients depend on the composition of the mixture, and since the composition changes dramatically in the region of interest, the calculation requires concentration data for all flame species.

Treatment of the diffusion of the HMWM required Lennard-Jones parameters. Details of the approach will be published. The correlations of Bird, Stewart, and Lightfoot[10] for the Lennard-Jones parameters as a function of critical temperature (Tc) and critical pressure (Pc) were used. The technique of Forman and Thodos[11] for estimating critical properties from molecular structures of hydrocarbons gave values of T_c and P_c. From available data on the molecular structures of flame species observed at the low end of the range of the HMWM, reasonable assumptions were made concerning the molecular structures of expected constituents of the HMWM. The HMWM was assumed to consist of polycyclic aromatic hydrocarbons in the most peri-condensed structures possible for a given carbon number. Peri-condensed PAH structures are the most closely packed arrangement of aromatic rings. For the series of most peri-condensed molecules having only six-membered rings, Lennard-Jones parameters were estimated, and correlated with the molecular weight. Values of the correlated Lennard-Jones parameters for the midpoints of the 50-amu ranges considered (e.g., at 375 amu for the 350-400 amu range) were taken as the Lennard-Jones parameters for that 50-amu range, each range being treated as an individual flame species in the flux and net reaction rate calculations. In the course of the work, Lennard-Jones parameters for fullerenes, and hence species containing both five- and six-membered rings, were also estimated. It was found that replacing the

above calculated transport parameters for the 700-750 amu range with those predicted for C_{60} resulted in only slight quantitative and no qualitative changes in the results.

FLUX AND RATE CALCULATION RESULTS

Mole fraction profiles for selected mass ranges are shown in Figure 1. The profiles exhibit behavior consistent with that of a chemical intermediate; they are first created then destroyed. However, the material heavier than 350 amu is not completely destroyed in the flame being studied. The calculated net reaction rates (Figure 2) also reflect behavior typical of intermediate species, the profiles for each 50-amu fraction having a region of net production followed by one of net consumption. (The wiggles at the extremes of the rate profiles are artifacts of the numerical smoothing and differentiation techniques[12].)

BEHAVIOR OF 700-750 AMU MATERIAL

The results for the 700-750 amu material are different from all the other HMWM profiles. The peak of the mole fraction profile is much broader and occurs much farther downstream than is the case for any of the other HMWM ranges. The peak value of the mole fraction is also larger than what would be expected from the observed trend of decreasing peak value with increasing molecular weight. The same observations also hold for the molar flux profiles. These results are also reflected in the net reaction rates calculated for the 700-750 amu material. The net production region is wider than that for any of the other 50-amu fractions and the peak is broader. The ratio of the peak destruction rate to the peak production rate is also lower for the 700-750 amu material than for the other HMWM.

The results for the 700-750 amu material show that there is a larger amount of material than expected in this molecular weight range, that it is produced over a larger region of the flame, and that it is destroyed more slowly, leading to an accumulation of mass in this size range. The results cannot be explained as the result of PAH coagulation, or in terms of especially stable PAH, but could be expained in terms of an especially stable species which would take longer to form and be more stable than the other PAH species.

The rsults are consistent with the presence of C_{60} in the near-sooting flame. The stability of C_{60} against attack by radicals has been observed[13], and in general, the relative abundance of C_{60} compared to other carbon clusters is increased under more severe reaction conditions. Due to its stability, C_{60} is likely to be destroyed more slowly than the HMWM, consistent with the accumulation of mass in the 700-750 range. The special structure of C_{60} would likely require more time to be formed than would a flat PAH molecule of comparable size, consistent with the delayed peaks in the 700-750 amu profiles.

COMPARISON WITH OTHER OBSERVATIONS OF C_{60}

Comparison of these results with those of Homann et al.[3-5] will be published. Briefly, both studied employed the same type of benzene

flames at the same pressure, but the species measured and the
equivalence ratio (ϕ) used in the two cases are different. Therefore
the comparison is somewhat complicated and requires explanation. The
number concentration profile of 700-750 amu HMWM at ϕ=1.8 from the
present study is comared with the number concentrations of C_{60}^{+} at
ϕ=1.9 and C_{60}^{-} at ϕ=2.15 found by Homann et al.[3-5]. The HMWM as
measured by Bittner[1] does not include ions. The ions of each species,
including C_{60}, are expected to be in much lower concentration than the
neutrals. Also, the 700-750 amu HMWM would be expected to include
other species in addition to mass 720. For these reasons, the C_{60}^{+} and
C_{60}^{-} concentrations should be considerably less than that of the 700-
750 amu HMWM. On the other hand, the lower ϕ of the HMWM measurement
would be expected to give considerably lower concentrations than would
be observed at the higher ϕ's of the ion measurements. Considering
these opposing effects, the two sets of data are found to compare
favorably, with no obvious inconsistencies.

REFERENCES

(1)   Bittner, J.D.   A Molecular-Beam Mass Spectromete Study of
Fuel-Rich and Sooting Benzene-Oxygen Flames; Sc.D. thesis, Department
of Chemical Engineering, Massachusetts Institute of Technology, 1981.

(2)   Bockhorn, H.; Fetting, F.; Wenz, H.W.   Ber. Bunsenges. Phys.
Chem. 1983, 87, 1067.

(3)   Gerhardt, Ph.; Loffler, S.; Homann, K.H.   Chemical Physics
Letters 1987, 137, 306.

(4)   Gerhardt, Ph.; Loffler, S.; Homann, K.H.   Twenty-Second
Symposium (International) on Combustion, The Combustion Institute,
1988.

(5)   Loffler, S.; Homann, K.H.   Twenty-Third Symposium
(International) on Combustion, The Combustion Institute, 1990.

(6)   Howard, J.B.; Bittner, J.D.   Soot in Combustion Systems and
its Toxic Properties, eds. J. Lahaye and G. Prado; Plenum: New York,
1983.

(7)   Pope, C.J.   Fluxes and Net Reaction Rates of High Molecular
Weight Material in a Near-Sooting Benzene-Oxygen Flame; M.S. thesis,
Department of Chemical Engineering, Massachusetts Institute of
Technology, 1988.

(8)   Fristrom, R.M.; Westenberg, A.A.   Flame Structure; McGraw-
Hill: New York, 1965.

(9)   Wilke, C.R.   Chemical Engineering Progress 1950, 46, 95.

(10)   Bird, R.B.; Stewart, W.E.; Lightfoot, E.N.   Transport
Phenomena; Wiley: New York, 1960.

(11)   As discussed in Reid, R.C.; Sherwood, T.K.   The Properties of

Gases and Liquids, 2nd ed.; McGraw-Hill: New York, 1966.

    (12)   Savitsky, A.; Golay, M.J.E.   Analytical Chemistry 1964, 36,
1627.   See also corrections by Steinier, et al., Analytical Chemistry
1972, 44, 1906.

    (13)   Zhang, Q.L. et al.   Journal of Physical Chemistry 1986, 90,
525.
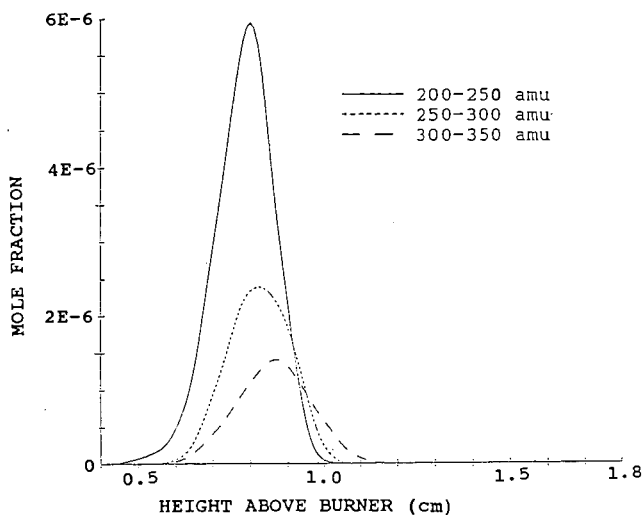
Figure 1:   Mole fraction profiles, 200-350 amu.
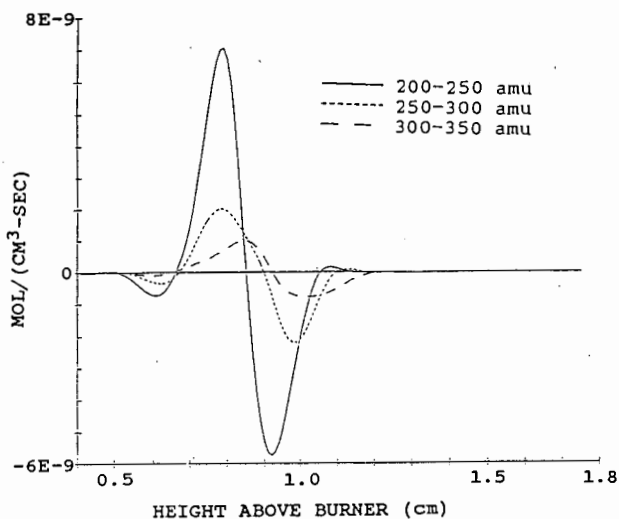
Figure 2: Net reaction rate profiles, 200-350 amu.
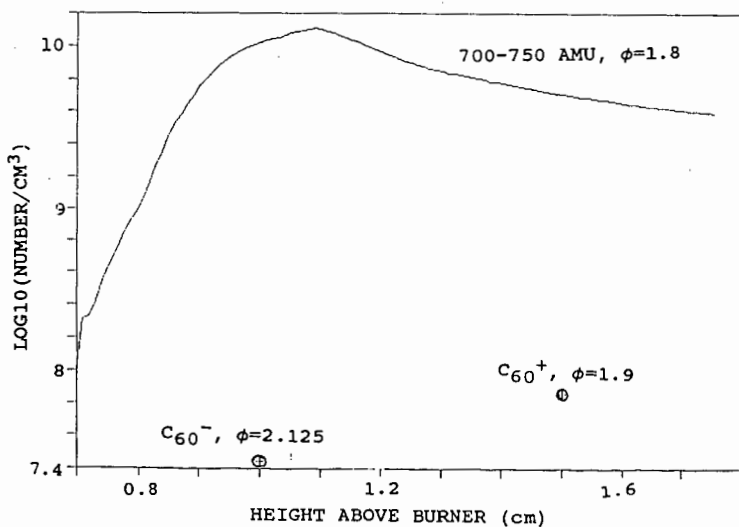
Figure 3: 700-750 mole fraction vs. Homann C_{60} ion measurements

A SHOCK TUBE INVESTIGATION OF SOOT FORMATION FROM TOLUENE/METHANOL
MIXTURES. Alexiou, A. and Williams, A., Department of Fuel and Energy,
Leeds University, Leeds, LS2 9JT, UK, and Abdalla, A.Y., Helwan
University, Cairo, Egypt.

ABSTRACT

Soot formation in toluene and toluene/methanol/argon mixtures was studied behind
reflected shock waves using a laser beam attenuation technique. The experiments
were undertaken over the temperature range 1484 - 2232K, pressure range 1.69 -
2.77 bar and total carbon atom concentrations for the toluene alone in the range
2.7×10^{17} - 1.1×10^{18} atoms/cm^3 (0.5 to 1.5 mol %) and for toluene/methanol
mixtures in the range 23 - 66 mol % methanol.

The results indicate that the soot yield decreases with an increase in methanol
concentration but the effect is not marked until the addition is greater than 50%
methanol. The rates of soot formation from toluene and toluene/methanol mixtures
have been determined and exhibit an Arrhenius dependence which was expressed by a
correlation equation. The induction periods for soot formation were measured and
were found to increase with methanol addition although the maximum soot yields
were found to decrease.

INTRODUCTION

Methanol is of considerable practical significance as an alternative fuel or as a
blend with petroleum for internal combustion engines. Earlier studies have shown
that methanol produces much less soot than typical hydrocarbon fuels but the
addition of aromatics greatly increases soot formation (1,2). In contrast, in
diesel engines, blends of diesel fuel oil with methanol produce substantially
smaller amounts of soot. Surprisingly there has been little previous work on the
gas phase combustion of these mixtures and only the benzene-methanol system has
been studied by shock-tube techniques (1). In diffusion flames the decreasing
fuel type is given by Glassman (3): aromatics > acetylene > olefins > paraffins >
alcohols. Since there is usually agreement in the behaviour in diffusion flames
and in shock tubes concerning soot tendency, we undertook a shock tube study to
evaluate the soot suppression effect. We confined our work to toluene and
toluene/methanol mixtures and we present in this paper data on the soot
suppression effect of methanol added to toluene mixtures, rather than the
alternative approach of adding aromatic fuels to enhance the radiation from
methanol flames.

EXPERIMENTAL

The experiments were performed in reflected shock waves and details of the shock
tube facility have been previously published (4). The test gas mixtures were
prepared manometrically, ANALAR toluene and methanol were further purified by
repeated freezing and evacuation. The experimental conditions are summarised in
Table 1.

A laser technique was employed and the absorption of the beam at 632.8 nm was
used to measure the concentration of soot. Only toluene concentrations up to 1.5
mol % could be studied because of the high levels of absorption. The soot yields
were calculated according to Graham's model (5).

$$Y = \frac{C_{soot}}{C_{total}} = \left[N\rho\lambda/72.\pi.E_{(\overline{m})}.\ell.C_{total}\right]\ell n\left[I_{(o)}/I_{(t)}\right] \qquad (1)$$

where C_{soot} = concentration of the particulate carbon per unit volume, C_{total} = the total concentration of carbon atoms per unit volume, N = Avogadro's number, ρ = density of soot, λ = wavelength of the measurement, I = intensity of radiation which is function of time, t, $E_{(m)}$ = imaginary part of the function $(m^2-1)/(m^2+2)$, m = the complex refractive index.

Since the soot yield is a function of the refractive index an accurate value is necessary. Many workers, including our previous work, have used the value of Lee and Tien (6) which at this wavelength would give a value of $E_{(m)}$ = 0.174. In the present work we used the value of $E_{(m)}$ = 0.253 based on the in flame measurements of Charalampopoulos and Chaung (7). If we had used the Lee and Tien data we would have overestimated the total soot yield as previously observed by Frenklach et al (10); indeed if data by some of the earlier researchers had been used the position would have been worse.

EXPERIMENTAL RESULTS

The results obtained in the toluene pyrolysis experiments are shown in Fig. 1. The amount of soot yield increased monotonically with the amount of toluene pyrolysed. The maximum slope on the oscillogram was measured and defined as the apparent rate of soot formation. The correlation equation of apparent rate of toluene pyrolysis is shown in Fig. 2 for the different concentrations which are given in Table 1. The RH on this figure stands for the fuel concentration term, in this case toluene. The rates exhibited an Arrhenius dependence given by a correlation equation:

$$R_{soot} \text{ (mol/m}^3\text{s)} = 1.38 \text{ } 10^8 \text{ } [C_7H_8]^{1.32} \exp(-11,900/T) \tag{2}$$

The activation energy which is valid up to 1950 K (1532 - 1950 K) is in agreement with the values quoted by Simmons and Williams (9), namely 99 - 118 kJ/mol depending on the value of the refractive index. The constant and the fuel exponent have changed because of the improved accuracy of the present data. The fuel exponent is now consistent with the value of 1.48 reported by Wang et al (8).

During the course of toluene/methanol pyrolysis mixtures an induction time was observed before any absorption occurred. This induction time was the time between the reflected shock wave and the onset of soot formation. Figure 3 shows the results for the induction times. As it can be seen the induction time increased with the amount of methanol added to the toluene. The following equation for calculating the soot induction time, t_{soot}, based on a 5% rise in signal was obtained.

$$t_{soot} = 5.448 \text{ } 10^{-5} \text{ [total fuel]}^{1.92} \exp(-16,644/T) \tag{3}$$

where [total fuel] = $[C_7H_8 + CH_3OH]$. The soot yield decreased monotonically with the increase of the amount of methanol added to toluene as shown in Fig. 4.

The apparent rate of toluene/methanol pyrolysis are measured in the same way as toluene and could be expressed as follows:

$$R_{soot} \text{ (mol/m}^3\text{s)} = 1.9 \text{ } 10^5 \text{ [total fuel]}^{-0.412} \exp(-15,300/T) \tag{4}$$

which is valid in a temperature range 1580 - 1950 K.

Fig. 5 shows the correlation equation of the apparent rate of soot formation of toluene methanol mixtures at different concentrations (Table 1).

We attempted to obtain a correlation equation incorporating both $[C_7H_8]$ and $[CH_3OH]$ terms, but we had great difficulty in separating the terms in an equation

of, for example, the form $R_{soot} = C_1 [C_7H_8]^a \exp (-E_1/RT) - C_2 [CH_3OH]^b \exp (-E_2/RT)$. Even though the correlation which we obtained is not ideal it can be used to express the rates and by comparing equations (2) and (4) conclusions could be made about the role of added methanol. The experimental determined exponent of the fuel term indicates that an increase of methanol concentration will decrease the apparent rate of soot formation. In addition there are differences in the activation energies and in the pre-exponential factor which are very significant.

DISCUSSION

In the early work by Graham (5) the extent of conversion of initial carbon in the fuel to soot was determined at 2.5 ms. Based on this observation time the soot yield fell rapidly with increasing temperature from 100% at ≈1800 K to less than 5% at 2300 K. He developed his well-known scheme which involved condensation reactions at around 1000 to 1800 K and fragmentation reaction above that temperature. Later Frenklach (10) demonstrated that the soot yield is not universal, but is dependent on experimental controllable variables such as observation time, total pressure and laser wave-lengths. He postulated another model for soot formation included polymerisation and fragmentation reactions.

In our work we measure the maximum conversion of the fuel to soot irrespective of the time. As is shown in Fig. 1, the maximum yield occurs at ~ 1900 K above which fragmentation takes place resulting in a reduction in soot yield. Based on this observation we do agree with Frenklach (10) that the soot yield maximum is not universal and the condensation, fragmentation reactions take place according to experimental conditions.

The unimolecular decomposition of methanol at high temperature is considered to involve two reactions (11).

$$CH_3OH + M \longrightarrow CH_3 + OH + M \qquad (i)$$

$$CH_3OH + M \longrightarrow CH_2 OH + H + M \qquad (ii)$$
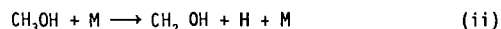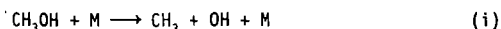
A computer model for toluene/methanol pyrolysis has been developed in which the initiation reactions (i) and (ii) of methanol together with the low activation energy reactions of H and CH_3 with CH_3OH has been used in order to evaluate the reduction of the soot yield. Preliminary results at about 1900 K not surprisingly demonstrate the importance and the rapid formation of OH and the products H_2O and CO increasingly as methanol is added to toluene. These reactions are also responsible for the increased soot induction period. Therefore it seems that the presence of OH radicals when methanol is added to toluene leads to the behaviour observed experimentally. These results are consistent with the role of OH as an oxidant in carbon-forming flames (12).

More recently, Frenklach (1), in his work on alcohol addition, explained that the reduction is also due to hydrogen atom scavenging. Alcohols undergo the H-abstraction reactions which results in the reduction in the superequilibrium of H atoms. In toluene pyrolysis the overshoot of hydrogen atoms beyond their equilibrium concentration is responsible for the propagation of the ring growth process. Our work is consistent with this since we demonstrate this soot reduction and this effect is not marked until the addition is greater than 50 mol % methanol.

Finally it should be noted that these results are consistent with the behaviour of methanol in fuel blends for gasoline engines. In the case of diesel engines the marked reduction in soot yields cannot arise from gas phase reactions alone and must arise from some physical change such as selective droplet evaporation or disruptive burning.

1549

CONCLUSIONS

The results of the present study show that methanol acts as a suppressing agent for soot formation. However this reduction is only achieved when the presence of methanol exceeds more than 50% in the total fuel mixture to be pyrolysed.

ACKNOWLEDGEMENTS

REFERENCES

1. M. Frenklach and J. Yuan. 17th Int. Symp. on Shock Tubes and Waves, 1989, pp 487-493.

2. M. Nakamuza, S. Koda and K. Akita. 19th Symp. Int. on Comb., 1982, pp 1395-1401.

3. I. Glassman. Combustion 2nd Edit. Academic Press, Orlando, Florida, 1987.

4. C.M. Coats and A. Williams. 17th Symp. Int. on Comb., 1979, p 611.

5. S.C. Graham, J.B. Homer, J.L.D. Rosenfeld. Proc. R. Soc. London, A344, 1975, pp 259-285.

6. S.C. Lee and C.L. Tien. 18th Int. Symp. on Comb., 1981, p 1154.

7. T.T. Charalampopoulos and H. Chaung. Comb. Scien. and Techn., 1988, vol. 59, pp 401-421.

8. T.S. Wang, R.A. Matula, R.C. Farmer. 18th Symp. Int. on Comb., 1981, pp 1149-1158.

9. B. Simmons and A. Williams. Comb. & Flame, 1988, 71, pp 219-232.

10. M. Frenklach, S. Taki, R.A. Matula. Comb. & Flame, 1983, 49, pp 275-282.

11. P.H. Gribb, J.E. Dove, S. Tamazuki. 20th Int. Symp. on Comb., 1984, pp 779-787.

12. K.G. Neon, J.D. Howard, A.F. Sarofim. Particulate Carbon Formation During Combustion, Plenum press, New York, 1981.

TABLE 1

	% Mol in Argon	T (K)	P (bar)	Carbon (atoms/cm^3)
1	0.5 C_7H_8	1580 - 2170	1.81 - 2.62	2.54×10^{17} - 3.01×10^{17}
2	1.0 C_7H_8	1532 - 2114	1.74 - 2.70	5.83×10^{17} - 6.56×10^{17}
3	1.5 C_7H_8	1584 - 2070	1.93 - 2.89	9.38×10^{17} - 1.07×10^{18}
4	1.0 C_7H_8 + 0.3 CH_3OH	1600 - 2096	1.85 - 2.67	6.19×10^{17} - 6.85×10^{17}
5	1.0 C_7H_8 + 0.5 CH_3OH	1580 - 2123	1.82 - 2.77	6.33×10^{17} - 7.19×10^{17}
6	1.0 C_7H_8 + 1.0 CH_3OH	1610 - 2087	1.88 - 2.79	6.65×10^{17} - 7.84×10^{17}
7	1.0 C_7H_8 + 2.0 CH_3OH	1664 - 2050	2.06 - 2.79	8.17×10^{17} - 8.94×10^{17}
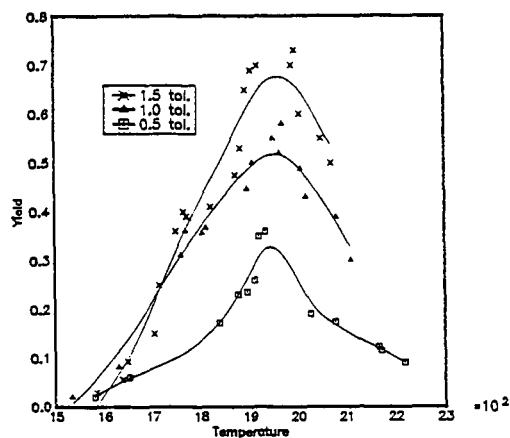
Fig. 1. Comparison of the soot yield at different toluene concentrations.
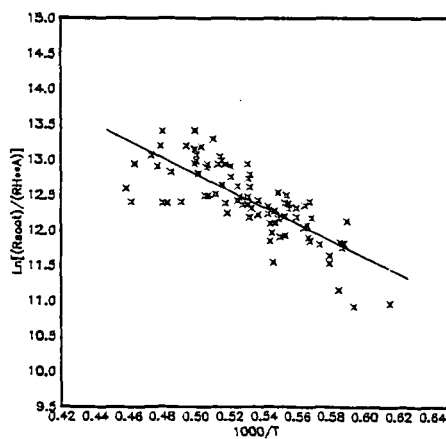
Fig. 2. Correlation equation of apparent rate of soot formation from toluene pyrolysis at different concentrations.
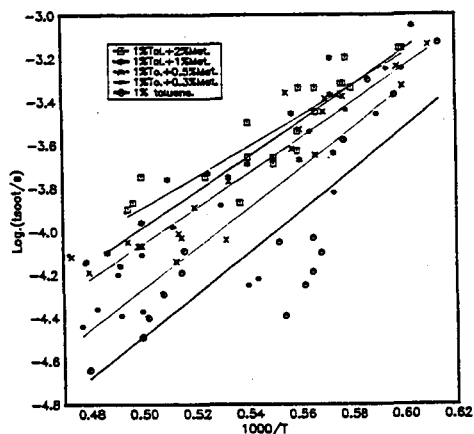
Fig. 3.   Induction times for soot appearance at different toluene/methanol concentration.
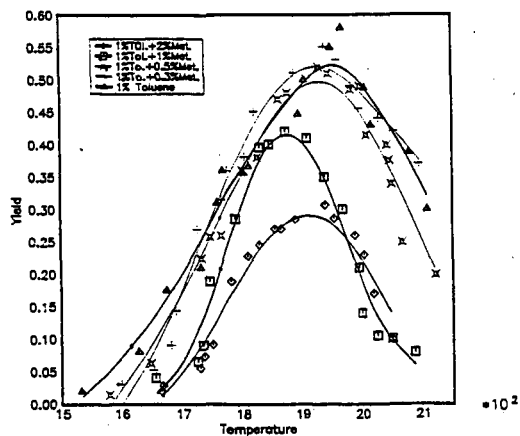
Fig. 4.   Comparison of the soot yield at different toluene/methanol concentrations.

1553
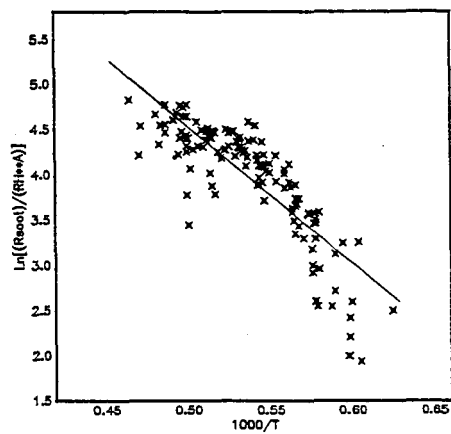
Fig. 5. Correlation equation of apparent rate of soot formation from toluene/methanol pyrolysis at different concentrations.

FORMATION OF VOLATILE PRECURSORS OF NO$_x$
IN THE RAPID PYROLYSIS OF NITROGEN-CONTAINING HETEROAROMATICS

J. C. Mackie and A. Doughty
Department of Physical and Theoretical Chemistry
University of Sydney
NSW 2006, Australia

INTRODUCTION

Identification of the reaction pathways whereby fuel-bound nitrogen evolves as NO$_x$ in the combustion of low rank fuels has attracted considerable recent attention. As models for the evolution of NO$_x$ from coal combustion, compounds containing the six-membered heteroaromatic pyridine ring and the five-membered pyrrole ring are being investigated. Recently, we have studied the kinetics of pyrolysis of pyridine[1] by single pulse shock tube techniques and developed a detailed kinetic reaction mechanism to model the observed products of decomposition. Pyridine was found to decompose principally via a hydrogen chain mechanism involving abstraction of the ring hydrogen *ortho* to the nitrogen atom, followed by ring scission of the *o*-pyridyl radical to an open-chain radical which could eliminate acetylene and form the HC=CH–CN radical which may eliminate H and form cyanoacetylene or produce acrylonitrile via an abstraction route. HCN was found to be largely a secondary product of pyrolysis of these organic nitriles and also of acetonitrile.

More recently, our investigations of the kinetics of pyrolysis of pyrrole[2] have shown that the five-membered heterocycle decomposes very differently from the six-membered heteroaromatic. Isomerization followed by ring opening to the open-chain C$_3$H$_5$CN isomers of pyrrole predominates the mechanism. Our interpretation of the kinetics has assumed that the decomposition is initiated by the reversible tautomeric reaction
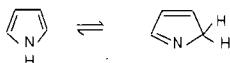
to form the 2-H pyrrole (pyrrolenine) with subsequent rupture of the weaker C2-N bond in the 2-H tautomer. It has been shown[2,3] that only through secondary decomposition of the C$_3$H$_5$CN products (principally cis- and trans- crotononitrile and allyl cyanide) are the NO$_x$ precursors including HCN produced. Thus, an understanding of the pathways of NO$_x$ formation from pyrrole rings requires a knowledge of the thermal decomposition kinetics of the C$_3$H$_5$CN isomers of pyrrole. This is considered in one part of this paper.

In heavy fuels heteroatoms are often found in condensed ring environments and in substituted rings rather than in the simple unsubstituted five- and six-membered rings. Evolution of NO$_x$ precursors might well depend upon the degree of heteroatomic ring substitution or condensation. The present work therefore involves, in part, a study of the simplest ring substituted heteroaromatic, 2-picoline (2-methylpyridine), the heteroaromatic analogue of toluene, whose stabilized radical, benzyl plays an important role in aromatic hydrocarbon pyrolyses and oxidations. Its heteroaromatic radical analogue, 2-picolyl might also be expected to be a key radical in heteroaromatic oxidations.

EXPERIMENTAL

Kinetics of pyrolysis of the nitrogen–containing products (cis– and trans–crotononitrile, allyl cyanide and 2–picoline) have been studied dilute in argon (0.1–0.4 mol%) in a single–pulse shock tube (SPST) over the temperature range 1100 to 1700 K, at pressures from 17–23 atm and at uniform residence times behind the reflected shock front of 600–800 μs. Analyses of products and remaining reactant have been made by capillary column GC. Product identifications have been made, where possible by comparison of retention times with standard samples, after initial identification by GC/MS and, in some cases, by FTIR spectrometry. The shock tube is equipped with pairs of UV–transmitting sapphire windows adjacent to the endwall. The absorption spectra of 2–picoline vapour and its products of decomposition have been measured over the wavelength range of 250–350 nm at a distance of 35 mm from the endwall with a detection system of time constant ≤5 μs. Details of the shock tube and ancillary analytical system are presented in our earlier publications.[1,2]
Samples of each compound studied were purchased from Aldrich of 98–99% purity and were further purified by several bulb–to–bulb distillations to greater than 99.8% (by GC) in all cases. Pressures and temperatures behind the reflected shock were computed from measurements both of incident and reflected shock velocities.

RESULTS AND DISCUSSION

Secondary Decomposition of Pyrrole Pyrolysis Products

Figures 1(a)–(d) illustrate the temperature profiles of all products of significance for both allylcyanide and crotononitrile pyrolysis. The same set of products was observed irrespective of whether the initial reactant was allyl cyanide or crotononitrile, with only the relative yields of the products changing with starting isomer. HCN, acetylene, acetonitrile and acrylonitrile were all observed at very low extents of decomposition, and remained the major products at high extents of decomposition. Minor nitrogen–containing products were ethyl cyanide, cyanoacetylene, and cyanopropyne/cyanoallene. Methane was also present in significant concentrations, along with smaller quantities of ethylene, propene and propyne. Traces of the following compounds could also be detected: cis– and trans– 1–cyano(1,3–)butadiene, benzonitrile, pyridine, diacetylene, 1,3–butadiene, 1–butene, benzene and toluene. The major difference in product distributions between the reactants crotononitrile and allylcyanide was that allylcyanide yielded significantly higher proportions of HCN, acetonitrile, acetylene and ethylene. C_3 hydrocarbons were also generated in higher concentrations for allyl cyanide when compared with crotononitrile. No dependence of the rate of decomposition of the reactant on initial concentration was observed.

The product distribution observed in the pyrolysis of the butenenitriles can best be described in terms of a free radical mechanism. The observation of a mixture of C_3H_5CN isomers in the product mixture shows that isomerization of the starting isomers occurs simultaneously with decomposition. Although there are considerable uncertainties in the thermochemistry of some of the nitrogen–containing radicals produced, it would appear that the most likely initiation reaction for the free radical mechanism would occur through single C–C bond fission. For crotononitrile, C_3–C_4 bond fission [reaction (1)] would be expected to take place whereas with allyl cyanide C_2–C_3 fission (2) would be most favourable.

$$CH_3CHCHCN \rightarrow CH_3 + HC=CHCN \qquad (1)$$

$$H_2C=CHCH_2CN \rightarrow H_2C=CH + CH_2CN \qquad (2)$$

Although initiation through C–H bond fission is possible, the significantly higher C–H bond energy

would make this only a minor initiation pathway. Thermochemical parameters for radicals and other species of importance in this study are given in Table 1. In the Table certain of the heats of formation have been obtained from kinetic modeling of pyrolysis kinetics. Entropies and heat capacities have been obtained by approximate Third Law calculations.

Formation of the major products, acetylene and acetonitrile, can be modeled by means of a simple abstraction chain mechanism in which the abstacting radical is CH_2CN. See Figure 2. A major intermediate in this mechanism would appear to be the cyanoallyl radical, C_3H_4CN. Analogous with allyl itself, we would expect this radical to possess resonance stability. Fission of a C–C bond in this radical would seem less likely than rearrangement to a less stable radical whose bond fission leads to C_2H_2 and to regeneration of CH_2CN. Both vinyl and its cyano– analogue, cyanovinyl (HC=CHCN), should readily undergo unimolecular C–H fission, on the one hand to acetylene, on the other, to produce the observed cyanoacetylene. Hydrogen atom addition, either to the double bond of C_3H_5CN to to the nitrile group can produce another set of observed products, including the major products acrylonitrile and HCN. (See Figures 3 and 4). A detailed kinetic model comprising 107 reactions which include both abstractions and H additions as well as isomerization reactions of the C_3H_5CN isomers, has been used to satisfactorily model the major and minor products of the pyrolyses of crotononitrile and allyl cyanide.[4] Examples of the comparison between model predictions and experiment are given for some major products in Figure 5.

Pyrolysis of 2–picoline

2–Picoline may be considered to be the nitrogen heteroaromatic analogue of toluene. Behind reflected shock waves at residence times of about 800 μs and 20 atm, 2–picoline begins to dissociate at about 1250 K. Principal products of decomposition are HCN and C_2H_2 although cyanoacetylene, acrylonitrile and acetonitrile are significant nitrogen containing products. 2–Ethylpyridine and pyridine, especially at lower tempertures, are also observed. By analogy with toluene, we would expect the pyrolysis to be dominated by reactions of the 2–picolyl radical, the analogue of benzyl. Troe et al[5,6] have made an extensive investigation of the electronic absorption spectra of benzyl and benzyl decomposition fragments in both thermal and laser decomposition of toluene and side–chain substituted derivatives. They found that the spectral region around 300 nm in shock heated toluene is dominated by benzyl radical and benzyl products spectra.

Similarly we find the the absorption spectrum between 300–340 nm of shock heated 2–picoline is dominated by absorbing species which show strikingly similar temporal behaviour to those reported by Troe et al[5,6]. Figure 6 gives an example of the spectrum of decomposing 2–picoline vapour (0.2%) in argon at a temperature of 1634 K. Note the rapid rise in absorption to an initial steady state, followed by a longer time steady rise in absorption. The absorption is most probably the consequence of at least two absorbers, the first a species which undergoes rapid equilibration followed by slower decomposition to a more stable product or products. Similar observations in toluene decomposition have by attributed by Troe et al[5,6] to the initial formation of benzyl radicals which equilibrate rapidly owing to an unexpectedly high value of the rate constant for recombination

$$PhCH_2 + H \rightarrow PhCH_3 \qquad (-3)$$

Slower decomposition was attributed to homogeneous recombination of benzyl radicals to produce dibenzyl which eventually underwent successive H fissions to the highly absorbing molecule, stilbene.

It is therefore tempting in our 2–picoline studies to assign the initial absorber of 330 nm radiation to the 2–picolyl radical, which, like benzyl, must also undergo rapid recombination with H atoms. The slower increase in absorption would therefore be associated with 2–picolyl reaction products

1557

which are sufficiently conjugated to absorb strongly around 330 nm. It would seem that such chromophores are not very volatile since no absorption around 330 nm can be detected in the absorption spectra of the products when cooled to room temperature.

More work is required to establish that the initial carrier of 330 nm radiation is the 2-picolyl radical in the pyrolysis of 2-picoline. If, tentatively, we assume that the pyrolysis of 2-picoline is initiated by H atom fission to form 2-picolyl (reaction 3) then the value given in Table 1 for the heat of formation of this radical is in accord with our experiments. Values for the entropy and heat capacity of this radical have been obtained by a Third Law calculation in which vibrational frequencies of the radical have been estimated from those of toluene, benzyl and 2-picoline[5,7] and moments of inertia calculated from an estimated geometry.

ACKNOWLEDGEMENTS

REFERENCES

1.   Mackie, J.C., Colket, M.B. and Nelson, P.F., J. Phys. Chem., 94, 4099, (1990).
2.   Mackie, J.C., Colket, M.B., Nelson, P.F. and Esler, M., Int. J. Chem. Kinet. (in press)
3.   Lifshitz, A., Tamburu, C. and Suslensky, A., J. Phys. Chem., 93, 5802, (1989).
4.   Doughty, A., B.Sc.(Hons.) Thesis, University of Sydney, 1990, Doughty, A. and Mackie, J.C. (to be published)
5.   Muller-Markgraf, W. and Troe, J., J. Phys. Chem., 92, 4899, 4905, (1988).
6.   Hippler, H, Reihs, C. and Troe, J., Z. Phys. Chem. N.F. 167, 1, (1990).
7.   Scott, D.W., Hubbard, W.N., Messerly, J.F., Todd, S.S., Hossenlopp, I.A., Good, W.D., Douslin, D.R. and McCullough, J.P., J. Phys. Chem., 67, 680, (1963).
8.   King, K.D. and Goddard, R.D., J. Phys. Chem., 80, 546, (1976).

Table 1. Thermochemical data for nitrogen-containing compounds

Species	$\Delta H_{f,300}$ kcal/mol	$S_{f,300}$ cal/K /mol	C_p cal/K/mol					Ref.
			300	500	1000	1500	2000	
CH_2CN	59.0	59.8	12.3	15.5	20.2	22.6	29.3	8
$HC=CHCN$	97.9	67.2	15.9	19.8	25.3	27.8	29.3	PW
$H_2C=CHCHCN$ (cyanoallyl)	77.0*	73.0	19.1	28.0	39.2	43.6	46.1	PW
$HC=CHCH_2CN$	91.6*	80.3	21.1	28.0	39.2	42.7	45.4	PW
$H_3CCH=CHCN$	85.0*	76.5	22.3	32.1	45.5	51.0	54.4	PW
$H_3CCH=CHCH=N$·	80.6	76.5	22.3	32.1	45.5	51.0	54.4	PW
Py·	81.7*	72.6	18.0	28.9	42.8	48.5	51.1	1
$PyCH_2$·[b]	65*	78.1	25.4	38.9	56.4	63.8	67.5	PW

·*ortho*-pyridyl radical   [b]*ortho*-picolyl radical   PW: present work
*Value derived from kinetic modeling.
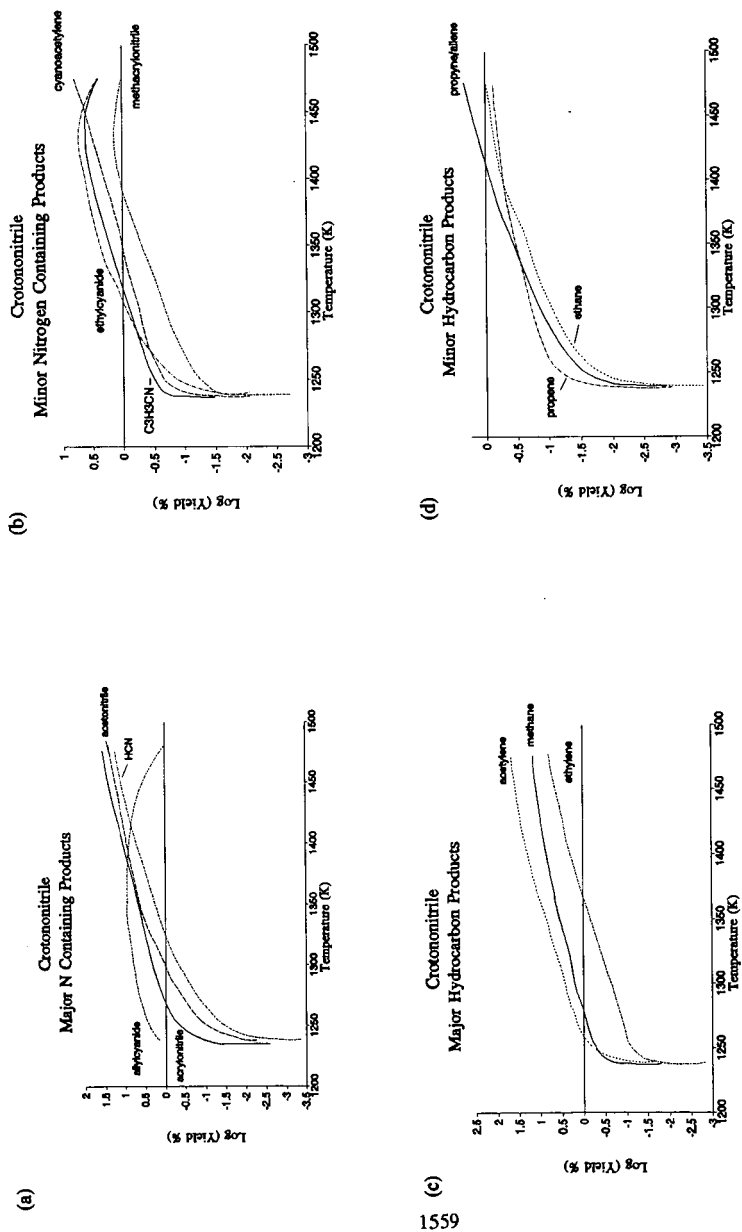
Figure 1. Products of pyrolysis of crotononitrile.

1559

Figure 4. H additions to the nitrile group

Figure 3. H additions across the double bond
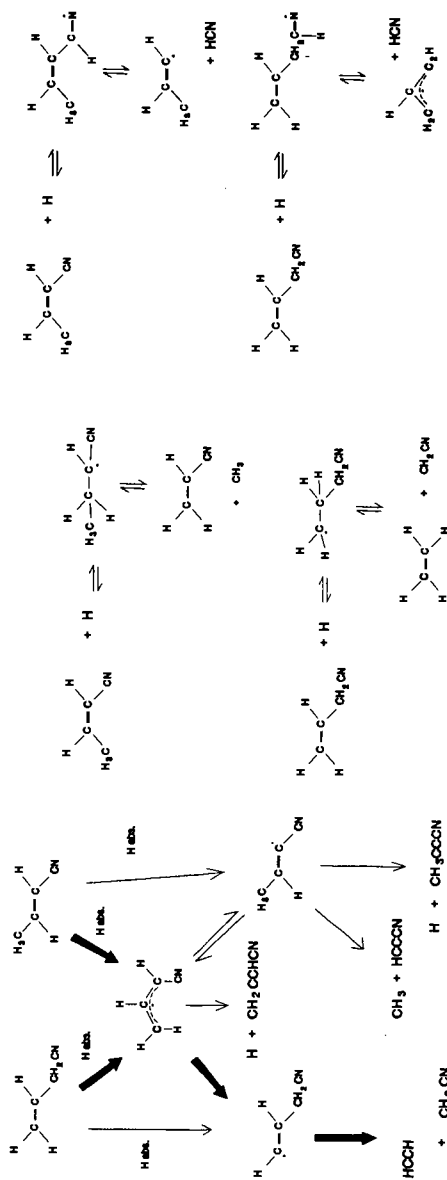
Figure 2. Free radical chain mechanisms.

1560

Butenenitrile Pyrolysis
Modeling Allylcyanide Concentration
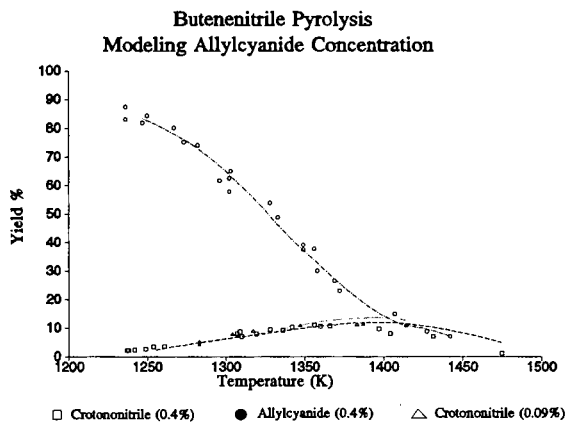
Figure 5(a). Modeling of Allylcyanide Concentration :
(points indicate experimental values , lines model predictions.)

Butenenitrile Pyrolysis
Modeling of Crotononitrile Concentration
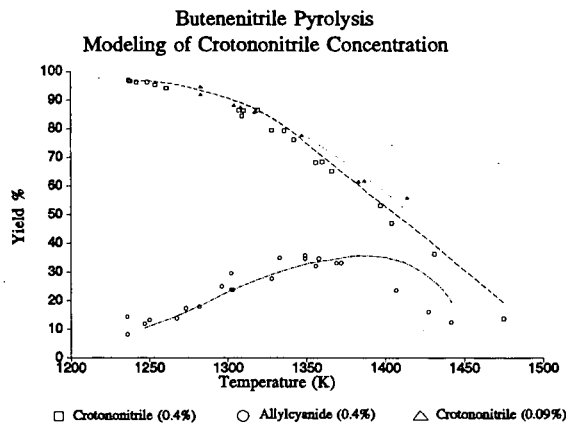
Figure 5(b). Modeling of Crotononitrile Concentration :
(points indicate experimental values , lines model predictions.)

Butenenitrile Pyrolysis
Modeling of HCN Formation
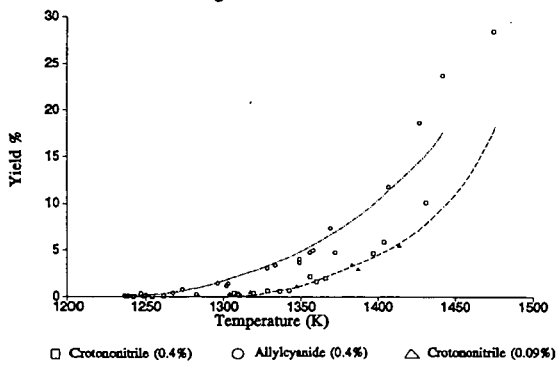
Figure 5(c). Modeling of HCN Formation :
(points indicate experimental values ; lines model predictions.)
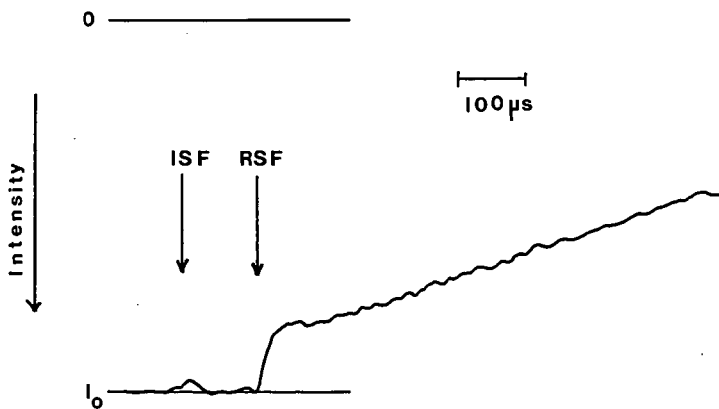
Figure 6.   Time dependence of an oscilloscope trace recording the absorption of 330 nm radiation in the pyrolysis of 2-picoline at 1634 K and 20 atm. ISF denotes the arrival of the incident shock front at the observation window, RSF denotes reflected shock front.

THERMAL RATE CONSTANT MEASUREMENTS BY THE
FLASH OR LASER PHOTOLYSIS-SHOCK TUBE METHOD:
RESULTS FOR THE OXIDATIONS OF H_2 AND D_2

J. V. Michael
Chemistry Division
Argonne National Laboratory
Argonne, IL 60439

INTRODUCTION

This article discusses the FP- or LP-ST technique. The modeling
of the oxidation of H_2 will be specifically featured. The reactions
that pertain to this oxidative system and that have been studied by
either the FP- or LP-ST technique, will be reviewed. These include,

$$H + O_2 \rightleftharpoons OH + O, \qquad (1)$$

$$O + H_2 \rightleftharpoons OH + H, \qquad (2)$$

$$H + H_2O \rightleftharpoons H_2 + OH, \qquad (3)$$

$$O + H_2O \rightleftharpoons OH + OH, \qquad (4)$$

$$H + O_2 + M \rightarrow HO_2 + M, \qquad (5)$$
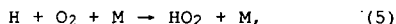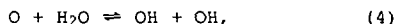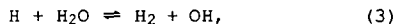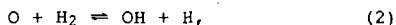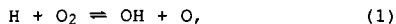
and their deuterated modifications. Both forward and reverse
processes will be included in the discussion since, in all cases, the
exising data indicate that the reactions are microscopically
reversible. Hence, data evaluations can be made over very large
temperature ranges.

EXPERIMENTAL

The FP-ST technique was first suggested by Burns and Hornig[1] and was
followed by some OH-radical reaction studies by Zellner and
coworkers.[2] The technique has recently been extended with the atomic
resonance absorption spectroscopic (ARAS) method of detection.[3] This
extension naturally follows from the earlier work.[1,2] A less
ambiguous experiment is now possible since spectroscopic absorption
by atomic species is stronger than by diatomic or polyatomic
radicals, and thus, smaller concentrations can be detected thereby
eliminating complications from secondary reactions. This development
has allowed absolute bimolecular rate constants to be directly
studied over a large T-range, ~650 to 2500 K.

The shock tube methods that are used in FP- or LP-ST studies are
traditional.[4] A schematic diagram of a recently constructed
apparatus[5] is shown in Fig. 1. The technique has been described
previously,[5,6,7] and therefore, only a brief description will be given
here. The method utilizes the double heating effect that can be
obtained by reflected shock wave methods. The nearly stagnant gas in
the reflected shock wave regime is subjected to either flash or laser
photolyis thereby producing an atomic species in the central hot gas
region. The time dependence of the atomic species is then radially
monitored as it reacts with an added reactant molecule. It is

necessary to have a source molecule present which, on photolysis, gives the atomic species of interest.

If the transmittance for any atomic absorption experiment can be held above ~0.8, then Beer's law will hold to a good approximation if the line is not too highly reversed. In FP- and LP-ST experiments with unreversed or only partially reversed resonance lamps, it is therefore only necessary to measure the temporal behavior of absorbance, (ABS), where $(ABS) \equiv -\ln(I/I_o)$. Since Beer's law holds, the atom concentration, [A], is equal to $(ABS)/\sigma_A l$. In all cases, the reactant concentration is very much larger than that of the atom, and therefore, the decay of A will obey pseudo-first-order kinetics. Since [A] is proportional to (ABS), it is only necessary to measure the temporal behavior of absorbance, $(ABS)_t$, in a kinetics experiment. The rate of depletion of the atomic species is the product of the thermal rate constant times the concentrations of the reactant and the depleting atomic concentration. After integration, a plot of $\ln(ABS)_t$ against time will yield a decay constant that is equal to the product of the thermal rate constant times the reactant concentration. Fig. 2 shows a typical plot of an experiment. The top panel shows an actual raw data signal and the bottom panel shows the first-order plot derived from the top panel. The negative slope of the plot gives the decay constant which, on division by the reactant concentration, gives a measurement of the thermal rate constant at the conditions of the experiment as determined from the initial pressure, temperature, and the shock strength.

RESULTS

H + O$_2$ → OH + O and D + O$_2$ → OD + O: The first published LP-ST paper[8] showed that the photolysis of H_2O at 193 nm yields both H-atoms and OH-radicals at high temperatures. In recent LP-ST experiments,[9] H_2O photolyte was used at T≥1085 K. With the higher fluences from excimer laser photolysis, experiments could be performed with less H_2O being present than in an earlier FP-ST study that used the same technique of detection.[10] This has allowed experiments to be performed at substantially higher T, up to 2278 K. Fig. 2 shows a typical experiment. Data with both H_2O and NH_3 as photolyte molecules have yielded the Arrhenius result,

$$k_1 = (1.15 \pm 0.16) \times 10^{-10} \exp(-6917 \pm 193 \text{ K/T}) \text{ cm}^3 \text{ molecule}^{-1} \text{ s}^{-1}, \quad (6)$$

for 1103≤T≤2055 K. Similar results for reaction (1D) with D_2O as photolyte give the Arrhenius result,

$$k_{1D} = (1.09 \pm 0.20) \times 10^{-10} \exp(-6937 \pm 247 \text{ K/T}) \text{ cm}^3 \text{ molecule}^{-1} \text{ s}^{-1}, (7)$$

for 1085≤T≤2278 K. The reverse rate constants can be determined from JANAF equilibrium values,[11] and rate constants for forward and reverse processes are listed in Table I.

O + H$_2$ → OH + H and O + D$_2$ → OD + H: FP-ST experiments with NO as the O-atom source have been carried out on both the H_2[12] and D_2[5] reactions. The results for O + H_2 can be described by the Arrhenius equation,

$$k_2 = (3.10 \pm 0.20) \times 10^{-10} \exp(-6854 \pm 84 \text{ K/T}) \text{ cm}^3 \text{ molecule}^{-1} \text{ s}^{-1}, \quad (8)$$

for $880 \leq T \leq 2495$ K. $O + D_2$ can similarly be described by,

$$k_{2D} = (3.22 \pm 0.25) \times 10^{-10} \exp(-7293 \pm 98 \text{ K/T}) \text{ cm}^3 \text{ molecule}^{-1} \text{ s}^{-1}, \quad (9)$$

for $825 \leq T \leq 2487$ K. Earlier shock tube determinations are in reasonable agreement with these direct results. There are also a number of lower temperature determinations for k_2[12-16] and k_{2D}.[14-18] The most reliable low T data are those of Sutherland et al.,[12] Westenberg and deHaas,[13,17] Presser and Gordon,[16] and Zhu et al.[18] These data have been combined with the FP-ST data to give three parameter expressions that can be used over the entire experimental temperature range.

$$k_2 = 8.44 \times 10^{-20} \text{ } T^{2.67} \exp(-3167 \text{ K/T}) \text{ cm}^3 \text{ molecule}^{-1} \text{ s}^{-1}, \quad (10)$$

for $297 \leq T \leq 2495$ K,[12] and,

$$k_{2D} = 2.43 \times 10^{-16} \text{ } T^{1.70} \exp(-4911 \text{ K/T}) \text{ cm}^3 \text{ molecule}^{-1} \text{ s}^{-1}, \quad (11)$$

for $343 \leq T \leq 2487$ K.[5] Eqs. (10) and (11) agree within a few percent with all studies except that of Marshall and Fontijn.[15] Rate constants for the reverse reactions can be calculated from JANAF equilbrium constant values,[11] and the values for both forward and reverse rate constants are compiled in Table I.

H + H_2O → H_2 + OH and D + D_2O → D_2 + OD: There are only two direct studies of reaction (3), one being with the FP-ST[19] and the other being with the LP-ST[8] techniques. The results from these two studies are given in Arrhenius form as,

$$k_3 = (4.58 \pm 0.61) \times 10^{-10} \exp(-11558 \pm 243 \text{ K/T}) \text{ cm}^3 \text{ molecule}^{-1} \text{ s}^{-1}, (12)$$

for $1246 \leq T \leq 2297$ K, and,

$$k_3 = (3.99 \pm 0.42) \times 10^{-10} \exp(-10750 \pm 500 \text{ K/T}) \text{ cm}^3 \text{ molecule}^{-1} \text{ s}^{-1}, (13)$$

for $1600 \leq T \leq 2500$ K, respectively. These two equations agree within combined error limits over the range of T'overlap. At high T, there is only one direct FP-ST study[20] of reaction (3D). These results are described for $1285 \leq T \leq 2261$ K by the Arrhenius expression.

$$k_{3D} = (2.90 \pm 0.73) \times 10^{-10} \exp(-10815 \pm 356 \text{ K/T}) \text{ cm}^3 \text{ molecule}^{-1} \text{ s}^{-1} (14)$$

There are numerous earlier studies[21-25] of reaction (-3) with four being particularly notable.[21,23-25] JANAF equilibrium constants[11] have been used to transform these reverse rate constant data[25] to those for the forward process, and an evaluation has been carried out for $250 \leq T \leq 2581$ K. A three parameter expression describes the results.

$$k_3 = 1.56 \times 10^{-15} \text{ } T^{1.52} \exp(-9249 \text{ K/T}) \text{ cm}^3 \text{ molecule}^{-1} \text{ s}^{-1}. \quad (15)$$

Since the data are not as extensive, an extended expression for k_{3D} cannot be evaluated; however, values for the back reaction (-3D) can be derived from JANAF values.[11] This expression and the other derived expressions are given in Table I.

O + H₂O → OH + OH and theory for O + D₂O → OD + OD: There are three direct studies of reaction (4)[26-28] for the T-ranges, 1053-2033 K,[26] 1500-2500 K,[27] and 753-1045 K,[28] respectively. The FP-ST results from Sutherland, et al.[26] can be represented by the Arrhenius equation,

$$k_4=1.10 \times 10^{-10} \exp(-9929 \text{ K/T}) \text{ cm}^3 \text{ molecule}^{-1} \text{ s}^{-1}, \qquad (16)$$

for 1288≤T≤2033 K. The results from Lifshitz and Michael[27] are,

$$k_4=(1.12 \pm 0.20) \times 10^{-10} \exp(-9115 \pm 304 \text{ K/T}) \text{ cm}^3 \text{ molecule}^{-1} \text{ s}^{-1}, (17)$$

for 1500≤T≤2500 K. The activation energies are different with the latter being lower than the former by ~10%. Evenso, the agreement between the two studies is good with eq. (16) being ~30-40% lower that that of eq. (17). The spread in the data from each study is ~±15-20%, and the two sets overlap over the common T-range. Sutherland, et al.[26] have also carried out Flash Photolysis-Resonance Fluorescence (FP-RF) studies at lower T, 1053 to 1123 K, and these data are the most accurate to date for reaction (4). There are numerous experimental studies of the back reaction (-4).[22b,29] These data have been combined with that from the two FP-ST studies through the JANAF equilibrium constants[11], and a comparison between the combined database for reactions (4) and (-4) with theoretical calculations has been made.[7] The theoretical result,

$$k_4^{th} = 7.48 \times 10^{-20} \text{ T}^{2.70} \exp(-7323 \text{ K/T}) \text{ cm}^3 \text{ molecule}^{-1} \text{ s}^{-1}, \quad (18)$$

agrees with experiment within experimental error over the T-range, 700-2500 K. There are no data for the O + D₂O reaction. Therefore, a theoretical estimate that is consistent with the successful protonated case, eq. (18),[7] can be used as a starting point in experiment design and/or in chemical modeling experiments for the D₂/O₂ system. The calculated result for 700≤T≤2500 K is,

$$k_{4D}^{th} = 2.05 \times 10^{-19} \text{ T}^{2.56} \exp(-8286 \text{ K/T}) \text{ cm}^3 \text{ molecule}^{-1} \text{ s}^{-1}. (19)$$

These expressions and the transformed reverse rate constant values are listed in Table I.

H + O₂ + M → HO₂ + M: FP-ST results have been obtained for this reaction.[10] The third-order rate constant has been determined for 746≤T≤987 K to be $k_5=(7.1 \pm 1.9) \times 10^{-33}$ cm⁶ molecule⁻² s⁻¹ with Ar as the heat bath gas.[10] The Baulch et al.[30] recommendation is,

$$k_{H+O2+Ar} = 4.1 \times 10^{-33} \exp(+500 \text{ K/T}) \text{ cm}^6 \text{ molecule}^{-2} \text{ s}^{-1}. \qquad (20)$$

A recent flow tube study[31] for 298≤T≤639 K in He gives,

$$k_{H+O2+He} = (4.0 \pm 1.2) \times 10^{-33} \exp(+560 \text{ K/T}) \text{ cm}^6 \text{ molecule}^{-2} \text{ s}^{-1}. (21)$$

Since He and Ar have about the same effective collision efficiency, the FP-ST result can be compared to both eqs. (20) and (21). At the mean temperature, T = 850 K, eqs. (20) and (21) give respective values of 7.4 x 10⁻³³ and 7.7 x 10⁻³³ to be compared to the FP-ST result of 7.1 x 10⁻³³ cm⁶ molecule⁻² s⁻¹. These results combine to give excellent agreement for the recombination reaction over the

temperature range, 300 to ~1000 K. Since the Hsu et al.[31] result is the most direct to date, it is listed in Table I. Similar experiments for D + O_2 + M have not been reported, but eq. (21) can be used in D_2/O_2 modeling calculations as a first estimate.

CONCLUSION

The most important rate constants in the branching chain oxidations of H_2 and D_2 have now been measured by the direct flash and/or laser photolysis-shock (FP- or LP-ST) tube technique. The only exceptions are the O + D_2O and D + O_2 + M reactions. There are of course several other reactions of secondary importance that must be included in complete oxidation mechanisms, and these have been considered in most earlier studies. The importance of these reactions increases as the extent of reaction increases, and, in the large conversion H_2/O_2 studies where OH-radicals are observed throughout the entire course of the reaction, the relative effects of these secondary reactions are greater than in the small conversion studies where the initial stages of the reaction are only monitored. However, even in the high conversion studies, the five reactions considered here and their reverses, always exhibit higher sensitivity than all other reactions in sensitivity analysis calculations. It can therefore be concluded with these new direct FP- and LP-ST data that the main features of the oxidation mechanisms are now substantially solved.

The evaluated rate constants are given in Table I along with comments regarding accuracy and the T-range of applicability. We recommend that these rate constants be used as initial starting values in oxidation studies. To be sure, the rate constants are known only within certain error limits, and therefore, any adjustments within these error limits are certainly allowed. However, if a particular observation implies the use of rate constants that are substantially outside the bounds set by these direct studies, then an inconsistency exists. In this event, new explanations must be found, and this may imply modifications in the reaction rate constants for initiation and/or perhaps in secondary chemical processes.

ACKNOWLEDGEMENT

REFERENCES

1. Burns, G. and Hornig, D.F., Can. J. Chem. **38**, 1702 (1960).
2. (a) Ernst, J., Wagner, H. gG. and Zellner, R., Ber. Bunsen-Ges. Phys. Chem. **82**, 409 (1978). (b) Niemitz, K. J., Wagner, H. gG. and Zellner,   R., Z. Phys. Chem. (Frankfurt am Main) **124**, 155 (1981).
3. Michael, J. V., Sutherland, J. W. and Klemm, R. B., Int. J. Chem. Kin. **17**, 315 (1985).
4. Bradley, J. N., *Shock Waves in Chemisty and Physics*, Wiley, New York, 1962.
5. Michael, J. V., J. Chem. Phys. **90**, 189 (1989).
6. Michael, J. V., Adv. Chem. Kin. and Dynamics **1**, xxx (1991).
7. Michael, J. V., Prog. Energy and Combust. Sci., submitted.
8. Davidson, D. F. , Chang, A. Y. and Hanson, R. K., Symp. (Int.) Combust., [Proc.] **22**, 1877 (1988).

9. Shin, K. S. and Michael, J. V., J. Chem. Phys., in press.
10. Pirraglia, A. N., Michael, J. V., Sutherland, J. W. and Klemm, R. B., J. Phys. Chem. **93**, 282 (1989).
11. Chase, Jr., M. W., Curnutt, J. L., Downey, Jr., J. R., McDonald, R. A., Syverud, A. N. and Valenzuela, E. A., J. Phys. Chem. Ref. Data **15**, 1078 (1986).
12. Sutherland, J. W., Michael, J. V., Pirraglia, A. N., Nesbitt, F. L. and Klemm, R. B., Symp. (Int.) Combust., [Proc.] **21**, 929 (1986).
13. Westenberg, A. A. and deHaas, N., J. Chem. Phys. **46**, 490 (1967); ibid **50**, 2512 (1969).
14. Clyne, M. A. A. and Thrush, B. A., Proc. R. Soc. London Ser. A **275**, 544 (1963).
15. Marshall, P. and Fontijn, A., J. Chem. Phys. **87**, 6988 (1987).
16. Presser, N. and Gordon, R. J., J. Chem. Phys. **82**, 1291 (1985).
17. Westenberg, A. A. and de Haas, N., J. Chem. Phys. **47**, 4241 (1967).
18. Zhu, Y.-F., Arepalli, S. and Gordon, R. J., J. Chem. Phys. **90**, 183 (1989).
19. Michael, J. V. and Sutherland, J. W., J. Phys. Chem. **92**, 3853 (1988).
20. Fisher, J. R. and Michael, J. V., J. Phys. Chem. **94**, 2465 (1990).
21. Frank P. and Just, Th., Ber. Bunsen-Ges. Phys. Chem. **89**, 181 (1985). 2
22. (a) Kaufman, F. and delGreco, F.P., Discuss. Faraday Soc. **33**, 128 (1962); (b) Dixon-Lewis, G., Wilson, W. E. and Westenberg, A. A., J. Chem. Phys. **44**, 2877 (1966); (c) Greiner, N. R., J. Chem. Phys. **51**, 5049 (1969); (d) Stuhl, F. and Niki, H., J. Chem. Phys. **57**, 3671 (1972); (e) Westenberg, A. A. and deHaas, N., J. Chem. Phys. **58**, 4061 (1973); (f) Smith, I. W. M. and Zellner, R., J. Chem. Soc., Faraday Trans. 2 **70**, 1045 (1974); (g) Atkinson, R., Hansen, D. A. and Pitts, Jr., J. N., J. Chem. Phys. **63**, 1703 (1975); (h) Overend, R. P., Paraskevopoulos, G. and Cvetanovic, R. J., Can. J. Chem. **53**, 3374 (1975).
23. Ravishankara, A. R., Nicovich, J. M., Thompson, R. L. and Tully, F. P., J. Phys. Chem. **85**, 2498 (1981).
24. Tully, F. P. and Ravishankara, A. R., J. Phys. Chem. **84**, 3126 (1980).
25. Oldenborg, R. C., Harradine, D. M., Loge, G. W. and Winn, K. R., Paper presented at the Second International Conference on Chemical Kinetics, N. I. S. T., Gaithersburg, MD, July 24, 1989.
26. Sutherland, J. W., Patterson, P. M. and Klemm, R. B., Symp. (Int.) Combust., [Proc.] **23**, xxx (1990).
27. Lifshitz, A. and Michael, J. V., Symp. (Int.) Combust., [Proc.] **23**, xxx (1990).
28. Albers, E. A., Hoyermann, K., Wagner, H. Gg. and Wolfrum, J., Symp. (Int.) Combust., [Proc.] **13**, 81 (1970).
29. (a) Rawlins, W. T. and Gardiner, Jr., W. C., J. Chem. Phys. **60**, 4676 (1974); (b) Ernst, J., Wagner, H. Gg. and Zellner, R., Ber. Bunsenges. Phys. Chem. **81**, 1270 (1977); (c) del Greco, F. P. and Kaufman, F., Disc. Faraday Soc. **33**, 128 (1962) and Kaufman, F., Ann. Geophys. **20**, 106 (1964); (d) Wilson, W. E. and O'Donovan, J. T., J. Chem. Phys. **47**, 5455 (1967); (e) Breen, J. E. and Glass, G. P., J. Chem. Phys. **52**, 1082 (1970); (f) Westenberg, A. A. and de Haas, N., J. Chem. Phys. **58**, 4066 (1973); (g) McKenzie, A., Mulcahy, M. F. R. and Steven, J. P., J. Chem. Phys. **59**, 3244 (1973); (h) Clyne, M. A. A. and Down, S., J. Chem. Soc. Faraday Trans. II **70**, 253 (1974); (i) Trainor, D. W.

and von Rosenberg, C. W., Jr., J. Chem. Phys. **61**, 1010 (1974);
(j) Farquharson, G. K. and Smith, R. H., Aust. J. Chem. **33**, 1425
(1980); (k) Wagner, G. and Zellner, R., Ber. Bunsenges. Phys.
Chem. **85**, 1122 (1981).

30. Baulch, D. L., Drysdale, D. D., Horne, D. G. and Lloyd, A. C.,
    vol. 1 of *Evaluated Data for High Temperature Reactions*,
    Butterworths, London, 1972.
31. Hsu, K.-J., Durant, J. L. and Kaufman, F., J. Phys. Chem. **91**,
    1985 (1987); Hsu, K.-J., Anderson, S. M., Durant, J. L. and
    Kaufman, F., J. Phys. Chem. **93**, 1018 (1989).

Table I: Recommended $k = A\,T^n\,\exp(-B/T)$ expressions for the H_2/O_2 and D_2/O_2 Reactions from the FP- or LP-ST Studies.

Reaction	A/cm^3 molecule^{-1} s^{-1}	n	B/K	Comments and Reference
Protonated reactions:				
$H + O_2$	1.15(-10)[a]	0	-6917	1100 - 2050K, ±27%[9]
$OH + O$	8.75(-12)	0	1121	1100 - 2050K, ±27%[9,11]
$O + H_2$	8.44(-20)	2.67	-3167	297 - 2495K, ±30%[12]
$OH + H$	3.78(-20)	2.67	-2226	297 - 2495K, ±30%[11,12]
$H + H_2O$	1.56(-15)	1.52	-9249	250 - 2297K, ~±25%[11,25]
$OH + H_2$	3.56(-16)	1.52	-7513	250 - 2581K, ~±25%[25]
$O + H_2O$	7.48(-20)	2.70	-7323	700 - 2500K, ~±50%, theory[7]
$OH + OH$	7.19(-21)	2.70	1251	700 - 2500K, ~±50%, theory[7]
$H + O_2 + M$	4.0(-33)[b]	0	560	298 - ~1000K, ~±30%[31]
Deuterated reactions:				
$D + O_2$	1.09(-10)	0	-6937	1050≤T≤2300K, ±27%[9]
$OD + O$	9.73(-12)	0	526	1050≤T≤2300K, ±27%[9,11]
$O + D_2$	2.43(-16)	1.70	-4911	343≤T≤2487K, ±16%[5]
$OD + D$	1.04(-16)	1.70	-3806	343≤T≤2487K, ±16%[5,11]
$D + D_2O$	2.90(-10)	0	-10815	1285≤T≤2261K, ±27%[20]
$OD + D_2$	6.56(-11)	0	-3320	1285≤T≤2261K, ±27%[11,20]
$O + D_2O$	2.05(-19)	2.56	-8286	>700 K, theory[7]
$OD + OD$	1.85(-20)	2.56	452	>700 K, theory[7]

[a]parentheses denotes the power of ten; i. e., 1.15×10^{-10}. [b]units are cm^6 molecule^{-2} s^{-1}.
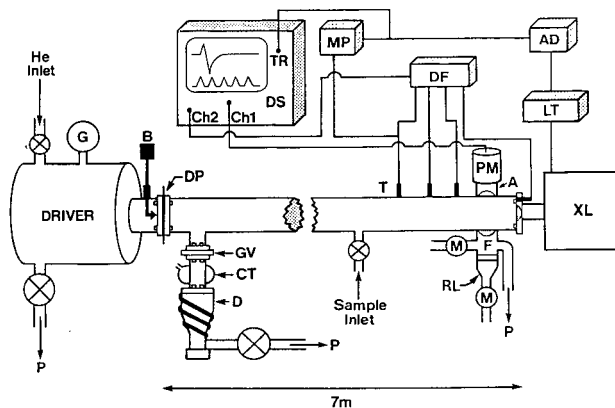
Fig. 1: Schematic diagram of the apparatus. P - rotary pump. D - oil diffusion pump.
CT - liquid nitrogen baffle. GV - gate valve. G - bourdon gauge. B - breaker.
DP - diaphragm. T - pressure transducers. M - microwave power supply.
F - atomic filter. RL - resonance lamp. A - gas and crystal window filter.
PM - photomultiplier. DS - digital oscilloscope. MP - master pulse generator.
TR - trigger pulse. DF - differentiator. AD - delayed pulse generator. LT - laser
trigger. XL - excimer laser.
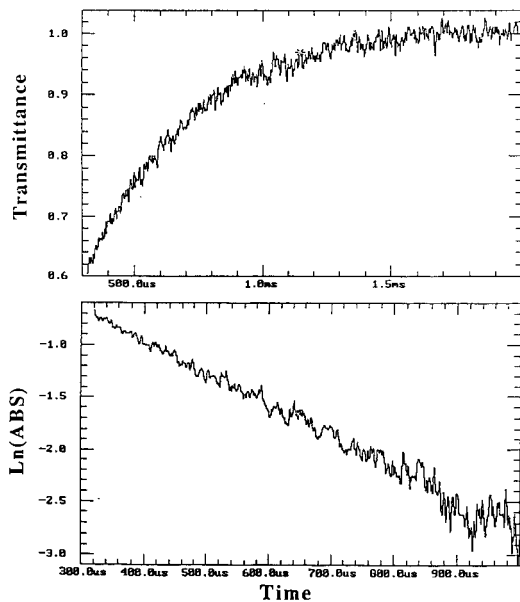
Fig. 2: Top: H-atom transmittance as a function of time after laser photolysis in the reflected
shock wave region. Bottom: First-order plot of ln[ABS]$_t$ against time that is obtained
from the top record.

1570

PHOTOIONIZATION MASS SPECTROMETRIC STUDIES OF THE COMBUSTION INTERMEDIATES CH$_2$OH AND CH$_3$O*

B. Ruscic and J. Berkowitz
Chemistry Division
Argonne National Laboratory
Argonne, IL 60439

I. INTRODUCTION

The radical species CH$_3$O and CH$_2$OH are believed to play important roles as intermediates in the combustion of hydrocarbon fuels.[1,2] Recently, absorption spectra in the visible-UV have been observed for both species,[3-10] primarily using laser methods. Accurate experimental vibrational frequencies are known for both species, and a rotational analysis (and hence geometric structure) is known for CH$_3$O. Despite this intensive study, the heats of formation of these species are still somewhat uncertain.

Cruickshank and Benson[11] studied the iodination reaction

$$CH_3OH + \rightarrow CH_2OH + HI \ ,$$
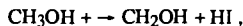
and obtained an endothermicity of 24.6±1.5 kcal/mol. Utilizing this value, Golden and Benson[12] compute $\Delta H^\circ_{f_{298}}$ (CH$_2$OH) = -4.2±1.5 kcal/mol. However, Golden and Benson also cite Buckley and Whittle,[13] who studied the corresponding bromination reaction, and inferred an endothermicity of <4.2 kcal/mol. From this latter observation, one can deduce $\Delta H^\circ_{f_{298}}$ (CH$_2$OH) ≤ -8.3 kcal/mol. In order to give some weight to the bromination data, Golden and Benson[12] chose $\Delta H^\circ_{f_{298}}$ (CH$_2$OH) = -6.2±2.5 kcal/mol. The compilation of Glushko et al.[14] selects $\Delta H^\circ_{f_{298}}$ (CH$_2$OH) = -4.8±2.4 kcal/mol as the middle range of several experiments, three of which are based on an incorrect ionization potential of CH$_2$OH (vide infra).

For ΔH°_f (CH$_3$O), most recent papers cite the experiments of Batt and co-workers.[15-17] Batt and Milne[16] determined the bond energy of CH$_3$O-NO by kinetic measurements (assuming no reverse activation energy) to be 41.8 kcal/mol. Using $\Delta H^\circ_{f_{298}}$ (CH$_3$ONO) = -16.0 kcal/mol from Silverwood and Thomas,[18] they obtained $\Delta H^\circ_{f_{298}}$ (CH$_3$O) = 4.2±0.7 kcal/mol. Subsequently, Batt and McCulloch[17] obtained $\Delta H^\circ_{f_{298}}$ (CH$_3$O) = 3.8±0.2 kcal/mol from the kinetics of dimethyl peroxide pyrolysis. Glushko, et al.,[14] surprisingly not citing Batt and co-workers, arrive at 3.1±1 kcal/mol from an examination of other sources.

At this point, it is convenient to introduce some *ab initio* calculations which have focused on the difference in stabilities of CH$_2$OH and CH$_3$O. Saebo et al.[19] show that CH$_3$O is 4.1 kcal/mol more stable than CH$_2$OH at the Hartree-Fock level (6-31 G** basis sets). However, when electron correlation is included, CH$_2$OH becomes more stable. At the MP3/6-31 G** level, and including zero point energies, CH$_2$OH is 5.0 kcal/mol more stable than CH$_3$O. At this level, the barrier to isomerization (CH$_3$O → CH$_2$OH) is found to be 36.0 kcal/mol. Later, Colwell[20] obtained an almost identical result - CH$_2$OH more stable by 5.86 kcal/mol, and a barrier height of 37.29 kcal/mol - using CI (singles and doubles) with a Davidson correction and a double zeta plus polarization basis set. However, in the recent calculation by Curtiss et al.[21] at the G2 level (more correlation) CH$_2$OH is found to be 8.8 kcal/mol more stable than CH$_3$O. Our prior analysis of experimental data would lead to a difference of (8.4 - 10.4) ± 2 kcal/mol. A previous experimental estimate of this quantity by Batt et al.[22] arrived at 7.5 kcal/mol.

The adiabatic ionization potential (I.P.) of a molecular species is the difference between the heats of formation of that species and the corresponding cation. Hence, if the heat of formation of the desired

cation is well known, and its adiabatic I.P. can be obtained, it offers an alternative route to the heat of formation of the neutral species. It turns out that $\Delta H°_f$ (CH_2OH^+) is rather well known from photoionization measurements[23] of the appearance potential of CH_2OH^+ from CH_3OH and C_2H_5OH. These measurements yield $\Delta H°_{f_o}$ $(CH_2OH^+) \geq 172.0 \pm 0.7$ and ≤ 171.7 kcal/mol, respectively. The adiabatic ionization potential of CH_2OH has been obtained in a photoelectron spectroscopic study by Dyke and co-workers,[24] who obtained I.P. $(CH_2OH) = 7.56 \pm 0.01$ eV. We shall re-examine this result in the experiments to be described below. Combining $\Delta H°_f$ (CH_2OH^+) and I.P. (CH_2OH), we obtain $\Delta H°_{f_o}$ $(CH_2OH) \leq -2.3 \pm 0.7$ kcal/mol, or $\Delta H°_{f_{298}}$ $(CH_2OH) \leq -3.9 \pm 0.7$ kcal/mol.

In the case of CH_3O, the heat of formation of its cation is very much in question. Dyke[25] reports 7.37 ± 0.03 eV as the adiabatic I.P. of CH_3O. Taking $\Delta H°_f$ $(CH_3O) \approx 4.0 \pm 1$ kcal/mol (vide supra), we infer $\Delta H°_f$ $(CH_3O^+) \approx 174$ kcal/mol. (We ignore for the moment the distinction between $\Delta H°_{f_o}$ and $\Delta H°_{f_{298}}$). By contrast, Burgers and Holmes[26] deduced $\Delta H°_f$ $(CH_3O^+) = 247 \pm 5$ kcal/mol from a somewhat complicated argument. First, they showed that the "CH_3O^+" ions previously believed to be produced by dissociative ionization of CH_3ONO and $(CH_3)_2O$ were really CH_2OH^+, and consequently earlier (lower) heats of formation of CH_3O^+ based on these measurements were invalid. They then prepared CH_3O^+ by charge reversal (starting with CH_3O^-). Upon measuring the metastable peak from the unimolecular decomposition process

$$CD_3O^+ \rightarrow DCO^+ + D_2 ,$$

they found that it had the same shape (i.e., the same kinetic energy release) as that from $CD_3OD^+ \rightarrow$ $[D_2COD^+] \rightarrow DCO + D_2$. Consequently, they argued that the transition state for formation of the DCO^+ metastable was the same, whether starting from CD_3O^+ or D_2COD^+, and that this transition state was "at or close above the enthalpy of formation of CD_3O^+." They measured the appearance potential of the metastable DCO^+ peak from CD_3OD (15.1 ± 0.2 eV) which, together with literature values for $\Delta H°_f$ (CD_3OD) and $\Delta H°_f$ (H), leads to a heat of formation of the transition state of 247 ± 5 kcal/mol. More recently, Ferguson, et al.[27] made an estimate of $\Delta H°_f$ (CH_3O^+) which provided some support for the value deduced by Burgers and Holmes. The argument is again somewhat involved, but they infer $\Delta H°_f$ $(CH_3O^+) = 245 \pm 6$ kcal/mol.

If $\Delta H°_f$ (CH_3O) is ~ 4 kcal/mol, then these latter inferences regarding $\Delta H°_f$ (CH_3O^+) imply I.P. $(CH_3O) \cong 10.5$ eV, very different from Dyke's 7.37 ± 0.03 eV. The major purpose of the current research was to resolve this huge discrepancy.

II. EXPERIMENTAL ARRANGEMENT

The experimental apparatus is a vacuum ultraviolet (VUV) photoionization mass spectrometer. It consists of a VUV light source (in this case, the emission spectrum from an electric discharge in molecular hydrogen), a 3-m VUV monochromator, a chamber where the gas to be studied is crossed by the light exiting from the monochromator, some ion optics and a quadrupole mass spectrometer. The apparatus operates windowless, with differential pumping, and hence can be utilized to much higher photon energies. The VUV light is monitored by a bare photomultiplier, while the ions strike another bare multiplier and are pulse counted. The data consist of ion intensity (normalized to light intensity) as a function of wavelength, which we refer to as the photoion yield.

Experiments of this sort for stable gases can be performed routinely. Transient species present more serious problems, because the number density is much smaller, and the methods of producing these transient species may generate additional noise. We have prepared CH_3O and CH_2OH by the reaction of F atoms with CH_3OH. Several previous studies have shown that H atom abstraction occurs at both the C and O position. McCaulley et al.[28] have recently studied this reaction, and review earlier results.

A schematic drawing of the apparatus for generating transient species *in situ* near the region of photoionization has been described previously.[29] In order to distinguish between CH_2OH and CH_3O, we have used isotopic variants of methanol, particularly CD_3OH and CH_3OD. With CD_3OH, CD_3O^+ occurs at m/e = 34, and CD_2OH^+ at m/e = 33; with CH_3OD, CH_3O^+ occurs at m/e = 31, CH_2OD^+ at m/e = 32.

1572

III. EXPERIMENTAL RESULTS

A. The F + CD₃OH reaction

1. CD₂OH⁺, M33

The photoion yield curve of M33, presumed to be CD_2OH^+ (CD_2OH), displays at least 3 sloping step-like features. They correspond in energy (approximately) to the positions of the peaks in Dyke's[25] photoelectron spectrum of CD_2OH. Hence, the dominant ionization process appears to be direct ionization. The half-rise of the first step occurs at 1644.3 ± 3 Å $\equiv 7.540 \pm 0.006$ eV, which we take to be the adiabatic I.P. of CD_2OH. Dyke gives 7.55 ± 0.01 eV for this quantity. In Dyke's spectrum (and also in ours), there is a weak peak (background in ours) at ~7.4 eV. In order to distinguish between a still lower threshold and a hot band, we performed a simple quasi-diatomic Franck-Condon calculation, assuming harmonic behavior and a frequency (presumed to be C-O⁺) of 1610 cm⁻¹, taken from Dyke. From the relative peak intensities, we calculate a change in bond length of 0.12 Å. Whangbo, et al.[30] have computed a contraction of 0.13 Å in the C-O bond length between CH_2OH and CH_2OH^+, in excellent agreement. Alternatively, if we assign the 0→0 peak as 0→1, we can calculate the intensity expected at the 0→0 position. The intensity of the weak peak at ~7.4 eV is about a factor 5 lower than the predicted intensity and the overall fit for higher peaks becomes much poorer. Hence, this weak feature is attributed to a hot band.

2. CD₃O, M34

The photoion yield curve of M34, presumed to be CD_3O^+ (CD_3O), displays a broad underlying "background," but an abrupt increase in ion yield occurs at 1155.9 ± 0.9 Å $\equiv 10.726 \pm 0.008$ eV. We take this to be the adiabatic I.P. of CD_3O. The underlying background has about the same shape as CD_2OH^+ from CD_2OH, but is about a factor 20 weaker. A possible source of this background may be the F + CD_3OH reaction itself, where some CD_2OD may be formed. Beyond threshold, one can observe sloping, step-like features with intervals of ~2400 cm⁻¹.

B. The F + CD₃OD, CH₃OD and CH₃OH reactions.

Some of these experiments are still in progress; consequently, these are preliminary results. The F + CD_3OD reaction yields CD_3O, and photoionization produces CD_3O^+ with essentially the same onset as obtained in the F + CD_3OH experiment. However, in the F + CD_3OD experiment CD_2OD is also formed, and its subsequent ionization yields ion intensity at the same mass, but at lower energy. Hence, CD_3O is identified as an increase in the photoion yield at m/c = 34, above that due to CD_2OD^+.

An adiabatic onset for CH_3O^+ is not observed at the wavelength expected in the F + CH_3OD and F + CH_3OH experiments. Some ionization at m/e = 31 is observed at shorter wavelength (higher photon energy). From zero point energy considerations,[21] the adiabatic I.P. of CH_3O should be the same as CD_3O, within about 0.001 eV. Hence, the absence of CH_3O^+ at the expected wavelength implies that it is unstable. In fact, HCO^+ is observed in this case, in the approximate abundance expected for the decomposition $CH_3O^+ \rightarrow HCO^+ + H_2$. The adiabatic I.P. of CH_2OH is found to be 1641.5 ± 1.3 Å $\equiv 7.549 \pm 0.006$ eV.

IV. DISCUSSION OF RESULTS

A. CH₂OH - CH₂OH⁺

The adiabatic I.P. of CH_2OH obtained in this study (7.549 ± 0.006 eV) is very nearly the same as that reported by Dyke[24,25] (7.56 ± 0.01 eV) by photoelectron spectroscopy. Taking $\Delta H°_f$ (CH_2OH^+) $\leq 172.0 \pm 0.7$ kcal/mol, we deduce $\Delta H°_f$ (CH_2OH) $\leq -2.1 \pm 0.7$ kcal/mol, or $\Delta H°_{f_{298}}$ (CH_2OH) $\leq -3.7 \pm 0.7$ kcal/mol, which is at the upper end of the range given in the Introduction.

B. CD₃O - CD₃O⁺

The I.P. for CD_3O obtained here (10.726 ± 0.008 eV) is obviously very different from Dyke's[25] 7.37 ± 0.03 eV. Dyke's experiment consisted of measuring the photoelectron spectrum of the pyrolysis products from dimethyl peroxide. The spectrum is suggestive of a blurred CH_2OH spectrum, but further speculation on our part is unwarranted. If we take $\Delta H^{\circ}_{f_{298}}$ (CH_3O) = 4.0 ± 1 kcal/mol, then ΔH°_f (CH_3O) = 5.9 ± 1 kcal/mol, and ΔH°_f (CH_3O^+) becomes 253.2 ± 1 kcal/mol (251.2 ± 1 at 298°K). This latter value is within the range deduced by Burgers and Holmes[26] (247 ± 5) and estimated by Ferguson, et al.[27] (245 ± 6 kcal/mol).

C. CH₃O⁺ - CD₃O⁺

Our failure to observe CH_3O^+, although CD_3O^+ was observed, suggests that zero point energy differences or tunneling could account for their relative stabilities. According to *ab initio* calculations,[21,31] the ground state CH_2OH^+ potential energy surface is a singlet, whereas that of CH_3O^+ is a triplet. Ionization of CH_3O will strongly favor formation of CH_3O^+, over CH_2OH^+, by Franck-Condon considerations. However, CH_3O^+ will initially be formed more than 3 eV above the ground state of CH_2OH^+, and above the thermochemical threshold for formation of $HCO^+ + H_2$ (which also represents a singlet surface). One can expect that there will be some crossing between the triplet CH_3O^+ surface and the singlet surface. Spin-orbit interaction should permit some mixing between the triplet and the singlet surface, and hence the crossing will become an avoided crossing, resulting in a potential barrier. In its lowest vibrational state, CD_3O^+ appears to be stable to decomposition by barrier penetration (on a time scale of ~10^{-5} sec) whereas CH_3O^+ is not. We look forward to the results of future *ab initio* calculations, which may clarify this point.

REFERENCES

1. "Oxidation of Organic Compounds", Advances in Chemistry Series (American Chemical Society, Washington, D.C., 1968), Vols. I, II, III.
2. K. L. Demerjian, J. A. Kerr, and J. G. Calvert, Adv. Environ. Sci. Technol. 4, 1 (1974).
3. T. Amano and H. E. Warner, Ap. J. Lett. 342, L99 (1989).
4. C. S. Dulcey and J. W. Hudgens, J. Chem. Phys. 84, 5262 (1986).
5. D. S. Bomse, S. Dougal, and R. L. Woodin, J. Phys. Chem. 90, 2640 (1986).
6. P. Pagsberg, J. Munk, A. Sillesen, and C. Anastasi, Chem. Phys. Lett. 146, 375 (1988).
7. G. R. Long, R. D. Johnson, and J. W. Hudgens, J. Phys. Chem. 90, 4901 (1986).
8. S. C. Foster, P. Misra, Y-T. D. Lin, C. P. Damo, C. C.Carter, and T. A. Miller, J. Phys. Chem. 92, 5914 (1988).
9. X. Liu, C. P. Damo, T-Y. D. Lin, S. C. Foster, P. Misra, L. Yu, and T. A. Miller, J. Phys. Chem. 93, 2266 (1989).
10. J. Kappert and F. Tanys, Chem. Phys. 132, 197 (1989).
11. F. R. Cruickshank and S. W. Benson, J. Phys. Chem. 73, 733 (1969).
12. D. M. Golden and S. W. Benson, Chem. Rev. 69, 125 (1969).
13. E. Buckley and E. Whittle, Trans. Far. Soc. 58, 536 (1962).
14. V. P. Glushko, L. V. Gurvich, G. A. Bergman, I. V. Veitz, V. A. Medredev, G. A. Khachkuruzov, and V. C. Yungman, "Termodinamicheskie Cvoistva Individuall'nikh Veshchestv, Vol. 1 and 2, Nauka, Moscow, 1978 and 1979.
15. L. Batt, K. Christie, R. T. Milne and A. J. Summers, Int. J. Chem. Kin. 6, 877 (1974).
16. L. D. Batt and R. T. Milne, Int. J. Chem. Kin. 6, 945 (1974).
17. L. Batt and R. D. McCulloch, Int. J. Chem. Kin. 8, 491 (1976).
18. R. Silverwood and J. H. Thmas, Trans. Far. Soc. 63, 2476 (1967).
19. S. Saebo, L. Radom, and H. F. Schaefer III, J. Chem. Phys. 78, 845 (1983).
20. S. M. Colwell, Theor. Chim, Acta 74, 123 (1988).
21. L. A. Curtiss, D. Kock and J. A. Pople, J. Chem. Phys. (to be submitted).
22. L. Batt, J. P. Burrows and G. N. Robinson, Chem. Phys. Lett. 78, 467 (1981).
23. K. M. A. Refaey and W. A. Chupka, J. Chem. Phys. 48, 5205 (1968).

24. J. M. Dyke, A. R. Ellis, N. Jonathan, N. Keddar, and A. Morris, Chem. Phys. Lett. $\underline{111}$, 207 (1984).
25. J. M. Dyke, J. Chem. Soc. Far. Trans. 2 $\underline{83}$, 69 (1987).
26. P. C. Burgers and J. L. Homes, Organic Mass Spectrom. $\underline{19}$, 452 (1984).
27. E. E. Ferguson, J. Roncin and L. Bonazzola, Int. J. Mass Spectrom. Ion Proc. $\underline{79}$, 315 (1987).
28. J. A. McCaulley, N. Kelly, M. F. Golde, and F. Kaufman, J. Phys. Chem. $\underline{93}$, 1014 (1989).
29. a) S. T. Gibson, J. P. Greene, and J. Berkowitz, J. Chem. Phys. $\underline{83}$, 4319 (1985); b) J. Berkowitz, J. P. Greene, H. Cho, and B. Ruscic, J. Chem. Phys. $\underline{86}$, 1235 (1987).
30. M.-H. Whangbo, S. Wolfe, and F. Bernardi, Can. J. Chem. $\underline{53}$, 3040 (1975).
31. W. J. Bouma, R. H. Nobes, and L. Radom, Organic Mass Spectrom. $\underline{17}$, 315 (1982).

A TIME-DEPENDENT FLAME MODEL UTILIZING THE METHOD OF LINES

H.D. Ladouceur and J.W. Fleming
Chemistry Division, Code 6110, Naval Research Laboratory
Washington, DC 20375-5000

ABSTRACT

We have developed a time-dependent flame model to interpret the temporal evolution of various chemical species generated by laser photolysis of a steady-state low-pressure (10 torr) CH_4/O_2 flame. The model includes the effects of diffusion, convection and elementary chemical kinetics. The diffusion and convection terms are represented by finite difference expressions in the species conservation equations which reduce them to a stiff system of ordinary differential equations. The latter system is solved as an initial value problem by Gear's method. The initial conditions on the model are determined by a photolysis mechanism which perturbs concentrations of the steady-state flame. The computations demonstrate the importance in low-pressure flames of mass transport and chemistry in the relaxation of the perturbed state.

I. INTRODUCTION

This paper describes a time-dependent flame model which utilizes the method of lines (MOL)[1]. This model was developed to correlate time-dependent relaxation measurements of steady-state CH_4/O_2 flames perturbed by laser photolysis. The conservation of various chemical species mass fractions (Y_k) within the flame is described by a system of coupled nonlinear partial differential equations[2] (PDEs) which depend upon the position, x, relative to the burner surface and the time, t. This system of PDEs and the associated boundary conditions are first discretized in the spatial variable by finite-difference formulae. Thus, the system of PDEs is reduced to a system of coupled ordinary differential equations (ODEs) in time. This system of ODEs is readily integrated using Gears method.[3]

The experiment to be modeled is the 193 nm excimer laser perturbation of a 10 torr CH_4/O_2 flame, $\Phi = 0.9$. The OH and CH concentration profiles as well as the temperature profile throughout the flame have been previously reported for the steady-state flame.[4] In this paper we present the results for OH following perturbation at a position of 3 cm in the post-flame region. As a result of the 193 nm perturbation, the OH concentration increases in the irradiated region. Laser-induced fluorescence is used to monitor OH concentration as it decays back to the steady-state value.

II. MODELING

A. Steady-state flame

We used a one-dimensional flame code[5], referred to as PREMIX, developed at Sandia for modeling premixed, laminar flames. The code predicts steady-state species spatial profiles from a given set of input variables which include: a chemical mechanism, total pressure, inlet gas composition, mass flux, and a vertical temperature profile. PREMIX uses CHEMKIN-II[6] and the Sandia thermodynamic data base[7] to calculate both forward and reverse chemical reaction rates as functions

of pressure, composition and temperature. The mass fluxes due to diffusion are computed from effective binary diffusivities[8] for the gas mixture utilizing Sandia's Transport Code[9] and the Lennard-Jones parameters for the various chemical species in the mechanism. Thermal diffusion (Soret effect) is neglected in the present calculations. The boundary conditions are that the mass flux fraction of each specie be specified at the origin and the spatial derivatives of each mass fraction go to zero downstream of the flame region. We chose the chemical mechanism of Miller and Bowman,[10] deleting reactions involving nitrogen. The resulting chemical mechanism consists of 33 chemical species and 150 chemical reactions along with their rate parameters.

The equation governing the spatial distribution of the kth species in a constant pressure, one-dimensional, laminar flame is

$$\rho(\partial Y_k/\partial t) = \dot{\omega}_k W_k - \rho u(\partial Y_k/\partial x) - \partial(\rho Y_k V_k)/\partial x , \qquad (1)$$

where Y_k denotes the mass fraction of the kth species (k=1,33), x the spatial coordinate, t the time, ρ the mass density, W_k the molecular weight of the kth species, $\dot{\omega}_k$ the molar production rate by chemical reaction of the kth species per unit volume and V_k the diffusion velocity of the kth species defined by

$$V_k = v_k - u, \qquad (2)$$

where v_k denotes the velocity of the kth species with respect to a stationary coordinate frame and u, the mass-averaged velocity, is given by

$$u(x) = \sum_k Y_k(x) v_k(x). \qquad (3)$$

In a burner-stabilized flame, the mass flux (ρu) is a known constant and the molar production rates, $\dot{\omega}_k$, are dependent on the temperature, pressure and composition. These rates are calculated from CHEMKIN-II. The Sandia code solves the steady-state version of Eqn. (1) via a damped Newton method. If convergence difficulties are encountered, a time integration procedure, based upon an Euler algorithm, is implemented to provide a better estimate of the solution. Computations have been carried out on a VAX 6310 computer, where typical computational (CPU) time is less than 30 minutes.

B. TDFLM: Time-dependent flame model

The initial conditions following laser photolysis for the system of ODEs depend upon specific assumptions about the flame and the perturbation laser wavelength. In the post-flame region of our 10 torr CH_4/O_2 flame only H_2O and O_2 have any appreciable absorption at 193 nm. We observe a prompt formation of OH ground-state radicals which relax back to the steady-state with a lifetime of 5 μs. The increased OH, H, and O concentrations and the decreased H_2O and O_2 concentrations from their steady-state values can then be used as the initial conditions for the time-dependent calculation. In the present paper we consider only water photolysis in calculating the initial conditions.

The steady-state flame solutions generated from PREMIX represent the relaxed state of the perturbation experiments. The relaxation after the perturbation is measured in real time and one must have an accurate time-integration scheme to model the experiments. In the MOL algorithm the spatial derivatives on the right-hand side of Eqn. (1) are replaced by finite-difference expressions, reducing the PDEs to a system of ODEs for $Y_k(j,t)$. Each j corresponds to a specified spatial

1577

position above the burner surface. Thus, Eqn. (1) becomes

$$dY_k/dt = \text{Chemistry} - \text{Convection} - \text{Diffusion}, \tag{4}$$

where

$$\text{Chemistry} = \dot{\omega}_k W_k/\rho$$

$$\text{Convection} = u_j[Y_k(j,t) - Y_k(j-1,t)]/[x_j - x_{j-1}]$$

$$\text{Diffusion} = [(\rho Y_k V_k)_{j+1/2} - (\rho Y_k V_k)_{j-1/2}]/[x_{j+1/2} - x_{j-1/2}]$$

Pictorially, this method divides the one-dimensional flame into a number of spatial slices, as represented in Figure 1. The center of each slice corresponds to a particular height above the burner surface. The temporal evolution of the chemical species is computed within each slice along a line parallel to the time axis. This computation is done by Gear's method using DGEAR,[3] an IMSL (International Math Science Library) subroutine. The complete solution of these equations requires appropriate boundary conditions and initial conditions. TDFLM computes a starting set of mole fractions at time zero by first reading the steady-state results from the PREMIX calculation for the corresponding position in the flame. The code includes a photolysis mechanism which can alter the concentration of one or more species. The boundary conditions are chosen to correspond to the steady-state PREMIX calculation, i.e., mole fractions are specified upstream (at the burner surface), and spatial derivatives vanish downstream (at the end of the post flame region).

III. DISCUSSION

In the experiment we perturbed a position in the flame 3 cm above the burner surface, which has a measured OH rotational temperature of 1770 ± 60 K, using an ArF excimer laser. The laser beam was masked to produce a measured width of 3 mm and an intensity of 4.0 ± 3.2 J/cm^2. There is a $117 \pm 15\%$ observed maximum OH concentration increase over the steady-state as a result of the perturbation. This corresponds to photolysis of 7.5% of the water at this height above the burner (based on the PREMIX results). Using temperature dependent absorption coefficients for H_2O and O_2,[11] and an observed increase in OH of 117% over the steady-state, the excimer laser intensity is estimated to be 1.2 J/cm^2. This estimate is consistent with the experimental number. Photolysis of 7.5% of the steady-state water concentration to produce OH and H is utilized as input to the TDFLM code. Concentrations for the perturbed condition are converted to renormalized mass fractions for all chemical species by the TDFLM code. The TDFLM code then calculates the relaxation of the OH concentration back to the steady-state solution. Figure 2 shows the experimental OH decay following the 193 nm laser perturbation (open circles). The experimental steady-state solution is indicated by the filled square, with $\pm 2\sigma$ experimental uncertainty. As can be seen in Figure 2, the OH concentration returns to its steady-state within 15 μs. The filled circles in Figure 2 are a least-squares fit of the experimental data to a single exponential. Error bars on the least-squares fit are a $\pm 1\sigma$ confidence limit. Figure 3 shows the results of the TDFLM calculation. The axis on the left is the same as Figure 2. The right axis in Figure 3 corresponds to the calculated OH concentration. The filled circles in this figure are taken from Figure 2. The dashed line in Figure 3 results from dropping the diffusion and convection terms in Eqn. (4).

This calculation predicts the OH concentration to decay to a value which is larger than the PREMIX steady-state value. Separate numerical calculations demonstrate that chemistry dominates the short time relaxation. However, in the long time limit the purely kinetic calculation predicts an equilibrium concentration which is slightly greater than the experimentally observed value.

The solid line in Figure 3 is calculated from Eqn. (4) where terms for diffusion, convection and chemistry are included in the calculation. The agreement between the calculated behavior and the experimental observation is good. The binary diffusion coefficient for most gases at 1 atm pressure is on the order of 0.1 cm^2/s.[12] The diffusion coefficient increases with temperature ($T^{3/2}$ dependence) and is inversely proportional to pressure.[13] At 1770 K and 10 torr, diffusion coefficients are on the order of 1000 cm^2/s. Neglecting the diffusion and convection terms in the calculation is equivalent to assuming a homogeneous gas-phase reaction at 1770 K in a closed system. The relative OH concentration decreases more rapidly when mass transport effects are included in Eqn. (4). In the long time limit these terms contribute to a steady-state balance which lies within the error bars of the experiment. At this position in the post-flame, the OH concentration gradient is relatively small, and the net effects of the transport terms is less than 10%.

Future studies will examine the effect of including the photolysis of O_2 in the perturbation mechanism. Also, calculations to model perturbation in the flame zone are planned. In the flame zone, large concentration gradients make the transport terms more important and essential for modeling the observed relaxation.

IV. ACKNOWLEDGEMENTS

V. REFERENCES

1. Galant, S., Eighteenth Symposium (International) on Combustion, (The Combustion Institute, 1981) pp 1451-1459.
2. Kuo, K.K., _Principles of Combustion_, (John Wiley & Sons, New York, 1986) ch. 3.
3. Gear, C.W., "The Automatic Integration of Ordinary Differential Equations", Comm. A.C.M., **14**, pp 176-179 (1971). See also IMSL, User's Manual, Vol. 1, Edition 9.2, IMSL Inc., 7500 Bellaire Boulevard, Houston, TX, U.S.A. (1984).
4. Fleming, J.W., Burton, K.A., and Ladouceur, H.D., "OH and CH profiles in a 10 Torr methane/oxygen flame: experiment and flame modeling," Chem. Phys. Lett. **175** (4), 395-400 (1990).
5. R.J. Kee, J.F. Grcar, M.D. Smooke, and J.A. Miller, "A Fortran Program for Modeling Steady Laminar One-Dimensional Premixed Flames," Sandia Report SAND85-8240 (1987).
6. R.J. Kee, F.M. Rupley, and J.A. Miller,"Chemkin-II: A Fortran Chemical Kinetics Package for the Analysis of Gas-Phase Chemical Kinetics," Sandia Report SAND 89-8009 (1989).
7. R.J.Kee, F.M. Rupley, and J.A. Miller,"The CHEMKIN Thermodynamic Data Base," Sandia Report SAND87-8215 (1989).
8. Curtis, C.F. and Hirshfelder, J.O., "Transport Properties of Multicomponent Gas Mixtures," J. Chem. Phys., **17**, p 550-555 (1949).
9. R.J. Kee, J. Warnatz, and J.A. Miller,"A FORTRAN Computer Code

Package for the Evaluation of Gas–Phase Viscosities, Conductivities, and Diffusion Coefficients," Sandia Report SAND 83-8209 (1983).

10. Miller, J.A. and Bowman, C.T., "Mechanism and Modeling of Nitrogen Chemistry in Combustion," Prog. Energy Combust. Sci. 15, pp 287-338 (1989).

11. Davidson, D.F., Chang, A.Y., Kohse-Höinghaus, K., and Hanson, R.K., "High Temperature Absorption Coefficients of O_2, NH_3, and H_2O for Broadband ArF Excimer Laser Radiation," J. Quant. Spectrosc. Radiat. Transfer, 42, No. 4, pp 267-278 (1989).

12. Bird, R.B., Stewart, W.E., and Lightfoot, E.N., Transport Phenomena, (John Wiley and Sons, New York, 1960) p 503.

13. ibid p 510.
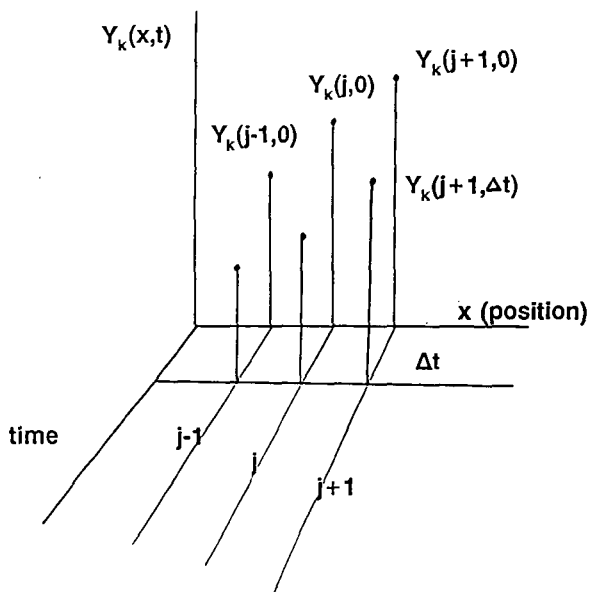
Figure 1. Schematic for the method of lines algorithm. Y_k denotes the kth species mass fraction at position j above the burner at time t.
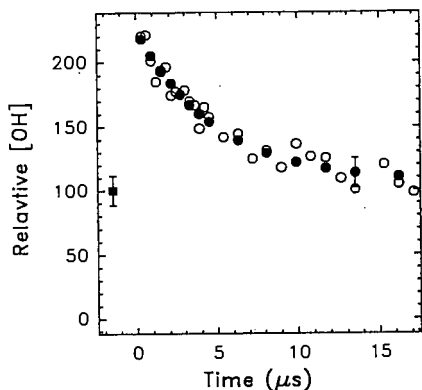
Figure 2. Relative experimental OH concentration at 3 cm above the burner surface in a 10 torr CH_4/O_2 flame as a function of time following 193 nm perturbation (open circles); Least-squares fit of the experimental OH decay to a single exponential (filled circles); relative experimental OH steady-state concentration (filled square). Error bars on the least-squares fit are a $\pm$ 1σ confidence limit.
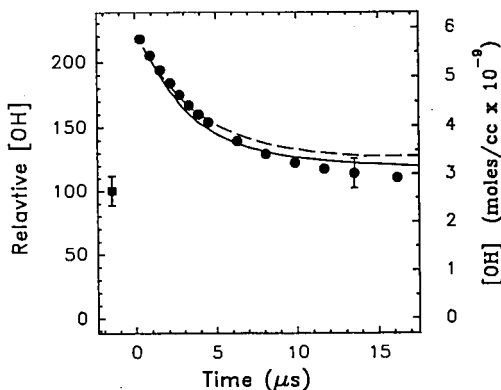
Figure 3. Least-squares fit of the relative experimental OH concentration at 3 cm above the burner surface in a 10 torr CH_4/O_2 flame as a function of time following 193 nm perturbation (filled circles, left axis); relative experimental OH steady-state concentration (filled square, left axis); TDFLM calculation with transport and chemistry (solid line, right axis); TDFLM calculation with no transport terms (dashed line, right axis). Error bars on the experimental steady-state represent $\pm$ 2σ experimental uncertainty. Error bars on the least-squares fit are a $\pm$ 1σ confidence limit. The left and right vertical axes have been chosen so that the relative experimental steady-state concentration equals the calculated PREMIX value.

CHEMISTRY OF SOLID PROPELLANT COMBUSTION STUDIED BY MASS SPECTROMETRY AND MODELLING.

O.P. Korobeinichev, L.V. Kuibida, A.A. Paletsky, A.A. Chernov, N.E. Ermolin
Laboratory of Kinetics of Combustion Processes
Institute of Chemical Kinetics and Combustion
Novosibirsk 630090, USSR

ABSTRACT

The flame structure of composite systems containing ammonium perchlorate with particle size < 50 μm and carboxy-terminated polybutadiene binder, component ratio close to stoichiometric (84% AP - 16% CTPB), was studied at a pressure of $8 \cdot 10^3$ Pa using the method of mass-spectrometric probing. The temperature and concentration profiles of 17 stable flame components were determined. Theoretical modelling of this flame structure was carried out by solving the differential equations describing a reacting multicomponent gas flow, involving heat and mass transfer as well as the kinetic mechanism, including 58 elementary steps and 35 components. Satisfactory agreement was achieved between the experimental and calculated data on concentration profiles of most of the 17 stable components and temperature. Rate constants of some little-studied or unstudied steps were estimated. The data obtained may be used to develop a model of the combustion of solid propellants based on ammonium perchlorate.

INTRODUCTION

The study of combustion mechanism at a molecular level is one of the most important problems of the combustion theory of condensed systems (CS). The experimental results on flame structure give the main information about the combustion chemistry, i.e., the kinetics and mechanism of chemical reactions in the combustion wave.

Earlier we have formulated and followed an approach to the study of the combustion chemistry of condensed systems (CS) which combines (a) experimental study of CS flame chemical structure by mass-spectrometric probing with (b) theoretical modelling of this structure by solving equations, describing the reacting multicomponent gas flow, and taking account of the multistep kinetic mechanism.[1-4] This approach has successfully been used to study the combustion chemistry of AP and RDX,[4] which made it possible to determine the most significant elementary steps and to estimate the rate constants of some little-studied or unstudied steps. In Reference 5, the above approach was employed to study the combustion chemistry of a homogenized composite solid propellant (CSP), containing ammonium perchlorate (AP) and polybutadiene binder with carboxy-terminated polybutadiene (CTPB) in a 77% AP-23% CTPB ratio of the components (thereafter, this composition will be referred to as composition No. 1) at $6 \cdot 10^4$ Pa. The aim of the present paper is to extend these studies. The experimental results are proposed for the flame structure of homogenized composite systems which are close to the stoichiometric ones.

EXPERIMENTAL

Experiments on flame structure were carried out at subatmospheric pressures ($8 \cdot 10^3$ Pa) in a helium flow by methods of mass-spectrometric probing of CS flames described in References 1, 2, and 5. The experiments consist of the following: a burning strand of solid fuel is moved toward the probe at a rate exceeding the burning rate, so that the probe is continuously sampling the gaseous species from all the zones including that adjacent to the burning surface. The sample is transported to the ion source of a time-of-flight mass spectrometer. Mass spectra of the sample are recorded with simultaneous filming of the probe and burning surface. The data allow us to identify stable components and to determine their concentrations and spatial distributions, i.e., the flame microstructure.

Apparata of two types have been developed for studying flame structure. In the first type (which was used in this work), a sample is transported to the ion source as a molecular flow. In the second type, the sample is transported to the ion source as a molecular beam.[4] A quartz cone (exterior and interior angles of 20° and 40-45°, respectively) with an orifice diameter of 20 μm was used as a

probe; the outer tip diameter was 0.3 mm. The thermal flame structure was studied with the help of microthermocouples (SiO_2-coated platinum and platinum-rhodium wires, 0.02 mm in diameter, and tungsten-rhodium wires, 0.02 mm in diameter) embedded in the propellant samples. A composition of 84% AP (particle size <50 μm) and 16% CTPB (composition No. 2) was used. The sample density was 1.5 g/cm, length - 15 mm, diameter - 8 mm. Cigarette paper served as armoured protection. The burning rate was 0.33 mm/s.

RESULTS AND DISCUSSION

Seventeen stable components (HCl, H_2O, CO, NH_3, CO_2, HClO, NO, O_2, H_2, NO_2, N_2, C_4H_6, C_2H_2, ClO_2, $HClO_4$, Cl_2, HCN) have been detected using mass-spectrometric probing. Concentration profiles of components in the flame were determined from the experimental data. As a rule, the sensitivity coefficients were estimated from the results of inlet system calibration against individual components. In some cases the mass spectra of combustion product samples and the balance equations for elements were used to determine the HCN and H_2O sensitivity coeffecients.

Dots in Fig. 1 (a,b) denote the experimental results from the flame structure, i.e. the dependences of component concentrations and of temperature in the flame under study, plotted as functions of the distance to the burning surface. The data show that the products of CTBP decomposition (C_4H_6, NH_3) are oxidized by those of AP dissociation and decomposition (ClO_2, $HClO_4$ and HClO) in the 1-mm zone of chemical reactions adjacent to the burning surface. These reactions result in HCl, HCN, C_2H_2, NO, CO, and H_2. The O_2 concentration passes through a maximum; that of Cl_2 decreases monotonically. The ammonia concentration in the combustion products decreases almost to zero, whereas in the combustion products of the fuel-rich composition No. 1, the concentration of ammonia was about 3%.

In Fig. 1(a,b), the solid lines represent the results of flame structure modelling using a stationary solution for the complete set of Navier-Stokes equations for reacting gas.[4] The experimental values of temperature and component concentrations were used as boundary conditions. In our calculations, we have used an abbreviated kinetic mechanism which involves 58 reversible steps and 35 components (Table 1),[5] which satisfactorily described the flame structure from composition No. 1. This mechanism has been isolated out of a complete one (258 reversible steps, 49 components).

Analysis of the data obtained shows that in the vicinity of the burning surface, the temperature gradient and the combustion zone width are especially sensitive to variations in the reaction rate constants of the following reactions:

$$NH_2 + O_2 \quad \rightarrow \quad HNO + OH \qquad \qquad [15]$$

$$CO + ClO \quad \rightarrow \quad CO_2 + Cl \qquad \qquad [57]$$

$$CO + ClO_2 \quad \rightarrow \quad CO_2 + ClO \qquad \qquad [58]$$

The most important step is the branching reaction 15. This reaction was studied experimentally in a number of papers, and its rate constant is most often taken from the paper by Dean.[6] However, to reach an agreement between experiment and theory, a rate constant that is 30-times higher must be used. In his recent paper, Dean[7] proposed another way:

$$NH_2 + O_2 \quad \rightarrow \quad NH_2O + O$$
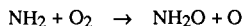
with the rate constant close to our value. There is a satisfactory agreement between experimental and calculated results of the flame structure under investigation. A better agreement with experiment can be achieved by increasing the rate constants for reactions 41 and 58 (see the Table) by 3 and 5 times. Note that the preexponential factors of these reactions are about 10 times as large as those of the same reactions used to calculate the flame structure of the composition No. 1 (with the equal rate constant of the other steps). In order to describe the experimental data on the flame structure of the different composition at various pressures, the mechanism presented in the Table should be improved. Having analyzed the data obtained, we can propose a scheme (Fig. 2) for the transformations of the main initial components (NH_3, C_4H_6, $HClO_4$, ClO_2) resulting from the reaction of oxidizer and fuel in the condensed phase in the AP-CTPB flame. This simplified scheme allows one to understand the main features of the chemical processes in the flame under consideration.

REFERENCES

1. Korobeinichev, O. P., *Fiz. Goreniya Vzryva* **1987**, *23*, No 5, 64.
2. Ermolin, N. E.; Korobeinichev, O. P.; Tereshchenko, A. G.; et al., *Fiz. Goreniya Vzryva*
   1982, *18*, No. 1, 46.
3. Ermolin, N. E.; Korobeinichev, O. P.; Tereshchenko, A. G.; et al. *Fiz. Goreniya Vzryva*
   1982, *18*, No. 2, 64.
4. Ermolin, N. E.; Korobeinichev, O. P.; Kuibida, L. V.; et al. *Fiz. Goreniya Vzryva* **1986**, *22*,
   No 5, 54.
5. Korobeinichev, O. P.; Chernov, A. A.; Emel'yanov, I. D.; et al. *Fiz. Goreniya Vzryva* **1990**,
   26, No. 3, 46.
6. Dean, A. M.; et al. *19th Symp. (Intern.) on Comb.*, Pittsburgh: The Combustion Institute, 97
   (1982).
7. Dean, A. M.; Bozzelli, J. W. *J. Phys. Chem.* **1982**, *93*, 1058.

Table 1. Rate coefficients in form $k_f = AT^b \exp(-E/RT)$, Ref. 5. Units are mol, cm^3, sec, K and cal/mol.

No.	Reaction	A	b	E
1.	$HClO_4 \rightarrow ClO_3 + OH$	1.00E+11	0.0	39100
2	$HClO_4 + HNO \rightarrow ClO_3 + NO + H_2O$	3.00E+13	0.0	6000
3	$HClO_4 + HCO \rightarrow ClO_3 + CO + H_2O$	5.00E+13	0.0	0
4	$HClO_4 + HCO \rightarrow ClO_2 + CO_2 + H_2O$	1.50E+12	0.0	0
5.	$ClO_3 \rightarrow ClO + O_2$	1.70E+12	0.5	0
6.	$Cl + O_2 + M \rightarrow ClO_2 + M$	6.00E+11	0.0	11200
7.	$ClO + NO \rightarrow Cl + NO_2$	6.80E+12	0.0	311
8.	$ClOH + ClO \rightarrow Cl_2 + HO_2$	1.00E+14	0.0	10000
9.	$ClOH + OH \rightarrow ClO + H_2O$	1.80E+13	0.0	0
10.	$HCl + OH \rightarrow Cl + H_2O$	5.00E+11	0.0	750
11.	$Cl_2 + H \rightarrow HCl + Cl$	8.40E+13	0.0	1150
12.	$NH_3 + ClO \rightarrow NH_2 + ClOH$	4.24E+11	0.5	6400
13.	$NH_3 + Cl \rightarrow NH_2 + HCl$	4.50E+11	0.5	100
14.	$NH_3 + OH \rightarrow NH_2 + H_2O$	1.00E+11	0.68	1100
15.	$NH_2 + O_2 \rightarrow HNO + OH$	6.00E+9	0.5	0
16.	$NH_2 + NO \rightarrow N_2 + H_2O$	2.40E+11	0.0	0
17.	$NH_2 + NO \rightarrow N_2H + OH$	6.00E+11	0.0	0
18.	$N_2H + NO \rightarrow HNO + N_2$	5.00E+13	0.0	0
19.	$HNO + OH \rightarrow NO + H_2O$	3.60E+13	0.0	0
20.	$HNO + O_2 \rightarrow NO_2 + OH$	1.00E+13	0.0	10000
21.	$HNO + H \rightarrow H_2 + NO$	1.00E+12	0.5	900
22.	$NO + H + M \rightarrow HNO + M$	3.20E+15	0.0	-600
23.	$N_2 + HO_2 \rightarrow HNO + NO$	8.00E+10	0.5	41800
24.	$NO + HO_2 \rightarrow NO_2 + OH$	3.00E+12	0.5	1800

25.	$NO_2 + H \rightarrow NO + OH$	5.00E+14	0.0	1740
26.	$H_2 + OH \rightarrow H_2O + H$	1.00E+8	1.6	3290
27.	$C_4H_6 + OH \rightarrow n\text{-}C_4H_5 + H_2O$	5.00E+12	0.68	1100
28.	$C_4H_6 + OH \rightarrow i\text{-}C_4H_5 + H_2O$	5.00E+12	0.68	1100
29.	$C_4H_6 + ClO \rightarrow n\text{-}C_4H_5 + ClOH$	5.00E+12	0.5	6400
30.	$C_4H_6 + ClO \rightarrow i\text{-}C_4H_5 + ClOH$	5.00E+12	0.5	6400
31.	$C_4H_6 + Cl \rightarrow n\text{-}C_4H_5 + HCl$	6.75E+12	0.5	100
32.	$C_4H_6 + Cl \rightarrow i\text{-}C_4H_5 + HCl$	2.25E+11	0.5	100
33.	$i\text{-}C_4H_5 + M \rightarrow n\text{-}C_4H_5 + M$	1.00E+14	0.0	6500
34.	$n\text{-}C_4H_5 \rightarrow C_4H_4 + H$	5.00E+14	0.0	45700
35.	$i\text{-}C_4H_5 \rightarrow C_4H_4 + H$	6.30E+15	0.0	58700
36.	$n\text{-}C_4H_5 \rightarrow C_2H_2 + C_2H_3$	5.00E+13	0.0	40000
37.	$i\text{-}C_4H_5 \rightarrow C_2H_3 + C_2H_2$	6.30E+10	0.0	32000
38.	$i\text{-}C_4H_5 + Cl \rightarrow C_4H_4 + HCl$	1.00E+14	0.0	1000
39.	$i\text{-}C_4H_5 + ClO \rightarrow C_4H_4 + ClOH$	1.00E+14	0.0	1000
40.	$C_4H_4 + H \rightarrow C_2H_3 + C_2H_2$	1.30E+14	0.0	1380
41.	$C_4H_4 + NO_2 \rightarrow CH_2 + HCN + HCO$	5.00E+13	0.0	0
42.	$C_2H_2 + C_2H_2 \rightarrow C_4H_4$	5.90E+12	0.0	44600
43.	$CH_2CO + OH \rightarrow CH_2O + HCO$	2.82E+13	0.0	0
44.	$CH_2OO + NO_2 \rightarrow CH_2O + CO + NO$	1.00E+13	0.0	6000
45.	$C_2H_3 + O_2 \rightarrow CH_2O + HCO$	6.00E+13	0.0	0
46.	$C_2H_2 + H \rightarrow C_2H_3$	5.50E+12	0.0	2330
47.	$C_2H_2 + OH \rightarrow CH_3 + CO$	2.00E+12	0.0	7000
48.	$CH_2O + M \rightarrow CO + H_2 + M$	2.50E+15	0.0	28600
49.	$CH_4 + Cl \rightarrow CH_3 + HCl$	2.50E+13	0.0	3830
50.	$CH_4 + ClO \rightarrow CH_3 + ClOH$	6.00E+11	0.5	5700
51.	$CH_4 + H \rightarrow CH_3 + H_2$	2.20E+4	3.0	8520
52.	$CH_4 + OH \rightarrow CH_3 + H_2O$	1.60E+6	2.1	2460
53.	$CH_3 + H \rightarrow CH_4$	6.00E+16	-1.0	0
54.	$HCO + M \rightarrow CO + H + M$	2.50E+14	0.0	16800
55.	$HCN + OH \rightarrow NH_2 + CO$	2.00E+11	0.0	0
56.	$CO + OH \rightarrow CO_2 + H$	4.40E+6	1.5	-740
57.	$CO + ClO \rightarrow CO_2 + Cl$	3.00E+12	0.0	1000
58.	$CO + ClO_2 \rightarrow CO_2 + ClO$	5.00E+10	0.0	0
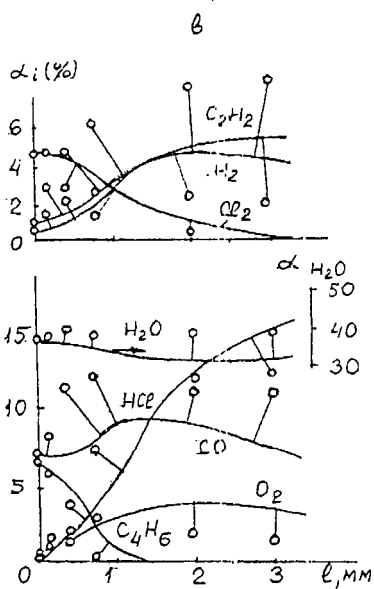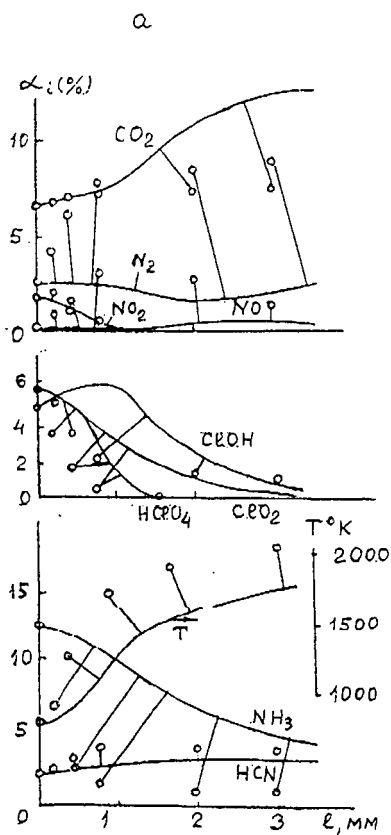
Fig. 1a, b. Temperature and concentrations of stable components in the studied flame vs distance to the burning surface: dots – experiment; solid lines – calculation.

Fig. 2. A scheme of chemical transformations in the AP – CTPB flame.

HOMOGENEOUS GAS-PHASE MODELING
OF BORON/OXYGEN/HYDROGEN/CARBON COMBUSTION

Louise Pasternack
Chemistry Division, code 6111
Naval Research Laboratory
Washington, D.C. 20375

keywords: boron combustion, combustion model

Introduction

The combustion of boron containing fuels is of importance in propulsion systems because of the potential large release of energy in going from boron to B_2O_3. The reaction scheme

$$2B(g) + 3/2\ O_2 \rightarrow B_2O_3(g)$$

is exothermic by 467 kcal/mole. The potential energy release from boron containing fuels is considerably greater than from liquid hydrocarbon fuels and from solid fuels containing metallic aluminum. This has resulted in increased attention to fuels composed of liquid hydrocarbons with boron particles suspended in a slurry. Calculations have shown this type of fuel to be an attractive candidate for air breathing propulsion systems which are volume limited.

The calculated advantage of these fuels is based on the assumption of complete combustion to water, carbon dioxide, and liquid B_2O_3. The combustion of boron containing fuels is a complex process involving both heterogeneous and homogeneous chemistry. First, the boron particles must be volatilized in heterogeneous processes to form gaseous boron containing species. These gas phase species then undergo homogeneous gas phase oxidation to form a mixture of boron oxide and boron oxyhydride species. The final step involves the condensation of the cooling product gases to form liquid B_2O_3. There are two major limitations to extracting the desired performance of these fuels which have been encountered. One is that boron fuel particles are coated with B_2O_3. This limits the initial vaporization of boron particles since B_2O_3 is difficult to remove either by vaporization or chemical reaction. The second problem is that the condensation of the final combustion products to liquid B_2O_3 may be slow, especially if boron oxyhydrides are formed as relatively long-lived intermediate species. For maximum efficiency of the combustion of boron containing fuels to be achieved, both the oxidation of the boron particles and the condensation to liquid boria must occur in the short residence time available in the system, typically less than 10^{-4} s.

Much attention has been focussed on these problems over the past several years. In this article, the homogeneous gas phase oxidation of boron, boron oxides, and boron oxyhydrides is discussed. In particular, the role of boron oxyhydrides as metastable species which contribute to the reduction of the overall combustion rate is explored. Efforts to understand this aspect of boron combustion have been hampered by the lack of basic thermodynamic and kinetic data on boron containing species. Modeling studies have been undertaken treating the gas phase oxidation step(1,2). This has helped to define some of the important species and reactions which require further study. Experimental and theoretical studies have focussed on the basic thermodynamics(3-5) and gas phase kinetics(6-10) of some of these systems. Using the results of these studies, the earlier model of homogeneous boron assisted combustion has been modified. The impact on the overall rate of combustion of these recent thermodynamic and kinetic measurements is discussed in this article. Several additional key reactions which may also have a significant impact on the model have been identified.

Model

The model used for this study is based on CHEMKIN gas-phase subroutines(11) and the SENKIN program(12) for predicting gas-phase kinetics with sensitivity analysis developed at Sandia. The modeling calculations predict the time dependence of a homogeneous gas-phase reacting mixture, based on a set of reversible or irreversible chemical reactions. As input, the code requires thermodynamic data in the form of polynomial fits to the heat capacities for all the species included in the mechanism. It also requires a list of all relevant chemical reactions, their rates, and initial species concentrations. The output of the calculation is processed using SENKPLOT graphics developed by D. Burgess of NIST.(13)

Species

The boron-containing species used in this model include B, BO, BO_2, HBO, B_2O_2(O=B-B=O), B_2O_3(O=B-O-B=O), and HBO_2(H-O-B=O). BH, BH_2, and BOH were also included in some cases. It is assumed that in order to obtain conditions where the B_2O_3 coating on the boron particles is volatilized (T>1800K), the hydrocarbon fuel is already oxidized. As a result, the H/O/C species used in this model include only H_2, H, O_2, O, OH, H_2O, H_2O_2, HO_2, CO, CO_2, and HCO. N_2 is included as a buffer gas, with total pressure of 1 atm.

Thermodynamics

The thermodynamic data base from Sandia(11) is augmented to include the boron compounds(14). Recently, Page(3) determined the heat of formation of HBO to be -60 kcal/mole using *ab initio* MCSCF with multireference CI techniques. This value of the heat of formation means that HBO is considerably more stable than was previously thought. The most recent JANAF recommended value for the heat of formation was -47.4 ± 3.0 kcal/mole(15). This difference has an impact on the overall boron combustion since HBO becomes a potential metastable species which could act as a bottleneck, preventing rapid combustion to B_2O_3 which is necessary for efficient energy release on the required timescale. The thermodynamic data base has been modified to include the polynomial fit to the thermodynamic properties as determined using statistical mechanics from the geometries, vibrational frequencies and heats of formation calculated by Page for HBO(3). In addition, BOH has been added to the thermodynamic data base, with the values determined in a similar manner.(5)

Kinetic Mechanism

A schematic diagram of the gas phase boron combustion pathways is shown below, which includes only the major species and the pathways which make the largest contributions to their production rates.
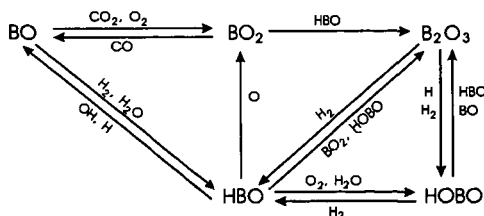
For our detailed kinetic mechanism, several modifications to the mechanism of Yetter, et al.(1) have been considered. All the elementary reactions included in the different mechanisms are listed in Table 1. The rates are tabulated in the form $k(cm^3mol^{-1}s^{-1})=AT^n\exp(-Ea/RT)$. Many of the rate constants for reactions of the boron containing species are taken from reference 1. Most of these values are estimated, since only a few detailed experimental or theoretical values are available. The list of elementary reactions for the hydrogen, oxygen, and carbon species is from Yetter, Dryer, and Rabitz(16) with rates updated to reflect the more recent recommended values of Tsang and Hampson(17).

The change in the heat of formation of HBO results in several exothermic reaction pathways which were previously considered to be endothermic. In particular, the reactions of $BO+H_2 \rightarrow HBO+H$ and $BO+OH \rightarrow HBO+O$ are now calculated to be exothermic. The rate of $BO+H_2$ reaction has been measured in our laboratory and the rate of $BO+OH$ has been calculated from transition state theory. The reaction of $B_2O_2+H \rightarrow BO+HBO$ is also calculated to be exothermic.

Reactions of B with oxidants have been measured at room temperature by DiGiuseppe and Davidovits(18,19). Oldenborg and Baughcum(20) have measured the rate of the $B+O_2$ reaction at higher temperatures. Recently, in our laboratory, rates of the reactions of BO with $H_2(6)$ and $O_2(7)$ have been measured at temperatures up to 1000K. Transition state theory has also been used to characterize the reactions of $BO+H_2(3,6)$ and $BO+O_2(7)$. These experimental rates are included in Table 1. We have also used transition state theory to characterize the reaction of $BO+OH$.

The remainder of the rate constants are estimated. The rate of reaction of $B_2O_2+H=BO+HBO$ is determined by comparison to other B_2O_2 reactions as estimated by Yetter, et al.(1) Several additional B and BO_2 reactions have been added, primarily to include boron hydrides in the kinetics. The rates are determined by analogy to similar reactions listed in reference 1. Reactions of BH have also been included in some of the test mechanisms. The rates of BH with O_2 and H_2O have been measured in our laboratory at temperatures up to 750K.(8) The rate of BH with CO_2 has only been measured at room temperature.(9) We assumed the same activation energy for O_2 and CO_2 reactions. The remainder of the BH reaction rates were estimated. BH_2 is not expected to play a major role in boron combustion; we have included a rate for the hydrogen abstraction from BH_2 by BO in the model which is similar in magnitude to other BO hydrogen abstraction rates.

Reactions have also been added to the mechanism to include the formation and reaction of BOH. Although this radical is not as stable as HBO, it may have a role in the combustion of boron. Rates were determined by comparison to similar reactions involving HBO and BO.

HBO reactions with O_2 and H_2O to form HBO_2 have been added. Several different rates for these reactions have been investigated in alternative mechanisms. The rates of these reactions listed in Table 1 are taken to be the same as Yetter, et al.(1) include for $HBO+OH=HBO_2+H$. However, the reactions of HBO with O_2 and H_2O involve more rearrangement than the substitution reaction of $HBO+OH=HBO_2+H$. Consequently, the rates may be slower.

Additional reactions of BO_2 abstracting hydrogen from HBO and HCO have also been included with rates analogous to the BO_2+OH and BO_2+H_2 reactions which were included by Yetter, et al.(1) A competing reaction for $BO_2+HBO=B_2O_3+H$ was also included.

Additional HBO_2 removal pathways by reaction with BO and HBO to form B_2O_3 have been added to the mechanism. The reaction with BO can proceed by substitution and its rate is determined by analogy to other similar substitution reactions included in the mechanism. The reaction with HBO is a four center reaction and might be expected to be slower.

Several additional oxidation pathways for $B_2O_2 \rightarrow B_2O_3$ have been added to the mechanism with rates of 6×10^{11} cm^{3}mol^{-1}s^{-1}. Their actual rates may be slower since these reactions would involve considerable rearrangement of an intermediate.

Results

Several different initial conditions have been considered in order to probe the effects of the different mechanisms and the importance of various reactions on the overall rate of boron combustion. The set of initial conditions listed in reference 2 which were derived from equilibrium calculations on a fuel rich mixture of JP4 and B(s) in air has been used. In addition, initial conditions which test the effects of all the boron being in either the form of HBO or BO have been investigated. The effects of assuming either complete hydrocarbon oxidation with H_2O and CO_2 as the hydrogen and carbon species or incomplete combustion with CO and H_2 as initial species have also been investigated.

In addition to the different initial conditions, several modifications to the mechanism which reflect the additional reactions discussed in the previous section have been studied. The first modification to the model used by Yetter, et al.[1] included the more recent thermodynamic values for HBO and the measured rates of reaction for $BO+H_2$ and $BO+O_2$. The result of these changes is to slow the overall rate of boron combustion, although the final ratio of the concentrations of the boron containing species remains similar. In addition, HBO is shown to be a potential bottleneck in the overall combustion, as can be seen in figure 1a.

This model can be modified by the inclusion of additional HBO removal processes. Adding the reactions of HBO with O_2 and H_2O increases the rate of boron combustion significantly. If the rates are on the order of 10^{12} $cm^3mol^{-1}s^{-1}$, HBO is no longer a metastable species slowing the boron combustion, but instead rapidly converts to HBO_2, as shown in figure 1b. An analysis of the rate of production of HBO and sensitivity analysis of the combustion process show that these reactions are important and may in fact be controlling, especially $HBO+O_2=HBO_2+O$.

Adding BH reactions has little effect on the overall boron combustion rate since there are few effective pathways to formation of BH under these conditions. Adding reactions involving BOH has no major effect on the overall rate of combustion, although it does play a significant role in the depletion mechanism for BO. BOH is expected to be rapidly oxidized to HBO_2.

Conclusions

The model for boron combustion has been updated to include recent experimental measurements and theoretical calculations of basic thermodynamic and kinetic data. An examination of the effects of these changes on the overall combustion rate, the production rates of the individual species, and sensitivity analysis has shown that there remain several key reactions which are in need of further study. In particular, reactions of HBO appear to be critical to the overall combustion scheme.

Acknowledgment

References

1. Yetter, R. A.; Rabitz, H.; Dryer, F. L.; Brown, R. C.; Kolb, C. E.; Combustion and Flame **1991**, 83, 43.
2. Brown, R. C.; Kolb, C. E.; Yetter, R. A.; Dryer, F. L.; Rabitz, H. R., "Development of a Boron Assisted Combustion Model with Sensitivity Analysis", Aerodyne Research, Inc., Report No. ARI-RR-580.
3. Page, M., J. Phys. Chem. **1989**, 93, 3639.
4. Page, M.; Adams, G. F.; Binkley, J. S.; Melius, C. F. J. Phys. Chem. **1987**, 91, 2676.
5. Page, M., unpublished data.
6. Garland, N. L.; Stanton, C. T.; Nelson, H. H.; Page, M., J. Chem. Phys., submitted.
7. Stanton, C. T.; Garland, N. L.; Nelson, H. H. J. Phys. Chem., submitted.
8. Garland, N. L.; Stanton, C. T.; Fleming, J. W.; Baronavski, A. P.; Nelson, H. H., J. Phys. Chem.**1990**, 94, 4952.
9. Rice, J. K.; Caldwell, N. J.; Nelson, H. H.,J. Phys. Chem. **1989**, 93, 3600.
10. Pasternack, L.; Balla, R. J.; Nelson, H. H. J. Phys. Chem. **1988**, 92, 1200.
11. Kee, R. J.; Miller, J. A.; Jefferson, T. H., "CHEMKIN: A General-Purpose, Problem-Independent, Transportable, Fortran Chemical Kinetics Code Package", Sandia, Report No. SAND80-8003.
12. Lutz, A. E.; Kee, R. J.; Miller, J. A. "SENKIN: A Fortran Program for Predicting Homogeneous Gas Phase Chemical Kinetics with Sensitivity Analysis", Sandia, Report No. SAND87-8248.
13. Burgess, D. private communication.
14. Gordon, S.; McBride, B. J.,"Computer Program for Calculation of Complex Chemical Equilibrium Compositions, Rocket Performance, Incident and Reflected Shocks, and Chapman-Jouguet Detonations", NASA Report No. NASA SP-273.
15. Chase, M. W. Jr.; Davies, C. A.; Downey, J. R. Jr.; Frurip, D. J.;McDonald, R. A.; Syverud, A. N., J. Phys. Chem. Ref. Data Supp. 1 **1985**, 14.
16. Yetter, R. A.; Dryer, F. L.; Rabitz, H."A Comprehensive Reaction Mechanism for the Oxidation of Moist Carbon Monoxide", Fall Western States Section Meeting of the Combustion Institute, WSS Paper 84-96, 1984.
17. Tsang, W.; Hampson, R. F., J. Phys. Chem. Ref. Data **1986**, 15, 1087.
18. DiGiuseppe, T. G.; Davidovits, P., J. Chem. Phys. **1981**, 74, 3287.
19. DiGiuseppe, T. G.; Estes, R.; Davidovits, P. J. Phys. Chem. **1982**, 86, 260.
20. Oldenborg, R. C.; Baughcum, S. L., J. Phys. Chem., submitted.

Table 1. Elementary reactions included in B/O/H/C combustion mechanisms.

REACTION	A cm^3/(mol s)	n	Ea cal/mol
B+O2=BO+O	7.24E13	0.0	310.
B+OH=BO+H	6.03E13	0.0	0.
B+CO2=BO+CO	4.17E10	0.0	0.
B+BO2=2BO	3.63E13	0.0	0.
B+O+M=BO+M	1.10E15	0.0	-1990.
B+H2O=HBO+H	2.40E14	0.0	2680.
B+HCO=BH+CO	6.03E13	0.0	0.
B+H+M=BH+M	1.10E15	0.0	-1990.
B+H2+M=BH2+M	1.10E15	0.0	0.
B+H2O=BOH+H	4.80E12	0.0	0.
B+OH+M=BOH+M	1.10E15	0.0	-1990.
BH+O2=HBO+O	3.00E13	0.0	2400.
BH+H2O=HBO+H2	3.00E12	0.0	380.
BH+CO2=HBO+CO	9.00E11	0.0	2400.
BH+O+M=HBO+M	1.10E15	0.0	-1990.
BH+OH=HBO+H	3.00E13	0.0	2400.
BH+BO2=HBO+BO	9.00E11	0.0	2400.
BH+BO=HBO+B	9.00E11	0.0	2400.
BH+HBO2=2HBO	3.00E12	0.0	380.
BH+BO2=HBO+B2O2	9.00E11	0.0	2400.
BH2+BO=HBO+BH	6.03E11	0.0	0.
HBO+OH=BO+H2O	4.79E13	0.0	0.
HBO+O=BO2+H	4.79E12	0.0	0.
HBO+OH=BO2+H2	6.03E3	0.0	70000.
HBO+O2=BO2+OH	4.79E12	0.0	70000.
HBO+O2=HBO2+O	4.79E12	0.0	0.
HBO+O+M=HBO2+M	3.63E20	-0.5	50070.
BO+O2=BO2+O	4.21E12	0.0	-507.
BO+OH=BO2+H	2.40E12	0.0	-1990.
BO+O+M=BO2+M	1.10E15	0.0	0.
BO+H2O=BO2+H2	6.03E10	0.0	9940.
BO+CO2=BO2+CO	4.21E12	0.0	-507.
BO+H2O=HBO2+H	4.20E12	0.0	9940.
BO+OH+M=HBO2+M	3.63E14	0.0	-1990.
BO+H+M=HBO+M	1.10E15	0.0	-1990.
BO+H2=HBO+H	4.52E01	3.53	3160.
BO+H2=BOH+H	4.52E01	3.53	3160.
BO+OH=HBO+O	1.64E03	2.76	5015.
2BO+M=B2O2+M	3.63E13	0.0	-1990.
BO+BO2+M=B2O3+M	7.24E13	0.0	-1990.
BOH+H2O=HBO2+BO	4.20E12	0.0	-507.
BOH+CO2=HBO2+CO	4.20E12	0.0	-507.
BOH+O2=HBO2+O	4.20E12	0.0	-507.
BOH+OH=HBO2+H	2.40E12	0.0	0.
BOH+H2O=HBO2+H2	2.40E12	0.0	0.
BOH+O+M=HBO2+M	6.00E10	0.0	9940.
BOH+O=BO2+H	1.10E15	0.0	-1990.
BOH+D=BO2+H	4.80E13	0.0	0.
BOH+HBO2=B2O3+H2	4.80E11	0.0	0.

REACTION	A	n	Ea
BOH+OH=BO+H2O	4.80E13	0.0	0.
BOH+O=BO+OH	4.80E13	0.0	0.
BO2+H2=HBO2+H	1.82E12	0.0	2980.
BO2+OH=HBO2+O	1.82E12	0.0	990.
BO2+BH=HBO2+B	1.82E12	0.0	990.
BO2+BH2=HBO2+BH	1.82E12	0.0	990.
BO2+HBO=HBO2+BO	1.82E12	0.0	990.
BO2+HCO=HBO2+CO	1.82E15	0.0	-1990.
BO2+H+M=HBO2+M	6.03E10	0.0	9940.
2BO2=B2O3+O	1.20E12	0.0	990.
BO2+HBO=B2O3+H	4.80E12	0.0	990.
HBO2+OH=BO2+H2O	4.80E11	0.0	0.
HBO2+BO=B2O3+H	3.63E13	0.0	0.
HBO2+HBO=B2O3+H2	3.63E13	0.0	0.
B2O2+H=BOH+BO	6.03E8	0.0	0.
B2O2+O=BO+BO2	6.03E8	0.0	0.
B2O2+OH=BO+HBO2	6.03E8	0.0	0.
B2O2+OH=BO2+HBO	1.21E14	0.0	69940.
B2O2+O2=2BO2	3.01E13	0.0	80080.
B2O2+OH=B2O3+H	6.03E11	0.0	0.
B2O2+CO2=B2O3+CO	6.03E11	0.0	0.
B2O2+O2=B2O3+O	6.03E8	0.0	11920.
B2O3+OH=HBO2+BO2	6.03E8	0.0	11920.
B2O3+H2O=2HBO2	1.21E14	0.0	0.
HCO+H=CO+H2	3.00E13	0.0	0.
HCO+OH=CO+H2O	3.01E13	0.0	0.
HCO+O=CO+OH	5.12E13	0.0	1690.
HCO+O2=HO2+CO	1.51E14	0.0	23650.
HO2+O=CO2+OH	4.39E6	1.5	-740.
CO+OH=CO2+H	1.69E13	1.5	52660.
CO2+O=CO+O2	5.0664	-0.91	16520.
H+O2=OH+O	4.58E9	2.67	6290.
O+H2=OH+H	6.19E7	1.9	17100.
H+H2O=OH+H2	1.75E12	1.9	18410.
H2O2+OH=H2O+HO2	1.69E14	0.0	-400.
O+H2O=2+OH	1.75E13	0.0	320.
H+HO2=2OH	6.62E14	0.0	874.
H+HO2=H2+O2	1.45E16	-1.0	2130.
OH+HO2=H2O+O2	5.42E16	-1.0	0.
H2O2+O2=2HO2	3.01E13	0.0	39740.
HO2+H2=H2O2+H	1.81E18	-1.00	26030.
O2+M=O+O+M	2.20E14	0.0	118100.
H2+M=H+H+M	2.41E15	0.0	96000.
OH+M=O+H+M	1.29E33	-4.86	99360.
H2O+M=2O+H+M	3.49E15	0.0	53250.
H2O+M=OH+H+M	1.21E19	-1.18	105120.
HO2+M=H+O2+M	2.51E13	0.0	48410.
CO2+M=CO+O+M	5.11E21	-2.14	87000.
HCO+M=H+CO+M	2.41E13	0.0	20420.
H+HBO2=H2O+OH			3970.

1593

Figure 1.   Species profiles as a function of time for an adiabatic, constant pressure (1atm) system. The initial species mole fractions, derived from the equilibrium gas phase calculations of reference 2, are as follows: $X(HBO)=9 \times 10^{-3}$, $X(B_2O_2)=2.8 \times 10^{-3}$, $X(B_2O_3)=5 \times 10^{-4}$, $X(HBO_2)=3 \times 10^{-4}$, $X(O_2)=4.4 \times 10^{-2}$, $X(CO)=0.18$, $X(H_2)=0.20$, $X(H)=1 \times 10^{-4}$, $X(H_2O)=1 \times 10^{-5}$, and $X(N_2)=0.56$, with an initial temperature of 1800K. a) The mechanism includes the more recent thermodynamic value for the heat of formation of HBO and the measured rates of reaction for $BO+H_2$ and $BO+O_2$, as described in the text. b) Additional HBO removal processes are added to the mechanism.

OXIDATION OF NITROGEN OXIDE IN HOMOGENEOUS GAS PHASE REACTIONS: COMBUSTION EMISSIONS CONTROL MODELING

K. P. Kundu
National Aeronautics and Space Administration
Lewis Research Center
Cleveland, Ohio

J. M. Deur
Sverdrup Technology, Inc.
Lewis Research Center Group
Brook Park, Ohio

Abstract

An analytical study on the oxidation of NO in homogeneous gas phase reactions is presented. Although NO is readily oxidized to NO_2 at room temperatures, the conversion rate falls with increasing temperature. However, aliphatic alcohols and hydrocarbons generate HO_2 which appears to oxidize NO at higher temperatures. In a medium containing oxygen and aliphatic alcohols or hydrocarbons, NO oxidizes to NO_2 even at 1000 K; but NO_2 returns to NO after these compounds are consumed. Various aliphatic compounds (ethane, butane, methanol, and ethanol) will be considered in this discussion. These chemicals may be useful in the treatment of emissions from stationary combustion systems for removal of NO_x.

Introduction

Nitrogen oxides (NO_x) pose serious environmental concerns due to their role in smog and acid rain formation.[1] These oxides are natural products of combustion, where high temperatures lead to their formation through reactions between dissociated nitrogen and oxygen (thermal NO_x) or through oxidation of nitrogenous compounds created during the combustion process (prompt NO_x).[2,3]

The extent of NO_x formation depends on the initial fuel/air mixture ratio, with greater amounts of NO_x generated with fuel-lean and stoichiometric mixtures. Thus, to control NO_x formation during combustion, one might be tempted to burn a fuel-rich mixture. However, this leads to excessive production of unburned hydrocarbons and carbon monoxide, which also pose severe environmental problems. All of these pollutants can be controlled through careful combustor design (4), but the resultant configuration may have other undesirable characteristics.

Post-combustion treatment of the exhaust to remove NO_x provides an alternative means of reducing the pollution problem. One method introduces various nitrogenous compounds (5-9) into the exhaust stream to react with the NO_x, reducing its concentration. However, this technique is limited to a narrow range of temperatures.[10]

Another post-combustion process removes the NO_x by scrubbing with water. Unfortunately, the poor solubility of most nitrogen oxides precludes direct application of this technique. NO_x is typically comprised of three species: NO, NO_2, and N_2O; and, although nitrogen dioxide (NO_2) is fairly soluble in water, nitrogen oxide (NO) predominates due to the high temperatures associated with combustion. To make the scrubbing technique feasible, the NO needs to be converted to NO_2.[1]

Lyon, et al, improved NO to NO_2 gas phase oxidation through treatment with methanol.[11] The present study expands on this theme by examining NO oxidation in the presence of methanol, ethanol, ethane, and butane.

Physical/Computational Models and Kinetics Mechanisms

Nitrogen oxides are indirect products of combustion, with the extent of formation dependent on temperature and residence time in the combustor. Although combustion is typically complete within a millisecond, NO_x in a fuel-lean mixture grows steadily with time as long as the temperature remains high. However, although equilibrium levels of nitrogen oxides are very high (Fig. 1), NO_x concentrations rarely reach these levels in conventional combustion processes. Thus, while the exhaust stream composition may approach equilibrium in general, the NO_x concentration will not.

The ability of hydrocarbons and alcohols to oxidize NO_x in an exhaust stream that, apart from the NO_x, is at equilibrium will be examined using the LSENS program of Bittker and Radhakrishnan.(12) In particular, the code's plug flow reaction model is used to compute concentrations at various times during the combustion process.

The starting point for these calculations will be the fuel-lean mixture described in Table I. As shown in the table, all of the NO_x is in the form of NO. This follows from the argument that, in the absence of hydrocarbon fragments, any NO_2 present would be converted to NO at the high temperatures being considered.

The kinetics mechanism for the calculations (shown in Appendix A) is essentially identical to that of Miller and Bowman (13), with a few species deleted to fit the constraints of the LSENS program. Additional reactions involving methanol, ethanol, and butane are taken from Westbrook and Dryer.(14) Finally, thermodynamic data has been obtained from B. J. McBride (Lewis Research Center) and the Sandia National Laboratory.(15)

Oxidation of NO in the Presence of Methanol

The fractional conversion of NO to NO_2 at various temperatures is shown in Fig. 2. As seen in the observations of Lyon, et al, the oxidation of NO occurs more quickly at higher temperatures.(11)

Hori (16) observed the formation of NO_2 in fuel-rich combustion and suggested that NO was oxidized by HO_2, while a similar result was reported by Sano (17) in a calculation of a hot gas mixing with cold air. The HO_2 is predominately formed from methyl alcohol and the CH_2OH radical, both products of methanol decomposition.(11) To test these findings, the reaction:

$$HO_2 + NO \rightarrow NO_2 + OH$$

was deleted from the model, and the NO_2 concentration was recalculated. The initial mixture composition was retained, and the initial temperature was set at 1100 K. This temperature was chosen because it had been found previously to result in the rapid formation of NO_2. With the above reaction removed, however, the formation of NO_2 was now negligible; but, when the forward reaction was restored but not the reverse reaction, significant NO_2 formation again took place. Hence, NO oxidation is dependent on: 1) the formation of HO_2, and 2) the reaction between HO_2 and NO.

Once all of the alcohol is consumed, NO_2 reverts to NO. This follows from the reactions involved in the chemical reduction of NO_2:

$$NO_2 + M \rightarrow NO + O$$

$$NO_2 + H \rightarrow NO + OH$$

$$NO_2 + O \rightarrow NO + O_2$$

$$NO_2 + OH \rightarrow HO_2 + NO$$
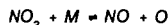
By varying the rates for the above reactions, it was found that all but the first reaction can reduce the NO_2 concentration. When methanol is consumed, these reactions act to lower the NO_2 concentration. The activity of the reactions also explains why NO_2 concentration is lower at higher temperatures.

To determine if the concentration of methanol has any effect on NO oxidation, the oxidation process was examined at different concentrations of CH_2OH using 1100 K as the reaction temperature. It appears that, in the presence of large amounts of methanol, the speed of the oxidation process increases. Heat is released in such cases, and it has already been noted that NO oxidation occurs more quickly at higher temperatures. However, if the amount of excess methanol is small, the rate of oxidation is not affected. Understandably, since their work did not consider mixtures with large amounts of methanol, Lyon, et al, reported only this latter finding.(11)

The effect of oxygen on NO oxidation in the presence of methanol was also studied. It was determined that increases in O_2 concentration do not affect the rate.

Oxidation of NO in the Presence of Ethanol

Since ethanol and methanol are very similar chemically, it can be expected that ethanol will behave similarly in

the oxidation of NO. Unfortunately, there is no experimental data available; therefore, the choice of the kinetic model is very important to insure the accuracy of the analysis. The mechanism of Westbrook and Dryer was chosen, as it was found to have rate parameters that were very similar to those of the methanol mechanism.

The calculations made with this mechanism showed that ethanol oxidizes NO to NO_2 in a manner identical to methanol. The variations in NO_2 concentration with time and temperature are shown in Fig. 3. As expected, NO_2 formation initially rises with increasing temperature and then falls as the ethanol is consumed.

Oxidation of NO in the Presence of Ethane and Butane

Little experimental data is available on the oxidation of NO in the presence of hydrocarbons. Hori (16) found that, as with methanol and ethanol, hydrocarbon reactions also generate HO_2, while Malte and Kramlich (18) also saw evidence of NO_2 formation. In a similar situation, Jasma and Boreman (19) showed that small amounts of H_2 and CO led to NO to NO_2 conversion, while the first author (20) has demonstrated the use of methane and hydrogen to also promote NO oxidation. Thus, the presence of ethane and butane might boost NO oxidation.

Figs. 4 and 5 show the calculated NO_2 concentration at varying temperatures in the presence of ethane and butane, respectively. As with methanol, the major species involved in the oxidation of NO is HO_2. This was proved using a method similar to that followed in the case of methanol. In fact, it was found that ethane and methanol behave almost identically in the oxidation of NO. When a large amount of ethane is present, there is some reduction of the total NO_x, and the reduction increases at higher temperatures. This reduction is due to reactions involving hydrocarbon fragments.

The effect of adding large amounts of oxygen was also studied. As the oxygen concentration varied from 4% to 12%, NO_2 formation changed by only 10%.

Conclusions

Computer modeling has been used to study the formation of NO in the presence of methanol, ethanol, butane, and ethane. It appears that NO_2 is formed through oxidation of NO by HO_2 which is generated by these additives. The oxidation process is temperature dependent, with higher conversion rates at higher temperatures. However, at all temperatures, the NO_2 begins to revert to NO_x once the additives are consumed; but, as long as the additives are present, the oxidation rate is only slightly dependent on the actual additive concentration. Although the presence of oxygen is necessary for the formation of NO_2, excess oxygen does not affect the NO_2 conversion.

References

1. Rosenberg, H. S., Curan, L. M., Slack, A. V., and Oxley, J. H., *Prog. in Energ. and Comb. Sci.*, vol. 6, 1988, p. 287.

2. Zeldovich, Y. B., *Acta Physiochim*, vol. 21, 1946, p. 577.

3. Fennimore, C. P., *Comb. and Flame*, vol. 2, 1976, p. 1.

4. Sarofin, A. F., and Flagan, R. C., *Prog. in Energ. and Comb. Sci.*, vol. 2, 1976, p. 1.

5. Lyon, R. K., *U.S. Patent No. 3900554*, 1975.

6. Turchan, O. C., *U.S. Patent No. 4208386*, 1980.

7. Perry, R. A., *U.S. Patent No. 4731231*, 1988.

8. Arand, J. K., Muzio, L. J., and Scotter, J. G., *U.S. Patent No. 4208386*, 1980.

9. Wada, Y., and Yamatsuta, K., *Japanese Early Disclosure Patent No. 54028771*, 1980.

10. Lyon, R. K., and Benn, D., *17th Sym. (Intl.) on Comb.*, The Combustion Institute, Pittsburgh, 1979, p.601.

11. Lyon, R. K., Cole, J. A., Kramlich, J. C., and Chen, S. L., *Comb. and Flame*, Vol. 81, 1990, p. 30.

12. Radhakrishnan, K., and Bittker, D. A., *Eastern Section, Comb. Inst. Fall Meetings*, December 15-17, 1986.

13. Miller, J. A., and Bowman, C. T., *Prog. in Energy and Comb. Sci.*, Vol. 15, 1989, p. 287.

14. Westbrook, C. K., and Dryer, F. L., *Prog. in Energy and Comb. Sci.*, Vol. 10, 1984, p. 1.

15. Kee, R. J., Rupley, F. M., and Miller, J. A., *SAND87-8215*, 1987.

16. Hori, M., *22nd Sym. (Intl.) on Comb.*, The Combustion Institute, Pittsburgh, 1988, p. 1175.

17. Sano, T., *Comb. Sci. and Tech.*, Vol. 38, 1984, p. 129.

18. Kramlich, J. C., Malte, P. C., *Comb. Sci. and Tech.*, Vol. 18, 1978, p. 91.

19. Jasma, D., and Borman, G., *Comb. Sci. and Tech.*, Vol. 23, 1980, p. 83.

20. Kundu, K. P., Nguyen, H. L, and Kang, M. P., *AIAA 29th Aerospace Sciences Meeting*, Reno, Nevada, 1991.

Table I. Initial Mixture Composition.

Species	Mole Fraction	Species	Mole Fraction
O_2	0.0400	NO	0.0002
CH_3OH	0.0004	CO_2	0.0100
H_2O	0.1000	Ar	0.0080
N_2	0.8414		
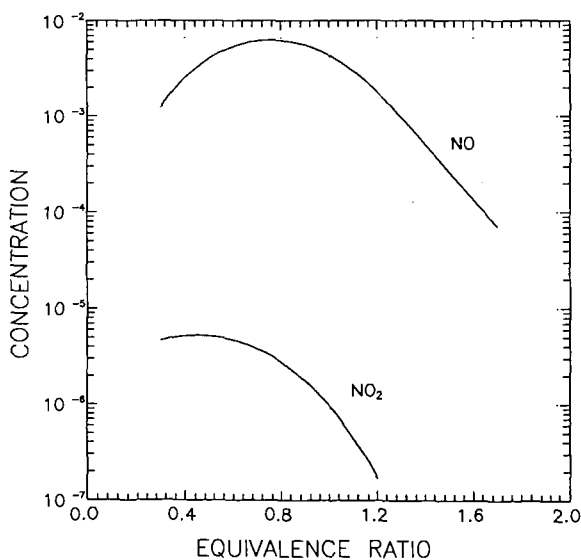
Figure 1. Equilibrium NO and NO_2 Concentrations (T = 800 K, p = 1 atm).
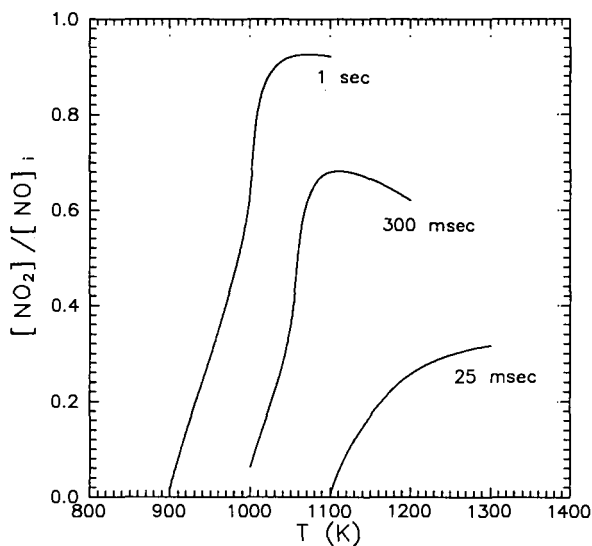
Figure 2. NO Conversion in the Presence of Methanol.
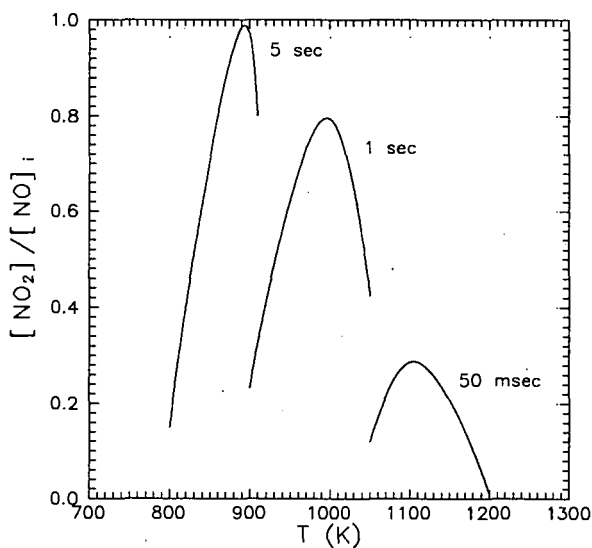
Figure 3. NO Conversion in the Presence of Ethanol.

1599
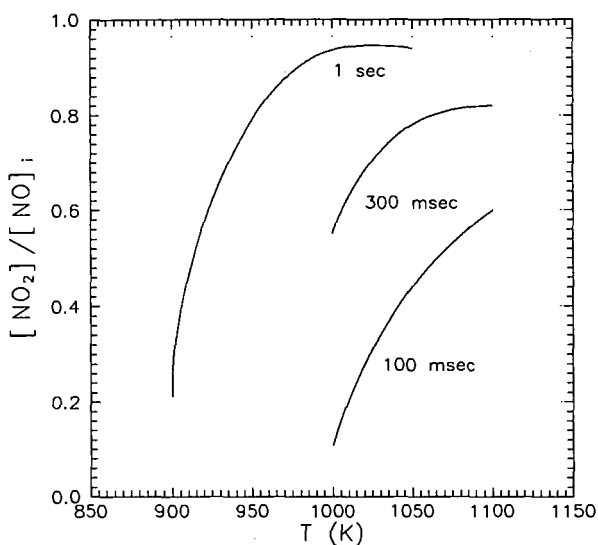
Figure 4. NO Conversion In the Presence of Ethane.
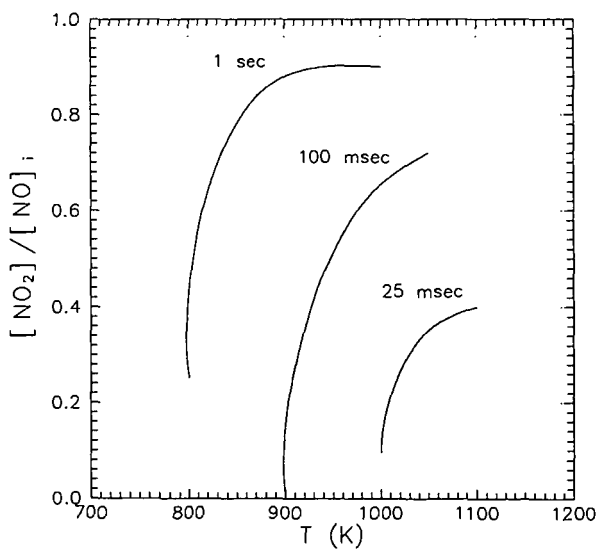
Figure 5. NO Conversion in the Presence of Butane.

Appendix A. Kinetics Mechanism.(13)

$$k = A \, T^B \, e^{-C/RT}$$

REACTION	A	B	C	REACTION	A	B	C
$M + 2CH_3 \rightarrow C_2H_6 + M$	9.03×10^{16}	-1.2	654.0	$CH + CH_2 \rightarrow C_2H_2 + H$	4.00×10^{13}	0.0	0.0
CO 2.0, H_2 2.0, CO_2 3.0, H_2O 5.0				$CH + CH_3 \rightarrow C_2H_3 + H$	3.00×10^{13}	0.0	0.0
$CH_3 + H \rightarrow CH_4 + M$	6.00×10^{16}	-1.0	0.0	$CH + CH_4 \rightarrow C_2H_4 + H$	6.00×10^{13}	0.0	0.0
CO 2.0, H_2 2.0, CO_2 3.0, H_2O 5.0				$C + O_2 \rightarrow CO + O$	2.00×10^{13}	0.0	0.0
$CH_4 + O_2 \rightarrow CH_3 \bullet HO_2$	7.90×10^{13}	0.0	56000.0	$C + OH \rightarrow CO + H$	5.00×10^{13}	0.0	0.0
$CH_4 + H \rightarrow CH_3 + H_2$	2.20×10^{04}	3.0	8750.0	$C + CH_3 \rightarrow C_2H_2 + H$	5.00×10^{13}	0.0	0.0
$CH_4 + OH \rightarrow CH_3 + H_2O$	1.60×10^{06}	2.1	2460.0	$C + CH_2 \rightarrow C_2H + H$	5.00×10^{13}	0.0	0.0
$CH_4 + O \rightarrow CH_3 + OH$	1.02×10^{09}	1.5	8604.0	$CH_2 \bullet CO_2 \rightarrow CH_2O + CO$	1.10×10^{11}	0.0	1000.0
$CH_4 + HO_2 \rightarrow CH_3 + H_2O_2$	1.80×10^{11}	0.0	18700.0	$CH_2 + O \rightarrow 2H + CO$	5.00×10^{13}	0.0	0.0
$CH_3 + HO_2 \rightarrow CH_3O + OH$	2.00×10^{13}	0.0	0.0	$CH_2 + O \rightarrow CO + H_2$	3.00×10^{13}	0.0	0.0
$CH_3 + O_2 \rightarrow CH_3O + O$	2.05×10^{19}	-1.6	29229.0	$CH_2 + O_2 \rightarrow 2H + CO_2$	1.60×10^{12}	0.0	1000.0
$CH_3 + O \rightarrow CH_2O + H$	8.00×10^{13}	0.0	0.0	$CH_2 + O_2 \rightarrow CH_2O + O$	5.00×10^{13}	0.0	9000.0
$CH_2OH + H \rightarrow CH_3 + OH$	1.00×10^{14}	0.0	0.0	$CH_2 + O_2 \rightarrow CO \bullet H_2O$	1.90×10^{10}	0.0	-1000.0
$M \bullet CH_2OH \rightarrow CH_2O + H$	1.00×10^{14}	0.0	25000.0	$CH_2 + O_2 \rightarrow CO_2 + H_2$	6.90×10^{11}	0.0	500.0
$CH_2OH + H \rightarrow CH_2O + H_2$	2.00×10^{13}	0.0	0.0	$CH_2 + O_2 \rightarrow HCO + OH$	4.30×10^{10}	0.0	-500.0
$CH_2OH + OH \rightarrow CH_2O + H_2O$	1.00×10^{13}	0.0	0.0	$CH_2O + OH \rightarrow HCO + H_2O$	3.43×10^{09}	1.18	-447.0
$CH_2OH + O \rightarrow CH_2O + OH$	1.00×10^{13}	0.0	0.0	$CH_2O \bullet H \rightarrow HCO + H_2$	2.19×10^{08}	1.77	3000.0
$CH_2OH + O_2 \rightarrow CH_2O + HO_2$	1.48×10^{13}	0.0	1500.0	$M + CH_2O \rightarrow HCO + H$	3.31×10^{16}	0.0	81000.0
$M + CH_3OH \rightarrow CH_3 + OH$	3.02×10^{18}	0.0	80000.0	$CH_2O + O \rightarrow HCO + OH$	1.80×10^{13}	0.0	3080.0
$H + CH_3OH \rightarrow CH_3 + H_2O$	2.00×10^{12}	0.0	5300.0	$HCO + OH \rightarrow H_2O + CO$	1.00×10^{14}	0.0	0.0
$H \bullet CH_3OH \rightarrow CH_2OH + H_2$	3.02×10^{13}	0.0	7000.0	$M + HCO \rightarrow H + CO$	2.50×10^{14}	0.0	16802.0
$OH + CH_3OH \rightarrow CH_2OH + H_2O$	3.98×10^{12}	0.0	2000.0	CO 1.9, H_2 1.9, CH_4 2.8, CO_2 3.0, H_2O 5.0			
$CH_3O + H \rightarrow CH_3 + OH$	1.00×10^{14}	0.0	0.0	$HCO + H \rightarrow CO + H_2$	1.19×10^{13}	0.25	0.0
$CH_3O + O_2 \rightarrow CH_2OH + HO_2$	3.98×10^{10}	0.0	50910.0	$HCO + O \rightarrow CO + OH$	3.00×10^{13}	0.0	0.0
$CH_3O + O \rightarrow CH_2OH + OH$	1.70×10^{12}	0.0	2290.0	$HCO + O \rightarrow CO_2 + H$	3.00×10^{13}	0.0	0.0
$CH_3OH + CH_3 \rightarrow CH_2OH + CH_4$	1.82×10^{11}	0.0	9800.0	$HCO + O_2 \rightarrow HO_2 + CO$	3.00×10^{13}	0.0	0.0
$CH_3OH + HO_2 \rightarrow CH_2OH + H_2O_2$	6.31×10^{12}	0.0	19360.0	$CO \bullet O \rightarrow CO_2 + M$	6.17×10^{14}	0.0	3000.0
$CH_3 + OH \rightarrow CH_2 + H_2O$	7.50×10^{06}	2.0	5000.0	$CO \bullet OH \rightarrow CO_2 + H$	1.51×10^{07}	1.3	-758.0
$CH_3 + H \rightarrow CH_2 + H_2$	9.00×10^{13}	0.0	15100.0	$CO + O_2 \rightarrow CO_2 + O$	1.60×10^{13}	0.0	41000.0
$M + CH_3O \rightarrow CH_2O + H$	1.00×10^{14}	0.0	25000.0	$HO_2 + CO \rightarrow CO_2 + OH$	5.80×10^{13}	0.0	22934.0
$CH_3O + H \rightarrow CH_2O + H_2$	2.00×10^{13}	0.0	0.0	$C_2H_6 + CH_3 \rightarrow C_2H_5 \bullet CH_4$	5.50×10^{-01}	4.0	8300.0
$CH_3O + OH \rightarrow CH_2O + H_2O$	1.00×10^{13}	0.0	0.0	$C_2H_6 + O_2 \rightarrow C_2H_5 + HO_2$	1.00×10^{13}	0.0	51000.0
$CH_3O + O \rightarrow CH_2O + OH$	1.00×10^{13}	0.0	0.0	$C_2H_6 + H \rightarrow C_2H_5 + H_2$	5.40×10^{02}	3.5	5210.0
$CH_3O + O_2 \rightarrow CH_2O + HO_2$	6.30×10^{10}	0.0	2600.0	$C_2H_6 + O \rightarrow C_2H_5 + OH$	2.51×10^{13}	0.0	6360.0
$CH_2 + H \rightarrow CH + H_2$	1.00×10^{18}	-1.56	0.0	$C_2H_6 + OH \rightarrow C_2H_5 + H_2O$	8.70×10^{09}	1.05	1810.0
$CH_2 + OH \rightarrow CH + H_2O$	1.13×10^{07}	2.0	3000.0	$C_2H_4 + H \rightarrow C_2H_3 + H_2$	1.10×10^{14}	0.0	8500.0
$CH_2 + OH \rightarrow CH_2O + H$	2.50×10^{13}	0.0	0.0	$C_2H_4 + O \rightarrow CH_3 + HCO$	3.32×10^{12}	0.0	1130.0
$CH + O_2 \rightarrow HCO + O$	3.30×10^{13}	0.0	0.0	$C_2H_4 + OH \rightarrow C_2H_3 + H_2O$	2.02×10^{13}	0.0	5955.0
$CH + O \rightarrow CO + H$	5.70×10^{13}	0.0	0.0	$CH_2 + CH_3 \rightarrow C_2H_4 + H$	3.00×10^{13}	0.0	0.0
$CH + OH \rightarrow HCO + H$	3.00×10^{13}	0.0	0.0	$M + C_2H_5 \rightarrow C_2H_4 + H$	2.00×10^{15}	0.0	30000.0
$CH \bullet CO_2 \rightarrow HCO + CO$	3.40×10^{12}	0.0	690.0	$C_2H_5 + M \rightarrow 2CH_3$	1.00×10^{14}	0.0	0.0
$CH + H \rightarrow C + H_2$	1.50×10^{14}	0.0	0.0	$C_2H_5 + O_2 \rightarrow C_2H_4 + HO_2$	8.43×10^{11}	0.0	3875.0
$CH + H_2O \rightarrow CH_2O + H$	1.17×10^{15}	-0.75	0.0	$C_2H_2 + O \rightarrow CH_2 + CO$	1.02×10^{07}	2.0	1900.0
$CH + CH_2O \rightarrow CH_2CO + H$	9.46×10^{13}	0.0	-515.0	$C_2H_2 + O \rightarrow HCCO + H$	1.02×10^{07}	2.0	1900.0

REACTION | A | B | C

REACTION	A	B	C
$C_2H_2 + O_2 \rightarrow 2HCO$	3.98×10^{12}	0.0	28000.0
$H_2 + C_2H \rightarrow C_2H_2 + H$	1.02×10^{07}	2.0	1900.0
$H + C_2H_2 \rightarrow C_2H_3 + M$	5.54×10^{12}	0.0	2410.0
H_2 2.0, CO 2.0, CO_2 3.0, H_2O 5.0			
$C_2H_3 + H \rightarrow C_2H_2 + H_2$	4.00×10^{13}	0.0	0.0
$C_2H_3 + O \rightarrow CH_2CO + H$	3.00×10^{13}	0.0	0.0
$C_2H_3 + O_2 \rightarrow C_2H_2 + HO_2$	1.00×10^{12}	0.0	10000.0
$C_2H_3 + O_2 \rightarrow CH_2O + HCO$	4.00×10^{12}	0.0	-250.0
$C_2H_3 + OH \rightarrow C_2H_2 + H_2O$	5.00×10^{12}	0.0	0.0
$C_2H_3 + CH_2 \rightarrow C_2H_2 + CH_3$	3.00×10^{13}	0.0	0.0
$C_2H_3 + C_2H \rightarrow 2C_2H_2$	3.00×10^{13}	0.0	0.0
$C_2H_3 + CH \rightarrow CH_2 + C_2H_2$	5.00×10^{13}	0.0	0.0
$OH + C_2H_2 \rightarrow C_2H + H_2O$	3.37×10^{07}	2.0	14000.0
$OH + C_2H_2 \rightarrow CH_2CO + H$	2.18×10^{-04}	4.5	-1000.0
$OH + C_2H_2 \rightarrow CH_3 + CO$	4.83×10^{-04}	4.0	-2000.0
$C_2H_2 + O \rightarrow C_2H + OH$	3.16×10^{15}	-0.6	15000.0
$CH_2CO + O \rightarrow CO_2 + CH_2$	1.75×10^{12}	0.0	1350.0
$CH_2CO + H \rightarrow CH_3 + CO$	1.13×10^{13}	0.0	3428.0
$CH_2CO + H \rightarrow HCCO + H_2$	5.00×10^{13}	0.0	8000.0
$CH_2CO + O \rightarrow HCCO + OH$	1.00×10^{13}	0.0	8000.0
$CH_2CO + OH \rightarrow HCCO + H_2O$	7.50×10^{12}	0.0	2000.0
$M + CH_2CO \rightarrow CH_2 + CO$	3.00×10^{14}	0.0	70980.0
$C_2H + O_2 \rightarrow 2CO + H$	5.00×10^{13}	0.0	1500.0
$H + HCCO \rightarrow CH_2 + CO$	1.00×10^{14}	0.0	0.0
$O + HCCO \rightarrow 2CO + H$	1.00×10^{14}	0.0	0.0
$HCCO + O_2 \rightarrow 2.0CO + OH$	1.60×10^{12}	0.0	854.0
$CH + HCCO \rightarrow C_2H_2 + CO$	5.00×10^{13}	0.0	0.0
$2HCCO \rightarrow 2CO + C_2H_2$	1.00×10^{13}	0.0	0.0
$C_2H + O \rightarrow CH + CO$	5.00×10^{13}	0.0	0.0
$C_2H + OH \rightarrow HCCO + H$	2.00×10^{13}	0.0	0.0
$2CH_2 \rightarrow C_2H_2 + H_2$	4.00×10^{13}	0.0	0.0
$CH_2 + HCCO \rightarrow C_2H_3 + CO$	3.00×10^{13}	0.0	0.0
$C_3H_3 + O_2 \rightarrow CH_2CO + HCO$	3.00×10^{10}	0.0	2868.0
$C_3H_3 + O \rightarrow CH_2O + C_2H$	2.00×10^{13}	0.0	0.0
$C_2H_2 + O_2 \rightarrow HCCO + OH$	2.00×10^{08}	1.5	30100.0
$M + C_2H_2 \rightarrow C_2H + H$	4.20×10^{16}	0.0	107000.0
$M + C_2H_4 \rightarrow C_2H_2 + H_2$	1.50×10^{15}	0.0	55800.0
$M + C_2H_4 \rightarrow C_2H_3 + H$	1.40×10^{16}	0.0	82360.0
$H_2 + O_2 \rightarrow 2OH$	1.70×10^{13}	0.0	47780.0
$OH + H_2 \rightarrow H_2O + H$	1.17×10^{09}	1.3	3626.0
$O + OH \rightarrow O_2 + H$	4.00×10^{14}	-0.5	0.0
$O + H_2 \rightarrow OH + H$	5.06×10^{04}	2.7	6290.0
$H + O_2 \rightarrow HO_2 + M$	3.61×10^{17}	-0.7	0.0
H_2O 18.6, H_2 2.9, N_2 1.3			

REACTION	A	B	C
$OH + HO_2 \rightarrow H_2O + O_2$	7.50×10^{12}	0.0	0.0
$H + HO_2 \rightarrow 2OH$	1.40×10^{14}	0.0	1073.0
$O + HO_2 \rightarrow O_2 + OH$	1.40×10^{13}	0.0	1073.0
$2OH \rightarrow O + H_2O$	6.00×10^{08}	1.3	0.0
$M + 2H \rightarrow H_2 + M$	1.00×10^{18}	-1.0	0.0
$H_2 + 2H \rightarrow 2H_2$	9.20×10^{16}	-0.6	0.0
$H_2O + 2H \rightarrow H_2 + H_2O$	6.00×10^{19}	-1.2	0.0
$H + OH \rightarrow H_2O + M$	1.60×10^{22}	-2.0	0.0
H_2O 5.0			
$H + O \rightarrow OH + M$	6.20×10^{16}	-0.6	0.0
H_2O 5.0			
$M + 2O \rightarrow O_2 + M$	1.89×10^{13}	0.0	-1788.0
$H + HO_2 \rightarrow H_2 + O_2$	1.25×10^{13}	0.0	0.0
$2HO_2 \rightarrow H_2O_2 + O_2$	2.00×10^{12}	0.0	0.0
$M + H_2O_2 \rightarrow 2OH + M$	1.30×10^{17}	0.0	45500.0
$H_2O_2 + H \rightarrow HO_2 + H_2$	1.60×10^{12}	0.0	3800.0
$H_2O_2 + OH \rightarrow H_2O + HO_2$	1.00×10^{13}	0.0	1800.0
$NO_2 + O \rightarrow NO + O_2$	1.00×10^{13}	0.0	600.0
$M + NO_2 \rightarrow NO + O$	1.10×10^{16}	0.0	66000.0
$NH + O_2 \rightarrow HNO + O$	1.00×10^{13}	0.0	12000.0
$NH + O_2 \rightarrow NO + OH$	7.60×10^{10}	0.0	1530.0
$NH + NO \rightarrow N_2O + H$	2.40×10^{15}	-0.8	0.0
$N_2O + H \rightarrow N_2 + OH$	7.60×10^{13}	0.0	15200.0
$M + N_2O \rightarrow N_2 + O$	1.62×10^{14}	0.0	51600.0
$N_2O + O \rightarrow N_2 + O_2$	1.00×10^{14}	0.0	28200.0
$N_2O + O \rightarrow 2NO$	1.00×10^{14}	0.0	28200.0
$N_2O + OH \rightarrow N_2 + HO_2$	2.00×10^{12}	0.0	10000.0
$NH + OH \rightarrow H_2O + N$	2.00×10^{13}	0.0	0.0
$NH + OH \rightarrow N + H_2O$	5.00×10^{11}	0.5	2000.0
$NH + N \rightarrow N_2 + H$	3.00×10^{13}	0.0	0.0
$NH + H \rightarrow N + H_2$	1.00×10^{14}	0.0	0.0
$NH + O \rightarrow NO + H$	2.00×10^{13}	0.0	0.0
$M + HNO \rightarrow H + NO$	1.50×10^{16}	0.0	48680.0
H_2O 10.0, O_2 2.0, N_2 2.0, H_2 2.0			
$HNO + OH \rightarrow NO + H_2O$	3.60×10^{13}	0.0	0.0
$HNO + H \rightarrow H_2 + NO$	5.00×10^{12}	0.0	0.0
$2HNO \rightarrow N_2O + H_2O$	3.95×10^{12}	0.0	5000.0
$HNO + NO \rightarrow N_2O + OH$	2.00×10^{12}	0.0	26000.0
$N + NO \rightarrow N_2 + O$	3.27×10^{12}	0.3	0.0
$N + O_2 \rightarrow NO + O$	6.40×10^{09}	1.0	6280.0
$N + OH \rightarrow NO + H$	3.80×10^{13}	0.0	0.0
$HO_2 + NO \rightarrow NO_2 + OH$	2.11×10^{11}	0.0	-479.0
$NO_2 + H \rightarrow NO + OH$	3.50×10^{14}	0.0	1500.0
$2NH \rightarrow 2H + N_2$	7.20×10^{13}	0.0	0.0

UNITS: A cm-mol/sec; B -; C cal/mol

LASER-INDUCED FLUORESCENCE MEASUREMENTS TO TEST CHEMICAL MECHANISMS OF PROMPT NO IN METHANE FLAMES

Dwayne E. Heard, Jay B. Jeffries, Gregory P. Smith and David R. Crosley
Molecular Physics Laboratory
SRI International
Menlo Park, CA 94025

ABSTRACT

Laser-induced fluorescence measurements have been made of the OH, CH and NO radicals in slightly rich methane/air flames burning at 30, 70 and 120 Torr; in the 30 Torr flame atomic hydrogen is also measured. Absolute NO and OH concentrations were determined using separate calibration experiments. Temperature profiles were deduced from OH rotational excitation scans, and fluorescence quenching rates for NO and CH were determined. Predicted profiles of the concentrations of these radical species as a function of height above the burner were obtained from a computer model of the flame, and comparison made with experiment. Good agreement is achieved for the relative concentration profiles, the absolute NO concentration, and concentration ratios between 30 and 70 Torr, although slight disagreement with the CH profile indicates there remain some unknown aspects of the flame chemistry.

INTRODUCTION

Although natural gas is a clean burning fuel, containing virtually no fuel-bound nitrogen or sulfur, its combustion in air forms NO_x pollutants. These emissions limit its use, and the degree of regulation is expected to become more stringent in the future. Thus reduction of NO_x emissions in practical natural gas systems is an important objective. A major part of attaining that goal is the development of a predictive computer model of the pertinent chemistry, validated by sensitive laboratory experiments.

At temperatures below 2000 K, the major method of NO production in hydrocarbon/air flames is by the prompt-NO route, especially for slightly fuel-rich conditions. This dominates in practical natural gas/air flames, which usually operate at temperatures below 2000 K. Even though average fuel/oxygen ratios may be on the lean side, there are always locally fuel-rich regions in a nonpremixed flame, which includes most practical burners.

The prompt NO mechanism, whose reactions occur near the flame zone, is largely that first postulated by Fenimore[1] in 1971. Much of this reaction mechanism has recently been extensively reviewed and discussed by Miller and Bowman.[2] The primary initiation reaction is that of the radical CH with the air nitrogen to produce HCN and nitrogen atoms. The HCN undergoes several oxidation steps to produce more N atoms; these atoms then react with OH and O_2 to form NO. Some of the NO can be back-converted to HCN through a series of reactions also involving CH radicals.

Much but not all of this chemistry is well understood. Because the desired level of prompt NO produced in natural/gas air flames is often tens of parts per millions, the reactive species responsible are also present at low concentrations. Accordingly, any sensitive test of the model predictions must involve measurements of these pertinent radical species with a high degree of spatial resolution. We have made laser-induced fluorescence measurements of atomic hydrogen and the free radicals CH, OH and NO in low pressure methane/air flames. The flame studied most extensively was burned at 30 Torr. A computer model of the flame chemistry was used to predict species profiles, and comparisons with experiment were made to identify key aspects of the prompt NO chemical mechanism.

EXPERIMENTAL DETAILS

The flames were supported on a 6 cm diameter porous plug McKenna burner, inside an evacuable chamber suitable for optical probing, described in more detail in Refs. 3 & 4. A shroud of Ar was employed to match the flame velocity at the burner surface and improve flame stability. The flame most extensively studied was slightly rich, with an equivalence ratio of 1.13, and at a pressure of 30 Torr. The high pressure flames were operated at the same equivalence ratio and same total flow rates, so they are positioned much closer to the burner surface. The flow rate was kept constant at all times for all flames studied in this work. All measurements were made using laser-induced fluorescence (LIF); the optical configuration remained the same whilst the burner was translated vertically with a minimum step size of 6 μm. Profiles as a function of height above the surface were typically measured with 125 μm between points and a spatial resolution between 0.2 mm and 1.0 mm.

Following laser excitation the fluorescence was collected at right angles and imaged onto a monochromator with attached photomultiplier (PMT), except in the case of H atoms, for which an interference filter centered at 656 nm was employed. The PMT signal was captured by a boxcar (SRS 250) and stored on computer through a CAMAC crate. Fluorescence lifetimes were measured using a Transiac 2001S 100 MHz digitizer. The laser energy was recorded in order to normalize the LIF signal on a shot-to-shot basis.

Collisions with the ambient flame gases quench the electronically excited states of the radicals, decreasing the fluorescence decay time from that given by the purely radiative rate. In the case of OH, the influence of quenching on the fluorescence quantum yield is avoided by the use of a short (20 ns duration) gate triggered promptly after the exciting laser pulse.[5] For NO and CH, the lower signal levels require integration over a large fraction of the decay pulse, and quenching must be accounted for to determine relative concentration profiles. In the case of NO, the decay time in the flame is also needed to calibrate the absolute concentration by comparison with LIF from a known room temperature concentration.

Decay measurements were made in the 30 and 70 Torr flames for both NO and CH, using the transient digitizer, with 10 ns resolution. The details are reported elsewhere,[6] where the experimental results for the 30 Torr flame are compared to those expected from current knowledge of species—specific cross sections for quenching of $A^2\Sigma^+$ NO and $A^2\Delta$ CH, together with a calculated composition of the flame. The agreement is good, within 20 to 30%. For both CH and NO, total quenching rate and thus fluorescence quantum yield were found[6] to be independent of flame position within experimental errors of 10%.

TEMPERATURE MEASUREMENTS

Accurate temperature determinations are crucial to any meaningful comparison between measured and calculated species profiles. This is because of the highly nonlinear dependence of reaction rates on temperature; it is especially true in the case of prompt NO formation, owing to the considerable temperature dependence for reactions including $CH + N_2$. As discussed below, a systematic error of 40 K through the flame (about 2.5%, and the same as our random error bars) would alter the predicted NO concentration by nearly 25%.

The temperature profiles are also needed to reduce measured LIF intensities to ground state radical concentrations, accounting for the variation of the fraction of the molecules populating the absorbing level as a function of temperature. Accuracy is especially important for this purpose at the lower temperatures close to the burner surface.

LIF temperature measurements are made using rotational excitation scans in the (0,0) band of the OH radical, which provides strong signals throughout the flame. The special care that must be taken to avoid systematic errors in these measurements has been discussed.[7] These include: (1) use of a prompt detection gate, here 20 ns, to avoid problems caused by temperature and

rotational-level dependent quenching and radiative rates; (2) use of a detector with a uniform response over a wide bandpass, here 25 nm, to avoid biasing due to changes in the fluorescence spectrum with excited rotational level; (3) normalizing LIF signals by transmitted laser intensity to correct for non-zero optical depth; and (4) operating in a linear regime to avoid intensity anomalies due to satellites and line wings.

Temperatures were measured in the flame using a spectral fitting method. Fig. 1 shows how spectra taken at different heights above the burner surface vary with temperature. The top panel is near the peak, with a fitted temperature of 1672 K. The middle panel shows a spectrum at 1153 K, while the bottom panel exhibits the sparse spectrum found in the coolest region we could measure, 405 K at only 2.5 mm from the burner surface. Due to the near ambient temperature (achieved through water cooling) heterogeneous reactions at the burner surface are minimized.

The temperature profile in the 30 Torr flames is shown in the top left panel of Fig. 2. Temperature profiles were also measured in the 70 and 120 Torr flames, exhibiting a peak closer to the burner surface, but with approximately the same peak value. The error bars were larger in the higher pressure flames, and have been estimated at about 100 K. A smooth temperature profile was fitted to the data for each flame, and then used as input to the model as well as for analysis of the LIF intensity profiles to obtain species concentrations.

EXPERIMENTAL SPECIES PROFILES

OH--Most profiles were made using the $R_2(6)$ line of the (0,0) band of the A-X system; some checks using the $R_1(3)$ line showed excellent agreement after accounting for the difference in population fraction with temperature. The 20 ns duration, prompt gate avoided effects of quenching.[5] The absolute OH concentration was measured at its peak value by an absorption measurement of 2% per cm for the $R_2(6)$ line and 1.5% per cm for $R_1(3)$, corresponding to a peak concentration of $(6\pm3) \times 10^{14}$ molecules/cm^3, or a mole fraction of 0.0035 in the 30 Torr flame. Similar measurements at 70 Torr indicate approximately the same fractional peak concentration.

NO--The $Q_1(17)$ rotational line of the (0,0) band of the A-X system was used for the profiles, (again minimizing the temperature dependence of the absorption) while collecting the (0,2) fluorescence. The absolute NO concentration was obtained by calibration using LIF in known amounts of NO diluted in helium/argon mixtures, flowing through the burner at room temperature. The optical system was the same as in the flame; the ratio of the LIF signals under these conditions to those in the flame then furnished the desired calibration. In the room temperature flow, the decay is mainly radiative with a lifetime of 192 ns. The quenching rate in the 30 Torr flame at the peak of the NO signal is 2.9×10^7 s^{-1}. Taking the ratio of the two signals and the quenching and accounting for Boltzmann population difference of the absorbing rotational level yielded a peak NO concentration of $(7\pm4) \times 10^{11}$ molecules/cm^3, or a fractional concentration of 4 ppm in the flame. From comparison of the relative LIF signals at 30 and 70 Torr, and applying the necessary quenching correction, a peak NO concentration of $1-3 \times 10^{12}$ molecules/cm^3 was obtained at 70 Torr (3.2 ppm).

CH--Excitation and observation were performed in the (0,0) band of the A-X system. There was insufficient absorption to calibrate for an absolute CH concentration. However, the profiles taken at 30 and 70 Torr were used to obtain a ratio of the peak CH concentration at these two pressures, showing a decrease in CH concentration at 70 Torr, with the ratio [CH]$_{30 Torr}$/[CH]$_{70 Torr}$ being 1.7.

H Atoms--Hydrogen atoms were excited to the n = 3 level using two photons near 205 nm, with observation of the Balmer-α n = 3 → n = 2 emission at 656 nm. In addition to LIF, amplified spontaneous emission (ASE) was also observed along the laser axis in both the forward and backward directions.

All intensity profiles were corrected to account for the Boltzmann fraction of the absorbing level at the local temperature. Profiles in the 30 Torr flame are given in Fig. 2 over a wide range of

measurement well into the burnt gases. For OH and NO, the absolute concentrations are given; for CH only a relative profile was obtained. The time decay measurements showed quenching of NO and CH to be invariant with position, so no quenching corrections were performed; the OH profiles were obtained with a prompt gate so they are not influenced by quenching. Also shown is the OH(A) chemiluminescence profile measured with the laser off, a result of the CH + O_2 reaction, which creates OH directly in the emitting $A^2\Sigma^+$ state.

At this point, it is useful to qualitatively describe the profiles of the three species in the 30 Torr flame. CH is sharply peaked at about 1.0 cm above the burner surface, similar to that of the chemiluminescence from OH(A), which is a direct product of the CH + O_2 reaction. The concentration of NO, OH, and H rise more slowly above the burner, and extend well past the flame front into the burnt gases. NO displays a bisigmoidal rise and this feature is discussed below. Profiles in the 70 and 120 Torr flames are not shown but are qualitatively similar, including a bisigmoidal NO profile at 70 Torr.

FLAME MODEL CALCULATIONS

A computer model of the chemistry of low pressure methane/air flames was assembled to compare predicted concentrations with the experimental profiles, and to gain some insight into the controlling kinetics. A basic mechanism was constructed, with rate constants of our choice[8] based largely on the recommendations of Warnatz[9] for hydrocarbon oxidation and of Miller and Bowman[2] for the prompt NO submechanism. This latter subset was selected according to the authors' flowcharts, and included deNO$_x$ chemistry. A total of 148 reactions involving 38 species were included. Thermodynamic and transport input are from the Sandia databases,[10] with slight modifications for the thermodynamics of the methylenes, formaldehyde, CH_2OH, and NCO.[8] The OH(A) chemiluminescence is calculated according to production from the CH + O_2 reaction, and removal by collisional quenching on a time scale short compared to flow velocities or diffusion.

The flame model calculations were carried out using the Sandia flame code,[11] based on one dimensional fluid flow; it includes thermal diffusion, bimolecular and unimolecular kinetics, and sensitivity analysis for individual chemical reactions. Necessary inputs are the measured pressure and gas flow rates at the burner surface, and the measured temperature profile. Calculations were performed well out into the burnt gases, to a height of 10 cm above the burner for the 30 Torr flame. The cross-sectional area of the flame was assumed constant (see below). Predictions of the model are compared to experiment for order, peak position, width and shape of the species profiles, and the absolute concentrations. These comparisons form sensitive tests of our understanding of the flame chemistry.

SPECIES PROFILES

In Fig. 2, the computed concentrations have been matched to the maximum of the experimental values at 30 Torr. In relative position, the CH and OH(A) chemiluminescence reach their peaks at the half maximum point in the rise of ground state OH, i.e., at the flame front in both experiment and model. However, the predicted widths are slightly too small, by roughly a millimeter for CH, and the CH in the model rises a millimeter too late. This disagreement implies some errors in the chemistry controlling CH production and destruction, and thus entertains the expectation that the model will also be in error with respect to predicted NO production. Since the position of the OH rise is well predicted, it appears the overall oxidation chemistry is being modeled reasonably. The OH(A) chemiluminescence calculation appears to decay too rapidly, suggesting gaps in our mechanistic knowledge or a second production reaction.

The shapes of the NO and OH profiles are also adequately computed, although early OH is underpredicted, and the slight apparent decline of NO in the burnt gases is not calculated. The OH profile shows low but significant concentrations at early time (low height) due to diffusion. The rise and steepness of the OH are well predicted, within 1 mm, as is the decline in the burnt gases

1606

via reaction with CO. The leveling off after 2 cm, the presence of NO at low heights, and the bisigmoidality of the profile are well predicted by calculation. The match in absolute position of the NO rise is also good, although diffusion reduces the sharpness of the rise.

ABSOLUTE CONCENTRATIONS

Absolute concentration measurements form another sensitive test. The calculated peak OH concentration at 30 Torr is 50% above the measured value, just at the estimated confidence limit for the absorption measurement. The NO concentration calculated at 1.75 cm for the 30 Torr flame is 3.7 ppm compared to the measured, calibrated value of 4 ppm. This excellent agreement is surprising, given the uncertainty in the main rate constants to which NO is sensitive, in particular the controlling chemistry involving CH (see below).

Our choice of rate constant for the key $CH + N_2 \rightarrow HCN + N$ is based on the direct shock tube measurement of Dean et al.[12] A preliminary transition state theory extrapolation of these values to the lower temperatures of the flame indicates a simple Arrhenius expression is adequate. The value obtained from this rate constant expression is in substantial agreement at 1500 K with the value recommended by Miller and Bowman[2]. An absolute measurement of the CH concentration was not performed in these experiments. The calculation predicts a peak mole fraction of only 2 ppm, very similar to that from another recent modeling study of a 0.1 atm methane/air flame.[13]

Model calculations were also made for the 70 Torr flame with the same stoichiometry and flow rates, using the measured temperature profile as input. The calculated mole fraction of NO formed is the same, in good agreement with the observed ratio of 0.8. The model also predicts a peak mole fraction of CH at 70 Torr of 35% of the 30 Torr value, which agrees excellently with the observed 0.25 ratio. This good agreement, although at present for a very limited set of conditions, offers encouragement for being able to predict pressure effects on prompt NO formation.

We briefly examined a few aspects of the kinetics associated with the profiles of NO, HCN, and NH. The early peak of NO is due to diffusion and its failure to react away at lower temperature. If we analyze all production rates for NO, there are no significant reactive sources in this region. The rise in NO early in the flame front occurs from the $CH + N_2$ reaction, which forms N atoms that are rapidly converted by oxygen to NO. Examination of reaction rates shows that almost all NO is from the prompt mechanism. The other product from the $CH + N_2$ reaction, HCN, also has a wide distribution showing that it has also diffused back to a nonreactive region, and that it takes longer to burn out. The NH distribution, which is the final step in the HCN oxidation process before N and NO production, occurs later in the calculated flame. These last steps are responsible for the final curvature in the profile near 2 cm. The peak NH concentrations are predicted to be in the 10 ppm range, and its LIF profile could be a useful diagnostic for this last portion of the prompt NO mechanism.

Sensitivity analysis indicates the $CH + N_2$ reaction to be the most important step in NO formation. Quantitative measurement and control of CH and its kinetics are clearly indicated as the key to reduction of NO_x emissions which result from prompt NO chemistry.

CONCLUSIONS

Laser-induced fluorescence measurements have been made of the species OH, CH and NO in a low-pressure methane/air flame and compared with predictions from a detailed computer model. Through measurement of several radicals, assessment of the goodness of the model does not rely on a single species comparison, and we can see which part of the model needs further investigation.

The model prediction of both the NO profile and its absolute concentration in this flame are in excellent agreement with experiments. A sensitivity analysis shows that the key reactions

controlling prompt NO are CH + N$_2$ plus those which control the CH concentration and position. However, the CH concentration profile is not in such good agreement with experiment.

The development of a measure of the predicted temperature sensitivity shows that this parameter, whose profile is taken as input to the model, is extremely important in NO prediction. Uncertainty in the temperature severely limits the ability to calculate or control the amount of prompt NO formed, even with perfect knowledge of kinetics. This could be particularly important for practical burners with nonpremixed flames where there exist a variety of temperature/ concentration conditions.

The model also makes excellent predictions of the relative concentrations of both NO and CH as the pressure is raised from 30 Torr to 70 Torr. This suggests that the pressure dependence of the reaction rates is properly incorporated, and indicates that the model may be suitable for scaling to yet higher pressures. However, confirmation is needed at more than just this pair of pressures.

The success of the model is encouraging although there remain questions, especially concerning the ability to predict CH. Therefore we do not yet know the predictability of this reaction set, and need to make further measurements with different conditions (pressure and stoichiometry). Absolute measurement of the CH concentration would be a particularly useful addition to the results at hand, and a determination of NH would be valuable.

ACKNOWLEDGEMENT

REFERENCES

1. C. P. Fenimore, Thirteenth Symposium (International) on Combustion, The Combustion Institute, Pittsburgh, 1971, p. 373.

2. J. A. Miller and C. T. Bowman, Prog. Energy Comb. Sci. **15**, 287 (1989).

3. K. J. Rensberger, M. J. Dyer, and R. A. Copeland, Appl. Opt. **27**, 3679 (1988).

4. M. J. Dyer, L. D. Pfefferle, and D. R. Crosley, Appl. Opt. **29**, 111 (1990).

5. K. Kohse-Höinghaus, J. B. Jeffries, R. A. Copeland, G. P. Smith, and D. R. Crosley, Twenty-Second Symposium (International) on Combustion, The Combustion Institute, Pittsburgh, 1988, p. 1857.

6. D. E. Heard, J. B. Jeffries, and D. R. Crosley, Chem. Phys. Lett., in press (1991).

7. K. J. Rensberger, J. B. Jeffries, R. A. Copeland, K. Kohse-Höinghaus, M. L. Wise and D. R. Crosley, Appl. Opt. **28**, 3556 (1989).

8. G. P. Smith, Combust. and Flame, in preparation, 1991.

9. J. Warnatz, in Combustion Chemistry, W. G. Gardiner, Ed., (Springer-Verlag, N. Y., 1984).

10. R. J. Kee, F. M. Rupley, and J. A. Miller, Sandia National Laboratory Report SAND87-8215 (1987); R. J. Kee, J. Warnatz, and J. A. Miller, Sandia National Laboratory Report SAND83-8209 (1983).

11. R. J. Kee, J. F. Grcar, M. D. Smooke, and J. A. Miller, Sandia National Laboratory Report SAND85-8240 (1985).

12. A. J. Dean, R. K. Hanson, and C. T. Bowman, Twenty-Third Symposium (International) on Combustion, The Combustion Institute, Pittsburgh, 1991, in press.

13. M. C. Drake and R. J. Blint, Western States Meeting of the Combustion Institute, Paper 90-08, San Diego, Oct. 1990; General Motors Research Publication GMR-6922, 1990.
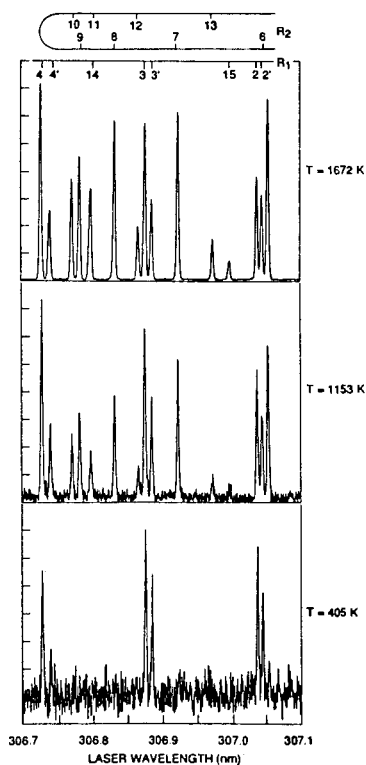
Figure 1 OH LIF rotational excitation spectra at three positions above the burner in the 30 Torr flame. Top: 3.22 cm height, 1672 K temperature; middle: 0.89 cm, 1153 K; bottom: 0.25 cm, 405 K.
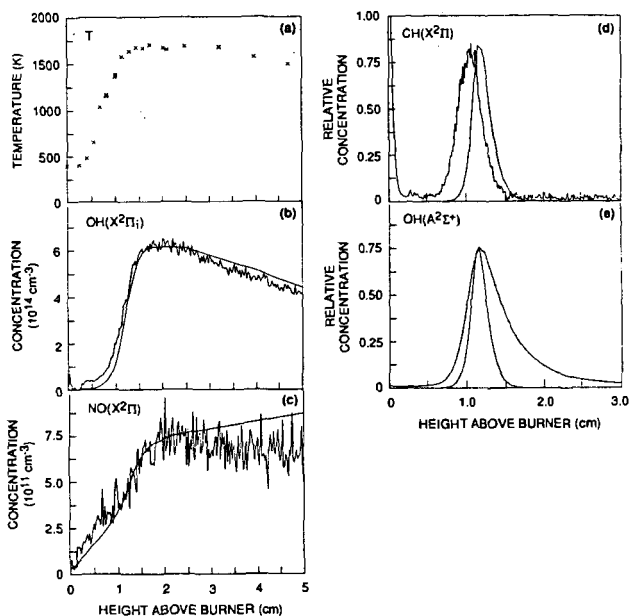
Figure 2   (a) Experimental temperature profile from OH LIF in the 30 Torr flame. A temperature of 399 K at the burner surface was assumed as a boundary condition for the flame model.

(b) - (e) Experimental and calculated species concentration profiles in the 30 Torr $\Phi = 1.13$ methane/air flame. Note the horizontal scale change for (d) $CH(X^2\Pi)$ and (e) $OH(A^2\Sigma^+)$. Model profile species are given by the smooth lines, and the OH values have been scaled by a factor of 0.67 to match the peak experimental value. Scattered laser light from the burner surface can be seen in the CH profile (d).

LASER-INDUCED FLUORESCENCE DIAGNOSTICS AND MODELING OF 10 TORR METHANE/OXYGEN FLAMES

J.W. Fleming, K.A. Burton[a], and H.D. Ladouceur
Chemistry Division, Code 6110
Naval Research Laboratory, Washington, DC 20375-5000.

Keywords: methane, flame modeling, CH radical

[a] NRC/NRL Postdoctoral Research Associate

ABSTRACT

Spatial concentration profiles for CH have been obtained using laser-induced fluorescence in several 10 torr CH_4/O_2 flames at equivalence ratios (Φ) between 0.8 and 1.3. The experimental flow rates, temperature profiles, and a published chemical mechanism have been used in Sandia's flame code to predict CH spatial positions. A comparison of experimental results and computer calculations are presented.

I. INTRODUCTION

The flame environment is one of the most interesting and complex chemical systems. Experimental efforts have been directed to identifying and quantifying molecular and atomic species in flames using a variety of techniques. An increasing experimental kinetics data base and computer modeling advances have made it possible to correlate experimental measurements with computer predictions. It is clear that experimentally monitoring all of the chemical species in any hydrocarbon combustion problem is impractical if not impossible. The ability to predict the behavior of most flame species based on a few experimental parameters is attractive and sometimes necessary for practical applications.

The flame zone is several millimeters wide at 10 torr which allows for the examination of CH with sufficient spatial resolution to resolve its growth and decay. This paper presents modeling and experimental comparisons for CH which extends our previous work.[1] The current work details the behavior of CH (experimental and predicted) for several 10 torr methane/oxygen flames of differing fuel equivalence ratios. We were particularly interested in the results for-fuel-rich flames. We monitor OH radical distributions (for temperature measurements) and CH radical concentrations with laser-induced fluorescence, LIF.

II. EXPERIMENTAL

Measurements characterizing a steady-state 10 torr methane/oxygen flame have been outlined previously.[1] Experiments were carried out in a water-cooled, stainless steel 6-way cross containing a water-cooled flat-flame burner.[2] Pressure measurements were made at the top of the cross using MKS baratron heads. Pressures were maintained at 10 torr to within $\pm$ 0.5 %. The flames are supported on a sintered bronze 6-cm diameter mantel. A shroud gas flow of Argon was used whose flow rate was adjusted to match the total mass flow through the burner for each flame studied. CH_4/O_2 flames were studied with equivalence ratios and flows listed in Table 1. The flow rates were measured with calibrated mass flow meters (Tylan). The methane and oxygen were premixed upstream from the burner. Total mass flow was maintained constant for all of the flames studied at 1.140 $\pm$ 0.005 mg/s-cm^2. The previously studied flame had a mass flow of 1.040 $\pm$ 0.005 mg/s-cm^2. Vertical translation of the burner via a bellows assembly with micrometer adjustment allowed a 10 cm range above the burner to be probed with a position reproducibility of $\pm$ 0.03 cm.

The CH and OH radicals were detected by LIF with the output of an excimer-pumped dye laser (Lambda Physik 101MSC/FL2002). The diameter of the probe beam was 0.8 mm. We measured CH intensity profiles as a function of position along the burner centerline by tuning the probe laser wavelength to the $P_1(6)$ transition in the $A^2\Delta$ - $X^2\Pi$ (0,0) band at 431 nm (Coumarin 440 dye, Exciton). A Corion 4500 interference filter (433 nm center, 60 nm FWHM) allowed the collection of CH fluorescence in the (0,0) band. The probe laser energies were kept $\leq$ 4 μJ/pulse. There was essentially no scattered light in the CH experiments. Zeroes were obtained by tuning off of the peak. A second PMT monitored the probe laser intensity using scatter from a roughened aluminum plate. Gated integrators (SRS) monitored signals from the PMT's. The fluorescence signals were weighted by the temperature-dependent Boltzmann population of the probed level determined from the experimental temperature profile. The detected fluorescence signals were also corrected for obscuring of the LIF signal by the burner itself. We assumed a uniform CH electronic quenching rate throughout the flame which has been demonstrated to be reasonable in similar flames.[3,4]

The flame temperature profiles were obtained using a Pt/ 13% Pt-Rh thermocouple (Omega - Type R, 0.01 inch diameter wire). The thermocouple leads were housed in a ceramic tube. The bare thermocouple was acid washed and then coated with a high temperature adhesive cement[5] (Ceramabond 569) which was cured using the manufacture's recommended procedure. The coated junction was positioned above the center of the burner with the leads parallel to the burner surface. For OH temperature measurements, OH excitation spectra were obtained using the frequency doubled output of the dye laser (coumarin 540A, Exciton). The OH probe laser had a diameter $\leq$ 0.8 mm and the energy was kept below 0.5 μJ/pulse. OH radicals were excited in the $A^2\Sigma$ - $X^2\Pi$ (1,0) band from 281 to 285 nm. A Corning 7-54 filter (320 nm center, 120 nm FWHM) transmitted fluorescence in the (1,0) and (0,0) band. Radiation corrections[6] for the thermocouple readings were calibrated using the OH LIF rotational temperature measurements in the Φ = 0.9 flame previously studied. The radiative effect of the burner surface to the thermocouple was accounted for by a view factor for a sphere to a disk.[7]

III. MODELING

We have previously shown that OH and CH relative concentration profiles could be reasonably modeled in a Φ = 0.9 flame using the chemical mechanism of Miller and Bowman,[8] excluding the nitrogen containing species. The same mechanism is used in this study and consists of 33 chemical species and 150 reversible reactions. Chemical thermodynamic data and rate coefficients were evaluated using CHEMKIN-II which can account for the pressure dependence of the appropriate reactions.

To model the CH profiles we used PREMIX,[9] a one-dimensional flame code developed at Sandia for modeling premixed, laminar flames. PREMIX calculates the steady-state species spatial profiles and requires the following as input: a chemical mechanism, transport properties, total pressure, flow rate, burner diameter, and the vertical temperature profile.

IV. RESULTS AND DISCUSSION

A. Temperature measurements

Thermocouple measurements were made throughout each flame as a function of height above the burner. The thermocouple temperature readings were corrected as outlined above. Listed in Table 1 are the maximum corrected temperature reading for each flame. The corrected temperature profiles are shown in Figure 1. Typical corrections for the 0.15 cm diameter coated junction varied from 100 to 550 K over the measurement range of 1000 to 1700 K. These corrections are large but consistent with the large junction diameter used in these experiments. Such large diameters were necessary to insure the integrity of the coating. Uncoated thermocouple temperature measurements have been shown to be completely unusable in a similar flame due to the very large catalytic effect.[1] Flame

deposited SiO_2 coatings were found to be very fragile and could be used in only for a few measurements before the coating deteriorated. The Ceramabond coating was very sturdy, lasting for numerous flames, and is easy to apply.

Also presented in Figure 1 are the LIF OH rotational temperature measurements for the Φ = 0.8 flame. The agreement is very good for this flame which has a 10% higher gas flows than the calibration flame. Temperatures at 1.5 cm above the burner for all of the flames were measured using OH excitation spectra as a check on the correction method used. Very good agreement was found for all of the flames at this position, the corrected reading always within the $\pm$ 2 σ experimental uncertainty.

B. Concentration measurements

Experimental relative concentration profiles for CH are shown in Figure 2 for flames Φ = 0.8, 0.9, and 1.0. Results for flames Φ = 1.15 and 1.3 are presented in Figure 3. Symbols in both of these figures are connected with a dashed line and the symbol legend is presented in Figure 1. All experimental concentrations are on the same relative scale (left axis). Also shown in Figures 2 and 3 with solid lines are the PREMIX calculated steady-state CH profiles (right axis) for the respective equivalence ratios. The two vertical axes (relative and absolute) have been chosen such that the maximum experimental concentration for Φ = 1.0 flame equals the PREMIX calculated maximum for that flame.

The qualitative shape of these profiles were as expected. Ground state CH radicals peak in each of the flames and the distances of these peaks above the burner surface are found to increase with higher equivalence ratio. Such behavior has also been observed in 40 torr C_2H_2 flames.[10] The general shape of the calculated CH steady-state profiles is in qualitative agreement with the experimental profiles. Higher CH concentrations are observed for higher flame equivalence ratios. Table 2 summarizes the quantitative comparison of the significant results: location of the profile maximum, the profile width, and concentration. The location of the profile maximum above the burner is reasonably well predicted for all of the flames. The model predicts the peak location to be approximately 1 mm closer to the burner than observed experimentally for each of the flames. This difference appears to be constant for all of the flames. For the profile widths, the calculated widths (FWHM) are the same as the experimentally observed widths within experimental uncertainty. For the concentration comparison, the calculated concentrations were divided by the relative experimental concentrations and then multiplied by the experimental profile for the Φ = 1.0 flame. Table 2 shows that the Φ = 0.8, 0.9, 1.0, and 1.15 flames are in good agreement within experimental uncertainty assuming the above scaling method. The largest difference is the slight over prediction of the Φ = 1.3 flame. This may be due to the presence of higher hydrocarbons in the richer system which are not in the chemical mechanism. Another assumption made is that the quenching rate is a constant as a function of height above the burner. Although this is valid for methane flames, it has been shown to break down in flames using higher hydrocarbon fuels.[11]

CH concentration profiles are very sensitive to the spatial temperature profile. The very good agreement of the location of the concentration maxima between predicted and calculated and the good agreement for the Φ = 0.8 flame between corrected thermocouple readings and LIF OH measurements, suggest that the thermocouple coating and correction method employed here is valid. The position of 1.5 cm above the burner for comparing the corrected thermocouple measurements with the OH rotational temperatures was chosen because of the fairly small temperature gradient at this position and the fairly good temperature separation of the flames (see Figure 1). A small systematic error in the temperature measurement in the region just above the burner is difficult to determine due to the very large temperature gradient present there and the finite probe size for both a thermocouple or a laser probe beam.

VI. CONCLUSIONS

The agreement between experimental measurements and modeling calculations of CH concentration profiles for 10 torr methane/oxygen flames has extended confidence in the predictive ability of the behavior of this specie in fuel-lean to slightly fuel-rich flames. These results indicate that the chemical mechanism used is consistent with the experimental observations but are not a confirmation of the mechanism or a verification of any individual kinetic rate. These results along with other species measurements, primarily other radical species, will begin to verify the chemical mechanism. Although CH is a minor chemical player in any hydrocarbon flame, the presence of ground-state CH only in the flame front makes the ability to predict its behavior extremely useful.

VII. ACKNOWLEDGEMENTS

VIII. REFERENCES

1. Fleming, J.W.; Burton, K.A. and Ladouceur H.D., Chem. Phys. Lett. **175** (4), 395-400 (1990).
2. Low-pressure model flat-flame burner obtained from McKenna Products, Inc, Pittsburg, CA.
3. Cattolica, R.J.; Stepowski, D.; Puechberty, D. and Cottereau, M., J. Quant. Spectrosc. Radiat. Transfer, **32**, 363-370 (1984).
4. Rensberger, K.J.; Dyer, M.J. and Copland, R.A. Appl. Opt., **27**, 2768-2775 (1988).
5. Aremco Products, Inc., 23 Snowden Ave,. Ossining, NY 10562.
6. Fristrom, R.M.; Westenberg, A.A., Flame Structure; McGraw-Hill, New York, 1965; pp 150-152.
7. Siegel, R.; Howell, J.R., Thermal Radiation Heat Transfer; McGraw-Hill, New York, 1981; p.830.
8. Miller, J.A. and Bowman, C.T., Prog. Energy Combust. Sci. **15**, 287-338 (1989).
9. "PREMIX: A Fortran Program for Modeling Steady Laminar One-Dimensional Premixed Flames," Kee, R.J.; Grear, J.F.; Smooke, M.D. and Miller, J.A., Sandia Report SAND85-8240 (1987).
10. Joklik, R.G., Daily, J.W. and Pitz, W.J. Twenty-first Symposium (International) on Combustion, (The Combustion Institute, 1988) pp 895-904.
11. Rensberger, K.J.; Dyer, M.J. and Copland, R.A. Appl. Opt., **27**, 3679-3689 (1988).

Table 1. Experimental Conditions[a,b]

Φ	CH$_4$ (slpm)	O$_2$ (slpm)	Maximum T^c (K)
0.8	0.44	1.10	2006
0.9	0.67	1.08	2093
1.0	0.53	1.06	2169
1.15	0.59	1.03	2273
1.3	0.65	1.00	2286

[a] Total mass flows for each of the flames was 1.140 ± 0.005 mg/s/cm^2.

[b] Argon shroud gas was flowed to match the mass flow rate in the burner.

[c] Radiation corrected temperature (see text).

Table 2. Comparison of Experimental and Modeling Results

Flame Φ	Profile Maximum Location (cm)			Profile Width (cm)		Peak Height Ratio Model/Experiment
	Experiment[a]	Model	Difference (Exp - Model)	Experiment[b]	Model	(Scaled to Φ = 1.0)[c]
0.8	0.55	0.49	0.06	0.80	0.64	0.79 ± 0.19
0.9	0.60	0.51	0.09	0.71	0.68	1.07 ± 0.21
1.0	0.65	0.55	0.10	0.75	0.72	1.00
1.15	0.75	0.66	0.09	0.86	0.78	1.27 ± 0.22
1.3	0.95	0.84	0.11	1.03	0.93	1.72 ± 0.29

[a] ± 0.08 cm uncertainty includes the measured positional uncertainty and the laser probe radius.

[b] ± 0.16 cm uncertainty.

[c] ± 2 σ.
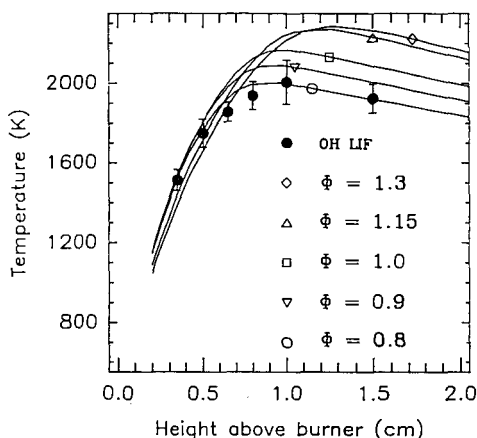
Figure 1. Temperature measurements as a function of height above the burner for the flame listed in Table 1: Corrected readings for a coated Pt/Pt-13% Rh thermocouple (solid lines); OH LIF temperatures derived from excitation spectra (filled circles) for the $\Phi = 0.8$ flame.
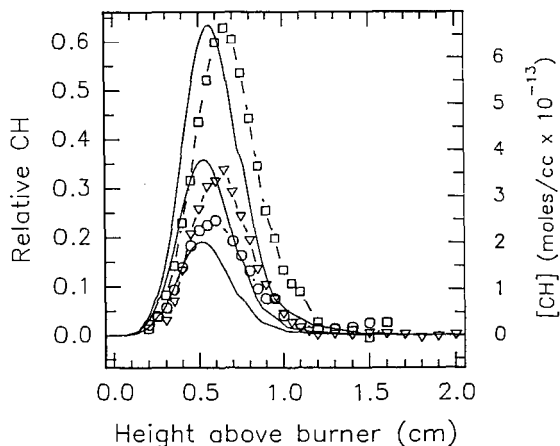
Figure 2. Concentration profiles for CH versus height above the burner for the flames $\Phi = 0.8, 0.9,$ 1.0, listed in Table 1 (symbol legend defined in Figure 1): Experimental concentration profile (symbols connected with a dashed line, left axis); PREMIX calculated CH radical profile using chemical mechanism listed in Reference 8 (solid line, right axis). Relative experimental concentrations have been scaled to the PREMIX calculated maximum value for the $\Phi = 1.0$ flame.
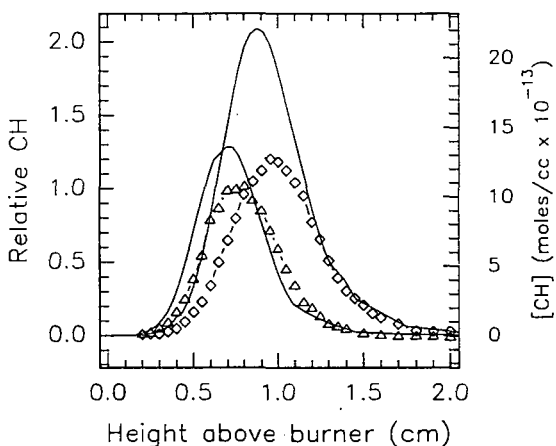
Figure 3. Concentration profiles for CH versus height above the burner for flames $\Phi = 1.15$ and 1.3, listed in Table 1 (symbol legend defined in Figure 1): Experimental concentration profile (symbols connected with a dashed line, left axis); PREMIX calculated CH radical profile using chemical mechanism listed in Reference 8 (solid line, right axis). Relative experimental concentrations have been scaled to the PREMIX calculated maximum value for the $\Phi = 1.0$ flame.

CONVERSION OF WASTE POLYMERS TO ENERGY PRODUCTS

P. Assawaweroonhakarn, Z. Fan, J.L. Kuester
Dept. of Chemical, Bio & Materials Engineering
Arizona State University
Tempe, Arizona 85287-6006

ABSTRACT

A project was performed to determine the feasibility of converting waste
polymers into diesel fuel.   The primary waste polymer source of interest
was disposable diapers, consisting of a mixture of cellulosic and synthetic
polymer material in the presence of biological wastes.   The overall project
consisted of five phases: (1) reaction equilibrium calculations, (2) batch
pyrolysis study, (3) continuous pyrolysis study, (4) continuous liquefaction
study, and (5) integrated system demonstration.   The integrated system
consists of a circulating solid fluidized bed pyrolysis system to produce a
synthesis gas for a fluidized bed catalytic liquefaction reactor.   The objective
for the pyrolysis system is to optimize the composition of hydrogen, carbon
monoxide and ethylene in the synthesis gas for conversion to diesel fuel in
the catalytic liquefaction reactor.   The liquefaction reactor produces a
product very similar to commercial No. 2 diesel fuel.

INTRODUCTION

Approximately 18% by volume of municipal solid waste consists of waste
plastics (1).   The 15.8 billion disposable diapers used annually comprise
about 2% of the total waste stream.   Due to increasing landfill costs and
environmental and regulatory pressure, a flurry of activity has emerged to
seek alternatives to landfill disposal of these materials.   Proctor & Gamble,
for example, has announced an "accelerated composting" program for their
disposable diaper products (2).   Separation steps are implemented to
segregate the non-compostable parts from the cellulosic parts. The intent is
to convert the cellulosic parts into "soil enhancer" (compost).   Presumably,
the plastics part still goes to the landfill.   The questions would be the market
for the "soil enhancer" and the probable   necessity to still landfill the
plastics.   An alternative approach would be to convert the bulk diaper (all
components) into marketable products with minimal landfill requirements.
This approach has been developed at Arizona State University (ASU)
utilizing   over 100 different feedstocks, generally falling into the categories

of industrial wastes, municipal wastes, hazardous wastes and various agricultural and forest residues. An indirect liquefaction approach is used, i.e., gasification of the feed material to a gas followed by liquefaction of the gas to a No. 2 diesel grade transportation fuel. The sequence is illustrated in Figure 1. The objective in the gasification step is to maximize the production of hydrogen, carbon monoxide and ethylene while the objective in the second step is to maximize the production of diesel fuel from these three reactants. A high octane product can be produced via conventional catalytic reforming of the diesel material. The potential products are thus liquid hydrocarbon fuels, medium quality gas (ca. 500 BTU/SCF) and/or electricity (via heat recovery or combustion of the fuels). Alternative operating conditions and catalysts for the second stage reactor could produce other products (e.g., alcohols, methane etc.).

Prior work on this process has been described elsewhere (see, for example, references 3-6). This paper will present the application for disposable diapers. A five phase approach was used (reaction equilibrium calculations, batch pyrolysis study, continuous pyrolysis study, continuous liquefaction study, integrated system demonstration) with performance limited to an 11 month period. The intent was to minimize the project risks and costs for scale-up to a commercial configuration. Using the composition of a particular disposable diaper product ("Huggies") as an example, the maximum yields of diesel fuel (wet and dry basis) are illustrated in Figure 2. Realistic actual liquid product yields are expected to be in the 50-100 gals/ton range (dry basis).

EQUILIBRIUM CALCULATIONS

Composition analysis for three commercial disposable diaper products is shown in Table 1. Since the compositions are similar, Huggies will be used for example calculations. Assuming a gas product slate of hydrogen, carbon monoxide, ethylene, ethane, acetylene, methane and carbon dioxide, the equilibrium product composition was calculated as a function of temperature by minimizing the Gibb's free energy of formation subject to atom balance constraints. Results are shown in Figure 3. As shown, all components decrease with temperature except hydrogen and carbon monoxide. The desired hydrogen/carbon monoxide ratio of ca. 1.2 (based on prior work) is achieved at ca. 1100 K (1550 F). No ethylene is predicted at equilibrium, as expected in the presence of hydrogen.

BATCH PYROLYSIS STUDY

These experiments were performed in a Chemical Data Systems Model 122 Pyroprobe coupled to a Carle Gas Chromatograph Model AGC111H . The

Pyroprobe consists of a temperature programmed ampule containing a sample of the desired feedstock with product gas being swept to the gas chromatograph via helium carrier gas. A full factorial designed experiment was performed for the factors temperature and water composition. The experimental design is given in Figure 4 with the results shown in Table 2 using Huggies as the example feedstock. The base condition for temperature was set by results from the reaction equilibrium calculations. The three responses of interest are: (1) hydrogen + ethylene + carbon monoxide, (2) hydrogen/carbon monoxide, and (3) ethylene. The superior level for all three responses is at the high level for each factor (experiment E). The factor ranking (via analysis of variance calculations) and experimental error (as calculated by base point replication range divided by factorial experiment range) is shown in Table 3. All response results are considered to be favorable for further investigation in a continuous system.

CONTINUOUS PYROLYSIS STUDY

This task was performed in a reactor constructed from 3 inch schedule 40 pipe with a length of 3 feet. A fluidized bed configuration was utilized with electrical heating, a screw type solids feeder, overhead scrubber and recycle gas system via a compressor. Thus this phase was to be continuous with respect to feed and product withdrawal but batch with respect to the fluidized solid. Operating conditions for an experiment to study temperature effect on gas composition using a Huggies sample are shown in Table 4. The "steady state" conditions reported were determined by relatively stable periods of reactor temperature. Some problems were encountered in achieving consistent feed rates in this task. Gas composition results are shown in Table 5. The gas phase results are considered reasonable and favorable for liquid fuels production.

CONTINUOUS LIQUEFACTION STUDY,

A 2 inch fluidized bed reactor was used for this study (continuous gas feed, electrical heaters, cooling coils, continuous product withdrawal via a condenser and trap, catalytic noncirculating fluidized solid). The factors temperature, pressure and residence time were studied with regard to the responses of liquid product yields, bulk properties and yields. Gas feed was from cylinders based on the compositions achieved from the batch and continuous pyrolysis studies. A cobalt/alumina catalyst was used. Yields in the 20-30 gals/ton range were achieved in limited experimentation. These yields would be expected to improve substantially by implementing the following: (1) recycle of the off gas, (2) feed gas composition improvement, (3) catalyst improvement, and (4) liquefaction reactor optimization. Product quality information is provided in Table 6 as compared with commercial

materials. In general, this comparison indicates that the liquid fuel is a competitive product without any additional refining steps.

INTEGRATED SYSTEM DEMONSTRATION

This task was performed in an existing integrated system (Figure 5) consisting of a circulating solid fluidized bed gasification system followed by a fluidized bed catalytic liquefaction reactor. The intent was to run the system for an extended period of time at fixed operating conditions as determined by the previous tasks in order to report commercially realistic mass and energy balances for economic and scale-up studies. Unfortunately, this effort was hampered by lack of availability of a suitable solids feeder within the budgeted performance period. The problem is considered to be readily solvable with proper effort. Gasification composition data for a relatively stable period is shown in Figure 6.

SUMMARY AND CONCLUSIONS

The production of liquid hydrocarbon fuels from biologically contaminated disposable diapers is a technically viable concept.. Favorable synthesis gas compositions can be produced. High quality liquid hydrocarbon fuel products can be produced from the synthesis gas. Additional research and development work is required to establish reliable mass and energy balances before scale-up is considered. To accomplish this objective, a reliable solids feeder system needs to be designed and tested. This is not considered to be a major obstacle.

REFERENCES

1. "Pressure for Plastic Recycling Prompts A Mix of Tough Laws and Cooperation", *Wall Street Journal*, page B7 (February 2, 1990)
2 "This Baby is Growing Up in Disposable Diapers", Procter & Gamble advertisement in *Newsweek* (October 15, 1990)
3. Kuester, James L. , "Conversion of Guayule Residues into Fuel Energy Products", *Bioresource Technology* 35, pp. 217-222 (1991)
4. Kuester, James L., "Electrical Power and Fuels Production from Wastes", in *Instrumentation in the Power Industry*, ISA, 32, pp. 69-74 (1989)
5. Prasad, B. and J.L. Kuester, "Process Analysis of a Dual Fluidized Bed Gasification System", *Industrial and Engineering Chemistry Research*, 27(2), pp. 304-310 (1988)
6 Davis, E., James L. Kuester and Marvin Bagby, "Biomass Conversion to Liquid Fuels: Potential of some Arizona Chaparral Brush and Tree Species", *Nature*, 307(5953), pp. 726-728 (1984)

TABLE 1

Elemental Analysis of the Waste Polymer Samples.

COMPOUND	ELEMENT	SAMPLE 1 Huggies	SAMPLE 2 Luvs	SAMPLE 3 (gmole) Pampers
Cellulose	carbon	1.3	1.3207	1.4417
	oxygen	1.00	1.1073	1.2088
	hydrogen	2.17	2.2045	2.4085
Polypropylene	carbon	0.331	0.2402	0.1865
	hydrogen	1.04	0.4799	0.3723
SAM	carbon	0.133	0.2142	0.2039
	hydrogen	0.147	0.2336	0.2224
	oxygen	0.102	0.1428	0.136
	sodium	0.031	0.0532	0.0507
Polyethylene	carbon	0.2	0.3286	0.304
	hydrogen	0.4	0.6576	0.608
Styrene	carbon	0.108	0.1635	0.3742
	hydrogen	0.143	0.2145	0.4955
Polyurethane	carbon	0.0126	0	0
	hydrogen	0.0168	0	0
	oxygen	0.0056	0	0
	nitrogen	0.0014	0	0
Urea	carbon	10.72	10.72	10.72
	oxygen	5.36	5.36	5.36
Feces	carbon	1	1	1
	oxygen	0.5	0.5	0.5
TOTAL	carbon	2.2949	2.2674	2.3104
	hydrogen	15.6569	15.5118	15.825
	oxygen	7.0576	7.1101	7.2048
	nitrogen	0.0014	0	0
	sodium	0.031	0.0532	0.0507

Source: Kimberly-Clark Corporation.

Uncorrected for gums

Urea	3.6	3.6	3.6
Feces	5	3	5
Rubber	0.31	0.075	0.015

TABLE 2

Gas Compositions from Huggies
(Factor: Temperature and Water Addition).

EXPERIMENT	A	B	C	A	D	E
# OPERATING CONDITION						
COIL TEMPERATURE (K)	1575	1467	1377	1575	1377	1467
(°F)	2012	2181	1939	2012	1839	2181
REACTION TEMPERATURE (K)	1093	1178	1020	1108	1006	1177
(°F)	1508	1663	1376	1535	1392	1651
WATER ADDED (WT %)	44.3	0	0	44.3	74.3	74.3
(ml/Ahr of sample)	0.18	0	0	0.18	0.36	0.36
# GAS COMPOSITION (MOLE %)						
H_2	26	29	14.5	21	22	22
CO	19	19	26	16	20	22
C_2H_4	7	5	5	7	4	7
C_3H_6	2	1	3	2	1	1
C_2H_6	0	0.2	0	0	0	2
CH_4	13	11	10.8	14	14	14
CO	32	34	30.7	33	32	32
H_2/CO RATIO	0.80	0.83	0.47	0.85	0.65	0.98

TABLE 3

Analysis of Variance Calculation Results.

RESPONSE	FACTOR RANK	% ERROR
$H_2 + CO + C_2H_4$	Temperature, Water	9.6
H_2/CO	Temperature, Water	9.8
C_2H_4	Water, Temperature	0

TABLE 4

Experimental Details

Reactor:
material.............. 316 stainless steel
diameter.............. 3 in. sch.40
length................ 3 feet

Sample: Huggies & synthetic urine

Operating Conditions:
Pressure............. ≈ 3 psig
θ.................... ≈ 0.3 min
feed rate............ ≈ 0.7-0.8 lbm/hr.
solid type........... Alumina (80 mesh)
solids loading....... 0.028 ft³
fluidizing gas....... Recycle pyrolysis gas

Factor: Temperature............ 1400°F-1700°F
Response: Gas Composition

TABLE 5

Task 3: % gmole of Gas Product at "Steady" State

EXPERIMENT	A	B	C	D	E
Average Temperature (degree F)	1441.625	1532	1719.5	1638.5	1544
Range of time (min)	34	18	32	14	5
Hydrogen	34.05	34.71	56.72	48.74	39.94
Carbon dioxide	9.09	4.62	4.50	3.31	5.04
Ethylene	7.20	5.31	0.57	1.70	4.19
Ethane	1.27	0.97	0.20	0.22	1.26
Nitrogen	1.01	1.09	0.71	0.71	0.62
Methane	19.42	19.05	2.90	9.64	14.88
Carbon monoxide	27.97	34.25	34.61	35.68	34.08

TABLE 6

Properties of Fischer–Tropsch Product and Commercial Fuel Oils

	No. 2 Diesel	Kerosene	JP-4	Waste Polymers Feedstock
Specific Gravity	0.8360	0.8108	0.7588	0.7470
Gravity, API °	37.6	43	55	57.9
Boiling point range, °F				
Evaporated at 10%	369	335	147	179
Evaporated at 50%	458	410	302	308
Evaporated at 90%	563	478	438	529
Calculated cetane index	44.2	44.2	37.8	45.7
Heating value, BTU/lb.	19080	21878	22440	19056

1623

FIGURE 1

Gas (2300 Btu/SCF)

Gas (700 Btu/SCF)

Gas (500 Btu/SCF)

Biomass,
Industrial Wastes,
Agricultural Wastes,
Urban Wastes → Pyrolysis → Fischer-Tropsch → Reformer → High Octane Gasoline

Paraffinic Fuel
(Diesel, Kerosene, Jet)

Normal Propanol,
Water
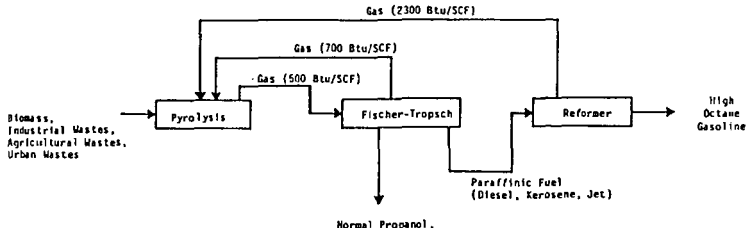
Basic Chemical Conversion Scheme

FIGURE 2

Huggies → Diesel

$$C_{2.3}H_{15.7}O_{7.1} \rightarrow C_{10}H_{22} + Other$$
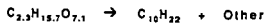
Composition (wt%)

	Huggies (wet)	Huggies (dry)	Diesel
C	17.54	53.44	84.51
H	9.97	7.64	15.49
O	71.92	37.19	0
N	0.02	0.04	0
Na	0.56	1.70	0

Maximum yield : 67 $\frac{gals\ diesel}{ton\ Huggies\ (wet)}$
(carbon balance)

189 $\frac{gals\ diesel}{ton\ Huggies\ (dry)}$

FIGURE 3

Equilibrium Gas Compositions of Huggies (wet)
as a Function of Temperature.

1624
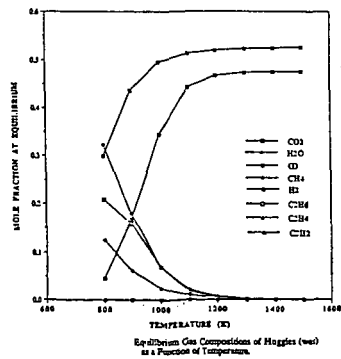
FIGURE 4

FACTOR	LEVEL		
	−1	0	+1
Temperature (K)	1019	1102	1185
(°F)	1375	1525	1675
Water (wt%)	0	64.3	78.3
(μl/0.1 mg.)	0	0.18	0.36

PRESSURE: 1 atm
RESIDENCE TIME: 20 seconds

Experimental Design for Huggies.

FIGURE 5

CONVERSION SYSTEM SCHEMATIC

GASIFICATION   LIQUID FUELS SYNTHESIS

FIGURE 6

PYROLYSIS GAS VS. TEMPERATURE
(N2 concentration less than 1 percent)

1625
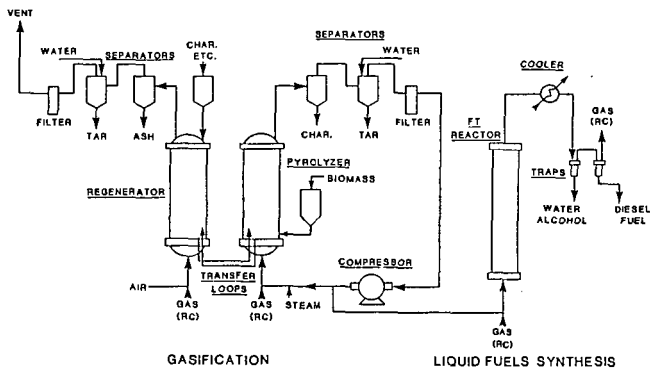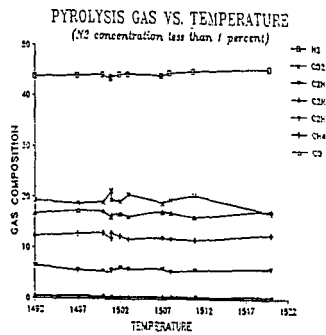
GASIFICATION OF WASTE PLASTICS FOR THE PRODUCTION OF FUEL-GRADE GAS

Laura Sharp
Robert O. Ness
Energy and Environmental Research Center
University of North Dakota
Box 8213, University Station
Grand Forks, ND 58202

Keywords: gasification, waste, fluid-bed reactor

INTRODUCTION

Many areas of the United States are experiencing waste disposal problems stemming from both a shortage of landfill space and a public concern for the environmental impacts and the appearance of landfilling. Although it is still the cheapest method of disposal, the rising cost of landfilling is making energy from waste more economically feasible. Incineration, another popular waste disposal method, faces ever more stringent emissions regulations, making it an increasingly less attractive alternative economically. New gasification and pollution control technologies are making it possible for waste materials to be used as environmentally acceptable sources of energy. Two possible waste materials which might be used as a feedstock for energy production, ebonite and automotive shredder residue, are being investigated at the Energy and Environmental Research Center at the University of North Dakota.

Several tests have been conducted with ebonite in a thermogravimetric analyzer (TGA) and a 1 to 4-lb/hr continuous fluid-bed reactor (CFBR) using K_2CO_3 and Paris limestone catalysts. Tests are scheduled for the automotive shredder residue. Data from the tests include carbon conversion, gas production, wastewater production, heavy metal analysis, and chlorine analysis. Analysis of the data includes discussion of the effects of the benefits of producing a fuel gas and the decrease in landfill volume, the environmental impacts of heavy metal disposal from the ash produced in the system, and the technological requirements for gas cleanup.

WASTE FEED MATERIAL

Automotive shredder residue is a waste product generated in the dismantling of automobiles. After removal of the gas tank and battery, the automobile is shredded to provide a material approximately less than 4 inches in size and composed of approximately 50% organic and 50% inorganic fractions. Magnetic separation is then used to separate out ferrous scrap. Air cyclone separators isolate a low density "fluff" from the nonferrous fraction (aluminum, copper, etc.). This fluff (shredder residue) is composed of a variety of plastics, fabrics, foams, glass, rubber, and an assortment of contaminants[1]. This waste product contains a wide variety of heavy metals and halogens, making it an excellent test material, as it will present many of the common problems to be considered when using waste as a gasification feedstock. Tests on automotive shredder residue are scheduled in the TGA and in the 1 to 4-lb/hr CFBR to investigate its gasification potential.

Ebonite, a hard rubber material used primarily in car battery casings, was tested both in a TGA and in the CFBR. Three tests in the TGA included one test at 800°C, with potassium carbonate as a catalyst, and two tests at 900°C, one of these with potassium carbonate and one with Paris limestone. The tests in the 1 to 4-lb/hr CFBR were all carried out using potassium carbonate as a catalyst, since it accelerated the process to the greatest degree. Table 1 shows the proximate and ultimate analyses of the ebonite.

EBONITE TGA GASIFICATION TESTS

Tests were conducted in the thermogravimetric analysis (TGA) instrument to determine test matrix conditions for further experiments to be run in the 1 to 4-lb/hr bench-scale unit. Ebonite reactivity with steam and two catalysts were investigated at temperatures of 800° and 900°C (Figure 1-4).

In all tests, the reactant mixtures containing -60-mesh ebonite were heated to the desired reaction temperature and held at temperature until approximately half of the fixed carbon in the sample had been converted to gas, at which point the reaction was terminated by cutting off the steam and heat supply. A -60-mesh ebonite was used due to the difficulty in obtaining samples of reproducible size distribution from the bulk samples. The +60-mesh-size fraction had the same TGA proximate analysis as the -60-mesh fraction, implying the difference (if any) in their reactivities would likely not be chemical, but due to a difference in surface area. All tests were performed under flowing argon gas.

To determine the point at which half of the fixed carbon had been converted, TGA proximate analyses were carried out on each sample prior to the reactivity tests. These analyses (Table 2) showed that volatiles are removed from the reactant mixtures, and the remaining material consists of about 63% fixed carbon and 37% ash for ebonite with catalyst and about 76% fixed carbon and 23% ash for ebonite without catalyst.

The TGA graphs start at time = 0. This point marks the beginning of the heat-up period. Weight loss during the heat-up period (as measured by a decreasing weight percent value) is due to moisture loss and devolatilization. When the reaction temperature is achieved (at which point devolatilization is essentially complete), the weight percent value is manually reset to a y-value of 100%, and steam is added. When 50% of the fixed carbon is converted, heat is turned off and the steam flow terminated. The point at which 50% of the fixed carbon is converted is determined by examination of proximate analysis data. As stated, each reactivity test was terminated when about half of each devolatilized sample had been converted to gas: 31.5 weight percent of the sample in the case with catalyst and 38.1 wt% of the sample in the case with no catalyst. After the termination of heat and steam, the conversion line still continued until the instrument was turned off, since some residual steam was still present, but it was not linear.

The catalysts investigated were Paris limestone (calcium carbonate) and potassium carbonate. All catalyst tests were performed using mixtures of ebonite and 10 weight percent-added catalyst. The ebonite/limestone test was performed at 900°C, and ebonite/potassium carbonate tests were performed at 800° and 900°C. The TGA data indicated that Paris limestone had a minor effect on the reactivity of the ebonite at 900°C (Figure 2), compared with the reactivity of ebonite without catalyst at the same temperature (Figure 1). Potassium carbonate, however, significantly affected reactivity. Conversion at 800°C (Figure 3) and at 900°C (Figure 4) with a potassium carbonate catalyst occurred quite rapidly. The residence time required for complete conversion at 800°C is 5.5 minutes and at 900°C is 2 minutes, whereas conversion time at 900°C is 18 minutes. Residence times for 50% and 100% conversion were found graphically. The point for 100% conversion was found by extrapolating the linear portion of the conversion line. The reaction appears to be zeroth order with respect to carbon. As conversion approaches 100%, the reaction is no longer strictly zeroth order because unreactable material (ash) limits access to carbon, but the order goes up only to approximately 0.2, introducing a very small error into the calculated time for total conversion.

EBONITE CFBR GASIFICATION TESTS

Bench-scale testing was performed in a 1 to 4-lb/hr fluid-bed reactor system, shown in Figure 5. Preheated gas and steam are introduced into the bottom of a 3-inch-

diameter reactor. The lower section of the reactor, which is attached to the coal feed system, is made of 3-inch pipe and is 33 inches in length. The freeboard section is made of 4-inch pipe, 18.75 inches in length. Solids remain in the bed until, through weight loss from gasification, they reach the top of the 3-inch section and fall out through the top bed drain leg, where they are collected in an accumulation vessel. Unreacted fines and some ash particles are entrained and separated from the gas stream by a 3-inch cyclone. Liquids are condensed in one of two parallel indirect cooled condensation trains. Gas is then metered and sampled by an on-line mass spectrometer.

The particle-size distribution of the ebonite was determined by sieve analysis; the results of which are shown in Table 3. Cold flow fluidization tests indicated a well-fluidized bed at 0.6 to 0.8 ft/s.

Carbon conversion for the ebonite was found to be approximately 90% at 900°C, with most of the unreacted ebonite found in the condensation train, indicating that fines blew out of the bed before having sufficient residence time for complete conversion. A narrower particle size for the feed, a lower fluidization velocity, or a larger diameter freeboard section would most likely raise this conversion by reducing fines entrainment. Alternatively, a reactor/cyclone recycle system that is designed for this particular feedstock would also produce higher conversions. Comparing the amount of material in the bed with the feed rate indicates that the residence time for the test was less than 1 hour. The residence time is extremely dependent on temperature and heat-up rate. Ebonite agglomerates at temperatures below about 800°C. If the reactor is not above 850°C and at a high heat-up rate, the ebonite will agglomerate, and the reaction rate and overall conversion are greatly reduced.

Gas produced from gasification and from water-gas shift reactions is between 220 to 280 lbs per 100 lbs of MAF ebonite feed material. Average composition of the product gas is shown in Table 4. Gas produced has a Btu content of approximately 260 Btu/scf. This number does not include nitrogen used in fluidization.

Water conversion was found to be 1.5-2.0 mole water/mole fixed carbon based on material balance data. Trace-element analysis showed considerable loss of lead from the ebonite, going from 660 ppm in the feed to 257 ppm in the product char. Antimony also decreased considerably, starting off at 696 ppm and ending up at 129 ppm. Chlorine content went from 160 ppm to 149 ppm.

ENVIRONMENTAL IMPACTS OF GASIFYING WASTE MATERIAL

Gasification of ebonite offers not only the benefit of energy production, but also decreases waste volume that needs to be landfilled. Density of the feed material (ebonite) is approximately 0.73 g/mL. Density of the reacted material (top bed drain) is approximately 0.56 g/mL. On an as-received basis, 12.8 ft^3 out of 100 ft^3 fed will be left over for landfill (assuming the 90% conversion). If 100% conversion is achieved, 14.5 grams per 100 grams of feed will be left over to landfill, resulting in a volume decrease of 87%.

Wastewater from the process may contain some heavy metals, including lead and antimony. Acid leaching the ebonite prior to gasification would be desirable to eliminate as much of the heavy metals as possible in downstream operations. Additionally, leachability studies will need to be conducted on the unconverted material. Gas cleanup problems will include the need to eliminate sulfur- and chlorine-containing compounds such as H_2S and HCl from the gas stream, as well as trace metals that may vaporize and recondense as particulates. The ebonite feed material is fairly high in sulfur, having an as-received sulfur content of 3.9%.

FUTURE TESTS

Further tests are planned to determine:

- the yield structure for automotive shredder residue and to verify the yield structure for ebonite
- optimal fluidization velocity
- carbon conversion with reduced fluidization velocity
- the effect of steam to carbon ratio
- the effect of increased pressure on gas yields
- the fate of vaporized heavy metals
- methods of ash stabilization
- the feasibility hot-gas cleanup
- leachability properties of unreacted material

Two of the key reactor design parameters that need further investigation include the fluidization velocity and the steam to carbon ratio. Carbon conversion could be increased if the fines could be kept in the reactor. The steam to carbon ratio coupled with the reactor pressure could change the output of carbon monoxide and hydrogen produced in the system. The heavy metals that are vaporized will either condense in the condensate train, which will cause scaling over a long period of time, or possibly recondense as particulates in the gas stream. More information will be needed on where these metals condense in order to determine the best way to deal with them.

SUMMARY

The future of waste disposal appears to be moving away from landfilling and incineration and toward recycling and using waste materials as a source of energy. New technology in pollution control and in energy generation techniques, such as gasification, make energy production from waste materials an environmentally acceptable alternative. Testing on ebonite, a hard rubber waste material, indicates that a high Btu gas can be produced in a reasonable residence time. Some work remains to be done to optimize operating conditions and to determine how to deal best with heavy metals and chlorine and sulfur compounds.

REFERENCES

1. Schmitt, R.J. "Automobile Shredder Residue-The Problem and Potential Solutions," Center for Materials Production, January 1990.

TABLE 1

EBONITE ANALYSIS

	As Det.	As-Received	MF	MAF
Proximate				
Moisture	1.98	2.00	N/A	N/A
Volatile Matter	37.1	37.1	37.85	44.4
Fixed Carbon	46.45	46.43	47.39	55.59
Ash	14.46	14.46	14.73	N/A
Ultimate				
Hydrogen	4.82	4.82	4.69	5.5
Carbon	70.34	70.34	71.76	84.18
Nitrogen	1.12	1.12	1.14	1.34
Sulfur	3.91	3.91	3.99	4.68
Oxygen	5.34	5.34	3.65	4.28
Ash	14.46	14.46	14.76	N/A

TABLE 2

PROXIMATE ANALYSES OF EBONITE/CATALYST MIXTURES

	Ebonite/10% $CaCO_3$	Ebonite/10% K_2CO_3
Moisture	1.70	2.76
Volatile Matter	36.53	36.97
Fixed Carbon	39.77	37.64
Ash	22.00	22.66

TABLE 3

EBONITE PARTICLE-SIZE DISTRIBUTION

Tyler Mesh Size	Weight Percent Retained
4	1.38
6	8.01
8	15.73
20	31.00
60	21.32
325	14.79
-325	7.71

TABLE 4

GAS ANALYSIS[1]

H_2	50.1
CO_2	28.8
H_2S	0.9
CH_4	4.5
CO	15.0

[1] Without nitrogen fluidizing gas.
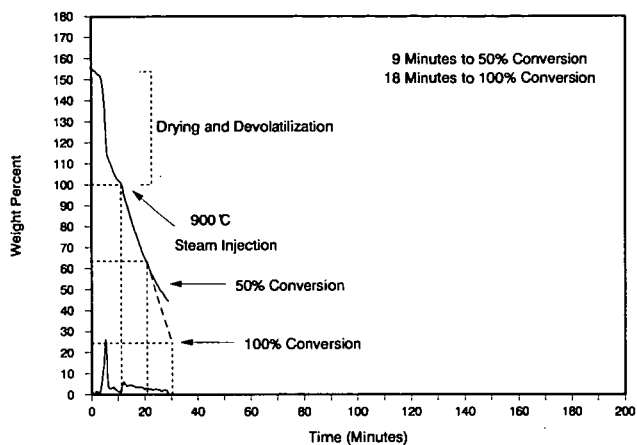
Figure 1. Steam reactivity of ebonite at 900°C.
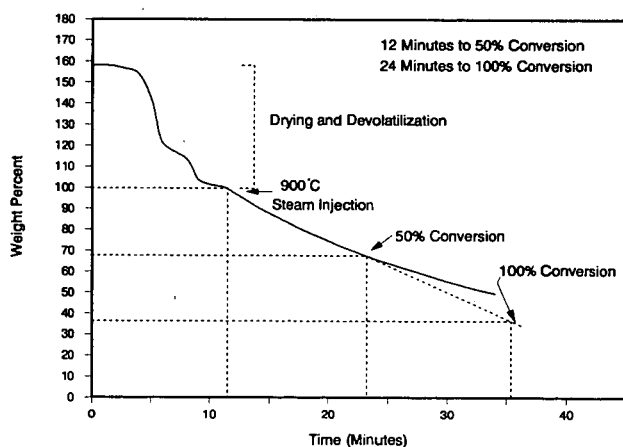
Figure 2. Steam reactivity of ebonite and calcium carbonate catalyst at 900°C.

1631
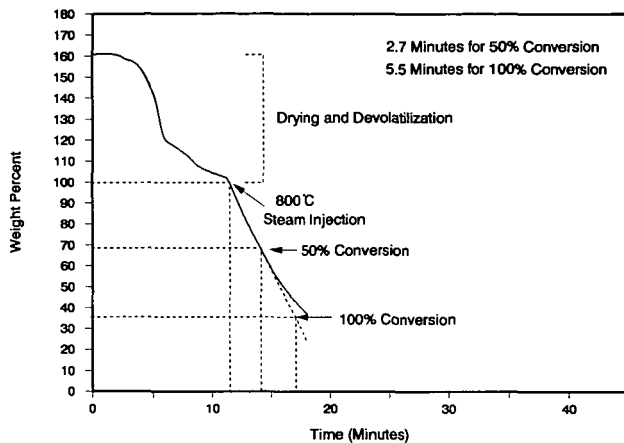
Figure 3. Steam reactivity of ebonite and potassium carbonate catalyst at 800°C.
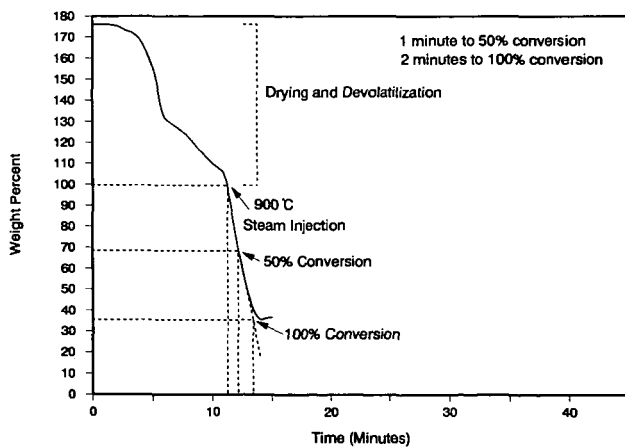
Figure 4. Steam reactivity of ebonite and potassium carbonate catalyst at 900°C.
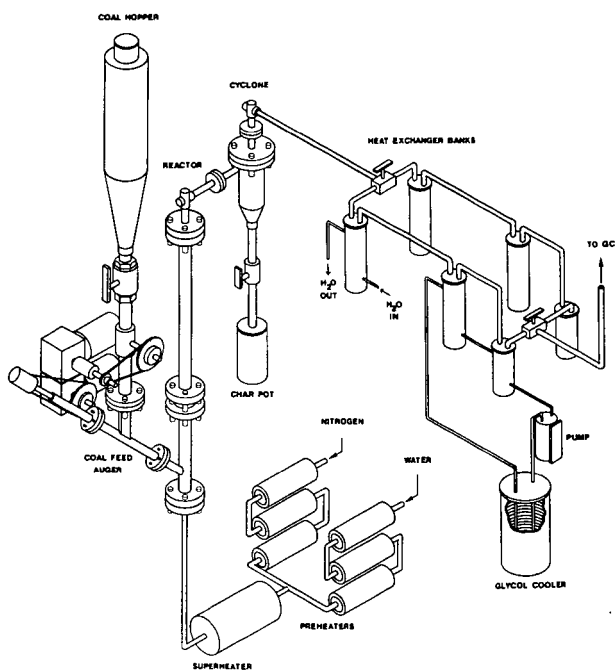
Figure 5. 1-4 lb/hr CFBR schematic.

RECOVERY OF ENERGY FROM MSW

M. D. Ackerson
E. C. Clausen
J. L. Gaddy
Department of Chemical Engineering
University of Arkansas
Fayetteville, AR 72701

ABSTRACT

Methods for disposal of MSW that reduce the potential for groundwater or air pollution will be essential in the near future. Seventy percent of MSW consists of paper, food waste, yard waste, wood and textiles. These lignocellulosic components may be hydrolyzed to sugars with mineral acids and the sugars may be subsequently fermented to ethanol or other industrial chemicals. This paper presents data on the hydrolysis of the lignocellulosic fraction of MSW with concentrated HCl and the fermentation of the sugars to ethanol. Yields, kinetics and rates are presented and discussed. Design and economic projections for a commercial facility to produce 20 MM gallons of ethanol per year are developed. Novel concepts to enhance the economics are discussed.

INTRODUCTION

The United States generates about 200 million tons of MSW annually, or about 4 pounds per capita per day (US EPA, 1981). The average composition of MSW is given in Table 1, and varies slightly with the season (Ng, et al., 1983). This material has traditionally been disposed of in landfills. However, recent environmental concerns over groundwater pollution, leaching into waterways, and even air pollution, as well as increasing costs, have resulted in this technology becoming unacceptable in most areas. Few new landfills are being approved and the average remaining life of operating landfills is only about five years.

Alternatives to landfilling include incineration, composting, anaerobic digestion, and recycling. Incineration can result in energy recovery as steam. However, concerns over hazardous components in exhaust gases and high capital and operating costs detract from this alternative. Large areas required for composting and the ultimate use or disposal of compost with high metals content makes this technology uncertain. Very slow reaction rates and large reactors for anaerobic digestion makes this technology uneconomical at present.

Recycling of glass, metals, plastics, and paper reduces the quantity of material to be landfilled by about 60 percent, as seen from Table 1. Most states have decided that recycling offers the best solution to the environmental concerns associated with solid waste disposal and many have implemented regulations for curbside segregation of recyclable components. Markets for recycled aluminum and steel are well established, however, markets for recycled paper, glass, and plastics are not well developed. Low prices (negative in some areas for paper) will impede the application of recycling.

Alcohol Production

The United States currently imports about half of its crude oil and must produce another 120 billion gallons of liquid fuels annually to become energy self sufficient. Ethanol can be produced from lignocellulosic matter, like paper, by hydrolysis of the polysaccharides to sugars, which can be fermented into ethanol. This technology would enable the use of the entire carbohydrate fraction of MSW (paper, yard and food waste, wood and textiles), which consti-

tutes 75 percent of the total, into a useful and valuable product. Ethanol can be blended with gasoline and, currently, nearly one billion gallons of ethanol, primarily made from corn, are used as a transportation fuel in this country. The potential market (at 10 percent alcohol) is 10 billion gallons per year. Blending of ethanol with gasoline reduces emissions and increases the octane rating. Some states, like California and Colorado where air quality has degraded seriously in metropolitan areas, are mandating the use of alcohol fuels.

The purpose of this paper is to describe a process for converting the lignocellulosic fraction of MSW into ethanol. The residue is contacted with concentrated mineral acid at room temperature to give theoretical yields of monomeric sugars, which are readily fermented into ethanol. Procedures to give high sugar concentrations are described. Data for fermentation in immobilized cell columns in a few minutes are presented. The economics of this process is then developed and key economic parameters identified.

HYDROLYSIS/ETHANOL PRODUCTION

The hydrolysis of biomass to sugars and fermentation of glucose to ethanol are technologies that have been commercial around the world for many years. The U. S. produced up to 600 million gallons of ethanol per year by fermentation during World War II. Also, the Germans produced fuel ethanol from wood by hydrolysis and fermentation during World War II. Today, Brazil produces most of its liquid fuel from sugar cane.

Hydrolysis Technology

Biomass materials are comprised of three major components: hemicellulose, cellulose, and lignin. The composition of various biomass materials is shown in Table 2. As noted, most of these materials contain 50-70 percent carbohydrate (hemicellulose and cellulose). These polysaccharides can be hydrolyzed to monomeric sugars, which can be converted by microorganisms into fuels or chemicals. The lignin cannot be hydrolyzed, but has a high heating value and can be used as a source of fuel. From Table 2, it is noted that most of the MSW biomass is cellulose.

The carbohydrate hydrolysis can be carried out by contact with cellulase or xylanase enzymes, or by treatment with mineral acids. Enzymatic hydrolysis has the advantage of operating at mild conditions and producing a high-quality sugar product. However, the enzymatic reactions are quite slow (30 hour retention time), and the biomass must be pretreated with caustic or acid to improve the yields and kinetics. The expense of pretreatment and enzyme production, and the large reactors required make this an uneconomical alternative.

Acid hydrolysis is a much more rapid reaction and various combinations of temperature and acid concentration may be used. Two methods of acid hydrolysis have been studied and developed: a high temperature, dilute acid process (Grethlien and Converse, 1982; Rugg, 1982) and a low temperature, concentrated acid process (Clausen and Gaddy, 1983; 1985). For example, complete conversion of the hemicellulose and cellulose in corn stover into monomeric sugars requires mineral acid concentrations of 2N at temperatures of 100-200°C (Clausen and Gaddy, 1982). However, acid concentrations of 10-14N yield complete conversions at room temperature (30°C).

At high temperatures, xylose degrades to furfural and glucose degrades to 5-hydroxymethyl furfural (HMF), which are both toxic to micro-organisms. Yields from dilute acid processes are typically only 50-60 percent of theoretical because of sugar losses by degradation and reverse polymerization at high temperatures. Also, equipment corrosion at high temperatures is a serious problem. Work in our laboratories has focused attention on concentrated acid

processes which produce theoretical yields at low temperatures. However, since high acid concentrations are used, acid recovery is an economic necessity (Clausen and Gaddy, 1983).

Studies in our laboratories have resulted in both single step and two-step hydrolysis processes, using concentrated mineral acids, which result in nearly 100 percent yields of sugars from hemicellulose and cellulose. The reactions are conducted at room temperature, without significant degradation or reverse polymerization (Prieto, et al., 1988a; Clausen and Gaddy, 1985). An acid recovery process has been developed and tested, yielding an energy efficient method of separating sugar and acid (Clausen and Gaddy, 1987). The resulting sugar solution has been successfully fermented to ethanol and other chemicals without pretreatment (Prieto, et al., 1988b).

Process Description. Figure 1 shows the proposed process for the acid hydrolysis of MSW, consisting simply of a mixed reactor where acid and MSW are contacted at a constant temperature. The unconverted solids (lignin and ash) are separated by filtration, washed, and used as fuel. Acid and sugars are separated and the acid returned to the reactor.

If desirable to separate the sugars, the hemicellulose, which degrades at milder conditions, may be first hydrolyzed to produce a mixture of five and six carbon sugars. The solids from this first stage reactor are separated and contacted with acid in a second step to hydrolyze the cellulose. Only six carbon sugars are obtained from cellulose in this second stage. This two step hydrolysis gives two streams; a xylose rich prehydrolyzate and a glucose rich hydrolyzate; and may be used where sugar separation is desirable. In the usual case, as with MSW, the simpler single step process will be preferred.

Hydrolysis Conditions. The two major factors which control the hydrolysis reactions are temperature and acid concentration. Studies in our laboratories have been made to define the appropriate conditions to maximize reaction rates and yields. Sugar degradation is promoted more at high temperature than at high acid concentration. Also, fast rates of hydrolysis are achieved at acid concentrations exceeding 12N. Therefore, the best conditions are a high acid concentration (80 percent H_2SO_4 or 41 percent HCl) and a mild temperature (~40°C).

The sugar concentrations and yields from a typical hydrolysis of MSW from our laboratories are given in Table 3 (Clausen and Gaddy, 1985). The prehydrolysis step yields 8 percent of the initial MSW as xylose. The combined yield of glucose is 60 percent. These yields represent nearly complete conversion of hemicellulose and cellulose to sugars. However, very dilute (3-7 percent) sugar solutions result from these reactions.

Hydrolyzate Fermentation/Ethanol Production.

Glucose may be fermented to ethanol efficiently by the yeast Saccharomyces cerevisiae, or the bacterium Zymomonas mobilis (Waldron et al., 1988). Batch fermentation experiments were carried out to compare the production rates of ethanol from hdyrolyzates and synthetic glucose. Saccharomyces cerevisiae (ATCC 24860) was used in the study. Identical results were found when fermenting synthetic glucose and hydrolyzate. Ethanol yields were also nearly identical. As noted in Table 4, the fermentation proceeded well in the presence of a small amount (0.25 percent) yeast extract, which can be obtained by recycle. Almost total conversion of sugars is obtained in only 16 hours. The concentrations of furfural and HMF in the hydrolyzates were found to be negligible. These low levels of by-products are believed to be the major reason for this highly efficient fermentation.

Xylose fermentation is much more difficult and the xylose might be used as a

source of energy for generating steam and power. However, future possibilities for xylose fermentation will improve the economics. Recent work with Pachysolen tannophilus shows promise for xylose conversion to ethanol (Schneider et al., 1981) but, at present, this technology is not fully developed. Ethanol may also be produced by converting xylose to xylulose, followed by fermentation with yeast (Gong, et al., 1981).

Continuous Fermentation. The standard technology for fermenting sugars to ethanol is in batch vessels. Batch fermentation is used so that contamination and mutation can be controlled. Sterilization between batches and the use of a fresh inoculum insure efficient fermentation. However, most batch alcohol fermentations are designed for thirty hour (or more) reaction time, which results in very large and expensive reactors.

The reactor size can be reduced substantially by using continuous flow fermenters. When fermenting acid hydrolyzates, the problems with maintaining sterile conditions are substantially reduced, since the substrate has been sterilized by contact with the acid. Therefore, the use of continuous fermentation is a natural application for producing alcohol from MSW hydrolyzates.

A number of continuous fermentation schemes have been studied, including the CSTR (Cysewski and Wilke, 1978), cell recycle reactor (Elias, 1979), flash fermentation (Cysewski and Wilke, 1977), and immobilized cell reactors (Sitton and Gaddy, 1980; Vega et al., 1988). Immobilized cell reactors (ICR) show potential in substantially decreasing reactor size and decreasing substrate and product inhibition (Vega et al., 1988; Gainer et al., 1981; Linko, 1981; Rowe and Margaritis, 1981). Reaction rates for ethanol production in an immobilized cell reactor are as high as 10 times the values obtained in a stirred tank reactor (Sitton and Gaddy, 1980). A wide variety of immobilization techniques have been employed, including cross-linking, entrapment, and covalent bonding (Vega et al., 1988).

Data are given in Figure 2 for laboratory columns with immobilized S. cerevisiae. The glucose profiles are given for initial sugar concentrations from 50-200 g/L. As noted, 90 percent conversion is achieved in one hour or less. Productivities to achieve 99 percent conversion were about 40 g/L-hr, or about an order of magnitude greater than the CSTR and 60 times more than the batch reactor. Furthermore, alcohol inhibition and toxicity to other inhibitors are reduced in the ICR. The reactor volume of the ICR for MSW hydrolyzate fermentation is about 5 percent that of the batch fermenter and substantial capital savings result.

Increasing the Sugar Concentration

Perhaps the single most important factor in the economics of this process is the sugar concentration that results from acid hydrolysis. Dilute concentrations increase both the equipment size and the energy required for purification. Methods to increase the sugar and ethanol concentrations have been developed.

Solids Concentration. The ultimate sugar and alcohol concentrations are direct functions of the initial solids concentration in the hydrolysis. Since fluidity in a stirred reactor is a requirement, a 10 percent mixture has been considered maximum. Therefore, the resultant sugar concentrations have been only 2-7 percent and alcohol concentrations only half as much.

If the limiting factor is considered to be fluidity in the reactor instead of the feed mixture, the feed concentration could be increased by roughly the reciprocal of one minus the solids conversion in the reactor. Of course, solids and liquid would have to be fed separately, which could also save equipment

1637

cost. For biomass, containing 75 percent carbohydrate, the reactor size could be reduced to one-fourth the size with a ten percent feed concentration. Attendant reductions would also result in the filtration and washing units.

Equally important are the resultant increases in sugar concentrations. The glucose concentration would be quadrupled to about 280 g/L (28 percent). Energy and equipment costs in the fermentation area would be reduced proportionately. This simple alteration in the process has a profound impact on the economics. It is estimated that the capital cost is reduced by 40 percent in the hydrolysis and acid recovery sections and 60 percent in the fermentation and utilities areas. Furthermore, the energy requirements for distillation are reduced by 60 percent.

Acid Recycle. Another method to increase the sugar concentration is to recycle a portion of the filtrate (acid and sugar solution) in the hydrolysis step. The acid would catalyze further polysaccharide hydrolysis to increase the sugar concentration. Of course, recycle of the sugars would also increase the possible degradation to furfural and HMF.

Experiments have been conducted to determine the enhancement possible with acid recycle. Various amounts of the acid and sugar solution from the filtration were recycled to determine the resulting sugar and by-product concentrations. Acid and solids concentrations and temperatures were kept constant. These experiments have shown that the sugar concentrations can be increased sixfold at total recycle. It should be noted that not all the filtrate can be recycled, since a portion adheres to the solids in filtration. In order to minimize sugar decomposition, a recycle fraction of 50 percent has been used, which results in doubling the sugar composition, without significant furfural or HMF levels.

The effect of acid recycle on the economics is significant. A recycle rate of 50 percent, coupled with high solids concentrations, would result in a xylose concentration of 15 percent and a glucose concentration of over 50 percent could be achieved. Practically, sugar concentrations should not exceed 25 percent, so a smaller recycle fraction is required. It should be noted that these concentrations have been achieved in the laboratory, while maintaining furfural and HMF less than 0.05 percent. These high concentrations reduce the equipment size in the acid recovery section by 50 percent and in the fermentation section by another 60 percent. Energy consumption is also reduced another 60 percent.

Acid Recovery. Acid recovery is essential when using concentrated acid hydrolysis. Processes for recovery of both hydrochloric and sulfuric acids have been developed. A number of possible recovery schemes were examined, including electrodialysis, distillation, etc.

The recovery technology that has been selected is based upon solvent extraction. Solvents have been identified that extract HCl and H_2SO_4 from the aqueous sugar solutions. Near complete acid recovery is possible and solvent losses are minimized. For HCl, the acid is separated from the solvent by distillation, and the solvent recycled. A hexane wash of the sugar solution is used to recover trace quantities of solvent, and hexane is separated by distillation for recycle.

Some solvent is lost in the process; however, the losses are quite small and solvent replacement costs are only $0.02 per gallon of alcohol. Acid losses are minimized and acid costs are $0.025 per gallon of alcohol. The total heat requirement for solvent and acid recovery is low and amounts to less than $0.05 per gallon of alcohol. As shown later, the energy cost may be recovered from the lignin and xylose streams.

1638

ECONOMIC PROJECTIONS

To illustrate the economics of this process, a design has been performed for a facility to convert MSW into 20 million gallons per year of ethanol, utilizing the acid hydrolysis procedures previously described. The capital and operating costs are summarized in Table 5.

MSW would be collected and delivered to the plant site as needed. Feedstock preparation consists of plastic, metal and glass removal, shredding, grinding and conveying to the reactors. The cost of the removal of glass and metals is not included in the feed processing cost, as reports indicate that resale of these materials will offset the capital and operating costs of separation. The hydrolysis section, as shown in Figure 1, consists of continuous reactors. Acid resistant materials of construction are necessary for this equipment. Ethanol fermentation in the ICR and typical distillation units are included. The total capital cost for this plant is $35 million, including all utilities, storage and offsites.

The annual operating costs are also shown in Table 5. These costs are also given on the basis of unit production of alcohol. As mentioned previously, no cost is included for MSW. A lignin boiler is used to reduce the energy requirements, and energy costs are only $0.08 per gallon. Fixed charges are computed as a percentage of the capital investment and total $5.6 million per year. The present ethanol price of $1.50 per gallon will yield a pre-tax profit of $18.5 per year ($.93/gal) or 53 percent per year.

It should be noted that this process does not include utilization of the pentose stream. Acid recovery is included, but fermentation of the xylose is not provided. Xylose could be fermented to alcohol, acids or other valuable chemicals, which would improve the economics. However, since this technology is not perfected, such products have not been included.

Sensitivity analyses show that the economics are particularly sensitive to capital cost and revenue. A 20 percent reduction in capital cost raises the pre-tax return to 70 percent. Similarly, a 20 percent increase in the ethanol price increases the return to 70 percent. A tipping fee of $20 per ton of MSW would increase the return to 65 percent. Increasing the plant size would have a similar positive affect on the economics.

CONCLUSIONS

Concentrated acid hydrolysis of residues, such as MSW, requires mild temperatures and results in near theoretical yields. The resulting hydrolyzates, containing primarily xylose and glucose, can be fermented to ethanol or other chemicals. The acid can be recovered for reuse by solvent extraction. The sugar concentration can be increased by using high solids reactions with acid recycle. Continuous fermentation of the hydrolyzates can be achieved in an hour or less in an immobilized cell column. The capital cost for a process to produce 20 million gallons of ethanol is estimated to be $35 million. The pre-tax profit from this facility is sufficient to encourage commercialization.

REFERENCES CITED

Clausen, E. C. and Gaddy, J. L., "Production of Ethanol from Biomass," Biochem. Engr. (1982).

Clausen, E. C. and Gaddy, J. L., "Economic Analysis of Bioprocess to Produce Ethanol from Corn Stover," Biotech. and Bioengr., 13 (1983).

Clausen, E. C. and Gaddy, J. L., "The Production of Fuels and Chemicals from MSW," Biotechnology Applied to Environmental Problems, CRC Press, (1985).

Clausen, E. C. and Gaddy, J. L., "Acid Hydrolysis/Recovery," SERI Review Meeting, Golden, CO (October 1987).

Cysewski, G. R. and Wilke, C. R., Biotech. Bioeng., 20, 1421 (1978).

Cysewski, G. R. and Wilke, C. R., Lawrence Berkeley Laboratory Report 4480, (March 1976) Biotech. Bioeng., 19, 1125 (1977).

Elias, S., Food Engineering, p 61 (October 1979).

Gainer, J. L. et al., "Properties of Adsorbed and Covalently Bonded Microbes," presented at AIChE National Meeting, New Orleans (1981).

Gong, C. S., McCracken, L. D., and Tsao, G. T., Biotech Letters, 3, 245-250 (1981).

Grethlein, H. E. and Converse, O. C., "Continuous Acid Hydrolysis for glucose and Xylose Fermentation," presented at International Symposium on Ethanol from Biomass, Canertech Ltd, Winnipeg (1982).

Linko, P., "Immobilized Microbial Cells for Ethanol and Other Applications," presented at AIChE National Meeting, New Orleans (1981).

Ng, A. S., Wong, M. K. Stenstrom, Larson, L., and Mah, R. A., "Bioconversion of Classified Municipal Solid Wastes: State-of-the-Art Review and Recent Advances," Fuel Gas Developments, CRC Press, (1983).

Prieto, S., Clausen, E. C. and Gaddy, J. L., "The Kinetics of Single-Stage Concentrated Sulfuric Acid Hydrolysis," Proceedings Energy from Biomass and Wastes XII, (1988a).

Prieto, S., Clausen, E. C., and Gaddy, J. L., "Ethanol from Biomass by Concentrated ACid Hydrolysis and Fermentation," Proceedings Energy from Biomass and Wastes XII, (1988b).

Rowe, G. and Magaritis, A, "Continuous Ethanol Production in a Fixed-Bed Reactor Using Immobilized Cell of Zymomonas mobilis," presented at AIChE National Meeting, New Orleans, (1981).

Rugg, B., "Optimization of the NYU Continuous Cellulose Hydrolysis Process," SERI Report No. TR-1-9386-1, (1982).

Schneider, H., Yang, P. Y., Chan, Y. K., and R. Maleszka, Biotech. Letters, 3, 89-92 (1981).

Sitton, O. C. and Gaddy, J. L., Biotech. Bioeng., 22, 1735, (1980).

Vega, J. L., Clausen, E. C., and Gaddy, J. L., "Biofilm Reactors for Ethanol Production," Enzyme and Microbial Tech., 10(3), 389 (1988).

Waldron, R. D., Vega, J. L., Clausen, E. C., and Gaddy, J. L., "Ethanol Production Using Zymomonas mobilis is Cross-Linked Immobilized Cell Reactors," Appl. Biochem. and Biotech., 18, 363 (1988).

_____ U. S. E. P. A., "Technical Environmental and Economic Evaluation of Wet Processing for Recovery and Disposal of Municipal Solid Waste," SW-109C (1981).

Table 1. Municipal Solid Waste Composition
(Weight Percent as Discarded)

Category	Summer	Fall	Winter	Spring	Average
Paper	31.0	38.9	42.2	36.5	37.4
Yard Waste	27.1	6.2	0.4	14.4	13.9
Food Waste	17.1	22.7	24.1	20.8	20.0
Glass	7.5	9.6	10.2	8.8	9.8
Metal	7.0	9.1	9.7	8.2	8.4
Wood	2.6	3.4	3.6	3.1	3.1
Textiles	1.8	2.5	2.7	2.2	2.2
Leather & Rubber	1.1	1.4	1.5	1.2	1.2
Plastics	1.1	1.2	1.4	1.1	1.4
Miscellaneous	3.1	4.0	4.2	3.7	3.4

Table 2. The Composition of Selected Biomass Materials

Material	Percent Dry Weight of Material		
	Hemicellulose	Cellulose	Lignin
Tanbark Oak	19.6	44.8	24.8
Corn Stover	28.1	36.5	10.4
Red Clover Hay	20.6	36.7	15.1
Bagasse	20.4	41.3	14.9
Oat Hulls	20.5	33.7	13.5
Newspaper	16.0	61.0	21.0
Processed MSW	25.0	47.0	12.0

Table 3. MSW Acid Hydrolyzates

	Concentration g/L	Yield g/100g
Prehydrolyzate		
Xylose	9.5	8.0
Glucose	18.5	16.0
Hydrolyzate		
Xylose	0.0	0.0
Glucose	67.8	44.0
Combined		
Xylose		8.0
Glucose		60.0

Table 4. Hydrolyzate Fermentation to Ethanol Percent Sugar Utilization

| Fermentation Time (hrs) | Hydrolyzate | | | |
| | With Vitamins and | | | With Yeast |
	Amino Acids	$NH_4(PO_4)$	Amino Acids and $NH_4(PO_4)$	Extract
16	15.9	21.9	27.3	97.5
23	19.3	24.9	35.8	97.5

Table 5. Economics of 20 Million Gallon Per Year Ethanol Facility

A. Capital Cost

	Million $
Feedstock Preparation	3.0
Hydrolysis	5.0
Acid Recovery	8.5
Fermentation & Purification	8.0
Utilities/Offsites	6.5
Engineering	4.0
	35.0

B. Operating Cost

	Million $/yr	$/gal
MSW	-	-
Utilities	1.5	0.08
Chemicals	1.9	0.09
Labor	2.5	0.13
Fixed Charges		
Maintenance (4%)	1.4	0.07
Depreciation (10%)	3.5	0.18
Taxes & Insurance (2%)	0.7	0.02
Pre-tax Profit (53%)	18.5	0.93
	$30.0	$1.50/gal
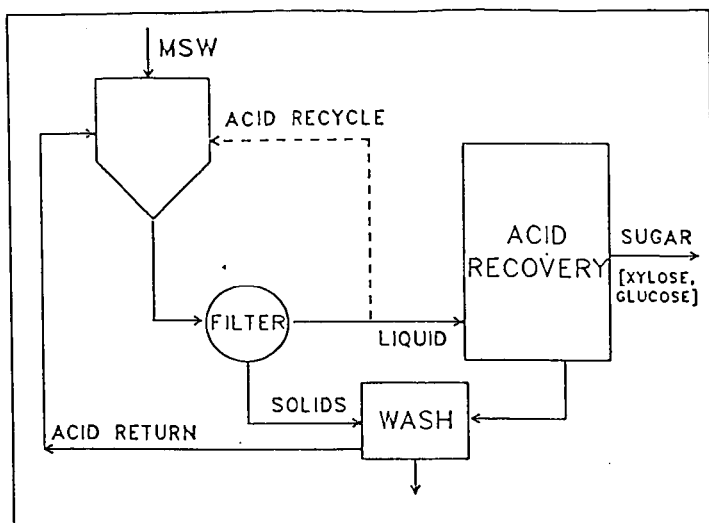
Figure 1. Schematic of Acid Hydrolysis Process
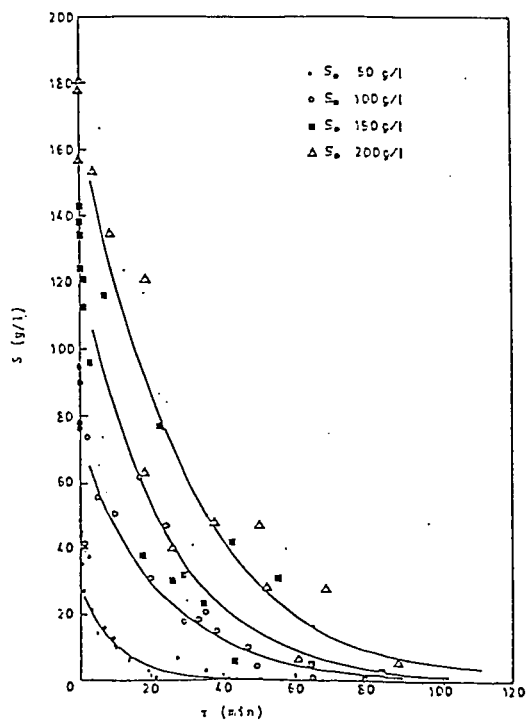
Figure 2. Glucose Profile in the ICR

CLEAN ENERGY FROM MUNICIPAL WASTE

" The environmental advantages of the controlled
combustion of municipal wastes as sources of energy".

Francis J. Cashin, D Eng. PE
Alfred J. Angiola, PE
Cashin Associates, PC
255 Executive Drive
Plainview, NY   11803-1707

Keywords: THERM (100,000 BTU's); TPD (Tons of Refuse per Day); SSRDF (Source-
Separated Refuse Derived Fuels)

ABSTRACT

This paper reviews the incinerator technology commonly employed in large
municipalities prior to 1970 (the introduction of EPA regulation; and, more
specifically the Clean Air Act of 1971); then, revisits the same technology as
it could be applied in the 1990's, but with...an environmentally aware public,
a vastly modified waste stream, the effects of recycling, controlled collection
procedures, and the latest technology (being developed and/or imported from
Europe).

In so doing, the review addresses: solid waste incineration prior to regulation
(pre-1970); the experiences in introducing regulation (1970-1990); and, the
significant environmental advantages in applying the latest knowledge,
methodology, and technology to the reduction of municipal wastes by combustion,
producing energies with a minimum adverse impact on the environment.

The delicate balances among the exposures (air, groundwater, land misuse),
factors not properly addressed in the early stages of environmental control
implementation are analyzed; and, scenarios are developed showing the overall
environmental advantages when a portion of (up to 10-15%) solid waste as a fuel,
replaces fossil fuels as a basic source.

PRECIS

The accumulation of solid wastes and the disposal of same had evolved into fairly
well established procedures by the 1960's. In most of the highly developed
countries of the world (Western Europe, North America, and the Pacific rim) solid
waste was collected and disposed of under controlled conditions. Actually,
population density determined the options to be selected by the local
communities.

Except to when collection procedures affect the disposal system (such as in
recycling), said procedures will not be developed hereinafter. Accordingly, the
emphasis will be in the disposal of solid wastes in areas of the denser
populations. This will represent an estimated 90% of the solid waste of
approximately 90% of the populations. The comparison of these disposal
procedures of this era (prior 1970) in the United States, will be developed,

herein, using that section of Long Island not of New York City (except for the Far Rockaway area of Queens). This area coincides with the area served by the Long Island Lighting Company (LILCO), for which there is considerable statistical data available; essentially, the United States Bureau of Labor Statistics Nassau-Suffolk reporting area.[1]

INCINERATION TECHNOLOGY - PRIOR 1970

In the 1960's, the incineration of solid wastes was being developed into a fairly sophisticated technology. The concepts being introduced included:

a. Continuously fed furnaces were replacing batch fed furnaces.
b. Systems for controlling combustion air at the grates, in the ignition chamber, and in the combustion chamber... were evolving.
c. Equipment effectuating complete combustion and removing particulate from the flue-gases were being installed (electrostatic precipitators).
d. Six major companies who were supplying grate systems/furnaces, all of whom were active in further development/improvement of their systems.
e. The American Society of Mechanical Engineers established a section,"The Incineration Committee" later to be made a division, until through mesne titles, it is referred to today as the "ASME WASTE PROCESSING DIVISION"). This division started to set standards for destructive distillations of solid wastes, write codes for operation, and develop courses/manuals for "Incinerator Operations" and later "Incinerator Maintenance."
f. As a result of the ASME (see 5 above) the first criteria for flue gas (air) and ground-water pollution control were established in the 1960's; and, more important, functional requirements for these controls were developed.
g. The first real effective measure for flue gas (air) control and quench water (waste water) control were being field tested on operating incinerators.
h. It is interesting to note: Several systems for energy recovery were developed and actually installed on large municipal incinerators (Town of Hempstead and Town of Oyster Bay). These systems worked well, but their use was discontinued because they were not economically feasible. The extra cost for the operation and maintenance could not be justified, when electric power was being generated from $0.06 per gallon fuels in very efficient power plants. Only when the cost of utility fuels exceeded ten times that amount did energy recovery from solid waste (a clean fuel) became attractive.

The history of incineration in the United States for this period is well chronicled in the "Proceedings" of the Incinerator Conferences of the American Society of Mechanical Engineers (ASME) of 1964, 1966, 1968, 1970, and 1972[2] Basically, all the major cities and suburban areas had either built or were under contract to build large incinerators. The typical plants were 500 tons per day (TPD) usually with two or more processing lines of 150, 200, or 250 TPD with a common tipping area and a common stack; many disposal facilities consisted of two 500 TPD plants. In the larger cities (typically New York, Chicago, Philadelphia) even larger furnaces and plants were built. Each new plant, usually employed the latest technology with the generation cycle at roughly five-years, and furnace replacement scheduled in on approximately 20-year cycle. The natural evolution of incinerator technology was in place.

It was during that period that the public was awakening to the environmental concerns resulting from energy conversions. However, the operators, designers, and manufacturers of incineration plants were already working on these environmental problems and several techniques for flue-gas cleansing and waste water recycling were being tested at new and existing incinerator plants. These environmental programs included:

i. Electrostatic precipitators for removing particulate in flue-gas.
j. Scrubbers for removing particulate in flue-gas and for partially absorbing certain of the undesirable gas products such as SO2 and NOx's.
k. Setting ponds and filter systems which would permit the recycling of flue-gas contaminates water (acetic) and ash quenching water (basic).
l. Analyses of incinerator residue to establish standards for contaminates such as heavy metals and hazardous non-metallic compounds.
m. Studies of air dispersion patterns from stack emissions of flue-gases.

These industry wide programs of voluntary, industry-supported development and research was aborted circa 1970, upon the introduction of Federal Government regulations/controls. In developing these new regulations, and later controls, the draftsmen almost completely ignored the wealth of knowledge and experience already accumulated. This literally short-circuited all the private sector efforts. These newly ordained "experts" began programs of enforcement by federal, state, and local governmental regulating authorities newly created for this purpose. The result was devastating; and,is discussed further herinafter.

EMBRACING ENVIRONMENTAL REGULATION 1970 TO 1990

Once the Environmental Protection Agency was created and began trying to get a handle in environmental concerns, the programs for processing, and improving upon the processing, of solid wastes suffered greatly. Unfortunately, the original appointees (many of whom were attorneys and/or not technically trained professionals) to the higher positions in of these new regulatory agencies were almost completely unknowledgeable in environmental considerations; and, lacked the experience in setting-up standards and organizing for the regulation of same. This was disastrous to the solid waste processing industry. Segments of the environmental problems were regulated without regards to the overall environmental impacts. The Air Quality Act of 1971 epitomizes this. Standards were promulgated for air quality which were arbitrarily applied and thus adversely impacted the overall environmental quality. They were standards for which neither time for enforcement or even need for same was properly addressed.

One of the reasons for enforcing the air quality of incinerators had such high priority is that incinerators had no constituency while the total adverse effect of solid waste burning was probably less than two percent (and that adverse effect was particulate which is admittedly undesirable by not an noxious as the sulfates, nitrates, chlorocarbons, etc. of the other polluters). Regulations were enforced that had the effect of systematically closing down all incinerators, because of the (then considered) excessive costs of installing (as yet unproven) air pollution control equipage.

As a result of these actions of the regulatorys, not only were operating incinerators closed, but the several companies developing incinerator technology and building incinerators went out of the business and most of the scientists, engineers, and technologists turned to other fields of endeavor. This was unfortunate because the real causes of air quality diminuation in 1970 were:

```
              Automobile...............................62%
              Industry.................................17%
              Utilities................................16%
              All other*................................5%
                  *(Including incinerators).........(±2%)
                                                    ------
                          Total.................100%
```

A whole new group took over the solid waste processing industry. Engineers were replaced by attorneys and financial consultants as the solving of the solid waste problem was explored by many entities including: the giants of American industry, financiers supporting (suggested but untested) technologies, and federal and state grants to test new technologies. During this period, these newly ordained experts suddenly discovered "Resource Recovery" (just as other name for incineration) and a series of pilgrimages were made to study "European technology." Actually, "European technology" was nothing more that than advances on the same 1960's technology the development of which had not been interrupted by the actions of regulating authorities. As a result of this, several European countries have transferred their technology to the United States as part of their corporate structure, in partnership with or by license to United States companies.

The European countries did have an advantage in that the resource recovery (hot-water or steam) technology was much further developed in Europe. This was largely because of the relatively high cost of fossil fuel (particularly oil) in Europe, which was anywhere from five to ten times the cost American utilities were paying for low grade fuels.

While the incineration industry was completely disrupted by regulation commencing circa 1970, there were several developments which inure to the overall improvement of the technology particularly with respect to public awareness, establishment of true values, and pre-processing standards such as source separation, mandated soft-drink containers deposits, and recycling systems all of which have made possible:

n. A significant reduction in the non-combustibles in the waste-stream, thereby decreasing the bulk handled during processing and reducing significantly the volume and weight of the (contaminated) residue by approximately 10%.
o. The separation of yard wastes remain both surface and combined waters and reduces the heterogenous nature of the solid waste stream making it easier to process.
p. The reduction in non-combustibles as increases in the heat value per pound (not the overall heat values) of the waste stream up to 20%.
q. The collecting, storing, and forwarding of solid waste in disposable plastic bags reduces significantly the amount of surface water contaminating the waste stream. When equal parts of water (by weight) are added to the solid waste stream, the result is a significant reduction in the net heating value:

The Effect of Water in Solid Waste Combustion

```
 72 degrees F to 212 degrees F.............................-150 BTU/lb
212 degrees F (water) to 212 degrees F (steam)............-970 BTU/lb
212 degrees F (steam) to 2,212 degrees F (superheat)....-1,000 BTU/lb
                            Total.........................-2,020 BTU/lb


1 lb solid waste.........................................5,000 BTU/lb
1 lb water..............................................-2,020 BTU/lb
    Net heating value/lb................................2,980 BTU/lb
```

Regulation, education, and economics have significantly altered the factors for evaluating solid waste as a viable fuel. The remaining waste after this separation of rubble and yard wastes and the recycling of paper, plastics, glass, metal containers and certain hazardous fuel is Source Separated Refuse Derived Fuel SSRDF (not to be confused with the RDF product of mechanically processed solid waste streams). The SSRDF has there main components:

<u>Waste Stream Analyses</u> - Abstracted from Town of Oyster Bay Solid Waste Management Plan - November 1990 by Cashin Associates P.C. (Corrected for rubble removal)[3]

Products (Combined)	Pre-Recycle 1984	Post-Recycle 1990
Papers	41.4	42.5
Glass	6.5	3.0
Metals	5.7	6.3
Plastics	8.0	8.0
Rubber	0.3	0.3
Textiles	1.7	3.6
Wood	5.4	8.5
Food	9.3	4.7
Yard	13.8	10.5
Inorganic	4.3	5.3
Miscellaneous	3.6	1.6
	100.0	100.0

This SSRDF has a calculated heat value of approximate 5,000 BTU's per pound plus or minus 10%, which compares with other non-renewal fuels as follows:

TYPE OF FUEL[4]	HEATING BTU/lb	VALUE Therms/Ton	Equivalent Bulk Unit
Natural Gas	22,000	440	41.08 MCF
Fuel Oil NO2	19,430	389	6.61 BBL
Fuel Oil NO6	18,300	366	6.10 BBL
Coal	15,500	308	1 TON
Coal	13,000	260	1 TON
Coke	11,670	233	1 TON
Pulp	6,700	134	1 TON
Begasse	4,000	80	1 TON
SSRDF	5,000	100	1 TON
Paper/Cardboard	6,500	130	1 TON
Plastic-Average	16,000	320	1 TON

RESOURCE RECOVERY TECHNOLOGY AFTER 1990

In order to bring into focus the potential energy available in solid waste, a comparison of the renewable energies shows:

Solar Energy Annually Available To The World From Reusable Sources[5]

SOURCE	BILLIONS OF THERMS
Solar collectors	433,000
Waterfall	9,000
Land Vegetation	1,600
Tropical Waters	500
Wind	50
Heat Pumps	50
Solid Waste (United States)	23.62
Solid Waste (Nassau/Suffolk)	0.23

All Types of Energy Sources Used By LILCO For The Year-1990[6]

Fuel Oil	1.01	56%
Natural Gas	0.36	20%
Nuclear Power	0.07	4%
Purchased	0.36	20%
Total......................1.80		100%

With the above statistics, a program for energy recoverable from solid waste can be evaluated. Approximately ten percent of the total electrical energy for this designated area (LILCO) could be produced from the solid waste generated therein. Looking at this possible alternative and at the changes in conditions brought about in the twenty years (1970-1990) by the introduction of regulations and environmental consciousness has produced many benefits, which will make solid waste more feasible and more attractive as an annually renewable energy source.

In producing energy, the most important considerations are economic and environmental, which complement one another. When comparing SSRDF with the energy sources, it is most likely to replace, SSRDF has the advantage:

CONSIDERATION	ECONOMIC COST/DECA THERM	ENVIRONOMICAL Sulfur Content
Fuel Type	$	%
Fuel Oil	$2.18	1.0
Nature Gas	1.80	Trace
Nuclear Power	0.98	0
SSRDF		Trace

The costs given for alternate fuels are from LILCO and are the average 1990 costs. The nuclear power is produced by facilities in which LILCO is partner.

SSRDF has essentially no cost as the cost of disposal is eliminated, if the SSRDF is used as a fuel for energy conversion. However, the costs of set conversion are higher that the costs for an equivalent amount of other fuels generated in the larger more efficient utility power plants.

THE FUTURE OF RESOURCE CONTROL - CIRCA 2000

As a result of the factors mentioned above, between 1970 and 1990, the control of solid waste processing has shifted in part from the ultimate disposer (landfill manager/incinerator plant operator) to the consumer, who has been taking more and more responsibilities for recycling.

As the environmental consciousness continues to evolve and the general knowledge of the public increases, the control of solid waste processing will gradually shift to the generators. A series of controls are being enacted, considered, and/or planned by Federal/State Agencies to:

t.   Further expand beverage container control to all parts the country.
u.   Reduce or eliminate undesirable compounds from packaging and expendable products (Florocarbons, etc.).
v.   Require more reusable containers for consumer product delivery.
w.   Reduce excess packaging; particularly, when the solid packaging is several times the bulk of the product delivered.
x.   Require disposable products and packaging, when not readily biodegradable to be safety reducible by combustion.
y.   Provide recycling systems for hazardous consumabiles (chemicals, batteries, oil wastes, etc).
z.   Containers for liquids will be regulated as to size, shape, type of label, and all types of materials used.

The solid waste problem will never be completely resolved, but slowly over the next twenty year (by 2010), the waste stream in the country will be controlled by the cooperation of the producers, consumers, and disposers.

SUMMARY

If the experiences of the past twenty years are carefully reviewed, a program for solving the ecological exposures in processing our waste stream can be resolved, unfortunately, in recent years, well intented environmentalists, supported by opportunist politicians, have skewed the public's understanding of this environmental problem.

For the past several years the public has been exposed to perceptions, not facts. It is time for the technologically trained scientists, engineers, and educators to speak out on all the environmental issues and put these issues in their proper prospective.

FOOTNOTES

1The Long Island Lighting Company's (LILCO) operating area essentially coincides with the United States Bureau of Labor Statistics reporting area of Nassau and Suffolk Counties in New York State. This area has a diverse nature with a population of 2.3 million, which is approximately one percent of the population of the United States. This area is uniquely situated on an island surrounded by water on three sides and New York City to the west. This assures control of the solid waste steam, which is impacted neither by the importation of foreign wastes, nor the export of locally generated wastes, except as part of controlled disposal programs of local municipalities).

2The American Society of Mechanical Engineers (ASME) commenced holding biennial conferences in 1964, all of which have been published in these "Proceedings", which are available in local technical libraries or the Engineering Library of the Engineering Building 345 East 47th Street, New York, NY 10011; or, may be purchased (not all years available) from ASME, 345 East 47th Street, New York, NY 10011. These proceedings are chronology of the then state-of-the-art, the operating data, and program for research and development...of the Incinerator/Waste Processing Industry.

3The Town of Oyster Bay Solid Waste Management Plan - November 1990 by Cashin Associates P.C., 255 Executive Drive, Plainview, New York 11803. Contains a summary of a series of solid waste analyses made by CASHIN ASSOCIATES P.C. from which these data were abstracted.

4Steam/its generation and use-Babcock & Wilcox, 161 East 42nd Street, New York, NY 10017.

5Energy Sources - The Wealth of the World, Ayres and Scarlott - Mc Graw-Hill, 1221 Avenue Americas, New York, NY 10027.

6Long Island Lighting Company - 1990 - Annual Report and supporting documents. LILCO, 175 Old Country Road, Hicksville, NY 11801.

SEWAGE SLUDGE: A FASCINATING FEEDSTOCK FOR CLEAN ENERGY

M. Rashid Khan, M. McMahon, S. J. DeCanio
Texaco Research & Development, P.O.Box 509, Beacon, NY 12508

Sewage sludge is composed of organic and inorganic materials. The organic portion of the sludge is predominantly composed of C, H, N, and S. On a dry-basis, the heating value of sludge is greater than that of oil shale or tar sand. The volatile matter content of dry sludge can be higher than that of the high volatile bituminous coal. Available correlations in the literature, developed for coals, were applied to predict the experimentally determined heating values. In addition, the sludge compositional data (C, H, S, and ash) were used to develop a new correlation specifically for raw sewage sludge. Compared to the models tested, the new correlation developed in this study for sewage sludge provided a better fit between the measured and predicted values.

KEYWORDS: Sludge, heating value, composition, coal

INTRODUCTION AND BACKGROUND

Treatment plants receive tremendous quantities of waste-water containing dissolved and suspended solids from a variety of sources including domestic, industrial and urban-offs as well as from storm drainage. Consequently, a variety of organic and inorganic materials can be found in a waste-water treatment plant (1).

Traditionally, the solid residue or sludge, the principal product of primary and secondary treatments, has been ocean dumped or landfilled. However, current federal regulations restrict such traditional practices. The option to dispose of such materials by landfilling also suffers from psychological (e.g., "not-in-my-backyard" syndrome) and genuine environmental concerns (e.g., contamination of ground water or agricultural products and leaching). A recent survey of compositional characteristics of domestic sludges indicate that most sludges can be classified as "hazardous," and consequently not suitable for disposal by landfilling (2). Keeping these alternatives in mind, conversion of sewage sludge to clean fuels via gasification (which readily converts essentially all the organic constituents) to synthesis gas (CO and H_2) for power generation or as chemical feedstock, provides an excellent avenue to utilize this renewable resource (3).

The use of sewage sludge requires a better understanding of its physical and chemical properties. In particular, the ability to estimate its calorific value would indeed be of great importance keeping in mind that the measured heating values of sludge are generally not readily available and the reported data often suffer from a relatively large experimental variation (partly due to possible biological/chemical degradation of samples during various treatments). Correlations are important for justification and

modeling of the conversion processes now being developed.

The correlations between the coal composition and heating value were reported as early as 1940. Over 20 different equations are reported in the literature which enable one to calculate the heating value of coal based on the ultimate/proximate analyses (4-9). However, essentially nothing could be found in the literature that could be readily applied to specifically estimate the heating value of sludge.

To examine the utility of existing correlations (developed for coal), the most widely used equations were tested for sewage sludge. Mott and Spooner (1940) claimed that their equation will yield heating values agreeing within 200 btu for the whole range of fuels, from peat to anthracite (4). We, however, were much less successful with this equation for dewatered sewage sludge.

Mason and Ghandi (1980) developed a correlation based on coal samples from the Pennsylvania State University coal data base (6). A comparison of the experimental results and the predicted values (based on Mason and Ghandi's equation) was made. Compared to the equation by Mott and Spooner, this equation (termed Data Base [DB] Equation) did a better job in estimating the heating value of sludge.

EXPERIMENTAL

In this study dewatered sewage sludge samples (originating in various treatment plants of the country) were dried in a lab vacuum oven under N_2. The dry samples were characterized by monitoring the following: ultimate analysis (C, H, S, N), ash content and high heating value. A selected set of samples were characterized in multiple laboratories which included the following: Huffmann Laboratories, Inc. (Golden, CO), Institute of Gas Technology (IGT, Chicago, IL), and Texaco Research & Development (Beacon, NY) to ensure that analyses in various laboratories provide comparable results. In general, the data obtained from various labs were within the variation allowed by the conventional ASTM guidelines for each analyses. All analyses for a given sample were completed relatively rapidly to minimize degradation of samples due to bacterial growth.

The data (30 observations in total) were analyzed by using the Statistical Analytical System (SAS) package developed by SAS Institute (10). The regression programs available in this package were applied to develop an empirical model.

RESULTS AND DISCUSSION:

1.   The Heating Value of Sewage Sludge Compared to the Various Fossil Fuels

The mean heating value (gross) of sludge (based on 30 observations) compared to various fossil fuels is shown in Figure 1. The heating

value of oil shale (Green River formation of Mahogeny zone; Colorado; 33 gal/ton, described by Khan, 1987) was 3200 Btu/lb (10). The heating value of eastern Kentucky shale can be significantly lower than the western shale considered in this study. The heating value of the Asphalt Ridge basin tar sand (Khan, 1989) was less than 2000 Btu/lb (11). By contrast, the heating value of an average sewage sludge is considerably higher (6400 btu/lb). The heating value of an industrial biosludge observed in this study to be greater than 9000 btu/lb. However, no industrial sludges were included in the data base aimed at developing the new correlation.

Compared to essentially all fossil fuels (excluding petroleum based fuels), sewage sludge has a higher H/C (atomic) ratio (Figure 2). The mean H/C ratio of sewage sludge was 1.65 (based on 30 observations), considerably higher than that of the bituminous coals (Pitt#8) with H/C ratio of 0.89 or a sub-bituminous coal (H/C of 0.96 for Wyodak coal). The H/C of the sewage sludge is comparable to tar sand bitumen (with H/C of 1.5).

In addition to the elements described above, significant amounts of chlorine and various volatile metals can be present in sewage sludge. For example, the chlorine content of one sludge was as high as 0.6% (dry basis). Other volatile inorganics identified in the this sludge included the following: Beryllium (less than 0.02 ppm), Vanadium (less than 1 ppm), and Manganese (900 ppm). However, this study did not consider the role of chlorine or vaporizable metals on the heating value of sludge.

2. Variations in the Sewage Sludge Composition

The mean, standard deviation, minimum and maximum values for the compositional analyses are presented in Figures 3 and 4. The variations in the C, H, N and S content in different samples are shown in Figure 3. The sulfur content for various sludges ranged between 0.18 and 3.61 percent with a mean value of 1.71 (with a standard deviation of 1.05 about the mean). The oxygen content of sludge ranges between 3.5 and 27.8% with a mean of 16.5 (and a standard deviation of 6.3%).

The volatile matter content for the a given sludge ranged between 45 and 62% (dry basis). These values are significantly higher than the volatile matter content of a high volatile bituminous coal (with a volatile matter content of 35%, dry basis). The H/C (atomic) for the data set used ranges between 1.44 and 1.86 with a mean of 1.65 with a standard deviation of 0.106.

Figure 4 shows that the mean heating value of the sludge was 6409 with a standard deviation of 816 (based on 30 observations). The measured values for the sludge ranged between 5261 and 8811 Btu/lb. The heating value and the compositional characteristics of sludge are dependent on the nature of sludge as well as on the degree of digestion (or pretreatment) a sludge has undergone. The minimum ash content for the sludge was 18.9% while the maximum value for

the sludge was 58.68% (the mean was 40.5%). The higher ash content generally reflects that the sludge has either been digested or heat-treated to convert a large portion of the organic constituents.

The sludge composition is dependent on the nature of pretreatment a given sludge has experienced. For example, the sludge conditioned by a wet oxidation process (intermediate pressure, 300-400 psi; oxidizing atmosphere; temperature of 250-375 F) has a significantly different analysis and a lower heating value compared to an untreated sludge (low C, H but higher oxygen content compared to the untreated materials).

The compositional differences between various sludges can be significant; these differences will be discussed elsewhere. It is interesting to note that the pyritic sulfur is the dominant sulfur type for several sludge. The presence of this large concentration of pyrite is not typical of domestic sludges but suggests the formation of pyritic sulfur from organic sulfur by bacterial action.

3. Comparison of Various Correlations

Attempts were made to estimate the heating value of sludge using correlations widely reported in the literature applicable for coal (and oil shale). In particular, the equation by Mott & Spooner and the Data Base equations were compared with the newly developed correlation.

The percent variation between the measured and the predicted values were calculated for each model by the following equation:

% Variation = 100 x (Predicted-Measured)/Measured

The variations (between the measured and predicted values) for the three models are summarized in Figure 5. The model developed in this study provides a <u>mean variation</u> of 0.019% between the predicted and the measured values. The <u>maximum variation</u> between the measured and predicted values was never greater than 2.83%, based on the new model. In contrast, the Data Base Equation provides a maximum variation of 10.2% while the equation by Mott & Spooner yielded a maximum difference of 14.8% between the measured and predicted values.

Figure 6 compares the measured and predicted heating values based on the Data Base Model. The disagreement between the predicted and measured values in Figure 6 is much larger than those shown in Figure 7 (based on the new correlation developed in this study).

4. Evaluation of the New Correlation

Figure 7 compares the measured and predicted heating values calculated based on the correlation developed in this study. The following equation describes this model:

$$Q \text{ (Btu/lb)} = 241.89*C + 264.26*H + 236.2*S + 20.99*Ash - 4174.68$$

R^2 for the model is 0.99. The parameter measures the proportion of total variations explained by the regression. It is calculated by dividing the sum of squares due to regression by the total sum of squares. R^2 is related to correlation coefficient, r, by the following in simple linear regression: r = square root of R^2. In addition, r, has the same sign as the slope of the computed regression.

The F value for the model was 650.6. The F ratio is the ratio produced by dividing the mean square for the model by the mean square of error. It tests how well the model as a whole (after adjusting for the mean) accounts for the behavior of the independent variable.

The P value for the model was 0.0001. P defines the "observed level of significance." In statistical terms, the level of significance, alpha, of a test is defined as the probability of rejecting the null hypothesis (i.e., no linear relationship between the dependent and independent variables) given the null hypothesis is true. The P-value gives us the largest value of alpha that would lead to the acceptance of the null hypothesis. In other words, from statistical standpoint, the correlation developed is highly significant.

SUMMARY & CONCLUSIONS

The following conclusions are derived based on this study:

o   The heating value of dry municipal sewage sludge is considerably higher than tar sand or oil shale but lower than that of bituminous coal. The atomic H/C ratio of sewage sludge, however, is higher than that of bituminous coal, but comparable to the H/C ratio of oil shale. Some industrial biosludges can have heating value comparable to that of low rank coal.

o   The volatile matter content of sludge is higher than that of coal, oil shale or tar sand.

o   The compositional characteristics (C, H, N, S and ash) of sludge can vary widely among sewage sludge of different origin. Wet oxidation of sewage sludge significantly reduces its heating value as well as its C and H content.

o   The conventional equations developed for coal are not readily applicable for sewage sludge. The equation developed in this study serve reasonably well for estimating the heating value of sludge of various origin based on its analysis (C, H, S, and ash).

REFERENCES

1.   V. T. Chow, R. Eliassen and R.K. Linsley, Editors, "Wastewater

Engineering: Treatment, Disposal & Reuse", McGraw-Hill, 1979.
2. Federal Register, "National Sewage Sludge Survey: Availability of Information and Data, and Anticipated Impacts on Proposed Regulations; Proposed Rule," Vol 55., No. 218, 40 CFR Part 503, Nov 9, 1990.
3. Willson, W. G. et. al, "Low-Rank Coal Water Slurries for Gasification," Final Report by UNDEERC, EPRI Report No. AP-4262, Nov., 1985.
4. Mott, R. A. and Spooner, C. E., "The Calorific Value of Carbon in Coal," Fuel 19, 226-31, 242-51 (1940).
5. Selvig, W. A. and Gibson, F. H., "Calorific Value of Coal," in Lowry, H. H. ed., Chemistry of Coal Utilization 1, 139, New York, 1945.
6. Mason, D. M. and Ghandi, K., Am. Chem. Soc. Div. Fuel Chem Preprints, 1980, 25(3), 235.
7. Boie, W., "Fuel Technology Calculations," Energietechnic 3, 309-16, 1953.
8. Grummel, E.S., and Davis, I. A., "A New Method of Calculating the Calorific Value of a Fuel From Its Ultimate Analysis," Fuel 12, 199-203, 1933.
9. Neavel, R. C., S. E. Smith, E. J. Hippo, and R. N. Miller, Fuel 65, 3, pp. 312-320, 1986.
10. Khan, M. R., K. S. Seshadri, and T. E. Kowalski, Energy & Fuels, 3, 412-420, 1989.
11. Khan, M. R., Energy & Fuels, 2, 834-842, 1988.
12. SAS User's Guide: Basic, Version 5 Edition; SAS Institute; Cary, NC, 1985.

Figure 1

Comparison of Heating Values
of Various Feedstocks (Dry-basis)

Btu/lb, dry (Thousands)

Bit Coal (Pitt#8) Sub-bit (Wy) Oil Shale (Col#)Tar Sand (Asp)- Sewage Sludge

Feedstock

#33 GPT; Khan, Energy Fuels #87/-89

Comparison of H/C (Atomic)
of Various Feedstocks (Dry-basis)
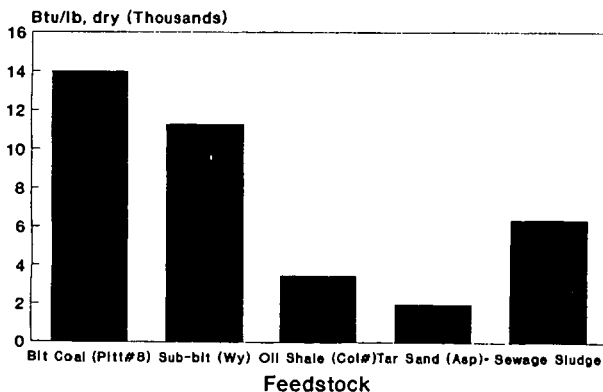
H/C (Atomic)
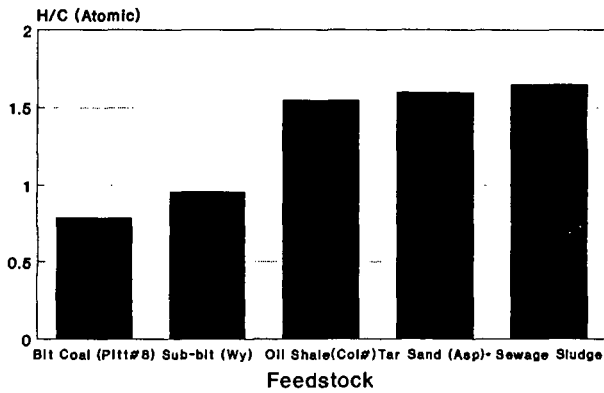
#33 GPT; Khan, Energy Fuels #87/·89

Figure 3

Figure 4

Variations in Sludge Heating Value   Variations in Ash Content
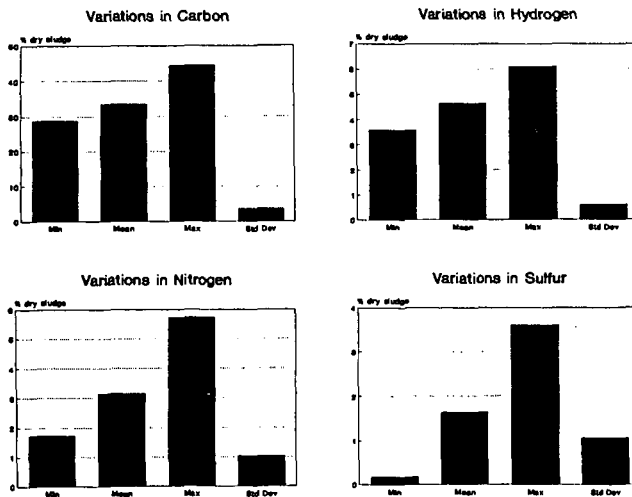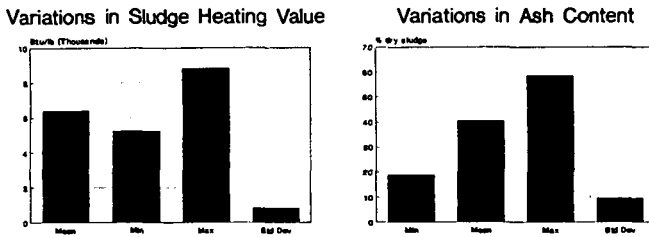
Figure 5

Comparison of Various Models
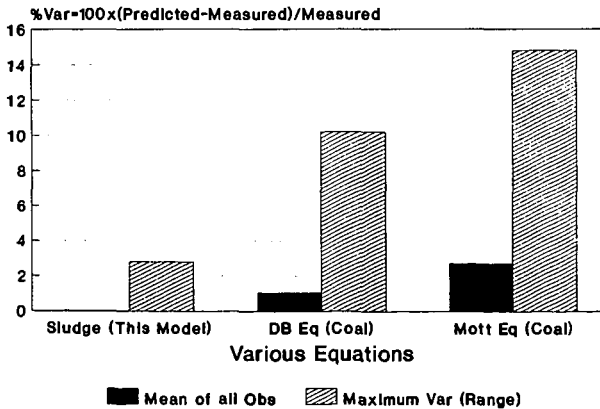
Figure 6

Predicted & Measured Heating Value For Sludge

DATA BASE EQUATION

Predicted & Measured Heating Value For Sludge

MODEL   DEVELOPED IN THIS STUDY
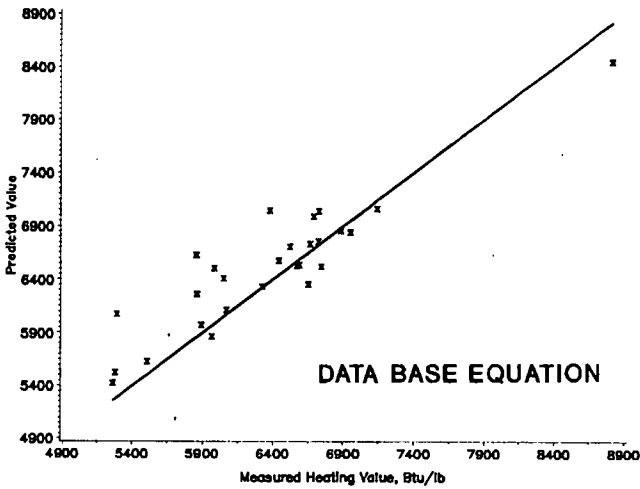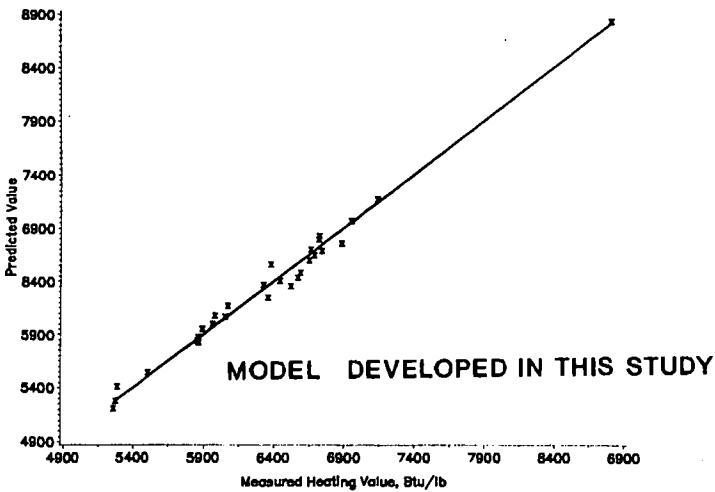
Figure 7

DRYING FUELS WITH THE CARVER-GREENFIELD PROCESS

Ernest A. Kollitides and Thomas C. Holcombe
Dehydro-Tech Corporation
6 Great Meadow Lane, E. Hanover, NJ 07046

Keywords: Drying, evaporation, solvent extraction

INTRODUCTION

Over 80 plants utilizing the Carver-Greenfield (C-G) Process ® have been licensed worldwide during the past 30 years to dry and convert a wide variety of sludges and other wastes into valuable products, such as fuel, animal feed, and fertilizer. Many of these plants generate energy from such wide-ranging feedstocks as sewage sludge, industrial bio-sludge, wool scouring waste, wood pulp mill sludge, chocolate processing waste, brewery sludge, and dye waste. Table I summarizes those C-G Process™ applications in which some or all of the dried wastes are used as fuels.

PROCESS DESCRIPTION

The patented C-G Process uses the innovative approach of dispersing the waste in a solvent and evaporating all the water out of the suspended solids. A simplified process flow diagram of the C-G Process is shown in Figure 1. The waste is mixed with a solvent to form a slurry containing about 5 lbs solvent/lb solids. The solvent properties can be optimized for the particular application. In cases where the dried solids are to be used as a fuel, a petroleum oil is typically used as the solvent. The waste/solvent slurry is circulated through an energy-efficient evaporator system to evaporate virtually all of the water from the solids. Water levels below 5 percent are typically achieved. Either multi-effect evaporation or mechanical vapor recompression is used to achieve very low energy requirements, in the range of 300 to 500 BTUs per pound of water evaporated, versus over 2000 BTUs per pound for conventional drying processes. The solvent fluidizes the mix and creates a low slurry viscosity, thereby ensuring high heat transfer coefficients and minimal scaling/fouling of the system as the water is evaporated. While evaporation of the water is going on, the solvent extracts oil-soluble contaminants from the waste as well. Since the slurry is raised to over 250°F during processing, any pathogens or other micro-organisms present in the waste are destroyed, thereby avoiding problems with product handling and storage.

After evaporating the water, the slurry is fed to a centrifuge to separate the bulk of the solvent from the dried solids. The residual solvent is removed from the centrifuge cake by "hydroextraction", a desolventizing step involving evaporation and gas stripping. Essentially all of the solvent is recovered and reused in the process. Extracted solvent-soluble compounds can be recovered by distilling the solvent and burned as a fuel separately from the solids.

Through commercial experience and continuing research, a simpler, less costly and highly reliable version of the C-G Process has been developed. The new process configuration eliminates the more complex equipment used in earlier plants, such as vacuum hydroextraction and slurry-to-slurry heat exchangers. Feedstocks with widely varying compositions can be handled easily, without the need for recycling dry solids.

SLUDGE DRYING

The drying of municipal sewage sludge is an important application of the C-G Process. As shown in Table I, the City of Los Angeles, the County of Los Angeles, and the City of Tokyo have all recently built C-G Process facilities to dry sludge prior to incineration for the generation of steam or electricity. Sewage sludge typically has an energy content of 6,500 BTU per pound of dry solids, although the moisture content has a major impact on the availability of the energy. As shown in Figure 2, drying sewage sludge completely creates a fuel with a net available heat of almost 4000 BTUs per pound of solids. Drying sludge also permits high flame temperatures (2000 to 3000 °F), thereby improving the quality of the flue gas by maximizing the destruction of any toxic compounds present.

The C-G Process facility at the City of Los Angeles is designed to handle over 400 dry tons per day of sewage sludge derived from 3.5 million people living in a 600 square-mile area. The dried sludge is fed to a fluidized bed gasifier which employs recycle flue gas followed by two stages of after-burning. This staged combustion of the pyrolysis gas results in minimum NO_x formation and results in air emissions below those experienced prior to this energy-recovery project. The design energy equivalent of the dried sludge is over 1000 barrels of oil per day.

PEAT DRYING

Most of the peat used to produce energy today is sun-dried in production fields. This method is obviously highly dependent upon the weather and has a short production season, especially in northern countries such as Finland. Working with the Technical Research Centre of Finland, laboratory and pilot plant tests were conducted to demonstrate the effectiveness and efficiency of the C-G Process in drying peat.

One of the important side benefits of the C-G Process is its ability to extract compounds from the solids during the drying steps. Bitumen is a major constituent of peat which can be extracted. Extracting bitumen prior to combustion or gasification is an advantage since the bitumen can be sold as a valuable by-product and it minimizes waxy depositions in the combusting equipment.

Studies were done to determine the solvent which optimizes total process performance. Iso-octanol was found to provide the best balance between bitumen extraction, fluidization capabilities, and cost.

REFINERY WASTES

Several tests have demonstrated the ability of the C-G Process to dry and detoxify refinery wastes, such as slop oils, DAF sludges, API separator bottoms, tank bottoms, bio sludges, and primary/secondary emulsions. In one typical study, a hazardous oily sludge was taken from a refinery wastewater pond in the Northeast and tested in DTC's laboratory. As shown in Table II, the material contained 1.3 pounds of indigenous hydrocarbons per pound of solids. One sample was treated with solvent once. A second sample was treated with distilled solvent twice. The concentrations of indigenous hydrocarbons in the solids were only 2.0 and 0.2 weight percent, respectively, after treatment. The original slop oil was unsuitable for landfilling due to the presence of a variety of hazardous hydrocarbon compounds. After treatment by the C-G Process, an independent testing laboratory determined that both solids samples met all the requirements for non-hazardous landfilling as specified by the U.S. EPA. The extracted indigenous hydrocarbons can be recycled to the front end of a refinery or burned as high BTU content fuel.

CONCLUSIONS

The C-G Process, licensed by Dehydro-Tech Corporation, is a versatile process for drying and solvent extracting wastes to produce fuels and byproducts. It has been used for a wide variety of applications and is being considered for new applications, such a peat and refinery wastes. The technology should play a growing role in the "waste to energy" markets.

REFERENCES

Bress, D. F., "Energy from Sludge-derived Fuels: the Hyperion Energy Recovery System", April, 1986.

"Carver-Greenfield Process ® for a Cleaner Environment", Dehydro-Tech Corporation brochure, 1988.

Crumm, Clifton James, and Kathryn A. Pluenneke, "Development of an Efficient Biomass Drying Process and its Commercial Use for Energy Recovery", presented to the Institute of Gas Technology Symposium, Orlando, Florida, February 1, 1984.

"EPA Examines Oil-based Extraction Process", Process Engineering, June, 1990.

Greenfield, Charles, "Treatment of Industrial Wastes by Multi-Stage Evaporation Drying", presented at the 67th Annual Conference of the New Jersey Water Pollution Control Association, Atlantic City, New Jersey, May 12, 1982.

Holcombe, Thomas C., et al, "Use of the Carver-Greenfield Process for the Cleanup of Petroleum-contaminated Soils", presented at the New York-New Jersey Environmental Expo '90, Secaucus, New Jersey, October 17, 1990.

Johnsson, P., et al, "Possibilities and Benefits of Bitumen Recovery in Peat Drying", presented at the International Symposium on Peat/Peatlands Characteristics and Uses, Bemidji, Minnesota, May 16-19, 1989.

"The L.A. Solution", Heat Engineering, January-April, 1986.

Makansi, Jason, "Power From Sludge", Power, February 1984, p. S-1.

U.S. Environmental Protection Agency, "Dehydro-Tech Corporation (Carver-Greenfield Process for Extraction of Oily Waste)", The Superfund Innovative Technology Evaluation Program: Technology Profiles, EPA/540/5-89/013, November 1989, p. 31.

Walters, Sam, "Benefits from Biowaste," Mechanical Engineering, April 1985, p. 70.

TABLE I
CARVER-GREENFIELD PROCESS WASTE TO FUEL APPLICATIONS

Location	Capacity (US DTPD)	Feed Type	Feed Solids (wt%)	Product Use	Startup Date
Los Angeles	420	Digested municipal sludge	19	Combustion for electricity generation	1992
Japan	50	Undigested municipal sludge	20	Combustion for energy and cement additive	1989
Italy	1.3	Digested municipal sludge	40	Combustion for electricity generation	1988
Los Angeles	400	Digested municipal sludge	20	Combustion for electricity generation	1987
Russia	48	Dye wastes	14.3	Fuel	1986
Italy	55	Dye waste sludge	20	Fuel	1985
Virginia	20	Bio-sludge and wool scouring waste	2	Fuel and lanolin	1985
Denmark	1	Refuse derived fuel and sewage sludge	10-50	Utility boiler fuel	1985
Washington State	50	Wood pulp mill activated sludge	13	Animal feed and fuel	1979
Indiana	24	Pharmaceutical plant wastes	2-4	Fuel	1978
Pennsylvania	0.3	Chocolate waste	2	Fuel	1978
Colorado	30	Brewery undigested sludge	4	Animal feed and fuel	1977
Japan	15	Undigested and digested municipal sludge	4.5-5	Utility boiler fuel	1976
Japan	25	Primary sewage sludge	2	Utility boiler fuel	1975
Mexico	7.2	Pharmaceutical wastes	6	Fuel	1975
Japan	1.3	Primary sewage sludge	20	Fuel	1973
Indiana	9.6	Pharmaceutical wastes	2-4	Fuel	1970
Pennsylvania	10	Undigested air floatation sludge	8	Utility boiler fuel	1964
Total	1,167.70				

TABLE II
SLOP OIL TREATMENT RESULTS

Component	Feed Composition (weight percent)	Treated Solids Composition (weight percent)	
		Treated Once	Treated Twice
Solids	12.0	97.8	99.6
Indigenous Hydrocarbons	16.0	2.0	0.2
Water	72.0	0.1	0.1
Solvent	0.0	0.1	0.1
Total	100.0	100.0	100.0

FIGURE 1
SIMPLIFIED CARVER-GREENFIELD PROCESS FLOW DIAGRAM
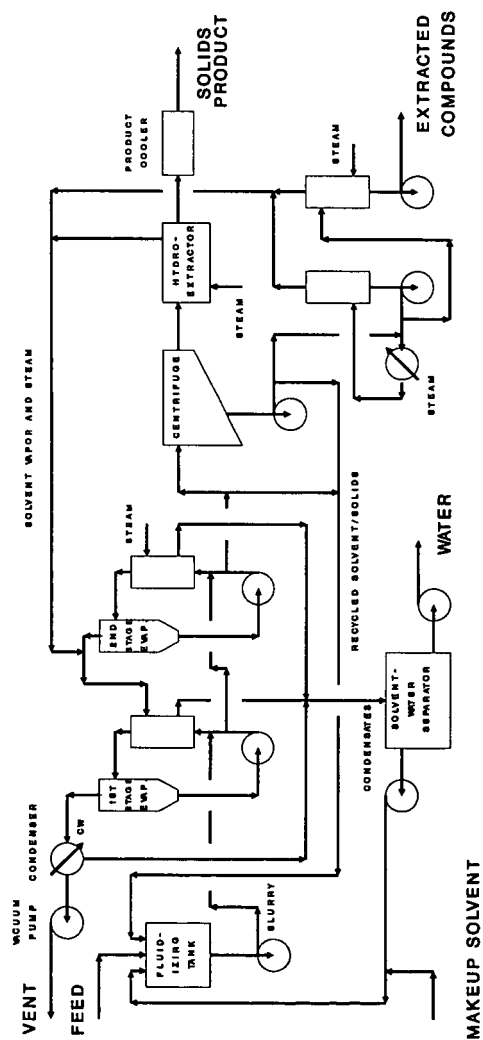
FIGURE 2
NET HEAT AVAILABLE IN SEWAGE SLUDGE
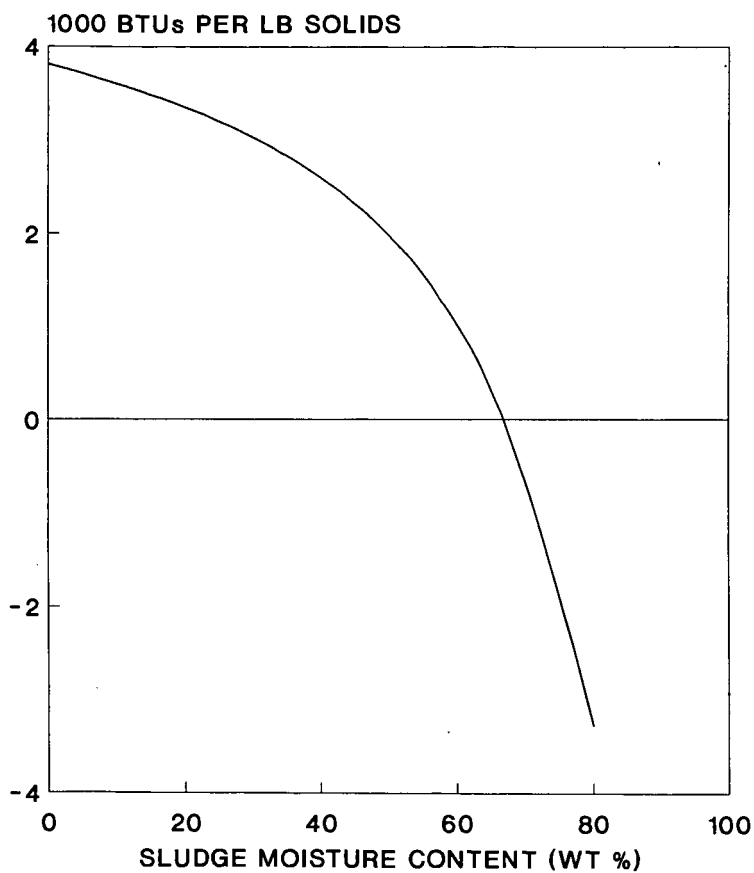
BASIS: 1400 DEG F, 50% EXCESS AIR

PRETREATMENT OF MUNICIPAL SEWAGE SLUDGE FOR GASIFICATION

Matthew A. McMahon, M. Rashid Khan, C. Albert and R. McKeon
Texaco Research and Development
P. O. Box 509, Beacon, NY 12508

ABSTRACT

The flow behavior of coal water slurry is significantly degraded
when untreated sludge is mixed with coal at a sufficient
concentration. Various methods of treating sludge were evaluated in
an effort to make coal slurries (containing more than 25 per cent
sludge) or treated sludge relatively more fluid so that they could
be pumped through pipes and nozzles into a pressurized gasifier.
Drying sludge in commercial dryers at temperatures ranging from 180
to 400°F significantly improved its slurrying characteristics with
coal. The fluid characteristics could also be improved by removing
water under vacuum, dewatering with high intensity filter presses
and subjecting the sludge to shear stresses. Slurry viscosity
measurements were made at 70 to 212°F in viscometers.

INTRODUCTION

Over 26 billion gallons of waste water are treated by about 15,000
publicly owned treatment works in the United States serving >70% of
the population (1). This treatment results in the production of 7
million metric tons per year of sewage sludge. Most of this is
applied to the land while about 20% is incinerated and another 6%
is dumped into the ocean. The recent ban on ocean dumping along
with a decreasing number of landfills and other environmental
concerns have created a need for environmentally sound sewage
disposal alternatives.

The Texaco Coal Gasification Process, which has operated
satisfactorily in large scale facilities for several years, appears
to offer attractive features as such an alternative. Coal slurries
containing about 60% coal are a usual feed for the process and
concentrated sludge slurries in the form of sludge filter or
centrifuge cakes containing 70 to 80% water are a usual product of
water treatment plants. Sludge in this form is a low quality
fuel, however, with an insufficient btu content to be gasified
alone in the process. It must therefore be mixed with an auxiliary
higher quality fuel such as coal, oil or gas to form a satisfactory
feed for the process.

In addition to having a satisfactory heat content, slurry mixtures
that are suitable feeds for the process must be pumpable at high
concentration and must contain sufficient sludge to justify the
incremental cost of handling it.

This paper describes the results of our efforts to characterize the fluidity properties of sludge/coal slurries and to identify a treatment process that would enable sludge concentrations in pumpable slurries with coal to be increased to practical levels.

The hydraulic transport of particulate solids has recently been reviewed (2). Campbell and Crescuolo examined the rheological characteristics of dilute sludge slurries (3). Beshore and Giampa reported on the rheological properties of concentrated coal slurries containing small amounts (up to 10%) of sludge (4). No detailed studies of the rheological characteristics of coal slurries containing high concentrations of raw or thermally treated sludge have been reported. A fuel comprised of raw (undewatered) sludge and coal has also been claimed to be pumpable and useful as a boiler fuel (5).

EXPERIMENTAL

The viscometer used for this work was developed in our laboratory and calibrated with oils of known viscosity. Usually, apparent viscosity vs. solids concentration curves were obtained from which we determined the total solids that could be included in a slurry at a given viscosity. Replicate measurements indicated that the standard deviation of measurements using this technique was 0.79. About 80 grams of slurry was required for each measurement. Slurries were prepared by mixing the desired amounts of sludge, coal and water to a measurable consistency in the measuring cup and noting the torque at a stirrer speed of 600 rpm. Measurements were then repeated as incremental amounts of water were subsequently added. Torques were related to viscosities by measurements on the oils of known viscosity. In addition, a Haake viscometer RV-100 was also used for rheological measurements.

To establish the patterns of sludge behavior, dewatering of sludge was achieved by an advanced dewatering technique, high intensity press (HIP). The HIP was simulated by distributing dewatered cake on a 4"x4" piece of filter fabric which was supported by a specially designed perforated square metal tray. This was surrounded by a square metal box. A similar piece of fabric was placed over the sample followed by an upper square tray. Pneumatic piston pressure was then applied to the upper tray forcing out entrapped water. The applied pressure was changed in various retention times (zones 1 through 4) to simulate the actual HIP zone pressures. Upon completion of the pressure cycles, the pneumatic lever was pushed up and the pressure box removed quickly. HIP applied a mechanical pressure of 125 psi (compared to only 25 psi for commonly used belt press filters) to effect dewatering. It is important to minimize contact of the dewatered sludge with the wet belt to avoid resorption of moisture by the sludge. The solid content was determined by actual measurement and the throughput was calculated by empirical equations developed by Andritz, the manufacturer of the device.

RESULTS AND DISCUSSION

1. Sludge Characteristics

The digested sludge used for most of the measurements made in this study was obtained from water treatment plants in Los Angeles County, Los Angeles City and San Bernadino County in California. The as-received filter cakes were amorphous, fibrous materials containing 20 to 30% total solids.   These materials were not pumpable but could be made so by diluting to about 15% total solids.   Polymeric flocculating agents were employed in their preparation. Their composition is compared with coal and peat in Table 1. Digested sludge solids generally contain: 30-60% volatile solids, 5-20% grease and fats, 5-20% protein, 10-20% silica and 8-15% cellulose (6).

2. As Received Sludge/Coal Slurries

For the purposes of this work we needed to know the maximum amount of sludge that could be incorporated into a pumpable slurry with coal.   Economics dictated   that commercially viable sludge containing feeds should include at least 25% sludge and have a total solids content of above 50%. Experience with coal slurries indicates that slurries having apparent viscosities of about 1000 cP are pumpable. Results of viscosity measurements on a number of sludge/coal slurries containing varying amounts of Los Angeles sludge in Utah-Sufco coal showed that the amount of total solids which can be incorporated into a pumpable slurry decreases with increasing sludge content. It was also apparent that in the 1000 to 2000 cP range, small increases in total solids content of slurries effect large increases in viscosity. None of these mixtures was considered a satisfactory fuel because either their sludge or total solids content was too low at the 1000 cP pumpable viscosity.

3. Rheology of Evaporatively Dried Sludge

Thermal treatment of sludge improves its slurrying characteristics. Heat treated sludge is readily dewatered on filters to solids concentrations of 30 to 50%, while unheated sludge is usually dewatered to about 20 to 30% only with the aid of polymeric or inorganic conditioning agents (6,7,8).

Dilute sludge slurries containing less than 5% solids are thermally treated on a commercial scale throughout the country in different types of dryers and thermal treatment units.   Thermal treatment over the wide temperature range encompassed by these processes did, in general, improve slurrying properties. The products of various treatment processes are physically and compositionally different from raw sludge (Table 2).   Some of the products are dry homogeneous powders somewhat coal-like in appearance while others are quite fibrous containing about 60% moisture.   The moist products could not be ground into a powder

1672

satisfactorily for slurry testing without drying them first.

Results of viscosity tests on slurries prepared from these materials are summarized in Table 3. We usually measured the slurrying characteristics of the neat sludges and of mixtures containing 30% sludge and 70% coal (dry basis). Clearly, all of these materials demonstrated slurrying characteristics far superior to those of untreated sludge. Some treated sludges were coal-like in slurry behavior hardly affecting the fluidity of the coal at low concentrations, while the other materials degraded the fluidity of the slurries to varying extent. This behavior is not unexpected since these materials have not only been heated at different temperatures but under different conditions. For example, sludge is heated while suspended in oil in one process in a manner that oil soluble compounds can be extracted from it, while in others, organic components in sludge are simply volatilized. Overall, the rheological characteristics of sludge and the sludge we treated in various ways were found to be very consistent. The rheology of a thermally treated sludge, as a function of shear rate is shown in Figure 1.

Thermally dried sludge could also be slurried in oil but the viscosity of the slurry oil determined to some extent the amount of slurry solids that could be included in a pumpable mixture.

Another factor that influences the rheology of sludge slurry is the applied shear rate. At relatively low shearing rates, the untreated sludge filter cakes could be reduced from an intractable solid with no meaningful viscosity to pourable liquids. This behavior is consistent with the thixotropic nature of sludge. As would be expected, more of this sheared product could be incorporated into a pumpable slurry than the "as received" sludge. This phenomenon is attributable to at least two factors: the first of these is the simple shearing of the cellulosic and polyamide flocculating polymers in the sludge. The second is a consequence of the shearing stresses on the flocculated colloidal particles. The drag forces and unfolding of the flocculated particles probably release trapped water and make it available as a carrier fluid with a consequent decrease in viscosity (Figure 2).

In an effort to explore various means for treating sewage sludge for improving its slurrying characteristics with coal, we have found that virtually any means of removing water trapped in the raw sludge filter cake (including thermal treatment, advanced dewatering, shearing, vacuum drying and simple air drying) appear to improve the slurrying characteristics.

REFERENCES

1. R. K. Bastion, " An Overview of Sewer Sludge Programs in the U.S.", Proceeding of the National Conference on Sewage Treatment Plant Sludge Management, May, 1987.
2. P. A. Shamlou, "Handling of Bulk Solids, Theory and Practice",

Butterworth and Company, Ltd., 1988.

3. H. W. Campbell and P.J.Crescuolo, "The Use of Rheology for Sludge Characterization," <u>Water Science and Tech.</u>, pp. 475, 1982.

4. D. G. Beshore and V.M. Giampi, U.S.Patent 4,762,527, "Slurry Fuel Comprised of Heat Treated, Partially Dewatered Sludge with a Particulate Solid Fuel and its Method of Manufacture", 1988.

5. L. A. Rodriguez, R.A. Ashworth, R. Armstead, P.A. Aristedes and N.B. Spake, U.S. Patent 4,405,332, "A Fuel Composition", 1983.

6. V. T. Chow, R. Eliassen and R.K. Linsley, Editors, "Wastewater Engineering: Treatment Disposal Reuse", McGraw-Hill, 1979.

7. T. P. Nichols, J.N.Lester and R. Perry, "The Influence of Heat Treatment on the Metallic and Polycyclic Hydrocarbon Content of Sewage Sludge," Science Total Environment, 14 (1), 19, 1980.

8. D. Reimann, "Thermally Conditioned Sewage Sludge", Umwelt, (6), 332, 1987.

9. W. D. Hatfield, "The Viscosity or Pseudo-plastic Properties Sludge," Sewage Work Journal, 10 (1), 3, 1938.

10. C. L. Doyle and D.M. Haight," Sludge Conditioning with Organic Polyelectrolytes," Proceedings of the National Conference on Municipal Treatment Plant Sludge Management, p. 103, 1986.

Figure 1

Apparent Viscosity vs. Shear Rate for 38.02 wt% Thermally Dried Sludge at 30, 60 and 90 C.
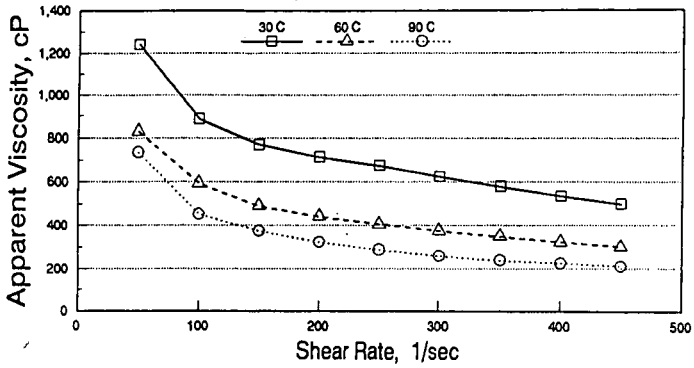
Figure 2
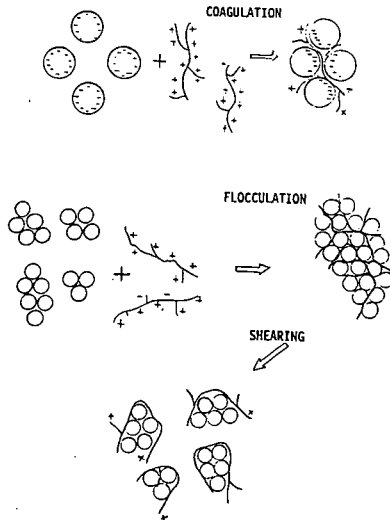
TABLE 1 TYPICAL ANALYSES OF SEWAGE SLUDGE AND OTHER SOLID FUELS								
FUEL	MOISTURE %	ASH	C	H	N	O BY DIFF	S	BTu/lb (DRY)
SEWAGE SLUDGE	80	36	31	4.8	3.9	22.1	1.7	6400
PEAT	83.7	3.4	47.1	5.4	1.4	42.6	0.1	
LIGNITE, TX	29.3	21.5	55.7	4.5	1.0	15.8	1.4	9788
SUBITUMINOUS C, WYOMING	28	7.8	68.1	4.9	1.1	17.2	0.6	11840
BITUMINOUS PITTSBURGH 8	0.8	8.6	76.5	5.1	1.4	5.8	2.5	13765

TABLE 2 ANALYSES OF DRIED SLUDGE FROM VARIOUS PROCESSES					
	LOS ANGELES AS RECEIVED	PROCESS A	PROCESS B	PROCESS C	PROCESS D
% MOISTURE	80.2	3.03	7.93	2.79	9.2
% ASH	36.3	50.91	32.29	31.38	44.0
% C	31.3	30.48	34.71	33.8	28.9
% H	4.84	4.49	4.99	5.32	3.81
% N	3.92	3.96	5.52	2.57	3.21
% S	1.66	1.6	.71	0.62	1.11
% O (BY DIFF)	22.00	8.6	21.8	26.3	19.0

TABLE 3 SLURRYING CHARACTERISTICS OF COMMERCIALLY AVAILABLE THERMALLY TREATED SLUDGES					
PROCESS	MAX TEMP, F	% ASH	SLURRY COMPOSITION SLUDGE %	COAL %	TOTAL SOLIDS AT 1000 CP
A	250	50.9	30 100	70 –	51.0 36
B	1200	32.29	30 100	70 –	58.5 48.2
C	365	33.8	30 100	70 –	45 30
D	358	44.0	30 100	70 –	62 53

PRODUCTION OF CLEAN MEDIUM Btu GAS FROM GASIFICATION OF SLUDGE WASTES

by

K. Durai-Swamy, Prent C. Houck, Qiao D. Feng,
13080 Park Street, Santa Fe Springs, California 90670

Momtaz N. Mansour
5570 Sterrett Place, #206, Columbia, Maryland 21044

Experimental tests were conducted to assess performance of an indirectly-heated, fluidized bed, sludge gasification process employing pulse enhanced heat transfer. Feedstocks included sewage sludge, RDF, lignite, sub-bituminous coal, mild gasification char, SRC residue and black liquor and wastes from pulp mills. Feedstocks were reacted with steam at temperatures of 1150°F - 1500°F to produce a clean medium Btu fuel gas with a higher heating value of approximately 400 Btu/SCF. Heat for the gasification reaction was supplied by means of an integrated pulse combustion system consisting of multiple firetubes immersed within a fluidized bed. This process is being scaled up from laboratory scale (20 lb/hr) to field test demonstration units (2,000 to 6,000 lb/hr). This unique gasification process does not require an oxygen plant to produce medium-Btu gas, thus reducing capital costs significantly. This paper presents the detail of results and progress of scale-up activities.

INTRODUCTION

The potential for recovering energy from renewable sources and organic waste products has been recognized for many years. In recent years and with the realization that fossil fuels (oil and gas in particular) are unrenewable and being depleted at an accelerated rate, the need for an effective technology for utilizing renewable organic sources of energy is a prime consideration for a U.S. Energy Policy.

The paper mill biomass waste is representative of materials discharged from virgin pulp mills and recycle mills located throughout the United States. These sludges typically contain 70 percent moisture as delivered from a belt press. Many mills are currently installing screw presses to reduce the moisture content to 50 percent. The presence of chlorinated organics (such as dioxins) in the sludges from virgin pulp mills, and plastics in the sludges from recycling mills poses serious problems for the landfilling of these wastes. The Hazardous and Solid Waste Act of 1984 (HSWA) restricts land disposal and requires pretreatment at the source prior to final disposal. Increasing disposal costs, diminishing landfill sites, and social and environmental factors are forcing mills to find unique solutions.

MTCI has developed a unique process that reduces the volume of the solid wastes, destroys the chlorinated or-ganics such as dioxins and produces clean fuel gas for use in the mill replacing natural gas.

BACKGROUND

A pulse-enhanced, indirectly heated fluidized bed gasifier system was constructed and tested by MTCI during 1985-1986 for gasification of waste feedstocks under the Phase II of a DOE/SBIR Program. The results of these tests confirmed the technical feasibility of the steam gasification of various feedstocks using the resonance tubes of the MTCI pulse combustor technology as an in-bed heat exchanger. In fact, the system demonstrated a capability for generating a medium-btu product gas of a quality superior to that attainable in air-blown, direct gasification system. The system's overall simplicity, due to the compact nature of the pulse combustor, and the high heat transfer rates attainable within the pulsating flow resonance tubes, provided a decided and near-term potential economic advantage for the MTCI system when compared to alternative direct or indirect gasification systems.

Under Phase II of this DOE/SBIR grant, testing of the gasifier was limited to biomass feedstocks only. In early 1987, Weyerhaeuser Paper Company expressed an interest in testing the MTCI gasifier using black liquor feedstocks. The pulp and paper industry has an ongoing and substantial interest in developing new black liquor recovery methods since the existing technology has significant economic, safety, and environmental shortcomings.

Preliminary feasibility tests were conducted in a 33 lb/hr reactor, which verified the feasibility of the MTCI gasifier with black liquor feedstocks. In order to further develop this technology for mill sludge waste

gasification and black liquor recovery, MTCI received funding from the Department of Energy; the Weyerhaeuser Company; and the California Energy Commission's Energy Technologies Advancement Program (ETAP). A scale-up reactor (200 lb/hr) was constructed and tested for verification of the technology. The tests emphasized the collection of definitive process data on conditions and with a broad range of feedstocks.

These projects were completed in 1989 and have yielded extremely successful results confirming the commercialization potential of the MTCI technology to process a wide spectrum of biomass feedstocks as well as the ability to process mill biomass waste from recycling operations. In these tests, the MTCI gasifier was operated using samples of paper mill biomass waste provided by the Gaylord Container Corporation. This waste is currently being landfilled at a significant expense to Gaylord. Despite the high moisture content and presence of plastic material in these waste products, the MTCI gasifier operated without problems.

DESCRIPTION OF THE PULSE COMBUSTOR

The indirect gasifier tested under this program is supplied heat through the resonance tubes of a pulse combustor. The use of pulse combustion significantly enhances the performance and economics of the indirectly-heated gasifier since heat transfer coefficients can be obtained which are 3 to 5 times that achievable in steady-flow systems.

The physical principles involved in the operation of a pulse combustor are essentially the same as those which govern the undesirable pulsations that sometime plague conventional combustion, however, pulsations or combustion-driven oscillations are induces by design and are intended to improve combustion rates, heat transfer, and system performance. The frequency, intensity, and nature of these self-induced combustion oscillations depends upon the precise geometry of the pulse combustion apparatus.

The pulse combustor consists of three main components: an air inlet valve, a combustion chamber, and a tailpipe or resonance tube. The pulse combustor operates over a natural oscillation cycle as shown in Figure 2. In the first step (Figure 2-1), fuel and air ignite within the combustion chamber. Ignition is spontaneously triggered from hot gases of the previous cycle and is not controlled by a spark plug or other external means. In the second step (Figure 2-2), the combustion-induced pressure rise forces the burning mixture to expand outward toward the tailpipe exit. Although some gases escape through the air inlet, the fluidic design of the air valve significantly impedes flow in this direction. In the third step (Figure 2-3), the momentum of the out-rushing combustion gases creates a suction within the combustion chamber. This results in the purging and recharging of the chamber with fresh air and fuel. The fourth and final step (Figure 2-4) involves recompression of the fuel/air mixture within the chamber. This is followed by spontaneous ignition to repeat the natural pulsation cycle.

Chamber pressure fluctuations are commonly achieved in pulse combustors. These pressure fluctuations are translated into velocity fluctuations of 600 ft/sec within the resonant tailpipe. The velocity fluctuations, which occur at a frequency characteristic of the combustor (30-300 Hz), intensely scrub the convective boundary layer inside the tube surface, thereby enhancing heat transfer rates.

In the conceptual commercial gasifier designed for atmospheric operation, as shown in Figure 3, the pulse combustors are constructed in modules which can be inserted into the side-wall of a refractory-lined containment vessel. The pulse combustor modules can be installed using techniques employed for conventional heat exchange tube bundles. Each pulse combustor will comprise an individual combustion chamber connected to a multitude of resonant heat exchange tailpipes. Since the pulse combustor is of a modular construction, scale-up of the gasifier is anticipated to be straightforward. In fact, MTCI has tested individual pulse combustors at firing rates of 6 MMBtu/hr which are comparable to the size expected for use in commercial systems.

Using the resonance tubes as a firetube bundle substantially alleviates heat transfer limitations on the flue gas side. This is due to the presence of a vigorous oscillating flow field contained within the resonance tubes. The oscillatory flow field, which causes periodic flow reversal, induces a significant level of turbulence in the boundary layer on the inner walls of the firetubes. This, in turn, gives rise to effective heat transfer coefficients (40 to 50 $Btu/hr/ft^2/°F$) which is about five times higher than that for conventional firetubes. Thus, the characteristics for the pulse-enhanced, indirectly-heated gasifier overcomes many of the limitations of the state-of-the-art gasifier systems.

GASIFICATION TESTS

1678

Test Systems

Two separate pulse-enhanced gasifier systems were constructed under this program. The first unit consisted of a 20 cm fluid bed reactor (35 lb/hr) enclosing two pulse combustor resonance tubes. This unit was employed to define essential gasification process data. The second gasifier consisted of a 48 cm reactor (90 Kg/hr) containing eight pulse combustor resonance tubes. The larger unit was intended to provide scale-up design criteria for integration of large, multi-tube, heat exchange bundles. Both of these reactors shared essentially similar basic designs.

The main components of the gasifier test rigs used until 1989 are shown in Figure 3.

Steam was supplied to the fluidized bed reactor (R-1) from a boiler (H-1) where it was injected at the base of the bed through a series of sparge tubes. The fluidized bed consisted of sized calcium carbonate (limestone) particles. The pulse combustor (X-2) was fixed to the base of the reactor with its resonance tubes positioned to penetrate the bed in a U-tube arrangement. Combustion gases were then vented through an induced draft fan (F-2). The feed was injected into the fluid bed using a screw feeder. The feeder was charged periodically with a lock hopper.

Product gas from the reactor entered a hot cyclone (V-2) and disengaged particulate matter which was collected in drum (V-3). The product gas was then incinerated (H-2) and scrubbed (V-4) prior to being vented to the atmosphere. In 1990 a quench scrubber and a condensate heat exchanger were added to remove the water from product gas.

In a commercial operation, a portion of these medium Btu product gases would be delivered to the pulsating heat exchanger as a fuel source. Combustion of these gases provides the heat necessary for the indirect gasification process.

Waste heat at the exit of the pulsating heat exchanger is utilized to superheat the process heat. Additional waste heat is available for feedstock drying, if necessary, or for generation of export steam to be used elsewhere in an integrated plant.

Gas samples were extracted downstream of the hot cyclone. The sample gas was cooled in a condenser and knock-out pot prior to being analyzed by gas chromatography. The condensate was collected and sent to an independent laboratory for analysis of tars and oils. In addition, a screw sample valve, located on the reactor shell, allowed continuous monitoring of the bed carbon content.

Test Results

System testing of the indirect gasifier on biomass/waste feedstocks was conducted. The test results provided detailed information on gas compositions, char and tar/oil yields, and bed carbon inventory levels.

Tests were performed using three different biomass feeds - pistachio shells, woodchips, and rice hulls; two different sludge waste products from a recycle paper mill; and a Kraft mill sludge (the two sludge wastes differed primarily in their plastic content). Table 1 summarizes the ultimate analysis for mill waste and other biomass feedstocks employed in the test program. The ash content of the sludge waste exhibited a high degree of statistical variation.

The waste paper sludge was obtained from a mill located in Northern California. The sludge fraction is composed of short fiber and plastic reject material which is recovered from a clarifier. The dilute waste stream is dewatered in a belt press and delivered to a pile where some additional draining occurs. Currently, the product is hauled by truck to a landfill site for disposal. Disposal costs represent a significant expense for the mill and exceeds $600,000 annually. These sludge wastes are representative of high moisture waste materials which are generated in similar mills located throughout the United States.

Table 2 summarizes the operating conditions for the various test runs. Temperatures were varied over the range of approximately 1215°F to 1450°F. Steam to biomass ratios varied from approximately .75 to 2.6. Test run durations typically ranged from four to ten hours. No process operating problems were encountered for any of the runs, including those with rice hulls which have a high ash content and low ash fusion point.

Selected gas compositions for the various feedstocks are summarized in Table 3. The methane content

1679

appears to be relatively constant (8 percent to 12 percent) over the range of feeds and processing conditions tested. Higher hydrocarbons show a decreasing trend with increasing temperature and a concomitant increase in hydrogen yields. The ratio between carbon monoxide and carbon dioxide appear relatively constant. The dry gas heating value typically ranged from 370 to 418 Btu/scf.

As seen in Table 3, carbon conversion to dry gas ranged from 92 percent to 94 percent for pistachio shells and woodchips. Char and tar/oil yields for pistachio shells diminished noticeably with increasing temperature (1.3 percent at 987°K). Significantly higher char yields were obtained for both rice hulls and paper mill sludge wastes. The increase in char yields for rice hulls is probably due to the associated high ash content of this feed which tends to inhibit the gasification reaction. The higher char yields for the sludge waste is believed to be due to high rates of entrainment exhibited by this fine, fibrous material. Also, since the sludge waste contained high moisture levels, vaporization of the feed moisture resulted in gas superficial velocities within the fluid bed which were generally higher than for the other feeds tested, thus further exacerbating the entrainment problem. It is anticipated that closer control of gasifier superficial velocities and modest recycle of fly ash can significantly enhance carbon utilization rates. It should be noted that the char and tar/oil levels obtained in these tests are comparable to those achieved for similar feeds in other gasifiers which operate at significantly higher temperatures.

CONDENSATE

Effluent from the gasifier includes condensed steam which contains tar/oil and particulate products. The Biological Oxygen Demand (BOD) level for the condensate was measured at 3920 mg/L. However, a significant portion of the BOD is in the form of carbon particulate which can be clarified or filtered. Further investigation will be needed to determine the achievable quality of wastewater discharge from the gasification plant.

DIOXIN REDUCTION

A key objective of the sludge gasification trial was to determine the dioxin destruction efficiency of the indirect gasifier. Dioxin, which is present in the feed sludge, has been attributed to the pulp-bleaching operation which includes a chlorination step. Dioxin levels were measured for the feed sludge, cyclone ash, condensate, and gasifier bed material. The dioxin feed and effluent results are summarized in Tables 4 and 5. As seen in Table 4, the feed sludge contains a total dioxin concentration of 1543 ppt. By comparison, the gasifier ash effluent contains only 100.2 ppt of dioxin. Including the effect of mass reduction, the net dioxin destruction efficiency is approximately 97.5 percent. It should be noted that dioxin concentrations in the gas product were not measured. However, the gas condensate showed very low dioxin levels and any dioxin that might be present in the gas phase is likely to be destroyed with high efficiency upon subsequent combustion.

The high destruction efficiency for the indirect gasifier is thought to be attributed to the use of calcium material within the fluid bed which serves to absorb HCl released during gasification, and the absence of oxygen in the reducing environment of the reactor.

Recent studies (Ref. Hagenmaier, H., et al) on the occurrence of dioxin in fly ash from waste incinerators have implicated a metal-catalyzed dioxin formation reaction which is facilitated by the presence of surplus oxygen at a temperature regime of approximately 575°F. Above 1100°F dioxin destruction rates exceeded dioxin formation rates. However, at somewhat lower temperatures, it was postulated that a Deacon-type mechanism was responsible for the release of molecular chlorine as shown below:

$$CaCl_2 + \tfrac{1}{2}O_2 \rightarrow CaO + Cl_2$$
$$CaO + 2HCl \rightarrow CaCl_2 + H_2O$$

$$2HCl + \tfrac{1}{2}O_2 \rightarrow H_2O + Cl_2$$
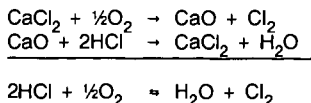
Under this assumption, oxygen in the incinerator flue gas reacts with $CaCl_2$ or other metal chlorides contained in the fly ash to form chlorine which subsequently gives rise to the formation of organochlorine compounds and finally dioxins.

1680

These studies further showed that no such dioxin formation occurred in an oxygen-deficient (nitrogen) environment. On the other hand, dioxin formation increased in an air stream spiked with HCl.

Based on this evidence, there is reason to conclude that gasification of chlorinated waste material may avoid the dioxin-forming reactions that contribute to dioxin emissions from incineration processes.

ASH TOXICITY

EP toxicity extract tests were performed on a typical feed, bed and cyclone ash materials. The results of tests are summarized in Table 6. The results indicate that cyclone char/ash disposal should not present a problem.

CONCLUSIONS

The test results confirmed the ability of the MTCI indirect gasifier to handle a wide range of biomass feedstocks including those with high moisture content, low ash fusion temperature, and high plastic materials content. Also, product gas quality was shown to be quite insensitive to feedstock moisture level.

The gasifier does not require any special feedstock preparation such as pelletization. The gasifier produces a medium-Btu gas without the consumption of oxygen. The reactor is easily scaled, since the pulse combustor tube bundles are constructed in modules. The gasifier produces a gas with a hydrogen to carbon oxide ratio considerably higher than oxygen-blown systems, thus making it particularly attractive for methanol production. The gasifier integrates well with both methanol and high purity hydrogen plants.

The results of these tests have provided a significant data base for preparing designs at the 50 ton/day level. MTCI will field demonstrate the gasifier at a commercial paper mill in the fall of 1991.

SCALE-UP AND COMMERCIALIZATION PLANS

MTCI is currently engaged in the design of scaled up units for 2 ton/hr (TPH) black liquor gasification and 1 TPH mill sludge gasification. The 2 TPH black liquor gasifier will be constructed and field-tested in 1991-1992, and the sludge gasifier will be constructed and operated in 1991-1992. The list of sponsors of these field test plants includes California Energy Commission, Department of Energy, Weyerhaeuser Paper Company, James River Paper Co., and Mead Paper Company. There are other paper companies interested in MTCI technology.

REFERENCES

"Testing of an Advanced Thermochemical Conversion System," MTCI, DOE Contract No. DE-AC06-76RLO1830, January 1990.

Hagenmaier, H., et al., "Catalytic Effects of Fly Ash from Waste Incineration Facilities on the Formation and Decomposition of Polychlorinated Dibenzo-p-dioxins and Polychlorinated Dibenzofurans" Environ. Sci. Technol., 21:1090-1084 (1987).

ACKNOWLEDGMENT

TABLE 1
ANALYSIS FOR FEEDSTOCKS TESTED IN PULSE-ENHANCED INDIRECT GASIFIER

ULTIMATE (MAF Basis)	Pistachio Shells	Wood Chips	Rice Hulls	Recycle Mill Fiber Waste	Kraft Mill Sludge	RDF Sand Bed	MSW Sand Bed
Carbon	49.51	49.33	49.09	50.00	59.36	46.96	58.20
Hydrogen	6.18	6.74	6.17	6.55	6.90	7.58	8.42
Oxygen	43.96	43.67	44.19	42.76	28.02	43.84	26.45
Sulfur	0.11	0.16	0.04	0.31	1.04	0.86	1.63
Nitrogen	0.24	0.10	0.51	0.38	4.68	0.77	5.30
Total	100.00	100.00	100.00	100.00	100.00	100.00	100.00

PROXIMATE (As rec'd wt %)							
Moisture	8.74	20.46	8.67	49.50	62.40	17.04	5.47
Ash	0.41	0.18	20.48	2.80	7.10	12.66	32.58
Volatile	N/M	N/M	N/M	N/M	N/M	60.23	60.82
Fixed Carbon	N/M	N/M	N/M	N/M	N/M	10.07	1.13
Total	9.15	20.64	29.15	52.30	69.50	100.00	100.00
HHV (Btu/lb), dry	8334	8334	8334	8850	10353	7515	6607

TABLE 2
OPERATING AND PROCESS CONDITIONS FOR BIOMASS TEST RUNS

FEEDSTOCK	TEMP. (F)	AVERAGE FEED RATE (lb/hr)	STEAM RATE (lb/hr)	STEAM TO BIOMASS (lb/lb)	TOTAL FEED (lbs)
Pistachio Shells	1317	35.5	26.0	0.73	337.1
Pistachio Shells	1216	30.6	31.5	1.03	115.3
Wood Chips	1286	22.9	31.4	1.37	205.7
Rice Hulls	1326	30.8	26.0	0.84	185.5
Recycle Paper Mill Sludg	1250	17.6	36.5	2.07	118.8
Kraft Mill Sludge Waste	1250	17.6	36.5	2.07	299.6
RDF (sand bed)	1450	11.0	29.0	2.64	66.0
MSW (sand bed)	1410	12.0	28.0	2.33	62.0
MSW (limestone bed)	1306	15.2	27.0	1.78	84.0

TABLE 4
DIOXIN LEVELS IN PAPER MILL SLUDGE
FEED AND GASIFIER EFFLUENTS
(In parts per trillion, ppt)

	DIOXIN	TCDD	TCDD	PCDD	HXCDD	HPCDD	OCDD
FEED SLUDGE	1543	74	33	69	580	150	670
BED MATERIAL	10.0	N/D	N/D	N/D	N/D	2.9	7.2
CYCLONE ASH	100.2	53	27	14	14	9.5	9.7
CONDENSATE	0.33	0.23	0.07	N/D	N/D	N/D	0.33

TABLE 5
DIOXIN AND FURAN ANALYSIS OF RDF FEEDSTOCK AND CYCLONE CAUGHT ASH IN THE DECEMBER 7, 1990 TEST (ng/g)

	RDF FEEDSTOCK		CYCLONE CAUGHT ASH	
	DETECTION LIMIT	CONCEN-TRATION	DETECTION LIMIT	CONCEN-TRATION
DIOXINS				
TOTAL TCDD	0.56	ND	0.089	ND
TOTAL PeCDD	0.76	ND	0.13	ND
TOTAL HxCDD	0.11	ND	0.091	ND
TOTAL HpCDD	*	0.27	0.23	ND
TOTAL OCDD	*	1.70	0.21	ND
FURANS				
TOTAL TCDF	0.30	ND	0.29	ND
TOTAL PeCDD	0.22	ND	0.13	ND
TOTAL NxCDD	0.30	ND	0.20	ND
TOTAL HpCDD	0.23	ND	0.21	ND
TOTAL OCDD	0.48	ND	0.13	ND

* = Not Supplied

TABLE 6
EP TOXICITY METALS ANALYSIS FOR A TYPICAL GASIFIER FEED AND EFFLUENT

ELEMENT	FEED	BED	ASH
	(mg/L in the EP Tox Extract)		
Ag	<.01	<.01	<.01
As	<.1	<.1	<.1
Ba	<.5	<.5	<.5
Cd	<.01	<.01	<.11
Cr	0.01	<.01	<.01
Hg	<.0005	<.0005	<.0005
Pb	<.05	<.05	<.05
Se	<.1	<.1	<.1

H-1   X-1   X-2   R-1   F-1   V-2   V-3   H-2   V-4   P-2   F-2

STEAM   SLIDE GATE   PULSE   THERMOCHEMICAL   FORCED   HOT   SOLIDS   INCINERATOR   QUENCH   CIRCULATION   I D FAN
BOILER   LOCK HOPPER   COMBUSTOR   REACTOR   DRAFT FAN   CYCLONE   CATCH-DRUM   SCRUBBER   PUMP
    FEEDER
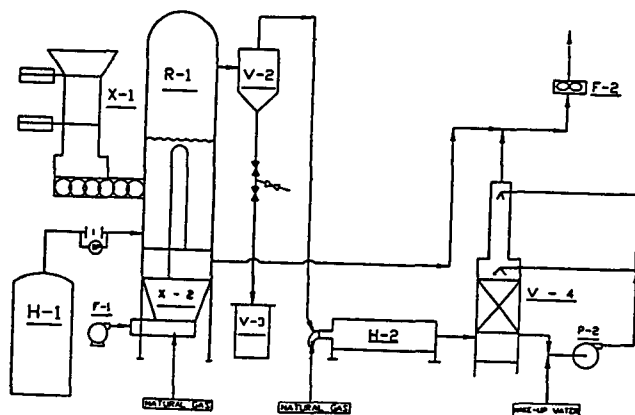
FIGURE 3. PROCESS FOR INDIRECT GASIFICATION PILOT PLANT

TABLE 3
SELECTED GAS COMPOSITIONS AND PRODUCT YIELDS FOR BIOMASS AND
MILL SLUDGE TESTS CONDUCTED INPULSE-ENHANCED INDIRECT GASIFIER

COMPOSITION (VOL%)	PISTACHIO SHELLS	PISTACHIO SHELLS	WOOD CHIPS	RICE HULLS	RECYCLE MILL FIBER WASTE	RECYCLED WASTE PAPER W/PLASTIC	KRAFT MILL SLUDGE	RDF SAND BED	MSW SAND BED	MSW LIMESTONE BED
H₂	37.86	35.04	48.11	42.83	38.86	50.50	52.94	45.54	55.21	54.40
CO	18.84	23.43	22.91	19.67	23.34	19.26	11.77	25.26	28.10	25.46
CO₂	28.73	25.20	20.18	24.40	23.27	20.10	21.94	14.51	5.95	5.66
CH₄	10.65	11.31	8.32	11.56	8.31	8.42	8.95	8.30	5.00	5.86
C₂+	3.92	5.02	0.48	1.54	6.40	1.72	3.00	6.38	5.74	8.62
TOTAL	100.00	100.00	100.00	100.00	100.00	100.00	98.60	100.00	100.00	100.00
HHV (Btu/scf)	370	406	329	367	412	364	372	418	374	448
TEMP (°F)	1317	1216	1286	1326	1250	1326	1250	1450	1410	1306
YIELD (% CARBON)	94.1	92.1	93.0	N/A	86.8	N/A	56.0	83.6	93.7	83.8

B-1	V-1	V-2	E-4	B-1	E-1	E-2	X-1	E-3
GASIFIER	RECIRCULATION CYCLONE	FINES CYCLONE	STEAM SUPERHEATER	AIR BLOWER	PROCESS GAS BLOWER	BFW PREHEATER	VENTURI SCRUBBER	COOLER
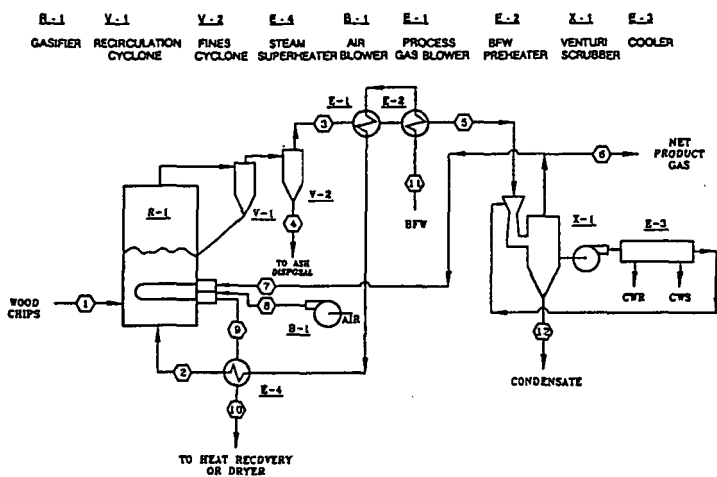
FIGURE 1. PROCESS FLOW DIAGRAM FOR INDIRECT GASIFIER

1. IGNITION AND COMBUSTION

2. EXPANSION

3. PURGE AND RECHARGE

4. RECHARGE AND COMPRESS
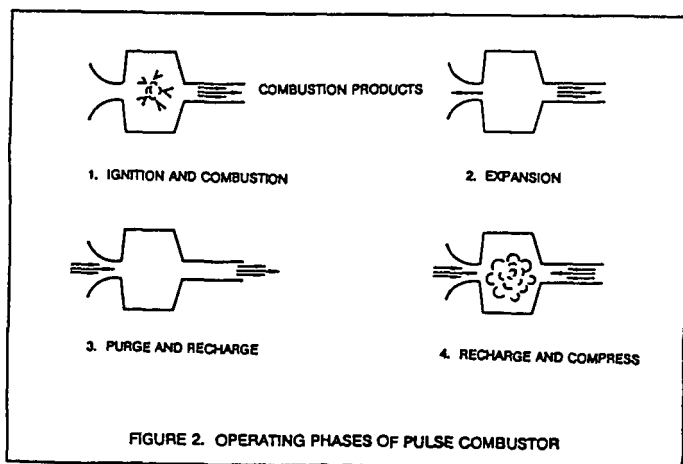
FIGURE 2. OPERATING PHASES OF PULSE COMBUSTOR

BIOMASS FUELED GAS TURBINE DEVELOPMENT

Joseph T. Hamrick
Aerospace Research Corporation
5454 Aerospace Road
Roanoke, Virginia 24014

Keywords: Biomass Fuel, Gas Turbines, Power Generation

INTRODUCTION

Research and development on a 3000 kw wood burning gas turbine power generating system has progressed to the production stage. A system using a General Electric aircraft derivative gas turbine is being prepared for installation at Huddleston, Virginia. The generated power will be sold to the Virginia Power Company. The R&D system located at Red Boiling Springs, Tennessee, will be upgraded for operation with the General Electric engine. Tests were conducted with sugar cane bagasse with good results. Sorghum and sugar cane promise to be major sources of fuel in the future.

Sweet sorghum and sugar cane juices are readily converted to alcohol by yeast fermentation. Sweet sorghum can be grown throughout the United States as well as the tropic and temperate zones of the earth. These plants have the highest conversions of solar energy into biomass of any of the species in the plant kingdom, substantially greater than trees. With the use of bagasse as a fuel for gas turbines in the generation of power, it is possible for the income from power sales to reduce the cost of ethyl alcohol well below that for gasoline. The sorghum grain can be used for fermentation or food. The high volume, high temperature exhaust gases from the turbine can be used to concentrate the juice, make alcohol, dry the bagasse or generate steam for injection into the turbine. There is adequate heat to concentrate the juice and dry the bagasse for year-round use during the harvest period.

Growth of sugar cane and sorghum on the 66.4 million acres of land taken out of production in the U.S. between 1981 and 1988 can supply enough energy to generate 34 percent of the power that was generated in 1986, enough to supply increased power demands into the next century. At the current rates paid by Virginia Electric Power Company for power generated with renewable fuels, 25.4 billion gallons of alcohol can be produced from the profits earned on power sales, enough to supply gasohol to the entire nation.

The system, which can be located at any point where there is a power distribution line and a sorghum or sugar cane source, can provide jobs in the area and an alternative crop for farmers while saving billions of dollars on set-aside payments. At $20/barrel, approximately $8 billion would be saved on the trade imbalance by the reduction of oil imports.

BACKGROUND INFORMATION

Research on wood burning gas turbines was started by Aerospace Research Corporation in 1978. It culminated in the operation of an Allison T-56 gas turbine power generating system at a facility located in Red Boiling Springs, Tennessee. Over two million dollars in U.S. Department of Energy funds and a matching amount of private funds were spent in carrying out the program. In addition, gas turbine engines were furnished by the Air Force and Naval Air Systems Command. A view of the research and development facility is shown in figure 1.
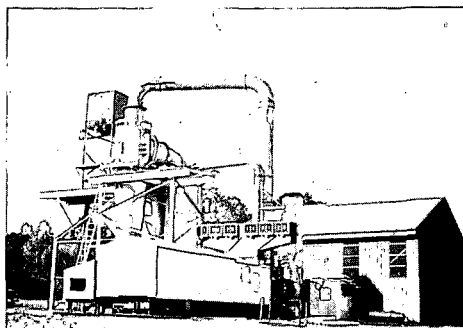
FIGURE 1 View Of Facility At Red Boiling Springs, Tennessee

Operational difficulties which resulted in learning curves peculiar to the system
such as wood processing, conveying, drying, combustion, ash removal, engine start-
ing, synchronization with the TVA power distribution grid, and development of
emergency procedures are covered in reference 1.* Feeding a pulverized solid into
a high pressure chamber and dealing with turbine blade fouling presented the great-
est challenge. An anticipated problem that was most feared at the outset, eroding
of the turbine blades, never materialized. In over 1500 hours of operation, no
erosion has been detected. The measures taken to resolve the two problems and the
approach taken with the General Electric LM 1500 gas turbine in meeting the prob-
lems are presented.

Modern aircraft engines which require very high power to weight ratios are designed
for high turbine inlet temperatures and high compressor discharge pressures. As
turbine blade cooling techniques, advanced materials, and more sophisticated design
methods have become available the pressure ratios and allowable turbine inlet temp-
atures have increased to high levels. As a result, the modern aircraft deriviative
gas turbines are less suitable for operation with biomass than the earlier models.
The current need for low turbine inlet temperature and low combustor pressure with
biomass makes the earlier models more compatible. The LM 1500 gas turbine fits
well into the biomass picture.

THE ROTARY AIR LOCK FEEDER

The rotary air lock feeder is also referred to as a rotary valve. A schematic view
of a rotary feeder is shown in figure 2.
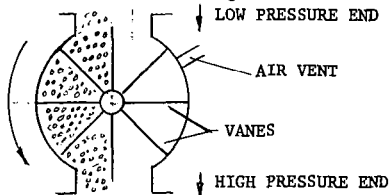
FIGURE 2 Schematic Of A Rotary Air Lock Feeder With Eight Wiper Vanes
* A list of references is included at the end of the paper.

1687

Referring to figure 2, the tips and sides of the vanes are fitted with seals that compartmentalize particles fed into a low pressure sector for movement around to a zone of high pressure and thence into the combustor. A major effort was directed toward development of long lasting sealing methods and materials. Sawdust is an extremely abrasive material that requires special techniques that were developed in the program. To meet the 130 psig requirement of the R&D installation two air lock feeders operating in series proved adequate. To provide conservative design margins, it is planned to use two feeders in series for the 90 psig pressure requirements of the Huddleston installation as well as in succeeding installations up to 6000 kw.

TURBINE BLADE FOULING

At the outset of the R&D program reports on work involved with solids fueled gas turbine systems (References 2 through 5) were reviewed at length. The primary problem with coal fired turbines was erosion of the turbine blades. A secondary problem was fouling of the blades. In work performed by the Coal Utilization Research Laboratory at Leatherhead, England (Ref. 2) it was determined that single cyclones in series adequately cleaned the ash from the combustion gases to prevent erosion. Therefore, it was decided to use only single cyclones in the wood burning program. As a result, there has been no erosion of the turbine blades in the more than 1500 hours of operation with the gas turbines used in the R&D program. In the R&D performed by the Australians (Ref. 3) on brown coal it was found necessary to limit the turbine inlet temperature to 1200°F to avoid deposition of ash on the turbine blades. In the R&D performed at Leatherhead, England with stationery blades there was no significant deposition at 1450°F after 1000 hours of operation with black coal. In tests with pine sawdust in early operation at Roanoke with a small Garrett turbine no significant deposition occurred at 1450°F in 200 hours of operation. In tests with the Allison T-56 at Red Boiling Springs it was found necessary to periodically clean the turbine blades with milled walnut hulls when firing with a mixture of oak and poplar sawdust at 1450°F turbine inlet temperature. Above 1450°F the particles adhered to the blades and could be removed only by scraping. The 1248°F turbine inlet temperature needed to produce 4000 kw with the LM 1500 gas turbine in the Huddleston installation is well below any problem zone for deposition with sawdust.

DISCUSSION OF LM 1500 GAS TURBINE PERFORMANCE
AND FACTORS FAVORING ITS SELECTION

When the advancement was made from the Garrett 375 kw gas turbine to a larger engine, the Allison T-56-9 gas turbine selection was made on the basis of its perceived easy adaptability to the system and the availability of used engines from the U.S. Air Force. As the R&D program advanced, it became clear that the turbine inlet temperature would have to be restricted to 1450°F to avoid excessive turbine blade fouling. The turbine inlet temperature of the T-56-9 is 1700°F at its normal rated overall electrical output of 2332 kw. With a 1450°F turbine inlet temperature the output drops to 1500 kw, a value too low for economical operation.

A search for a more suitable gas turbine from standpoints of availability, adaptability to wood fueling, and electrical output led to selection of the General Electric J-79 gas generator and companion power turbine. The combined gas generator and power turbine was given the designation LM 1500 by General Electric. For aircraft propulsion the hot gases leave the engine at high velocity, propelling the airplane forward. For use in power production the hot gases are ducted to a power turbine. A favorable feature of a two shaft arrangement, such as this one, is that the gas generator can operate efficiently at part load by adjusting its speed downward while the power turbine operates at the required constant speed for

1688

power generation. The compressor efficiency is high over a broad range. This is made possible by adjustment of variable stators in the first six stages of the compressor. By adjustment of the stators to match the compressor speed and air flow, rotating stall is avoided and good compressor efficiency is maintained. Rotating stall is a phenomenon associated with flow separation on the compressor blades as the angle of attack on the blades increases with changes in rotative speed and air flow. Compressor efficiency over the speed range results in economical operation over a wide range of power production. Detailed information on turbine inlet temperature, compressor discharge pressure, and wood feed rate as a function of power output was derived from General Electric specification MID-S-1500-2.

Turbine Inlet Temperature – Figure 3 shows a straight line relationship between
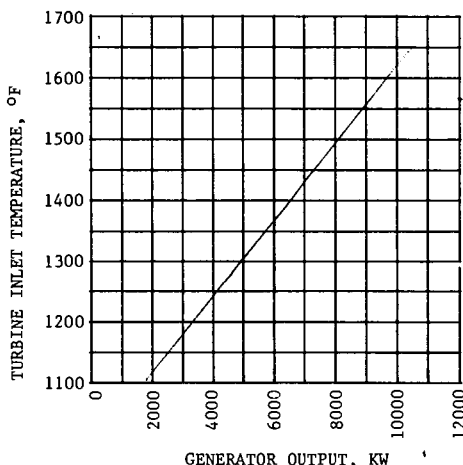
FIGURE 3   Plot Of Turbine Inlet Temperature Versus Generator
Output With The G.E. LM 1500 GAS TURBINE At 1000 ft.
Altitude And Compressor Inlet Air At 70°F

turbine inlet temperature and generator output. This characteristic provides a significant amount of latitude in operation with untried species of plants or sources of fuels such as clean waste. For example, it can be safely predicted that in the worst case the turbine inlet temperature of 1200°F required for a 3400 kw output will not result in excessive or difficult to clean accumulations on the turbine blades. Minimum performance guarantees would be warranted in such cases. With most wood species a 7000 kw output probably can be tolerated.

Compressor Discharge Pressure – Figure 4 shows a straight line relationship between compressor discharge pressure and generator output. The primary concern with pressure is the feeding of solid fuel into the combustion chamber. The demonstrated maximum sustained pressure in the R&D system is 130 pounds per square inch. Thus, the ability to sustain feeding of sawdust from 3000 kw to approximately 7500 kw is assured. The pressure required to produce the 4000 kw projected for the production facility now being prepared for installation at Huddleston, Virginia is only 90 psig.
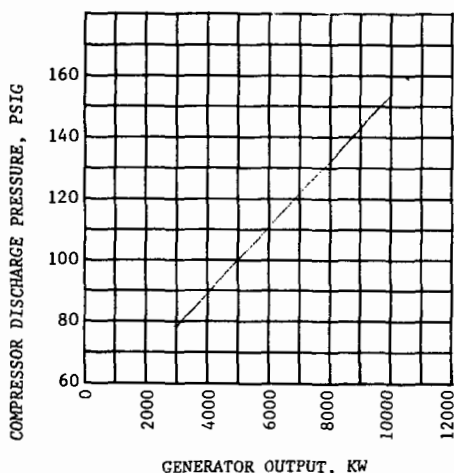
FIGURE 4   Plot Of Compressor Discharge Pressure Versus Generator
Output With The G.E. LM 1500 GAS TURBINE At 1000 ft.
Altitude And Compressor Inlet Air At 70°F

Wood Feed Rate - The wood feed rate in figure 5 is based upon a heat value of 8,200 Btu/lb for sawdust. The heat value ranges from 8100 Btu per pound for oak to 8,600 Btu per pound for yellow pine. Green sawdust as delivered from the mill averages
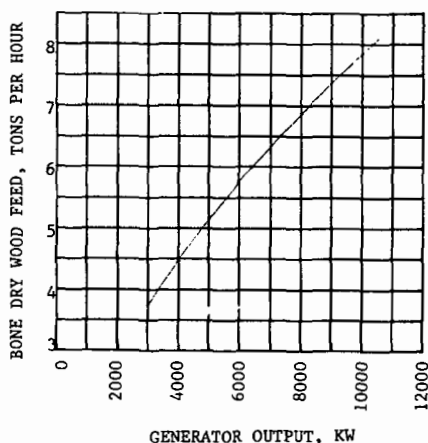

FIGURE 5   Plot Of Wood Feed Versus Generator Output With
G.E. LM 1500 GAS TURBINE At 1000 ft. Altitude
And Compressor Inlet Air At 70°F

1690

approximately 45 percent water content. Trailers 40 ft. long normally deliver on the order of 25 tons of green sawdust per load. For the 4000 kw output projected for the Huddleston facility five trailer loads per day will be required. Shelter for approximately fifty truck loads will be needed to assure continued operation in the winter months when sawdust delivery can be erratic due to weather conditions.

ENGINE DURABILITY

A question frequently arises as to the life of an aircraft derivative gas turbine in stationary power applications. The answer is that the lower power output and lower turbine inlet temperature that are projected for this application make for very favorable longevity for the LM 1500 gas turbine. A twelve year life or greater before overhaul is predictable. The gas generator in the stationary application is never exposed to the extreme power requirements and high turbine inlet temperatures that exist during airplane take off. The primary requirement for long engine life in stationary applications is adequate filtration of the air entering the compressor.

SUGAR CANE AND SWEET SORGHUM FUELS

Sweet sorghum which is highly drouth resistant can supply two to three times as much fiber energy per acre as trees in some areas in addition to the sugar produced for alcohol and grain for food. The yield from sugar cane, in the areas where it can be grown, is even higher than from sweet sorghum. A further advantage is that there is no stigma attached to its use as a fuel, as there is with trees. This renewable fuel will result in a zero net increase in carbon dioxide. Based on the published research results (Reference 6) for sweet sorghum, the 66.66 million acres taken out of production between 1981 and 1988 can supply the energy to generate 34 percent of the power generated in 1986 in the U.S. The annual payment for setting land aside is estimated to be over $5 billion. Much more additional acreage can be easily devoted to sorghum as an alternative crop. Besides providing fuel for electric power the grain and sugar can produce in excess of 25.4 billion gallons of ethanol which equals fifteen percent of the energy supplied from imported oil. Intensive cultivation of sugar cane and sorghum in states bordering the Gulf of Mexico can result in tripling these outputs.

SUMMARY

The General Electric LM 1500 gas turbine has been chosen for use in the wood burning power production system because of its highly compatible performance characteristics, the ease with which it can be mechanically adapted to the system, and its ready availability. Salient points are as follows:

1. The 4000 kw power output projected for the production system being readied for installation at Huddleston, Virginia can be achieved with a 1250°F turbine inlet temperature and compressor discharge pressure at 90 psig. Both are well below the 1450°F turbine inlet temperature and 130 psig compressor discharge pressure found acceptable in the R&D program.

2. Power outputs up to 7500 kw can be achieved with oak sawdust while remaining below the 1450°F turbine inlet temperature and 130 psig compressor discharge pressure found acceptable in the R&D program.

3. There is adequate distance between the compressor and turbine to adapt the engine to the external burner required for wood and other biomass fuels.

4. J-79 gas generators are readily available on the overhaul and used market. New power turbines are available from manufacturers. In addition, a limited number of

serviceable complete LM 1500 sets are available for immediate use.

5. Both the Red Boiling Springs and Huddleston facilities are ideally located for demonstration of combined electrical power and fuel alcohol production from sweet sorghum.

REFERENCES

1. Hamrick, J.T., Development Of Biomass As An Alternative Fuel For Gas Turbines, Report PNL-7673, UC-245 April 1991 DOE, Pacific Northwest Laboratory, Richland, Washington.

2. Roberts, A.G., Barker, S.N., Phillips, R.N. et al, Fluidised Bed Combustion, NCB Coal Utilisation Research Laboratory Final Report, U.S. Department of Energy Report FE-3121-15(a), 1980. National Technical Information Service, Springfield, Virginia.

3. F.L. McCay, Chairman, The Coal-Burning Gas Turbine Project, ISBN 0642001499, 1973. Australian Government Publishing Service, Canberra, NSW, Australia.

4. Summary of The CPU-400 Development, Staff, Combustion Power Company, Inc., U.S. Environmental Protection Agency Report on Contracts 68-03-0054 and 68-03-0143, October 1977. National Technical Information Service, Springfield, Virginia.

5. Yellot, J.I. et al, Development of Pressurizing, Combustion, and Ash Separation Equipment For a Direct-Fired Coal-Burning Gas Turbine Locomotive, ASME Paper 54-A-201, 1954. American Society of Mechanical Engineers, Washington, D.C.

6. Jackson, D.R., Arthur, M.F. et al, Development of Sweet Sorghum As An Energy Crop, Report BMI-2054 (Vol. I) May, 1980. Battelle Columbus, Columbus, Ohio.

FUEL EVALUATION FOR THE U-GAS® FLUIDIZED-BED GASIFICATION PROCESS

A. Rehmat and A. Goyal
Institute of Gas Technology
Chicago, Illinois 60616

Keywords: Gasification; U-GAS Process; Fuel Evaluation

ABSTRACT

The gasification characteristics of a solid carbonaceous fuel in the U-GAS fluidized-bed gasification process can be predicted by laboratory examination of the fuel, which includes chemical and physical characterization, and thermobalance and agglomeration bench-scale tests. Additional design information can be obtained by testing the feedstock in the U-GAS process development unit or the pilot plant.

INTRODUCTION

The Institute of Gas Technology (IGT) has developed an advanced, single-stage, fluidized-bed gasification process, the U-GAS process, to produce a low- to medium-Btu gas from a variety of solid carbonaceous feedstocks, such as coal, peat, wood/biomass, sludge, etc. The development of the process is based on extensive laboratory testing of these feedstocks as well as large-scale tests in a low-pressure (50 psig) pilot plant and a high-pressure (450 psig) process development unit conducted over a period of several years. Up to 98% feedstock utilization with long-term steady-state operation has been achieved. The testing has provided information related to the effect of various gasification parameters, such as pressure, temperature, and steam-to-carbon feed ratio, on gasification characteristics of the feedstocks. The concept of in-situ desulfurization by simultaneous feeding of dolomite/limestone has also been established. Reliable techniques have been developed for start-up, shutdown, turndown, and process control. The process represents the fruition of research and development in progress at IGT since 1974. The product gas from the process will be a low-Btu gas that is usable as a fuel when operating with air, and a medium-Btu or synthesis gas when operating with oxygen. The medium-Btu or synthesis gas can be used directly as a fuel, can be converted to substitute natural gas, or can be used for the production of chemical products such as ammonia, methanol, hydrogen, and oxo-chemicals. The low- and medium-Btu gas can also be used to produce electricity generated by a combined cycle or by fuel cells.

On the basis of the operational results with numerous feedstocks, IGT has developed an experimental program for the evaluation of a solid carbonaceous fuel for use in its fluidized-bed gasification technology.

U-GAS PROCESS

The U-GAS process employs an advanced single-stage fluidized-bed gasifier (Figure 1). The feedstock, which is dried only to the extent required for handling purposes, is pneumatically injected into the gasifier through a lockhopper system. Within the fluidized bed, the feedstock reacts

with steam and air or oxygen at a temperature dictated by the feedstock
characteristics; the temperature is controlled to maintain nonslagging
conditions of ash. The gases are introduced into the gasifier at different
compositions at different points at the bottom of the gasifier. The operating
pressure of the process depends on the ultimate use of the product gas and may
vary between 50 and 450 psi. Upon introduction, the feedstock is gasified
rapidly and produces a gas mixture of hydrogen, carbon monoxide, carbon
dioxide, water, and methane, in addition to hydrogen sulfide and other trace
impurities. Because reducing conditions are maintained in the bed, nearly all
of the sulfur present in the feedstock is converted to hydrogen sulfide.

       The fines elutriated from the fluidized bed are separated from the
product gas in two stages of external cyclones and are returned to the bed
where they are gasified to extinction. The product gas is virtually free of
tars and oils due to the relatively high temperature of the fluidized-bed
operation, which simplifies the ensuing heat recovery and gas cleanup steps.
The process yields a high conversion, especially because of its ability to
produce ash agglomerates from some of the feedstocks and selective discharge
of these agglomerates from the fluidized bed of char.

FUEL EVALUATION

       Three steps are required to evaluate the suitability of a potential
feedstock for the process:

1. Laboratory analyses

2. Bench-scale tests

3. Process development unit (PDU) or pilot plant gasification test.

Laboratory Analyses

       Table 1 lists those fuel properties that are normally determined for
assessing a solid fuel for use in the process. Additional analyses are
performed as required with unusual feedstocks. For example, run-of-mine coals
with a high mineral content may require mineral identification and evaluation
of the effect of high mineral content on ash fusion properties.

       The bulk density, heating value, ash content, and elemental composition
of the organic portion of the feedstock usually have no direct effect on the
behavior of the feedstock in fluidized-bed gasification. However, they do
influence the oxygen requirement, the gas yield, and the gas composition. The
higher heating value (HHV) is a measure of the energy content of the feed-
stock. It relates, with other factors, to the amount of oxygen needed to
provide the desired gasification temperature levels. If a feedstock has a low
HHV, more oxygen is needed to maintain the gasifier temperature at an accept-
able operating level. If the HHV is higher, less oxygen will be required to
maintain the desired temperature levels.

       The ash fusion temperature reflects the ease of agglomeration of the ash
in the gasifier. The free swelling index (FSI) indicates the caking tendency
of the feedstock; for highly caking feedstocks, a proper distribution of the
feed material, as it enters the gasifier, is critical. In the U-GAS process,

the Pittsburgh No. 8 bituminous coal with an FSI of 8 has been successfully gasified and agglomerated with overall coal utilization of 96%. The feedstock is generally sized to 1/4-inch x 0 before it is fed to the gasifier. If a finer size is available, the fluidization velocity is reduced accordingly.

To utilize a feedstock today, one needs to know a great deal about it prior to purchase. It is essential to know the sulfur content to comply with airborne emissions standards and the ash content and its constituents to ensure compliance with solid waste regulations. Other standards are still evolving as new environmental and energy legislation is enacted.

The range of various properties of the feedstocks that have been tested in the U-GAS process development unit or pilot plant is given in Table 2.

Bench-Scale Tests

Three types of bench-scale tests are conducted to evaluate the fuel. These bench-scale tests establish a range of operating conditions that can be used to plan tests in the process development unit or the pilot plant facility, and to perform material and energy balances for the gasifier and estimate its throughput. These tests are described below.

Thermobalance Tests

The gasification of a solid carbonaceous fuel consists of two major steps: 1) initial rapid pyrolysis of the feedstock to produce char, gases, and tar and 2) the subsequent gasification of the char produced. (In addition, some combustion reactions take place if gaseous oxygen is present; these reactions are very rapid.) Because the rate of the second step is much slower than that of the first step, the volume of a gasifier (or the carbon conversion in the gasifier) is primarily dependent on the gasification rate of the char. Due to the relatively well-mixed nature of a fluidized-bed gasifier, the char particles undergoing gasification are exposed to gases consisting primarily of CO, CO_2, H_2, H_2O, and N_2.

The thermobalance testing is performed to determine a relative reactivity constant for the feedstock for comparison with the reference coal, Western Kentucky No. 9 bituminous coal, which has been extensively tested in the thermobalance (Goyal et al., 1989) as well as in the U-GAS process. In the thermobalance, a small quantity of the feedstock is continuously weighed while being gasified at a specific temperature, pressure, and gas composition. This measured weight loss data versus time and the thermobalance operating conditions and analyses of feed and residue are used to calculate the specific relative reactivity constant for the feedstock. The kinetic data, in conjunction with the reference coal information, are used to plan tests in the PDU or pilot plant. As an example, Figure 2 shows the gasification rate for maple hardwood char, peat char, and bituminous coal char, as determined by the thermobalance.

Ash-Agglomeration Tests

Prior to the large-scale testing, the ash-agglomeration tests are conducted in the laboratory to determine the possibility of agglomerating the feedstock ash in the gasifier. These tests are performed in a 2-inch fluidi-

zed-bed reactor capable of operating at temperatures up to 2200°F. Several tests have successfully demonstrated that ash agglomerates can be produced in this bench-scale unit at conditions that can be related to the pilot plant operating conditions. The 2-inch reactor has a unique grid design that allows close simulation of the pilot plant fluidized-bed dynamics and mixing characteristics, which are essential for proper ash agglomerate formation, growth, and discharge. The tests are generally conducted at different temperatures, superficial velocities, gas compositions, and operating times to evaluate conditions favoring ash agglomerate formation and growth. The results are quantified using size distribution curves of feed, residue, and fines to show size growth of particles. Visual evaluation of the agglomerates includes separation of the +8 mesh fraction (normally 100% agglomerates) in the residue and, if required, separation of agglomerates by float-sink techniques for each size fraction. The agglomerates thus separated can be easily photographed or examined petrographically. An example of the test results with different coal samples is given in Table 3.

Fluidization Test

A fluidization test in a glass column at ambient conditions may also be conducted to determine the minimum and complete fluidization velocities of the material. This information is then translated into the necessary operating velocity in the PDU or pilot plant test. The fluidization test is conducted only if the feedstock is unusual or if the feedstock size is different than that typically used (1/4 in. x 0) in the process. This test is conducted with the char produced from the feedstock.

Process Development Unit (PDU) or Pilot Plant Test

IGT has two continuous U-GAS gasification units: 1) The 8-inch/ 12-inch dual-diameter high-pressure process development unit, which can be operated at up to 450 psig and has a nominal capacity of 10 tons per day (at 450 psig operation), and 2) The 3-foot-diameter low-pressure pilot plant, which can be operated at up to 50 psig and has a nominal capacity of 30 tons per day. In addition, a 2-foot/3-foot dual-diameter high-pressure pilot plant has recently been constructed at Tampere, Finland, and its shakedown has begun. Plans are under way to further test various coals, peat, wood and bark waste, and pulp mill sludge in this unit.

A test in the PDU or pilot plant provides the following information:

● It confirms the suitability of the candidate feedstock for the U-GAS process.

● It establishes the base design operating conditions as well as an operating window for the gasifier.

● Design data for fines characteristics, ash agglomeration characteristics, and gas characteristics are obtained.

● Estimates for gas quality, gas yields, and process efficiency are established.

- Necessary environmental data to define the environmental impact are taken.

- Various samples, such as bed material samples, ash discharge samples, fines samples, and wastewater samples, are collected and saved and provided as needed for use during detailed engineering.

The PDU testing is recommended where high-pressure gasifier operation would be required. Each test in the PDU usually consists of 2 days of operation, whereas one 5-day-duration test is usually conducted in the pilot plant with the candidate feedstock. During the test, the gasifier is operated in ash-balanced, steady-state conditions, during which most of the design data are procured. A detailed test plan is generally prepared based on a comparison of the feedstock with a similar feedstock or from information obtained from bench-scale testing. Depending on the feedstock characteristics, the gasifier is operated at a temperature of up to 2000°F and a superficial velocity of up to 5 ft/s.

Numerous solids samples are collected regularly during the test run so that accurate material balances can be prepared. Process sample points include the coal feed, fluidized bed, ash discharge, and cyclone diplegs (for the pilot plant). Samples from the fluidized bed are also collected and analyzed hourly during the test to help the operators determine and maintain steady-state operation.

All process solids and gas flow streams are measured and recorded. Temperatures are recorded for all process streams and at several locations within the reactor. Redundancy is provided for the reactor pressure taps used for bed density and height.

A product gas sample stream is drawn continuously from the gasifier freeboard for chromatograph analysis. The chromatograph system provides accurate on-line analysis for CO, CO_2, CH_4, H_2, N_2, H_2O and H_2S. The chromatograph sequencing is microprocessor-controlled for flexibility in the scope and frequency of the analysis. The product gas samples are also collected in gas bombs for later laboratory analyses.

Special sampling and instrumentation are available for complete chemical characterization (organic compounds as well as trace elements) of the product gas and wastewater streams. Test results of this nature are necessary to satisfy environmental permitting requirements and for proper design of downstream processing equipment. Equipment is also available for determination of product gas dust loading after one, two, or three stages of cyclone separation.

These units use a microprocessor-based data acquisition system to ensure accurate, timely, and reliable collection of all process data of interest. About 85 process data points (temperature, pressure, flow, etc.) for the pilot plant and about 40 data points for the PDU are scanned repeatedly throughout the test. A full scan is completed in approximately 10 seconds and is repeated at 3-minute intervals. The reactor operating status, including various flows, pressures, temperatures, and velocities (grid, venturi, bed, freeboard, cyclone), bed density, bed height, etc., is calculated and dis-

played on the computer CRT screen. The data are stored on magnetic tape in both raw signal and converted form. The converted data are averaged hourly, and an hourly average report of all data points and the operating status is automatically printed in the control room; in addition, a shift report is printed every 8 hours to allow a shift engineer to review the operation of a previous shift. Particular emphasis is placed on the use of the data acquisition system as an operating tool. Specialized programs have been developed to aid the operators in the approach to and confirmation of steady-state operation. This results in more steady-state operating time, and therefore more useful design data, per test run.

The details of the PDU system and some test results are given by Goyal *et al.*, (1989, 1991). The details of the pilot plant system and some test results are given by Goyal and Rehmat (1984, 1985).

In September 1989, IGT entered into a licensing agreement with the Power Industry Division of Tampella, Ltd., Tampere, Finland, which will result in the commercial application of the process. Tampella selected the pressurized fluidized-bed technology because of its versatility and applicability to a wide variety of feedstocks, including coal, peat, forestry waste, etc. As a first step toward commercialization, a 10-MW pressurized (450-psi) pilot plant has been designed and constructed at Tampella's R&D Center in Tampere, Finland. Various coals, peat, wood and bark waste, and pulpmill sludge will be tested in this unit. To demonstrate the application of the technology to the Integrated Gasification Combined Cycle (IGCC), a detailed engineering of a 650-ton/day plant will begin in 1991 and will be commissioned in 1993-1994. Tampella also plans to demonstrate its IGCC process in other parts of the world, including the United States.

REFERENCES

Goyal, A., B. Bryan and A. Rehmat, "Gasification of a Low-Rank Coal," in *Proceedings of the Fifteenth Biennial Low-Rank Fuels Symposium*, p. 447-464, DOE/METC-90/6109, CONF-890573, May 1989.

Goyal, A., B. Bryan and A. Rehmat, "High-Pressure Gasification of Montana Subbituminous Coal," in *Proceedings of the Sixteenth Biennial Low-Rank Fuels Symposium*, May 1991.

Goyal, A. and A. Rehmat, "The U-GAS Process -- From Research to Commercialization," Paper presented at the AIChE Annual Meeting, San Francisco, California, November 25-30, 1984.

Goyal, A. and A. Rehmat, "Recent Advances in the U-GAS Process," Paper presented at the 1985 Summer National AIChE Meeting, Seattle, Washington, August 25-28, 1985.

Goyal, A., R. F. Zabransky and A. Rehmat, "Gasification Kinetics of Western Kentucky Bituminous Coal Char," *Ind. Eng. Chem. Res.*, *28*, No. 12, 1767-1778, (1989) December.

Table 1. LABORATORY ANALYSES OF THE FUEL

- Proximate Analysis
- Ultimate Analysis
- Higher/Lower Heating Value
- Bulk Density
- Particle-Size Distribution
- Grindability
- Equilibrium Moisture
- Free Swelling Index
- Ash Fusion Temperatures (Reducing Atmosphere)
- Ash Mineral Analysis

Table 2. RANGE OF FEEDSTOCK PROPERTIES
TESTED IN THE U-GAS PROCESS

Moisture,* %	0.2 to 41
Volatile Matter,** %	3 to 69
Ash,** %	6 to 78
Sulfur,** %	0.2 to 4.6
Free Swelling Index	0 to 8
Ash Softening Temperature, °F	1980 to 2490
Higher Heating Value,** Btu/lb	2,330 to 13,630

*   As received
** Dry basis

Table 3. 2-INCH ASH-AGGLOMERATION TESTS WITH VARIOUS FEEDSTOCKS

Coal Sample	Run Temp., °F	Char Initial Ash, %	Run Time, h	Fluidizing Velocity, ft/s	Comments
FC-1	1985	31.5	2.0	1.0	Sinter particles plus some agglomerates
FC-1	2100	31.5	1.5	1.5	Agglomerates formed, little or no sinter
FC-2	1990	45.5	1.0	1.5	Small agglomerates present
FC-2	1988	45.5	1.3	1.5	Larger agglomerates found
FC-3	2080	45.4	2.5	1.5	Agglomerates formed
FC-4	1960	15.5	1.0	2.1	No agglomerates found
FC-4	1920	20.9	3.0	1.5	Small agglomerates found
FC-4	2000	15.5	2.5	1.6	Greater number of large agglomerates
KY #9	2000	51.0	1.3	1.5	Many agglomerates produced
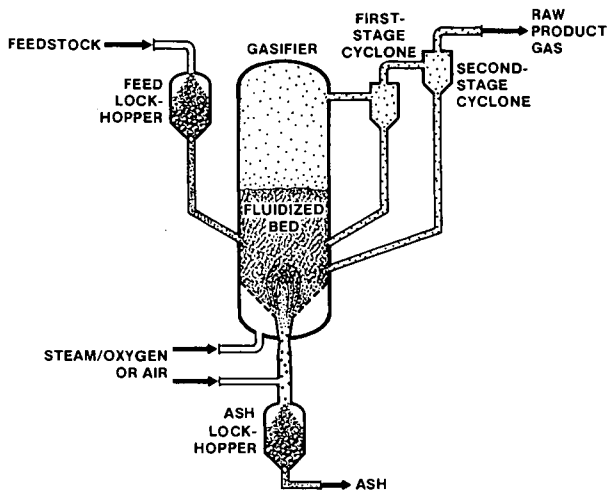
Figure 1. SCHEMATIC DIAGRAM OF THE U-GAS GASIFIER
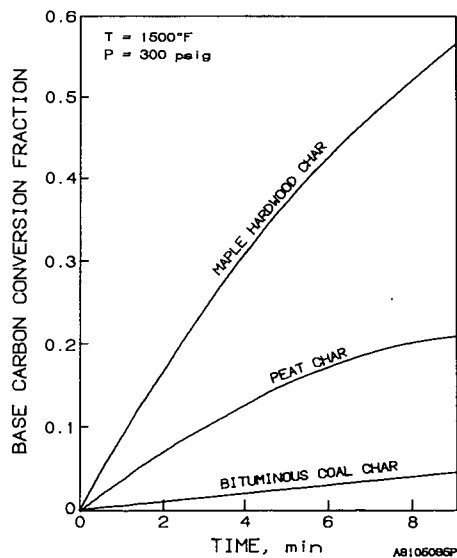
Figure 2. GASIFICATION RATES FOR MAPLE HARDWOOD CHAR,
PEAT CHAR, AND BITUMINOUS COAL CHAR

1701

TREATMENT OF MUNICIPAL SOLID WASTE (MSW) BY THE HYDROCARB PROCESS

Meyer Steinberg
Process Sciences Division
Department of Applied Science
Brookhaven National Laboratory
Upton, NY 11973

Keywords: Solid waste, carbon, methanol.

INTRODUCTION

It is now generally known that the municipal solid waste problem has become an ever increasing problem in populated areas in the U.S. The increase in the standard of living manifested by a vast array of consumer goods has added to the problem of disposal of industrial and municipal solid waste (MSW). The land-fill disposal sites around metropolitan areas have become exhausted so that tipping fees are soaring. Municipalities are opting for more waste incineration or mass-burn plants. Legislation is being passed to require separation of waste for recycling and resource recovery. Because separated waste is market demand dependent, the cost of recycling is highly time and location variable. In fact, there are a number of municipalities that pay carters to remove and transport recyclable the waste to other locations which instead of becoming s source of income becomes a liability. MSW roughly consists of 50% paper and plastic and the remainder being glass, metal and kitchen waste. Industrial waste includes paper, wood and used rubber tire discard.

The most traditional waste disposal method is incineration. The modern and improved method for the same process is now termed mass-burn. In some cases, the energy generated is used to produce steam for electricity generation which can be sold, and therefore constitutes a positive value. The problem here is that the mass-burn plant generates potentially polluting gaseous and solid residue effluents. In the gaseous effluent, dioxin has been one of the most elusive and worrisome pollutants and has caused the shutting down of a number of incinerator plants. There are other gaseous pollutants, including volatile refractory organics, chlorine containing compounds, and particulates from plastic and organic waste. The chemical and biological activity in the remaining solid ash residue from incinerators is also a problem which still requires landfilling or other methods of disposal. There is concern that leachates from incinerated ash will eventually contaminate the aquifers. Municipalities are also passing legislation forbidding the use of materials which do not degrade and tend to remain in long-term storage in the landfill, such as plastics. A number of communities are outlawing disposable plastic products and appear to be returning to paper bags and containers. Much effort is also going into developing biodegradable plastics. Whether this is a sound environmental solution is yet to be determined.

HYDROCARB WASTE PROCESS

The HYDROCARB Process offers a viable alternative. The process was originally conceived for the purpose of processing our vast resources of coal to produce a clean carbon fuel.[1,2] However, the process can operate as well with virtually any carbonaceous raw material and certainly a large fraction of MSW qualifies as a carbonaceous material. The process is new and unique and the products formed can be used primarily as premium clean fuels as well as for the commodity market. The process depends on two basic steps, (1) the hydrogenation of coal to form a methane-rich gas while leaving the ash behind and (2) the thermal decomposition of the methane-rich gas to form carbon black and hydrogen which is recycled. The excess hydrogen and oxygen from the co-products can be a hydrogen-rich co-product which can either be hydrogen, methane, methanol or water. Figure 1 shows a

Figure 1
HYDROCARB PROCESS
CLEAN CARBON FROM CARBONACEOUS FEED STOCK WITH METHANOL AND GASOLINE CO-PRODUCT

1703
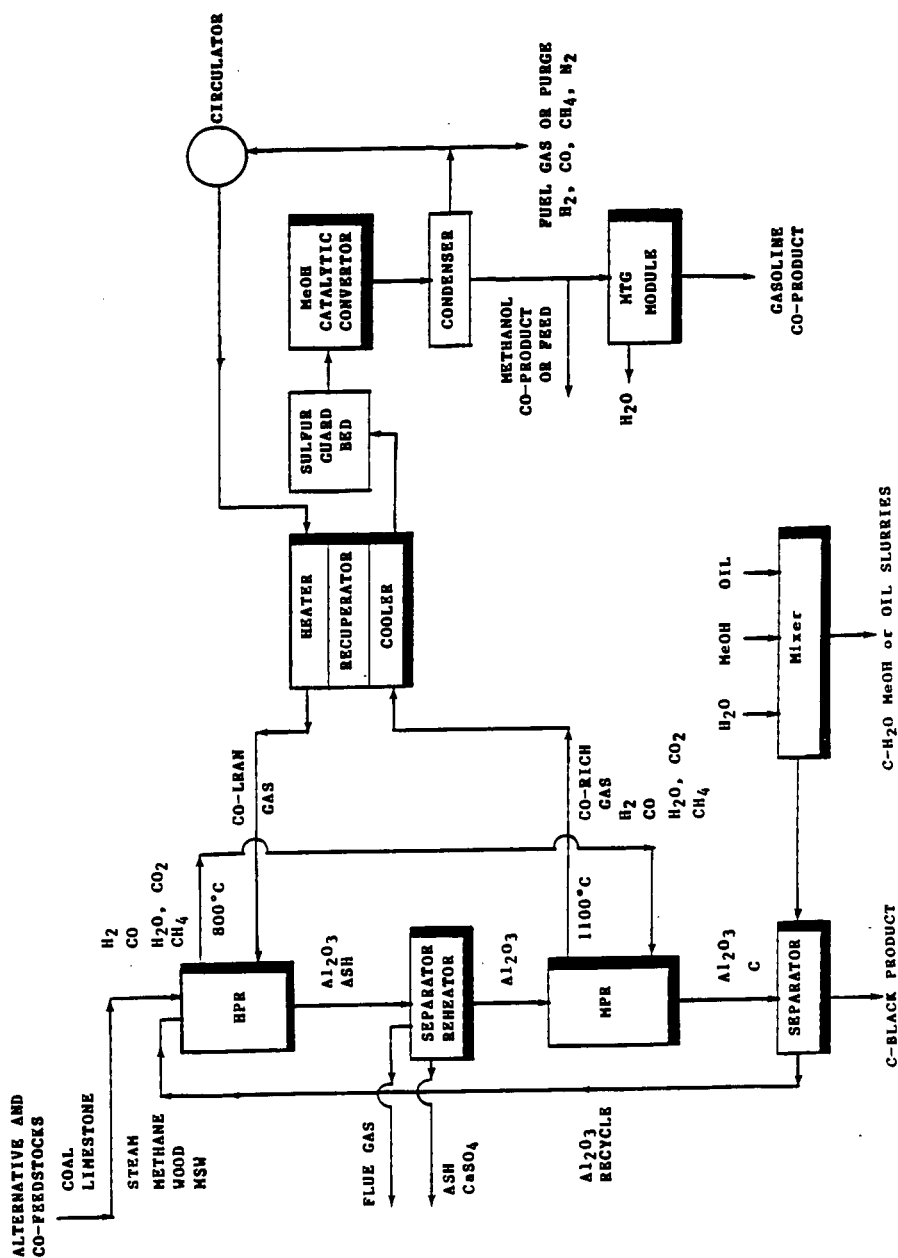
schematic flow with alternative feedstocks, coal, wood or MSW and with co-feedstock additions.

Figure 1 gives a schematic of the process listing various feedstock materials, additives and co-products. The process can be made very efficient because the only raw material used is the carbonaceous material. The energy required to operate the process is relatively small. The overall reaction is thermally neutral. The primary product is always carbon black which can be used as a clean burning fuel and can also supply the market for vulcanization of rubber for automotive tires, pigment for inks and paints and for lubricants. The co-product hydrogen-rich gas can primarily be used as a burner fuel and the methanol as an automotive fuel, or as a commodity chemical, or can even be converted to gasoline. The process is fundamentally different than mass-burn in that it operates in a reducing atmosphere rather than in an oxidizing atmosphere and it is run in a closed system under pressure. Temperature conditions are about the same or perhaps even somewhat lower than in mass-burn incinerator plants. Because of the elevated operating pressure and reducing atmosphere, no dioxin can be formed and all the oxygen containing organic material is reduced to carbon and methane and any metals that may be present in the waste are kept in their reduced state as opposed to mass-burn where the metals can become oxidized. The following describes how the process can be effectively used in processing MSW and the economic dynamics of the process.

The process can be used with either separated or non-separated waste. To simplify the example and avoid discussion of head-end costs, we will give examples of the process operating on separated waste. Thus, the main MSW feedstock is paper and plastic and we can include rubber tires for this example. Since paper is essentially produced from wood, the process can be represented by the following chemical stoichiometric formula, limiting the products to carbon and methanol.

$$CH_{1.44}O_{0.66} \quad + \quad 0.44CH_{1.5} \quad + \quad 0.14CH_4 \quad - \quad 0.92C \quad + \quad 0.66\ CH_3OH$$
paper   +   plastic   +   nat. gas   =   carbon   +   methanol
              methane   black
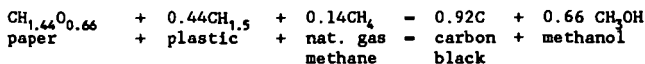
Notice that the formula for plastic contains only C and H, like rubber and methane. The oxygen containing material in paper is in the form of hemi-cellulose. The above equation is based on an assumed MSW composition such that the amount of plastic is 25% of the weight of paper. This can be changed for specific sites and the mass balance adjustment can be made by varying the amount of natural gas added. The gas can be purchased from the local gas company in the particular area where the waste is being processed. We now have to set the production capacity of the plant. Mass-burn incinerator plants have been built in the 2,000-3,000 T/D capacities in and around metropolitan areas. Of course, around New York, for example, it might be worthwhile building a 10,000 T/D or more of waste paper and plastic HYDROCARB plant. However, for this and generally more widespread applications, we will fix on a 3,000 T/D MSW processing capacity which would contain 2,400 T/D paper and 600 T/D plastic.

We now calculate that to run this plant, we have to add 226 T/D of natural gas from the natural gas pipeline company's distributing company. This natural gas is equivalent to 10.7 million SCF/D of methane, which must be purchased from the gas company. The separated MSW is thus co-processed with natural gas.

ECONOMICS

We now must estimate the capital investment of the plant. We can obtain this estimate by scaling down from a large plant we estimated in detail, operating on 25,000 T/D of coal. Because this is a volumetrically controlled process, we can scale it by the well known 0.6 power factor of capacity. The 25,000 T/D plant

making carbon and methanol from coal is estimated to cost 800×10^6. Thus, the 3,000 T/D waste plant will cost:

$$800 \times 10^6 \ \times \ \left(\frac{3000}{25000}\right)^{0.6} - \$200 \times 10^6$$

We can now calculate a selling price for the carbon black fuel and methanol co-product. The financial parameters operating on the capital investment are as follows: capitalization 80% debt/20% equity, 20 yr depreciation, 11% interest on debt, 25% return on equity (ROE) and 38% tax on ROE before taxes. This results in a 21.9% annual fixed charge operating on the total capital investment.

We assume a high natural gas cost from the gas company of $5.00/MSCF which equals a cost of $0.119/lb CH_4. We then add operation and maintenance cost and the 21.9% fixed charges on the $200 million capital investment. We can now calculate the $\underline{G}$ price of the MSW value of the waste taken from the municipality, which can range from a negative value, in which case the community pays the processor to take the waste away, to a positive value in which case the processor pays the community to acquire the waste for processing. We shall first calculate a breakeven G price for the waste in $/Ton in Table 1, assuming we obtain $5.00/MMBtu for the resulting fuel products.

TABLE 1
HYDROCARB WASTE PROCESSING PLANT
Plant Factor 90%, Efficiency 90%, capacity 3,000 T/D
Production Capacity of Fuel - 11,000 Bbl/D Fuel Oil Equivalent

Production Cost	$/Day
Waste Cost —	3,000 T/D x $G/Ton
Nat. Gas — 0.119 x 226 x 2,000 —	53,000
Op & Maint — $\frac{3,000}{25,000}$ x 120,000 —	20,000
Fixed Charges — $\frac{0.219 \times \$200 \times 10^6}{328}$ —	133,000
	206,000 + 3,000 G

Thus,
$$206,000+3,000 \ G - 0.9 \times (3000+226 \ T/D) \times \underline{\frac{22.9 \ MMBtu}{Ton}} \ \times \ \underline{\frac{\$5.00}{MMTU}}$$

Solving for G — $41.50/Ton; this is what the processor can afford to pay the town for taking the MSW for processing and while still obtaining a 25% return on equity.

The above is based on a fuel value for a C-methanol composition makeup mixture of 34.3% carbon in 65.7% methanol by weight. The plant produces 700,000 gal/Day of this C-methanol slurry which is equivalent to 11,000 Bbl/D of fuel oil equivalent.

If we assume the processor obtains the waste from the town free, so that G — $0/Ton, we can then calculate the selling price of $3.10/MMBtu for both co-products carbon and methanol. This is equivalent to $18.70/Bbl oil or $0.44/gal.

Now if the town pays the processor $25/Ton to cart the waste away (as some towns on Long Island have already done), then the selling price for carbon and

methanol can come down to only $2.00/MMBtu which is equivalent to $12.00/Bbl fuel oil equivalent or $0.28/gal while maintaining a reasonable return on the investment equity.

At $2.50/MMBtu which is highly competitive with oil at $15.00/Bbl, the town would only have to pay $13.50/Ton to a processor to take it away.

The conclusion is that even at a waste capacity of 3,000 T/D and an investment of $200 x 10^6, the processor can sell the carbon and methanol as a clean burner fuel for domestic and industrial boilers, as well as for diesel and turbine engines at an economically attractive price. Additional return can be obtained by the processor selling the methanol and carbon at a higher price to the chemical commodity market so that the cost of waste disposal would even bring a profit to the town by selling the waste to the processor at a higher price.

The above indicates that the HYDROCARB Process for the disposal of MSW is highly attractive and should be taken up for development on a fast track schedule. Because this process utilizes natural gas for co-processing waste in a reducing atmosphere, not only is the process environmentally acceptable but is potentially economically attractive and thus it should be worthwhile to develop this process in conjunction with a municipality that is generating the waste.

REFERENCES

1. Grohse, Edward W. and Steinberg, Meyer. Economical Clean Carbon And Gaseous From Coal And Other Carbonaceous Raw Material, Brookhaven National Laboratory, Upton, NY, BNL 40485, (1987).

2. Steinberg, Meyer. Coal To Methanol To Gasoline By The HYDROCARB Process, Brookhaven National Laboratory, Upton, NY, BNL 43555 (1989).

COMMERCIAL APPLICATION OF
WASTE-FUEL FIRED HYBRID FLUIDIZED BED BOILERS

Robert H. Vander Molen and
Robert Rossi
Combustion Power Company
1020 Marsh Road
Menlo Park, CA 94025

Keywords: Fluidized Bed Combustor, Waste Fuels, Boilers

INTRODUCTION

In the early 1980's, developments in California created opportunities for aggressive developers. The California Public Utilities Commission (CPUC) ordered the states utilities to sign power contracts with anyone willing to pay a nominal fee. A range of contract types were ordered. Amongst them was the Standard Offer No. 4 (SO4) type contract which calculated payments on avoided costs that utilities would have incurred had they installed new capacity. The SO4 contract resulted in very attractive payments for both capacity and energy. Before the CPUC rescinded the SO4 contract, nearly 12000 MW were signed up for by developers. Many of these contracts were for small power plants less than 50 MW in size. By staying below 50 MW, review of permits and need by the California Energy Commission was not required. And in most cases, plants burning solid fuels sized less than 30 MW could avoid US EPA review under the Prevention of Significant Deterioration (PSD) regulations.

Combustion Power entered this market with a hybrid circulating fluidized bed boiler. The system uses the positive attributes of a bubbling/turbulent bed combined with a bed-solids circulating loop to develop system performance and emissions profiles which possess substantially enhanced performance characteristics. First commercial operation of the technology was December 1986. At present, a total of 12 units are operating or under construction for a combined steam generation capacity of about 2,500,000 lb/hr (300 MWe). These FI CIRC^{TM} boilers are designed to burn coal and/or a variety of waste fuels having sulfur levels of up to 5.0% and nitrogen up to 3.0%. SO_2 is controlled in typical fluidized bed combustor fashion by introducing limestone into the bed. NOx control, where required such as in California, is attained using a Combustion Power proprietary ammonia injection technique which was developed specifically for the California applications.

DESIGN CONCEPT

The hybrid approach was created by the need in California during the early 1980's to design a solid fuel fired boiler that could meet the very stringent emissions standards in that state. The emissions standards for NOx and SO_2 were typically 0.05 lb/mmBTU for both pollutants. These levels are 5% and 8% respectively of today's Federal EPA New Source Performance STandards for SO_2 and NOx.

Combustion Power has acquired significant fluid bed R&D and operational experience since 1970. This experience, combined with the experience of others, convinced us that the best technical approach for a "California" fluid bed boiler was a hybrid combination which could meet the following design criteria:

- Meet or exceed the most stringent SO_2, NOx and CO emissions standards.
- Have reliable scale-up from pilot plant data.
- Be largely shop-fabricated for low cost field fabrication.

- Designed for ease of maintenance and minimal erosion potential.

Figure 1 is a chart that is often used to classify the three major classes of fluid bed technologies by degree of fluidization. The chart is a plot of superficial gas velocity versus bed expansion with a comparison made between mean gas velocity (gas passing unhindered through the solids bed) and mean solids velocity. As the differential (slip velocity) decreases between these two velocities, the degree of bed expansion (i.e., solids carryover) increases to the point where the solid particle passes unhindered through the process.

Over the range of this expansion there is Type A, classical bubbling bed; Types B and C, circulating fluid beds; and Type D, transport reactors. As depicted, there are four types of beds in these three categories, with two being circulating beds.

At low velocities the Type "A" bed has a defined fluidized-solids/freeboard interface that is readily visible. A very high proportion of product solids is discharged from the bed via a gravity overflow or underflow technique. This is the well known bubbling bed concept.

Higher gas velocity creates a higher rate of particle elutriation (carryover). Also the fluidized-solids/freeboard interface becomes less defined. This is a Type "B" bed, often called a turbulent layer bed which is the bed closest to a FI CIRC™ combustor. This bed typically elutriates over 50% of its incoming solids to the recirculation cyclone for enhanced particle reprocessing. In a fluid bed boiler this reprocessing means improved carbon burnout and lime sulfation.

The Type "C" circulating bed differs in that much higher gas velocities are used. Extensive product recycling creates a condition known as particle "clustering". These clusters have much higher transport velocities which explains the greater slip velocities at increasing solids throughput.

Both Type "B" and "C" beds are considered true circulating fluid beds due to their greater solids elutriation and subsequent extensive recycling via cyclones when compared to Type "A". It is important to remember, however, that both "B" and "C" still retain a dense lower bed relative to the lower density upper zone. In some respects this dense lower bed is similar to a bubbling bed but with much greater gas-solids heat and mass transfer.

A key difference between the FI CIRC™ design and Type "C" beds is the utilization of multiple small-diameter, high-efficiency cyclones to recycle a larger cut of fine particles contained in the elutriated solids. Type "C" beds typically utilize only one or two large diameter cyclones, which do not have as small a fine particle Dp_{50} as a smaller diameter cyclone. Typical Dp_{50} for these larger cyclones is over 75 microns, whereas the FI CIRC™ cyclone Dp_{50} is 15 microns.

Since a significant portion of unsulfated calcium oxide and carbon particles are found in the larger particle cuts, the FI CIRC™ cyclones will recycle the majority of those particles that need to be recycled. The net result is that FI CIRC™ attains the same or better degree of fuel carbon burnout (98 to 99.5+) and lower Ca/S ratios (1.6 to 1.8 at 90% SO_2 suppression) at much lower solids recirculation rates than the Type "C" bed.

The cyclones are critical in FI CIRC™, as with any circulating bed design, since they greatly affect carbon burnout and lime utilization. But with FI CIRC™ they serve the extra function of constantly "doping" the lower bed with a large portion of small particles. It is this "doping" that creates the fine bed particle size average of 300 to 600 microns. With this fine bed average particle size a significant portion of the bed is elutriated, even at velocities of 3-6 ft. per second.

This "doping" also creates a dense bed having a fluidized bulk density of 40 to 60 lbs/ft³. It is well know that decreasing solids fluidized bulk density decreases the bed side heat transfer

coefficient. Increased fluidized bulk density increases the heat transfer coefficient. At these high densities, the bed side heat transfer film coefficient is typically over 100 Btu/hr-ft^{2}F.

FI CIRC^{TM}, with its higher heat transfer rate and denser combustion bed using in-bed tube bundles, controls steaming rate by pneumatic removal of bed solids into an external bed material silo. By dropping bed level and exposing tube surface, the steaming rate drops. A one-inch drop in bed level has a noticeable effect in steaming rate.

Because small bed level changes result in noticeable steam rate change, it is possible to maintain boiler MCR (Manufacturer's Continuous Rating) SO$_2$, CO and HC emissions levels as low as 60% MCR. All of these pollutants require residence time (bed depth) in an oxidizing mode to be thoroughly abated. Since bed level does not greatly change, FI CIRC^{TM} can therefore maintain excellent emissions levels at low MCR ratings.

In summary, the FI CIRC^{TM} fine particle recycling technique gives this design the flexibility to:

- Obtain very turbulent dense bed heat and mass transfer equivalent to higher velocity circulating bed designs without the high velocities or increased solids recirculation ratio and consequent erosion potential:

- Capture the fine particles and introduce them into the lower dense bed, thereby enhancing carbon burnout and greatly improving sulfur capture while also reducing lime consumption.

- Introduce a very high and stable bed side heat transfer coefficient which allows for accurate steaming rate control over a wide MCR range without sacrificing fuel efficiency or emissions control. The design overall heat transfer coefficient (Uo) is greater than 65 BTU/hr-ft^2-F and is constant within 60-to-100% of MCR.

- Permit combustion of low ashing fuels such as petroleum coke and wood waste without the need for either supplemental or costly bed makeup.

- Create a fine particle bed which at lower velocities is much less likely to erode critical in-bed metal components and refractory.

Figure 2 is a cross-sectional view of a typical FI CIRC^{TM} fluid bed boiler and depicts many of the key design features. These features are:

- A standardized modular design, whereby each design "module" consists of:

  - one cyclone and dipleg
  - five fuel guns
  - four in-bed tube bundles
  - 112 ft^2 of tuyere area.

  Each "module" is capable of generating 25 KPPH to 40 KPPH of steam, depending on fuel and emissions standards. Each boiler, regardless of size, utilizes these "building block" modules to reduce scale-up variances. The FI CIRC^{TM} pilot plant has a 4 ft^2 bed area so the maximum process scale-up factor for any size boiler is 112 ft^2 ÷ 4 ft^2 or 28:1.

- Under bed above-stoichiometric air introduction to ensure uniform fluidization and complete combustion burnout in the lower zone where boiler water evaporation and sulfur removal control are critical. An oxidizing lower bed eliminates reducing gas initiated metal corrosion and ensures complete sulfur capture.

1709

- Patented flat plate directional flow tuyeres which continuously move unfluidized particles to the gravity bed drain. This ensures optimal air introduction, fuel/air mixing and elimination of gas "jetting" with subsequent solids impingement on metal surfaces.

- Pneumatic fuel guns which positively and accurately introduce fine sized solids fuels under-bed, thereby enhancing fuel/air contact.

- Air swept spreaders or gravity drop pipes, which evenly distribute coarse particle fuels above-bed.

- Flanged, removable in-bed heat exchanger tube bundles which are located in the upper region of the dense bed to ensure uniform oxidation and minimize erosion. The upper bed placement also allows for quick and easy startup and fine steam rate control "on-the-run". They are also designed to be removed, turned over, and rotated, thereby extending wear life.

- A high freeboard region allows for coarse particle disengagement, thereby reducing refractory erosion in the cyclones. The freeboard also provides for final burnout and temperature stabilization which is required for good NOx removal without proprietary ammonia injection system.

- Multiple, small diameter, high efficiency cyclones which recycle fine particles ($Dp_{50} = 15$ microns) of unburned fuel and undersulfated lime particles into the lower dense bed via gravity diplegs.

- Forced circulation water flow through the tube bundles to ensure nucleate boiling in the evaporators. The net result is a low height profile, bottom supported fluid bed boiler.

FUEL PROPERTIES

Since 1977, Combustion Power has converted waste or low grade fuels to useable energy using fluidized bed combustors. Previous to then, the company was primarily doing research and development in the area of waste-to-energy conversion. Earliest work was with conversion of municipal solid waste processed to refuse derived fuel (RDF). A 100 TPD pilot plant was operated during the 1970's with continued work in a smaller unit through 1985. The pilot plant work consisted of pressurized fluidized bed combustion, atmospheric fluidized bed boiler development, and oxygen blown gasification. Typical RDF properties were as shown on Table I. Numerous other waste and low-grade fuels were burned in various Combustion Power Company pilot scale fluidized bed combustors, including high sodium North Dakota lignite, Texas lignite, pulp and paper industry sludges, wood wastes, waste oils, aircraft paint stripping wastes, etc.

These experiences with waste fuel combustion influenced design of the FI CIRC™ boiler. Low fluidizing velocities (high residence times) and high rates of solids recirculation are two examples of this. Currently operating or in construction boilers are being fired with or designed for, ponded coal fines, delayed petroleum coke, fluid petroleum coke, pat, mixed industrial wastes, log yard debris, pulp and paper sludge, municipal sludge, and rubber tires. Typical properties of some of these fuels are shown on Table II.

EMISSIONS CONTROL

Aside from particulates, there are four major gaseous species which are of most concern today: SO_2, NOx, HC and CO.

The FI CIRC™ system utilizes the principle of temperature, time and turbulence to effect extensive and cost efficient reduction of all these pollutants. SO_2 is controlled by the addition of calcium carbonate (limestone), bed temperature control, excess air, and dense bed height. CO and HC are controlled by operating temperature, excess air, and dense bed height. NOx is controlled by the addition of ammonia with gas temperature control.

All of these pollutants have temperature control in common and it is within the FI CIRC™ combustion region that the optimum range of temperatures is found. The optimum temperature range to remove each pollutant is as follows:

NOx with NH_3 reductant:	1500 - 1750°F
SO_2 with limestone:	1500 - 1750°F
CO with excess air:	above 1600°F
HC with excess air:	above 1550°F

Therefore the best temperature operating range is 1500 to 1600°F in the combustor bed and 1550 to 1650°F in the freeboard. The uniform temperatures long residence times at the proper temperatures and good solids-gas mixing are the key reasons why fluid bed combustors outperform older solid fuel combustion techniques, such as stokers and pulverized coal systems.

SO_2 is controlled by the chemical absorption of SO_2 with active calcium oxide primarily in the fluidized dense combustion bed. Some removal also occurs in the freeboard region. There are several simultaneous chemical reactions which occur to effect SO_2 removal.

CxHyOzNiSj + O_2	--->	CO_2 + H_2O + N_2
Fuel Combustion	--->	CO + NOx + SO_2/SO_3 + HC
		+ ash and char

The SO_2 portion is absorbed by calcium oxide after the calcium oxide is first formed by calcination of limestone:

Ca CO_3	--->	CaO + CO_2
CaO + SO_2 + 1/2 O_2	--->	$CaSO_4$
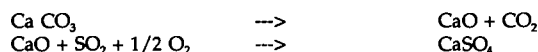
The conversion to $CaSO_4$ does not occur unless oxygen is present. Also it is critical that the dense bed temperature remain below 1700°F to minimize calcium consumption. With FI CIRC™, the important Ca/S ratio is optimized via several techniques.

• Dense bed temperature control below 1700°F using in-bed heat exchange tube bundles.

• A dense bed high enough and operating at a low enough gas velocity to ensure excellent gas/solids contact time.

• Excess oxygen in the combustion zone to "drive" the sulfation reaction.

• Extensive fine particle recycling to ensure that elutriated and unreacted CaO is given another opportunity to sulfate.

The above techniques yield not only very low SO_2 emissions levels, as high as 98% suppression, but do so at very economical Ca/S ratios. Figure 3 depicts the relationship in a FI CIRC system between Ca/S ratio and SO_2 suppression.

In fluidized bed combustors operating at temperatures of 1700F or below, NOx is generated by the combustion of fuel-bound nitrogen. This NOx is destroyed by ammonia injected into the

freeboard region at the proper residence time and temperature according to the following reactions:

$$4\ NH_3 + 4\ NO + O_2 \quad \longrightarrow \quad 4\ N_2 + 6\ H_2O$$
$$4\ NH_3 + 2\ NO + 2\ O_2 \quad \longrightarrow \quad 3\ N_2 + 6\ H_2O$$
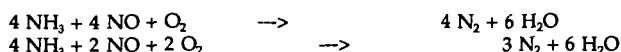
Excessive ammonia introduction will create "ammonia slip" which is free ammonia leaving the stack as well as increasing CO production. This later relationship is as depicted on Figure 4. NOx control, as practiced by Combustion Power, is proprietary. This is due to the careful control required to ensure that NOx is indeed destroyed without undesired side effects, such as CO production and ammonia slip.

Both CO and hydrocarbon emissions are controlled by temperature and excess air:

$$HC + O_2 \quad \longrightarrow \quad CO_2 + H_2O$$
$$CO + 1/2\ O_2 \quad \longrightarrow \quad CO_2$$
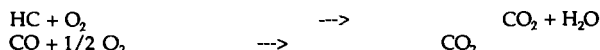
As with SO_2 control, these pollutants are controlled in the FI CIRC™ boilers by:

• Dense bed temperature control using in-bed heat exchange tube bundles.

• A dense bed high enough and operating at a low enough gas velocity to enhance gas/gas reaction times.

• Excess oxygen in the combustion zone to essentially complete the oxidation reactions.

• Careful ammonia injection control to minimize CO production.

This extensive emissions control technology has resulted in California FI CIRC™ plants being permitted at very low SO_2, NOx and CO levels. Of the 33 fluid bed boiler plants in California, 1/3 are FI CIRC™ systems.

Table III shows permitted and actual emissions from six petroleum coke fired plants in southern and northern California.

REFERENCES

1. G. Goldbach, et.al, Program to Develop MSW Fired Fluidized Bed Boiler, CPC Final Report, U.S. DOE sponsored project under Contract No. AC02-80CS24321, June 1983.

2. Ebbe Skov, et.al, Low Emissions Profile from Efficient Fluidized Bed Power Plants Using Petroleum Coke, Paper presented at ASME Industrial Power Conference, St. Louis, MO, October 1990.

3. Michael A. O'Hagan, The California Applications of the Fines Circulating Fluidized Bed Technology, Paper presented at ASME Industrial Power Conference, Hartford, CT, October 1989.

TABLE I: REFUSED DERIVED FUEL CHARACTERISTICS
            (composition on a dry basis*)

	Proximate Analysis (ASTM D 3172)			Ultimate Analysis (ASTM D 3176)	
	wt % (mean)	(σ)		wt % (mean)	(σ)
Ash	18.4%	(2.54%)	Ash	18.36%	(2.54%)
Volatile	71.5%	(2.27%)	C	41.66	(1.25%)
Fixed Carbon	10.1%	(2.86%)	H	5.41	(0.23%)
			N	.74	(0.17%)
			Cl	.37	(0.10%)
Heating Value	7272	(283 Btu/lb)	S	.27	(0.09%)
	Btu/lb		O	33.20	(2.12%)

*Based on 11 samples taken over 6 mo. period with average moisture content of 26%

• • • • • • •

TABLE II: TYPICAL WASTE FUEL PROPERTIES

Property	Ponded Coal Fines	Delayed Pet Coke	Fluid Pet Coke	Peat	Mixed Ind. Wastes	Wood Wastes	Municipal Sludge	Rubber Tires
Moisture, wt%	15.0	3.1	0.2-0.8	37.6	35	50	70	0.5
Volatiles, wt%	NA*	9.0	4.7-6.4	35.9	35	45	NA	62.3
Ash & Inerts, wt%	25.5	0.2	0.2-0.3	1.9	8	1.5	NA	5.7
Ultimate Anal, wt%								
C	45.2	86.0	90-92	NA	NA	25.5	58.3	83.2
H	3.3	3.6	1.8-2.2	NA	NA	2.9	8.5	7.1
O	9.7	0.5	0.4-1.2	NA	NA	19.8	22.9	2.5
N	0.6	1.4	2.3-3.0	NA	2	0.1	8.8	0.3
S	0.6	5.2	2.7-3.5	0.3	NA	0.2	1.6	1.2
Cl	0.1	0.04	0.4-1.2	NA	NA	NA	NA	NA
Higher Heating Value, Btu/lb	8,150	14,770	14,550	6,481	6,423	4,500	3,600	16,329

*NA = Not Available

• • • • • • •

TABLE III: FI CIRC™ EMISSIONS BURNING PETROLEUM

Plant	Fuel	SO$_x$[1]	NOx[1]	CO[1]	Total Part[2]
Torrance, CA	Delayed pet coke	21/13	19/8	190/13	7.8/1.7
Contra Costa County, CA (5 plants)	Fluid pet coke	54/20	50/25	117/25	3.0/1.8

(1)   Values in table are given as Permit/Actual in ppm, dry, standard conditions, corrected to 3% O$_2$. Data taken from emissions compliance test conducted to obtain operating permit.

(2)   Total particulate values are given as Permit/Actual in lb/hr.
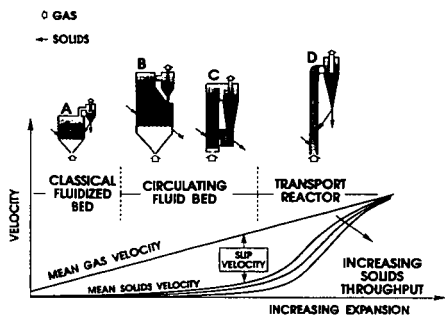
1713

TYPES OF FLUIDIZED BEDS

Figure 1

FICIRC™ FLUIDIZED BED BOILER SEGMENT
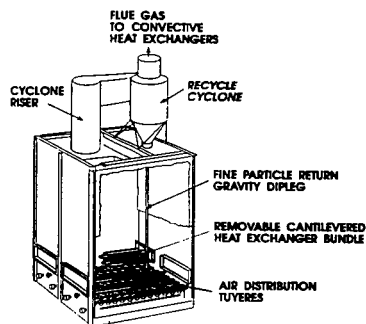
Figure 2

SO$_2$ CONTROL BY CALCIUM ADDITION
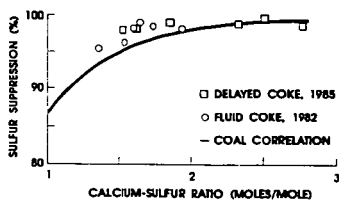
Figure 3

TYPICAL CARBON MONOXIDE PRODUCTION UPON AMMONIA INJECTION
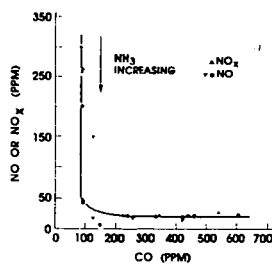
Figure 4

1714

TRANSITION METALS AS CATALYSTS
FOR PYROLYSIS AND GASIFICATION OF BIOMASS

Les A. Edye, G.N. Richards, G. Zheng
Wood Chemistry Laboratory
University of Montana
Missoula, MT 59812

INTRODUCTION

We envision a two stage process for the conversion of lignocellulosic waste (such as sawdust or newsprint) into useful chemicals and simple gases. In the first stage, vacuum pyrolysis at relative low temperatures produces a charcoal, a condensible organic liquid (pyrolysis tar) and a noncondensible low Btu fuel gas. In the second stage, the charcoal which contains a major portion of the energy content of the feedstock is either pyrolyzed at high temperatures, or gasified to produce simple gases. The gasification is free from tar forming reactions, with the energy balance and product gas composition dependent on the composition of the reactant gas.[1,2]

The production of LG from vacuum pyrolysis of pure cellulose and wood has frequently been reported.(e.g.[3,4]) Higher yields of LG from wood pyrolysis were obtained by prior removal by acid washing of the indigenous metal ions bound to the hemicellulose in the wood. We have recently[5] studied the effect of individual metal ions (ion exchanged into wood) on gaseous products from pyrolysis of wood using coupled TG/FTIR. These studies showed that K but not Ca, acts as a catalyst in pyrolysis reactions resulting in formation of CO_2, CO, and formic acid (especially from polysaccharides), acetic acid (from hemicellulose), and methanol (from lignin). This type of study has now been extended to include a wider range of metal ions, and to embrace newsprint as well as wood. Since the major motivation in this work lies in the thermochemical utilization of lignocellulosic waste, we have especially included metal ions which are known to increase char yield and to act as catalysts in char gasification.

In this paper we are specifically concerned with air gasification of the chars doped with metal ions that result from LG producing pyrolyses (i.e. Fe and Cu-doped chars). Several studies have been made of the catalytic effects of copper and its salts in accelerating the oxidation of graphite.[6-9] In fact, copper is reported to be the most effective catalyst of the carbon-air reaction (for Spanish lignite char) of the first transition series of elements.[10,11] The same authors report (for air gasification of Cu-doped lignite char) a dramatic jump from a region of low reactivity and high apparent activation energy to a region of high reactivity and low apparent activation energy for a 5°C temperature increase.[12]

This laboratory has also observed this jump phenomenon for copper catalysis[13] and for iron catalysis[14] in the air gasification of cellulosic chars. For this study we utilized carboxymethylcellulose (CMC) for incorporation of ion exchanged cations and cellulose fibers (CF-11) for incorporation of salts by sorption from aqueous solution. The doped cellulosic fibers were then pyrolyzed to chars for gasification studies. We were able to report "jump temperatures" (T_j, defined by Moreno-Castilla et al.[12] as the lowest temperature of the high reactivity region) for ion-exchanged Cu CMC and sorbed Cu salt CF-11 samples.

Part of this paper reports our continued study of this jump phenomenon. We use the approach described above (viz. copper doped CMC and CF-11 samples) since we are able to achieve particularly exact control of the distribution of the metal species in the cellulosic substrates and hence in the char.

EXPERIMENTAL

The ion-exchanged wood (milled cottonwood sapwood, *Populus trichocarpa*) and carboxymethylcellulose (CMC) and salt-sorbed samples were prepared as described earlier.[15, 16] Newsprint samples were prepared from the Wall Street Journal, macerated with deionized water (or salt solutions for salt-sorbed newsprint) in a Waring blender, filtered and air-dried to a mat ca. 2 mm thick. The mats were cut into cubic pellets (ca. 2 mm³) before pyrolysis. Metal ion contents were measured by inductively coupled argon plasma spectrometry (see *Tables 1* to *4*).

Pyrolyses were carried out at 2 Torr under flowing nitrogen as described previously[17] with tars condensed at room temperature and "distillate" condensed at -50°C. LG contents of tars were determined by GLC of tri-O-methylsilyl ethers[17] and the compounds in the second condensate (other than water) were determined by ^{1}H NMR.[18] The yield of levoglucosenone (LGO) in the second distillate was determined by relating the integrated signal for the C-1 hydrogen (5.31 ppm, s, 1H)[19] to the internal standard (2-methyl-2-propanol; 1.21 ppm, s, 9H).

The thermogravimetry system used to measure gasification rates has been described.[13] The samples were first pyrolyzed at a heat treatment temperature (HTT) for 15 min in nitrogen *in situ* (80 mL min⁻¹), and subsequently gasified (gasification temperature = GT) in air (80 mL min⁻¹, 22% O_2). The TG balance was purged with helium (20 mL min⁻¹). The temperature program and weight loss curve of a typical gasification experiment are shown in *Figure 1*.

The apparatus for measuring differences in sample and furnace temperatures is described elsewhere.[20] Essentially, a thermocouple was placed in the furnace near to the sample (similar to TG temperature measurement) and a second thermocouple embedded in the sample. The temperature program and gas flow control was similar to a typical gasification, and during the course of the experiment the two thermocouple readings were compared.

RESULTS AND DISCUSSION

Pyrolysis of Ion-exchanged Wood
The yields of char, tar, and distillate from the pyrolysis of ion-exchanged wood are shown in *Table 1*. The alkali metal and calcium wood samples showed increased char formation, low tar and high distillate yield compared to acid-washed wood. All other ion-exchanged wood samples showed char and tar yields similar to acid-washed wood, with the transition metals especially favoring tar formation. The analysis of the tar for LG shown in *Table 1* indicates that the tars from Li, K and Ca wood samples were not only obtained in reduced yield, but also contained a lower proportion of LG than tar from acid-washed wood. All other metal ions produced yields of LG above 10.5% compared with 5.4% from acid-washed wood. In other words, wood samples ion-exchanged with transition metals gave higher yields of a cleaner tar.

The best yield of LG observed was 15.8% from the ferrous wood sample. Assuming that LG is derived only from cellulose and that the latter represents 50% of the wood,[21] then the conversion of cellulose to LG was 31.6%. This yield may be compared with 41.5% obtained from pure cellulose (CF-11 cellulose).

The mechanism whereby the yield of LG is increased by the presence of these metal ions is not known. However, since cupric acetate sorbed in pure cellulose does not catalyze the formation of LG, we tentatively conclude that catalysis of LG formation in wood may involve some interaction with lignin. The low yield of LG from original wood (0.4%) is probably associated with two inhibiting factors, *viz.* indigenous metal ions (especially K and Ca) and lignin. When the metal ions are removed by acid washing, the LG yield increases to 5.4% (*i.e.* 10.8% based on cellulose), but the lignin effect presumably holds the LG yield well below that from cellulose (41.5%). The presence of some metal ions, especially the transition metals, may decrease the interference by lignin in the conversion of cellulose to LG.

Pyrolysis of Wood Sorbed with Salts
Since the improved yields of LG from wood pyrolysis induced by the presence of added metal ions are of considerable interest (in connection with thermochemical utilization of biomass), this study was extended to determine whether it is necessary to remove the indigenous cations in the wood, and whether the "beneficial" metal ion can be added more simply and economically as salts by sorption rather than by ion-exchange. This study concentrated on cuprous and ferrous salts because these ions were most effective in increasing LG and charcoal yields when ion-exchanged, and also because the chars from such pyrolyses are likely to contain elemental Cu or active Fe species which are known to be catalysts of gasification reactions.[13]

The products of pyrolysis of wood sorbed with cupric acetate, ferrous acetate and ferrous sulfate are shown in *Table 2*. The addition of cupric ion by sorption of the acetate salt in acid-washed wood (to 0.45% Cu) is effective in increasing LG yield to 11.2%; higher concentrations of copper did not significantly improve the LG yield. When the indigenous ions (predominantly K and Ca) are not removed by acid washing before addition of the cupric acetate, the improvement in LG yield is much less marked. The indigenous cations negate some of the catalytic influence of the Cu. The results with sorbed ferrous acetate were similar, although the LG yield with the salt sorbed in the acid-washed wood (7.5%) was considerably less than for the corresponding ion-exchanged wood (15.8%).

The pyrolysis of wood sorbed with ferrous sulfate was studied as an example of an anion likely to remain in the pyrolyzing solid and to generate acid conditions (acetate ions are lost from the solid at the pyrolysis temperature). Acid-washed wood containing ferrous sulfate yielded 6.1% LG and an additional 3.0% levoglucosenone (1,6-anhydro-3,4-dideoxy-β-D-glycero-hex-3-enopyranos-2-ulose, LGO), which was found in the distillate. LGO is a known product of acid-catalyzed cellulose pyrolysis[22] and its formation was observed only in the presence of the sulfate anion.

Application to Newsprint
Newsprint comprises about one-third of the solid municipal waste in developed countries, it is likely soon to be excluded from landfill disposal and there is a limit to the proportion which can be recycled into paper. Thermochemical processes have the potential to account for the utilization of large amounts of waste newsprint. Our sample contained 24% lignin.[23] It was therefore expected, on the basis of the above experiments with wood, to be similarly amenable to the "beneficial" effects of ferrous sulfate in terms of increased LG and LGO yields.

Table 3 shows the influence of sorbed ferrous sulfate on products of pyrolysis in nitrogen at 400°C for 30 min. In the absence of added ferrous sulfate, pyrolysis of newsprint yielded 3.2% LG, but no LGO. Sorption of ferrous sulfate (to 2.08% $FeSO_4$) before pyrolysis increased the yield of LG to 16.6%, and also yielded 4.2% LGO. Char yield also increased from 15% for newsprint to 20% for $FeSO_4$ sorbed newsprint. Thus we have a procedure to generate chemical

feedstocks (LG and LGO) from pyrolysis of newsprint, while simultaneously forming in increased yield a char which already contains an efficient gasification catalyst.

Gasification of Cu and Fe ion-exchanged CMC chars

We have previously reported the effect of HTT and mode of addition of metal ions on the Tj of Cu-doped chars.[16] Jump temperatures were determined in a series of gasification experiments where GT was successively lowered 5°C until the low reactivity region was reached. The Tj for Fe-doped CMC char (HTT 400°C, [Fe] 2.47% d.a.f.), determined by the same method, was 295°C. *Figures 2* and *3* show rate-time plots for the gasification in air of Cu- and Fe-doped cellulose chars (HTT 400°C) at and below the jump temperature (Tj = 255°C for Cu and 295°C for Fe). Copper appears to be a superior catalyst over iron; the Tj of Cu is lower and the rate maximum (Rg(max)) is higher. In the case of Cu-doped chars, the initial rate of gasification increases *ca.* 160-fold for a 5°C temperature increase at Tj.

In a series of experiments to determine the effect of Cu concentration on Tj we gasified Cu-doped CMC chars in a temperature program (HTT 400°C, GT 200°C + 5°/min). *Table 4* shows the effect of Cu concentration on the apparent Tj. Increasing Cu concentration in the range shown in *Table 4* effected a decrease in the apparent Tj but did not change Rg(max). We expected to measure Tj as the temperature at which the rate suddenly increased, and that the Tj of our CuCMC-1 sample would be as previously determined (*i.e.* 255°C). However, the Tj of CuCMC-1 determined by this method was significantly different. We conclude that this jump in reactivity is also affected by the thermal history of the char.

Effect of oxygen chemisorption on sample temperature in the furnace

It seemed likely, based on the observation of small spikes in the TG thermocouple reading on the introduction of air into the furnace (see *Figure 1*), that the TG apparatus may not be recording the true temperature of the sample during rapid gasification. In fact, when a *ca.* 20 mg CuCMC-1 char (HTT 400°C) was gasified (GT 260°C) with a thermocouple in contact with the char, the temperature of the char ran ahead of the furnace temperature soon after air was admitted (see *Figure 4*).

We have reported[20] that for calcium-doped chars prepared at relatively low temperatures (*e.g.* HTT 400°C), the initial rate of gasification in air (Rg(max) from TG) is extremely high for a short time. This effect was shown to be due to "run away" temperature increase associated with exothermic oxygen chemisorption. In this case the effect can be avoided by pre-sorption of oxygen below the gasification temperature. However, unlike calcium-doped chars, in the copper-catalyzed gasification the initial high Rg(max) peak at GT 260°C could not be eliminated by pre-sorption of oxygen at 200°C (see *Figure 5*). We conclude that exothermic oxygen chemisorption contributes to, but does not fully account for the jump phenomenon in copper catalysis of gasification.

It seems likely that this jump in reactivity is associated with the mobility of the metal species acquired at the Tammann temperature,[12] and that jumps in reactivity below the Tammann temperature can be explained by the thermal history of the sample and its heat capacity, and by the heat generated by oxygen chemisorption.

REFERENCES

1. Walker P.L., Rusinko F., Austin L.G. (1959), *Advan. Catal.* **11**, 133-221.
2. Brink D.L., Thomas J.F., Faltico G.W. (1977), in *Fuels and Energy from Renewable Resources*, Eds. Tillman D.A., Sarkanen K.V., Anderson L.L., Academic Press, N.Y., 141-168.
3. DeGroot W.F. (1985), *Carbohydr. Res.* **142**, 172-178.
4. Ponder G.R., Qiu H.-X., Richards G.N. (1990), *App. Biochem. Biotechnol.* **24/25**, 41-47.
5. Pan W.-P., Richards G.N. (1989), *J. Anal. Appl. Pyrolysis* **16**, 117-126.
6. McKee D.W. (1970), *Carbon* **8**, 131.
7. McKee D.W. (1970), *Carbon* **8**, 623.
8. Patrick J.W., Walker A. (1974), *Carbon* **12**, 507.
9. Turkdogan E.T., Vinters J.V. (1974), *Carbon* **12**, 189.
10. Fernandez-Morales I., Lopez-Garzon F.J., Lopez-Peinado A., Moreno-Castilla C., Rivera-Utrilla J. (1985), *Fuel* **64**, 666.
11. Moreno-Castilla C., Rivera-Utrilla J., Lopez-Peinado A., Fernandez-Morales I., Lopez-Garzon F.J. (1985), *Fuel* **64**, 1220.
12. Moreno-Castilla C., Lopez-Peinado A., Rivera-Utrilla J., Fernandez-Morales I., Lopez-Garzon F.J. (1987), *Fuel* **66**, 113-118.
13. Ganga Devi T., Kannan M.P., Richards G.N. (1990), *Fuel* **69**, 1440-1447
14. Ganga Devi T., Kannan M.P. (1991), *Personal Communication*.
15. Pan W.-P., Richards G.N. (1989), *J. Anal. Appl. Pyrolysis* **16**, 117-126.
16. Kannan M.P., Richards G.N. (1990), *Fuel* **69**, 999-1006.
17. Lowary T.L., Richards G.N. (1988), *J. Wood Chem. Tech.* **8**, 393-412.
18. Richards G.N. (1987), *J. Anal. Appl. Pyrolysis* **10**, 251-255.
19. Halpern Y., Riffer R., Broido A. (1973), *J. Org. Chem.* **38**, 204-209.
20. Edye L.A., Ganga Devi T., Kannan M.P., Richards G.N. (1991), *in preparation*.
21. DeGroot W.F., Pan W.-P., Rahman M.D., Richards G.N. (1988), *J. Anal. Appl. Pyrolysis* **13**, 221-231.
22. Shafizadeh F., Chin P.P.S. (1977), *Carbohydr. Res.* **71**, 169-191.
23. Iiyama K., Wallis A.F.A. (1988), *Wood Sci. Tech.* **22**, 271-280.

Table 1. Vacuum pyrolysis of ion-exchanged wood

Sample	Metal ion (% d.a.f.)[a]	char (% d.a.f.)	Tar (% d.a.f.)	Distillate (% d.a.f.)	LG (% d.a.f.)
Acid-Washed Wood	---- [b]	19	43	16	5.4
Li	----	19	25	44	0.7
Mg	0.08	16	45	29	10.5
K	0.20	22	21	40	0.4
Ca	0.14	20	32	27	4.1
Mn[II]	0.19	15	44	29	10.6
Fe[II]	0.37	15	50	30	15.8
Co[II]	0.20	15	49	29	12.4
Ni[II]	----	14	56	25	13.0
Cu[II]	0.19	17	54	26	13.5
Zn	0.26	16	45	31	11.4
CF-11 cellulose	----	13	67	14	41.5
CuAc$_2$/CF-11[c]	----	24	51	14	31.0

a % weight based on dry ash free wood. Pyrolysis at 350°C/30 min.
b Not determined
c Cupric acetate sorbed on CF-11 (not ion-exchanged)

Table 2. Vacuum pyrolysis of wood sorbed with salt solution

Sample	Metal ion (% d.a.f.)[a]	char (% d.a.f.)	Tar (% d.a.f.)	Distillate (% d.a.f.)	LG (% d.a.f.)
Original wood		15	25	24	0.4
Acid-Washed (AW)		19	43	16	5.4
AW/CuAc$_2$	0.45	29	38	--- [b]	11.2
AW/CuAc$_2$	0.74	30	40	---	11.2
AW/CuAc$_2$	1.10	20	42	---	12.5
CuAc$_2$	0.43	15	43	21	5.9
AW/FeAc$_2$	3.34	22	24	26	7.5
FeAc$_2$	3.18	28	19	28	5.2
AW/FeSO$_4$[c]	1.43	38	18	25	6.1

a % weight based on dry ash free wood. Pyrolysis at 350°C/30 min.
b Not determined
c Pyrolysis at 300°C/60 min

1720

Table 3. Vacuum pyrolysis products from newsprint (NP)[a]

Sample	char	Tar	Distillate	LG	LGO
Original NP	15	44	32	3.3	ND
NP + 2.08% FeSO$_4$	20	43	37	16.6	4.2

a   % weight based on dry ash free wood. Pyrolysis at 400°C/30 min.
ND not detected

Table 4. The Effect of Copper Concentration on the Apparent Jump Temperature[a]

Sample	Cu in char (% d.a.f.)	Tj (°C)	Rg(max) (min^{-1})
CuCMC-1	2.82	312	1.6
CuCMC-2	1.54	320	1.8
CuCMC-3	0.67	340	1.8

a For HTT 400°C, GT 200°C + 5°/min

Figure 1.   CuCMC-1 Gasification in air
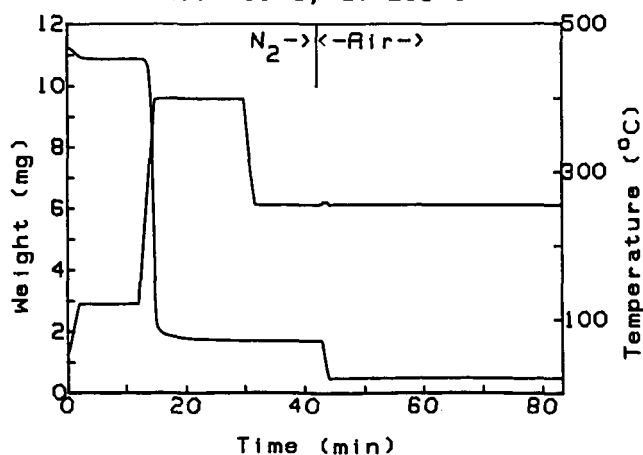HTT 400°C, GT 255°C

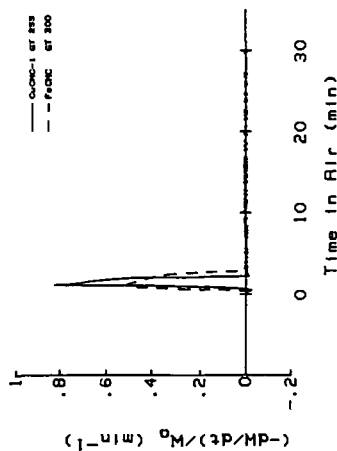Time (min)

Figure 2. DTG Curves for Fe and Cu CMC at T_J
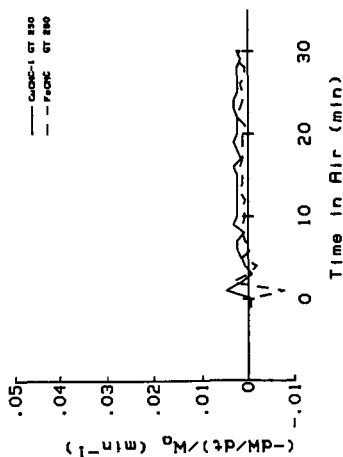
Figure 3. DTG Curves for Fe and Cu CMC Below TJ

Figure 4. CuCMC-1 Gasification in Air (HTT 400)
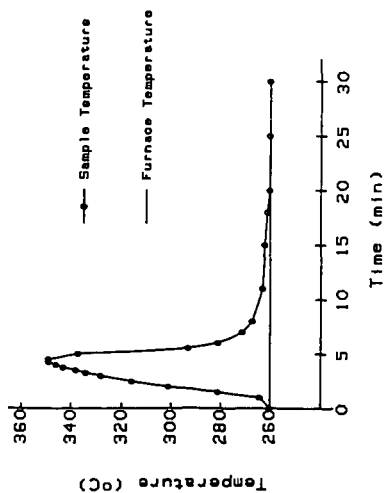
Figure 5. CuCMC-1 Gasification with Pre-sorption at 200°C
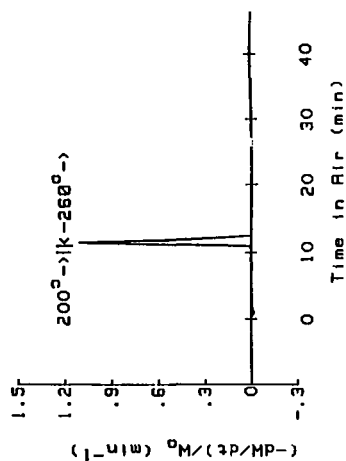
Metals Emissions Control Technologies
For Waste Incineration

J.R. Donnelly
Davy Environmental
San Ramon, California

Keywords: Incineration, Heavy Metals, Air Pollution Control

INTRODUCTION

A major issue facing industrialized nations is the environmentally sound disposal of municipal solid wastes and industrial hazardous wastes. The amounts of these wastes generated has shown an annual growth rate over the past several decades [1] and improper disposal has resulted in numerous environmental problems. Incineration in properly designed combustion systems has been demonstrated as a method of achieving a very high degree of destruction and control for these wastes and is often combined with heat recovery systems to simultaneously recover energy in the form of steam or electricity. A wide variety of incinerator types as well as boiler and industrial furnaces are used for destroying these wastes.

Incineration of municipal and hazardous waste has the potential for increasing air pollution due to emissions of constituents contained in these waste streams and products of their combustion. Municipal and hazardous wastes are likely to contain sulfur and chlorine compounds as well as a wide number of toxic heavy metals (e.g. arsenic, beryllium, cadmium, chromium, lead, mercury, and silver). During combustion sulfur and chlorine compounds are converted to the acid gases SO_2 and HCl. Heavy metals are converted to their oxide or chloride forms. The high combustion temperature employed in modern incinerators will cause many of the metal compounds present to volatilize and be carried out of the incinerator device with the hot flue gases. These compounds then condense out as fine particulate matter or in some instances can leave the system still in the vapor form.

The increase in waste incineration has been accompanied by increased public concerns over air pollution and an increase in local, state, and federal regulations. The USEPA has recently revised federal regulations to further limit incinerator emissions. This increased regulatory climate has resulted in an increase in the complexity and efficiency of air pollution controls employed for emissions controls.

This paper presents a review of the current U.S. regulations covering incinerator emissions and describes technologies used for their control. Typical emission levels and control efficiencies achievable are presented.

AIR POLLUTION REGULATIONS

Air pollution regulations applied to incinerator flue gas emissions vary widely in the compounds controlled, emissions levels, removal efficiencies ies required, averaging times and testing requirements. On the national level, municipal waste incinerators are regulated under Clean Air Act provisions whereas hazardous waste incinerators are regulated under the Resource Conservation and Recovery Act (RCA). In addition to national regulations, local or state permitting agencies may require more stringent emissions controls or control of additional pollutants as a part of a facility's operating permit. The EPA has recently been active in setting standards for municipal waste incinerators, hazardous waste incinerators and boilers and industrial furnaces which burn hazardous wastes.

Municipal Waste Incinerators

EPA promulgated "New Source Performance Standards and Emissions Guidelines for Existing Facilities" for Municipal Waste Combustors in February 1991. These standards are summarized in Table 1.

In setting these standards, EPA recognized differences in facility size, type of incineration (mass burn fired versus refuse derived fuel fired) and new sources versus existing sources. The facility capacity refers to the total burn rate for all refuse combustors at a single site. EPA selected total particulate matter emission limits as the way of controlling trace heavy metal emission limits. EPA will add emission limits based on applying Maximum Achievable Control Technology (MACT) for mercury, cadmium and lead emissions in the coming year. EPA has until late 1992 to establish comparable emission standards for smaller combustors, those less than or equal to 250 tons per day per train.

Emissions limits are established for total emissions of poly-chlorinated dibenzyl-dioxins (PCDD) plus polychlorinated dibenzyl-furans (PCDF). These compounds were selected as surrogates for organic emissions because of their potential adverse health effects. In addition , EPA has established carbon monoxide (CO) emission limits as a measure of "good combustion practices" which limit the formation of PCDD, PCDF and their key precursors. CO emission limits vary from 50 to 150 ppm (1 at 7% O_2 dry gas conditions) depending on the type of combustion.

Acid gas emission limits (HCl and SO_2) are based on either a percent reduction or a maximum stack emission level whichever is the least stringent. Nitrogen Oxides (NO_x) emissions levels are proposed only for large new sources.

Hazardous Waste Incinerators

In April 1990, the EPA published a proposed rule and requests for comments in the Federal Register for Standards for Owners and Operators of Hazardous Waste Incinerators and Burning of Hazardous Wastes in Boilers and Industrial Furnaces". [3] The final rules for "Burning Hazardous Wastes in Boilers and Industrial Furnaces" was published in the Federal Register in February 1991. [4] Key provisions of these regulations are presented in Table 2.

EPA proposed extending current emissions limits covering Destruction and Removal Efficiencies for organic constituents and for particulate matter. EPA proposed to establish risk-based emission limits for individual toxic metals, hydrogen chloride, and organic emissions. EPA added limits for chlorine when they published their final rule for Boilers and Industrial Furnaces. [4] Reference Air Concentration (RAC's) were proposed for maximum modeled annual average ground concentrations of these pollutants. The RAC's for the carcinogenic metals were set at levels which would result in an increased cancer risk for a Maximum Exposed Individual of less than 1 in 100,000. The RAC's for the non-carcinogenic metals, and chlorine were set at 25 percent of the reference dose (RfD) with the exception of lead which was set at ten percent of the National Ambient Air Quality level. The RAC for HCl is based directly on inhalation studies. RfD's are estimates of a maximum daily exposure (via injection) for the human population that is not likely to cause deleterious effects.

In setting these standards, EPA established a three tiered approach for demonstrating compliance. The tiers are arranged from the easiest to demonstrate and most conservative to the more complex and less conservative. Compliance with any tier is considered to prove compliance with these regulations.

Tier I   EPA established conservative maximum feed rates (lb/hr) for each constituent as a function of effective stack height, terrain and land use. In setting these limits, EPA assumed no partitioning in the incinerator, no removal in an air pollution control system, and reasonable worst case dispersion. Demonstration of compliance is through monitoring of feed composition. Two examples of Tier I screening limits are 2.4×10^{-4} to 4.1×10^{-3} pounds per hour for arsenic and 9.4×10^{-3} to 1.6 pounds per hour for lead, depending on stack weight, terrain and land use.

Tier II	EPA established conservative emission rate limits for each constituent as a function of effective stack height, terrain, land use and assumed reasonable worst case dispersion. Demonstration of compliance in through periodic stack emission testing and continuous emission monitoring of carbon monoxide, hydrocarbons and oxygen. Two examples of Tier II screening limits are 3.1×10^{-5} to 5.3×10^{-3} grams per second for arsenic and 1.2×10^{-3} to 2.0×10^{-1} grams per second for lead.
Tier III	EPA established RAC's which must be met for each component. Demonstration of compliance is through periodic emissions testing and site specific dispersion modeling to demonstrate actual (measured) emissions do not exceed the RAC's. For the carcinogenic metals, the ratios of each metal's measured value to its RAC's are added to give a cumulative value which must be below ONE (a risk of 1 in 100,000). Tier III RAC's for all metals are shown in Table 2.

The standards will be implemented through limits on specific incinerator and air pollution control system operating parameters. In addition, emissions testing of all dioxin/furan tetra-octa congeners, calculation of toxic equivalents, dispersion modeling and health risk assessments will be required for incinerators equipped with a dry particulate control device (electrostatic precipitator of fabric filter operating at an inlet temperature between 450 and 750°), or if hydrocarbon emission levels exceed 20 ppmv (d).[4]

AIR POLLUTION CONTROLS

Heavy metals emissions from municipal and hazardous waste incinerators are controlled primarily through the use of particulate collection devices (electrostatic precipitators, fabric filters, wet scrubbers) or acid gas control systems (dry injection, spray dryer absorption, wet scrubbing). The major fraction of heavy toxic metals in the flue gas exists as fine particulates and is effectively controlled by properly sized electrostatic precipitators or fabric filters. Additional control of vaporized toxic metals is achieved in spray dryer absorption system or wet scrubbers.

Spray dryer absorption (SDA) has been widely applied for municipal waste incinerator emissions control and has demonstrated high collection efficiencies for most heavy toxic metals present in the flue gas. SDA has been specified as Best Available Control Technology (BACT) in a number of municipal waste incinerator air permits. Typical control efficiencies and emission levels achieved using SDA are presented in Table 3.

Figure 1 shows simplified process flow diagram for the SDA process. The SDA system is comprised of a spray dryer, absorber, a dust collector and a reagent preparation system. Incinerator flue gas enters the spray dryer where it is contacted by a cloud of finely atomized droplets of reagent (typically hydrated lime slurry). The flue gas temperature is decreased and the flue gas humidity is increased as the reagent slurry simultaneously reacts with acid gases present and evaporates to dryness. In some systems a portion of the dried product is removed from the bottom of the spray dryer, while in others it is carried over to the dust collector. Collected reaction products are sometimes recycled to the feed system to reduce reagent consumption.

Several different spray dryer design concepts have been employed for incinerator SDA applications. These include single rotary, multiple rotary and multiple dual fluid nozzle atomization; downflow, upflow and upflow with a cyclone pre-collector spray dryers; and single and multiple gas inlets. Flue gas retention times range from 10 to 18 seconds and flue gas temperatures leaving the spray dryers range from 230°F up to 300°F.

Heavy toxic metals removal in the downstream dust collector is enhanced through cooling of the incoming flue gas (from 450°-500°F) as it passes through the spray dryer with the subsequent condensation of some vaporized metal forms, and through impaction and agglomeration of fine particulate matter with the very high number of lime droplets produced by the atomization devices.

Generally, the lower the spray dryer outlet temperature, the more efficient acid gas absorption and vaporized toxic metals removal. The minimum reliable operating outlet temperature is a function of the spray dryer and dust collector design and the composition of the dry fly ash reaction product mixture. The spray dryer outlet temperature must be maintained high enough to ensure complete reagent evaporation and the production of a free flowing product. Low outlet temperature operation requires efficient reagent atomization, good gas dispersion and mixing, adequate residence time for drying and design of the dust collector to minimize heat loss and air in-leakage.

The dust collector downstream of the spray dryer may be an electrostatic precipitator, a reverse-air baghouse or a pulse-jet type baghouse. The selection of a specific type of dust collector is dependent on site specific factors such as particulate emission limits, overall acid gas removal requirements and project economics. Each of these dust collection devices offers process advantages and disadvantages that are evaluated on a site specific basis. Generally where high acid gas control is required, (95+ % HCl, 85+ % SO$_2$), a baghouse is utilized as it functions as a better chemical reactor than an electrostatic precipitator. Heavy toxic metals control efficiencies achievable with a SDA system are quite high (99+%) except for the relatively highly volatile mercury. Mercury emissions however, can be controlled at greater than 90 percent efficiency through the use of additives such as sodium sulfide or activated carbon. [1,7]

SDA has also been shown to be an effective method of controlling heavy toxic metals emissions from hazardous waste incinerators [6,3,8], however, wet scrubbing systems have been most commonly applied for overall emissions control. Wet scrubbing has been applied either alone or after a dust collection device to achieve acid gas control or to act as a polishing step for particulate and heavy toxic metals control. In some instances, wet scrubbers have been installed downstream of SDA systems with evaporation of the scrubber blowdown in the spray dryer to eliminate a liquid effluent stream. Figure 2 shows a typical emissions control system process flow scheme for hazardous waste incinerators.

Flue gases at approximately 2200°F are ducted from the incinerator to a quench tower (or a high temperature spray dryer) where they are cooled to 300-450°F. The cooled flue gas then enters a fabric filter (or electrostatic precipitator) where the majority of particulate matter and heavy toxic metals are removed. From the dust collection device, the flue gas enters a saturator venturi where the flue gas is further cooled to 160-200°F. Here HCl and some additional particulate matter as well as heavy toxic metals are removed. The flue gas then enters a packed tower where it is contacted with a caustic scrubbing solution for removal of SO$_2$.

The flue gas may then enter the induced draft fan or may pass through a secondary scrubber for additional fine particulate and heavy toxic metal removal. This secondary scrubber is typically a charged droplet or condensation type designed for light inlet particulate loading and fine particulate control.

Table 4 presents hazardous waste incinerator particulate and heavy toxic metals emissions levels achievable with these types of emissions control systems. The first column indicates conservative estimated removal efficiencies used by EPA in establishing Tier II screening levels for the ten heavy toxic metals of concern. These values are based on using a spray dryer absorption system incorporating a fabric filter as the dust collector or a system consisting of a four-field electrostatic precipitator followed by a wet scrubber as the control device. The next column presents data believed to be more representative of control efficiencies achieved in trial burns where these types of air pollution controls are employed. The final column presents typical ranges of emission rates for particulate matter and the toxic heavy metals. These values are obtained from our in-house emission data base compiled from a wide range of sources. These values are used to estimate incinerator metals emissions in permit support activities.

CONCLUSIONS

The increased use of incineration for control and destruction of municipal and hazardous wastes has lead to increasingly stringent air pollution control regulations. EPA has recently promulgated New Source

Performance Standards for municipal waste combustors which require health risk based emissions limits for specific metals to be established within the next year. EPA has proposed hazardous waste incinerator emissions limits which include risk based emissions limits for ten toxic heavy metals.

Spray dryer absorption is considered to represent BACT for many municipal waste incinerator application and is capable of achieving high collection efficiencies for the metals of concern. Spray dryer absorption is also used for emissions control from hazardous waste incinerator. Dust collectors followed by wet scrubbers or also often used to control metals emissions from hazardous waste incinerators. Both types of systems have demonstrated the ability to achieve high collection efficiencies for the ten toxic heavy metals proposed for regulation. Emission rates from medium to large incinerators equipped with properly designed air pollution control systems are capable of achieving the required emission levels.

REFERENCES

1.   J.R. Donnelly overview of "Overview of Air Pollution Controls for Municipal Waste Combustors" Second International Conference on Municipal Waste Combustion, Tampa, April 1991

2.   USEPA, "New Source Performance Standards and Emissions Guidelines for Existing Municipal Waste Combustors" 40 CFR Part 60 Ca, Federal Register, Volume 56, No. 28, February 11, 1991

3.   USEPA "Standards for Owners and Operators of Hazardous Waste Incinerators and Burning of Hazardous Wastes in Boilers and Industrial Furnaces; Proposed and Supplemental Proposed Rule, Technical Corrections and Request for Comments, 40 CFR Parts 260, 261, 264 and 270", Federal Register Volume 55, No. 82, April 27, 1990

4.   USEPA "Burning of Hazardous Waste in Boilers and Industrial Furnaces; Final Rule, 40 CFR Part 260 et al", Federal Register, Volume 56, No. 35, February 21, 1991

5.   T.G. BRNA and J.D. Kilgroe, "The Impact of Particulate Emissions Control of The Control of Others MWC Air Emissions", Journal of the Air and Waste Management Association, volume 40, No. 9, Pages 1324-1330, September 1990

6.   J.R. Donnelly and S.K. Hansen, "Joy/Niro Spray Dryer Acid Gas Removal System for Hazardous Waste and Sewage Sludge Incineration", HMCRI-Sludge 8T, Boston, May 1987

7.   J.R. Donnelly, S.K. Hansen, M.T. Qurch, "Joy/Niro Control Technology Concepts for Hazardous Waste Incinerators", 1986 Annual Meeting, Minneapolis, June 1986

8.   EPA/530-SW-91-004, "Metal Control Efficiency Test at a Dry Scrubber and Baghouse Equipped Hazardous Waste Incinerator", September 1990

9..   "E.I. Dupont Company Trial Burn Test Program, Emission Test Results, Sabine River Works, Final Report" Alliance Technologies Corporation, August 1990

Table 1. USEPA Municipal Waste Combustion Emission Standards. [2]

	New Source Performance Standards	Emission Guidelines For Existing Facilities	
Capacity-Tons/day	Unit	Unit	Facility
	>250	>250 ≤ 1100	>1100
Particulate Matter-(gr/dscf)	0.015	0.030	0.015
Opacity-%	10	10	10
Organic Emissions-ng/dscm Total Chlorinated PCDD Plus PCDF			
-Mass burn units	30	125	60
-RDF fired units	30	250	60
Acid Gas Control % Reduction or Emissions-(ppm)			
HCl	95 (25)	50 (25)	90 (25)
SO_2	80 (30)	50 (30)	70 (30)
NO_x	(180)	None	None
Carbon Monoxide, ppm	50-150*	50-250*	50-250*

All emissions limits are referenced to dry gas conditions at 7% oxygen concentration.
Range of values reflect differing types of MWC's

Table 2. USEPA Proposed Hazardous Waste Incineration Standards [3]

Destruction and Removal Efficiency (DRE)		99.9999% Dioxin - Listed Wastes 99.99% All Other Wastes	
Particulate Matter		0.08 gr/dscf	@ 7% O_2
Carbon Monoxide (Tier I)		100 ppmv (d)	@ 7% O_2
Hydrocarbons (Tier II)		20 ppmv (d)	@ 7% O_2
Continuous Emissions Monitoring		CO, O_2, HC	

Tier III Reference Air Concentrations
(annual limits, $\mu g/m^3$)

Hydrogen Chloride	0.7	Free Chlorine	0.4
Carcinogenic Metals		Non Carcinogenic Metals	
Arsenic	2.3×10^{-3}	Antimony	0.3
Beryllium	4.1×10^{-3}	Barium	50
Cadmium	5.5×10^{-3}	Lead	0.09
Chromium	8.3×10^{-4}	Mercury	0.3
		Silver	3
		Thallium	0.3

Table 3. Typical Refuse Incinerator Uncontrolled and Controlled Emissions.

Pollutant	Uncontrolled Emissions	Controlled Emissions	Percent Reduction
Particulate Matter, gr/dscf	0.5-4.0	0.002-0.015	99.5+
Acid Gases ppmdv			
HCl	400-100	10-50	90-99+
SO_2	150-600	5-50	65-90+
HF	10-0	1-2	90-95+
NO_x	150-300	60-180	30-65*
Heavy Metals mg/nm^3			
Arsenic	<0.1-1	<0.01-0.1	90-99+
Cadmium	1-5	<0.01-0.5	90-99+
Lead	20-100	<0.1-1	90-99+
Mercury	<0.1-1	<0.1-0.7	10-90+
Total PCDD/PCDF ng/nm^3	20-500	<1-10	80-99

Reference conditions - Dry Gas @ 12%CO_2

Table 4. Hazardous Waste Incinerator Emissions Estimates

	EPA * Conservative Estimated Efficiencies	Typical Actual Control Efficiencies	Typical Range of Emissions Rates ▰ g/Nm^3
Particulate Matter	99+	99.9+	0.005-0.02 gr/dscf
Arsenic	95	99.9+	1-5
Beryllium	99	99.9	<0.01-0.1
Cadminum	95	99.7	0.1-5
Chromium	99	99.5	2-10
Antimony	95	99.5	20-50
Barium	99	99.9	10-25
Lead	95	99.8	10-100
Mercury	85-90	40-90+	10-200
Silver	99	99.9+	1-10
Thallium	95	99+	10-100

*Based on spray dryer fabric filter system or 4 field electrostatic
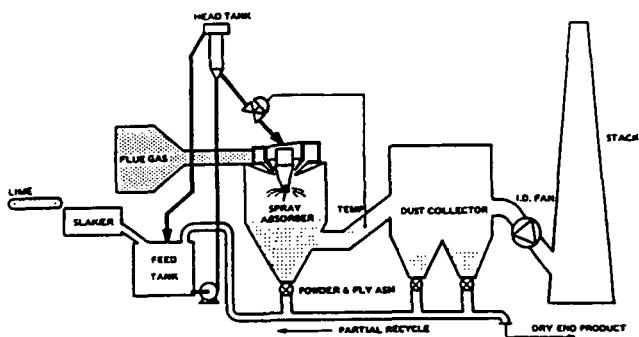precipitator followed by a wet scrubber [3]

Figure 1. Spray Dryer Absorption Process
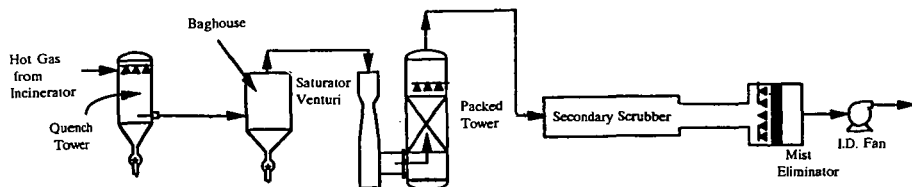(Courtesy of Niro Atomizer)

Figure 2. Hazardous Waste Incinerator - Emissions Control Scheme

CHARACTERIZATION AND CONTROL
OF CADMIUM, LEAD, AND MERCURY FROM RDF
MUNICIPAL WASTE COMBUSTORS

R. Michael Hartman
ABB/Resource Recovery Systems
7 Waterside Crossing
Windsor, CT 06095

INTRODUCTION AND SUMMARY

Title III of the 1990 Clean Air Amendments mandates EPA to propose maximum achievable control technology (MACT) standards for cadmium, lead and mercury air emissions from municipal waste combustors (MWC's) by November 1991. There is growing concern in this country and in Europe regarding environmental levels of lead and mercury, and a fear exists that MWC's may be a major contributor to these levels. Finally, Congress will soon be debating amendments to RCRA, the Solid Waste Act, which will likely consider disposal and reuse requirements for ash from MWC's where questions of leachability of trace metals, particularly cadmium (Cd), lead (Pb), and mercury (Hg) will be of concern.

Because of these important factors, this paper will primarily focus on air and ash emissions for these three trace metals from refuse derived fuel (RDF) type MWC's. Secondarily, the paper will attempt to point out what emission controls are being, and could be, imposed, and what future trends are likely to occur to reduce these emissions. Thirdly, the paper will put into perspective the contribution that Hg emissions from MWC's have to the global emissions of Hg.

Most of the data that will be presented comes from the Mid-Connecticut RDF facility located in Hartford, Connecticut. That facility is a 2,000 ton/day facility owned by the Connecticut Resources Recovery Authority and designed and constructed by ABB Resource Recovery Systems (ABB/RRS). The facility contains a waste processing facility that produces RDF which is operated by the Metropolitan District Commission. Slides will be presented which illustrate how this facility produces RDF (see Figure 1). Slides will also be presented showing how pre-processing MSW to produce RDF can reduce levels of Cd, Pg and Hg by 33% - 90% prior to combustion.

Next, the paper will describe the power block facility (see Figure 2) which is operated by ABB/RRS. Slides will be presented which describe the boiler, the combustion controls, the dry scrubber, and the reverse air fabric filter from this facility. Slides will also be presented which summarize the uncontrolled levels of Cd, Pb and Hg in the flue gas before the scrubber as well as the controlled levels of these same pollutants after the baghouse. These levels will be compared for different steam loads, combustion conditions and scrubber settings. Finally, data will be presented showing the high removal efficiencies for these trace metals in the flue gas (i.e. 97.6 - 100%) and the impact that varying the calcium to sulfur stoichiometric ratio has on removal efficiency.

Next, the paper will describe the facility ash handling system. Slides will be presented showing both the concentration (ug/g) and quantity rates (kg/hr) of Cd, Pb, and Hg in the RDF and the various ash fractions. These slides will illustrate the concentration buildup of these trace metals in fly ash. Slides

will also be presented which show results of leachability studies on the ash using sequential batch extraction and TCLP leach tests.

Finally, the paper will conclude with general observations on trends in control of Cd, Pb, and Hg from all types of MWC's, and what EPA may be considering in the new air regulations that must be promulgated soon. The paper will discuss general confusion that currently exists about the magnitude that MWC's may play in contributing to environmental levels of Hg. The paper will put Hg emissions from MWC's into perspective and compare them to emissions from other sources.

ABB Resource Recovery Systems

Municipal Solid Waste Processing – Single Line
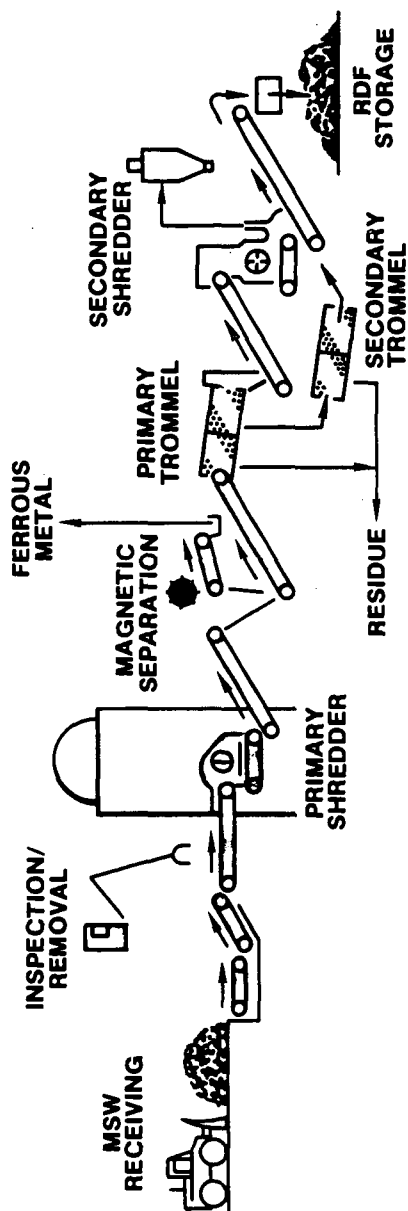
FIGURE 1

ABB Resource Recovery Systems

Prepared Fuel Steam Generation System

Environmental Components

Enclosed Bins and Feeders Prevent Dust and Odors

Continuous Monitoring and Regulation of Combustion Parameters Maximizes Efficiency of Performance and Controls Formation of Organic Compounds

The Dry Scrubber System Injects a Lime Solution Into the Exhaust Stream to Neutralize Acid Gases

Combustion Gases Preheat Boiler Water in the Economizer to Increase Boiler Efficiency

Fabric Filters Trap and Remove Particulate Matter and Other Pollutants

Gas Scrubber

Particulate Collectors

Economizer

Boiler

Combustion Air is Preheated to Increase the Thermal Efficiency of the Steam Generator

Air Preheater

Enclosed Conveyor System Under Negative Pressure Captures and Contains Odors

Enclosed RDF Feed Conveyors

RDF Metering and Feed System

ABB CES Travelling Grate Stoker

Zone Control of Underfire Air

The ABB Travelling Grate Stoker Contains Zoned Control of Underfire Air for Proper Air Distribution and Improved Combustion of RDF

Ash Conveyor(s)

Ash Collection

Nitrogen Oxides Removed from Combustion Gases

Ferrous and Non-Ferrous Metals Can Be Removed from the Ash
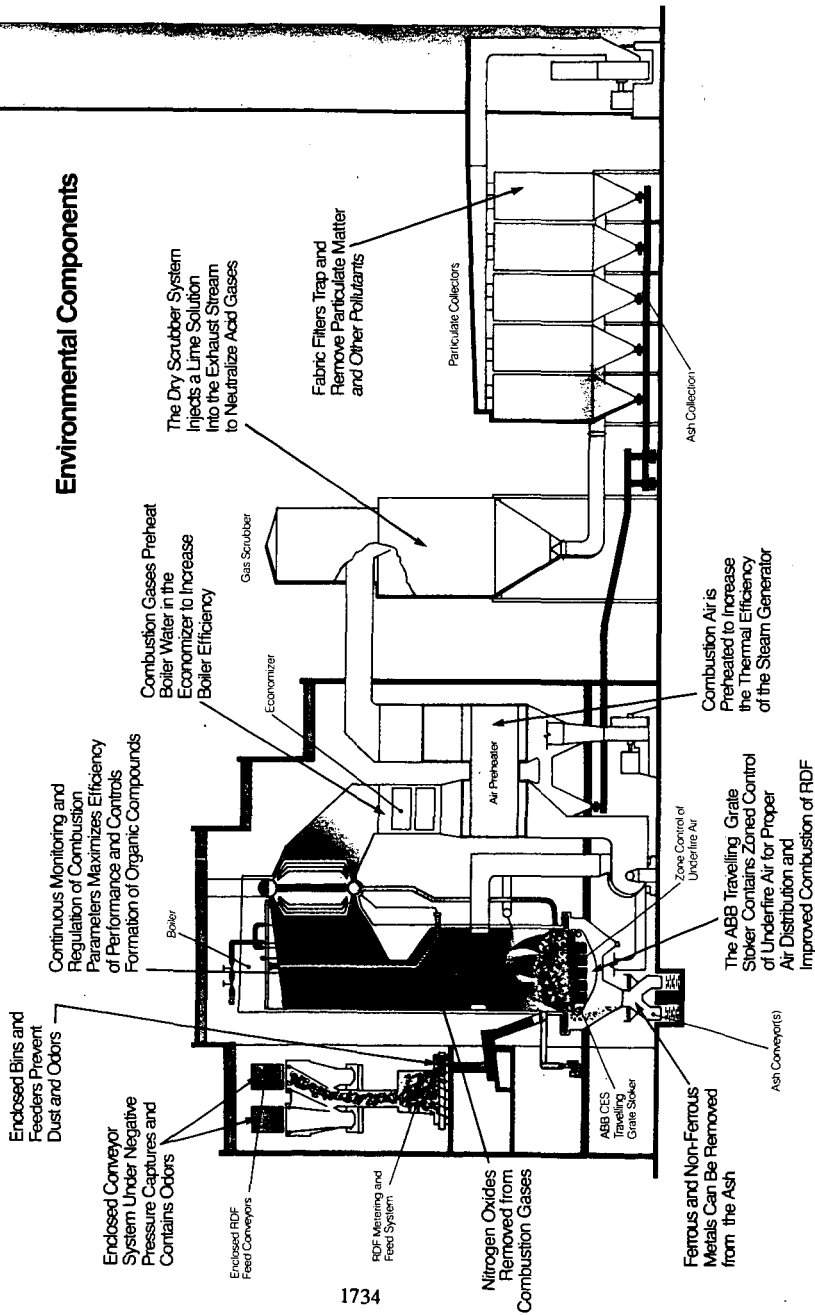
1734

FIGURE 2

METALS BEHAVIOR DURING MEDICAL WASTE INCINERATION

C.C. Lee and G.L. Huffman
U.S. Environmental Protection Agency
Risk Reduction Engineering Laboratory
Cincinnati, Ohio 45268

ABSTRACT

Medical waste contains toxic metals such as lead, cadmium, and mercury. Consequently, the incineration of medical waste may result in the emissions of trace metals into the environment, if incinerators are not properly designed and operated. EPA's Risk Reduction Engineering Laboratory initiated a study in 1988 to document what is known about medical waste treatment, particularly in the area of medical waste incineration. This paper is to summarize the findings from this study regarding the behavior of metals in incineration processes. Highlights of these findings are as follows:

- Lead and cadmium are the two most-often-found metals in medical waste.

- Metals can partition into different phases (gas, liquid or solid) but cannot be destroyed during incineration.

- There are several potential pathways that metals follow to reach the environment. They exit incinerators with sifting, bottom ash, fly ash, scrubber waste, and flue gas.

- Data on the capture efficiency of metals by air pollution control equipment used at medical waste incinerators is very limited.

- Wet scrubbers generally capture cadmium moderately well but normally perform poorly in removing chromium and lead. Fabric filter systems efficiently capture all metals.

INTRODUCTION

It has been well known that medical waste contains toxic metals such as lead, cadmium, and mercury. These metals will only change forms (chemical and physical states) but will not be destroyed during incineration. They can be emitted from incinerators on small particles capable of penetrating deep into human lungs. Thus, the emission of trace amounts of heavy metals from medical waste incinerators is one of the major concerns to those who are involved in medical waste management. A clear understanding of metals behavior in medical waste incinerators is critically needed.

EPA's Risk Reduction Engineering Laboratory initiated a study in 1988 to document what is known about medical waste treatment, particularly in the area of medical waste incineration. Potential toxic metal emissions from medical waste incineration was one of main subjects studied. This paper is to summarize the findings of that study.

METAL SOURCES

Researchers at the University of California at Davis conducted a study to identify the sources of toxic metals in medical wastes (Hickman, 1987). The research effort focused on lead and cadmium because they were the two most-often-found metals in medical waste. They concluded that plastics in the waste contributed most to the presence of these two metals. Cadmium is a component in common dyes and thermo- and photo-stabilizers used in plastics. Lead was found in many materials including plastics, paper, inks, and electrical cable insulation. However, the primary source of lead appeared to be plastics. Like cadmium, lead is used to make dyes and stabilizers which protect plastics from thermal and photo-degradation. It is ironic to note that the dyes made from lead and cadmium are used to color plastic bags. Thus, part of the lead and cadmium emissions could be due simply to the "red bags" that infectious waste is placed in.

Under the hazardous waste program of the Resource Conservation and Recovery Act of 1976, EPA has identified ten (10) metals of most concern from 40 CFR 261 Appendix VIII. Four of the ten metals are classified as carcinogenic and the other six metals are considered to be toxic. The EPA's Carcinogen Assessment Group has estimated the carcinogenic potency for humans exposed to low levels of carcinogens. An assigned "Unit Risk" indicates the relative health threat of the metals. Unit Risk (UR) is the incremental risk of developing cancer to an individual exposed for a lifetime to ambient air containing one microgram of the compound per cubic meter of air. Inhalation is the only exposure pathway considered in determining UR.

Toxicity data are used to define concentrations for the six toxic metals below which they are not considered dangerous. Ambient concentrations should not exceed this concentration. The EPA has defined the maximum toxic concentration, or Reference Air Concentration (RAC), for each metal. If ground level concentrations of any of these metals exceeds its RAC, adverse health effects are likely. The Unit Risk of the four carcinogenic metals and the RAC of the six toxic metals are listed in Tables 1 and 2 (EPA, 4/91).

EMISSION PATHWAYS

A majority of metal emissions is in the form of solid particulate matter and a minority is in vapor form. It was generally concluded that particulate emissions from the incineration of medical wastes are determined by three major factors:

(1) Suspension of noncombustible inorganic materials;

(2) Incomplete combustion of combustible materials (these materials can be organic or inorganic matter); and

(3) Condensation of vaporous materials (these materials are mostly inorganic matter).

The ash content of the waste feed materials is a measure of the noncombustible portion of the waste feed and represents those materials which do not burn under any condition in an incinerator. Emissions of noncombustible materials

result from the suspension or entrainment of ash by the combustion air added
to the primary chamber of an incinerator. The more air added, the more likely
that noncombustibles become entrained. Particulate emissions from incomplete
combustion of combustible materials result from improper combustion control of
the incinerator. Condensation of vaporous materials results from
noncombustible substances that volatilize at primary combustion chamber
temperatures with subsequent cooling in the flue gas. These materials usually
condense on the surface of other fine particles.

Figure 1 shows the transformation of mineral matter during combustion of
metals-containing waste. The Figure is self-explanatory. There are several
potential pathways to the environment that metals may follow. Most metals
remain in the bottom ash. A small fraction of the ash (on a weight basis) is
entrained by the combustion gases and carried out of the primary chamber as
fly ash. Volatile metals may vaporize in the primary combustion chamber and
leave the bottom ash. These metals recondense to form very small particles as
the combustion gases cool. Some of the entrained ash and condensed metals are
captured in the air pollution control equipment (APCE). The rest enters the
atmosphere. Four key variables affecting the vaporization of metals are (EPA,
4/91):

- Chlorine concentration in the waste;

- Temperature profiles in the incinerator;

- Metal species concentration in the waste; and

- Local oxygen concentration.

CURRENT CONTROL PRACTICE

Two strategies are used to minimize metals emissions: (1) The primary chamber
is operated at conditions which do not promote vaporization or entrainment of
metals; and (2) Any metals which do escape can be captured in the APCE, if
present. The parameters usually used to control the escape of metals from the
primary chamber are the primary chamber temperature and gas velocity. The key
APCE parameters used are specific to the device which is utilized.

(1)   Combustion control: Most operating medical waste incinerators are
      simple single-chamber units with an afterburner located in the stack.
      The ability of batch incinerators to control metals emissions is
      limited because only the temperature in the stack is usually
      monitored.

      Most new incinerators are starved-air units. The primary chamber is
      designed to operate at low temperatures and low gas flow rates. This
      minimizes the amount of materials entrained or vaporized.

      To ensure that metal emissions are minimized, operators must maintain
      the primary chamber at the temperatures and gas flow rates for which
      it was designed. Usually the only parameter that system operators

can directly control is feed rate. High feed rates can lead to high temperatures and high gas velocities. Thus, many operators carefully control the feed rate. The feed rate is reduced when primary temperatures increase.

(2) APCE control: When metals reach the APCE, they are present in one of three forms. Non-volatile metals are on large entrained particles. Metals which have vaporized and recondensed are usually present on fly ash particles with diameters less than 1 micron. Extremely volatile metals are present as vapors. Table 3 summarizes the ability of common APCE to control these different metal forms. The Table is based on data and worst case predictions. Wet scrubbers are often used to minimize the temperature of the flue gases. Use of low temperatures ensure that all metal vapors have condensed. As indicated in Table 3, vapors are much more difficult to capture than particles (EPA, 4/91).

EMISSION DATA

Figure 2 compares the concentration of arsenic (chosen merely for illustrative purposes) in flue gases before any APCE, and in emitted gases for a variety of incinerators. As shown, a wide variety of flue gas cleaning equipment is used. The Figure indicates the effectiveness of the various types of APCE. Arsenic is predicted to be relatively volatile, compared to other metals. Significant amounts of arsenic are therefore expected to vaporize in an incinerator (EPA, 4/91).

CONCLUSION

Some metals and metal species found in waste materials are volatile and will vaporize at the conditions found in incinerators. The vapors are carried away from the waste by the exhaust gas and they recondense as the gas cools. The vapors condense both homogeneously to form new particles and heterogeneously on the surfaces of existing fly ash particles. To control metal emissions, metals which are of a highly volatile nature are of main concern in terms of installing the proper APCE. Because there are many APCE sizes and types, it is very important to fully understand metal emissions characteristics, combustion control and operating possibilities, and expected APCE performance so that metal emissions can be minimized.

REFERENCES

(EPA, 4/91), "State-of-the-Art Assessment of Medical Waste Thermal Treatment," A Draft Report to EPA's Risk Reduction Engineering Laboratory, April 1991.

(Hickman, 1987), "Cadmium and Lead in Bio-Medical Waste Incinerators," Master of Science Thesis, University of California, Davis, 1987.

TABLE 1. UNIT RISK (UR) VALUES FOR FOUR CARCINOGENIC METALS	
Metals species	Unit risk
Arsenic (As)	0.0043
Beryllium (Be)	0.0025
Cadmium (Cd)	0.0017
Chromium (Cr^{+6})	0.012
UR: incremental lifetime cancer risk from exposure to 1 μg/cubic meter	

TABLE 2. REFERENCE AIR CONCENTRATIONS (RACs) FOR SIX TOXIC METALS	
Metals species	RAC (μg/m^3)
Antimony (Sb)	0.025
Barium (Ba)	50.00
Lead (Pb)	0.09
Mercury (Hg)	1.70
Silver (Ag)	5.00
Thallium (Tl)	500.00

TABLE 3. TYPICAL APCE CONTROL EFFICIENCIES			
	Control Efficiency(%)		
APCE	Particulate	Fume	Vapor
Venturi scrubber 20" pressure drop	90	85	60
Venturi scrubber 60" pressure drop	98	97	90
Fabric filter	95	90	50
Spray drier/ fabric filter	99	95	90
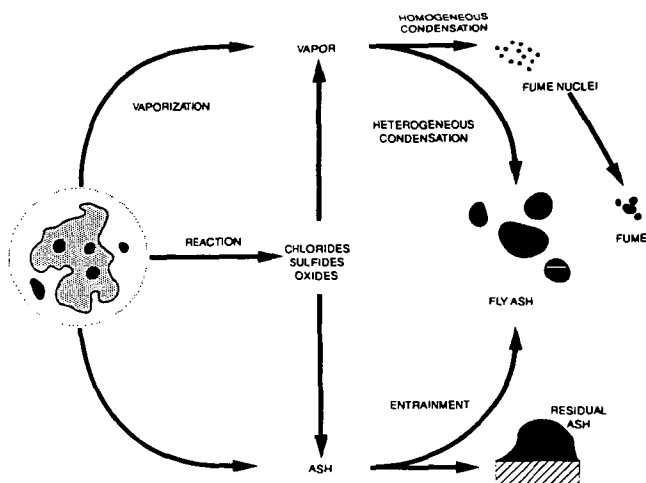
FIGURE 1. METAL TRANSFORMATION DURING INCINERATION (EPA, 4/91)

FIGURE 2.   ARSENIC EMISSIONS   (EPA, 4/91)

FUNDAMENTALS OF HEAVY METAL REMOVAL BY DRY SORBENTS

Mohit Uberoi[+] and Farhang Shadman
Department of Chemical Engineering
University of Arizona
Tucson, AZ 85721

[+] Present Address: W.R. Grace & Co.-Conn., Research Division, 7379 Route 32, Columbia MD 21044

Abstract

Emission of toxic metal compounds is a major problem in many combustors and incinerators. In the present work, using cadmium chloride as a model compound, the use of solid sorbents for removal of toxic metal compounds from high temperature flue gases is investigated. The sorbents tested were silica, alumina, kaolinite, emathlite and lime. Compounds containing aluminum oxide show high cadmium removal efficiency. In particular, bauxite has the highest rate and capacity for cadmium capture. The overall sorption process is not just physical adsorption, but rather a complex combination of adsorption and chemical reaction.

Introduction

Cadmium compounds are considered to be among the most toxic trace elements emitted into the environment during fuels combustion and waste incineration. Cadmium and cadmium compounds are primarily used in the fabrication of corrosion resistant metals. Cadmium is also used as a stabilizer in poly-vinyl chlorides, as electrodes in batteries and other electrochemical cells, and for numerous applications in the semiconductor industry [1]. Due to this wide range of applications, cadmium is present in many municipal and industrial wastes. Cadmium is also present in coal in trace quantities [2]. Consequently, emission of cadmium compounds is a problem in many waste incinerators and coal combustors. The chemical form and concentration of these compounds depend on a number of factors including feed composition and operating conditions [3].

The increased use and disposal of cadmium compounds, combined with their persistence in the environment and relatively rapid uptake and accumulation in the living organisms contribute to their serious environmental hazards. The present technology is inadequate to meet the expected cadmium emission standards. Therefore, new and effective methods need to be developed and investigated for controlling the emission of cadmium and other toxic metals in combustors and incinerators.

A promising technique for the removal of metal vapors from high temperature gases is through the use of solid sorbents to capture and immobilize the metal compounds by a combination of adsorption and chemical reactions. The sorbent can be

used in two ways:
- a. It could be injected as a powder (similar to lime injection) for in-situ removal of cadmium compounds.
- b. The cadmium containing flue gas could be passed through a fixed or fluidized bed of sorbent. The sorbent could be used in the form of pellets, beads, or monoliths (for high dust applications).

Previous studies by us and other investigators indicate that solid sorbents can be very effective in removing alkali and lead vapors from hot flue gases (4-7). In the present work, a number of potential sorbents were screened and compared for their effectiveness in removing cadmium compounds from hot flue gases. Details of the sorption mechanism were investigated for the selected sorbents.

Experimental

Materials

In the first part of this study, several model compounds and naturally available materials were evaluated as potential sorbents for removal of gaseous cadmium compounds from hot flue gases. The model compounds included silica (MCB grade 12 silica gel) and alpha alumina (Du Pont Baymal colloidal alumina, technical grade). The naturally available materials included kaolinite (52% SiO_2, 45% Al_2O_3, 2.2% TiO_2, 0.8% Fe_2O_3), bauxite (11% SiO_2, 84% Al_2O_3, 5% Fe_2O_3), emathlite (73% SiO_2, 14% Al_2O_3, 5% CaO, 2.6% MgO, 3.4% Fe_2O_3, 1.2% K_2O) and lime (97% CaO). Cadmium chloride was used as the cadmium source. For the screening experiments, the sorbents were used in the form of particles, 60 - 80 mesh in size. For the kinetic and mechanistic study the sorbents were used in the form of thin flakes (disks). The flake geometry is easy to model and characterize using analytical techniques. All the sorbents were calcined at 900°C for two hours and stored under vacuum until used. All the experiments were conducted in a simulated flue gas atmosphere containing 15% CO_2, 3% O_2, 80% N_2 and 2% H_2O.

Equipment and Procedures

Screening Experiments: The main components of the experimental system were a Cahn recording microbalance, a quartz reactor, a movable furnace and analyzers for determining the composition of the gaseous products. This system has been previously used for screening of sorbents for removal of lead compounds. Therefore, only the salient features of the system are described here. Details can be found in a previous publication[4]. The cadmium source was suspended by a platinum wire from the microbalance, which monitored the weight change during the experiments. A fixed bed of the sorbent particles was made by placing 100 mg of the sorbent particles on a 100 mesh stainless-steel screen in a quartz insert. All experiments in this study were performed with the source at 560°C and the sorbent at 800°C. This method ensured that the concentration of cadmium vapors around the sorbent was much below saturation, thereby preventing any physical condensation on the outer surface of the sorbent.

Heating of the cadmium source resulted in vaporization of CdCl$_2$ which was carried by the flue gas through the sorbent fixed bed. The percentage of cadmium adsorbed was determined from the amount of cadmium delivered (microbalance measurement) and the cadmium content of the sorbent at the end of the experiment. The cadmium content of the sorbent was determined by dissolving the samples in a H$_2$O/HF/HNO$_3$ (2/1/1 proportion by volume) mixture and subsequently analyzing the solution by atomic absorption spectroscopy. Separate water leaching experiments were performed to determine the water soluble fraction of adsorbed cadmium. The leaching of cadmium was conducted at 40°C in an ultrasonic bath for two hours. The cadmium content of the solution was subsequently determined by atomic absorption spectroscopy.

Study of Sorption Details: A microbalance reactor system was used for studying the sorption details. The sorbent flakes were suspended by a platinum wire from the microbalance. The weight of the sorbent was continuously monitored during the experiments by the microbalance. The cadmium source was placed in the horizontal arm of the reactor. The simulated flue gas from the gas preparation section was split in two parts. One part entered the reactor from the inlet below the balance and the remaining gas entered through the horizontal arm in which the cadmium source was placed. The cadmium source was heated by a heating tape and a furnace heated the sorbent flakes. All experiments were conducted with the source temperature of 560°C and the sorbent temperature of 800°C. When steady flow rates and cadmium concentrations were achieved, the sorbent was exposed to the cadmium containing flue gas. The sorbent weight was continuously recorded as it captured the cadmium vapors. The microbalance was continuously purged with ultra high purity nitrogen gas.

Results and Discussion

<u>Screening Experiments</u>

The results obtained from the screening experiments are given in Figure 2. Multiple experiments were conducted for most of the sorbents and good reproducibility was obtained. Since all experimental parameters except the sorbent type were kept constant, the amount of cadmium adsorbed is a good indication of the sorbent effectiveness (rate) for cadmium removal from hot flue gases. The most obvious feature of these results is the difference in the ability of the sorbents to capture cadmium from the flue gas passing through them. Alumina and bauxite had the highest cadmium capturing efficiencies. A large fraction of the cadmium captured by these two sorbent was water insoluble. Silica and kaolinite were not effective for removal of cadmium. Since cadmium chloride has a high water solubility, the formation of water insoluble compounds on sorption by alumina and bauxite leads to the conclusion that chemical reaction is the dominant mechanism of cadmium capture by these sorbents. Lime, a sorbent used for removal of sulfur compounds, did not have a high cadmium capturing efficiency. Since most of the cadmium captured by lime was water soluble, physical condensation is the dominant mechanism of cadmium capture for lime. From the screening experiments, it seems that compounds containing aluminum oxide have a

high cadmium capturing efficiency. Bauxite was therefore further studied to determine the mechanism of cadmium capture. Since previous studies have indicated that kaolinite is a good sorbent for removal of lead and alkali compounds, it was also included in the mechanistic study.

Details of the Sorption Process:

In the first part of this study, the cadmium sorption capacity of kaolinite and bauxite was investigated at 800°C. In these experiments the sorbent flakes were exposed to cadmium vapors until no further mass change was observed. The profiles for sorption for both kaolinite and bauxite are shown in Figure 3. The rate of sorption decreases with time and a final limit is achieved beyond which no further cadmium sorption takes place. The observed initial rate for cadmium capture by kaolinite was much slower than that for bauxite. This is consistent with the results from the screening experiments, where kaolinite captured much less cadmium compared to bauxite. Also, the final saturation limit for kaolinite (18%) was found to be lower than that for bauxite (30%) (Figure 3). When the concentration of cadmium in the flue gas wa reduced to zero, no desorption from either sorbent was observed indicating that reversible physical adsorption was not the dominant sorption mechanism.

X-ray diffraction (XRD) analysis was used to identify the final products formed by sorption of cadmium chloride on kaolinite and bauxite. Analysis of kaolinite flakes exposed to cadmium vapors indicated the formation of a cadmium aluminum silicate compound, $CdAl_2Si_2O_8$, which is water insoluble. Based on XRD results, the following reaction scheme is proposed for capture of cadmium :

$$Al_2O_3.2SiO_2 + CdCl_2 + H_2O \ \text{----} \quad CdO.Al_2O_3.2SiO_2 \ + \ 2HCl \quad (1)$$
metakaolinite
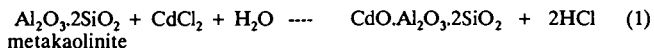
where metakaolinite is the dehydration product of kaolinite. Holland et al. ([8]) also observed the formation of this compound when a solid mixture of cadmium carbonate and kaolinite was heated to 800°C for twenty hours. Based on the stoichiometry of the overall reaction, 1 kg of kaolinite can capture 0.51 kg of cadmium, forming a product which is water insoluble and therefore safely disposable. The maximum weight gain postulated from this reaction (58% by weight) is much higher than that obtained experimentally in the microbalance reactor setup (18 wt%).

To further understand the reasons for low sorbent utilization, a kaolinite flake which had captured cadmium to its maximum capacity was mounted in epoxy and analyzed by SEM and EDX analysis. A cadmium map of the flake shows that cadmium is concentrated on the kaolinite edge (Figure 3). An EDX line scan on the flake surface indicated that the concentration of cadmium varied from 49 wt% at the edge to 2 wt% at the center. The concentration of cadmium at the edge (49%) is close to the value calculated from the postulated reaction mechanism assuming complete conversion (51%). This indicates that the surface of kaolinite was completely converted by reaction to form a cadmium aluminosilicate. Silicon and aluminum maps on the kaolinite surface indicate complete uniformity of distribution of these elements on the kaolinite surface. Since this flake had captured cadmium to its maximum capacity (microbalance data, Figure 3), the non-uniform distribution of cadmium indicates incomplete sorbent

utilization. Since the volume of the cadmium aluminosilicate phase is higher than that of the aluminum silicate phase, the formation of cadmium aluminum silicate at the outer surface probably blocks the sorbent pores, resulting in incomplete sorbent utilization.

XRD analysis of bauxite particles exposed to cadmium vapors indicated the formation of two crystalline compounds: a cadmium aluminum silicate and a cadmium aluminate. Since the cadmium aluminate has a higher water solubility compared to that of the aluminosilicate, bauxite has a larger fraction of water soluble cadmium in the screening experiments. The amount of SiO_2 present in bauxite is not enough to combine with all Al_2O_3 to form an aluminosilicate compound. Based on the stoichiometry of Reaction 1 and the amount of SiO_2 present, 1 kg of bauxite can capture 0.10 kg of cadmium to form a cadmium aluminosilicate. Based on the remaining alumina, 1 kg of bauxite can capture 0.94 kg of cadmium oxide forming a cadmium aluminate according to the following reaction mechanism:

$$Al_2O_3 + CdCl_2 + H_2O \ ---- \quad CdO.Al_2O_3 \ + \ 2HCl \tag{2}$$

If all the alumina and silica reacted with kaolinite to form cadmium aluminum silicate and cadmium aluminate (Reactions 1 and 2), the maximum weight gain possible is 1.06 kg per kg of bauxite. This is higher than the value obtained in the microbalance experiments conducted to completion (0.30 kg/kg bauxite).

To further understand the sorption mechanism, a bauxite flake exposed to cadmium vapors to the point of "no further weight change" was mounted in epoxy and analyzed by SEM and EDX analysis. The cadmium map on the bauxite surface indicated a non-uniform cadmium distribution (Figure 4). Comparison of the cadmium map with the aluminum and silicon maps on the flake surface indicated that regions high in both alumina and silica have high concentrations of cadmium. As confirmed by the XRD analysis, the cadmium present in the alumina phase reacts to form a cadmium aluminate. Regions rich in both alumina and silica combine with cadmium to form a cadmium aluminum silicate. EDX analysis of regions high in both aluminum and silicon indicated that the cadmium concentration was 26 wt%. EDX analysis of regions high in alumina indicated that the cadmium concentration in this phase (11 wt%) was much lower than that postulated by Reaction 2. This indicates that the alumina phase does not completely react with cadmium to form a cadmium aluminate. This could be due to the alumina phase having low porosity thereby preventing complete sorbent utilization. Also, formation of a higher volume product on the outer surface could inhibit further capture of cadmium.

From the mechanistic study it is clear that the sorption process under present experimental conditions is influenced by diffusional resistances. In practical systems, the rate of sorption can be increased by optimization of the sorbent pore structure to facilitate intraphase transport of cadmium vapors into the sorbent. The interphase mass transport limitations can also be reduced to increase the overall sorption rate. For in-situ applications, the efficiency of the sorbent can be increased by decreasing the particle size.

Conclusions

1. Bauxite and, to a lower degree, kaolinite are effective sorbents for removal of cadmium in combustors and incinerators.

2. The sorption mechanism and the nature of final products formed have important implications in the way each sorbent may be used. Compared to kaolinite, bauxite has a higher sorption rate and capacity; however, the products of sorption in bauxite are more water soluble. Therefore, kaolinite is more suitable when no leaching from the spent sorbent can be permitted.

3. The overall sorption process is a complex combination of adsorption, condensation, diffusion and chemical reactions.

4. In adsorbing cadmium chloride, chlorine is not retained by either kaolinite or bauxite. Additional cleanup steps may be needed in systems where the presence of chlorine in the flue gas cannot be tolerated.

Literature Cited

(1)   Palmer, S.A.K.; Breton, M.A.; Nunno, T.J.; Sullivan, D.M.; Suprenant, N.F. Metal/Cyanide Containing Wastes: Treatment Technologies **1988.**

(2)   Pacnya, J.M.; Jaworski, J. Lead, Mercury, Cadmium and Arsenic in the Environment **1987.**

(3)   Barton, R.G.; Maly, P.M.; Clark, W.D.; Seeker, R. Proceedings of 1988 National Waste Processing Conference, **1988,** 279.

(4)   Uberoi, M.; Shadman, F. AIChE J., **1990,** 36(2), 307.

(5)   Uberoi, M.; Punjak, W.A.; Shadman, F. Progress in Energy and Combustion Science **1990,** 16, 205.

(6)   Lee, S.H.D.; Johnson, I.J. J. Eng Power **1980,** 102, 397.

(7)   Bachovchin, D.M.; Alvin, M.A.; Dezubay, E.A.; Mulik, P.R. A Study of High Temperature Removal of Alkali in a Pressurized Gasification System, DOE-MC-20050-2226, Westinghouse Research and Development Center, Pittsburgh, PA. **1986.**

(8)   Holland, A.E.; Segnit, E.R.; Gelb, T. Journal of The Australian Ceramic Society **1976,** 10, 1.
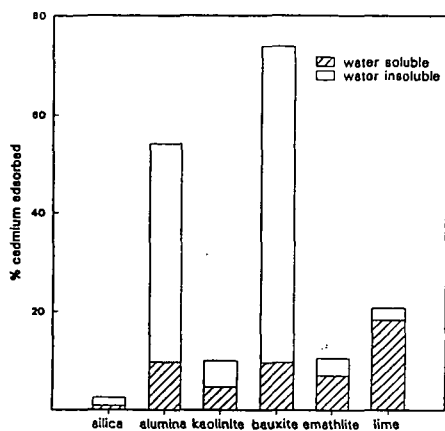
Figure 1: Cadmium removal efficiencies of various sorbents. Mass of sorbent used = 100 mg. T=800°C. Amount of cadmium vaporized in each experiment = 6.5 mg.
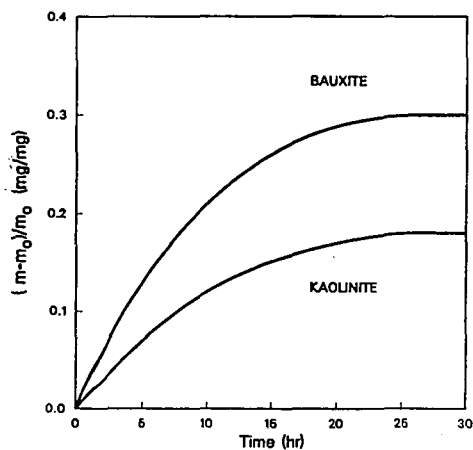
Figure 2: Temporal profiles of cadmium sorption on kaolinite and bauxite. T=800°C. Flow rate = 200 cc/min. Mass of flake = 15.1 mg (bauxite); 20.4 mg (kaolinite). Flake thickness = 0.71 mm (bauxite); 1.1 mm (kaolinite)

1748
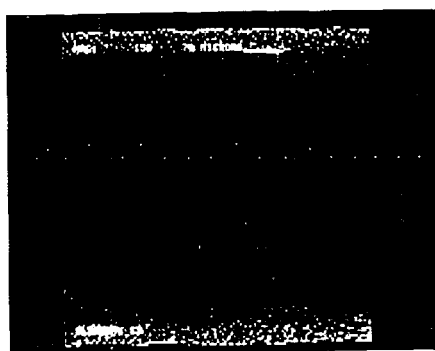
Figure 3: Cadmium concentration map on kaolinite flake surface
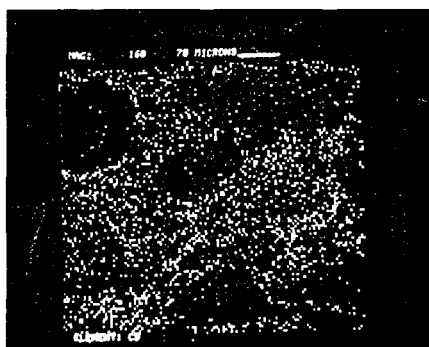
Figure 4: Cadmium concentration map on bauxite flake surface.

CELLS ON FIBERS FOR WASTE CLEAN UP

Robert Clyde
Clyde Engineering   (
POB 740644
New Orleans, Louisiana 70174

INTRODUCTION: Fibers have a large surface area so many cells
can be immobilized. Sulfur can be taken out of coal, metals
removed from wastewater, pulp mill effluent decolorized, and
a non-corrosive road deicer made.

At a recent conference in Boston (1) uses and methods of making
CMA (calcium magnesium acetate) were discussed. Beer told how(2)
calcium acetate could be sprayed into burning coal to remove
70% of the sulfur in the stack gas. Acid rain causes much
damage to trees and lakes. Yang (3) described methods of making
CMA from lactose (cheese whey) with organisms on cotton. Chapter
16 of a new book (4) teaches producing CMA from glucose with
cells on rotating fibers, covered in Clyde's patent 4,407,954.
CMA is also a non corrosive road deicer. Salt causes millions of
dollars damage 'to bridges, cars and plant life. Using woody bio-
mass or old newspapers as a raw material would reduce the cost.

Patent 4,530,763 describes removing uranium and other metals
from wastewater. Recently it has been found that when a strip
of Tyvek©fiber with Zymomonas mobilis on it was put into lead
and six valent chromium, the metals got not only on the section
immersed, but climbed right up the fiber and got on the fingers
of the holder, all in a couple seconds. The EPA will soon lower
the limits on lead in drinking water, and Cr6 is also very toxic.

Thousands of lawsuits have been filed against paper mills for
putting deadly dioxin into rivers. It also gets in milk cartons,
fish, tea bags, and diapers. The fungus Phanerochaete chrysos-
porium grows on fibers and high area Celite entrapped in fibers,
to decolorize pulp mill effluent. When an RBC (rotary biological
contactor) is run half full and a light shone in the top, the
light hits a thin moving film. UV light destroys dioxin. In
most photo reactors,colored solution blocks the light.

Methanol can be made from coal(5) and dissociated to clean burn-
ing CO and H_2 with 20% increase in energy (because waste heat
from the exhaust is utilized) as in patent 4,420,462.

Wayman (6) confirms that sugar . can be fermented to alcohol for
gasohol in 15 minutes. Dale (7) reports that when yeast is im-
mobilized on fiber, high rates of mass transfer are achievable
even at low agitator speeds.

Old cars and trucks that use leaded gasoline put the lead into
air and rain washes it into drinking water supplies. If gasohol
were used this would not be a problem. Sugar can be converted
to alcohol as follows:

A few spoons of Celite®(from Manville Company, Denver, CO) are
slurried in water and poured into a fermenter with rotating
fibers (Reemay 2033 from Reemay Co. Old Hickory, Tenn.) of
polyester. The unit is sterilized and <u>Zymomonas mobilis</u> (NRRL
14023, US Department of Agriculture, Peoria, Il.) is added. It
takes about 30 hours for the cells to grow and attach to the
fibers, and then the fermenter is flushed with four times its
volume of nutrient which is 10% glucose, 10g/l yeast extract
(from Difco) and 1 g/l of three salts $(NH_4)_2SO_4$ $MgSO_4$, and
KH_2PO_4.   If the pH is lower than 6, K_2HPO_4 is used instead of
KH_2PO_4. After flushing, aliquotes are taken and in 10 minutes
4% ethanol is measured by HPLC. This is an 80% yield, since
one mol of glucose is fermented to two of ethanol and two of CO_2
and the molecular weights of these are about the same (46 and 44)
so the theoretical yield is 51 g/l. The unit can then be run for
several weeks with residence times of 10 minutes. Some alcohol
can be stripped off and sugar recycled. If 96% yield is desired,
it can be run with a 15 minute residence time as Wayman did.
We believe that this reactor design is so efficient because
nutrients have intimate contact with cells, and the same thing
should apply to other applications. Membranes are expensive
but Tyvek®fiber from DuPont is not (only 75¢/sq.yd) and it has
small pores and many fibers so we plan on using Tyvek®in place
of Reemay. Zymomonas on Tyvek is shown in Fig. 1.

REFERENCES

1. The conference was held in Boston May 14-16 and sponsored by Northeastern
University.
2. J.M. Beer is from the Combustion Research Institute at MIT in Cambridge.
3. Shang Yang is from the Chem. Eng. Dept. at Ohio State Univ. in Columbus.
4. The CMA book is published by Elsevier and edited by Don Wise at Northeastern
University.
5. The book HOW TO PRODUCE METHANOL FROM COAL is published by Springer
Verlag and Emil Supp from Lurgi GmbH is the author.
6. Wayman M. et al Process Biochem. June '89 pg. 88-91
7. Dale,B. and Bringi,V. Biotech. Progress May/June '90 pg. 205-209

ZYMOMONAS MOBILIS ON TYVEK® FIBER
FIG. 1

10μm ×1250 13kV

Feed

Rotating Fibers
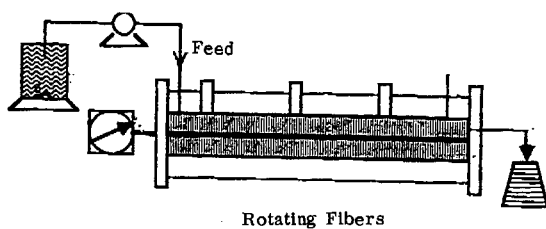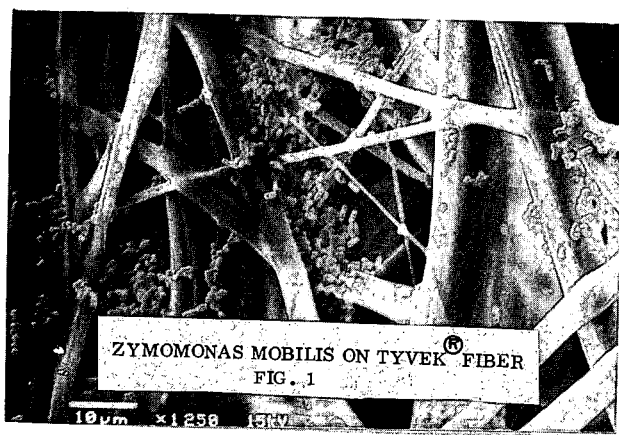
UTILIZATION OF COAL GASIFICATION SLAG: AN OVERVIEW

Vas Choudhry and Steven R. Hadley
Praxis Engineers, Inc.
852 North Hillview Drive
Milpitas, California 95035

ABSTRACT

Coal gasification generates solid waste materials in relatively large quantities, and their disposal can represent a significant expense. For example, a 100-MW power plant based on IGCC technology using 1000 tons of 10% ash coal per day may generate over 110 tons/day of solid waste or slag, consisting of vitrified mineral matter and unburned carbon. As coal gasification technologies, considered clean and efficient methods of utilizing coal, find increasing applications for power generation, it becomes imperative that slag utilization methods be developed, tested, and commercialized in order to address the costly problems associated with its disposal as solid waste. This paper presents an overview of the experimental work that has been conducted to characterize samples of slag from various gasifiers and to identify and test a number of commercial applications for their utilization, and discusses various issues with regard to slag utilization. In the course of examining various utilization applications for a number of coal gasification slags that parallel those developed for fly ash, a better understanding of slag as a construction material has been achieved. The applications tested include the use of slag as an aggregate for road construction, cement concrete and asphalt concrete, and production of lightweight aggregate from slag.

HISTORICAL PERSPECTIVE ON COAL WASTE UTILIZATION

In the past decade, fly ash, bottom ash, and boiler slag have increasingly been utilized in construction and other applications. In 1984, 51 million tons of fly ash was generated nationwide, of which 10 million tons, or 19.6%, was utilized in a number of applications. In Europe and Japan combustion solid wastes are utilized to a greater extent; this is attributed to the demand for construction aggregate and fill materials, the shortage of space for waste disposal, and environmental and economic factors.

The search for utilization applications for coal gasification slag parallels that of fly ash, which has been tested successfully for a variety of applications including aggregate stabilization in airport, highway, and dam construction, engineered backfill, soil amendment, cement additive, and lightweight aggregate production. A number of similar applications for gasification slag have been studied by Praxis Engineers, Inc. under a series of contracts funded primarily by the Electric Power Research Institute (EPRI) with additional support from Texaco, Inc. and Southern California Edison.

DEVELOPMENT OF SLAG UTILIZATION TECHNOLOGY

Using fly ash utilization as a model, Praxis started work in 1986 to develop the utilization of gasification slag. The steps involved in this approach can be summarized as follows:

o   Measurement of physical and chemical properties expected to affect the utilization of slag,

o   Screening of conventional industrial and construction materials and products for potential slag utilization applications,

o   Comparison of the properties of gasification slag with the specifications established for other materials to identify possible slag substitution,

o   Testing of promising applications at the bench scale,

o   Enhancement of the properties deemed significant from the utilization viewpoint by simple, low-cost preparation techniques, and

o   Selection of successful applications for further testing at the pilot or demonstration level.

Initial testing was performed using slag samples from the Cool Water Demonstration Plant (CWDP) to demonstrate this methodology. The Cool Water plant was based on the Texaco gasification process. Sixteen potential applications for the utilization of gasification slag were initially identified based on a comparison of the preliminary characteristics of CWDP slag with those of ash by-products. The most promising of these applications included use of slag as a soil conditioner, abrasive grit, roofing granules, ingredient in cement and concrete manufacture, road construction aggregate, and lightweight aggregate. The results of this work were summarized in a paper[1] and presented in an EPRI report[2].

Once successful utilization concepts had been identified for this slag, samples of another slag generated at CWDP from a different coal feedstock and three other slags generated from different gasifiers were also evaluated[3]. The three additional gasifier technologies were the Shell Coal Gasification Process, the British Gas Corporation/Lurgi Slagging Gasifier, and the Dow Entrained-Flow Gasification Process, using single-stage operation.

In a parallel study, use of slag for the production of synthetic lightweight aggregate was investigated. The findings of this study were presented in an EPRI report[4]. In a follow-on project, the production of lightweight aggregate from slag was successfully advanced to the pilot scale.

COAL GASIFICATION SLAG PROPERTIES

The physical and chemical properties of coal gasification slags were found to be related to the composition of the coal feedstock, the method of recovering the molten ash from the gasifier, and the proportion of devolatilized carbon particles (char) discharged with the slag. The rapid water-quench method of cooling the molten slag inhibits recrystallization, and results in the formation of a granular, amorphous material. Some of the differences in the properties of the slag samples that were characterized may be attributed to the specific design and operating conditions prevailing in the gasifiers. For instance, the British Gas/Lurgi gasifier produced a slag with a distinct iron-rich phase in addition to the silicate phase, and the Texaco gasifier generated slag containing a higher proportion of discrete char particles.

In general, slag is nominally in the 5-mm x 0.3-mm size range, which is equivalent to the classification for fine aggregates used in cement concrete and asphalt concrete. The apparent specific gravity of slag ranges between 2.64 and 2.81, and its dry compacted unit weight is between 70.1 and 104.9 lb/ft^3. The water absorption capacity of slag varies from 2 to 16% and increases with its char content.

The elemental composition of the slag samples with respect to both major and trace elements is similar to that of the gasifier feed coal ash, as shown in Table 1. The major constituents of most coal ashes are silica, alumina, calcium, and iron. Slag fluxing agents, when used to control molten ash viscosity inside the gasifier, can result in an enrichment of calcium in the slag.

The Cool Water slag was classified as nonhazardous under the RCRA regulations. EP toxicity and ASTM extraction tests were run on a number of slags to evaluate their leachability. The slags appear to be nonleachable with respect to RCRA-listed metals. Tests for eight common anions were run, with only sulfate anions being detected at significant concentrations (25 to 200 mg/l).

EVALUATION OF POTENTIAL UTILIZATION CONCEPTS

Selection of applications to utilize gasification slag must take into account the fact that it is in competition with conventionally used materials whose acceptability has been established over long periods. In this effort, the emphasis was placed on evaluating the functional requirements of various applications (such as compressive strength in the case of cement concrete) in order that existing specifications--written for natural materials--do not rule out slag utilization. Ultimately, if slag is found to satisfy the functional requirements of an application, suitable standards can be established for its use in particular cases. A precedent for this procedure is the creation of a standard such as ASTM C 989-87a which was adopted for utilization of ground blast-furnace slag as cement.

Selection of the specific utilization concepts was guided by the following criteria:

o   Similarity between the properties of slag and those of the material it replaces, and

o   Achievement of comparable final products meeting the necessary functional requirements.

Based on these criteria, a number of utilization concepts were identified. These include:

Agriculture: Soil conditioner, lime substitute, low analysis fertilizer, carrier for insecticides

Industrial material: Abrasive grit, catalyst and adsorbent, roofing granules, industrial filler, mineral (slag) wool production, filter media

Cement and concrete: Concrete aggregate, mortar/grouting material, pozzolanic admixture, raw material for portland cement production, masonry unit production

Road construction and
maintenance: De-icing grit, fine aggregate for bituminous pavement, base aggregate, subbase aggregate, seal-coat aggregate

Synthetic aggregate: Lightweight construction aggregate, landscaping material, sand substitute

Landfill and soil
stabilization: Soil conditioner to improve stability, structural fill, embankment material

Resource recovery: Source of carbon, magnetite, iron, aluminum, and other metals

Of these, a number of high-volume applications were tested at the laboratory scale and found to be suitable. For example, the potential for using slag as a fine aggregate for base, subbase, and

1755

backfill applications is suggested by the slag size gradation. Shear strength, permeability, and compaction test data also indicate that slag would perform well as an aggregate fill material. While these applications would consume large quantities of slag they provide few economic incentives to the industry to replace cheap and abundant conventional materials with slag at this stage. However, as concern about the environment increases and recycling of waste products becomes a priority, this situation could change rapidly.

USE OF SLAG IN ROAD CONSTRUCTION

The use of slag in road construction was studied by testing various asphalt mix designs incorporating slag. By itself, the slag was not found to be suitable for surface pavement applications due to the lack of coarse particles and the tendency to degrade when abraded. However, its use as a subbase and base material in road construction is quite feasible as it meets a number of requirements for resistance values, e.g., the California Department of Transportation standards for Class 1, Class 2, and Class 3 subbases, and Class 2 aggregate base. To compensate for the high proportion of fine material in the slag, it may need to be mixed with a coarser material for use in specification base material and as an asphalt concrete aggregate.

Asphalt concrete hot mixes containing varying concentrations of asphalt and 30-50% slag by weight as the fine aggregate were tested for their strength (S-values) in a laboratory. A mix in which 30% slag was combined with 6% asphalt yielded an S-value of 50, which is much higher than the minimum value of 30-37 required for various grades of asphalt concrete. This mix, which had good workability, compares favorably with the standard test mix containing 5% asphalt, with an S-value of 58.

USE OF SLAG IN CEMENT AND CONCRETE

The composition of the slag and its natural pozzolanic properties are similar to the raw material used to make portland cement clinker. In this application, the slag carbon (char) content may be beneficial and may provide some of the fuel needed to make the clinker. The slag could also be added to cement clinker and ground with it.

The carbon content of some of the slags is far higher than the 1% limit placed on aggregate. This makes it necessary to recover the unburnt carbon from the slag, both in order to meet the standard for aggregate and to improve the process economics. Char removal was accomplished by means of simple specific gravity devices. The recovered char is a usable by-product.

Several batches of concrete were prepared using slag to replace varying quantities of the sand in the mix. Specimens in which 50% and 75% of the sand was replaced by slag had compression strengths of 2786 and 2483 psi respectively, over a 28-day curing period. This compared well with the control sample containing no slag, which had a compression strength of 3407 psi. These results indicate that slag could be used to replace a large proportion of the fine aggregate in making light-duty nonstructural concrete.

Tests to replace some of the fine aggregate used to make concrete with slag were performed by substituting 50% of the sand by slag. The test specimens achieved satisfactory results, with compressive strengths ranging from 3000 to 3500 psi, compared with a control strength of 3900 psi at the same cement content. These results satisfy typical compressive strength requirements of 2000 psi for concrete pads for sidewalks, driveways, and similar applications.

Another series of tests involved using slag ground to a fine powder as a cement replacement. Cement additive requirements have been established for blended cements in ASTM C 595 which covers five classes of blended hydraulic cements made from conventional materials for both general and specific applications. Following initial exploratory tests, it was concluded that it was necessary

to process the slag samples to remove potentially deleterious substances. The lighter char fraction was removed from one of the slags by density separation, and an iron phase was recovered from another slag by magnetic separation. The percentages of cement replaced by slag in these tests was 15% and 25% respectively. The use of processed slags resulted in a more successful replacement of cement by slag. All of the 15% slag-cement blend samples exceeded the 3-, 7-, and 28-day strength requirements of 1800, 2800, and 3500 psi respectively, and one of the four slags tested exceeded these requirements at the 25% replacement level. The other three 25% replacement level slag samples achieved the required 28-day strength but did not satisfy the 3- and 7- day requirements. The average 28-day strength for the 15% blend was 5600 psi, and that of the 25% blend was 4900 psi.

The success of the prepared slag-cement blends in achieving long-term compressive strength suggested that the ground slag would also qualify as a pozzolanic mineral admixture. A pozzolan is a finely ground siliceous material which can react with calcium ions, in the presence of water and at room temperature, to form strength-producing calcium silicate minerals in a manner similar to cement reactions. A 35% replacement of cement by slag was evaluated in accordance with the procedures outlined in ASTM C 311. The success of a pozzolanic test is measured by the Pozzolanic Index, which indicates the ratio of the sample's compressive strength to that of an ordinary portland cement control sample. All of the concrete samples thus produced exceeded the Pozzolanic Index requirement of 75%, with index values ranging between 90 and 118%.

SLAG LIGHTWEIGHT AGGREGATE

Lightweight aggregates (LWA) have unit weights that are approximately 40-60% those of standard aggregates. Annual consumption of LWA in the United States for various applications is approximately 15 million tons. Major applications of LWA are in the production of lightweight structural concrete used in highrise buildings and lightweight precast products such as roofing tiles, masonry blocks, utility vaults, cement concrete pipes, etc. Conventional LWAs are produced by pyroprocessing of naturally occurring expansible shales or clays at temperatures ranging between 1880 and 2200°F after pulverizing, working into a paste, and extruding them to produce pellets of the desired size. The strength requirements for lightweight concretes made from LWA are given in Table 2.

Slag-based lightweight aggregates (SLA) were produced by duplicating the processing methods used for commercial LWA manufacture. These steps included grinding the slag, mixing it with a clay binder and water, and extruding it to form long strands that were cut to the desired sizes. These wet green pellets were then dried and fired in a laboratory muffle furnace at 1800°F for 4 minutes. A unit weight of 45 lb/ft^3 was measured for the SLA, which is below the minimum coarse LWA specification of 55 lb/ft^3. Concrete made from the SLA had a 28-day compressive strength of 3100 psi and a unit weight of 105 psi, which exceeds the ASTM requirements shown in Table 2.

Further tests have confirmed that the density of the SLA can be controlled as a function of the firing temperature, as shown in Figure 1. This indicates that SLA products can be produced to meet specific density requirements such as those for cement concrete LWA, lightweight concrete masonry units, or ultra-lightweight material used in insulating concrete.

Tests on discrete 2-mm particles of each slag showed that they also expand to form a lightweight material when fired at 1600-1900°F. Further tests on all particles larger than 0.3 mm, without pelletization, confirmed this phenomenon. The materials resulting from these tests had unit weight values of 15-25 lb/ft^3. The concrete produced from one of the expanded slag samples had a unit weight of 33 lb/ft^3, which qualifies it to be classified as an insulating concrete. However, it had a compressive strength of only 125 psi which is somewhat lower than the strength of commercially available insulating concretes at 200-250 psi. It is expected that the strength can be considerably

1757

increased with minor adjustments to aggregate gradation and the cement proportions used to formulate these test samples.

The experimental work on slag utilization has been developed to the continuous pilot scale for the production of SLA from slag. The results from this test program have been very encouraging and have confirmed the bench-scale test results. During the tests, engineering information on energy requirements, scale-up information, and off-gas analysis was obtained, and the mechanism of slag expansion was investigated. The energy requirements for SLA production are considerably lower than those for conventional LWA production due to the lower kiln temperatures required for slag. Samples of the SLA generated during the pilot tests are undergoing extensive testing.

CONCLUSIONS

Gasification slag has been determined to be an environmentally nonhazardous material, whose unique properties may be attributed to the composition of the mineral matter in the coal feedstock and the method of quench-cooling applied in the gasifier. Bench-scale test data have shown that there are a number of promising applications for the utilization of gasification slags. In particular, the utilization of slag in applications such as road and construction aggregates, cement additives, and lightweight aggregates has been demonstrated. Production of slag-based LWA (or SLA) is feasible and should be established as a priority. The high unit price of LWAs will permit SLA to be transported for greater distances while remaining economically competitive, thus rendering slag utilization less sensitive to the location of the gasifier.

FUTURE OF SLAG UTILIZATION

Currently, in most utilization scenarios, gasification slag would be used as a replacement for materials that have a relatively low unit cost, such as road aggregates. Unless potential commercial users of slag are provided with extensive characterization and utilization data, the economic incentives alone are unlikely to be sufficient to cause them to incorporate slag into their production scenarios. The initial resistance to the use of new materials that may be encountered in the construction materials manufacturing industry can be addressed in two ways. First, the slag producer can supply complete engineering data on slag utilization to the prospective end user, who would then be responsible for any processing steps that might be required for a particular application. An alternative, more comprehensive approach would be for the slag producer to deliver the slag to the end user in a form that meets the user's specifications; these specifications could vary depending on the market demand in the vicinity of the gasifier. If recent legislation in California can be used to gain an insight into coming regulatory trends, at least 50% of the slag produced in the state will be required to be utilized in the coming decade, thereby creating additional incentives for producers and prospective end users to work together to realize its utilization potential.

REFERENCES

1.   V. Choudhry, D. Deason, and R. Sehgal, "Evaluation of Gasification Slag Utilization Potential." Presented at the 6th EPRI Coal Gasification Contractors' Conference, Palo Alto, California, October 1986.

2.   Potential Uses for the Slag from the Cool Water Demonstration Plant, Electric Power Research Institute, Palo Alto, Calif., February 1987. Final Report for Projects 985-9 and 1654-35, prepared by Praxis Engineers, Inc. EPRI AP-5048.

3.   "Characterization of Coal Gasification Slags," EPRI Contract No. RP2708-3. Final report in preparation.

4. *Synthetic Lightweight Aggregate from Cool Water Slag: Bench-Scale Confirmation Tests*, Electric Power Research Institute, Palo Alto, Calif., May 1991. Final Report for RP1654-38 prepared by Praxis Engineers, Inc. EPRI GS-6833.

Table 1

COMPARATIVE COMPOSITION OF TYPICAL BLAST-FURNACE SLAG, COOL WATER FEED (UTAH) COAL ASH, AND COOL WATER SLAG

Mineral	Blast Furnace Slag	Cool Water (Utah) Coal Ash	Cool Water Slag
SiO_2	32-42	48.0	40-55
Al_2O_3	7-16	11.5	10-15
CaO	32-45	25.0	10-15
MgO	5-15	4.0	2-5
Fe_2O_3	0.1-1.5	7.0	5-10
MnO	0.2-1.0	NA	NA
S	1.0-2.0	NA	<1

Table 2

UNIT WEIGHT, MINIMUM COMPRESSIVE STRENGTH, AND TENSILE STRENGTH
(28-Day Requirements for Structural Concrete, ASTM C 330)

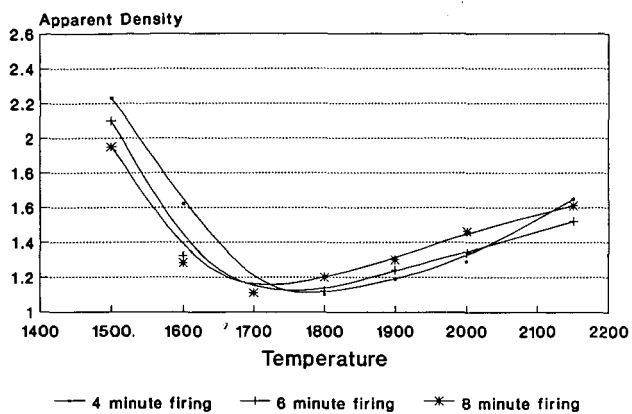| 100% LWA mix		Sand/LWA Mix	
Unit Weight lb/ft³	Compressive Strength, psi	Unit Weight lb/ft³	Compressive Strength, psi
115	--	115	4000
110	4000	110	3000
105	3000	105	2500
100	2500	100	--

Figure 1. Time/Temperature/Density Relationship for Expansion of Slag Pellets

ASH UTILIZATION AND DISPOSAL
by

CARL A. HOLLEY
PRESIDENT
FERRO-TECH, INC.
WYANDOTTE, MI 48192

ABSTRACT

There are many changes taking place in the utilization and disposal of
ash and related materials and each day it seems that there are more
restrictions on the disposal of ash. In one project, mass burn ash
has been screened to remove the plus one inch pieces and then combined
with the fly ash and portland cement to produce a pellet that is non-
leaching with all of the heavy metals "fixed".

In the northeastern United States, the ash from circulating fluidized
bed combustors needs to be pelletized so it can be transported back to
the mine for easy disposal. The ash can also be blended with digested
municipal sewage sludge to form a soil additive which contains lime
and nutrients.

The new clean air standards are making it necessary for utilities to
install sulfur dioxide scrubbers which produce gypsum. This gypsum
filter cake can be pelletized so that the pellet produced can be
utilized in the final grind of Portland cement or can be disposed of
in a non-leaching pile.

We have taken the lead in producing these agglomeration techniques and
many more processes which we will describe and show the detailed
process flow diagram for each of these methods.

INTRODUCTION

The utilization and disposal of fly ash in a legal and environmentally
safe manner is becoming a major engineering challenge because of
rapidly changing government laws and regulations.

There are many changes taking place in ash management based on the
fact that pellets can be produced which are non-leaching. Pellets can
be moved with conventional bulk material handling equipment without
producing a dusty environment. The pellets can be disposed of in any
type site and do not need to be placed in a lined landfill.   In
addition, slight modifications to the pelletizing process can produce
usable products such as lightweight aggregate or aggregate to be
utilized in asphalt.

We see that each situation or plant needs to be treated as a separate
problem and a process developed to solve that particular problem. The
two key pieces of equipment required to process fly ash are the Ferro-
Tech-Turbulator™ (Figure 1) and the Ferro-Tech Disc Pelletizer (Figure
2).   The Ferro-Tech-Turbulator™ is a proprietary, intense, highly
efficient, agitative agglomeration device. The unit has maximum effi-
ciency because it operates by fluidizing the material and atomizing
the injected liquid. Each whirling dust particle is uniformly coated
with a very thin layer of water or other binder. These coated dust

particles, moving at a high velocity in suspension, collide and impact with great force with the other coated, spinning particles within the turbulent wake created behind the pins, forming a very uniformly sized and dense particulate or microgranule. The thick, resilient polymer liner in the Turbulator™ combined with critical close pin tip tolerance causes the pins to fully sweep or wipe the liner, eliminating product build-up on the inner casing of the Turbulator™ body. Because of the intensity of the Turbulator™, it can efficiently pre-blend, de-dust, blend, condition, densify, hydrate and micropelletize all types of fine powders, dust, fume and hard-to-wet particulates. The fly ash particles are uniformly coated with water in the Turbulator™ before they are discharged to be pelletized in the disc pelletizer. The conditioning step in the Ferro-Tech-Turbulator™ compensates for the variation in particle size and surface area which is an inherent quality of fly ash, due to changes in combustor operations and variation in fuel.

CIRCULATING FLUIDIZED BED COMBUSTOR ASH AGGLOMERATION

Most of the new cogeneration plants are utilizing a circulating fluidized bed combustor principle which burns coal having reasonable levels of sulfur (up to 3%). The ash from these combustors consists of two fractions, bed drain or bottom ash and fly ash. The bed drain ash is approximately 25 to 30% of the total ash. The best ash systems keep the two ash fractions separated so they can be blended uniformly together for agglomeration. The fly ash can be agglomerated alone, but the bed drain ash must be blended with at least 50% fly ash before quality pellets can be produced.

The basic process flow diagram for producing a 1/4" x 1/2" pellet is shown in Figure 3. This system includes two (2) surge bins with feeders feeding the ash into a Ferro-Tech-Turbulator™ where most of the water required for pelletizing is added. The conditioned ash from the Turbulator™ discharges directly into the disc pelletizer where pellets are formed. This disc pelletizer is designed for this specific agglomeration application. The pellets or green balls from the disc pelletizer have a modest amount of strength so that they can withstand the treatment of the material handling system to the pellet curing area. The pellets require some curing if they are to be moved by normal material handling methods. After curing, a typical 1/2" diameter pellet may require a force of 300 pounds to crush it. These pellets can easily be utilized as road bed material or as aggregate in concrete.

CIRCULATING FLUIDIZED BED COMBUSTOR ASH AGGLOMERATION
(High Sulfur Coal)

When a high sulfur coal (above 3%) is burned in a circulating fluidized bed combustor, this fly ash acts very differently. When water is added to the fly ash in a Ferro-Tech-Turbulator™, the ash very quickly (5 to 10 minutes) gains temperature. A typical temperature is shown in Figure 4 where the temperature rose to 290° F in seven minutes. If enough water has been added to produce pellets, the pellets will quickly heat up and will completely disintegrate becoming an even finer dust than it was in the beginning.

The process flow diagram necessary to produce pellets from this fly ash on which Ferro-Tech holds a patent is shown in Figure 5. The conditioned fly ash from Turbulator™ No. 1 is discharged directly into a conditioning bin where the fly ash hydrates and the temperature increases to as much as 300° F. The conditioned material from Turbulator™ No. 1 is retained in the conditioning bin until all of the water which was added in Turbulator™ No. 1 has chemically reacted and the fly ash is completely dry. During the hydration phase, the chemical reaction will produce much finer particles with a lower bulk density than the original fly ash. The material from the conditioning bin is fed into Turbulator™ No. 2 where most of the water for pelletizing is added. Again, the material from the Turbulator™ is discharged directly into a disc pelletizer where pellets are formed. The pellets are placed in a curing area where they cure and gain strength.

FLY ASH LIGHTWEIGHT AGGREGATE

One of the better uses for Class F and Class C fly ash from pulverized coal power plants is to produce lightweight aggregate. This aggregate can be utilized to produce lightweight concrete block and other masonry forms. The basic process flow diagram for the process is shown in Figure 6. The aggregate seems to have many advantages over other lightweight aggregates including its spherical shape. The aggregate produced by this process bonds to the mortar with both a mechanical bond and a chemical bond instead of just a mechanical bond as is true of other non-reactive aggregates.

The bulk density of the aggregate is approximately 45 to 50 lbs./cu.ft. The typical sieve analysis (ASTM C136) of the aggregate for concrete block is:

Sieve Size	Product Percent Passing	Specification Percent Passing
1/2"	100	100
3/8"	99	90 - 100
4 mesh	83	65 - 90
8 mesh	49	35 - 65
16 mesh	31	---
50 mesh	19	10 - 25
100 mesh	15	5 - 15

SYNTHETIC GYPSUM & FLY ASH PELLETIZING

One of the major problems at pulverized coal power plants burning high sulfur coal which have a wet line scrubber is how to dispose of the synthetic gypsum slurry. One very simple solution is to produce a pellet by blending dry fly ash with the gypsum filter cake or even with the gypsum slurry. Figure 7 shows the basic process flow diagram for the required system. In this system, the filter cake is metered into the Ferro-Tech-Turbulator™ at a constant rate. The feed rate of the fly ash is controlled by a Ferro-Tech patented moisture control system on the disc pelletizer. This system adjusts the feed rate to maintain a constant surface moisture on the pellets which are about to discharge from the disc pelletizer.

The pellets from the disc pelletizer are placed in a curing pile where they gain strength before being placed in a landfill. The pellets increase in strength quickly and can then be transported in standard material handling equipment.

MASS BURN ASH AGGLOMERATION

The processing of mass burn ash is in a state of change since there is obviously a need to produce a product that has all of the heavy metals "fixed" so they do not leach from a landfill. The requirement is to process both the bottom ash and the fly ash. Processing the bottom ash alone is very difficult because of the extreme variation in the size of the pieces and in the high moisture of the material. A finger screen can be utilized to separate the plus one inch particles from the minus one inch pieces even though the moisture may be as high as 20 to 25% as shown in Figure 7.

Once the oversized pieces are removed, the available fly ash is added uniformly along with 15 to 20% Portland cement. These are all fed directly into a disc pelletizer which is equipped with a reroll ring. Moisture is added to the disc pelletizer through spray nozzles until pellets are produced. It normally requires a total of 16 to 20% moisture to produce pellets.

The completed pellets are discharged from the disc pelletizer pan into the reroll ring where 1 to 3% Portland cement is added to coat the pellets. The coating of the pellets with Portland cement serves two purposes. The first purpose is to seal the surface of the pellets which will assist in eliminating any leaching, the second purpose is to keep the pellets from sticking together as they cure in the tote bin.

After approximately seven days of curing, the heavy metals in the ash are fixed to the point that they will pass the T.C.L.P. leaching test. The pellets will have strength enough to be easily handled and should not crush under normal handling.

CONCLUSION

Essentially any fly ash can be agglomerated into non-dusting and non-leaching agglomerates. The requirements for the agglomerates keep changing and become more restrictive as the regulators try to make the environment safer. Our goal is to assist the customer in developing the best process to fulfill the regulators present and future demands. Many of the processes appear to be simple, but there has been much experience involved in the development. We feel that the simplest process is the best process if it meets all of the customer's goals. We know that each situation is unique and a process must be adapted to the special ash from a specific plant. It is advisable to cooperate with a supplier who has the most experience so you can have confidence in their recommendations.
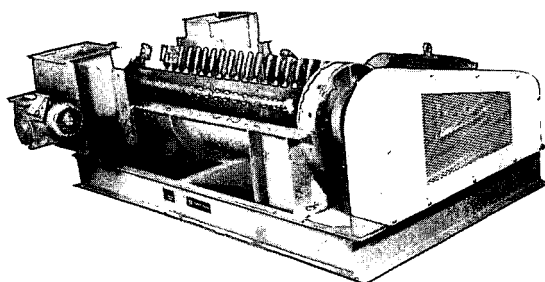
FIGURE 1
FERRO-TECH-TURBULATOR™
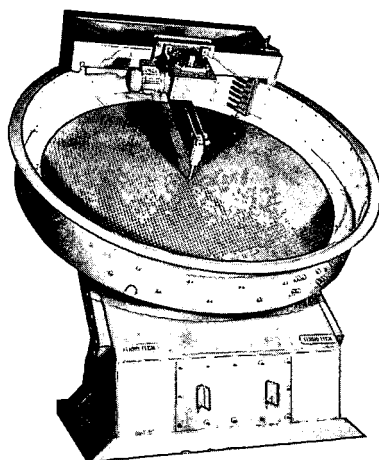
FIGURE 2
DISC PELLETIZER

HYDRATION TEMPERATURE

TEMPERATURE DEGREES F

300+ 300 280 260 240 220 210 200 180 160 140 120 100

TIME IN MINUTES

1 2 3 4 5 6 7 8 9 10 11

Temperature Curve
Figure #4

C.F.B. Ash Pelletizing System
Figure #3

WASTE
PORTLAND CEMENT
SURGE BIN
BIN DISCHARGER
FEEDER
FIXING AGENT
TURBULATOR
WATER
DISC PELLETIZER
STACKER CONVEYOR
PELLET CURING

FERRO—TECH INC.
467 EUREKA RD.
WYANDOTTE , MI   48192

FiT

Fly Ash Light-Weight Aggregate
Figure #6

C.F.B. Ash Pelletizing System
High Sulphur Coal
Figure #5

FERRO–TECH INC.
467 EUREKA. RD.
WYANDOTTE , MI   48192
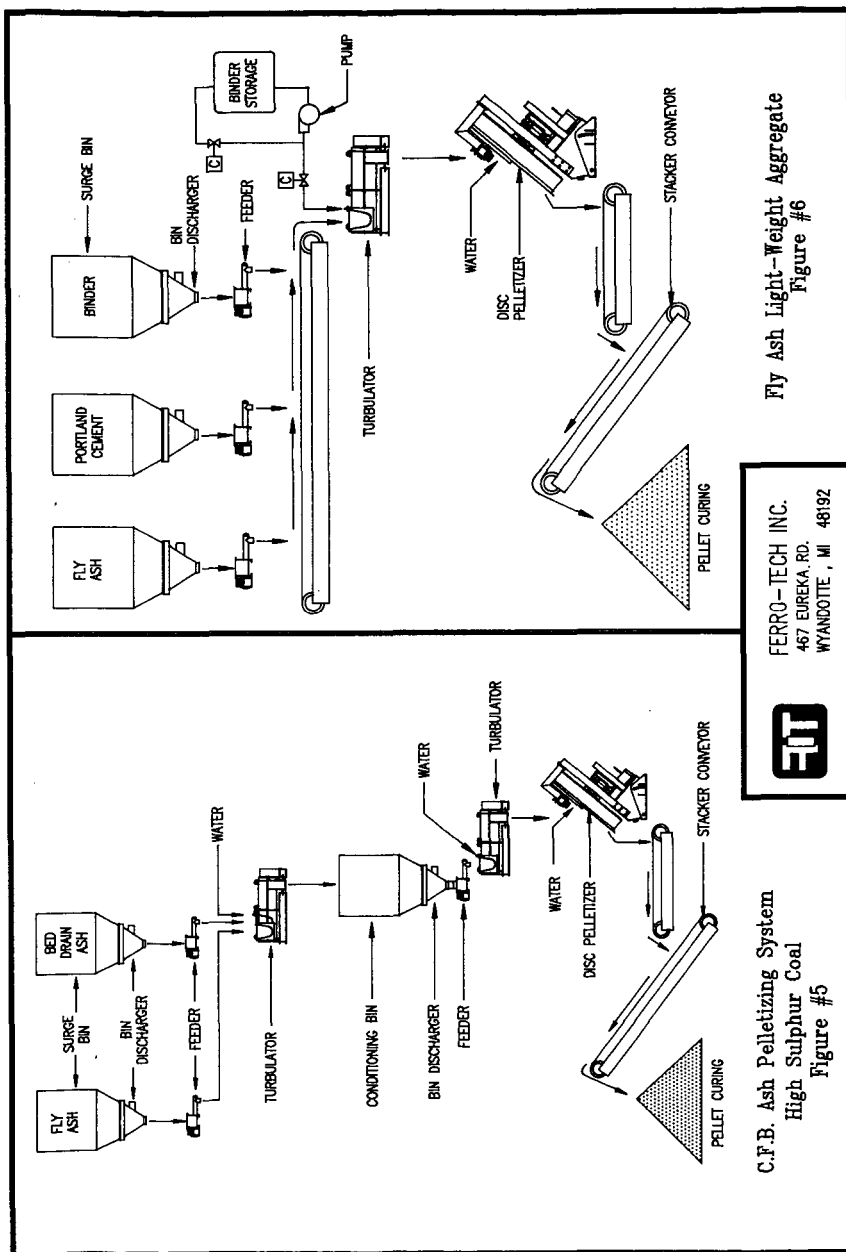
Mass Burn Ash Agglomeration
Figure #8
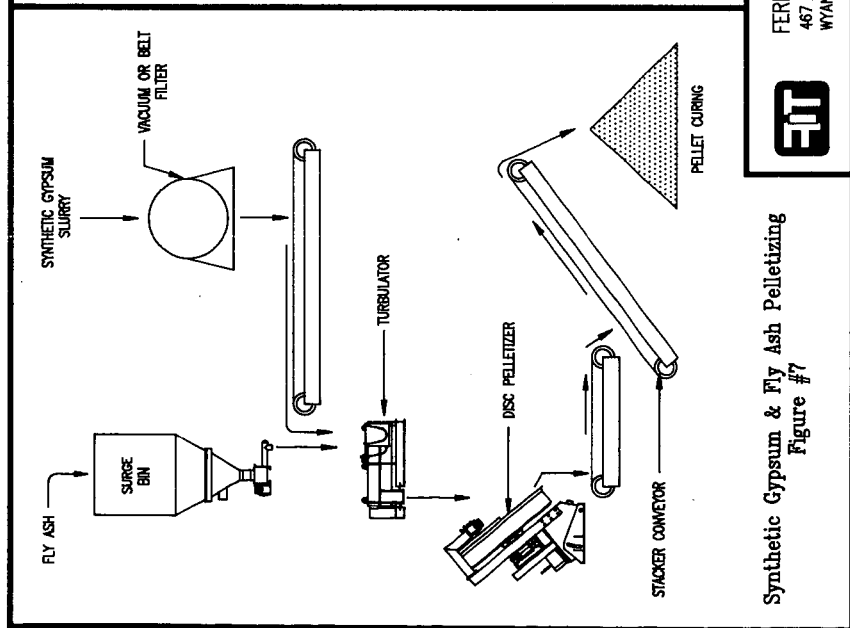
Synthetic Gypsum & Fly Ash Pelletizing
Figure #7

FERRO—TECH INC.
467 EUREKA, RD. .
WYANDOTTE , MI 48192

HIGH-STRENGTH PORTLAND CEMENT CONCRETE
CONTAINING MUNICIPAL SOLID WASTE INCINERATOR ASH

James T. Cobb, Jr., C. P. Mangelsdorf, Jean R. Blachere,
Kunal Banerjee, Daniel Reed, Clayton Crouch, Coby Miller,
Jingqi Li, and Jeannette Trauth

School of Engineering, University of Pittsburgh
Pittsburgh, Pennsylvania 15261

Keywords: municipal solid waste, incinerator ash, Portland cement concrete

ABSTRACT

A variety of methods are being examined by numerous organizations to render
hazardous solid residues non-hazardous and to create beneficial uses for ash from
municipal solid waste incinerators. One method for both purposes is the replacement
of a portion of the fine aggregate in Portland cement concrete. The strength of the
concrete drops significantly as the portion replaced increases, even with normal
additives. This paper presents the greatly improved strengths obtained with ash,
which has been exposed to a new additive. These results show that up to 35% of
the concrete can be made up of ash, while still obtaining compressive strengths of
over 5000 psi (34.5 MPa). Micrographs of the original ash, ash and additive,
concrete with ash but without additive, and concrete with ash and additive indicate
the role of the additive. TCLP extractions of this novel new concrete have yet to be
conducted. The economics, commercialization and extension of the development to
other situations are discussed.

INTRODUCTION

As landfill space becomes more limited, it becomes more attractive to reduce the
volume of materials being disposed there. Recycling is one approach, waste
minimization is a second method, and combustion for energy production is the third,
and ultimate, one. Ash from municipal solid waste (MSW) combustors can have less
than 10% of the original volume entering the facility. A further reduction in
landfilling, though, can be realized by developing a beneficial use for the ash. The
most commonly considered beneficial use of ash is as an aggregate in either
bituminous or Portland cement concrete. This method has the further advantage of
displacing sand and gravel, which must be mined from sometimes environmentally
sensitive locations. Another short-term advantage of this method is its ability to bind
the toxic metals, entering with the MSW [1], into the concreted mass. Controversy
over the long-term implication of the presence of these metals in the concrete has
arisen, however. The Environmental Defense Fund has expressed vigorous concern
for the long-term release of these metals as the concrete eventually degrades or is
reduced to rubble [2].

Utilizing MSW incinerator ash in Portland cement concrete has been investigated by
several organizations. At a number of locations, bottom ash (slag) from high-
temperature combustors is utilized as coarse aggregate in regular concrete (see for
example References 3 and 4). Utilization of low-strength concretes containing either

fly ash or mixed fly and bottom ash (combined ash) are moving toward commercial use in three directions.

One of these directions is to make block secondary products, such as artificial reef blocks, construction blocks, and shore protection devices [5]. Artificial reef blocks consist of 85% combined ash and 15% Portland (Type II) cement and have compressive strengths of about 1000 psi (6.9 MPa). By comparison, standard precast Portland cement concrete contains 40% coarse aggregate, 40% fine aggregate and 20% Portland cement and has a compressive strength of over 3500 psi (24.2 MPa). Construction blocks consist of 35-60% combined ash, 25-50% sand, 15% Portland (Type IP) cement, and sufficient Acme-Hardesty superplasicizer to allow the mix to flow easily. Compressive strengths vary from 1600 psi (11.0 MPa) to 2600 psi (17.9 MPa). A boathouse, built recently at the State University of New York at Stony Brook from 14,000 such construction blocks, is being evaluated for structural and environmental acceptability. Finally, shore protection devices require the use of a patented admixture, Chloranan (manufactured by Hazcon, Inc., of Brookshire, Texas) at a ratio of cement to admixture of 10:1. Using cement percentages between 17 and 33, compressive strengths up to 4200 psi (29.0 MPa) are reported.

A second approach is the accretion of combined ash with Portland cement (8-14%) into coarse aggregate for use in roadbeds and concrete [6]. This level of concretization provides aggregate with strengths of about 1200 psi (8.3 MPa), similar to the material, described in Reference 5. Finally, a third approach is the stabilization of combined ash with Portland cement (6-10%) to create land fill covers [7]. In all of these approaches, the ability of Portland cement concrete to reduce the leachability of trace metals from the concreted mass to meet TCLP standards has been a key element of their development.

A major area which these projects do not address is the precast concrete market. For entrance into this arena, compressive strengths between 3500 psi (24.2 MPa) and 5500 psi (38.0 MPa) must be achieved. In addition, extensive physical testing must be applied and minumum standards met. These tests include tensile strength, freeze-thaw, deicing, and abrasion. As the preceding brief review shows, obtaining the compressive strengths required by precasters has proven impossible with significant amounts of combined ash, even with standard additives. Only those concretes made with the addition of large amounts of Chloranan enter this range.

The School of Engineering at the University of Pittsburgh has recently discovered an inexpensive method which permits high-strength concrete to be produced, containing large amounts of combined ash from a MSW combustor. The method, which has just been disclosed to the University as the first step in the patent process, will now be described as thoroughly as possible within the limits imposed by that process.

PORTLAND CEMENT CONCRETE MANUFACTURE

In October 1988 the University of Pittsburgh began to study the utilization of MSW combustor ash in Portland cement concrete. Four 750-lb (1650-kg) samples of ash have been obtained during the past two years from the MSW combustor at Poughkeepsie, New York, operated for the Dutchess County Resource Recovery Agency by Dutchess Resource Energy, a subsidiary of the Resource Energy Systems

Division of Westinghouse Electric Corporation. The primary combustor in this facility is an O'Conner water-wall rotary kiln. The bottom ash drops into a water-filled pit, from which it is reclaimed past a grizzly to take out large particles, and a magnet for iron removal. The hot gases from the primary combustor pass through a secondary combustor, a boiler, and a dry scrubber. The fly ash and spent limestone (injected in the scrubber for acid gas removal) are added to the bottom ash just before the combined ash is loaded into trailers for hauling to a land disposal site.

The first two samples of ash were composited from 5-pound (11-kg) sub-samples of combined ash, collected six times daily for 25 days. Ash Sample #1, combined ash collected from mid-July to early September 1989, contained 8-21% moisture, 15.1% calcium oxide, 2.21% sulfur trioxide and 7.2% iron oxide and exhibited a 7.26% loss of ignition. Ash Sample #2 was bottom ash collected during January 1990. Ash Samples #3 and #4 were bottom ash collected in essentially one quick draw on May 24-25, 1990, and March 1-2, 1991, respectively. Ash Sample #3 contained 11.9% calcium oxide, 2.58% sulfur trioxide and 9.8% iron oxide and exhibited a 8.04% loss of ignition.

Six batches of concrete were made with Ash Sample #1 and fifteen batches with Ash Sample #2. The basic recipe was 17% coarse aggregate, 40% ash and 43% Portland cement. An air entrainment additiive, a water reduction additive and a silica fume additive were all tried individually with certain of these batches. The slump of each batch was held as close as possible to 1.75 inches (4.45 cm) by varying the water content. Concrete batches were produced in a small commercial mixer in the Concrete Laboratory of the Civil Engineering Department, following standard procedures. A number of cylinders (3 inches (7.6 cm) in diameter and 6 inches (15.2 cm) long) were formed from each batch. Cylinders were stored in an environmentally controlled room. Compressive strengths were measured on a Baldwin hydraulic compression tester, also located in the Concrete Laboratory of the Civil Engineering Department. Sets of four cylinders were cracked, and the load at breaking were averaged to obtain reported values of compressive strength.

Compressive strengths were generally in the range of 1000 psi (6.9 MPa) to 2300 psi (15.9 MPa). The ash in the first six batches of concrete were subjected to the Standard Extraction Procedure Method (the EP TOX procedure). The extractions were performed in the Environmental Laboratory of the Civil Engineering Department and leachates were sent to a commercial laboratory for analysis. Neither the ashes nor the concretes exceeded the EP TOX limits for any constituent. However, the ash and one of the six concrete batches (which happened to contain a lower amount of Portland cement a higher amount of coarse aggregate than according to the usual recipe, and which also contained some sand) exceeded the NYCRR limits for cadmium and lead. The presence of fly ash in Ash Sample #1 appeared to cause a number of "popouts". A white crystalline material, identified as a physical assemblage of aluminum chloride and calcium oxide crystals, was found at the focal point of all the popouts examined.

As Ash Sample #2 was running out, it was decided to attempt to modify the chemical and/or physical makeup of the surface of the ash particles to increase the strength of the bond between the ash and the cement. Two different commonly available chemicals were tried as additives in the last two batches of concrete made from Ash Sample #2. One of these novel additives did, in fact, yield compressive

strengths of nearly 4000 psi (36.0 MPa). Therefore, a set of batches with varying amounts of this effective, inexpensive, novel additive were prepared with ash from Ash Sample #3. The results are shown in the Table 1. The amount of additive is given as a percentage of the weight of cement present in each batch. A second batch of concrete, Batch Number 44, was made with the last portion of Ash Sample #3, using the same recipe as Batch Number 32.

Samples of ash and concrete were examined in the Scanning Electron Microscope (SEM) in the secondary electron imaging mode. The phases present were also compared using X-ray microanalysis in the SEM. Figures 1 and 2 are examples of micrographs for Batches Number 42 and 44, respectively, in the secondary electron imaging mode. It appears from an examination of these micrographs that, even with a 12-fold increase in additive from Batch Number 42 to Batch Number 44, the same basic cement structure is present in both concretes.

Figures 3 and 4 are SEM micrographs of ash. Figure 3 is for Ash Sample #4 as received. Figure 4 is for Ash Sample #3, which has been mixed with an aqueous solution of the chemical additive, using the same amounts of ash and additive as was used in preparing Batch Number 32. It may be observed from an examination of these micrographs that the surface of the as-received ash is heavily contaminated with fine particles, which are not present on the treated ash.

It is hypothesized from the observations reported above that the elimination of the fine particles in the concrete formulations with the chemical additive renders the surface of the ash particles (serving as fine aggregate) more amenable to strong bonding with the hydrated Portland cement, yielding high-strength concrete as a product.

A preliminary cost analysis of one ton (4400 kg) of concrete (dry basis), composed of

- 420 pounds (930 kg) coarse aggregate
- 750 pounds (1650 kg) of ash
- 830 pounds (1830 kg) of Portland cement
- chemical additive at the level of Batch Number 32

shows that purchase of the materials for its manufacture would require $23.50. The cost of materials for a 2:2:1 precast concrete is $10.00. The ash-containing concrete with the formulation of Batch Number 32 would be $13.50 more expensive than the standard concrete. Since the former contains 750 pounds of ash, the ash would have to be forced into this beneficial use with a tipping fee of $36.00 per ton, which is less than one-third of the current tipping fee at landfills.

FUTURE WORK

One final technical step in developing concrete with the same recipe as Batch Number 32 needs to be taken. Durability tests (tension strength, expansion, freeze/thaw, deicing and abrasion) and a TCLP extraction need to be carried out. When these results are available, precasters in the vicinity of the MSW combustor, operated by the Dutchess County Resource Recovery Agency, can make an informed technical decision on the use of the ash from this combustor in their products.

Regulatory permission for this use of the MSW combustor ash would then have to be sought from the State of New York.

Several other aspects of the beneficial use of MSW combustor ash in Portland cement concrete should be examined. First, the current 0.5:0.9:1 recipe may not be the optimal one for commercial use. A range of formulations should be explored. Second, additives similar to the one used in these first experiments could be tried, especially if durability and TCLP tests uncover any problems. Third, ash from other types of combustors could be tested for the applicability of the new additive . These combustors would include other MSW combustors with different methods for ash removal from the unit. They could also include industrial and hazardous waste combustors.

ACKNOWLEDGEMENTS

REFERENCES

[1] Franklin, M. A., "Sources of Heavy Metals in Municipal Solid Waste in the United States, 1970 to 2000," Proceedings of the Third International Conference on Municipal Solid Waste Combustor Ash Utilization, Arlington, Virginia, November 13-14, 1990.

[2] Denison, R. A., "The Hazards of Municipal Incinerator Ash and Fundamental Objectives of Ash Management," presented at "New Developments in Incinerator Ash Disposal," Northwest Center for Professional Education, April 26, 1988.

[3] Hartlen, J.," Incinerator Ash Utilization in Some Countries in Europe," Proceedings of the First International Conference on Municipal Solid Waste Combustor Ash Utilization, Philadelphia, Pennsylvania, October 13-14, 1988.

[4] Mahoney, P. F., and J. F. Mullen, "Use of Ash Products from Combustion of Shredded Solid Waste," Proceedings of the First International Conference on Municipal Solid Waste Combustor Ash Utilization, Philadelphia, Pennsylvania, October 13-14, 1988.

[5] Roethel, F. J., and V. T. Breslin, "Stony Brook's MSW Combustor Ash Demonstration Programs," Proceedings of the Third International Conference on Municipal Solid Waste Combustor Ash Utilization, Arlington, Virginia, November 13-14, 1990.

[6] Huitric, KR. L., J. L. Korn, and M. M. Wong, "Characterization and Treatment of Ash Residue at the Commerce Refuse-to-Energy Facility," Proceedings of the Third International Conference on Municipal Solid Waste Combustor Ash Utilization, Arlington, Virginia, November 13-14, 1990.

[7] Chesner, W. H., "The Long Island Ash Utilization Program -- Preliminary Engineering, Economics and Environmental Findings, and Guidelines for MSW Combustor Ash Utilization," Proceedings of the Third International Conference on Municipal Solid Waste Combustor Ash Utilization, Arlington, Virginia, November 13-14, 1990.

TABLE 1. Variation of Compressive Strengths with Additive

Batch Number	Additive (%)	90-Day Compressive Strength, Psi (MPa)
29	3.47	0 (0)*
30	1.73	4940 (34.1)
32	0.87	6200 (42.8)
36	0.65	3750 (25.9)
37	0.43	3210 (22.1)
34	0.17	2260 (15.6)
42	0.07	1560 (10.8)**

*   All cylinders of this batch broke apart by 90 days.
**   14-day compressive strength.

FIGURE 1.   SEM micrograph of the fractured surface of Batch Number 42, made
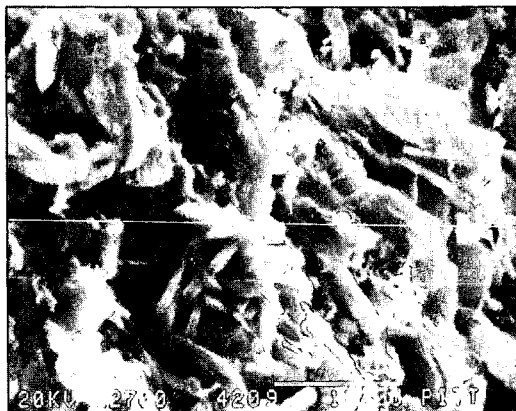with 0.07% additive; the bar is 10 micrometers.

FIGURE 2.   SEM micrograph of fracture surface of Batch Number 44, made with
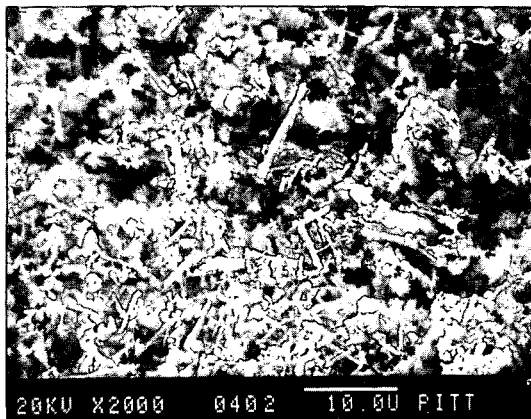0.87% additive; the bar is 10 micrometers.

FIGURE 3. SEM micrograph of Ash Sample #4 as received; the bar is 10 micrometers.
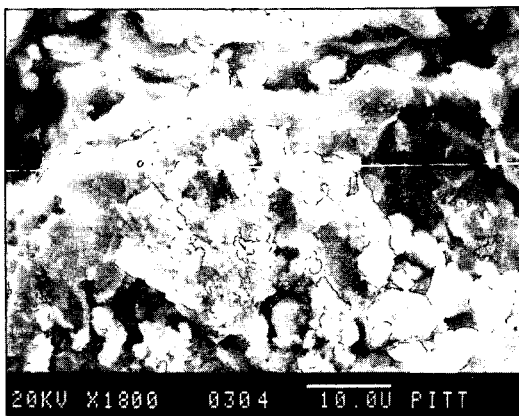

FIGURE 4. SEM micrograph of Ash Sample #3, mixed with additive; the bar is 10 micrometers.

CHARACTERIZATION OF MUNICIPAL WASTE
BY SCANNING ELECTRON MICROSCOPY AND OPTICAL MICROSCOPY

Melanie A. Behrens, M. Rashid Khan, Tristan A. Laurion,
Ronald J. McKeon

Texaco, Inc.
P.O. Box 509
Beacon, New York   12508

ABSTRACT

The use of municipal waste in conjunction with coal gasification is
becoming an increasingly attractive option for disposal of this
waste. Characterization of the properties of the waste material is
necessary before it can be utilized as a feedstock. There are
considerable differences in the municipal waste generated by
different communities and regions of the country and these differ-
ences can affect the gasification process. Scanning Electron
Microscopy (SEM) with Energy Dispersive X-ray Microanalysis (EDX),
using a backscattered electron detector, was used to examine the
mineral content and morphology of the municipal waste. The fiber
content and morphology was also characterized, using both optical
microscopy and SEM.

INTRODUCTION

Disposal of municipal waste has been an environmental issue in
recent times. Methods of disposing of this waste by incineration
and composting have drawbacks. Composting requires space and time,
while incineration is wasteful of the energy inherent in the
sludge, and distasteful to the public. The continuing development
of the coal gasification process allowing incorporation of the
sludge as part of the feedstock in this process is an option for
the disposal of this waste.   Conversion of the sludge to electric
power by this process rather than wasting its inherent energy value
is the result. In terms of energy conservation this factor makes
the process attractive.

There are several processing aspects which must be considered in
utilizing municipal waste as a feedstock. Municipal waste must be
partially dewatered before it is shipped to the gasification plant.
The viscosity of the mixed coal/sludge slurry is important because
it must be pumped into the reactor. Beyond the mixing ratio, some
of the factors influencing the viscosity of the sludge will be due
to the composition of the material, particularly the fiber conte-
nt.[1] Wastes from different parts of the country and different
communities will have different compositions. For instance,
municipal waste from Passaic County, NJ is known to have a high
content of kaolinite due to the concentration of paper producing
plants in the region. Some municipalities produce a sludge with a
higher fiber content than others. Minerals containing elements
which are volatile at gasification temperatures may be found in

higher concentrations in one region as opposed to another. The
nature of the mineral content of the sludge will have an effect on
the slag produced and volatile elements may initiate formation of
deposits.

Although bulk elemental analysis of sludge is essential to the
characterization of the material, microanalysis through the use of
optical and scanning electron microscopy techniques and Energy
Dispersive X-ray microanalysis also has its place. Municipal waste
is an extremely heterogeneous material and examination of this
material by these techniques can provide insight on associations of
the minerals with the organic content of the sludge and morphology
of the fibers. Presented here are the results of microscopic
characterizations performed on raw and treated samples of dewatered
sludge from Los Angeles County, CA, and Passaic County, NJ.[2]

EXPERIMENTAL

SAMPLE PREPARATION
For the SEM analysis, a small amount of each sample was mounted and
carbon coated using an evaporative coater to produce a conductive
surface. In addition, several of the LA County samples were
sputter coated with gold in order to obtain improved imaging
results for documentation. The optical microscopy was performed on
larger portions of the sludge.

OPTICAL MICROSCOPE
A Nikon SMZ-10 stereoscopic optical microscope was used to take
color photomicrographs of the raw and treated LA County, CA munici-
pal waste.

SCANNING ELECTRON MICROSCOPE
The instrumentation used for this study was an AMRAY 1645 SEM
equipped with a lanthanum hexaboride (LaB6) electron emitter source
and imaging detectors for secondary and backscattered electrons. A
Tracor Northern TN-5500 Energy Dispersive X-ray microanalysis
system (LSI 11/73 CPU with 3 MByte working memory and 30 MByte mass
storage capacity) with a lithium-drifted silicon detector was used
for semiquantitative analysis of elements with an atomic number
greater than 10 and less than 92. Elemental spectral analysis was
performed using standardless software routines with ZAF correction
factors. The SEM conditions for analysis were 20KV acceleration
voltage, 100 micron emission, 200 micron final aperture, spot size
4, working distance 24 millimeters, 0 degrees tilt, and a calculat-
ed take-off angle of 28.6 degrees. In addition to elemental
analysis and photomicrography, X-ray mapping and digital image
acquisition were performed on the LA County samples.

RESULTS

Optical microscopy was used to get an overview of the morphological
characteristics of the municipal waste. As the figures show, the
raw sludge contained a large amount of fibrous material. In addi-
tion, sprouting seeds and plastic bandage materials were found.
The treated sludge materials looked darker and more granular, with
little fibrous material present.

1778

SEM/EDX microanalysis was used to verify these results and to characterize the mineral content of the waste material. It is important to understand that only a small portion of sludge was examined by microanalysis and therefore the elemental analysis is not representative of the bulk of the municipal waste.

Morphological study by both methods indicated that many of the untreated sludge particles were held together by fibrous material, mostly hair and cellulosic plant fibers. In the LA County sludge, the hair was usually long and curled around the organic material while the plant fibers which were present were thicker and often served as a base on which the organic material could anchor. The Passaic sludge was matted together, with short fibers holding the organic material together in a matrix.

Seen in the untreated LA County sludge, along with the discrete woody cellulosic materials, fibers, and mineral particles, were many particles of organic material. These had inclusions of smaller particulate mineral matter, which were often silicates. Also included within the organic matrix were fibers, woody material and even plastics or spongy material. Other inorganic mineral matter found within the matrix of these samples contained iron, barium, aluminum, zinc, magnesium, phosphorus, calcium, sulfur, potassium, and titanium. In addition to these elements, a Houston municipal waste which was characterized contained cadmium, nickel, and lead. The treated LA sludge samples were devoid of the fibrous and cellulosic material. Mineral inclusions were still present within the matrix of the organic material.

The backscattered electron detector was used to locate particles containing inorganic elements and to obtain photomicrographs when charging problems prevented good imaging by secondary electrons. X-ray mapping was useful in locating associations between elements on a broader scale. Figures 1 and 2 show the labeling of the analyzed points of solid sludge particles. The tables beneath these figures give the EDX microanalysis of the marked points. The other figures present morphological information about the different municipal wastes.

ACKNOWLEDGEMENTS

REFERENCES

1. L. A. Rodriguez, R. A. Ashworth, R. Armstead, P. A. Aristedes and N. B. Spake, U. S. Patent 4,405,332, "A Fuel Composition", 1983.
2. D. G. Beshore and V. M. Giampi, U. S. Patent 4,762,527, "Slurry Fuel Comprised of Heat Treated, Partially Dewatered Sludge with a Particulate Solid Fuel and its Method of Manu facture", 1988.
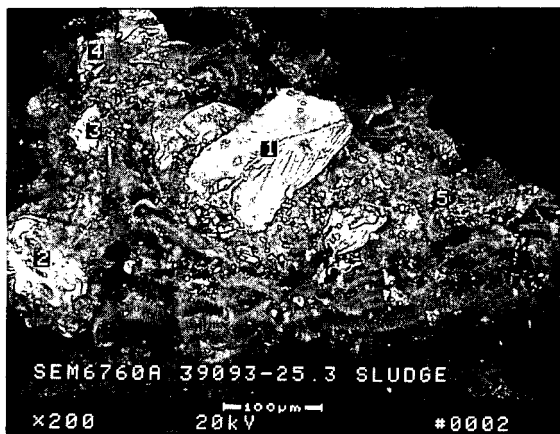
Fig.1 Los Angeles Raw Sludge (200X): A particle of sludge composed of both mineral matter and organic matter.

Analysis Table (normalized results):

ELEMENTAL ANALYSIS   (WEIGHT % OF MINERAL MATTER)

POINT	Mg-K	Al-K	Si-K	P-K	S-K	Cl-K	K-K	Ca-K	Ti-K	Fe-K	Cu-K	Ni-K	Zn-K
1	--	1	94	1	1	--	-	--	--	--	3	--	--
2	1	6	3	1	1	--	7	2	3	64	9	1	2
3	1	4	1	-	1	--	-	14	1	73	5	--	-
4	5	17	2	-	1	3	-	--	-	24	41	2	4
5	2	10	19	15	13	3	1	18	2	10	5	1	1
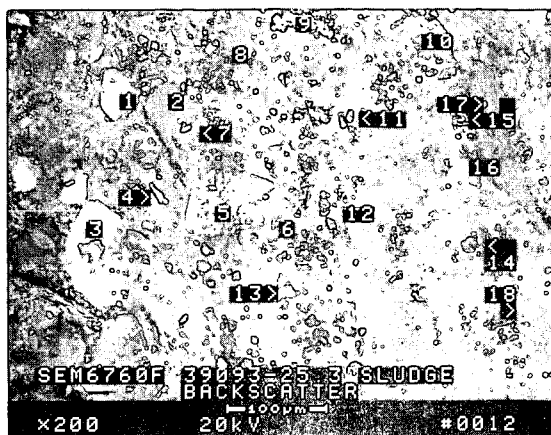
Fig.2 LA County Raw Sludge (200X): Portion of a sludge particle showing its heterogeneous nature.

Analysis Table (normalized results):

ELEMENTAL ANALYSIS   (WEIGHT % OF MINERAL MATTER)

POINT	Mg-K	Al-K	Si-K	P-K	S-K	Cl-K	K-K	Ca-K	Ba-K	Ti-K	Fe-K	Cu-K	Zn-K
1	--	--	96	1	-	--	-	--	--	--	1	1	--
2	--	2	2	2	78	2	-	3	--	--	4	5	1
3	--	1	92	1	-	--	-	--	--	--	1	4	--
4	--	5	3	1	2	1	1	24	--	1	51	9	2
5	--	1	96	-	-	--	-	--	--	--	--	2	--
6	2	8	14	17	12	1	1	16	--	2	23	3	1
7	1	2	4	5	24	1	-	3	50	1	8	2	-
8	3	8	10	9	24	3	1	16	--	-	14	10	1
9	2	5	2	1	1	-	-	1	--	4	84	1	-
10	1	1	1	1	-	-	-	95	--	--	1	1	-
11	--	25	56	1	1	1	-	14	--	--	1	1	-
12	2	10	15	6	19	4	3	18	--	--	11	10	1
13	--	1	92	2	1	-	-	--	--	--	1	2	-
14	12	19	30	-	1	-	-	1	--	--	35	1	-
15	--	4	17	7	11	1	6	23	--	3	14	9	5
16	--	--	96	1	-	-	-	--	--	--	1	1	-
17	20	6	47	4	7	1	1	4	--	--	6	3	1
18	2	4	5	9	12	29	1	18	--	6	11	3	-
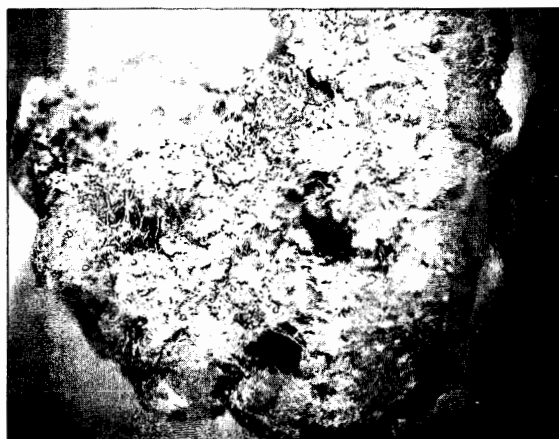
Fig.3 Los Angeles County Raw Sludge (6X) Optical Photomicrograph: The fibrous material holding this piece together is visible, along with some particles of inorganic material.

Fig.4 Los Angeles County Raw Sludge (18X) Optical Photomicrograph: A sprouting seed found in this municipal waste.
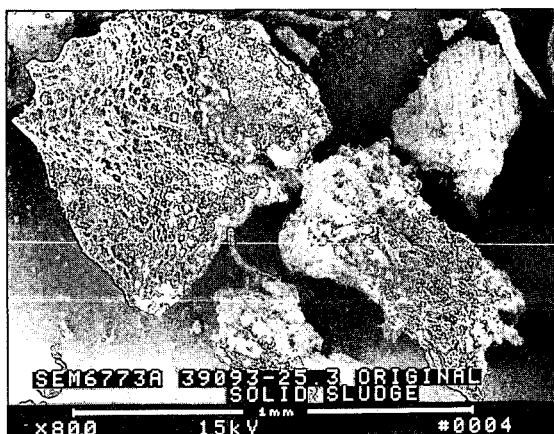
Fig.5
Raw LA County Sludge (80X): The honeycombed particle was aluminum silicate, the upper right corrugated particle was cellulosic, and two lower ones were organic matter with mineral inclusions.
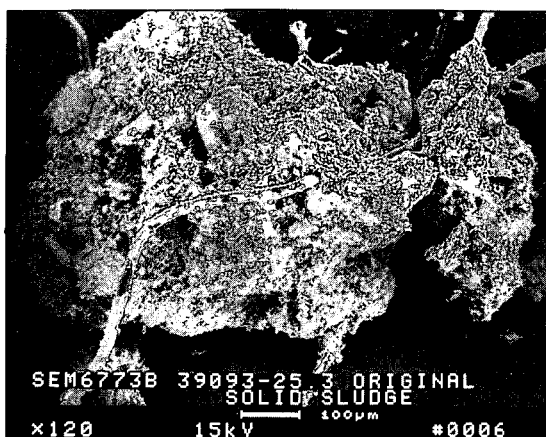
Fig.6 Raw LA County Sludge (120X): Organic particle with fibers and mineral particles included in the matrix.
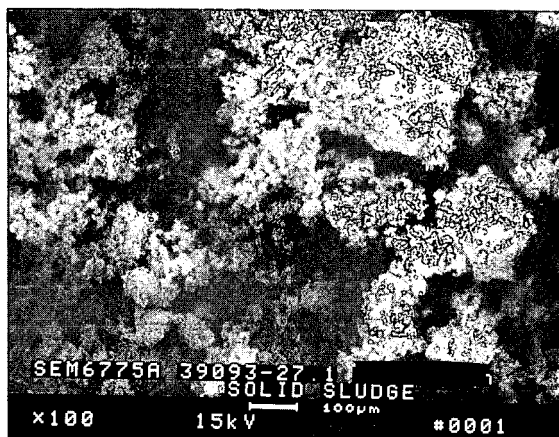
Fig.7 LA County Sludge after treatment process (100X): Fibers have disappeared and material is more homogeneous.
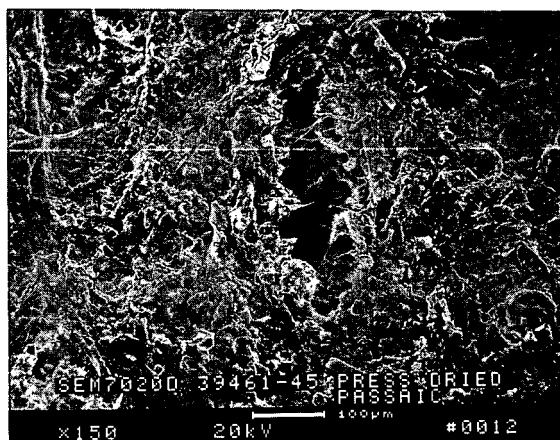
Fig. 8 Passaic Valley, NJ Sludge (150X): Fibrous sludge with mat-like morphology.

Trace Metals Analysis of Fly Ash by
Inductively Coupled Plasma Atomic Emission Spectrometry

Bassam S. Attili
Dr. Kenneth E. Daugherty*
University of North Texas
Denton, Texas

A binding agent has been developed for pelletized densified refuse derived fuel (dRDF). Initial studies showed that calcium hydroxide (Ca(OH)$_2$) is effective in reducing the rate of biological and chemical degradation of dRDF pellets. A commercial test of dRDF, with Ca(OH)$_2$ as a binder, was conducted at Jacksonville, Florida Naval Air Station in the summer of 1985.

In June/July of 1987 a full-scale cofiring of a binder densified refuse derived fuel (bd-RDF) and high sulfur content coal was conducted at Argonne National Laboratories (ANL). About 567 tons of bd-RDF pellets was cofired with coal, at 0, 10, 20, 30, 50 percent d-RDF Btu content and 0, 4, 8 percent calcium hydroxide binder. Results indicated that some trace elements decreased in fly ash with the increase in dRDF percentage while others increased.

The most toxic elements of concern are As, Ba, Be, Cd, Cr, Cu, Hg, Ni, Pb, Sb, Se, Tl, V and Zn. A microwave oven dissolution method was used to dissolve the ash in a mixture of aqua-regia and hydrofluoric acid using a Parr bomb. The solution was then analyzed by Inductively Coupled Plasma Atomic Emission Spectroscopy after approximate dilution.

Introduction

Incineration of municipal solid waste is an attractive solution to landfills[1-4] . However the physical and chemical characteristics of ash are becoming more and more important for safe disposal[5] . Some trace metals are important in the ash because of their potential toxicity, which plays a role in characterizing the ash as hazardous, and how and where to dispose of it.

Mass burn incineration produces ash residues amounting to 15 to 25 percent by weight and 5 to 10 percent by volume of the incoming Municipal Solid Waste (MSW)[3,6] . Ash comes in two forms. Fly ash the fine particles in the flue gas collected by electrostatic precipitators or bag house, and bottom ash the material dropped from the grate in the furnace. The ashes during the 1987 study at ANL were collected three times a day for six weeks from both the bag house and the grate.

Trace element concentrations in ash are of great interest because of their relationship to regulatory criteria under the Resource Conservation and Recovery Act (RCRA) regarding toxicity. Trace metals in fly ash were analyzed using Inductively Coupled Plasma Atomic Emission Spectroscopy (ICP-AES).

Several investigators have examined the feasibility of ICP-AES for the rapid, precise, and accurate multi-element analysis[7-13]. ICP-AES permits the determination of a large number of elements with high sensitivity and precision and with relative freedom from chemical interferences[14-17].

Methodology
Fuel Preparation

The binder enhanced d-RDF pellets for the 1987 ANL study were supplied by two facilities, one located at Thief River Falls, (Future Fuel Inc.) Minnesota, and the other at Eden Prairie, Minnesota (Reuter Inc.). The dRDF was made with 0, 4, 8 percent $Ca(OH)_2$ binder. High-sulfur Kentucky coal is normally burned in the power plant of Argonne National Laboratory at the rate of nine tons per hour.

Before each test run, d-RDF pellets and coal were blended together using a front-end loader until the material looked roughly homogenous. Three volumes of coal and one volume of d-RDF produces a blend close to 10 percent d-RDF by Btu content. Then the blend was moved by front-end loader to the coal pit and transported by conveyor to coal bunker prior to use in the ANL stoker fired boiler.

Sampling Plan

A total of 567 tons of d-RDF pellets were cofired with 2,041 tons of sulfur-rich coal in 12 test runs. The runs were classified according to the different Btu contents of d-RDF in the fuel and different binder content of d-RDF. Runs 1 and 12 used coal alone in order to establish base line data. In between the different runs and to avoid cross-contamination, coal runs were performed to cleanout the d-RDF from the previous run. Details of the test plan and sampling locations have already been published[3,18,19,20].

Sample Collection

During the test runs, samples were collected from various plant locations that were of interest in the study. Economizer, multicyclone fly ash and bottom ash samples were collected in aluminum containers and then transferred to plastic zip-lock bags for subsequent analysis at the University of North Texas.

Equipment

Parr Bombs

Parr Teflon acid bombs were obtained from Parr Instrument Company. The bomb is made of a microwave transparent polymer. A compressible relief disc is built into the closure to release excessive pressure. Over 1500 psi the relief disc will be compressed to a point where support for the O-ring will be lost and it will blow out. In most cases all parts of the bomb were reusable except for the O-ring.

Microwave Oven.

A Kenmore commercial microwave oven was used in this work. The oven has a variable timing cycle from 1 second to 100 minutes and a variable heating cycle based on power setting from 10% through 100% full power (700 w).

Inductively Coupled Plasma Atomic Emission Spectrometry ICP-AES

A Perkin-Elmer ICP-5500 Atomic Emission Spectrometer with a 27.12-MH, RF generator was used in this analysis. A Perkin-Elmer Model-10 data station was used with a Pr-100 printer.

Sample Analysis

After the samples were returned to the laboratory, they were arranged on the shelves according to the dates and times they were collected. About 10 grams of a homogenous sample was ground to pass at least a 75 mesh sieve. A 400 mg sample was placed in a polyteflon container and treated with 1 mL of hydrofluoric acid and 3 mL of aqua regia. The teflon container was then placed in the bomb and the bomb was tightly capped. The bomb was placed in the microwave oven and heated for 4 minutes and left for several hours to cool. After cooling, the PTFE container was uncapped and 2 mL of saturated boric acid was added quickly. The container was then recapped, returned to the microwave oven and reheated for 1 more minute, then cooled again.

At this stage some uncombusted carbon remained, so the solution with the residue was filtered, washed with deionized water and the filtrate was diluted to 50 mL in a polyethylene volumetric flask.

The microwave heating procedure has been used to determine minor and major constituent in the past. The solution was finally analyzed by ICP-AES using a blank and a standard solution containing the same amounts of acids. Standards with varied concentrations of As, Hg, Pb, Sb, Se, Tl, Ba, Be, Cd, Cr, Cu, Ni, V, Zn, were used for the analysis.

Results and Discussion

The chemical composition of coal/dRDF ash depends on geological and geographic factors related to the coal deposits, the combustion conditions and the efficiency of air pollution control devices. The fly ash samples which were investigated by ICP-AES were the Economizer fly ash samples. The results are summarized in Table 2. Thirteen elements were investigated; As, Cd, Hg, Pb, Sb, Se, Te, Ba, Be, Cr, Cu, Ni, V, and Zn. The metals As, Cd, Hg, Pb, Sb, Se and Tl are not included in the table because their concentrations were too low to be detected by ICP. Table 3 shows the ICP detection limits of all elements studied.

Effect of d-RDF content on trace metals:

Processing of MSW to RDF removes much of the unwanted trace metals. The metal content of coal/RDF blend ash is expected to be affected by the different percentages of RDF.

The trace metal concentration is economizer fly ash are listed in Table 2. Elements such as Cd, Cr, Cu, Hg, Pb and Zn are known to be enriched in RDF related to coal.

Table 2 and the graphs shows the percent bd-RDF versus concentration (ug/g) for each element alone at a constant level of binder. The top graph shows 0, 10, 20 ,30 percent bd-RDF versus element concentration at 0 percent binder. The middle graph shows the 10,20,30,50 percent bd-RDF versus element concentration at 4 percent binder. The bottom graph shows the concentrations at 8 percent binder. The graphs shows how the elements are increasing or decreasing in concentration with the increase in bd-RDF.

From Table 2 and the graphs, the most prominent increase in concentration resulting from cofiring coal/RDF mixtures were Cu and Zn. Ba and Cr were increased slightly in economizer fly ash. This increase is due to these elements being more enriched in RDF ash than in coal ash, while Be, Ni and V content were lower or close to those in coal ash.

References

1. K.E. Daugherty, "An Identification of Potential Binding Agent for Densified Fuel Preparation for Municipal Solid Waste, Phase 1, Final Report", U.S. Department of Energy, (1988).

2. O. Ohlsson, et. al., "Densified Refuse Derived Fuel - An Alternative Energy Source", Proceedings of the American Association of Energy Engineers, (1986).

3. M. Poslusny, et. al., "Emission Studies of Full Scale Co-firing of Pelletized RDF/Coal", American Institute of

Chemical Engineers Symposium Series, 265,(1988).

4. Gershman, Brincker and Bratton, Inc., "Small Scale Municipal Solid Waste Energy Recovery Systems", Van Nostrand Reinhold Company, N.Y., (1986).

5. Hecht, Norman, "Design Principles in Resource Recovery Engineering", Ann Arbor Science, Butterworth Publishers: Boston, (1983), pp 23-33.

6. Marc J. Rogoff, "How to Implement Waste-to-Energy Projects", Noyes Publications: Park Ridge, New Jersey, (1987), p 39-45.

7. N.R. McQuarker, D.F. Brown, P.D. Kluckner, Analytical Chemistry, 51, (1979).

8. A. Sugimae, Taiki-Osen Gakkaishi, 14,(1979).

9. A. Sugimae, Bunseki Kagaku, 29, (1980).

10. M.A. Floyd, V.A. Fasel, A.P. D'Silva, Analytical Chemistry, 50, (1980).

11. A. Sugimae, ICP Inf. Newsl., 6, (1981).

12. S.L. Harper, J.F. Welling, D.M. Holland, L.J. Pranger, Analytical Chemistry, 55, (1983).

13. A. Sugimae, Anal. Chem. Acta, 144, (1982).

14. X.B. Cox, S.R. Bryan, R.W. Linton, Anal. Chem., 59, (1987).

15. A. Sugimae, R. Barnes, Anal. Chem., 58, (1986).

16. R.A. Nadkarni, Anal. Chem., 52, (1980).

17. P.M. Beckwith, R.L. Mullins, D.M. Coleman, Anal. Chem., 59, (1987).

18. M. Poslusny, K.E. Daugherty, P. Moore, Chemosphere, 19, (1989).

19. Jen-Fon Jen, "Analysis of Acid Gas Emissions in the Combustion of the Binder Enhanced Densified Refuse Derived Fuel by Ion-Chromatography", Ph.D. Dissertation, University of North Texas, Denton, Texas, (1988).

20. J.F. Jen, K.E. Daugherty, J.G. Tarter, Journal of Chromatographic Science, 27, (1989), p 504-510.

Table 2. Summary of Toxic Metals Concentration
        in Economizer Fly Ash (ug/g).*

Run#	Ba	Be	Cr	Cu	Ni	V	Zn	Btu%dRDF	Binder%
1.	158.2	25.3	105.2	152.7	130.0	223.4	324.8	0	-
2.	240.1	27.7	111.3	199.5	135.3	234.1	338.5	10	0
3.	202.2	19.6	100.3	151.8	122.2	177.9	293.7	10	4
4.	144.4	14.7	94.9	143.7	100.8	160.7	390.8	10	8
5.	227.7	20.2	143.8	243.4	137.4	231.0	404.6	20	0
7.	155.7	11.3	108.3	208.5	149.0	187.1	478.2	20	4
8.	182.8	13.3	127.6	243.6	121.3	193.4	466.7	20	8
9.	160.1	11.4	114.4	360.6	92.7	181.3	443.6	30	0
10.	158.3	10.5	115.9	207.9	75.6	149.6	455.9	30	4
6.	190.2	10.5	112.2	227.6	130.5	161.3	470.8	30	8
11.	228.5	14.9	126.1	353.5	97.7	179.8	372.1	50	4
12.	177.4	16.6	93.5	217.1	97.8	171.6	240.3	0	-

* Average of Three Replicates.

Table 3. Detection Limits of ICP (ug/g).

As (ug/g)	62.5
Ba	12.5
Be	0.63
Cd	6.25
Cr	6.25
Cu	6.25
Hg	125.0
Ni	12.5
Pb	125.0
Sb	125.0
Se	62.5
Tl	125.0
Zn	6.25

Cr, in Economizer Fly Ash

Ni, in Economizer Fly Ash

Cu, in Economizer Fly Ash

Zn , in Economizer Fly Ash

V, in Economizer Fly Ash

0% Binder

4% Binder

8% Binder

Percent RDF

Ce, in Economizer Fly Ash

0% Binder

4% Binder

8% Binder

Percent RDF

Ba, in Economizer Fly Ash

0% Binder

4% Binder

8% Binder

Percent of RDF

1792
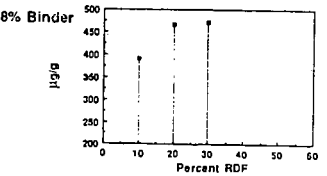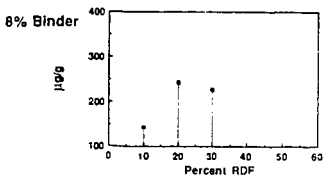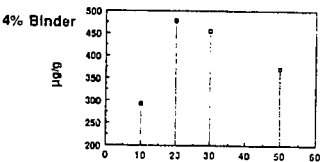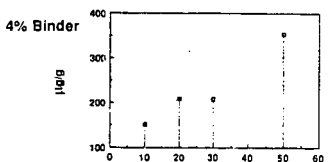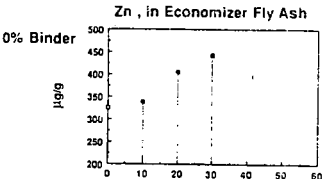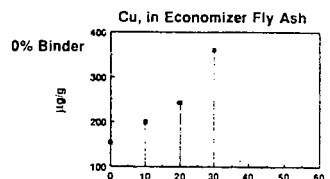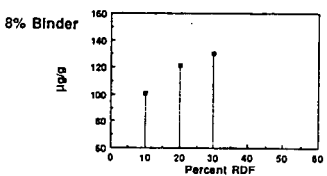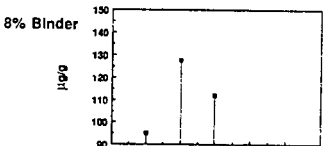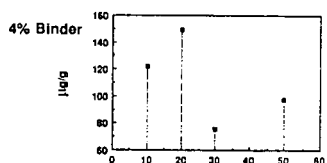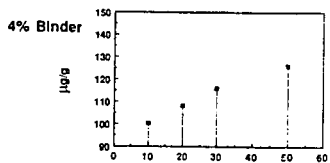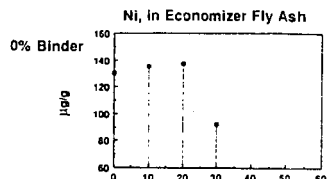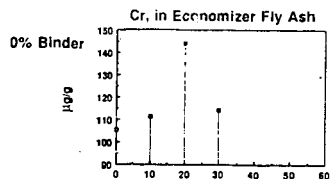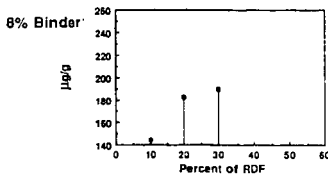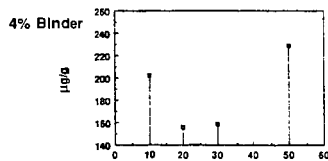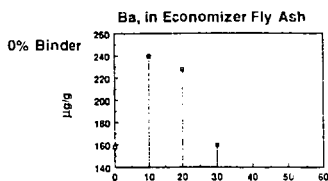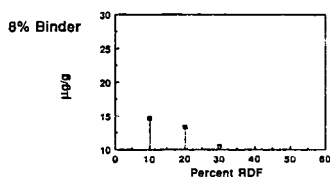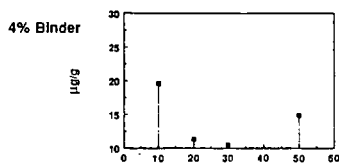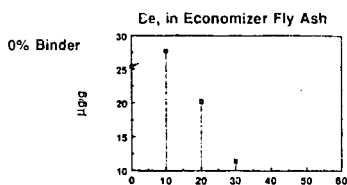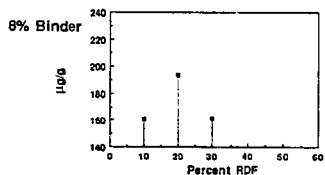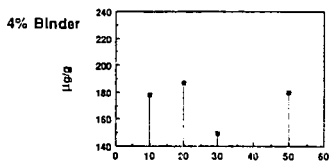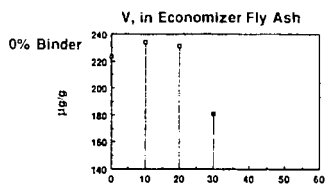
PHASE CHARACTERIZATION OF UNMODIFIED PETROLEUM COKE AND COAL GASIFICATION SLAGS

Mitri S. Najjar
Texaco Research Labs at Beacon (TRCB), P. O. Box 509,
Beacon, NY 12508

John C. Groen and James R. Craig
Department of Geological Sciences, Virginia Polytechnic Institute and State University
Blacksburg, VA 24061-0420

Keywords: coal-ash, petroleum-coke, slag, phase characterization

ABSTRACT

The slags produced in gasifiers using petroleum coke as a feedstock differ compositionally and texturally from the ash and slag formed during combustion of coal. Hence, the chemical and slagging behavior of petroleum-coke ash under gasification conditions must differ markedly from the behavior of coal ash. Whereas the latter is reasonably well understood, the former has been much less well studied. The present work is part of an ongoing study aimed at understanding the physical and chemical characteristics of the phases formed in the slags that are produced during petroleum coke gasification.

INTRODUCTION

The partial oxidation of liquid hydrocarbonaceous fuels such as petroleum products and slurries of solid carbonaceous fuels such as coal and petroleum coke to form alternative fuels is now a common practice. An evolving trend in the feedstocks for such processes is that they are becoming increasingly heavy and of poorer quality. To compensate for this trend, refiners must employ more "bottom of the barrel" upgrading to provide the desired light products. The current industry workhorse to provide this upgrading is some type of coking operation (either delayed or fluid). A good deal of current refinery expansion includes the installation or expansion of coker units, and this coking will be a process of general use for some time to come.

The production of light hydrocarbon fuels from coal or petroleum feedstocks results in the formation of ash or slag which concentrates most of the contaminants originally present in the coal or petroleum. Coals contain significant amounts of clays, quartz, pyrite, and carbonates, along with a broad range of less abundant solid mineral phases (Jenkins and Walker 1978). Petroleums contain less solid mineral matter but may contain significant amounts of other contaminants such as iron, nickel, vanadium and sulfur. Consequently, the residual concentration of elements is significantly different depending upon the feedstock materials. The resulting phases affect gasifier operation and the ultimate use or disposal of the ash or slag.

PROCESS DESCRIPTION

The Texaco Gasification Process is a partial oxidation reaction to produce mixtures of CO and H_2, known as synthesis gas. A carbon containing feedstock is reacted with a controlled, sub-stoichiometric quantity of oxygen in a fuel rich, exothermic reaction. The process is carried out in a pressurized reaction chamber with the temperature maintained above the melting point of the coal or petroleum-coke ash, thus making a slag (molten ash), by controlling the individual feed rates of the reactants. The feeds are introduced together, through the top of the gasifier, and pass through it concurrently with the product gases transporting the solids, making it an entrained flow gasifier. It is fundamentally a simple system that leads to high reliability, and it can be adapted readily to fit many applications economically.

The chemical reaction path is quite complicated, and includes many simultaneous and sequential reactions such as devolatilization, combustion and interactions between the feeds and intermediate or final products. The chemistry is depicted in a schematic sense in Figure 1. The conversion of feedstock slurry to synthesis gas is normally in excess of 95% and can be over 99%.

The use of coal as a feedstock, either in direct combustion or as a gasifier feedstock results in most of the ash being converted to slag, a nearly carbon-free, inorganic material. After water quenching, the slag is normally a glass-like solid, with a maximum size of one-half inch. In all cases evaluated to date, the slag from coal gasification, including the fine fractions that are co-mingled with carbon-rich char, have been classed as a non-hazardous waste.

The high temperature gases, char and molten ash, or slag, produced in the gasifier are normally cooled prior to cleanup, by either of two methods: quenching, i.e., direct contact with water, or indirect heat exchange to make high pressure steam in a special syngas cooler.

The molten slag is cooled with the gas and is collected in a water pool either in the bottom of the radiant cooler or in the quench vessel located under the gasifier. The slag is removed from the system by means of a water-filled lockhopper system. The carbon-rich char can be disposed of with the slag or separated for recycle.

The cooled gas is scrubbed with water to remove the remaining fine particulates. Following particulate scrubbing, gas purification is completed by sulfur removal. A variety of subsequent processes can then be used, with the choice made to fit the overall project needs. The cleaned gas can be used for many purposes, such as fuel for power generation or process heat, synthesis of ammonia or other chemicals, or as a reducing gas.

SAMPLE PREPARATION AND ANALYSIS

The slag samples examined in this study occur both as fragmental materials that are discharged routinely from the gasifiers and as solid incrustations that build up on the interior walls of the gasifier. Megascopically, most samples appear as dark brown to black, porous to solid, irregular masses ranging from less than one-fourth to more than several inches across. The samples removed from the gasifier walls are commonly layered, apparently reflecting episodic buildup.

Representative portions of slags were cast in a low viscosity, cold-setting epoxy resin. Porous samples were vacuum impregnated by placing them in a vacuum desiccator in which vacuum was alternated with normal air pressure. This procedure removed trapped air and forced the epoxy into pores and cracks. Samples were then polished using standard techniques employed for optical microscopy and electron microprobe analysis as described in Craig and Vaughn (1981).

GASIFIER SLAGS

Characterization of slags produced in gasifiers is important in determining the ultimate use and/or disposal of the slags. Furthermore, a prior knowledge of the nature of the slag phases is necessary if it becomes desirable to alter slag properties that adversely affect the operability of gasifiers. To these ends, we have been carrying out investigations on the physical and chemical properties of slags produced both from coal and from petroleum coke feedstock. The slags produced from the different feeds are markedly different, as evidenced in the data presented in Table 1, 2, and 3.

The conditions under which coal and petroleum-coke ash and slags form are similar in that they all involve partial to full combustion. The principal difference is that direct combustion is generally more oxidizing and hence will permit formation of more oxidized phases (eg. ferric rather than ferrous phases). Coal bottom ash, fly ash, and slags have been examined by numerous investigators in recent years as noted in Table 2 and by a wide variety of techniques (eg. Huggins and Huffman, 1979; Weaver 1978; Voina and Todor, 1978; Eriksson et al. 1991). Typical coal ash as noted in Table 1 is rich in SiO_2 with major but variable amounts of Al_2O_3, Fe_2O_3, and CaO. Coal slag are generally dominated by glass phases which, though highly variable, are always rich in SiO_2 and contain significant Al_2O_3. Some glasses are also sufficiently rich in reduced iron to be referred to as "ferrous glasses" (Huffman et al. 1981). The number and variety of other mineral analogous

phases are considerable (Table 2) but often constitute only small proportions of the bulk material. Furthermore, several percent unreacted or partially reacted carbon-char are commonly present.

The glass phases display flow, banding, indicating some flow of compositionally distinct zones. Crystalline phases range from skeletal to fibrous laths (commonly mullite or anorthite; Hulett et al. 1980; Huggins et al. 1981) to skeletal and cruciform spinels (Chen et al. 1986).

Petroleum-coke slags are also highly variable in composition but generally contain less SiO_2, less Al_2O_3 and less CaO but greater amounts of Fe_2O_3, V_2O_5, NiO and sulfur (included in "others" Table 1). The iron and vanadium contents are reported as given by ASTM analytical procedures; however, iron and vanadium actually occur in lower oxidation states in these slags. These gross compositional differences reflect the nature of the source materials. Coals contain abundant included clays and carbonate minerals, whereas petroleum contains less discrete fragmental mineral matter but often contains significant amounts of organic sulfur and porphyrins that hold iron, nickel, vanadium, and chromium.

A general result of these differences in composition is the fusibility of the ash. Typical coal ash has initial deformation (ID) temperatures of 2120°-2140° F, softening temperatures (ST) of 2150°-2210°F, and fluid temperatures (FT) of 2250°-2430° F. In contrast, typical petroleum coke ash remains undeformed and does not melt until temperatures exceed 2700° F.

PETROLEUM COKE SLAGS

The present study has concentrated especially on slags formed during gasifier operation using petroleum coke without any additives to alter constituents or behavior, and are part of an ongoing study to characterize the physical and chemical characteristics of such slags (Craig et al. 1990; Craig and Najjar 1990; Groen et al. 1991).

The investigators have found that the slags formed, display a variety of textures and phases; these apparently reflect differing locations and hence conditions within the gasifiers as well as differences in the feedstock. In general, the types of slags may be summarized as (1) glass-rich, (2) V-oxide rich, (3) sulfide-rich, (4) CaMgFe-silicate-rich. These no doubt represent end members of a continuum, but most samples extracted from the gasifiers conveniently fall into one of these categories. The total of the wide variety of phases that the investigators have found to date are listed in Table 3. Below briefly described are each of the major types of slags noted above:

Glassy Slags - These generally range from black to brown glasses that occasionally exhibit well developed flow textures evidencing their slow flow down the sides of the gasifier. Typically, they contain significant quantities of very fine spherical iron sulfide droplets. The droplets greater than 1 mm in diameter appear to have been formed along with the glass. Finer droplets, down to less than 1 micrometer, appear to have formed primarily through exsolution on cooling. Glassy slags commonly contain dispersed skeletal to cruciform spinels which also appear to have formed on cooling as the liquidus boundary was intersected.

V-oxide-rich slags - These slags are relatively SiO_2-poor and represent slag formation within the gasifier where vanadium phases crystallize as relatively coarse crystals (~100 micrometers). The V-oxide phases occur as interlocking laths with interstitial spinel crystals and droplets of glass and sulfide-oxide intergrowths. The coarseness of the crystals and the absence of flow structures and exsolution features indicate that the V-oxide phases were stable and forming directly under the conditions of gasifier operation.

Sulfide-rich Slags - Many chunks of slag consist primarily of intimate iron sulfide-iron oxide intergrowths. The iron sulfide ranges from pure FeS (troilite) to $Fe_{1-x}S$ (hexagonal pyrrhotite) and the iron oxide is FeO (wustite). The intergrowths are symplectic in nature and are often so fine (1 micrometer and less) that they are barely resolvable with an optical microscope. The textures are characteristic of the unmixing of phases from a homogenous melt on rapid cooling. Nickel may substitute on a minor scale for the iron in the pyrrhotite and may, in nickel-rich areas, occur as Ni_3S_2 (heazlewoodite) or as $(Fe, Ni)_9S_8$ (pentlandite). The iron sulfide-iron oxide masses commonly contain dispersed drop-like to cruciform crystals of free iron-nickel alloy. Also scattered throughout

the sulfide-oxide matrix are droplets of glass and euhedral to skeletal iron aluminum spinels which may concentrate significant amounts of vanadium and chromium.
CaMgFe-silicate slags - These occur as local segregations within sulfide-rich slags. The sulfide phase cannot accomodate Ca, Mg, or Si within its structure, hence these elements concentrate sufficiently to form a variety of CaMgFe silicates.

SUMMARY

It is apparent that the differences in the bulk chemistries of the petroleum coke and coal slags are reflected in the behavior and nature of the phases within each. The high silica and alumina contents of the coal slags result in lower melting temperatures and the development of predominantly glassy products. In contrast, the low silica and alumina contents of the petroleum coke slags, coupled with high transition metal contents, result in the development of a variety of crystalline phases. Most notable are aluminate spinel phases that concentrate iron, vanadium, chromium and nickel, and sulfide-oxide intergrowths in which nickel becomes concentrated in both sulfide and accessory alloy phases.

REFERENCES

1. Chen, T.T., Quon, D.H.H., and Wang, S.S.B. (1986) Compositions and micro structures of furnace-bottom deposits produced from beneficiated western Canadian bituminous coals. Canad. Mineral. 24, 229-237.

2. Craig, J.R. and Najjar, M.S. (1990) Elemental partitioning in Coke gasification slags. in W. Petruk, et al. eds., Process Mineralogy IX, The Minerals, Metals and Materials Soc., 473-483.

3. Craig, J.R., Najjar, M.S., and Robin, A.M. (1990) Characterization of Coke gasification slags. in W. Petruk, et al. eds., Process Mineralogy IX, The Minerals, Metals and Materials Soc., 473-483.

4. Craig, J.R. and Vaughan, D.J. (1981) Ore Microscopy and Ore Petrography, Wiley Interscience, New York, 406pg.

5. Groen, J.C., Craig, J.R., and Najjar, M.S. (1991) Chemical phases in petroleum coke gasification slag. Amer. Chem. Soc. Preprints Div. of Fuel Chem., 36, 207-215.

6. Eriksson, T., Zygarlicke, C., Ramanathan, M., and Folkedahl, B. (1991) Composition and particle size evolution of Kentucky #9 Amer. Chem. Soc. Preprints Fuel Chem. Div., 36, 158-164.

7. Fessler, R.R., Skidmore, A.J., Hazard, H.R., and Dimmer, J.P. (1980) Composition and Microstructure of a furnace ash deposit from a coal-fired utility boiler. Jour. Engin. for Power 102, 692-697.

8. Huffman, G.P., Huggins, F.E., and Dunmyre, G.R. (1981) Investigation of the high-temperature behavior of coal ash in reducing and oxidizing atmospheres. Fuel 60, 585-597.

9. Huggins, F.E. and Huffman, G.P. (1979) Mössbauer analysis of iron-bearing phases in coal, coke, and ash, in C. Karr ed., Analytical Methods for Coal and Coal Products, Academic Press, New York, Vol.III, pp. 371-473.

10. Huggins, F.E., Kosmack, D.A., and Huffman, G.P. (1981) Correlation between ash-fusion temperatures and ternary equilibrium phase diagrams. Fuel 60, 577-584.

11. Hulett, L.D. and Weinberger, A.J. (1980) Some etching studies of the microstructure and composition of large alumino silicate particles in fly ash from coal-burning power plants. Envir. Sci. and Tech 14, 965-970.

12. Hulett, C.D., Weinberger, A.J., Northcutt, K.J., and Ferguson, M. (1980) Chemical species in fly ash from coal-burning power plants. Science 210, 1356-1358.

13. Jenkins, R.G. and Walker, P.L. (1978) Analysis of mineral matter in coal, in C. Karr ed., Analytical Methods for Coal and Coal Products, Academic Press, N.Y. Vol.II, 265-292.

14. Quon, D.H.H., Wang, S.S.B., and Chen, T.T. (1984) Viscosity measurements of slags from pulverized western Canadian coals in a pilot-scale research boiler. Fuel 63, 939-942.

15. Raask, E. (1982) Flame imprinted characteristics of ash relevant to boiler slagging, corrosion and erosion. Jour. Engin. for Power 104, 858-866.

16. Voina, N.I. and Todor, D.N. (1978) Thermal analysis of coal and coal ashes, in C. Karr ed., Analytical Methods for Coal and Coal Products, Academic Press, N.Y. Vol.II, 619-648.

17. Weaver, J.N. (1978) Neutron activation analysis of trace elements in coal, fly ash and fuel oils, in C. Karr ed., Analytical Methods for Coal and Coal Products, Academic Press, N.Y. Vol.I, 372-401.

GASIFICATION REACTION SCHEMATIC

REACTANTS:

OXIDANT (OXYGEN, O_2)

+

SLURRY COKE (C, H, S, N, O, ASH, H_2O)

PRODUCTS:

MAJOR
(> 2%) :
$\left\{\begin{array}{l} CO \\ H_2 \\ CO_2 \\ H_2O \\ Slag\ (melted\ ash) \\ Char \end{array}\right.$

MINOR
(1000 ppm - 2%) :
$\left\{\begin{array}{l} CH_4 \\ H_2S \\ N_2 \\ NH_3 \end{array}\right.$

TRACE
(1 - 1000 ppm) :
$\left\{\begin{array}{l} COS \\ CN^- \end{array}\right.$

UNDER
1 ppm :
$\left\{\begin{array}{l} Higher \\ Hydrocarbons \end{array}\right.$
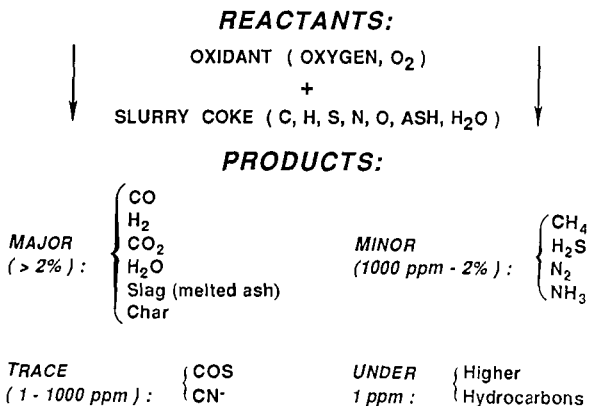
Figure 1. Simplified schematic diagram of the partial oxidation reaction occurring in a petroleum coke gasification.

Table 1. Typical ash composition in wt % of coal and petroleum-coke generated ash.

	Coal		Petroleum Coke	
	Eastern	Western	Type A	Type B
SiO_2	52.1	42.0	4.4	40.6
Al_2O_3	15.4	25.0	1.5	9.6
Fe_2O_3	7.3	20.9	23.0	6.3
CaO	17.4	9.5	7.5	1.4
MgO	3.7	--	--	2.4
NiO	--	--	20.9	14.0
V_2O_5	--	--	40.3	16.6
Others	4.1	2.6	2.5	9.1
Carbon %	9.5	9.7	0.5	0.9
	Ash Fusibility, °F			
ID	2120	2140	--	--
ST	2150	2210	--	--
FT	2250	2430	>2700	>2700

TABLE 2.

COAL COMBUSTION ASH / SLAG PHASES

Phase Composition	Remarks	Mineral Name	Reference
FREE ELEMENTS:			
C	unreacted char	Graphite	Quon et al., 1984
FeSi	....	....	Quon et al., 1984
SULFIDES:			
FeS	......	Troilite	Huffman et al., 1981
$Fe_{1-x}S$	......	Pyrrhotite	Huffman et al., 1981
SULFATES:			
$CaSO_4$	Result of Ca from calcite reacting with SO_2	Anhydrite	Huffman et al., 1981
OXIDES:			
FeO	......	Wüstite	Huffman et al., 1981
Fe_3O_4	......	Magnetite	Quon et al., 1984
$(Fe,Al)_3O_4$	......	Hercynite	Huffman et al., 1981
Ferrite phases	Cited as mostly Fe_3O_4	....	Huffman et al., 1981
Ferrite phases	Cited as calcium ferrite	....	Huggins et al., 1981
$Fe_{3-x}M_xO_4$	M = V, Cr, Mn, Co, Ni, Zn	....	Hulett et al., 1980
Fe_2O_3	In oxidized ash	Hematite	Quon et al., 1984
Al_2O_3	....	Corundum	Huggins et al., 1981
TiO_2	....	Rutile	Quon et al., 1984; Chen et al., 1986
SiO_2	....	Cristobalite	Quon et al., 1984; Chen et al., 1988
SiO_2	Residual phase ?	Quartz	Hulett et al., 1980; Hulett and Weinberger, 1980; Raask, 1982; Quon et al., 1984; Chen et al., 1986
Glass	Highly variable Si-Al-dominated ferrous glass	Obsidian	Fessler et al., 1980; Huffman et al., 1981; Raask, 1982; Quon et al., 1984; Chen et al., 1986
Silicates:			
Fe_2SiO_4	......	Fayalite	Huffman et al., 1981
$Al_6Si_2O_{13}$	......	Mullite	Hulett et al., 1980; Hulett and Weinberger, 1980; Raask, 1982; Quon et al., 1984; Chen et al., 1986
$CaAl_2Si_2O_8$	......	Anorthite	Huggins et al., 1981; Quon et al., 1984
$Ca_2Al_2SiO_7$	....	Gehlenite	Huggins et al., 1981

TABLE 3.

PETROLEUM COKE GASIFIER SLAG PHASES

Phase Composition	Texture	Ideal Composition	Mineral Name
FREE ELEMENTS:			
FeNi-alloys (up to >70 atomic percent Ni)	Dendritic to blocky crystals & irregular blebs all in sulfide matrix	Complete Fe to Ni solid solution	Native Iron & Native Nickel
C	Aggregates of radiating to fibrous microcrystalline subgrains	C	Graphite
SULFIDES:			
(Fe,Ni)S	Matrix phase often symplectic with "FeO", & as irreg. blebs in glass	FeS	Troilite
(Fe,Ni)$_{1-x}$S	Matrix phase often symplectic with "FeO", & as irreg. blebs in glass	Fe$_{1-x}$S	Pyrrhotite
(Fe,Ni)$_9$S$_8$	Irregular separations in sulfide matrix	(Fe,Ni)$_9$S$_8$	Pentlandite
(Ni,Fe)$_3$S$_2$	Irregular blebs in V-oxide rich slags	Ni$_3$S$_2$	Heazlewoodite
CaS	Irregular blebs	(Ca,Mn)S	Oldhamite
(Fe,Ni,Cr)VS$_2$	Dendritic crystals in sulfide matrix	....	....
Undeciphered sulfides	Euhedral micron-scale crystals in sulfide matrix	....	....
SULFATES (?):			
Undeciphered M-S-O phases	Euhedral micron-scale crystals in sulfide matrix	....	....
OXIDES:			
(Fe,Mg,V,Ni)O	Symplectically intergrown in sulfide matrix, and as dendritic crystals and rounded blebs in sulfide matrix	FeO	Wüstite
(Ni,V,Fe)O	Alteration rind on bleb of (Ni,Fe)$_3$S$_2$	NiO	Bunsenite
(Fe,Ni,Mg)(Fe,Al,V)$_2$O$_4$	Euhedral massive crystals in V-oxide rich matrix	Fe$_3$O$_4$	Magnetite

Phase Composition	Texture	Ideal Composition	Mineral Name
$(Fe,Mg)(Cr,V)_2O_4$	Euhedral crystals in glassy matrix (residual from refractory brick?)	$FeCr_2O_4$	Chromite
$(Mg,Fe)(Cr,Fe,Al,V)_2O_4$	Euhedral crystals in glassy matrix (residual from refractory brick?)	$MgCr_2O_4$	Magnesiochromite
$(V,Cr)V_2O_4$	Euhedral massive crystals in sulfide matrix	V_3O_4	....
$(Fe,V,Cr,Ni)V_2O_4$	Euhedral massive to dendritic crystals in sulfide matrix	FeV_2O_4	Coulsonite
$(Mg,Ni,Fe)(Al,V,Cr,Fe)_2O_4$	Euhedral massive to dendritic crystals in V-oxide rich matrix	$MgAl_2O_4$	Spinel
$Fe(Al,Fe)_2O_4$	Irregular grains w/ FeS interstitial between dendritic FeO crystals	$FeAl_2O_4$	Hercynite
$(Ni,Fe)(Fe,Al)_2O_4$	Euhedral skeletal crystal in V-oxide rich matrix	$NiFe_2O_4$	Trevorite
$(Ni,Mg)(V,Fe,Al,Cr)_2O_4$	Euhedral massive crystals in V-oxide rich matrix	....	....
$(Fe,V,Al,Cr)_2O_3$	Oxidation crusts on sulfide-rich and glassy slag surfaces	Fe_2O_3	Hematite
$(Cr,Fe,Al,V)_2O_3$	Exsolved lamellae in chromite crystals	Cr_2O_3	Eskolaite
$(Al,Fe,V,Cr)_2O_3$	Slender acicular crystals & as irregular cores of spinel crystals	Al_2O_3	Corundum
$(V,Fe,Cr)O_2$	Bladed euhedral crystals in V-oxide rich slag	VO_2	....
$(V,Al,Fe,Cr)_2O_3$	Crust on Fe-Ni sulfide/oxide symplectic intergrowths	V_2O_3	Karellanite
$(Ca,Mg,Ni)V_2O_6$	Bladed to feathery euhedral crystals in V-oxide rich slag	CaV_2O_6	....
$(Fe,Mg,Mn)(V,Al,Fe)_2O_6$	Prismatic diamond-shaped euhedral crystals in V-oxide rich slag	FeV_2O_6	....
$(Na,Fe)(V,Al,Fe)_5O_{15}$	Feathery euhedral crystals in V-oxide rich slag	NaV_5O_{15}	....
$(Na,Ni)(Ca,Ni)(V,Fe,Al,Cr)_9O_{20}$	Feathery euhedral crystals in V-oxide rich slag	$NaCaV_9O_{20}$	....
$(Fe,Ce)VO_4$ or $CaFeV_2O_7$ (?)	Bladed to feathery euhedral crystals in V-oxide rich slag	$FeVO_4$ or $CaFeV_2O_7$	....
$(Si,Al,V)O_2$	Matrix phase & as rounded blebs in sulfide- and V-oxide rich slags	SiO_2	Obsidian

Silicates:

Phase Composition	Texture	Ideal Composition	Mineral Name
$(Al,Fe)_2(Si,V,Cr,Al)O_5$	Euhedral, diamond shaped, acicular crystals in glass matrix	Al_2SiO_5	Andalusite or Sillimanite
$(Fe,Mg,Ca,Mn)_2(Si,Al)O_4$	Matrix of tiny subhedral crystals intergrown w/ Pigeonite crystals	Fe_2SiO_4	Fayalite
$(Ca,Fe,Mg,Mn)(Mg,Fe)(Si,Al)_2O_6$	Matrix of tiny subhedral crystals interg. w/ Fayalite crystals	$(Mg,Fe,Ca)(Mg,Fe)Si_2O_6$	Pigeonite
$(Mg,Fe)Ca_2(Si,Al)_2O_7$	Equant euhedra in glass matrix w/ spinel, sulfide, & other silicates	$MgCa_2Si_2O_7$	Akermanite
$(Na,Ca)_2Al_3(Al,Si,V,Fe)_3Si_6O_{24}$	Euhedral, w/ spinel, glass spheres, & Fe_2O_3 in V-oxide rich slag	$(Ca,Ne)_2Al_3(Al,Si)_3Si_6O_{24}$	Sarcolite
Undeciphered silicates	Small euhedral crystals	....	....

Analysis of PCB's and PCDD's from the Combustion of Quicklime BInder Enhanced Densified Refuse Derived Fuel/Coal Mixtures

Russell Hill
Baoshu Zhao
Dr. Kenneth Daugherty*
University of North Texas
Denton, Texas

Dr. Matthew Poslusny
Marist College
Poughkeepsie, New York

Dr. Paul Moore
International Paper
Mobile, Alabama

Keywords: RDF, Quicklime, Dioxins/Furans/PCB's

Introduction

Two of the nations current major concerns are energy and municipal solid waste. The combustion of Refuse Derived Fuels (RDF) is increasingly being viewed as an attractive solution to both problems. Densification of RDF producing dRDF is typically performed to minimize the problems of handling, transporting and storing the low bulk volume material. When densification is performed with the use of a binding agent additional performance and environmental benefits can be gained.

In 1985 the University of North Texas (UNT) under contract with Argonne National Laboratory investigated over 150 potential binding agents. Evaluations were made based upon economics, toxicity, availability and performance. The top 13 binder candidates were tested in a large scale demonstration. End results found calcium hydroxide or quicklime ($Ca(OH)_2$) to be the best performing binder. UNT also hoped that this binder's basic nature might help reduce the emission of acid gases. Further conjecture was made that the binder might physically absorb halogens, such as chlorine and thus reduce the production of polychlorinated biphenyls and dioxins. (1,2)

These hypotheses were tested at a pilot plant operation at Argonne National Laboratory in 1987. The six week program combusted over five hundred tons of binder enhanced dRDF (bdRDF) blended with Kentucky coal at heat contents of 10, 20, 30 and 50 percent. The $Ca(OH)_2$ binder content ranged from 0 to 8 percent by weight of dRDF. Emission samples were taken both before and after pollution control equipment (multicyclone and spray dryer absorber). All samples were taken to UNT for analysis.

Experimental

Isokinetic samples were taken for the analysis of polychlorinated biphenyls (PCB's), polyaromatics (PAH's), polychlorinated dioxins (PCDD's) and polychlorinated furans (PCDF's). The following sampling sites were investigated.

Site 1   combustion zone (2000°F), sample site (1200°F)
Site 2   prior to pollution control equipment (300°F)
Site 3   after pollution control equipment (170°F)

Sample collection was completed using an EPA Method 5 modified sampling train, and a XAD-2 resin for trapping the majority of organics. After extractions, sample clean-up was accomplished using various acid/base modified silica and alumina gels to remove interferents. Response factors, recovery and detection limits were established through internal standards. The gas chromatography mass spectrometer analysis was performed with a Hewlett-Packard Model 5992B. (3)

Results and Discussion

The EPA's sixteen most hazardous PAH's (Table 5) and all congener groups of PCB's were tested. The results of site 2 and site 3 sampling areas are found in Tables 1 and 2. Figures 1 and 2 clearly depict a reduction in PAH and PCB emission as the binder concentration is increased. Data is not available on all compositions due to the mixing and sampling methods used. Tables 3 and 4 show the calcium and chloride contents of fly ash from the multicyclone for a series of specific compositions. The calcium is used as an indicator of the binder present in the boiler system during a particular sampling period. The increase in calcium occurring between the first coal "blank" run and the second blank occurring 3 weeks later, suggest a build-up of residual binder throughout the boiler configuration. It is noteworthy that the increase in water soluble chloride in the fly ash for the 10% RDF samples is on the same order as the reduction of PCB's seen in Figure 2. This is presumably due to the lime's ability to bind the chloride in the combustion area. The much higher chloride content of the second coal blank ash relative to the first blank can be explained by assuming a longer contact time for chloride absorption on the residual binder as the binder became saturated throughout the boiler system. (4)

The dioxin and furan analysis initially concentrated on the tetra chlorinated species present after the pollution control equipment at sample site 3. Table 6 shows that no dioxins or furans were found at the listed detection limits. Composited fly ash samples were also analysed for absorbed PCDD's and PCDF's, and again results were below detection limits. Additional analysis was performed for penta, hexa, hepta, and octa congeners at sample site

3.   In all cases, no dioxins or furans were detected.   These
results were confirmed by collaborating with Triangle Laboratories
at Research Triangle Park, NC, using their high resolution mass
spectrometer. Detection limits were generally improved only on the
order of one magnitude, and as before, no detectable quantities of
dioxins or furans were found. (5)

Conclusion

Results of the pilot plant program indicates that the binder
enhanced densified refuse derived fuel can be cofired with coal,
at the levels tested, without producing detectable amounts of
dioxins or furans.   PCB's and PAH's are apparently reduced as a
function of the quicklime binder content.

References

1.   Daugherty, K.E., Ohlsson, O., Safa, A., and Venables, B.J.,
      "Densified Refuse Derived Fuel - An Alternative Energy Source"
      Proceedings for the American Power Conference, 1986, pp. 930-
      935.

2.   Daugherty, K.E., "An Identification of Potential Binding
      Agents for Densified Refuse Preparation from Municipal Solid
      Waste: Phase 1 Final Report, U.S. Department of Energy, 1986,
      ANL/CNSV-TM-194.

3.   Poslusny, M., Moore, P., Daugherty, K., Ohlsson, O., Venables,
      B., "Organic Emission Studies of Full-Scale Cofiring of
      Pelletized RDF/Coal", American Institute of Chemical Engineers
      Symposium Series, 1988, Vol. 84, No. 265, pp. 94-106.

4.   Matthew Poslusny Ph.D. Dissertation, "Analysis of PAH and PCB
      Emissions From the Combustion of dRDF and the Nondestructive
      Analysis of Stamp Adhesives", University of North Texas, May
      1989.

5.   Paul Moore Ph.D. Dissertation, "The Analysis of PCDD and PCDF
      Emissions From the Cofiring of Densified Refuse Derived Fuel
      and Coal, University of North Texas, August 1990.

Table 1

Polyaromatic Hydrocarbons (PAH's);

Polychlorinated Biphenyls (PCB's) at Site 2

Run#/Sample#	Site	mg PAH's cubic meter of gas sampled	mg PCB's cubic meter of gas sampled
Run 1 Sample 1	2	1.7×10^{-2}	6.2×10^{-3}
Run 2 Sample 2*	2	1.0×10^{-3}	1.3×10^{-2}
Run 2 Sample 2	2	7.6×10^{-2}	2.7×10^{-1}
Run 3 Sample 1	2	1.6×10^{-2}	1.4×10^{-2}
Run 4 Sample 1	2	4.0×10^{-3}	7.6×10^{-3}
Run 4 Sample 2	2	8.1×10^{-3}	$7.7 \text{ xx } 10^{-3}$
Run 5 Sample 1	2	3.5×10^{-2}	9.7×10^{-3}
Run 5 Sample 2	2	4.6×10^{-2}	7.7×10^{-3}
Run 7 Sample 1	2	2.2×10^{-1}	2.0×10^{-3}
Run 7 Sample 2	2	3.5×10^{-1}	2.9×10^{-1}
Run 8 Sample 2	2	2.4×10^{-1}	1.3×10^{-2}
Run 8 Sample 4	2	3.0×10^{-1}	3.4×10^{-3}
Run 12 Sample 1	1	3.4×10^{-1}	5.4×10^{-3}
Run 12 Sample 2	2	1.3×10^{-1}	3.9×10^{-4}

* This sample was lighter in color than all the rest

<u>Table 2</u>

Polyaromatic Hydrocarbons (PAH's);

Polychlorinated Biphenyls (PCB's) at Site 3

<u>Run#/Sample#</u>	<u>Site</u>	mg PAH's cubic meter <u>of gas sampled</u>	mg PCB's cubic meter <u>of gas sampled</u>
Run 1 Sample 1	3	4.6×10^{-3}	5.3×10^{-4}
Run 2 Sample 1	3	6.3×10^{-3}	1.2×10^{-3}
Run 2 Sample 2	3	1.5×10^{-2}	*
Run 2 Sample 3	3	8.1×10^{-3}	1.6×10^{-3}
Run 3 Sample 1	3	7.3×10^{-3}	$9.1 \times 10^{-3}n$
Run 4 Sample 1	3	7.3×10^{-3}	$1.1 \text{ xx } 10^{-4}$
Run 4 Sample 2	3	3.1×10^{-3}	3.1×10^{-3}
Run 5 Sample 1	3	3.6×10^{-4}	2.8×10^{-4}
Run 5 Sample 2	3	4.0×10^{-3}	1.2×10^{-3}
Run 7 Sample 1	2	7.9×10^{-2}	$4.2 \text{ xx } 10^{-2}$
Run 7 Sample 2	3	4.9×10^{-2}	6.5×10^{-3}
Run 8 Sample 1	3	1.0×10^{-3}	2.4×10^{-3}
Run 8 Sample 2	3	8.1×10^{-3}	8.5×10^{-4}
Run 12 Sample 1	3	7.0×10^{-2}	4.0×10^{-3}
Run 12 Sample 2	3	1.4×10^{-3}	4.3×10^{-4}

* Interference made it impossible to determine the quantity
of PCB's in this run

Table 3

Calcium Levels in Fly Ash

Fuel	ppm of Calcium
First coal blank	3,000
Coal - 10% dRDF (0% binder)	6,700
Coal - 10% dRDF (4% binder)	10,600
Coal - 10% dRDF (8% binder)	15,000
Second coal blank	4,200

Table 4

Inorganic Chloride Levels in Fly Ash

Fuel	ppm of Chloride
First coal blank	100
Coal - 10% dRDF (0% binder)	190
Coal - 10% dRDF (4% binder)	280
Coal - 10% dRDF (8% binder)	320
Second coal blank	280

Table 5

EPA Priority PAH's

Napthalene	Benzo-a-anthracene
Acenapthylene	Chrysene
Acenapthene	Benzo-b-fluoranthene
Flourene	Benzo-k-fluoranthene
Phenanthrene	Benzo-a-pyrene
Anthracene	Dibenzo-a,h-anthracene
Fluoranthene	Benzo-g,h,i-perylene
Pyrene	Idendo-1,2,3,-g,d-pyrene

1807

<div align="center">

Table 6

Tetra-Chlorinated Dioxins and Tetra-Chlorinated
Furans at Site 3

</div>

Run#/Sample#	Site	Tetra-Chlorinated Dioxin Level	Tetra-Chlorinated Furan Level	Detection Limit
Run 1 Sample 1	3	BDL	BDL	0.72 ng/m^3
Run 2 Sample 1	3	BDL	BDL	1.99 ng/m^3
Run 2 Sample 2	3	BDL	BDL	4.07 ng/m^3
Run 2 Sample 3	3	BDL	BDL	5.24 ng/m^3
Run 3 Sample 1	3	BDL	BDL	4.80 ng/m^3
Run 4 Sample 1	3	BDL	BDL	4.27 ng/m^3
Run 4 Sample 2	3	BDL	BDL	4.27 ng/m^3
Run 5 Sample 1	3	BDL	BDL	0.49 ng/m^3
Run 5 Sample 2	3	BDL	BDL	0.47 ng/m^3
Run 7 Sample 1	3	BDL	BDL	4.16 ng/m^3
Run 7 Sample 2	3	BDL	BDL	4.10 ng/m^3
Run 8 Sample 1	3	BDL	BDL	4.78 ng/m^3
Run 8 Sample 2	3	BDL	BDL	4.78 ng/m^3
Run 12 Sample 1	3	BDL	BDL	3.85 ng/m^3
Run 12 Sample 2	3	BDL	BDL	4.85 ng/m^3

ng/m^3 = nanograms per cubic meter
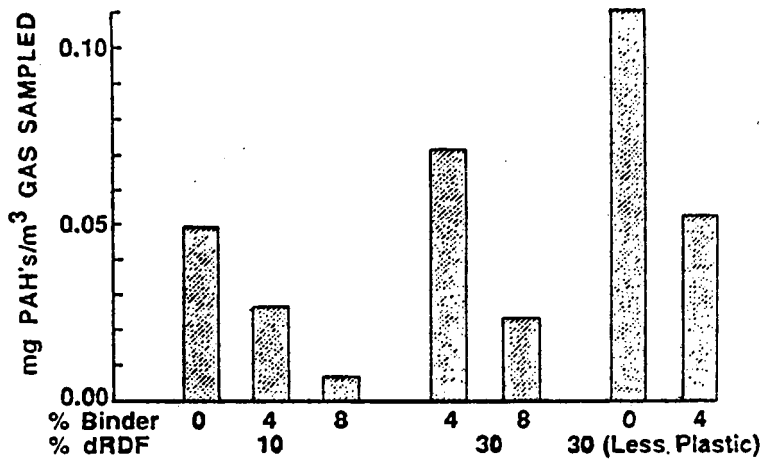
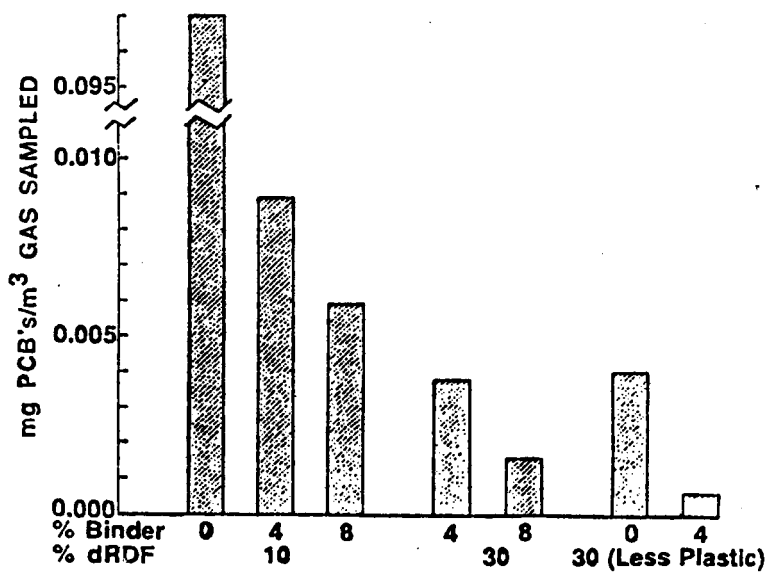BDL = Below Detection Limits

Figure 1

Figure 2

A METHODOLOGY FOR ASSESSING THE FEASIBILITY OF DEVELOPING AND TRANSFERRING NEW ENERGY TECHNOLOGY TO THE MARKETPLACE. Dr. H. M. Kosstrin and Dr. B. E. Levie, R. W. Beck and Associates, 1125 17th Street, Suite 1900, Denver, Colorado 80202.

Any new process intended to produce clean energy from waste should be characterized for its ultimate feasibility of becoming commercially successful. A four-phase strategy to analyze the process and plan for scaleup is presented. First, the new technology is assessed in terms of its market potential based on laboratory, bench scale or pilot data. A comparison with competing commercial technology is performed to compare the technology with its competition by estimations of factors such as life cycle cost, public acceptance, and adaptability to changing conditions and fuels. Second, the current status is reviewed with respect to theory, laboratory or pilot scale results, and available cost data. Third, the path to commercialization is outlined. The stages of scaleup and data required to prove the concept and remove risks of commercialization are identified. Finally, the financing needs for the various stages of scaleup and for a commercial unit are determined.

Introduction

Development of any new technology has traditionally been a controversial subject due to high expectations shared by proponents and results which many times fall short of these expectations. Solid and liquid waste management has seen both success and failure in the implementation of new technology. For example, promises to commercially produce liquid or gaseous fuels and/or chemicals from municipal solid waste (MSW) or refuse derived fuel (RDF) have so far been unfulfilled after several attempts at demonstrating various technologies. These failures encourage us to examine new and undeveloped technology in a more sophisticated and step-wise manner than has been previously done. By learning from past failures and taking a methodical and proactive approach to scaling-up suitable technology, we can better direct development so that realistic expectations can be made and met. The approach discussed here will increase chances for successful development of new waste management technologies.

The following phases outline the approach to be presented:

I.   Determine if a technology at its current state of development, either conceptual, bench, or pilot scale can be potentially competitive with commercial technologies today.

II. Establish the current status of the technology and what needs to be better understood before progressing.

III. Establish the path which would most logically be taken to result in commercializing the technology.

IV. Identify the requirements of different financing options necessary to commercialize the technology.

These phases follow a progression in which the results of each builds on the results from the preceding phases. This review can be started at any time in the development process and should be updated to account for new data on the technology, the competition, or the market as they become available.

Review and analysis of new technology can be biased according to the perspective of the reviewer. The investigators, developers, and sponsors all have vested interests in the technology which may prevent a balanced view of the technology, its development, or its commercialization. Investors and lenders typically look for independent reviews of the technology prior to committing large amounts of capital. This can best be accomplished by persons without conflicts of interest and with an adequate background reviewing development of the technology.

Review of the Concept

In this initial stage of analysis, the technology is looked at objectively to assess its niche in current markets. The first step is to identify the market or markets where the technology would most likely be competing and to broadly establish a range of competitive pricing for the service provided or product produced. It is important to consider all areas where the technology could potentially compete, including those outside the primary field of interest. High value chemicals, resins, and plastics, for instance, may be more economically feasible to produce than fuels from certain feedstocks.

Questions to resolve before proceeding are those which would be important to an investor. These generally will establish if the market is potentially strong and lasting. In the area of solid waste management, the following questions can be used as guidelines to ascertain the market's potential. Similar questions can be developed for any particular field.

- Is market expanding?

- Is it monpolistic or controlled by a few companies?

- What are the minimum or maximum requirements for waste needed to be processed?

- Is the waste composition changing due to recycling, composting, changes in consumption, etc.?

- Are markets localized, where are they located?

- Do long-term contracts either for feedstocks or products already exist which would interfere with this technology?

- What are the standards for the product produced?

- Can environmental permits be obtained?

- What are the characteristics of markets for byproducts of the process?

The next step in reviewing a new technology is to compare the technology with those commercial technologies currently in the identified market(s). This comparison can be as brief or extensive as is desired, depending on if we are considering a revolutionary change or just an evolutionary advance in the market. At a minimum, cost and environmental comparison should be made between the new technology and what is available in the market. The cost should be assessed on a life-cycle basis, accounting for capital, operation and maintenance, disposal of residue costs, and revenues from tipping fees, the primary product and any byproducts. The general environmental assessment could include a number of considerations including impacts on air, water, workers, noise, and flora and fauna.

There are many other considerations in performing this initial assessment. The feedstock must be compatible with the technology, and the product(s) compatible with the existing markets. Flexibility can be quite advantageous in the waste management industry, as the quantities and composition of waste is rarely fixed. While some technologies might only be competitive for a certain type and quantity of waste, others could take many types of waste, in a range of quantities. Effects on other related technologies should be assessed, as today municipalities and other organizations are interested in integrated solid waste management. Generally no one technology can solve the waste problems for a given location. Thus, technologies which can work effectively together may be more desirable than those which prevent other technologies and strategies from being employed successfully.

In order to compare the new technology with existing ones, it must be emphasized that the new technology should be judged on a realistic basis. A conservative estimate for costs, revenues and efficiency of the new process should be used for comparison purposes. Often a new technology assessment under estimates commercialization costs and greatly over estimates potential revenues from products.

Establishing Current Status of the Technology

The second phase of this review is to establish the current status of the new technology, providing a baseline or framework from which further development can be compared. The initial limited economic feasibility developed in Phase I, can be updated with new information gained in this phase. Technical and economic gaps in knowledge should be identified in this phase and either resolved now or targeted for later development work and/or analysis.

Existing Data Review

This stage of review is many times performed by the researchers in order to propose further expenditures or justify previous funding. Therefore, some data may already exist for this analysis.

The first part of establishing the current status is to verify that the process proposed is physically possible and practically attainable. This will require checking previous assumptions, reviewing theory and obtaining

correct parameter values for thermodynamic, kinetic and mass and heat transfer. Mass and energy balances should be done to check process feasibility. A second law analysis could be performed on the process to identify inefficiencies.

Once the theory has been reviewed, operational data from the lab, bench, and/or pilot facility should be assessed to determine the deviation from theory. This will allow a better estimate of expected yields as the process is scaled-up further. It will also serve to highlight areas where the process can be improved or is not performing as well as expected. In some cases, it will point to the fact that the data is inaccurate or insufficient for reasonable analysis and that additional and more accurate data must be obtained before further progress can be made. It is important in this review that sufficient data be available to determine the precision of the data. Furthermore, there should be an adequate review of the instrumentation and data acquisition system to determine any measurement biases which exist. For example, biases occur in high temperature measurements, and when measurements are made close to the detection limit of the instrumentation.

Once a thorough review of the available data has been accomplished, we need to update our original economic model. Existing cost data should be reviewed to better establish costs of the technology at its present state of development. These costs should be segregated as much as possible into standard technologies and developmental technologies to identify which areas need more accurate estimates as development proceeds. If possible, costs for each piece of equipment or unit operation should be tabulated.

Many costs will not be available based on pilot plant data, such as upstream and downstream equipment which may not be implemented at this stage of development. But this equipment can be estimated if standard technology is used. Equipment in this category may include material waste recovery systems, gas cleaning, liquid cleaning, heat recovery equipment, and emissions, effluent and residue treatment systems.

Costs for operation and maintenance (O&M) are difficult to determine as pilot scale or smaller equipment will rarely run for long continuous periods of time. Some costs may be determined such as on energy requirements, energy losses, and other requirements of the process such as gases, water, or other utilities. Costs associated with running the process for long periods of time will generally not be available. But preliminary estimates can be made, and ranges input to the economic model to establish a current economic status.

Technical and Economic Questions

The review of the current status will raise various questions on both a technical and cost basis. Technical questions which are easily resolved with current equipment should be addressed as soon as possible prior to going on to Phase III.

It is generally far less expensive to acquire data at the initial
stages of development than later on, and this data can provide many benefits.
The additional data taken may indicate unusual phenomena occurring which need
to be understood for successful scale-up. Extra information may point to
flaws in the technology such as larger heats of reaction than calculated, poor
kinetic rates, or poor catalytic activity. Such results might be indicated
using extra thermocouples, calorimetry, gravimetric monitoring, etc. These
may be economical to measure at this stage of development, but not once the
technology is scaled-up. Discrepancies between actual operating data and
theoretical projections may indicate poorly understood phenomena, inaccurate
data, or invalid assumptions in the theory. These technical data gaps may
need to be filled before further progress should be attempted.

Technical questions which may be unanswerable include environmental
impacts, reliability of equipment over time, labor necessary to run and
maintain operations full time, and degradation of process over time due to
unknown phenomena. These questions will need to be revisited in later phases
of development, and should be noted to trigger later activity.

Economic questions which may not yet be answered should be identified
at this point and noted for later resolution. These may include questions of
costs for upgrading the products and byproducts for sale, prices for the
products and byproducts, and disposal costs for residues and effluents. Some
of these questions are best left for later stages in development, when more
representative products and residues will be produced. By initially
establishing costs of upgrading or treating products or residues, it may be
revealed that further consideration needs to be given to different methods of
treatment. This may need to be worked on before, or concurrent to scaling-up.

Establishing a Path to Commercialization

Now that the current status of the emerging technology has been
established and we have updated the economic model with new information, which
still projects a competitive product, we can establish how to proceed. This
third phase of development can consume fairly large amounts of capital, so a
critical assessment should be conducted to establish a deliberate agenda so
that an investor may be convinced to fund this phase.

The initial task of this phase is a risk assessment to identify any
technical flaws in the concept, and establish a plan to address and overcome
any obstacles. As an example, the process data from bench scale operations has
confirmed the kinetic viability of the process but has left unanswered certain
mechanical questions. For instance, we know the reactor works but we have
assumed in our model a feeder that can use unprocessed feedstock. The problem
identified is, how do we introduce the solid feedstock in a uniform,
continuous manner without excessive preprocessing. This risk assessment,
which should include all components, is intended to identify components of the
process that either require further development prior to proceeding to the
first scale-up or to find an acceptable alternative.

The final piece of the risk assessment is to critically look at the question of scale-up. One may ask the question, how far can we proceed, in this initial step from bench scale? But the right question is, what is the maximum scale-up possible from the final development unit to the commercial demonstration? Answering this question is a key to determining the total path to commercialization. We can then decide on how many scale-up steps to take and when critical components should be scaled-up. These steps may include any or all of the following: an integrated pilot plant, a semi-works to prove out critical components or a complete demonstration system.

After planning the global technical approach, and the required component development has been identified, we need to feed any revisions to our overall cost model to reconfirm feasibility. The next stage is to determine the additional technical data, whether mechanical or process, that is required.

Typical questions which help identify such data include:

−   Does each component work as intended?

−   Does the system as a whole work together in a safe manner?

−   Does proper selection of materials take into consideration "corrosive and errosive elements in the process and can I maintain product specifications?

In addition, the duration of acquiring the answers to these questions should be established. Typical goals of this first scale-up may be 5,000 hours of total test time with perhaps 1,000 hours of continuous operation under design conditions. The purpose of this scale-up is to work through the operational and process problems, confirm yields and product quality, and obtain an indication of reliability. The "other" objective is to be able to again refine the economic model with the data obtained from this first scale-up for both capital and operations costs. We will need this information, since we are approaching the time that additional capital will be needed for the next scale-up or for a continuously operational demonstration facility.

Once we have established technically what type of data and scaled-up system the technology requires, we need to establish a cost of this phase of the work and raise additional capital. At this stage, it is important to consider if any revenue can be derived from the operation of the development unit to offset the operational costs. This may not be realistic, but an investor typically likes to see some "pay as you go" operation while development is progressing.

After the development unit has completed the technical data acquisition, it is again time to refine our feasibility model with new cost data, operational data and reliability data. The level of success of the

development unit will at times determine the type of financing that the process developer can consider. The final section discusses the various options.

The First Commercial Unit - How Can It Be Financed

As we complete Phase III, the additional data collected from the scaled-up operation is again fed back into the economic model to reconfirm feasibility. A positive result will now enable the project to proceed to raise the capital necessary to build a full scale facility which, by definition, when successful will be the first commercial unit.

Financing can be obtained from a variety of sources, ranging from total equity, where the investor assumes all the risk, to non-recourse project financing where the risk of failure is divided between the lender and the equity participant. Technologies concerned with the disposal or processing of solid waste are currently eligible to obtain tax exempt bonding authority. The lower cost of capital by using tax exempt bonds is a commonly used method to enhance the overall economics of a project.

Funding a new technology using non-recourse project financing, typically requires either some level of equity participation or a guarantee to pay back the debt, or some combination of the two. The level of equity participation or debt guarantee depends on the characteristics of the project and the projected economics as determined by an Independent Engineering Study. This Independent Engineering Review is critical to both lenders and equity participants, since it is intended to confirm both the technical and economic viability of the technology.

From a lender's point of view, the typical characteristics of a strong project include some or all of the following:

- A turnkey construction contract including a fixed price, fixed completion date, detailed performance test and penalties for nonperformance.

- An operations and maintenance contract with a fixed price and incentives for positive performance and penalties for poor performance.

- Independent projections based on the technology and contract structure which show adequate cash flow to cover all expenses and debt service. These projections should be done for both the expected operational scenarios and in cases where potential problems may arise that are either technical or economical in nature.

Raising the capital for a new technology can be as challenging as completing the technical development. However, this job is easier when the proper groundwork has been laid by following the methodology presented here.

CHARACTERISATION AND MODEL COMPOUND STUDIES ON Pd AND Ni/Mo HYDROUS TITANIUM OXIDES

Lindsey E. Hayes, Colin E. Snape and Stanley Affrossman
University of Strathclyde, Dept. of Pure & Applied Chemistry,
Thomas Graham Building, 295 Cathedral St., Glasgow G1 1XL, UK

ABSTRACT

Pd and Ni/Mo exchanged hydrous titanium oxides (HTOs) have high activities for hydrogenation and hydroprocessing reactions, respectively which arise principally from the effective dispersion of the active phases and the acidity of the substrate. This paper covers (i) the use of deuterated substrates to investigate the mechanism of pyrene hydrogenation with Pd-HTOs, (ii) the use of XPS and EXAFS to investigate the dispersion of the Pd and Ni/Mo and (iii) the impact of ion-exchange procedures on the activity of Ni/Mo-HTOs for hydrodesulphurisation (HDS) and hydrodenitrogenation (HDN). The deuteration experiments indicated that acidic hydrogen on the HTO does not participate in hydrogenation despite the broad correlation of activity with the substrate acidity. XPS and EXAFS indicated that the Pd and sulphided Mo phases on HTOs are smaller than on other substrates, such as γ-alumina where impregnation procedures are used. Indeed, EXAFS has provided evidence for the existence of a mixed "Ni-Mo-S' phase. Hydrogenation and hydrogenolysis activities and selectivities in HDS of dibenzothiophene and quinoline vary considerably as a function of substrate surface area, preparation procedure and calcination temperature.

INTRODUCTION

Hydrous metal oxide ion-exchange compounds of Ti, Zr, Nb and Ta were developed originally for the preparation of ceramic materials [1] and the decontamination of aqueous nuclear wastes [2]. However, the high surface areas and ion-exchange capacities, variable acidities and relatively good thermal stability make these amorphous materials ideal substrates for transition metal, metal oxide and metal sulphide catalysts. Indeed, research to date has shown that Pd-hydrous titanium oxides (HTOs, the cheapest hydrous metal oxide to prepare) have considerably higher activities than Pd-γ-alumina catalysts for the hydrogenation of polynuclear aromatic compounds, such as pyrene [3]. Active carbon is the only widely-used support for Pd that has been found to give comparable activities to the HTOs [4]. Moreover, activities of Ni/Mo-HTOs have been found to be broadly comparable to their γ-alumina counterparts for hydroprocessing coal tars [5] and heavy coal liquids [6] and they do not undergo rapid deactivation. However, there are a large number of variables involved in the preparation of HTOs and their compositions, particularly in relation to catalytic activity, remain important topics for research.

In this paper, the following aspects of structure and reactivity of HTOs are addressed.

(i)   The use of X-ray photoelectron spectroscpoy (XPS) and extended X-ray adsorption fine structure (EXAFS) to investigate the dispersions of Pd and sulphided Ni/Mo , respectively.
(ii)   The use of deuterated substrates to investigate whether acidic hydrogen participates in the mechanism for pyrene hydrogenation with Pd-HTOs.
(iii) The impact of ion-exchange and calcination procedures on activity and selectivity in hydrodesulphurisation (HDS) and hydrodenitrogenation (HDN).

EXPERIMENTAL

Catalyst preparation
Sodium hydrous titanium oxide substrates (Na-HTOs) were prepared as described [3-6] previously by hydrolysing the soluble intermediate formed from titanium tetraisopropoxyl and a methanolic solution of sodium hydroxide. The atomic ratio of Na to Ti was 0.5 for all the substrates used in this investigation. To increase the surface areas of the HTOs, about 15% w/w of silica was incorporated into the substrates using the appropriate amount of silicon tetraethyl in the preparation [7]. Pd was ion-

exchanged onto the Na-HTOs to give nominal loadings in the range 1-20% w/w using two procedures. In the first, Pd was dissolved in a mixture of concentrated nitric and hydrochloric acids and diluted to a pH of 1. Following ion-exchange with the appropriate volume of solution, the Pd-HTO was Filtered, washed with acetone/water and dried under vacuum. In the second method, The Na-HTO was contacted with an aqueous solution of $Pd(NH_3)_4Cl_2.H_2O$ and, after filtration and washing, the catalyst was acidified with phosphoric acid to a pH of 3-4. All the Pd-HTOs were calcined at 350°C for 10 minutes. For deuteration experiments, Pd-HTOs were prepared by these two methods but using the corresponding deuterated mineral acids.

A series of Ni/Mo-HTOs were prepared with a nominal loading of 10% Mo and the Ni concentration was varied between 1 and 7% w/w. Table 1 summarises the variables in the preparation procedure which included the substrate surface area, the order of ion-exchanging Ni and Mo in conjunction with substrate acidity, calcination temperature and whether or not the HTO was calcined in between ion-exchanging Ni and Mo. The nickel was loaded from nickel nitrate solution at a pH of 4 and Mo from ammonium heptamolybdate solution at the same pH. Sulphuric acid was used to acidify the HTOs in all the preparation stages.

Characterisation
Nitrogen BET surface areas of most of the HTOs were determined and typical values are summarised in Table 2. Incorporating silica into the substrate and exchaging Pd for Na greatly increased the surface area from the typical baseline value of 80 m^2 g^{-1} for the Na-HTO. Mo concentrations were determined directly from XRF and indirectly by AA using the ammonium heptamolybdate solutions after ion-exchange.

The Pd and Ni/Mo HTOs have been analysed using XPS at each stage in their preparation procedures. The spectrometer comprised a Vacuum Science Workshop 100 mm hemispherical analyser with an Al anode as the X-ray source giving AlK_α radiation at 1486.6 eV. The powdered samples were adhered to conventional SEM stubs with double-sided cellotape and evacuated to 10^{-6} torr before transfer from the entry to the main chamber for analysis. Ni EXAFS was carried out at the Daresbury laboratory using station 7.1. with monochromatic X-rays having a wavelength of 1.488 A°.

Activity measurements
Pyrene was hydrogenated at 100°C and 10 bar pressure using stainless steel tubing bomb microreactors (TBMR) immersed in a fluidised sandbath and agitated via a flask shaker and ball bearings in the reactors [3]. 0.1g of pyrene was used with n-hexadecane as an inert diluent and 20mg of catalyst. After the desired reaction period, the TBMRs were quenched in water and the reaction mixture was recovered for gas chromatographic (GC) analysis.

HDS and HDN activities of the Ni/Mo catalysts were assessed using dibenzothiophene and quinoline respectively. For purposes of comparison, tests were also carried out with a commercially available Ni/Mo-γ-alumina catalyst (Akzo 153). The catalysts were pre-sulphided at 400°C prior to the tests using a large stoichiometric excess of hydrogen sulphide in hydrogen. Both the HDS and HDN tests were conducted at 350°C and 70 bar pressure (cold) in TBMRs. These were loaded with 20 mg of catalyst and 1 cm^3 of 0.06 molar solutions of dibenzothiophene and quinoline in n-decane or n-hexadecane containing a different n-alkane as internal standard [8]. After the desired reaction period, the solutions were recovered and the product disributions were determined by GC.

RESULTS AND DISCUSSION

Hydrogenation activity and XPS characterisation of Pd-HTOs
The hydrogenation of pyrene to di- and tetrahydropyrenes can be conveniently modelled as a pseudo first order reaction [3]. The rate constants on a weight of catalyst basis are presented in Figure 1 for the two methods used to ion-exchange Pd onto the HTOs. As the Pd concentration is increased from 1 to 20% (maximum ion-exchange capacity of Pd is about 23% w/w of dry catalyst), the rate constants increase linearly, i.e. they remain virtually constant with respect to the weight of Pd. However, the activities of the HTOs prepared from Pd dissolved in aqua regia are vastly higher than those prepared from the tetra-amine salt. Apart from a possible inhibiting effect from the amine ligands, the key difference in the two methods is that with the tetra-amine salt, the catalyst is acidified after rather than during ion-exchange. As reported previously [3], activity does broadly correlate with substrate acidity

1818

as demonstrated by the fact that the neutral Pd-HTO gave an extremely low conversion, but other more subtle effects such as the Pd precursor used can also be important. For a given preparation method, the hydrogenation activity has been found to broadly correlate with the substrate BET surface area [4].

Figure 2 presents the surface atomic Pd/Ti ratios for the two methods used to prepare the Pd-HTOs. For the method employing the tetraamine salt as the Pd precursor, the Pd/Ti increases linearly with Pd concentration up to the highest loading used of 20% w/w in accord with the increase in the rate constant for pyrene hydrogenation (Figure 1) and suggesting that the dispersion of the Pd does not vary markedly. In contrast, for the method using Pd dissolved in aquq regia, the Pd/Ti ratios plateaus at approximately 5% Pd despite the hydrogenation rate constant increasing linearly with Pd concentration. Up to a loading of 5% Pd, both methods give the same Pd/Ti ratio. It is proposed that this apparent difference arises from a kinetic effect with much faster ion-exchange of Pd occurring on the HTO surface when the Pd is dissolved in acid.

The results above and previous work [3] suggest that the acidic protons on the HTOs may participate in the hydrogenation reaction in much the same way as with super acids. To test this ascertion, the Pd-HTOs deuterated acids were used instead of the corresponding mineral acids in the preparations of the Pd-HTOs. Moreover, the reactions with deuterium-labelled Pd-HTOs were carried out under conditions where the concentrations of acidic deuterium on the catalyst were vastly in excess of the amount of hydrogen required. GC-MS analyses of the hydrogenated pyrenes indicated that the acidic deuterium had not been incorporated in measureable quantities and, therefore, it is suggested that the primary role of the acidic substrate in hydrogenation and indeed, also in HDS and HDN, is to facilitate the adsorption of aromatic species.

Characterisation of Ni/Mo HTOs
Figure 3 presents the XPS-determined surface Mo concentrations for two Mo- and a Ni/Mo-HTO, together with that for the commercial γ-alumina catalyst. The surface Mo concentrations increase linearly with the bulk concentration up to a loading of 20% w/w. For nominal bulk loadings of about 10% Mo, the surface concentration is higher on the HTOs (Figure 3). EXAFS provides evidence that the dispersion of Ni is also superior on the HTOs than on γ-alumina. In the EXAFS transforms for supports containing only sulphided Ni, the characteristic Ni-Ni peak at about 3.0 Å was virtually absent for the HTOs whereas it was a prominent feature for γ-alumina. For the Ni/Mo catalysts, the peak due to the mixed Ni-Mo-sulphide phase at about 2.8 Å was less pronounced for the HTO than for the commercial γ-alumina catalyst (Figure 4). However, this difference is attributed to the fact that the HTO was calcined in between ion-exchanging Ni and Mo and that the Ni concentration was higher (5 cf 2.5 %) meaning that a smaller proportion of the Ni is likely to be in the mixed phase.

Hydrodesulphurisation and hydrodenitrogenation
Figures 5 and 6 summarise the product distributions obtained from the HDS and HDN tests on dibenzothiophene and quinoline, respectively with the Ni/Mo HTOs (M1A-M7A, Table 1) and the commercial γ-alumina catalyst. The highest activities for the HTOs were observed for those samples not calcined between ion-exchanging the Ni and Mo (M2A and M7A) possibly due to maximising the concentration of the catalytically active mixed Ni-Mo-sulphide phase. Indeed, the activities of these HTOs were comparable to that of the γ-alumina catalyst for HDS (Figure 5) and superior for HDN where higher concentrations of propylcyclohexane and propylbenzene were obtained (Figure 6). However, it should be pointed out that the activities of commercial γ-alumina catalysts can vary considerably and the HDN activity of Akzo 153 may be less than that of other corresponding samples.

All the HTOs discussed above were calcined at 500°C because results for thiophene indicated that HDS activity increased markedly as the calcination temperature is increased above 400°C. Figures 7 and 8 present the variations in HDS and HDN activity for dibenzothiophene and quinoline, respectively as the calcination temperature is increased from 350 to 550°C. For HDS, the activity increases considerably and the extent of hydrogenation as indicated by the concentrations of bicyclohexyl decreases. Similarly for HDN, an increase in hydrogenolysis activity for removal of the heteroatom is observed. Interestingly, these significant changes in activity with increasing temperature must be accompanied by increasing amounts of the amorphous HTOs being converted into crystalline titania (primarily anatase as indicated by XRD).

1819

REFERENCES

1. Dosch, R.G. and O'Neill, W.M., US Patent 3,699,044, 1972.
2. Dosch, R.G., Headley, T.J. and Hlava, P.F., J. Am. Chem. Soc., 1984, 67, 354.
3. Stephens, H.P. and Dosch, R.G., Proc. of 4th Int. Symp. on the Scientific Bases for the Preparation of Heterogeneous Catalysts, Belgium, Eds. Delman, B. and Yates, J.T., 1987, p271.
4. Hayes, L.E., Ph.D thesis, University of Strathclyde, in preparation.
5. Stephens, H.P., Bolton, C.and Snape, C.E., Fuel, 1989, 68, 161.
6. Stohl, F.V., Dosch, R.G. and Stephens, H.P., Proc. Direct Liquefaction Contractors Review meeting, Pittsburgh, Oct. 1988, p490.
7. Dosch, R.G., Stohl, F.V. and Richardson, J., Prepr. Am. Chem. Soc. Div. Fuel Chem., 1989, 34(4), 1415.
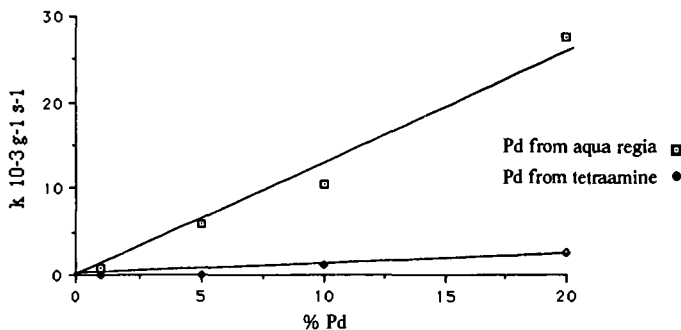8. Moreau, C., Durand, R., Zmimita, N. and Geneste, P., J. Catal., 1988, 112, 411.

FIGURE 1 RATE CONSTANTS FOR PYRENE HYDROGENATION

Table 1 Typical BET surface areas of the HTOs

Type of HTO	Surface area m^2 g^{-1}
Na-HTO (atomic Na/Ti ratio = 0.5)	98
Na-HTO/silica (about 15% w/w silica)	204
10% Pd-HTO	170
10% Pd-HTO/silica	310
Ni/Mo-HTO (about 3% Ni, 10% Mo)	73
Ni/Mo-HTO/silica	270

Table 2 Summary of high surface area Ni/Mo HTO/silica catalysts prepared

Designation	Ion-exchange sequence		No. of calcinations[a]	Removal of Na[b]
M1A	1. Mo	2. Ni	2	No
M2A	1. Mo	2. Ni	1	No
M3A	1. Ni	2. Mo	2	No
M4A	1. Mo	2. Ni	2	No
M5A	1. Mo	2. Ni	2	Yes (pH 2.5)
M6A	1. Mo	2. Ni	2	Yes (pH 4)
M7A	1. Ni	2. Mo	1	No

[a] = two corresponds to calcining between the ion-exchange steps.
[b] = sodium removed via acidification prior to ion-exchange of Mo.
The pH of the molybdate solution was adjusted to 4 except for M1A where it was 2.5.
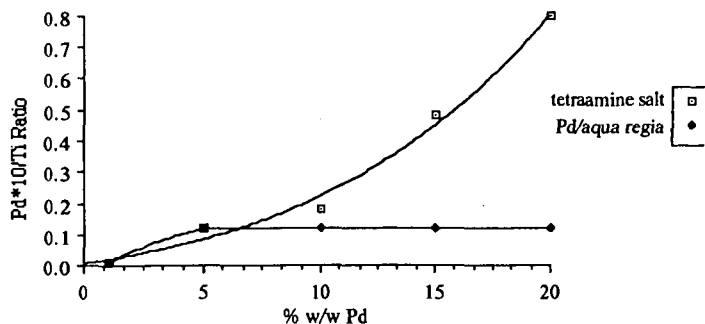
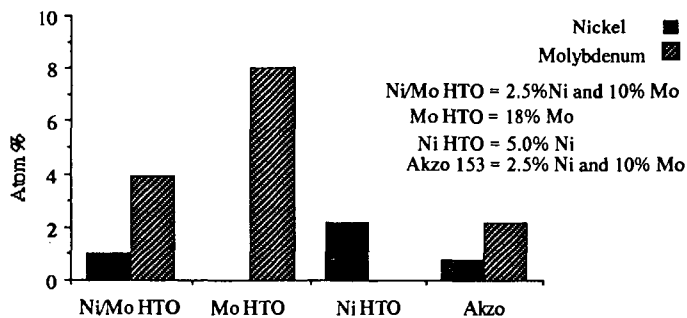FIGURE 2 Pd/Ti RATIOS VS. BULK Pd CONCENTRATIONS

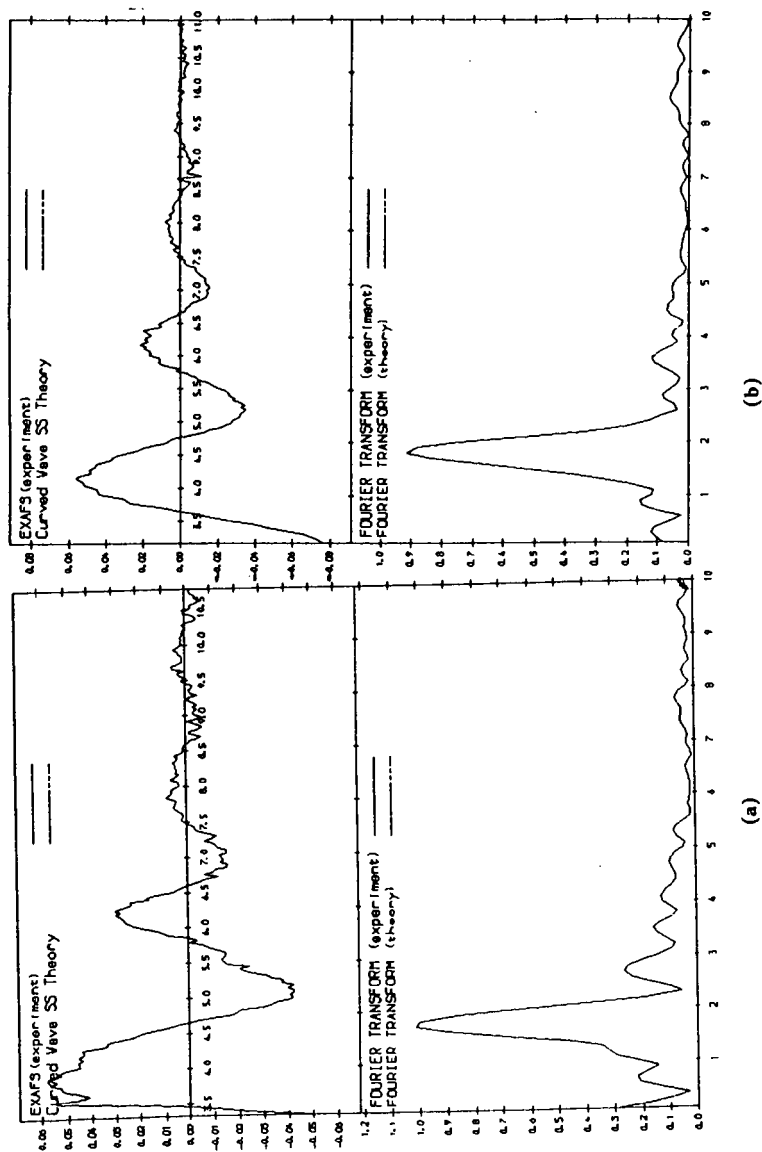FIGURE 3 XPS-DETERMINED SURFACE CONCENTRATIONS

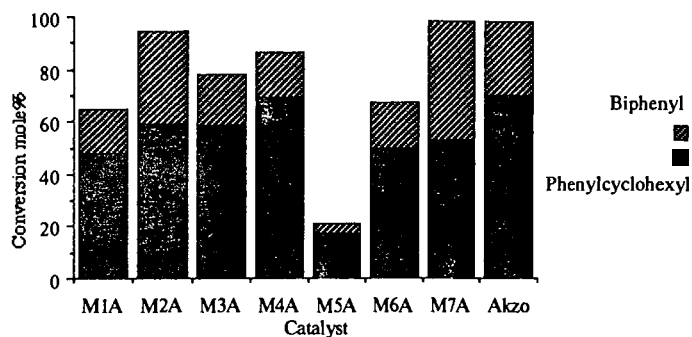FIGURE 4 RAW AND TRANSFORMED Ni EXAFS DATA FOR Ni/Mo (a) γ-ALUMINA AND (b) HTO CATALYSTS
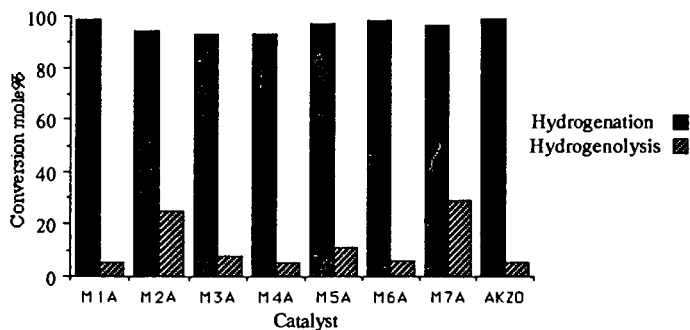
FIGURE 5 HDS OF DIBENZOTHIOPHENE
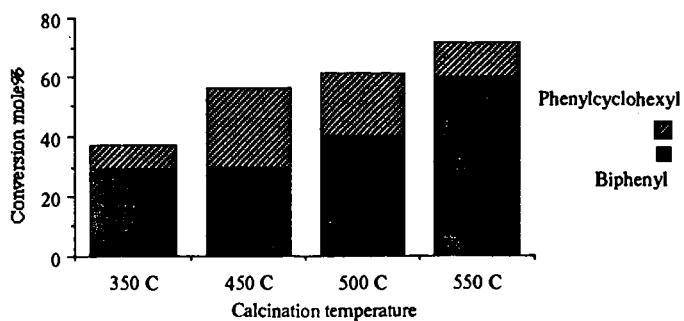

FIGURE 6 HDN OF QUINOLINE

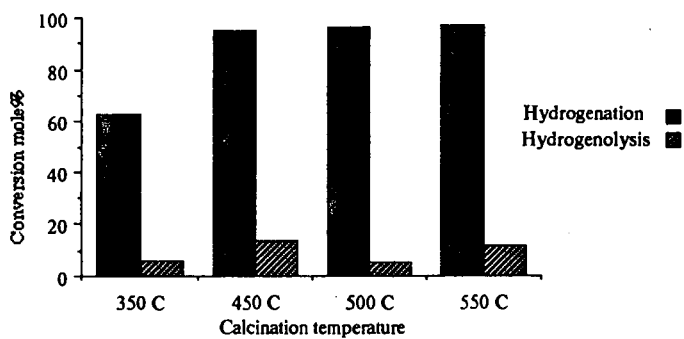FIGURE 7 EFFECT OF CALCINATION TEMP. ON HDS ACTIVITIES

FIGURE 8 EFFECT OF CALCINATION TEMP. ON HDN ACTIVITIES

REACTIONS OF PROPANE ON HYDROUS METAL OXIDE-SUPPORTED CATALYSTS

Zhentao Feng and Rayford G. Anthony
Department of Chemical Engineering, Texas A&M University
College Station, TX 77843

INTRODUCTION

There are strong economical incentives today to develop catalysts for the selective conversion of light paraffins, especially propane. Formation of propylene, aliphatics or aromatics is favorable. Previous work has shown catalytic conversion of propane on HZSM-5 (Inui and Okazumi, 1984; Kitagawa et al., 1986; Scurrell, 1988). The main products are benzene, toluene and xylenes. In this work, a relatively new type of catalyst is prepared for the reaction of propane, i.e., hydrous metal oxides.

Hydrous metal oxides were first used for waste water treatment and direct coal liquefaction (Stephens et al., 1985). Research on these materials identified several properties that might make hydrous metal oxides useful as catalyst supports. They include high surface area, large ion exchange capacity, dual ion exchange properties for cation and anion, and strong thermal stability (Lehto, 1987). This study employed hydrous metal oxides as catalyst supports for the synthesis of catalysts for the propane transformation.

EXPERIMENTAL

Catalysts. Sol-gel method was used to prepare two different types of hydrous metal oxides, i.e., hydrous silicon titanium oxide and hydrous zirconium oxide. The main procedure followed the patent by Dosch et al. (1985):

Tetraisopropyl titanate was mixed with tetraorthoethyl silicate to get a clear solution. Then slowly add the alkoxide mixture into a 10 wt% methanol solution of sodium hydroxide to get a very thick soluble intermediate. The intermediate was rapidly added to a solution of 1:10 water and acetone. The slurry was continuously stirred until it was homogenized. Filter the mixture and rinse with acetone. Collect the precipitate and dry it in vacuum at 80 °C overnight. This procedure was used to prepare hydrous silicon titanium oxide.

Hydrous zirconium oxide was synthesized by the same procedure, except that zirconium propoxide and potassium hydroxide were used. These two types of hydrous metal oxides were incorporated with Mo, Ni, Pd or Zr via ion exchange. After ion exchange, the catalysts were treated with sulfuric acid and then calcined in air at 540 °C.

Activity Tests. Activities of the catalysts were determined by their performance in the reactions of propane. Reactions were carried out isothermally in a Pyrex reactor under atmospheric pressure. Reaction temperature was 600 °C. The feed was 20% propane in nitrogen. Propane weight hour space velocity was 1.5 to 1.9. Composition of products was obtained with two GCs using a flame ionization detector and a thermal conductivity detector, respectively.

RESULTS

Characterization of Catalysts. Hydrous metal oxides as prepared were amorphous materials with 30% to 35% volatile. The surface areas of hydrous silicon titanium oxide and hydrous zirconium oxide were 390 m^2/g and 260 m^2/g, respectively. The pore volume was 0.6 cc/g with pore diameters in the range of mesopores. After ion exchange, the weight percent of Pd, Mo, Ni and Zr in the catalysts were 0.52%, 15%, 1.4% and 14% respectively based on dry weight. After calcination, hydrous silicon titanium oxide and hydrous zirconium oxide changed to their oxide forms, i.e., silica, titania and zirconia. X-ray diffraction showed that titania was predominately anatase with a small amount of rutile, while the phase of zirconia was cubic.

NaOH titration and temperature programmed desorption of ammonia experiments showed that the catalysts synthesized were weak acidic materials. Zirconia supported catalysts had higher acidity than the corresponding silica titania catalysts. Figure 1 is the ammonia TPD of Pd on zirconia and Pd on silica titania. Most of the ammonia desorbed below 250 °C, which indicates the absence of strong acid sites.

Activity Tests. Figure 2 is the summary of the activity tests on the catalysts. Dehydrogenation was the main reaction of propane and propylene was the largest reaction product. The change of propylene selectivity at different levels of propane conversion is shown on the figure. For silica titania supported catalysts, propane conversion ranged from 10% to 20% and propylene molar selectivity from 55% to 70%. For most zirconia supported catalysts, the conversion of propane was higher, up to 30% to 47%.

Besides propylene, the product consisted of methane, ethane, ethylene, small amounts of aromatics and C_4 to C_6 aliphatics. Figure 3 is the product distribution of propane reaction on silica titania supported molybdenum. Molar selectivities to light hydrocarbons ranged from 5% to 15% without significant change with time on stream.

Figure 4 shows the effects of active metals on propane conversion. The three catalysts were Pd, Mo and Ni supported on zirconia. The comparison indicated that palladium was the most active among these three metals.

DISCUSSION

From thermodynamic equilibrium point of view, propane converts to light hydrocarbons (methane, ethane, etc.) and aromatics much more favorably than to propylene. The results of this study showed just the opposite. Propylene was the main reaction product. Previous work (Riley and Anthony, 1986) on alkane transformation over HZSM-5 showed the formation and reactions of carbonium ions on the catalysts surface. On strong acid sites, carbonium ions would undergo cracking and aromatization reactions forming methane, ethane and aromatics. However, the catalysts in this study are weak acidic materials, consequently the formation and reactions of carbonium ions are less favorable. The mechanisms of propane

reaction on these catalysts are hydride abstraction on the dispersed metals. Hydride abstraction of propane produces propylene and hydrogen. Palladium has relatively strong interactions with hydrides and hence shows higher activity, which coincides with the experimental results. Beside hydride abstraction, carbonium ion formation and reactions, though not as important as that on zeolite, also contributes to the reaction. Zirconia supported catalysts have stronger acidity than titania supported ones, and hence higher amount of light hydrocarbons and aromatics are produced.

The equilibria conversion of propane to propylene at 600 °C is about 45%. Some catalysts in this study achieved about 35% to 45% conversion. Most catalysts showed high selectivity to propylene (about 60%). Therefore, hydrous metal oxides show considerable potential for the synthesis of catalysts for propane dehydrogenation.

REFERENCES
1.   Dosch, R.G., H.P. Stephens, and F.V. Stool, U.S. Patent 4,511,455, 1985.
2.   Feng, Z., M.S. Thesis, Texas A&M University, 1991.
3.   Inui, T., and Okazumi, "Propane Conversion to Aromatic Hydrocarbons on Pt/H-ZSM-5 Catalysts," Journal of Catalysis, 90, 366, 1984.
4.   Kitagawa, H., Y. Sendoda, and Y. Ono, "Transformation of Propane into Aromatic Hydrocarbons over ZSM-5 Zeolites," Journal of Catalysis, 101, 12, 1986.
5.   Lehto, J., "Sodium Titanate for Solidification of Radioactive Waste - Preparation, Structure and Ion Exchange Properties," Academic Dissertation, Department of Radiochemistry, University of Helsinki, 1987.
6.   Riley, M.G., and R.G. Anthony, "Transition-State Selectivity in the Cracking of N-Heptane over Modified ZSM-5 Catalysts," Journal of Catalysis, 100, 322, 1986.
7.   Scurrell, M.S., "Factors Affecting the Selectivity of the Aromatization of Light Alkanes on Modified ZSM-5 Catalysts," Applied Catalysis, 41, 89, 1988.
8.   Stephens, H.P., R.G. Dosch, and F.V. Stool, "Hydrous Metal Oxide Ion Exchangers for Preparation of Catalysts for Direct Coal Liquefaction," I&EC Proc. Res. Dev., 24, 15, 1985.

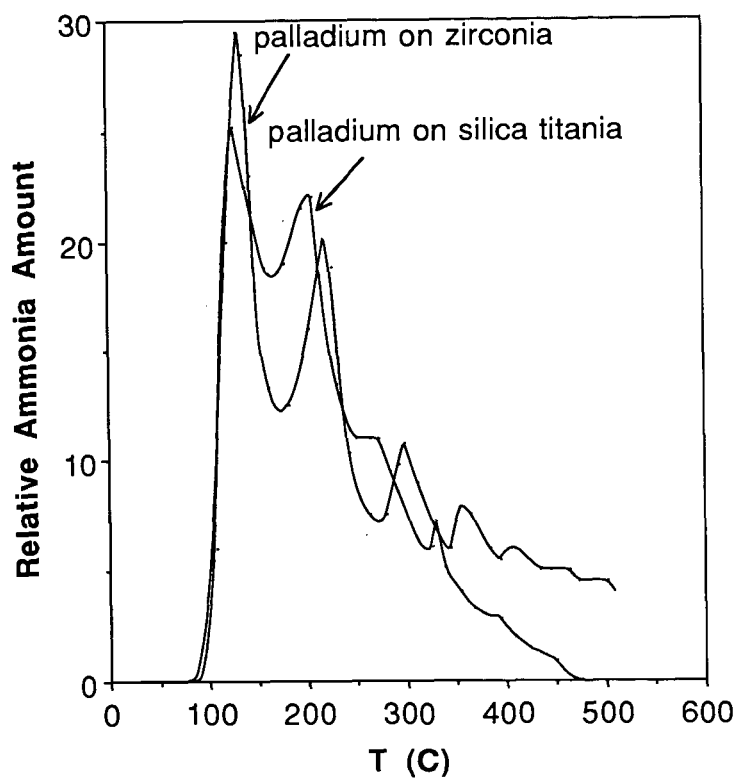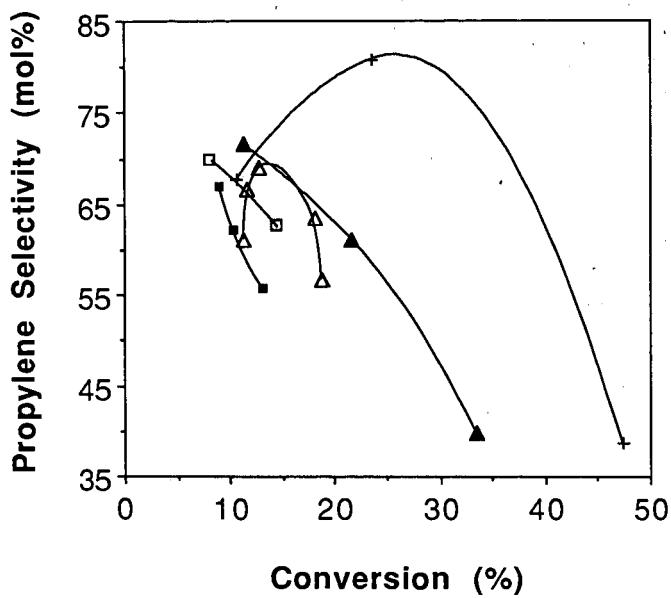Figure 1. Ammonia TPD of Catalysts

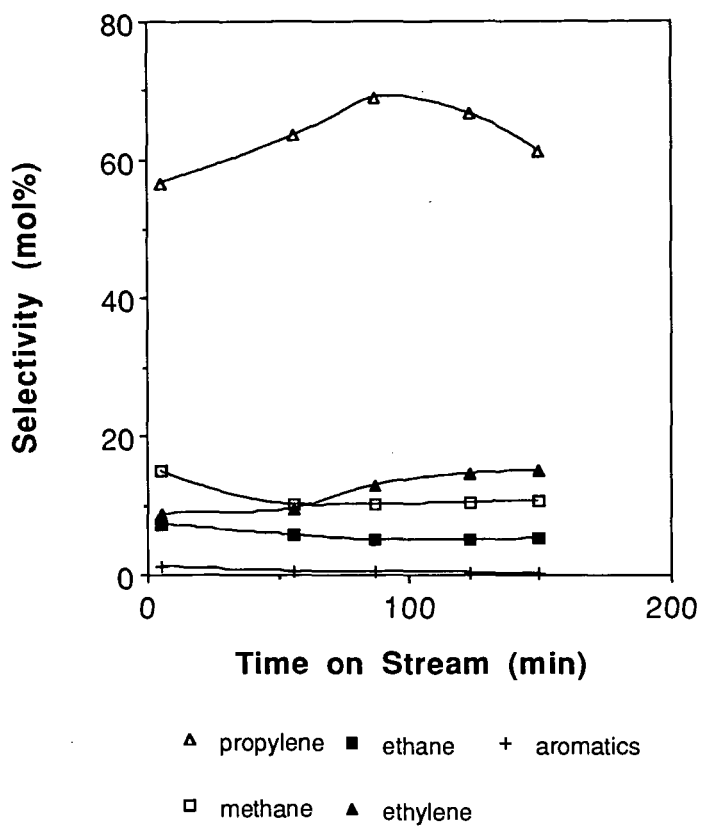Figure 2. Propylene Selectivity at Different Levels of Propane Conversion

Figure 3. Product Distribution of Propane Transformation
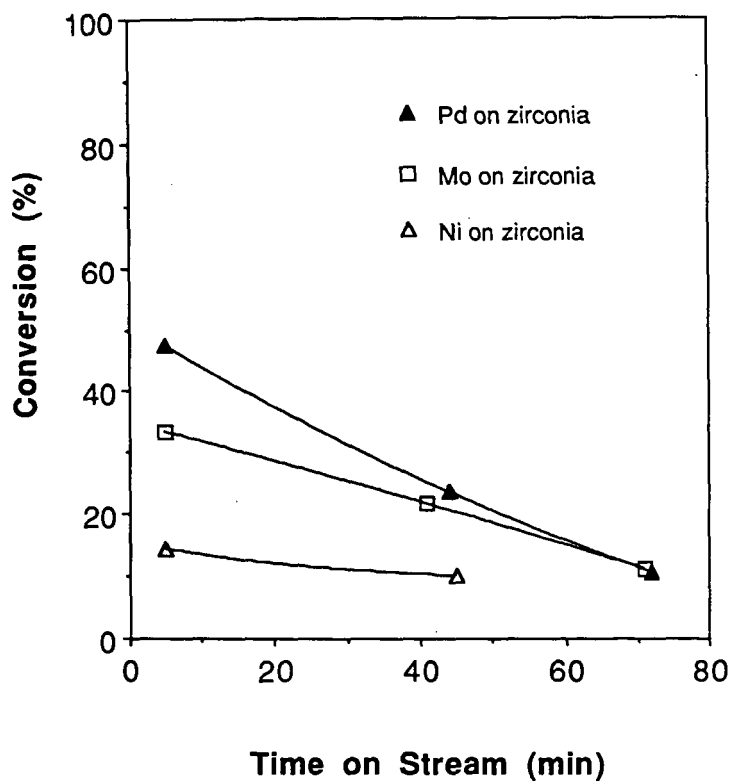for Mo on silica titania

Figure 4. Comparison of Different Active Metals

H-D EXCHANGE DURING SELECTIVE BENZENE HYDROGENATION TO CYCLOHEXENE

M. A. Richard, D. J. Taube, D. K. Yee, D. O. Durieux,
J. C. De Deken, P. Alcala, and H. Moreno

Catalytica, Inc.
430 Ferguson Drive
Mountain View, CA 94043

Keywords: benzene, hydrogenation, H-D exchange

INTRODUCTION

Ruthenium catalyzed hydrogenation of benzene to a mixture of cyclohexene and cyclohexane has been studied in gas phase (1-4) and slurry phase (5-9) reactions. The highest yields of cyclohexene, on the order of 30-40*%, have been observed in a four-phase slurry system consisting of a liquid benzene/cyclohexene/cyclohexane phase, an aqueous phase containing a dissolved transition metal salt, a solid heterogeneous ruthenium catalyst, and gas phase hydrogen. The presence of water and a transition metal promoter are generally required to achieve high selectivity to cyclohexene. There has been limited speculation on the role that water (1,2,4,8) and other promoters play in enhancing selectivity to cyclohexene. We have investigated the hydrogenation of benzene-d_6 with H_2 to probe mechanistic aspects of the four-phase slurry reaction. We have determined the extent of H-D exchange in the benzene feed and analyzed the H-D distributions in the products, cyclohexene and cyclohexane, at increasing benzene conversions.

EXPERIMENTAL

Benzene-d_6 hydrogenation was carried out in a 1 liter teflon-lined stirred reactor (Autoclave Engineers) at 150°C and 650 psig total pressure. A supported ruthenium catalyst (10) was reduced at 400°C in flowing hydrogen; a sample of the reduced catalyst was suspended in 150 cc of an aqueous solution of cobalt sulfate at 150°C in the teflon-lined reactor. Benzene-d_6 (250 cc) was preheated to 150°C and charged to the reactor. The total pressure was adjusted to 650 psig and maintained at 650 psig during hydrogenation. The reactor was sampled periodically and the organic phase composition determined by standard gas chromatographic methods. The H-D ratios and distributions in the organic components were determined by GC/MS.

RESULTS

Hydrogenation - Cyclohexene yield and selectivity vs. conversion are shown in Figure 1. Full conversion was reached after 100 minutes.

H-D Exchange in Benzene-d_6 - Less than 5% of the deuterium in benzene-d_6 was exchanged after 75 minutes (88% conversion). While the amount of hydrogen incorporated into the feed was very low, the amount increased as residence time in the reactor increased. The net make of benzene-h_6 increased from 0.2% after 11 minutes to 0.9% after 75 minutes.

H/D Ratios in Cyclohexane and Cyclohexene - The H/D ratios in the products, cyclohexane and cyclohexene, were determined at increasing benzene conversions by deconvolution and integration of the MS signals of the individual components. The ratios are shown in Table 1. We estimate that the error in these ratios is less than 5%. The expected ratios are 1.0 and 0.67 for cyclohexane ($C_6H_6D_6$) and cyclohexene ($C_6H_4D_6$), respectively, if one assumes no hydrogen incorporation by H-D exchange from H_2 or H_2O.

H-D Distributions in Cyclohexane and Cyclohexene - The distributions of H and D in cyclohexane and cyclohexene were determined by deconvolution of the GC/MS signals. The major products were $C_6H_6D_6$ and $C_6H_4D_6$; however there was significant scrambling of H and D giving the isotopic distributions shown in Figures 2 and 3.

DISCUSSION

Hydrogenation of benzene-d_6 was zero-order in benzene-d_6 up to 95% conversion; this is consistent with saturation of the catalytic sites with benzene-d_6. We were surprised to find no significant H-D exchange in the benzene-d_6 feed. This observation has two implications. First, it is unlikely that benzene adsorbs dissociatively. And second, cyclohexene disproportionation to benzene/cyclohexane does not occur to any measurable extent.

The data in Table 1 show that no H-D exchange occurred during hydrogenation of benzene-d_6 to cyclohexene and cyclohexane. However, the isotopic distributions in cyclohexane and cyclohexene (Figures 2 and 3) show that considerable *intermolecular* H-D exchange occurs *with conservation of deuterium*. The exchange of H and D between cyclohexene molecules to give the distributions observed supports the view that cyclohexene must adsorb and desorb numerous times so that the molecules can present both sides of the ring to the surface randomly. We believe that the key intermediate for the scrambling reaction is cyclohexene dissociatively adsorbed at the allylic position. As the reaction time in the reactor increases, the average residence time of the cyclohexene increases (it is continuously produced from benzene and continuously disappears as cyclohexane; thus, the residence time distribution of the cyclohexene molecules broadens as reaction time increases) and this results in increased scrambling with time as shown by the broadening of the distributions for cyclohexene in Figure 3. The less pronounced broadening of the cyclohexane distribution with time is consistent with little or no intermolecular exchange for the fully hydrogenated product; this is consistent with adsorption of cyclohexane being very weak relative to the adsorption strengths of benzene and cyclohexene.

The lack of a net hydrogen (H) incorporation into cyclohexene (or cyclohexane) is very surprising in view of the rampant scrambling that occurs. We believe that this is conclusive evidence supporting the view that the catalyst surface is hydrogen "starved" despite the very high hydrogenation rate (turnover frequency on the order of 10 sec^{-1} per exposed ruthenium site).

REFERENCES

1.   Don, J. A. and Scholten, J. J. F. Faraday Disc., Chem. Soc. 1982, 72, 145.
2.   van der Steen, P. J. and Scholten, J. J. F. Proceedings of the 8th International Congress on Catalysis 1984, 2, 659.

3.   Schoenmaker-Stolk, M. C., Verwijs, J. W., Don, J. A., and Scholten, J. J. F. Appl. Catal. 1987, 29, 73.
4.   van der Steen, P. J. and Scholten, J. J. F. Appl. Catal. 1990, 58, 281, 291.
5.   Niwa, S., Mizukami, F., Isoyama, S., Tsuchiya, T., Shimizu, K., Imai, S., and Imamura, J. J. Chem. Tech. Biotechnol. 1986, 36, 236.
6.   Niwa, S., Lopez Salinas, E., Mizukami, F., and Toba, M., Yukagaku 1989, 38(11), 938.
7.   Niwa, S., Mizukami, F., Toba, M., Tsuchiya, T., Shimizu, K., and Imamura, J. Shokubai 1989, 31(6), 421.
8.   Niwa, S. Mizukami, F., Imamura, J., and Itabashi, K. Sekiyu Gakkaishi 1989, 32(6), 299.
9.   Nagahara, H., et al. US 4,734,536 (1988), JP 63-243038 (1988), JP 63-88139 (1988), all assigned to Asahi Kasei Kogyo K. K.
10.   Details of catalyst preparation and characterization will be given in subsequent publications.

TABLE 1. H/D Ratios in Cyclohexane and Cyclohexene

Reaction Time, min	H/D, Cyclohexane	H/D, Cyclohexene
11	0.94	0.71
30	0.98	0.65
45	0.97	0.66
60	0.98	0.68
75	0.98	0.71
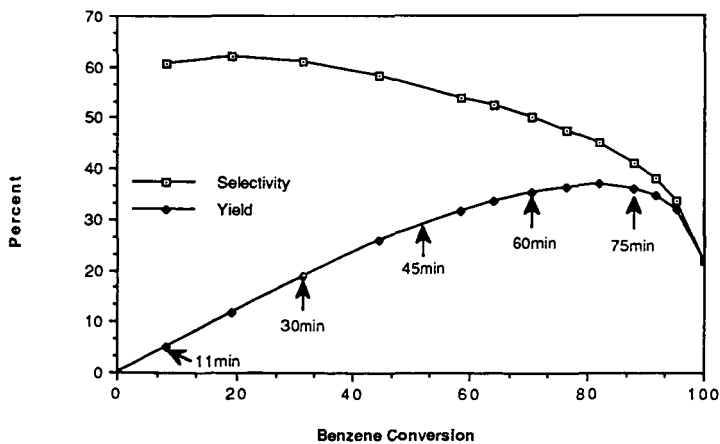
FIGURE 1. Cyclohexene selectivity and yield vs. benzene conversion. Note that the only products were cyclohexene and cyclohexane. The times noted correspond to the samples analyzed for H/D ratios and distributions.
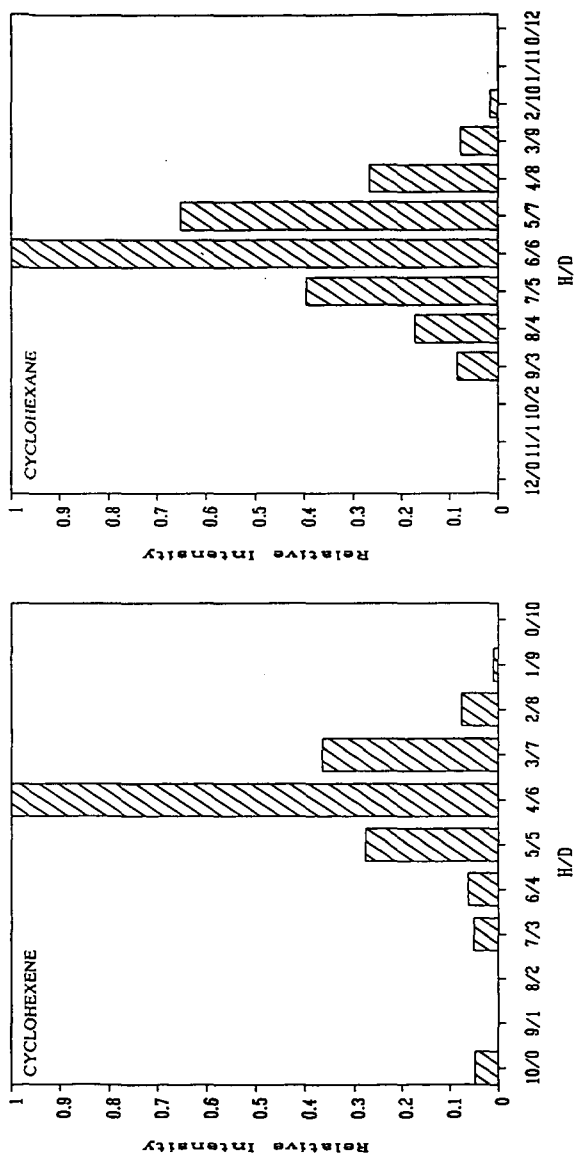
FIGURE 2. Isotopic distributions in cyclohexane and cyclohexene; 11 min sample.
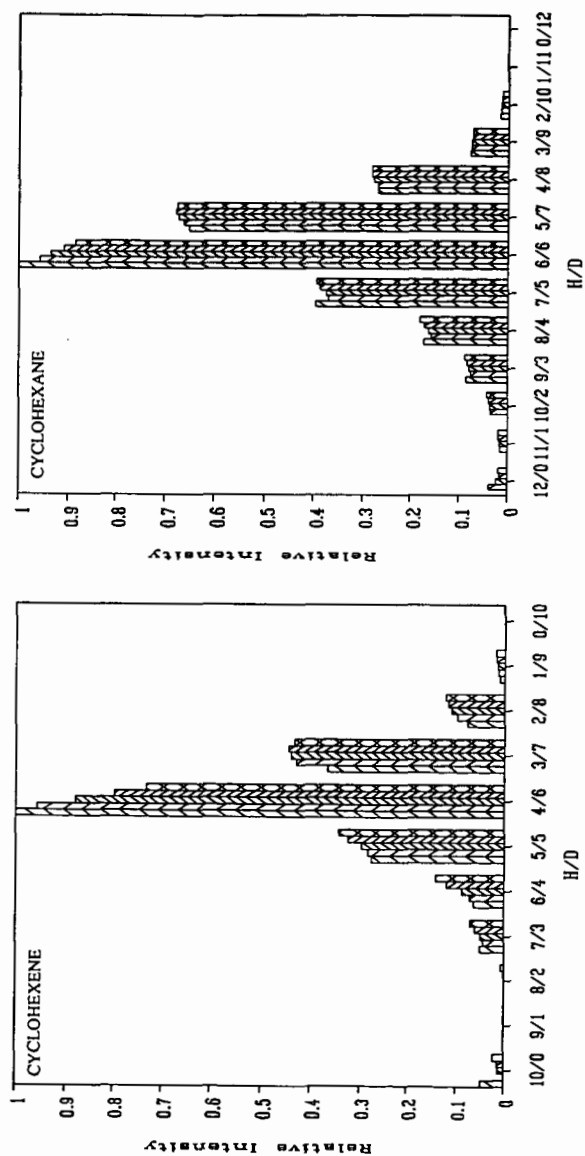
FIGURE 3. Isotopic distributions in cyclohexane and cyclohexene; reaction time increases from left-to-right (11, 30, 46, 60, 75 minutes) in each bar cluster.

Catalyst Selectivity in Hydrocarbon Reactions: Ethylene on Ru/SiO$_2$ and M-Ru/SiO$_2$

M. PRUSKI[α], D.K. SANDERS[βα], X. WU[βα], S.-J. HWANG[γα], T. S. KING[βα], and B.C. GERSTEIN[γα]

[α]Ames Laboratory, USDOE, and Departments of [β]Chemical Engineering, and [γ]Chemistry, Iowa State University, Ames, IA 50011

The nuclear spin dynamics of ^{1}H in adsorbed hydrogen, and ^{13}C in adsorbed ethylene on Ru/SiO$_2$ and M-Ru/SiO$_2$ (M≈Cu,Ag or Au) catalysts are used to probe surface concentrations of Ru and M, reactive intermediates, and selectivity in hydrocarbon conversion reactions. The temperature and exposure dependence of ethylene reaction on Ru/SiO$_2$ is investigated via various ^{13}C NMR techniques, as well as via ^{1}H multiple quantum coherence. Comparisons between monometallic and bimetallic catalysts are made.

Introduction.

Solid state NMR is becoming an increasingly important tool in the study of heterogeneous catalysis. The ability to directly study phenomena on the surfaces of underlined dispersed metal particles is one advantage offered by NMR. This is contrasted with mainstay ultrahigh vacuum techniques requiring single crystal surfaces, which may not always be good models for real catalysts. The objective of this paper is to demonstrate the application of several solid state NMR techniques to study the fundamental processes associated with hydrocarbon conversion over supported bimetallic catalysts. To this end, the interaction of hydrogen with M-Ru/SiO$_2$ (M=Cu,Ag or Au) is used to probe catalyst surface composition. An investigation of ethylene reaction on mono- and bimetallic catalysts at various temperatures, exposures and M composition is presented.

Experimental.

Catalyst samples were prepared as described previously.[1,2] ^{1}H NMR was performed on a 220 MHz homebuilt spectrometer, equipped with an 8-bit digital phase shifter.[3] Multiple quantum coherence was developed using a single quantum propagator.[4] ^{13}C NMR experiments were carried out on another homebuilt spectrometer operating at 100.06 MHz for ^{1}H and 25.16 MHz for ^{13}C. Transient techniques included cross polarization (CP) and direct excitation (Bloch decay), both of which were done with and without magic angle spinning (MAS) and proton decoupling. Special procedures were developed for low temperature (85-300K) experiments whereby samples were prepared, sealed, transferred to the spectrometer, and measured using CP/MAS without rise in temperature at any time.[5]

Results and Discussion.

NMR of Adsorbed Hydrogen: Establishing the Surface Composition of Bimetallic Catalysts

Studies on Cu-Ru/SiO$_2$ have shown that, at room temperature, hydrogen undergoes fast exchange between the two metals such that the observed lineshift, δ_{obs}, may be expressed as:

$$\delta_{obs} = X_{Ru}\delta_{Ru} + X_{Cu}\delta_{Cu/Ru}$$

where X_i is the surface concentration of metal i, δ_{Ru} and $\delta_{Cu/Ru}$ are the lineshifts for hydrogen chemisorbed on Ru/SiO$_2$ and the asymptotic limit as X_{Cu} approaches unity in Cu-Ru/SiO$_2$, respectively.[6] Thus, the surface composition of the bimetallic catalyst can be obtained from ^{1}H spectra (Fig. 1).
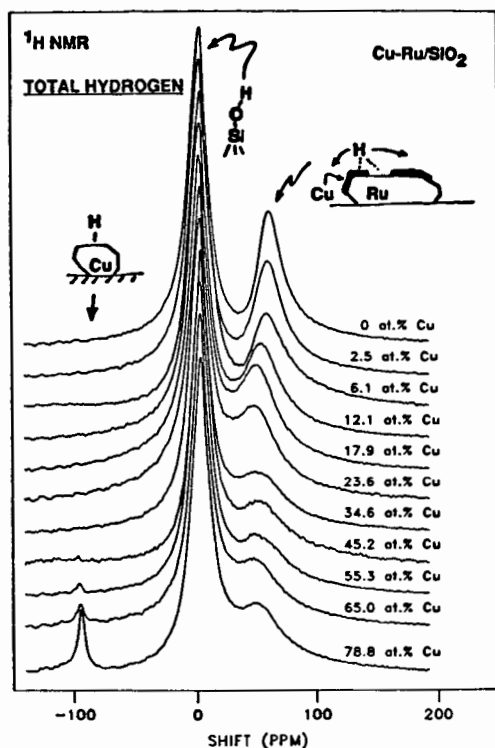
Fig. 1. NMR of adsorbed hydrogen on Cu-Ru/SiO$_2$ as a function of Cu concentration. The first moment of the upfield peak establishes the surface concentration of Ru.

Peak shifts in Fig. 1 demonstrate that X_{Ru} decreases quickly as the total Cu concentration increases from 0 to 20 at.%, before levelling off at ca. 35 at.%, and approaches zero at ca. 80 at.%, where complete masking of Ru is concluded. These trends suggest that Cu forms a thin monoatomic layer on Ru particles, until near complete coverage, after which 3-d Cu islands and/or pure particles begin to form, as evidenced by the emergence of a downfield peak indicative of hydrogen chemisorbed on bulk Cu (cf. Figure 1). Hydrogen uptake and ^{1}H NMR studies on Ag-Ru/SiO$_2$ and Au-Ru/SiO$_2$ indicate a higher tendency for these metals to form three dimensional aggregates.[2]

NMR of Adsorbed Ethylene: Weakly and Strongly Adsorbed Intermediates and Products
Ethylene on Ru/SiO$_2$

Transient NMR techniques were used to probe the development of intermediates and products as ^{13}C-labelled ethylene reacted over Ru/SiO$_2$ to establish:

(i)   concentrations of weakly and strongly adsorbed species (Bloch decay),

(ii)   possible identities of strongly adsorbed intermediates (Bloch decay, CP/MAS, dipolar dephasing), and

(iii)   identities of weakly adsorbed products (liquid state NMR techniques).

Intensity measurements indicated that no significant amounts of ^{13}C nuclei remain undetected in the Bloch decay studies. Assignments of weakly adsorbed species could be made unambiguously based on chemical shifts, relative intensities of the various peaks, and, in some cases, J-splittings. These experiments were performed at a high magnetic field (300 MHz), using slow MAS to remove broadening due to magnetic susceptibility. The identification of strongly adsorbed species based solely on NMR shifts is not straightforward. Although MAS can remove the effect of anisotropies of chemical shift, Knight shift, and magnetic susceptibility, considerable line broadening often remains due to the distribution of sites across the metal particles. The extent to which isotropic Knight shifts affect the identification of ^{13}C resonances of hydrocarbon species on highly dispersed, supported Ru is debatable. Dipolar dephasing and multiple quantum NMR were also used to probe possible identities of the strongly adsorbed species.

Selectivity and product distributions are strong functions of temperature and surface coverage. Fig. 2 shows an example of the temperature dependence of ^{13}C CP/MAS spectra of ethylene dosed on Ru/SiO$_2$ at 78K. The exposures (ϵ) were 0.5 and 1.5 ethylene molecules per surface Ru atom, and spectra were accumulated at 85K, at 185 K after reaction at that temperature for 2 days, and at 300 K after reaction at 300 K for 1 day.[7]
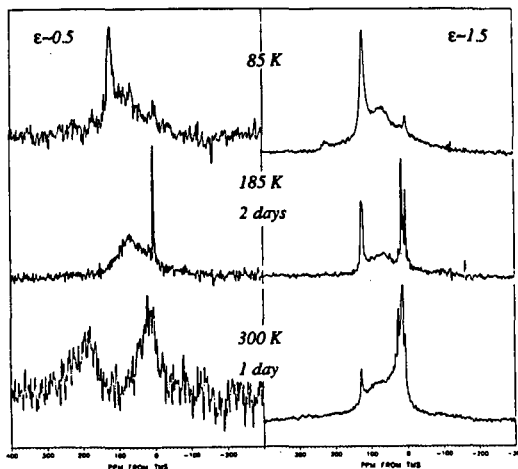
Fig. 2. NMR of ^{13}C in ethylene adsorbed on Ru/SiO$_2$ as a function of exposure (ϵ = 0.5 and 1.5), and temperature (85K≤T≤300K).

4

Both exposures give similar spectra at 85K. Peaks are assigned to weakly and strongly adsorbed ethylene, the strongly adsorbed species being either π, or di-σ bonded to the metal surface. To distinguish between the π and di-σ bound species, bond length measurements may be performed using the homonuclear dipolar coupling between ^{13}C nuclei. This work is in progress.

At 185K and $\epsilon = 0.5$, only ethane is observed in the weakly adsorbed layer. Changes in the spectrum also suggest a strongly bound C_2H_2 species in addition to the strongly bound C_2H_4. For $\epsilon = 1.5$, the increase in temperature leads to the development of weakly bound cis- and trans-butenes.

At 300K, for $\epsilon = 0.5$, broad peaks are observed at ca. 185 and 10 ppm, which are tentatively assigned to the $>$C- and -CH$_3$ carbons of ethylidyne, although experiments are underway to further investigate this assignment. At $\epsilon = 1.5$, the weakly adsorbed species were identified as ethane, butenes, and butane. Surface attached alkyl groups and acetylide are inferred to be present in the strongly bound layer.[1]

Evolution of weakly adsorbed products is shown in Fig. 3, for an $\epsilon = 5$ sample. At 140K,

$\epsilon \sim 5$, weakly adsorbed

130 K
ethylene

300 K
ethylene
c,t-butenes

370 K
ethane
c,t-butenes
butane

470 K
methane

PPM FROM TMS

Fig. 3. ^{13}C CP/MAS NMR of ethylene adsorbed on Ru/SiO$_2$ (ϵ = 5) as a function of temperature.

1842

only ethylene is observed. When the temperature is raised to 300K, cis- and trans- butenes are formed. Butadiene is observed as a transient during this temperature rise. Increasing temperature to 370K results in the formation of ethane and butane. At 470K only the fully hydrogenated products, methane, ethane and butane, are observed. The appearance of methane indicates that C-C bond cleavage has already occurred at or below 470K.

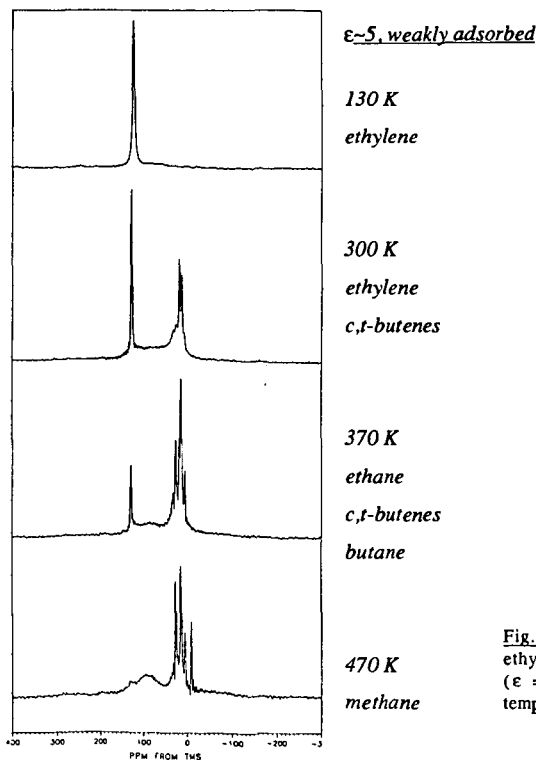As a means of further establishing identities of the strongly adsorbed species, multiple quantum spin counting was used.[4] Under the conditions imposed in this experiment for the development of multiple quantum coherence, the number of coupled spins is $k_{max} + 1$, where k_{max} is the highest order of observed coherence. The silanol protons of the support, separated by ca. 4Å, only develop double quantum coherence in a period sufficient to see $k > 8$ for the infinitely coupled ensemble of spins in adamantane. Fig. 4 shows the multiple quantum spectrum of the strongly adsorbed species resulting from ethylene adsorption on Ru/SiO_2. k_{max} sharply cuts off at a value of 5, indicating that species with no more than 6 strongly coupled protons are present in the sample. One possible candidate for the fragment with 6 coupled protons is metallocyclic $(Ru)CH_2CH=CHCH_2(Ru)$, which may be a participant in the formation of butenes. Small concentrations of this species cannot be excluded on the basis of ^{13}C NMR data.
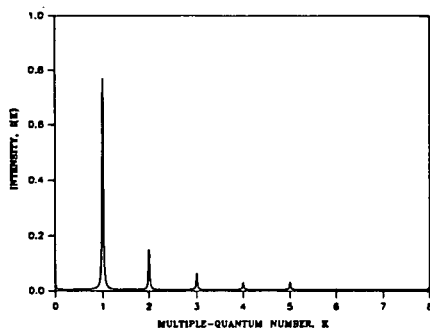
Fig. 4. Multiple quantum spectrum of strongly bound species from reaction of ethylene with Ru/SiO_2.

Ethylene on M-Ru/SiO$_2$

Unlike the extensive reaction of ethylene on Ru/SiO_2, no reaction is observed on Cu/SiO_2 at 300K. The bimetallic $Cu-Ru/SiO_2$ differs from the monometallic Ru/SiO_2 in that the ability of the catalyst to produce hydrogenated products is reduced. At room temperature, the intermediate, butadiene, is stabilized in the bimetallic system.[8] This is evidenced by Fig. 5, which shows the CP/MAS spectrum of ^{13}C in ethylene adsorbed on a 15 at. % Cu bimetallic catalyst.

Cu and Ru are known to be immiscible in the bulk.[9] Monte-Carlo simulations[10] indicate Cu-Ru bimetallic particles to be polyhedra in which the Cu selectively populates high coordination edge and corner sites, and then forms islands on the particle faces as Cu content increases. The equilibrium structure for a Cu-Ru particle with 15 at.% Cu, as predicted by Monte Carlo simulations, is shown in Fig. 5. It is therefore postulated that the selectivity towards highly

hydrogenated products is affected by the availability of edge and corner Ru sites, which become blocked by the adsorption of Cu.
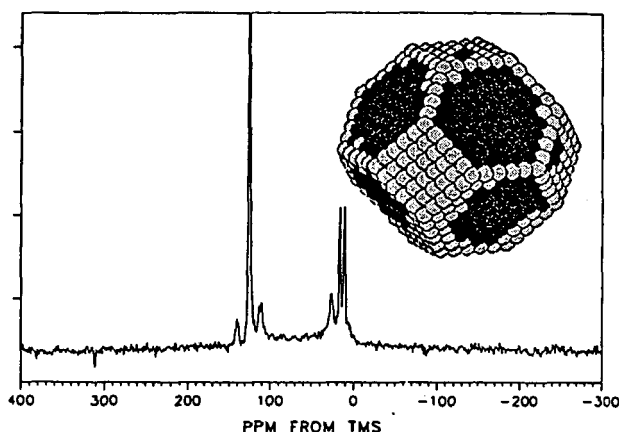
Fig. 5. NMR of ^{13}C adsorbed on Cu-Ru/SiO$_2$ at room temperature. Total metal loading = 4%, Cu = 15% of total metal.

Ethylene reaction on Ag-Ru/SiO$_2$ shows reduced hydrogenation[2] as compared to Ru/SiO$_2$, but not as much as for Cu-Ru/SiO$_2$. Although Ag tends to aggregate on Ag-Ru/SiO$_2$, this result suggests that it does block edge and defect-like sites to some extent, consistent with Monte Carlo simulations of Ag-Ru particles.[10] Prelimiary ^{13}C data on Au-Ru/SiO$_2$ indicate that the hydrogenation capability is also reduced. This is a surprising result, since, of the three metals studied, Au has the least tendency to efficiently cover the Ru surface.

Conclusions.

Product distributions, reaction intermediates, and surface metal concentrations are very important clues in understanding the mechanistic details of heterogeneous catalytic reactions. This paper demonstrates the wealth of information available via solid state NMR, illustrated by the study of ethylene reaction on mono and bimetallic catalysts. On Ru/SiO$_2$, this reaction is a complex function of both temperature and exposure. For example, the evolution of weakly adsorbed C$_4$ species is observed only at higher exposures, whereas the strongly bound species tentatively identified as ethylidyne is only observed at low exposures. Hydrogenation reaction is extensive on Ru/SiO$_2$. The addition of Cu, Ag or Au to the catalyst generally reduces hydrogenation activity, presumably by the blockage of catalytically active edge and corner sites.

References
1. Pruski, M., Kelzenberg, J.C., Gerstein, B.C., and King, T.S., <u>J. Am. Chem. Soc.</u> 1990, <u>112</u>, 4232.
2. Wu, X., Gerstein, B. C., and King, T. S., <u>J. Catal.</u> 1990, <u>123</u>, 43.
3. Gerstein, B.C., Han, J.-W., Hwang, S.-J., Pan, H.-J., and Skank, H., <u>Rev. Sci. Instr.</u> 1990, <u>61</u>, 2349.
4. Hwang, S.-J., and Gerstein, B.C., "Spin Counting in Dipolar Coupled Spin 1/2 Systems by Multiple Quantum Coherence", in <u>NMR: Basic Principles and Progress</u>, Springer-Verlag (Berlin) (in press).
5. Pruski, M., Sanders, D. K., King, T. S., and Gerstein, B.C., <u>J. Magn. Res.</u> (submitted).
6. Wu, X., Gerstein, B. C., and King, T. S., <u>J. Catal.</u> 1990, <u>121</u>, 271.
7. Sanders, D. K. Gerstein, B. C. King, T. S., and Pruski, M., manuscript in preparation.
8. Sprock, M., Pruski, M., Gerstein, B. C., and King, T. S., <u>Catal. Lett.</u> 1990, <u>5</u>, 395.
9. Hansen, M., <u>Constitution of Binary Alloys</u>, 2nd ed., McGraw-Hill, New York, 1958, p. 620.
10. Strohl, J. K., and King, T. S., <u>J. Catal.</u> 1989, <u>116</u>, 540.

SELECTIVE PARTIAL OXIDATION OF METHANE BY CATALYTIC SUPERCRITICAL WATER OXIDATION

Catherine N. Dixon and Martin A. Abraham
Department of Chemical Engineering
The University of Tulsa
Tulsa, Oklahoma 74104

ABSTRACT

The product spectrum obtained from catalytic partial oxidation in supercritical water has been compared to that obtained from catalytic oxidation in the gas phase. The presence of supercritical water inhibits the methane conversion but promotes the yield of methanol. The effect of oxygen concentration on the reaction in supercritical water has also been considered. High oxygen concentrations apparently inhibit the conversion reaction and decrease the yield of methanol. These results are considered in terms of consistent reaction pathways.

Keywords: Methane, Partial Oxidation, Supercritical Water

INTRODUCTION

Abundant supplies of natural gas exist within the United States. Methane, the major component of natural gas, is useful primarily as a fuel and, because it is difficult to transport, primarily at the wellhead. Partial oxidation to methanol or formaldehyde, or oxidative coupling to ethylene or other higher hydrocarbons, would greatly enhance the usability of methane both as a fuel source and as a raw material. Unfortunately, it is easier to convert partial oxidation products such as methanol to complete oxidation products than it is to form the partial oxidation products in the first place.

Research has centered on the identification of a selective catalyst which will provide high selectivity to partial oxidation products. Limited success has been obtained using selected metal-oxide catalysts, namely MoO_3 and Cr_2O_3 [Pitchai & Klier, 1986]. However, in these cases low conversion must be maintained so that the desired methanol product is not further converted to undesired complete oxidation products. The complete oxidation products, CO and CO_2, have little economic value. Low oxygen concentrations also have been used to increase the selectivity to partial oxidation products. Reports also indicate that, independent of the catalyst, the addition of water decreased the rate of methane conversion but increased the selectivity to methanol [Pitchai & Klier, 1986].

The use of supercritical water as a reaction solvent has previously been shown to alter the reaction pathways and thereby the product spectrum. Kinetic studies for the thermal oxidation of carbon monoxide, ammonia, and ethanol in supercritical water [Helling & Tester, 1987; Helling & Tester, 1988] revealed that secondary reaction pathways can be created through the addition of the supercritical fluid. Thermal oxidations of methane and methanol were accomplished in supercritical water [Rofer &

Streit, 1989] and a mechanism, modified from the gas-phase free radical mechanism, approximately described the kinetics. Extrapolation of the kinetics obtained from these experiments reveals that high methanol yields should be obtained from thermal oxidation in supercritical water [Dixon & Abraham, 1991].

Several investigators have also demonstrated that the addition of a supercritical fluid in a catalyzed reaction can influence the mechanism through which conversion is obtained. In one particular effort of interest, Dooley & Knopf [1987] selectively converted toluene to benzaldehyde through oxidation over CoO/Al_2O_3 in supercritical CO_2. In the oxidation of cumene hydroperoxide, Suppes & McHugh [1989] have shown that the addition of the catalyst can promote specific steps in a free-radical mechanism relative to others, which led to an observed change in the product selectivity.

Within the current paper, we present evidence to indicate that oxidation of methane in the presence of supercritical water can be used to promote the formation of the desired partial oxidation product, methanol. Gas phase catalytic oxidation is compared with catalytic oxidation in supercritical water, in terms of both methane conversion and methanol yield. Secondly, the influence of oxygen concentration on the conversion and methanol yield is considered.

EXPERIMENTAL

Batch reactions were used to determine the influence of supercritical water on the product spectrum of catalytic oxidation of methane. All reactions were carried out in separate 1.26 mL batch reactors, which have been described in detail elsewhere [Jin & Abraham, 1990]. Each reactor was loaded at room temperature with 0.8 mg of Cr_2O_3 catalyst [Aldrich Chemical]. For the reactions with supercritical water, 0.4 g deionized water was also added to the reactor. After the reactors were sealed, oxygen, methane, and nitrogen were added to the reactor in the desired proportions to a total pressure of 51.7 bar; for the high oxygen concentration study, a gas mixture containing 1.83% methane, 18.4% O_2 and the balance nitrogen [Scott Specialty Gases] was used. All materials were commercially available and used as received.

After loading, the reactors were placed into a high temperature fluidized sandbath (Tecam SBL-2), which had been pre-heated to the desired temperature. After the desired reaction time, the reactor was quenched by placing it into a cold water bath. Insertion into the sandbath and into the cold water bath corresponded to zero and the measured reaction time, respectively. Each experiment was repeated at least twice and the resulting values averaged to obtain the reported data. Heatup time for these reactors was approximately 1 minute, short compared to ultimate reaction times of up to 40 minutes.

The small reactor size, combined with the high temperature and pressure at the reaction conditions made measurement of the actual reaction pressure unfeasible. However, it was possible to estimate the actual pressure of the gas phase reaction using the assumption of the ideal gas law; this provided an estimate of the pressure as 118.8 bar. For the reactions in supercritical water, the actual pressure at the reaction temperature of 400 °C was greater than the gas phase reactions. Steam tables could be used to estimate the partial pressure of water at the reaction conditions as 325 bar, and then assuming Dalton's Law allows estimation of the total pressure as 444 bar.

Product analysis was accomplished by gas chromatography. For the gas analysis, an Hewlett Packard 5840 gas chromatograph with gas sampling valve, 30 ft Hayesep DB packed column, and thermal conductivity detector, was used in temperature programmed mode. Liquid analysis was accomplished with the HP 5840 instrument, using capillary column injection, 10 m DB-5 capillary column, and flame ionization detector. In both cases, product identification was accomplished by injection of pure component samples of the suspected material. Quantification was accomplished by comparison of peak areas with that of a standard, calibrated by injection of known amounts of materials. Inert nitrogen introduced with oxygen as air was the standard for the gas phase products while added naphthalene was used as a liquid phase standard.

RESULTS AND DISCUSSION

The conversion of methane is reported as a function of time in Figure 1, in which the gas phase conversion is compared directly with catalytic oxidation in supercritical water. Conversion increased monotonically with time in both cases. For the gas phase catalysis, approximately 0.6 conversion was achieved at 40 minutes, compared with approximately 0.3 conversion for the supercritical water case. At any given reaction time, the conversion achieved from gas phase catalysis was approximately twice that obtained from the reaction in supercritical water.

Experiments were accomplished at 400 °C and initial concentrations of oxygen and methane of 6.32 mol/L and 0.627 mol/L, respectively. The stoichiometry of the complete combustion reaction

$$CH_4 + 2\,O_2 \longrightarrow CO_2 + 2\,H_2O \tag{1}$$

indicates that only 2 moles of oxygen are required for complete conversion of methane to CO_2 and water. Thus, initial experiments were accomplished with greater than 500% excess of oxygen and should be well-represented by assuming that the kinetics are independent of oxygen concentration. Pseudo-first order kinetics for methane conversion provides

$$dx/dt = k\,(1-x) \tag{2}$$

which upon integration reveals

$$x = 1 - \exp(-kt) \tag{3}$$

Best fit analysis of the data of Figure 1 in terms of equation 3 provides estimated values of the rate constants as 0.0233 min^{-1} and 0.0115 min^{-1} for gas and supercritical water phase reaction, respectively. The solid lines in Figure 1 represent the predictions of the first order approximation and indicate the quality of the fit of the data.

Methanol yield is compared for the two cases in Figure 2. Essentially no methanol was observed for the gas phase catalysis at any reaction time. For the case of oxidation in supercritical water, the methanol yield ($y_{MeOH} = C_{MeOH}/C_{CH4,0}$) was also low, however, a maximum of approximately 0.7% yield was obtained at 5 minutes. The concentration decreased at longer reaction times, owing to subsequent conversion of methanol to complete combustion products CO_2 and water. Although the oxygen

concentration was in substantial excess, thereby favoring the production of total oxidation products, the yield of methanol was increased by more than one order of magnitude through the presence of the water. The lines in Figure 2 do not represent kinetics predictions but are used to more clearly indicate the trends in the data.

The presence of supercritical water serves to inhibit the initial conversion of methane, as evidenced by the data of Figure 1. This may occur by inhibiting adsorption of either methane or oxygen (or both), thereby decreasing the available concentration of the reactants. Alternatively, water may compete with the reactants for catalytic sites, or may poison some sites, limiting the effectiveness of the catalyst. It is not clear, however, what effect the water has on the reaction of methanol to CO_2 and water. Certainly, the presence of water promotes the formation of methanol, as indicated in Figure 2. From this observation, it would be suspected that the presence of water inhibits conversion of methanol to CO_2 and water, as well. The mechanism of this inhibition, while not determined within this study, could be attributed to the same factors used in understanding the inhibition of the methane conversion reaction.

Initial experiments were accomplished at high oxygen concentration, which would be expected to promote methane conversion but inhibit the formation of methanol. Several experiments were then accomplished to determine the effect of oxygen concentration on methane conversion and methanol yield. In these cases, the molar ratio of oxygen to methane is indicated in terms of the initial loading in the reactor, $\theta = C_{O2}/C_{CH4}$. Based on this definition and the stoichiometry of equation 1, $\theta = 2$ would correspond to stoichiometric oxygen.

Figure 3 reveals the effect of oxygen concentration on the methane conversion. At very low oxygen concentration, $\theta = 0.071$, conversion increased to approximately 0.1 after 5 minutes, and then remained steady at longer reaction times. In this case, the maximum conversion based on the stoichiometry and the oxygen loading should be approximately 0.035. However, if only methanol is produced, the reaction stoichiometry is

$$CH_4 + 1/2\ O_2 \longrightarrow CH_3OH \qquad\qquad (4)$$

and, given the oxygen loading, 0.14 conversion could be expected. Thus, it was likely that this low oxygen concentration reaction was oxygen-limited.

For oxygen concentration $0.6 < \theta < 0.8$, conversion increased steadily with reaction time, reaching approximately 0.25 conversion at 20 minutes. Little discrimination in conversion could be observed between the 3 experimental runs attempted within this concentration range. The high oxygen concentration data is repeated from Figure 1 for comparison purposes and reveals that conversion was slightly lower at $\theta = 8.72$ than at the lower concentration conditions. Although this was not expected, it is possible that the high concentration of oxygen inhibited methane conversion by preferential adsorption of oxygen onto the catalytic sites.

The effect of oxygen concentration on the yield of methanol is indicated in Figure 4. In all cases, a maximum in methanol yield was observed at a reasonable short reaction time. The highest yield was observed for $\theta = 0.071$, with a maximum yield of approximately 0.035 at 10 minutes. Considering that methane conversion was only 0.12 at this reaction time, the selectivity to methanol ($s = y/x$) was approximately 30%. As

the oxygen concentration was increased, the maximum yield of methanol decreased. For the intermediate range of oxygen, $0.6 < \theta < 0.8$, the maximum yield was approximately 0.015 at 15 minutes, and the maximum methanol yield was 0.005 for the high oxygen concentration case.

These observations for methanol yield are consistent with a series of reaction pathways described by equation 4 above followed by further reaction of methanol to CO_2 and water,

$$CH_3OH + 3/2\,O_2 \longrightarrow CO_2 + 2\,H_2O \tag{5}$$
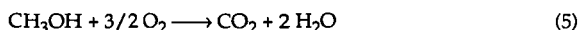
From Figure 4, this reaction is likely to be dependent upon the oxygen concentration, with higher concentrations of oxygen promoting methanol conversion. The data of Figure 3 suggests that the initial conversion of methane to methanol is essentially independent of oxygen concentration, although at high concentration, oxygen apparently inhibits the initial conversion. Under all conditions, reaction 5 is more facile than is reaction 4, leading to low methanol yield in all cases. However, the yield of methanol is greater in all cases where supercritical water was present than when the reaction was accomplished within the gas phase.

CONCLUSIONS

Methane oxidation was inhibited by the presence of supercritical water, with the rate of reaction being approximately one-half of that observed for gas phase oxidation. CO_2 and water were always the primary products of the reaction, but methanol was formed as an intermediate in low to moderate yield. The presence of supercritical water increased the yield and selectivity of methanol by approximately one order of magnitude compared to reaction in the gas phase. Little effect of increasing oxygen concentration was observed on the methane conversion reaction occurring within supercritical water, although inhibition was observed at very high oxygen concentration. At all oxygen concentrations, increasing oxygen led to a decrease in the maximum yield of methanol.

REFERENCES

Dixon, C. N., Abraham, M. A., "Direct Conversion of Methane to Methanol by Reaction with Supercritical Water", submitted to *Chem. Eng. Commun.*, 1991.

Dooley, K.M.; Knopf, F.C.; *I&EC Research*, 26(9):1910-16, 1987.

Helling, R.K.; Tester, J.W.; *Energy & Fuels*, 1(5):417-23, 1987.

Helling, R.K.; Tester, J.W.; *Environ Sci Tech*, 22(1):1319-24, 1988.

Jin, L., Shah, Y. T., Abraham, M.A.; *J. Supercritical Fluids*, 3(4):233-9, 1990.

Pitchai, R.; Klier, K.; *Catal. Rev. - Sci. Eng.*, 28:13, 1986.

Rofer, C.K.; Streit, G.E.; US DOE Hazardous Waste Remedial Actions Program, LA-11700-MS DOE/HWP-90, 1989.

Suppes, G.J.; McHugh, M.A.; *I&EC Research*, 28(8):1146-52, 1989.
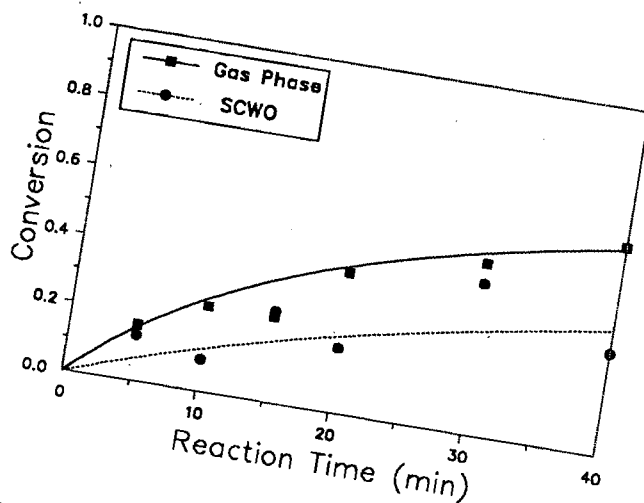
Figure 1: Comparison of methane conversion obtained from gas phase and supercritical water catalytic oxidation at 400 ℃.

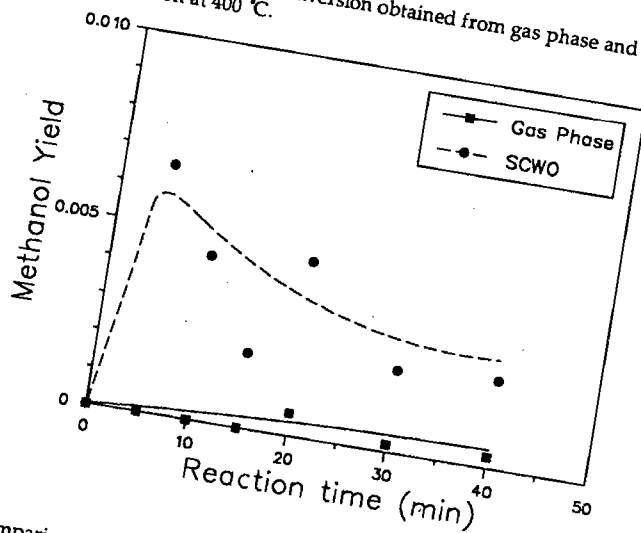**Figure 2:** Comparison of methanol yield obtained from gas phase and supercritical water catalytic oxidation at 400 ℃.

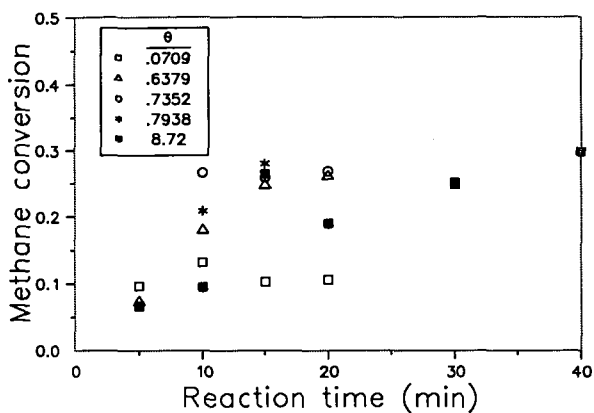**Figure 3:** Influence of oxygen concentration on the temporal variation of methane conversion during catalytic oxidation in supercritical at 400 °C.
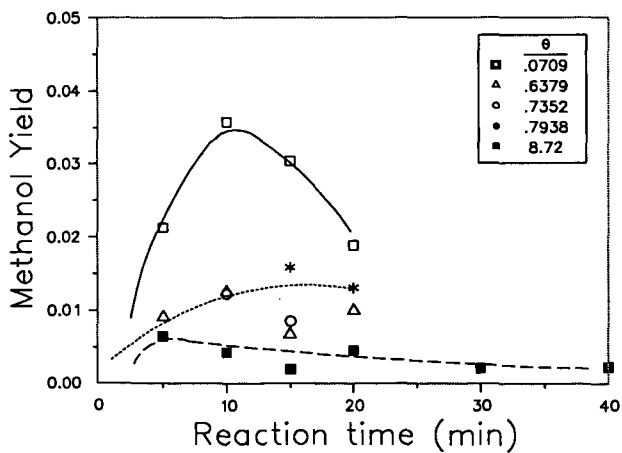

Figure 4: Influence of oxygen concentration on the temporal variation of methanol yield during catalytic oxidation of methane in supercritical at 400 °C.

Selectivity of γ-Al$_2$O$_3$ supported vanadium catalysts in the Hydrodemetallisation (HDM) of Ni-TPP and VO-TPP.

R.L.C. Bonné, P. van Steenderen and J.A. Moulijn[1]

Department of Chemical Engineering, University of Amsterdam, Nieuwe Achtergracht 166, 1018 WV Amsterdam (The Netherlands).

[1] *Present adress: Faculty of Chemical Technology and Materials Science, Delft University of Technology, Julianalaan 136, 2628 BL Delft (The Netherlands).*

abstract

The HDM reactions of nickel-tetraphenylporphin (Ni-TPP) and vanadyl-tetraphenylporphin (VO-TPP) over sulfided V/γ-Al$_2$O$_3$ catalysts have been studied in the liquid phase. Kinetic analysis revealed that both Ni-TPP and VO-TPP are demetallised through a reversible sequential mechanism via hydrogenated intermediate porphinic compounds. For the hydrogenation of the porphins a single site model, in which atomic hydrogen and porphins are adsorbed on the same type of sites, applies with a Langmuir-Hinshelwood type of kinetics for hydrogen. Hydrogenolysis is achieved on a different type of sites.

The HDM reactions of both Ni-TPP and VO-TPP are structure sensitive: increasing the vanadium loading of the catalysts initially results in an increased hydrogenation activity. The presence of crystalline materials on the catalysts suppresses the hydrogenation activity of the catalysts. Hydrogenolysis is not influenced by the presence of crystalline material but decreases almost linearly with increasing vanadium loading of the catalysts.

Introduction

Today's oil refining is facing major changes. The world's supplies of relatively easily refinable petroleum are decreasing whereas demands for clean refinery products (e.g. transportation fuels) are increasing. As a consequence, ever increasing quantities of low quality crude oils have to be processed, resulting in vast amounts of economically invaluable residual oils. The alternative which is rapidly becoming more important is to upgrade the residual oils into the desired products composition. In doing this, not only the C/H ratio of the feed has to be improved but a more thorough removal of hetero-atoms (sulfur, nitrogen and metal compounds) has to be achieved as well in order to protect 'down-stream' catalysts from rapid deactivation and to meet with stricter environmental legislations.

Unlike HDS and HDN, hydrodemetallisation (HDM) generates deposits of metal sulfides (mainly nickel and vanadium sulfides) on the catalysts, leading to an alteration of selectivity and eventually to an irreversible deactivation of the catalysts. Furthermore, the metallic constituents of petroleum tend to concentrate in the heavy fractions which makes the upgrading of residual oils even more cumbersome. In the improvement of existing processes and the development of new processes, kinetic data are highly desirable. Also the development of new types of catalysts with improved selectivity toward demetallisation as well as large metal storage capacity is to a large extent based on kinetics.

The objective of the current investigation is to relate structural aspects and sulfiding behavior of γ-Al$_2$O$_3$ supported vanadium catalysts to their activity and selectivity in the HDM of model metal compounds.

Experimental

1) Catalysts.
A listing of the catalysts applied in this study is given in table 1. All catalysts were prepared by pore volume impregnation of a wide-pore, high purity γ-Al$_2$O$_3$ support (Rhône-Poulenc SCM

99XL, specific surface area 156 m^2/g, pore volume 1.2*10^{-6} m^3/g and mean pore radius 13 nm). 75-150 μm particles were used. Further details on the preparation of the catalysts are given elsewhere [1].

Table 1. Catalysts applied

catalyst	vanadium loading	
	wt% V	atoms V/nm^2
V(0.9)/Al$_2$O$_3$	1.25	0.94
V(1.4)/Al$_2$O$_3$	1.79	1.35
V(1.8)/Al$_2$O$_3$	2.33	1.77
V(3.0)/Al$_2$O$_3$	3.93	2.98

Prior to the activity measurements, the catalysts were sulfided at 673 K in a gas mixture consisting of 15 vol% H$_2$S in H$_2$ (total flow rate: 13.67 μmol/s). The sulfiding mechanism of the catalysts is discussed in detail elsewhere [2]. The sulfiding procedure was as follows:
- Purging with Ar at 293 K to remove air.
- Isothermal sulfiding at 293 K in H$_2$S/H$_2$ for 1.8 ks.
- Temperature programmed heating (0.167 K/s) in H$_2$S/H$_2$ to 673 K.
- Isothermal sulfiding at 673 K in H$_2$S/H$_2$ for 7.2 ks.
- Purging with Ar at 673 K for 1.8 ks.
- Cooling down to 293 K in Ar.

2) HDM-activity measurements.
Vanadyl-meso-Tetraphenylporphin (VO-TPP) and Nickel-meso-Tetraphenylporphin (Ni-TPP) were used as model metal compounds. The HDM-activity measurements were performed in the liquid phase. The solvent employed in this study was o-Xylene (Janssen Chimica, p.a. grade). Because of the poor solubility of the model compounds at room temperature and their reactivity towards oxygen at elevated temperatures [3], they were dissolved under argon in refluxing o-Xylene for 7.2 ks. The porphin solutions thus obtained contained approximately 0.3 mol/m^3 VO-TPP or Ni-TPP and were stored under Ar or used immediately.

HDM-activity measurements of the presulfided catalysts were performed in a 2*10^{-4} m^3 stirred batch autoclave. The reactor was equipped with a sampling device from which samples were taken at regular intervals. After thoroughly purging the autoclave with argon, about 100 g of model compound solution was loaded into the reactor. The reactor was then evacuated and approximately 0.1 g of catalyst was introduced from a catalyst loader that had been mounted on the reactor to prevent the presulfided catalyst from contact with air. After purging with H$_2$ and subsequent evacuation the reactor was pressurised to approximately 0.3 MPa with a gas mixture containing 15 vol% H$_2$S in H$_2$. The H$_2$S/H$_2$ mixture was used as received. The reactor was further pressurised to 3 MPa with H$_2$ (99.9 %) which had been prepurified to remove traces of oxygen and water. After completing the loading and pressurising, the autoclave was closed and heated to 573 K while stirring its contents.
With each metalporphin, six runs were carried out at 573 K. In four of these runs the vanadium loading of the catalysts was varied while the liquid phase concentration of hydrogen was kept constant. The effect of the liquid phase concentration of hydrogen at 573 K was evaluated in three runs with the V(1.8)/Al$_2$O$_3$ catalyst. An overview of the HDM experiments with Ni-TPP and VO-TPP is given in table 2.
In each run 8-10 liquid samples of approximately 0.5 g were taken at various reaction times from the sampling port and analysed immediately with a Philips PU 8725 rapid scanning UV/VIS spectrophotometer. Porphins and metalloporphins are known to have distinct and intense absorption maxima in the visible range. The concentrations of the porphins and their

1854

hydrogenated intermediates were calculated from the UV/VIS spectra by applying Beer's law. The specific absorptions of each compound were corrected for overlap with other absorption bands in the spectra.

Table 2. **Overview of HDM experiments with Ni-TPP and VO-TPP over sulfided V/γ-Al₂O₃ catalysts**

catalyst	run	Ni-TPP $[H_2]$ (mol/m^3)	$[H_2S]$ (mol/m^3)	run	VO-TPP $[H_2]$ (mol/m^3)	$[H_2S]$ (mol/m^3)
V(0.9)/Al₂O₃	Ni-1	365.50	13.17	V-1	396.55	13.63
V(1.4)/Al₂O₃	Ni-2	388.78	13.51	V-2	381.02	13.40
V(1.8)/Al₂O₃	Ni-31	255.87	13.81	V-31	236.30	13.39
V(1.8)/Al₂O₃	Ni-32	381.02	13.40	V-32	404.31	13.73
V(1.8)/Al₂O₃	Ni-33	536.45	13.32	V-33	532.57	13.28
V(3.0)/Al₂O₃	Ni-4	400.43	13.68	V-4	392.67	13.57

In order to check for the presence in the liquid samples of metal compounds not detected by UV/VIS spectrometry, the total metal content of several samples was determined by Graphite Furnace Atomic Absorption Spectrometry (GFAAS, Perkin-Elmer HGA 500/560).
The actual concentrations of H_2 and H_2S at reaction conditions were calculated with the Peng-Robinson equation of state. Binary interaction parameters for H_2 and o-Xylene were obtained from literature [4]. Interaction parameters for H_2-H_2S and for H_2S-Xylene were set to zero. Also the density of the liquid phase at the reaction conditions was calculated with the Peng-Robinson equation of state. This made accurate calculation of the concentration of model compounds at these conditions possible.

3) Kinetic analysis.
Intrinsic kinetic parameters were obtained by evaluation of the concentration versus time curves with a non-linear regression programme (NLS). The objective function, defined as the sum of squares of deviations (residuals) between experimental and calculated concentrations, was minimised by using a combination of the Simplex and Levenberg-Marquardt methods.
With the NLS programme, several reaction mechanisms were tested. A fourth order Runge-Kutta method was used to numerically solve the sets of coupled differential equations for each kinetic model. Zero reaction time was taken at the moment the desired reaction temperature was reached. During the heating of the reactor and its contents some conversion of the reactants already occurred. In order to overcome this problem, concentrations of reactants and intermediates in the sample taken at zero reaction time were used as the initial concentrations in the kinetic analysis of the experiments.

Results

Typical concentration versus reaction time plots for HDM experiments with Ni-TPP and VO-TPP at 573 K are shown in figures 1 (run Ni-32) and 2 (run V-32). The experimentally obtained concentrations of reactants and hydrogenated intermediates are represented by markers. Solid lines represent calculated concentrations.

Ni-TPP has been shown to demetallise through a reversible sequential mechanism via the hydrogenated intermediate species Ni-TPC and Ni-TPiB [5-7]. In anology with Ni-TPP, VO-TPP appears to demetallise through a similar sequential mechanism. The concentration of VO-TPP as a function of reaction time rapidly drops while the concentrations of VO-TPC and VO-TPiB

1855

build up and then, after reaching a maximum, slowly decline indicating that these hydrogenated species are rather stable intermediates in the course of the HDM reaction of VO-TPP. No other vanadium containing species and metal-free porphins were detected in the liquid samples. Similar trends were observed in all the other HDM-experiments with VO-TPP, irrespective of vanadium-loading of the catalysts, liquid phase concentration of hydrogen and reaction temperature.

It can be seen clearly from figures 1 and 2 that VO-TPP is much more reactive than Ni-TPP at the conditions applied. Not only the concentration of VO-TPP drops faster and the concentration levels of hydrogenated intermediate species are much higher, but also the total content of vanadium in the liquid phase decreases faster than is the case with nickel.

Since the concentrations of reactants, reaction intermediates, hydrogen and hydrogen sulfide could be calculated at the reaction conditions applied, detailed kinetic analysis of the HDM reactions of both Ni-TPP and VO-TPP was possible.

Various kinetic models were tested which were all based on sequential reaction mechanisms. The most successful model is depicted in figure 3. In this model, which applies for both Ni-TPP and VO-TPP, the initial porphin is hydrogenated reversibly to its intermediates M-TPC and M-TPiB (M = Ni, VO). The intermediate M-TPiB then goes through a series of reactions, leading to the deposit of a metal sulfide on the catalyst and the fragmentation of the porphin macrocycle. The hydrogenolysis process is lumped into one irreversible step, represented by an apparant rate constant k_5.

It was carefully checked if inhibition by porphinic species occurs. No evidence was found for this at the conditions applied. Also in separate experiments with a flow reactor, in which the initial concentration of reactants as well as reaction temperatures were varied over large intervals, no evidence was obtained for inhibition of the HDM reactions by porphinic species.

Kinetic analysis of the HDM reactions of Ni-TPP and VO-TPP with respect to the liquid phase concentration of hydrogen revealed that both the hydrogenation reactions (1 and 3) and the hydrogenolysis step (5) exhibit fractional orders in hydrogen. The dehydrogenation reactions (2 and 4) appeared to be zeroth order in hydrogen. Similar results were obtained by Van Steenderen et al. [8] for the HDM reactions of Ni-TPP over a sulfided Mo/γAl$_2$O$_3$ catalyst at 613 K. The kinetic orders with respect to the liquid phase concentration of hydrogen are given in table 3. For comparison, the results obtained by Van Steenderen et al. are included.

Table 3. **Kinetic orders with respect to the liquid phase concentration of hydrogen**

catalyst	porphin	T (K)	α	β
V(1.8)/Al$_2$O$_3$	Ni-TPP	573	0.80	1.89
V(1.8)/Al$_2$O$_3$	VO-TPP	573	1.01	1.51
Mo(1.2)/Al$_2$O$_3$	Ni-TPP	613	0.73	1.78

The kinetic order in hydrogen of the hydrogenation reactions is represented by ·α. β represents the order in hydrogen of the hydrogenolysis step.

The fractional orders in hydrogen concentration indicate a Langmuir-Hinshelwood type of kinetics. Two kinetic models were considered based on the fact that no inhibition occurs by porphins and their hydrogenated intermediates or products. In the first model, adsorbed molecular hydrogen reacts with the porphins and their hydrogenated intermediates. In the second model, the porphinic species are thought to react with dissociatively adsorbed hydrogen. In both the models hydrogenolysis was considered to take place on either the same type of sites as

hydrogenation and dehydrogenation or on a different type of sites.

Although all models considered fitted reasonably well with the experimental data, for both Ni-TPP and VO-TPP the best results were obtained with the model of dissociatively adsorbed hydrogen with different types of sites for hydrogenation/dehydrogenation and hydrogenolysis. With this model, a value of $K_H=7.49^*10^{-5}$ m^3/mol was obtained. The hydrogenation and dehydrogenation rate constants were not introduced as variables but the ratios k_1/k_2 and k_3/k_4 were kept constant. They are in fact the equilibrium constants which were estimated from non-catalytic experiments and from various catalytic experiments in which liquid phase concentrations of hydrogen and hydrogen sulfide were widely varied. The estimated equilibrium constants at 573 K are given in table 4.

Table 4. Equilibrium constants of Ni-TPP and VO-TPP at 573 K

	Ni-TPP	VO-TPP
$K_{1,2}=k_1/k_2$	3.147^*10^{-3}	7.983^*10^{-3}
$K_{3,4}=k_3/k_4$	8.919^*10^{-4}	2.949^*10^{-3}

Plots of intrinsic rate constants for the HDM reactions of Ni-TPP and VO-TPP as a function of vanadium content of the catalysts are shown in figures 4 and 5, respectively.

It can be seen from figures 4 and 5 that VO-TPP is much more reactive than Ni-TPP. In both cases, the HDM reactions appear to be structure sensitive. This effect is for both Ni-TPP and VO-TPP most pronounced in the secondary hydrogenation rates (k_3). The (lumped) rate constant of hydrogenolysis (k_5) decreases almost linearly with increasing vanadium loading.

Discussion

The results obtained from the current investigation have demonstrated that the HDM of VO-TPP and Ni-TPP proceed through identical pathways. In both cases the initial porphin is reversibly hydrogenated to its chlorin, which in turn is reversibly hydrogenated to yield a metal-isobacteriochlorin.

Kinetic analysis of the hydrogen dependence of the HDM reactions revealed that both the hydrogenation and hydrogenolysis reactions exhibit fractional orders in the liquid phase concentration of hydrogen (table 3) whereas zeroth order applies for the dehydrogenation reactions. The non-integer orders in hydrogen indicate a Langmuir-Hinshelwood type of kinetics. It was shown that a single site model for hydrogenation and dehydrogenation reactions, in which porphinic species and atomic hydrogen are adsorbed on the same type of sites, fitted best with the experimental data, irrespective of the porphin used. The fact that the value for K_H is very low shows that the HDM reactions of both Ni-TPP and VO-TPP are only slightly inhibited by hydrogen at 573 K.

At present it is not clear whether the metal is removed from the metal-isobacteriochlorin, at which a very unstable metal-free porphinic molecule is formed, or metal removal takes place after destruction of the porphin macrocycle by e.g a combination of hydrogenation and cracking reactions. Fact is however that the hydrogenolysis reactions leading to the removal of metals from Ni-TPP and VO-TPP have fractional orders in hydrogen greater than 1 indicating that demetallisation is achieved via a sequence of reactions.

The HDM reactions of Ni-TPP and VO-TPP over sulfided V/Al$_2$O$_3$ catalysts are clearly demanding. Primary as well as secondary hydrogenation rates initially increase with increasing vanadium loading of the catalysts, the effect being most pronounced with the secondary hydrogenation rates. The catalyst with a vanadium loading of 3 atoms/nm^2 has a significantly lower

activity toward the hydrogenation reactions. Increasing of the vanadium loading of the catalysts has a dramatic impact on the hydrogenolysis step. Whereas hydrogenation rates initially increase with increasing vanadium loading, the hydrogenolysis rate decreases linearly with the vanadium content of the catalysts. This observation nicely confirms the conclusions that hydrogenation and hydrogenolysis are achieved on different types of sites.

It has been reported [1,2] that with V/Al_2O_3 catalysts prepared by pore volume impregnation with vanadium loadings up to 2 atoms/nm^2 the alumina surface contains an ill defined two-dimensional structure of vanadium oxide. At very low loadings the alumina surface contains species of tetrahedrally coordinated vanadium which, on increasing the vanadium loading, are transformed into octahedrally coordinated species. Further increasing of the vanadium loading is thought to result in an expanding of these relatively small clusters due to polymerisation into larger structures of octahedrally coordinated vanadium with a relatively less intimate interaction with the alumina surface than the former ones. At vanadium loadings exceeding 2 atoms/nm^2, V_2O_5 crystallites are present on the catalysts.

As for the sulfidability of V/Al_2O_3 catalysts, it was shown [2] that catalysts lacking crystalline V_2O_5 are nearly completely sulfided at 673 K whereas the major part of the sulfiding process of crystalline V_2O_5 takes place at temperatures well above 673 K. At temperatures up to 673 K, crystalline V_2O_5 is reduced to V_2O_3.

The ease with which the catalysts are sulfided and the observed sulfiding mechanism are indicative for the preservation of the characteristics (e.g. dispersion and support interaction) of the active phase. Also the temperature at which the sulfiding of the catalysts was performed is too low for solid state transformations or solid state diffusion processes to occur.

From the above, the impact of the vanadium loading of V/Al_2O_3 catalysts on the HDM of Ni-TPP and VO-TPP reactions can be rationalised as follows. The relatively low hydrogenation activities of $V(0.9)/Al_2O_3$ may be the result of the presence of the active phase in small clusters with a strong interaction with the support. On increasing the vanadium content, these clusters expand to larger structures which have a weaker interaction with the support. Due to this weaker interaction sulfur vacancies, which are thought to be the active sites for porphin adsorption and hydrogenation, may be formed with more easily. Also edges of the clusters of the active phase may contribute to the hydrogenation activity of the catalysts. It appears that after reaching a maximum with the $V(1.4)/Al_2O_3$ catalyst, the rate constants of hydrogenation slowly decline. This may be the result of the presence of larger clusters, formed out of small clusters, of the active phase with a relatively lower ratio of edges/mol V. The presence of crystalline material on the $V(3.0)/Al_2O_3$ catalyst results in a lowering of the hydrogenation activity for both Ni-TPP and VO-TPP. From this it is tentatively concluded that crystalline V_2O_3 has no hydrogenation capacity and, through coverage of the active sites, causes a lowering of the hydrogenation activity of V/Al_2O_3 catalysts.

The fact that the hydrogenolysis activity for both Ni-TPP and VO-TPP decreases linearly with increasing vanadium loading of the catalysts indicates that hydrogenolysis is to a large extent independent of the characteristics of the different phases in which the active material is present and supports the idea that hydrogenolysis is achieved on another type of sites.

As in hydrogenation, sites located at the edges of the active phase clusters apparently play an active role in the hydrogenolysis. Upon increasing the vanadium loading of the catalysts small clusters expand through polymerisation to larger clusters with a relatively lower ratio of edges/mol V resulting in a lowering of the hydrogenolysis activity.

Conclusions

- HDM of Ni-TPP and VO-TPP proceeds through a reversible sequential mechanism via hydrogenated intermediate compounds of similar nature: metal-tetraphenylchlorin and metal-tetraphenylisobacteriochlorin. VO-TPP is more reactive than Ni-TPP with respect to hydrogenation which can be seen from the faster decline of the concentration of VO-TPP and the substantially larger amounts of hydrogenated intermediates formed.

- A two-site mechanism is found to apply for the HDM reactions of both Ni-TPP and VO-TPP. In the hydrogenation and dehydrogenation reactions porphins, intermediates and atomic hydrogen are adsorbed on the same type of sites which are thought to consist of sulfur vacancies. Hydrogenolysis is achieved on another type of sites in which hydrogen sulfide is thought to play an important role.

- The HDM reactions of both Ni-TPP and VO-TPP are first order in porphins and hydrogenated intermediates. Hydrogenation reactions are approximately first order in the liquid phase concentration of hydrogen whereas dehydrogenation reactions are zero order in hydrogen. The hydrogenolysis reactions exhibit fractional orders in hydrogen greater than one.

- The fact that for hydrogenolysis, hydrogen orders are greater than one indicates the demetallisation of the porphins to proceed through a sequence of fast reactions.

- The HDM reactions of both Ni-TPP and VO-TPP over sulfided $V/\gamma Al_2O_3$ catalysts are clearly structure sensitive. With increasing vanadium loading of the catalysts hydrogenation rates for both Ni-TPP and VO-TPP increase untill, at loadings exceeding 2 atoms V/nm^2, crystalline V_2O_3 is present on the catalysts. The presence of crystalline V_2O_3 results in a loss of hydrogenation activity probably caused by coverage of active sites by crystalline material. The hydrogenolysis rate is not affected by the presence of crystalline V_2O_3.

Acknowledgements

Literature cited

1. Bonné, R.L.C., van Langeveld, A.D., Kieboom, M.N.H., and Moulijn, J.A., in preparation.

2. Bonné, R.L.C., van Duin, A.C.T., van Langeveld, A.D., and Moulijn, J.A., in preparation.

3. Agrawal, R., and Wei, J., Ind. Eng. Chem., Process Des. Dev. 23, 505 (1984).

4. Moysan, J.M., Huron, M.J., Paradowski, H., and Vidal, J., Chem. Eng. Sci. 38, 1085 (1983).

5. Hung, C.W., and Wei, J., Ind. Eng. Chem., Process Des. Dev. 19, 250 (1980).

6. Ware, R.A., and Wei, J., J. Catal. 93, 100 (1985).

7. Ware, R.A., and Wei, J., J. Catal. 93, 122 (1985).

8. Van Steenderen, P., Bonné, R.L.C., and Moulijn, J.A., in preparation.

Figure 1. Concentration versus reaction time plot of a HDM experiment with Ni-TPP at 573 K (run Ni-32). Experimental values are represented by markers. Solid lines represent calculated values.
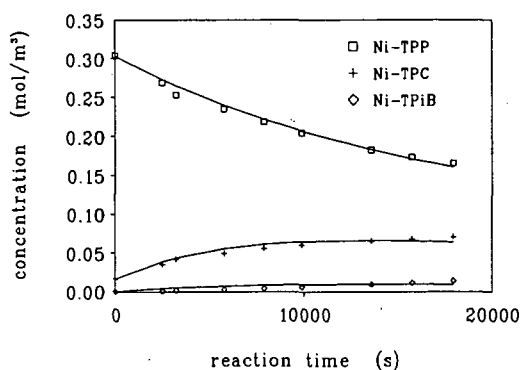
Figure 2. Concentration versus reaction time plot of a HDM experiment with VO-TPP at 573 K (run V-32). Experimental values are represented by markers. Solid lines represent calculated values.
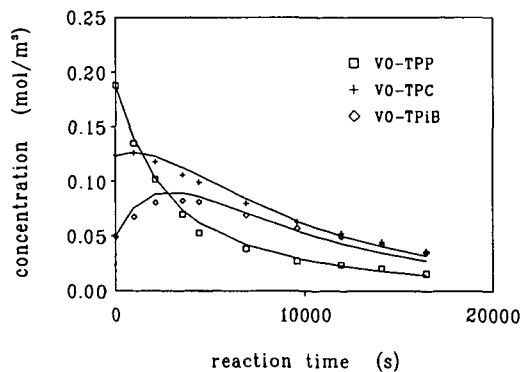
Figure 3. Reversible sequential reaction model for the HDM of M-tetraphenylporphins (M=Ni,VO). Deposited metal sulfides are represented by MS_x.
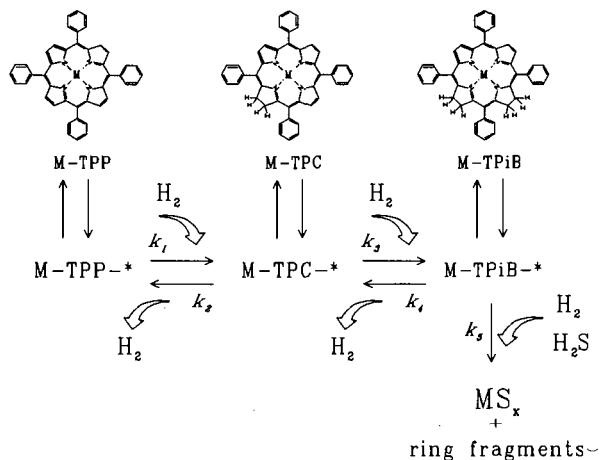
Figure 4. Intrinsic rate constants for the HDM of Ni-TPP at 573 K as a function of the vanadium loading of the catalysts (k_2, k_4 omitted).
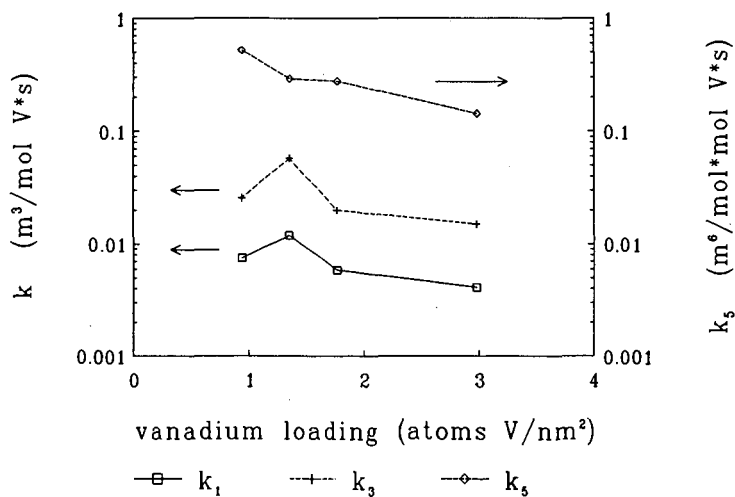
Figure 5. Intrinsic rate constants for the HDM of VO-TPP at 573 K as a function of the vanadium loading of the catalysts (k_2, k_4 omitted).
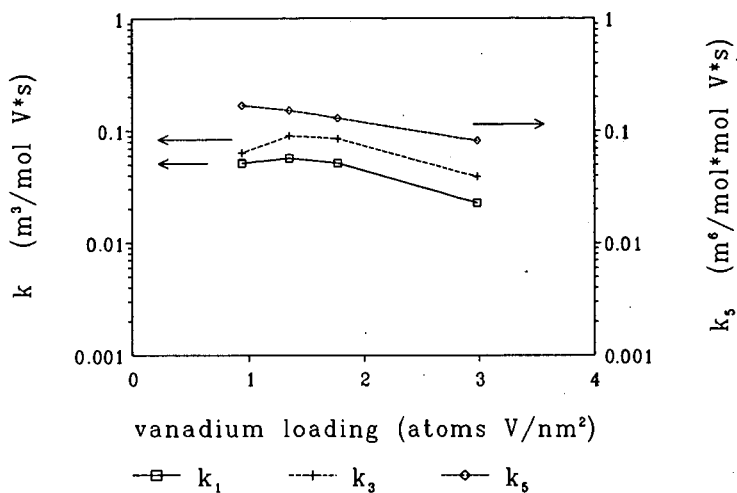
CRACKING PROPERTIES OF SAPO-37 AND FAUJASITES

M. BRIEND, A. LAMY, D. BARTHOMEUF, Laboratoire de Réactivité de Surface et Structure, URA 1106, Université P. et M. Curie, 4 place Jussieu, 75252, Paris Cédex 05.

Abstract :

SAPO-37 materials with Si atomic fraction from 0.12 to 0.22 are studied for their thermal stability, their acidity and their cracking activity. Most of the acid sites have a medium acid strength. A very small number of sites is very strong. The materials are thermally stable up to high temperatures. After pretreatment at 1175 K they are as active as an ultrastable faujasite in the cracking of n-octane.

IINTRODUCTION

SAPO-37, isotype of faujasite, is an active catalyst for cracking reactions (1,2). The present paper compares the properties of this material with those of faujasites.

EXPERIMENTAL

The samples are synthetised as described in (3) for sample Si-0.12 and Si-0.13 and in (4) for the other solids. The chemical analysis gives results in table 1.
XRD is used to determine the unit cell parameter of the as-synthetised samples. The heating chamber of a Guinier Lenné camera is employed to follow the changes in crystallinity and to determine the temperature for the loss of crystal structure.
TPD of NH_3 is followed using a quadrupole mass spectrometer Quadruvac PGA 100 Leybold-Heraeus.
The desorption of pyridinium ions from the H-SAPO-37 samples is followed by infrared spectroscopy.
The catalytic activity in the cracking of n-octane at 725 K is studied in a microreactor with H_2 as carrier gas.

RESULTS AND DISCUSSION

Si incorporation in the framework

The incorporation of Si in the SAPO-37 framework is seen by the decrease of the unit cell parameter a_0 (table 1) as the materials contain more Si.
The mechanism II of of substitution of Si for P in a theoretical $AlPO_4$ framework creates isolated Si atoms (1). Each Si atom generates one proton. According to mechanism III, 2 Si replace a pair Al-P in the $AlPO_4$ framework. In the case of SAPOP-37, Si containing islands are formed (2-5,7). This decreases the potential number of protons formed if no Al is included in those Si islands (5). Alternatively some Si-Al faujasite phase has been described (2,7). The table 1 shows that the Al fraction is often less than the theoretical value 0.50 which suggests the existence of Si islands. The difference from 0.50 increases as the Si content rises (except for the sample Si-0.20 which in fact contains some impurities of SAPO-20). This corresponds to an increasing amount of Si in islands. This is confirmed by the simultaneous decrease in the amount of occluded template (table 1) which indicates that a smaller number of charges have to be neutralized.

Thermal stability

The stability of the crystal structure studied in the heating XRD chamber is very high (table 1). In a flow of dry O_2 or of oxygen saturated with water at room temperature the structure collapses near 1200-1300 K which is similar to the case of the ultrastable LZY-82 zeolite (8). Nevertheless the SAPO-37 structure is not stable in ambient conditions for the template free samples (table 2). The instability occurs when the template free sample is contacted with water at temperatures lower than around 350 K. It probably results from the attack of Al-O-P bonds (8).

Acidity

The TPD of ammonia and of pyridine (table 3) gives one broad peak for all the SAPO-37 materials (free of template) located near 500 K or 665 K for the two bases respectively. Examples are given for Si-0.13 and Si-0.20 in table 3. The same experiment gives for HY and for a dealuminated sample (HYD) 2 peaks indicating two main average acid strength distributions. The mean acid strength of SAPO-37's is intermediate between the two which exist in faujasites (9). A detailed infrared study of the acid strength of protons followed by the limit temperature to evacuate the pyridinium ions shows (table 3) that higher temperatures are required (i.e. stronger acid present) for the SAPO-37 material than for HY or even than the dealuminated HYD compared to Si-0.13. This suggests the presence of very strong acid sites which infrared study showed to be in a very small amount (6).

The TPD peaks related to the medium acid strength which is the main source of acidity very likely reflects the protonic acidity associated to isolated Si-O-Al species. The very strong sites evidenced by infrared would be the Si-O-Al centers at the border of Si islands.

CATALYTIC ACTIVITY

The n-octane cracking carried at 725 K gives the results of table 4. After a pretreatment at 875 K for SAPO-37 and 675 K for HY (in order to avoid structure collapse) the % conversion and selectivities are reported in table 4. The very active HY had to be tested at a higher flow rate in order to decrease the % conversion to the SAPO's range. With a similar flow rate HY would be 15 to 20 times more active. The table 4 shows that similar products are formed with all the catalysts. Looking at the ratios olefin/paraffin, values of 1.9, 1.9 and 1.6 are obtained for Si-0.16, Si-0.20 and Si-0.22 while HY gives 1.2. This suggests lower hydrogen transfer reactions for SAPO's which might result from a higher distance between close sites than in Si-Al faujasites. For the branched to non branched hydrocarbons ratios, SAPO's give 0.6, 0.5 and 0.6 in the same order of materials as above and HY 0.65.

Increasing the pretreatment temperature up to 1225 shows that HY looses its activity near 1075 K and the SAPO's together with the ultrastable LZY-82 material near 1175 K. The table 5 compares the changes in per cent conversion for Si-0.22 and LZY-82. It shows that after pretreatment at 1175 K Si-0.22 is even more active than LZY-82. This stability for the catalytic properties at high temperatures may be related to the high thermal stability described above in tables 1 and 3.

In conclusion the main influence of phosphorus in SAPO's compared to Si-Al faujasites is an increased thermal stability which maintain catalytic properties after heating at high temperatures. It also give rise to a higher olefin to paraffin ratio suggesting a lower hydrogen transfer activity.

1864

REFERENCES

1   E.M. Flanigen, R.L. Patton, S.T. Wilson, Innovation in Zeolite Materials Science (P.J. Grobet et al., eds), Stud. Surf. Sci. Catal., 1988, 37, 13.

2   J.A. Martens, P.J. Grobet, P.A. Jacobs, J. Catal., 1990, 126, 299.

3   B.M. Lok, C.A. Messina, R.L. Patton, R.T. Gajek, T.R. Cannan, E.M. Flanigen, US Pat. 4 440 871 (1984).

4   G.C. Edwards, J.P. Gilson, V. Mc Daniel, US Pat. 4 681 864 (1987).

5   P.P. Man, M. Briend, M.J. Peltre, A. Lamy, P. Beaunier, D. Barthomeuf, Zeolites, 1991, in press.

6   S. Dzwigaj, M. Briend, A. Shikholeslami, M.J. Peltre, D. Barthomeuf, Zeolites, 1990, 10, 157.

7   L. Maistriau, N. Dumont, J.B. Nagy, Z.Gabelica, E.G. Derouane, Zeolites, 1990, 10, 243.

8   M. Briend, A. Shikholeslami, M.J. Peltre, D. Delafosse, D. Barthomeuf, J. Chem. Soc. Dalton Trans., 1989, 1361.

9   M. Briend, A. Lamy, S. Dzwigaj, D. Barthomeuf, Proceed. Int. Zeol. Symp., Prague, 1991.

Table 1. Characteristics of SAPO-37 materials

	Si 0.12	Si 0.13	Si 0.16	Si 0.20	Si 0.22
Si_x [a]	0.12	0.13	0.16	0.20	0.22
Al y	0.50	0.49	0.48	0.50	0.46
Pz	0.38	0.49	0.36	0.30	0.32
Occluded templates % [b]	22.3	20.7	21.9	19.7	18.5
a_0 (Å) [c]	24.76	24.76	24.74	24.70	24.71
Thermal stability (O_2) (K)	nd [d]	1270 ± 30	nd	nd	1320 ± 30
O_2 + H_2O (K)	nd	1275 ± 30	nd	nd	1240 ± 30

a : x, y, z molar fraction
b : weight %
c : as-synthetised samples
d : not determined

Table 2. Thermal stability

With template	stable	template decomposition	stable	
template free no water		stable		
template free + water	unstable	stable		
RT	~ 350 K	~ 850 K		1200-1300 K

Table 3. Acidity of SAPO-37 materials

	TPD NH_3	TPD Py	T desorption pyridinium
Si-O.13	500 [a]	665 [b]	723 [c]
Si-0.20	500	665	673
HY	455 520	545 735	623
HYD	455 520	545 735	673

a, b   peak (K) of the maxima in TPD of ammonia (a) or pyridine (b)

c   evacuation temperature (K) for the complete disappearance of the pyridinium ion (infrared spectroscopy)

Table 4. Selectivities (mole %) in the cracking of n-octane at 725 K

Products	Si-0.16[a]	Si-0.20	Si-0.22	HY [a]
methane [b]	4.4	3.9	3.8	3
ethylene [b]	2.8	2.2	2.1	1.7
ethane	7.9	5.9	6.7	4.7
propene + propane	24.8	23.0	24.9	25.4
iso-butane	3.1	5.2	5.2	7.1
n-butane	9.2	12.4	9.7	9.8
iso-butene	9.6	6.8	9.7	10.5
n-butene	3.9	5.0	4.4	4.1
cis-butene	4.8	5.7	5.0	4.9
trans-butene	6.7	7.9	6.8	6.8
iso-pentane	2.5	4.1	4.1	4.8
n-pentane	5.7	4.7	5.4	5.5
1-pentene	0.8	1.0	0.7	0.6
3-methyl-butene	0.3	0.4	0.4	0.5
trans-2-pentene	1.8	2.2	1.9	1.9
cis-2-pentene	5.4	3.6	3.2	3.5
2-methyl-2-butene	6.1	6.0	6.0	5.2
conversion %	1.3	1.3	1.6	2.7

(a) Flow rate 13 ml/min for SAPO's and 56.2 ml/mn for HY
(b) Thermal cracking

Table 5. % conversion in n-octane cracking at 725 K

	1075	1175	1225
Si-0.22	1.7	2.4	~ 0
LZY-82	> 6	1.5	~ 0

Carbon Materials - Activity and Selectivity in Hydrocracking Reactions.

M. Farcasiu, C.M. Smith, E.P. Ladner
U.S. Department of Energy
Pittsburgh Energy Technology Center
P.O. Box 10940, Pittsburgh, PA 15236

A.P.Sylwester
Sandia National Laboratory, Albuquerque, NM 87185

Keywords: carbon materials, hydrocracking catalysts, selectivity.

INTRODUCTION

The use of carbon materials in catalytic systems has been traditionally associated with their properties as supports (1). There are, however, some literature data describing their use as catalysts. It was reported that, after activation with ammonia, some carbon blacks are good oxidation catalysts (2) and that some activated carbons are active in the cracking of hydrocarbons (3). Our data (4,5), as well as recent data by Grunewald and Drago (6), show that some carbon materials could act as catalysts for specific reactions. Thus, a high surface area carbon molecular sieve was active for oxidative dehydrogenation reactions at temperatures of about 230°C (6). We have used carbon materials with variable surface area as catalysts for C-C cleavage in a reductive medium and at temperatures above 320°C (4,5).

In this paper, we describe a systematic study of the catalytic activity of carbon blacks of different surface area and origin and also the catalytic activity of carbon materials obtained by the pyrolysis of polymers such as resorcinol - formaldehyde and polyacrylonitrile.

EXPERIMENTAL

Materials and Analytical Procedures. 9,10-Dihydrophenanthrene (9,10-DHP) was obtained from Aldrich Chemical Co. Black Pearls 2000, Monarch, Mogul and Regal carbon blacks were provided by Cabot Corporation; graphite powder -325 mesh was supplied by ALFA. The carbon materials from the carbonization of polyacrylonitrile and resorcinol-formaldehyde polymers were prepared at Sandia National Laboratory and their methods of preparation have been described previously (7-11). The results of the analyses performed on different carbon materials used in this work are given in Tables 1, 2, and 3.

The elemental analyses were performed by Huffman Laboratories, Golden, CO, and at the Pittsburgh Energy Technology Center. The surface area of various carbon materials was measured in Prof. D. Smith's laboratories at the University of New Mexico in Albuquerque and at Sandia for the carbon materials from the polymer pyrolyses.

4(1-Naphthylmethyl)bibenzyl, I, was prepared in Prof. Paul Dowd's laboratory at the University of Pittsburgh and completely characterized, as previously reported (5). Dichloromethane was stored over 4A molecular sieves.
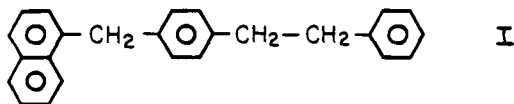
Glass reaction tubes were made of Pyrex tubing, 5 x 7 mm(i.d. x o.d.). Sealed sample tubes were approximately 75 mm long.

Gas chromatographic analyses were carried out on a Hewlett Packard Model 5890 gas chromatograph equipped with an SE-30 60m capillary column. Gas chromatography/Mass spectra (GC/MS) were obtained on a Hewlett Packard GC/MS Model 5985 instrument equipped with a 30 m SE-52 capillary column.

Identification of reaction products was accomplished by GC/MS analysis and, when possible, by GC comparison with authentic samples. Reported product yields and overall conversion of I are based on capillary GC.

General Experimental Procedure. The reaction components (9,10 DHP, ca. 100 mg, I,ca. 25 mg, and catalysts) were weighed into open- ended glass reaction tubes. The tubes were flame-sealed, and no precaution was taken to exclude air. Warm water was used to melt the hydrogen donor and ensure the mixing of the reactants. The samples were placed upright in a temperature-equilibrated Lindberg muffle furnace and heated at the indicated temperatures for given times. The samples were removed from the oven, cooled to room temperature, and diluted with ca. 0.5 mL of dichloromethane. The samples were filtered through a plug of MgSO₄ and glass wool. An additional 0.5 mL of dichloromethane was used to wash the filter and, in the catalytic reaction, the carbon black catalyst. An aliquot of the resulting solution was analyzed by gas chromatography. The recovery was checked for selected experiments with an internal standard.

Catalytic Activity. As a measure of the catalytic activity, we determined: the overall conversion (thermal + catalytic), the catalytic conversion, and the selectivity of the catalytic conversion toward cleavage of the C-C bond between the naphthalenic ring and the adjacent aliphatic carbon. The selectivity of the above-described cleavage is calculated as the percent of the catalytic conversion only.

Deactivation, Recovery and Reuse of Black Pearls 2000. Black Pearls 2000 was recovered from several different reactions, washed, and dried for reuse. In a typical procedure, the catalyst was recovered from a reaction using compound I and 9,10 DHP, which had been run at 420ºC for 1 h. The samples were prepared as described above in the general procedure. At the end of the reaction time, the tubes were cooled to room temperature. The reaction mixture was filtered through a filter paper and the retained catalyst was washed with dichloromethane and cyclohexane. The catalyst was washed

1870

exhaustively until the GC analysis indicated only the presence of the solvent. The Black Pearls was dried in vacuo at 105°C for 4 h. Surface area determination and elemental analyses of the used catalyst are presented in Table 1.

RESULTS AND DISCUSSION

Soon after observing the catalytic activity of carbon blacks for the cleavage of C-C bonds, we found that not all carbon materials act as a catalyst. Therefore, we initiated a study to determine what features make some carbon materials active. Obvious candidates were chemical composition, surface area, and the structure of the carbon skeleton. As a first step of this study, we looked at several carbon materials of different origin and properties and tested their catalytic activity for reactions of compound I in presence of 9,10 dihydrophenanthrene as H-donor.

Cabot Carbon Blacks as Catalysts   We used four carbon blacks (Table 1) obtained from Cabot Corp. and found that all four were active as catalysts for selective cleavage of C-C bonds. Their catalytic activity was proportional to their surface area. When the Cabot carbon blacks were present in quantities that provided equivalent surface area their catalytic activity and selectivity were very similar (Table 4). We found, however, that another commercial carbon black Norit (1300 m2/g) exibits only about 77% of the activity of BP2000 for equivalent surface area.

For comparison, Alpha graphite does not exibit any catalytic activity under our reaction conditions.

Carbon Materials from Carbonization of Organic Polymers   A variety of carbon materials can be obtained by carbonization of organic polymers under controlled conditions (7-11). We investigated the carbonization products of polyacrylonitrile and of resorcinol-formaldehyde foams prepared at Sandia NL.

    a.   Carbonized Polyacrylonitrile Polymers (PAN) as Catalysts   Polymers pyrolyzed at various temperatures (Table 2) were tested for their hydrocracking activity (Table 5). They have substantially lower surface area and catalytic activiy than the Cabot Carbon Blacks, but exibit the same selectivity. After 1h at 422°C, the catalytic conversion of 1g of I is 1.65 %/ m2 catalyst for carbon black BP2000 but only 1.1 %/ m2 catalyst for PAN 410. Also, while the surface area of PAN 410 (pyrolyzed at 1200°C) is almost twice as large as that of PAN 1448 (pyrolyzed at 2000°C), the catalytic conversion of I is ~ four times larger with PAN 410 than with PAN 1448. Obviously, surface area is one, but not the only, factor in the activity of carbon materials.

    b.   Carbonized Resorcinol-Formaldehyde Foams (CRF) as Catalysts   A systematic study of carbon materials as catalysts was possible because carbon materials could be obtained by controlled pyrolysis of resorcinol-formaldehyde foams (9). For each pyrolysis temperature, several surface areas of carbon material could be obtained (10). The samples used in this paper are described in Table 3 and their catalytic activity is presented in Table 6. It can be seen that for materials pyrolyzed at the same temperature the activity is

1871

proportional to the surface area, while for materials with the same surface area, the activity depends on the pyrolysis temperature (Fig.1). The CRF materials are the most active catalysts among the materials we have investigated so far. The catalytic conversion at 400ºC in 1h for 1g of I is 0.54%/m2 of CRF (pyrolyzed at 1050ºC) and only 0.34 % /m2 of BP2000.

Activity of the Reused Carbon Materials We have conducted some preliminary experiments in which carbon black BP2000 was recovered after reaction and re-used (see experimental part, Tables 1 and 7). These experiments showed that the reactivated BP2000 has an elemental composition different from the initial material and its surface area is reduced by ⁻30%. The catalytic activity of the recovered material is also reduced by 30%, but the selectivity remains the same.

Charge Distribution Analysis of Carbon Materials   Charge Distribution Analysis (CDA) is a new method, invented by F.Freund (12), which makes possible the determination of the charge on the surface of solids as a function of temperature. Several of the carbon materials used as catalysts in this work have been studied by F.Freund by CDA. In all cases, the carbon materials that are acting as catalysts started to develop positive charges on their surface when heated in an inert gas at temperatures around 300ºC. We have shown that carbon black BP2000 becomes catalytically active for the C-C cleavage reaction at ⁻ 320ºC, and we have discussed possible mechanistic implications (4,5). Further work is being carried out to determine whether the selectivity of carbon materials for the cleavage of C-C bond adjacent to a condensed polyaromatic structures is related to this positive charge on the surface of the catalyst.

CONCLUSIONS

Our results show that no simple relationship exists between the catalytic activity of some carbon materials for selective cleavage of carbon-carbon bonds adjacent to condensed polyaromatic rings and the elemental composition or surface area of these materials. The activity is dependent, however, upon the precursor used to generate the carbon material. Moreover, for a given precursor the activity is determined by the method of conversion to the carbon material. It remains to be established what elements of structure are responsible for the observed activity in carbon materials that are catalytically active.

ACKNOWLEDGEMENTS

DISCLAIMER
Reference in the paper to any specific commercial project, process, or service is to facilitate understanding and does not necessarily imply its endorsement or favoring by the United States Department of Energy.

REFERENCES

1. Kaminscky,M; Yoon, K.J.; Geoffroy,G.L.; Vannice, M.A. J.Catal.1985,91, 388. Venter, J.J.; Vannice, M.A. J.Amer. Chem. Soc. 1989, 111, 2377 and references therein.
2. Boehm,H.P., "Structure and Reactivity of Surfaces," C.Morterra, A.Zecchina and G.Costas Editors, Elseviers Science ublishers B.V., Amsterdam, 1989.
3. Greensfelder, B.S.; Voge, H.H.; Good, G.M. Ind.and Eng. Chem. 1949, 41, 2573.
4. Farcasiu, M.; Smith, C. Prepr. Pap. Am.Chem.Soc.Div.Fuel Chem. 1990, 35,404
5. Farcasiu, M.; Smith, C. Energy & Fuels 1991, 5, 83.
6. Grunewald, G.C.; Orago, R.S. J.Amer.Chem.Soc. 1991, 113, 1636.
7. Sylwester, A.P.; Aubert, J.H.; Rand, P.B.; Arnold, C.J.; Clough R.L. ACS PMSE Preprints 1987, 57, 113.
8. U.S.Pat. 4,832,881 (1989).
9. Pekala, R.W. J.Mat. Sci. 24, 1989, 3221.
10. Pekala, R.W.; Kong, F. ACS Polym. Preprints, 1989, 30, 221.
11. Aubert, J.H.; Sylwester A.P. J.Mat.Sci. 1991 (In Press).
12. Freund, M.M.,; Freund, F.; Batlo, F. Phys Rev.Lett. 1989, 63, 2096.
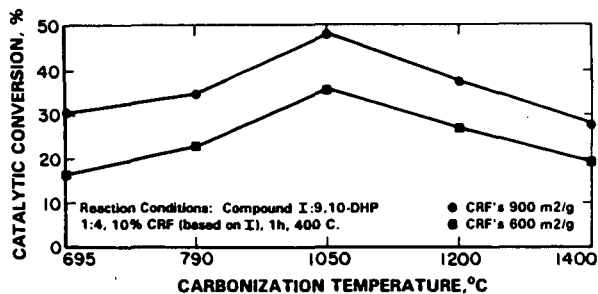
Fig.1   Influence of the Carbonization Temperature on the Catalytic Activity of CRF Carbon Materials.
Reaction conditions : I:9,100HP 1:4 (wt), 10 % CRF (based on I), 1h, 400ºC.

Table 1   Properties of Carbon Blacks form Cabot Co.

Material	Surface Area m2/g	Dry loss %	Elemental C	H	Analysis S	Dry O	Basis % Ash
Regal 400 R	86	2.3	95.9	0.5	0.9*	1.5	0.9
Mogul L	138	3.2	94.9	0.5	1.0	3.0	0.5
Monarch 1300	560	7.9	88.9	0.5	1.1	7.5	2.8
Black Pearls 2000	1475	10.9	96.1	1.4	1.4	1.4	1.2
Black Pearls 2000, recovered*	1026	0.0	96.5	1.7	0.3	0.6	0.8

* the recovery of the used BP2000 is described in the experimental section.

Table 2   Properties of Carbonized Polyacrylonitrile Polymers.

PAN #	Temperature of Carbonization C	Surface Area m2/g	Elemental C	H	Analysis wt. N	% O*
455	700	16	73.5	0.5	15.6	10.4**
662	800	17	75.4	0.2	13.4	10.0
1260	1100	22	94.3	<0.05	3.2	2.5**
410	1200	85	96.9	<0.05	1.8	0.6
1448	2000	48	>99.9	–	–	–

 * O by Neutron Activation Analysis
** O by difference

Table 3 Properties of Carbonized Resorcinol-Formaldehyde Polymers.

CRF #	Temperature of Carbonization °C	Surface Area m2/g	Elemental Analysis, wt.%			
			C	H	N	O*
654	695	900	93.69	1.45	<0.01	~4.9
626	695	700	--	--	--	-
654	790	900	·94.62	0.85	0.02	~4.1
626	790	700	--	--	--	-
1029	1050	900	94.22	0.59	0.20	~5.0
613	1050	600	92.33	0.63	0.18	~6.9
654	1200	900	97.57	0.19	0.21	~2.0
626	1200	600	--	--	--	-
571	1400	900	98.88	0.30	0.06	~0.8
624	1400	600	--	--	--	-

*   Oxygen by difference

Table 4   Experiments with Various Cabot Carbon Blacks at Equivalent Surface Area of Catalyst per gram of Compound I.
In all cases 1:4 ratio (wt) Compound I : 9,10 DHP, 1h.

Carbon Black	Cat. conc. m2 cat/g I	Temp. C	overall conv.%	catalytic conv. %	selectivity %
None	-	407	5	-	(43)*
Regal	15.6	407	15.3	10.3	100
Mogul	15.6	407	15.4	10.4	97
Monarch	15.6	407	13.5	8.5	100
BP2000	15.6	407	13.6	8.6	100
None	-	428	26	-	(40)*
Regal	14	428	42	16	100
Mogul	14	428	45	19	100
Monarch	14	428	35	9	100
BP2000	14	428	46	20	100

*   The selectivity of the thermal reaction is expressed as a percent of the C-C bond cleavage of the bond adjacent to the naphthalene ring vs overall conversion.

Table 5. Catalytic Properties of Carbonized PAN Polymers.
Reaction conditions: Compound I:9,10 DHP = 1:3 (by wt), 1h, 420°C.
Different PAN carbons were added to an equivalent surface area (4.25 m2 catalyst/g of I).

Carbonization temp. of PAN C	Surface Area m2/g	Overall conv. I %	Catalytic conv. I %	Catalytic Selectivity %
700	16	15.1	0	-
800	17	14.5	0	-
1100	21	20.1	3.8	> 93
1200	85	21.0	4.7	100
2000	48	17.5	1.2	> 90
Thermal		16.2		43*

* The selectivity of the thermal reaction is expressed as a percent of the C-C bond cleavage of the bond adjacent to the naphthalene ring vs. overall conversion.

Table 6. Catalytic Properties of Carbonized Resorcinol Formaldehyde Polymers.
Reaction conditions :
I : 9,10 DHP (wt) 1:4, 10 % wt CRF material(based on I), 400°C, 1h.

Carbonization temp. of CRF C	Surface Area m2/g	Overall conv. I %	Catalytic conv. I %	Catalytic Selectivity %
695	900	33.4	30.4	>99
790	900	37.8	34.8	100
1050	900	51.2	48.2	98
1200	900	40.6	37.8	100
1400	900	31.0	28.0	97
695	700	19.6*	16.4	>99
790	700	25.8*	22.8	100
1050	600	38.8	35.8	99
1200	600	30.0	27.0	100
1400	600	22.1	19.1	96
Thermal		3.0		43**

* the experimental values for the overall conversion for these catalysts have been reduced by the factor of 600/700 for comparison with the catalysts that have surface areas of 600 m2/g (samples carbonized at 1050, 1200 and 1400°C).

** the selectivity of the thermal reaction is expressed as a percent of the C-C bond cleavage of the bond adjacent to the naphthalene ring vs. overall conversion.

Table 7. Activity of Fresh and Recovered* BP2000

Reaction of I in presence of 9,10 DHP, 1h, 407°C 10% BP2000 (based on I)

Catalyst	Surface area m2/g	Overall conv. %	Catalytic conv. %	Selectivity %
None	-	5	-	44**
Fresh	1475	63	58	98
Recovered*	1026	45	40	98

* for the recovery conditions see Experimental Section.

** The selectivity of the thermal reaction is expressed as a percent of the C-C bond cleavage of the bond adjacent to the naphthalene ring vs overall conversion.

INDUSTRIAL CATALYSTS FOR AROMATICS REDUCTION IN GAS OIL

Arpad F. Somogyvari, Michael C. Oballa and Patricio S. Herrera
NOVA Husky Research Corporation
2928 16 - Street N.E., Calgary, Alberta, Canada T2E 7K7

ABSTRACT

Six commercially available Ni-Mo/Al$_2$O$_3$ catalysts were tested for HDN, aromatics reduction and HDS on a hydrocracked gas oil (249 - 524°C) in a fixed bed reactor operating in the upflow mode. Acceptable HDN, HDS, and aromatics reduction were obtained for three of the six catalysts. Total aromatics concentrations were determined using four different methods, two of which were also used to determine PNA concentrations. Each method gave a different aromatics concentration, however, linear correlations were established between the results obtained by each method. Contrary to expectations, superior HDN and HDS performance and comparable PNA reductions were observed in a heavier fraction (343+°C) than in the total liquid product.

INTRODUCTION

The expected depletion of the lightest conventional feedstocks has placed a greater emphasis on upgrading technologies. These technologies generally involve hydrocracking the "bottom of the barrel" and hydrotreating the resulting distillates to reduce the amounts of sulphur and nitrogen[1-3]. The substitution of conventional petroleum with synthetic crudes is on the rise. This trend is expected to shift the hydrocarbon distribution toward the aromatic at the expense of the saturates in the blended feedstocks[4]. Studies have shown that, due to their high content of aromatic components, combustion of synthetic fuels generates higher particulate concentrations than combustion of conventional fuels in both diesel engines and heating applionces. Because of the varied health hazards associated with particulate emissions[5,6], refiners are confronted with stricter regulations aimed at controlling particulate emissions and unburned hydrocarbons in diesel exhaust through reduced aromatics levels.

Thus, aromatics reduction has become a key upgrading parameter in light of stringent environmental regulations and industry trends toward low-quality component blends derived from conventional crudes and synthetic crude distillates. The optimization of product quality and product performance becomes critical both from an environmental and a marketing perspective. While regulations have focussed on aromatics determined by fluorescent indicator adsorption (FIA) in diesel fuels, the guidelines for aromatics determination in the gas oil fraction are much more ambiguous. Consequently, it is essential to have a reliable method for aromatics determination in these heavy cuts.

The work reported herein is part of a much larger study aimed at evaluating the performance of commercial catalysts during the hydrotreating of gas oil. One of the performance indicators in that study was the reduction in the amount of aromatic components. Many conventional hydrotreating catalysts (e.g., sulphided Ni-Mo/Al$_2$O$_3$), normally designed for hydrodesulphurisation, show excellent hydrodenitrogenation activity and perform aromatics reduction as well.

This paper provides technical information related to product properties upon hydrotreating a hydrocracked gas oil. The data will focus on aromatics determination and aromatics reduction for six commercially available hydrotreating catalysts.

EXPERIMENTAL

The hydrotreating experiments were performed in a stainless steel tubular fixed-bed reactor operating in the upflow mode. The key process parameters were T = 375°C, P = 1750 psig and LHSV = 0.5 h^{-1}. The feedstock was the fraction boiling between 249°C and 524°C obtained from hydrocracking a 50/50 volumetric blend of Cold Lake/ Lloydminster resid.

Specific gravities were determined at 15.5°C on a Paar DMA 48 instrument while dynamic viscosities were determined at 25°C on a Brookfield DV II instrument. Sulphur was determined on a Leco SC-132 sulphur analyzer while carbon and hydrogen as well as trace nitrogen were determined commercially. Both simulated distillations (ASTM D-2887) and vacuum distillations (ASTM D-1160) were performed in-house.

Carbon-13 NMR analyses were obtained on a Bruker ACE-200 instrument. Solutions were prepared by diluting 2.0 cm^3 of the sample with 2.0 cm^3 of a 0.10 mole dm^{-3} solution of tris(2,4-pentanedionato)chromium(III) in CDCl$_3$. The instrument was operated in the inverse gated decoupled mode for NOE suppression using a 6.5 us pulse (90°C) and a repetition time of 10 s. In a typical experiment 5000 transients were collected as 8K data points which were zero filled to 16K. A Lorentzian line broadening of 5 Hz was applied to the free induction decay prior to processing. Integration for paraffins, naphthenes and aromatics was as described by Young and Galya[7].

Low resolution mass spectrometric analyses for aromatic types were obtained commercially. The method of Robinson and Cook[8], which has been adopted as ASTM D-3239, was used with minor modifications. As well, the weight per cent of total aromatics was determined by a column chromatographic technique as described by Watson[9]. The method of Fitzgerald et al[10], for the determination of aromatic components by UV/Vis spectroscopy, was adapted in-house to account for expected differences in the sample composition.

RESULTS AND DISCUSSIONS

The project from which these data were derived concerned the selection of hydrotreating catalysts for the Bi-Provincial Upgrader facility[11] currently under construction. The design specifications for hydrotreated product quality included, among others, nitrogen at 500

wppm, sulphur at 400 wppm and total aromatics by Watson's method[9] at 45 wt.%. The properties of the feedstock and of the products obtained from hydrotreating this material using six different catalysts have been recorded in Table 1. The data indicate that all of the products exceed the design specifications for nitrogen and total aromatics content and that three of the six products meet the sulphur specifications as well.

The aromatics content of the feedstock and the six hydrotreated products have been measured using four different methods (Table 2). Both ^{13}C NMR[7] and the Watson method[9] measure total aromatics only. With ^{13}C NMR the paraffinic and naphthenic carbon content as well as the aromatic carbon content of the sample may be determined while with the Watson method, any moiety which has not been eluted from a silica containing chromatographic column with an oliphatic hydrocarbon is considered aromatic. Consequently, in this latter technique any compound which contains an aromatic unit would be considered as aromatic. The UV/Vis method[10] may be used to determine both total oromatics and polynuclear aromatics (PNA). The technique requires an *a priori* assumption or knowledge of the types of aromatic components in the sample so that the absorption maximo and absorptivities of corresponding model compound types may be used to calculate the concentrations of related components in the sample of interest. The method seems to be highly dependent on the materials chosen to represent the PNA components, the sensitivity has been found to be low, and the method was found to overestimate both PNA content and total aromatics content. However, the UV/Vis method may be useful for determining trends. The last method used for aromatics determination was a modification of Robinson and Cook's mass spectrometric technique[8]. Saturates are separated from aromatics by column chromatography and each fraction is introduced into the mass spectrometer for classification by Z number. Because "aromatics" is loosely and operationally defined, each of the techniques determines a different quantity and consequently results in method dependent values for aromatics content.

Among the various methods, the best agreement for total aromatics content appears to be between the UV/Vis and MS methods. Bearing in mind the limitations of the UV/Vis method, this correspondence may be more fruitious than real and probably reflects the large number of tetra- and penta-aromatic standards used in the technique and that the mono-aromatics account for the major portion of the total aromatics content of the samples. Also, it may be seen that while the absolute values for total aromatics vary considerably according to method, a relationship exists between the different methods. This relationship has been further explored by plotting the total aromatics content obtained via NMR, chromatographic and UV/Vis analyses in the hydrotreated total liquid product against that obtained from mass spectrometry (Figure I). Linear regression analysis has resulted in correlation coefficients of 0.971, 0.988 and 0.997 respectively for the following equations:

$$NMR = 0.31 \cdot MS + 3.95 \quad\quad\quad (1)$$
$$Watson = 0.84 \cdot MS + 10.0 \quad\quad\quad (2)$$
$$UV/Vis = 1.06 \cdot MS - 1.44 \quad\quad\quad (3)$$

Again, the fortuitous relationship between aromatics determined by the UV/Vis method and the MS method noted above has resulted in excellent correlations between the methods. However, it is noted that the correlation coefficient drops to 0.75 if the aromatics content of the feedstock is included in the regression analyses. It is possible that the deviation of the data point for the feedstock from the regression line encompassing the hydrotreated products may be due to the sensitivity of the method to the choice of reference standards. The inclusion of the data point for the feedstock in the remaining two methods alters the correlation coefficients only slightly but results in appreciable changes in the slope of the regression line.

One interpretation of equations 1-3 above could be that on average, only 31% of the carbon atoms are in aromatic rings, the remainder being in alkyl side chains and naphthenic substituents. Consistent with this, 16% of the aromatic components in the sample could be considered saturate on the basis of polarity because of long chain alkyl substituents on the aromatic moiety.

Only the UV/Vis method can be compared to the MS method for aromatics content by ring number. Meaningful results have been obtained for only mono-aromatics, di-aromatics and total PNA (Figure II). The insensitivity of the UV/Vis method to higher ring number components precluded further correlations. The data indicate that while the correlation coefficients were acceptable, the UV/Vis technique overestimates mono-aromatics while severely underestimating higher ring number aromatics.

Lee et al[12,13] have found similar correlations between aromatics determined by mass spectrometry and NMR, FIA (ASTM D-1319) and SFC for diesel fuels and middle distillates. Since the NMR analyses methodology adopted by these authors differed from our approach, no basis for data comparison existed. However, the fact that such correlations exist for diesel and middle distillate cuts[12,13] and for the gas oil fraction suggests that these correlations may be part of a more general phenomenon.

The heteroatom distribution as well as the PNA (UV/Vis meethod) and total aromatics (Watson method) content of the 343+°C fractions of the feedstock and hydrotreated products were determined (Table 3). The data indicate that both the heteroatom content and the aromatics content have increased in the feedstock while, for the most part, these values have decreased for the hydrotreated product relative to those in total liquid product. Suprisingly, this has resulted in higher conversions in the heavier gas oil fractions (Table 4) and consequently indicates the superior catalytic activity of these catalysts for the heavier components.

CONCLUSIONS

Although the Ni-Mo/Al$_2$O$_3$ catalysts used in this work will not perform deep aromatics hydrogenation, they will remove 30 - 60% of the total aromatics in the hydrocracked gas oil while at the same time exhibiting a 90 - 99% conversion of sulphur and nitrogen. The catalysts investigated show superior performance with the heavier gas oil fractions. The

amount of aromatics determined, and consequently the aromatics conversions, are method dependant. This must be considered in potential environmental legislation as well as in fuel oil and catalyst marketing and underscores the requirements for standardization. The trends determined for the very narrow range of compounds reported here may be part of a broader, more general phenomenon.

REFERENCES

1. S. Mohanty, D.F. Saraf and D. Kunzru, Erdol und Kohle, *Erdgas Petrochemie* 1990, **43**, 359.
2. J.F. Le page, G. Martino and C. Thonon, *J. Pet. Res.* 1989, **8**, 147.
3. R.A. Corbett, Oil Gas J. 1989, **87**, 49.
4. M.F. Wilson, I.P. Fisher and J.F. Kriz, *Ind. Eng. Chem. Prod. Res. Dev.* 1986, **25**, 505.
5. S.T. Bagley, L.D. Gratz, D.G. Leddy and J.H. Johnson, Prepr. Am. Chem. Soc. Div. Fuel Chem. 1991, **36**, 311.
6. J. Lewtas, Prepr. Am. Chem. Soc. Div. Fuel Chem. 1991, **36**, 319.
7. D.C. Young and L.G. Galya, *Liq. Fuels Technol.* 1984, **2**, 307.
8. C.J. Robinson and G.L. Cook, *Anal. Chem.* 1969, **41**, 1548.
9. A.T. Watson, *Anal. Chem.* 1952, **24**, 507.
10. M.E. Fitzgerald, J.L. Moirano, H. Morgan and V.A. Cirillo, *Appl. Spectros.* 1970, **24**, 106.
11. S. Chase., *The Husky Bi-Provincial Design Basis*, Paper presented at the Sixth Annual Heavy Oil and Oil Sands Technical Symposium, Calgary, March 8, 1989.
12. S.W. Lee, B.J. Fuhr, L.R. Holloway and C. Reichert, *Energy and Fuels* 1989, **3**, 80.
13. S.W. Lee, S. Coulombe and B. Glavincevski, *Energy and Fuels* 1990, **4**, 20.

TABLE 1

FEEDSTOCK AND HYDROTREATED PRODUCT PROPERTIES

	FEED-STOCK	PROD. A	PROD. B	PROD. C	PROD. D	PROD. E	PROD. F
Density (kg/dm^3)	923.3	872.8	890.2	890.2	886.3	889.2	880.4
Viscosity (cP)	38	13	22	21	19	22	16
Carbon (wt%)	87.09	86.60	87.04	87.02	86.91	86.78	86.50
Hydrogen (wt%)	11.61	12.74	12.15	12.26	12.47	12.38	12.65
Sulphur (wppm)	14123	795	984	517	393	391	247
Nitrogen (wppm)	1799	102	276	204	62	129	30
Sim. Dist. (wt%)							
IPB - 177	-	4.1	1.5	1.4	1.8	1.5	2.7
177 - 249	1.6	7.4	4.3	3.8	4.7	4.2	5.9
249 - 343	31.4	39.2	35.7	36.3	36.5	35.8	37.4
343 - 524	65.4	49.3	58.5	58.5	57.0	58.5	54.0
524+	1.6	-	-	-	-	-	-

Note: A, B, C, D, E, F are commercially available catalysts.

TABLE 2

TOTAL AROMATICS (WT.%) BY METHOD

METHOD	FEED-STOCK	PROD. A	PROD. B	PROD. C	PROD. D	PROD. E	PROD. F
^{13}C NMR	27.0	9.8	13.9	13.9	12.2	13.6	11.1
Watson	55.1	25.7	35.2	37.3	33.8	36.3	29.3
UV/Vis	32.4	18.1	30.7	33.8	28.0	30.6	24.0
Mass Spec.	50.45	18.94	29.92	33.72	27.45	30.55	23.73

1883

TABLE 3

HETEROATOM AND AROMATICS DISTRUBITION IN THE 343+°C FRACTIONS

	FEED-STOCK	PROD. A	PROD. B	PROD. C	PROD. D	PROD. E	PROD. F
Density (kg/dm^3)	940.6	888.7	905.4	904.2	900.7	903.4	895.4
Nitrogen (wppm)	2050	37	230	145	60	161	15
Sulphur (wppm)	16400	265	718	488	265	240	60
Aromatics, UV/Vis (wt%)							
Monoaromatics	23.3	16.7	25.1	29.9	25.7	27.0	21.5
Polynuclear Arom.	12.9	4.1	4.7	4.4	4.4	4.5	4.2
Total Aromatics	36.2	20.7	29.8	34.3	30.1	31.5	25.7
Aromatics, Watson (wt%)	57.9	22.1	35.9	38.4	33.8	37.1	28.0

TABLE 4

HETEROATOM AND AROMATICS CONVERSION (%)
IN THE TOTAL LIQUID PRODUCT AND THE 343+°C FRACTION

TEST	CAT. A	CAT. B	CAT. C	CAT. D	CAT. E	CAT. F
Total Liquid Product						
Sulphur	94.4	84.7	88.7	96.5	92.8	98.3
Nitrogen	94.4	93.0	96.3	97.2	97.2	98.2
Aromatics, Watson (wt%)	53.3	36.1	32.3	38.7	34.1	46.8
343+ Fractions						
Nitrogen	98.2	88.8	92.9	97.1	92.1	99.3
Sulphur	98.4	95.6	97.0	98.4	98.5	99.6
Aromatics, Watson (wt%)	61.8	38.1	33.7	41.7	36.0	51.7

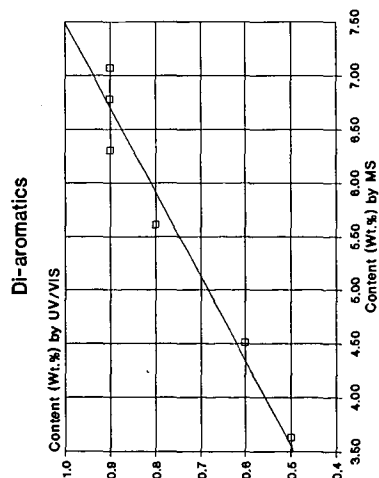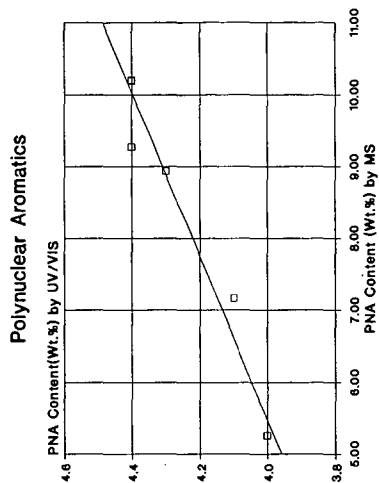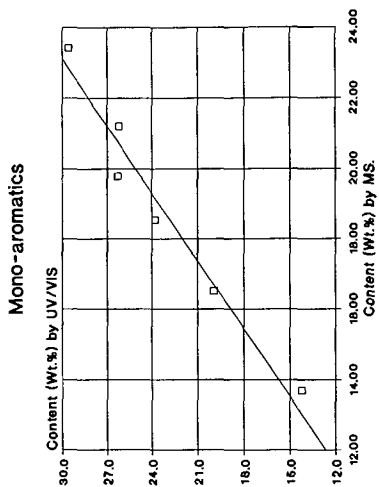Figure I. Effect of Analysis Method
on Aromatics Content in Gas Oil
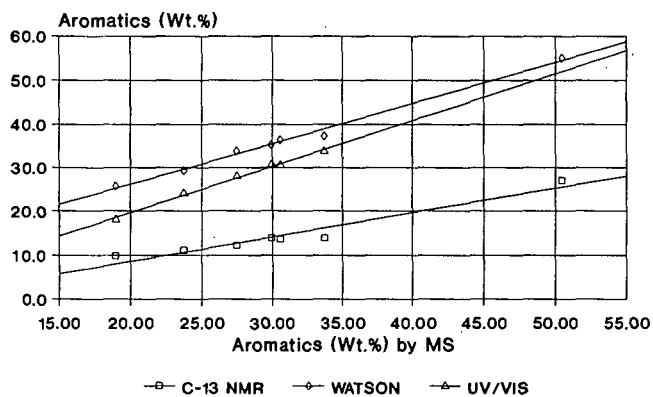
Figure II. Correlation Between UV/Vis and Mass Spectrometric Methods for Aromatics Content by Ring Number

COAL/OIL COPROCESSING USING SYNGAS

Yuan C. Fu, Makoto Akiyoshi. Fumiaki Tanaka and Kenichi Fujiya

Department of Applied Chemistry.
Muroran Institute of Technology.
Muroran, Japan 050

Keywords: Coprocessing. Model Compounds. Syngas

ABSTRACT

Coal and model compounds were hydrogenated and desulfurized in the presence of petroleum solvents and catalyst under coprocessing conditions by using syngas with steam in place of hydrogen. Nickel molybdate and cobalt molybdate catalysts impregnated with potassium carbonate exhibited good activities for hydrogenation and desulfurization of coal and model compounds(anthracene and benzothiophene) at 400-425℃ with the use of syngas. Some water gas shift conversion also took place simultaneously. The extent of hydrogenation and desulfurization obtained are comparable to those obtained in coprocessing using pure hydrogen. Iron catalysts such as synthetic pyrite exhibited good activities for coal conversion in coprocessing using hydrogen, but only moderate activities in coprocessing using syngas. Results from coprocessing of model compounds indicate that these iron catalysts have relatively low activities in the desulfurization of benzothiophene.

INTRODUCTION

In coprocessing of coal and petroleum residues to produce liquid fuels, the process economics could be improved significantly by using syngas(H_2+CO) and steam instead of hydrogen as feed gas to the reactor. The use of syngas, even only at the first stage of the current two-stage process being developed, could substantially reduce the hydrogen consumption and improve the overall thermal efficiency. It has been demonstrated that lignite[1] and bituminous coal[2] are liquefied and coal liquid[3] is hydrogenated by the use of carbon monoxide or carbon monoxide-containing gas.

In this study, coal model compounds(anthracene and benzothiophene) are coprocessed with petroleum solvents in the presence of catalyst, and the results of hydrogenation and desulfurization during coprocessing using syngas and hydrogen were compared. The catalysts used include NiMo, CoMo, and disposable Fe and $ZnCl_2$ catalysts. In general the catalyst activities are somewhat lower with the use of syngas than with hydrogen. It is shown, however, that NiMo and CoMo catalysts exhibit good activities with syngas and the performances are comparable to those obtained with hydrogen. Some coprocessing experiments using coal and petroleum solvents with syngas yielded moderately good coal conversions, but reaction conditions relating to H_2/CO ratio, steam/syngas ratio, solvent composition, catalyst, and process severity should be optimized to achieve better results.

EXPERIMENTAL

The coprocessing reactions of model compounds were conducted in a shaking 20-ml microreactor with syngas(H_2:CO=1:1) or H_2 at initial pressures of 70 Kg/cm² and temperatures of 350-400℃ for 45 minutes. Anthracene and benzothiophene were used as the model compounds, and mixtures of n-paraffin and cycloalkane and that added with tetralin were used as petroleum solvents. The ratio of solvent to coal model compounds was 5:1. With syngas, 10 weight % of H_2O based on the total amounts of the model compounds and solvent was added. The amount of ground catalyst powder added was also 10 weight %.

The conventional NiMo/Al$_2$O$_3$ and CoMo/Al$_2$O$_3$ catalysts and disposable synthetic pyrite(Mitsui Coal Liquefaction Co.) were used for coprocessing experiments using H$_2$. For experiments using syngas, the NiMo/Al$_2$O$_3$ and CoMo/Al$_2$O$_3$ catalysts and synthetic pyrite were impregnated with aqueous potassium carbonate solution(10 wt%). Additional catalysts tested for comparison purpose included a solid superacid catalyst of sulfate-promoted iron oxide[4,5] and a zinc chloride catalyst[6](30 wt%) supported on silica-alumina. The Fe$_2$O$_3$/SO$_4^{2-}$ (2 wt%) was prepared starting from iron(III) nitrate precipitated with an aqueous ammonia. The powdered precipitate was treated with ammonium sulfate, and then dried and calcined at 500°C.

Some coprocessing experiments using coal and petroleum solvents with syngas were also conducted. Illinois No.6 bituminous coal (River King) with an ultimate analysis of C, 78.3; H, 5.4; N, 1.32; O, 11.12; S, 3.86; Ash, 10.9(maf/basis) was used. The coal conversion was determined from tetrahydrofuran insolubles, and the solubles were analyzed by Yanaco G-6800 gas chromatograph using OV-1701 fused silica capillary column(60m x 0.25mm φ).

RESULTS AND DISCUSSION

Hydrogenation of Anthracene. Anthracene was initially hydrogenated in the presence of petroleum solvents and synthetic pyrite using H$_2$ and syngas. The results in Table 1 show that the hydrogenation proceed well at 350°C with H$_2$ irrespective of the type of solvent used. Paraffins and cycloalkanes did not participate in the reaction and hydrogen transfer from tetralin was not an important factor. The reaction with syngas at the same temperature gave only 65.9% anthracene conversion. It is observed that the conversion increased as the temperature increased to 400°C, and that this was accompanied by the increase of CO shift conversion.

Coprocessing of Model Compounds. Anthracene and benzothiophene were coprocessed with petroleum solvents to study the hydrogenation and desulfurization during coprocessing. It is seen in Table 2 that anthracene was hydrogenated easily with H$_2$ in the presence of synthetic pyrite, but desulfurization of benzothiophene did not take place easily. In the presence of NiMo/Al$_2$O$_3$ and CoMo/Al$_2$O$_3$, both hydrogenation and desulfurization progressed markedly. In the run using an n-dodecane/decalin mixture as the solvent, 23.8% of decalin was dehydrogenated(17.7% to tetralin and 6.1% to naphthalene). It is of interest to note that trans/cis ratio of the remaining decalin has increased to 4.6 from the original trans/cis ratio of 1.6 after the coprocessing reaction. Similar increase of trans/cis ratio was also observed in the run using an n-dodecane/decalin/tetralin solvent mixture. The occurrence of isomerization to trans decalin during extraction of coal was also observed by Clarke et al[7].

For comparison purpose, a sulfate-treated iron oxide catalyst and a ZnCl$_2$/SiO$_2$-Al$_2$O$_3$ catalyst were prepared and tested. Both catalysts showed moderately good activities for hydrogenation and desulfurization in coprocessing using H$_2$.

In coprocessing using a paraffin/ethylcyclohexane/tetralin solvent with syngas, NiMo and CoMo catalysts impregnated with K$_2$CO$_3$ exhibited good activities for both hydrogenation and desulfurization, as shown in Table 3. When a paraffin/decalin/tetralin solvent was used, the extent of hydrogenation and desulfurization decreased. It was noticed that no net conversion or dehydrogenation of decalin took place in this case. The trans/cis ratios of the remaining decalin were much lower than those observed for coprocessing using H$_2$, indicating limited occurrence of isomerization during coprocessing with syngas. As was suggested by Clarke et al[7], decalin could participate in hydrogen donation reactions in the presence of polyaromatic compunds, and this was more pronounced in the reaction with H$_2$ than with syngas. It is speculated that hydrogen donation reactions of decalin somehow relate to the occurrence of isomerization. With syngas,

synthetic pyrite, sulfate-treated iron oxide, and $ZnCl_2/SiO_2-Al_2O_3$ exhibited moderate activities for hydogenation, but poor activities for desulfurization. Presence of significant concentrations of hydrogen donating tetralin alone was not sufficient to give high conversion in coprocessing using syngas. It is also observed, in general, that hydrogenation and desulfurization progress with the progress of CO shift conversion.

Coprocessing of Coal with Petroleum Solvents. Table 4 shows the test results of coprocessing bituminous coal with paraffin/decalin/tetralin solvents. Fairly high coal conversions were obtained with $NiMo/Al_2O_3$, $CoMo/Al_2O_3$, and synthetic pyrite using H_2. The coal conversions obtained with syngas were only moderete, but it should be emphasized that the reaction conditions have not been optimized in these runs. Improved conversions should be obtainable if variables including steam/syngas ratio, H_2/CO ratio, solvent composition, catalyst, and process severity are properly chosen.

In the run using an n-dodecane/decalin/1-methylnaphthalene mixture as the solvent, high coal conversion was obtained even without the use of tetralin. Product analysis indicates that significant amounts of 1-methylnaphthalene may have participated in hydrogen exchanges with decalin and coal. In the similar run with syngas, the active participation of 1-methylnaphthalene was not evident, and the decalin conversion decreased. For syngas runs, again the trans/cis ratio of the remaining decalin was lower, probably suggesting that only limited participation of decalin in hydrogen donation reactions has taken place.

ACKNOWLEDGEMENTS

References

1. Appell,H.R.,Miller,R.D.,Wender,I., presented before the Division of Fuel Chemistry, 163rd ACS National Meeting, Boston, April 10-14,1972
2. Batchelder,R.F.,Fu,Y.C., Ind.Eng.Chem. Process Des. Dev. Vol.18,No.4,599(1979)
3. Stephens,H.P.,Kottenstette,R.J., presented before the Division of Fuel Chemistry, 194th ACS National Meeting, New Orleans, August 30-September 4,1987
4. Tanabe,K.,Yamaguchi,T.,Hattori,H.,Matsuhashi,H.,Kimura,A., Fuel Processing Technology, Vol.4, 247(1986)
5. Pradhan,V.,Tierney,J.W.,Wender,I., Preprrints, Div.Fuel Chem., Am.Chem.Soc. Vol.35, No.3,793(1990)
6. Sharma,R.K.,Diehl,J.W.,Olson,E.S., Preprints, Div.Fuel Chem., Am.Chem.Soc. Vol.35, No.2,414(1990)
7. Clarke,J.W.,Rantell,T.D.,Snape,C.E., Fuel, Vol.63,1476(1984)

Table 1 Hydrogenation of Anthracene Using H₂ and Syngas
(Initial Pressure: 70Kg/cm², Time: 45min)

Gas	H₂					Syngas (H₂:CO=1:1)	
Catalyst	FeS$_x$[a]					FeS$_x$[b]	
Solvent[c]	T	D/E	D/E/DL	D/E/T	D/E/T	D/E/T	D/E/T
Temperarure, ℃	350	350	350	350	400	350	400
Anthracene conversion,%	92.8	92.2	90.0	92.4	82.8	65.9	81.0
DHA formed,%	68.8	74.3	74.3	66.8	47.2	65.9	67.6
Conversion of tetralin,%	3.8	–	1.8[d]	6.7	20.2	1.5	8.3
CO conversion,%	–	–	–	–	–	2.0	8.3

[a] Synthetic pyrite [b] Impregnated with K₂CO₃ solution

[c] Equal wt% of each component [d] Conversion of decalin

D:n-Decane, E:Ethylcyclohexane, T:Tetralin, DL:Decalin, DHA:9,10-Dihydroanthracene

Table 2 Coprocessing of Model Compounds Using H₂
(Coal Model:Anthracene/Benzothiophene, Initial Pressure:70Kg/cm², Time:45min)

Catalyst	FeS$_x$	FeS$_x$	Fe₂O₃ /SO₄²⁻	ZnCl₂ /SiO₂-Al₂O₃	NiMo	CoMo	NiMo	NiMo
Solvent[a]	D/E/T	D/E/T	D/E/T	DO/E/T	D/E/T	D/E/T	DO/DL/T	DO/DL
Temperature, ℃	350	400	400	400	400	400	400	400
Anthracene conversion,%	90.8	81.7	68.4	87.1	97.0	96.8	97.2	89.4
Benzothiophene conversion,%	10.2	26.0	80.8	50.2	96.2	100	100	100
Conversion of tetralin,%	11.5	13.8	13.5	33.2	38.5	33.0	16.7	–
Decalin remained,%							86.4	76.2
cis							15.0	13.7
trans							71.4	62.5
trans/cis ratio							4.8	4.6

[a] Equal wt% of each component

T:Tetralin, D:n-Decane, E:Ethylcyclohexane, DO:n-Dodecane, DL:Decalin

Table 3 Coprocessing of Model Compounds Using Syngas(H₂:CO=1:1)
  (Coal Model:Anthracene/Benzothiophene,
   Initial Pressure:70Kg/cm², H₂O:10wt% of Reactants, Time:45min)

	FeSₓᵃ	FeSₓᵃ	NiMoᵃ	NiMoᵃ	NiMoᵃ	CoMoᵃ	Fe₂O₃/SO₄²⁻	ZnCl₂/SiO₂-Al₂O₃
Solventᵇ	D/E/T	D/E/T	D/E/T	DO/DL/T	TD/DL/T	D/E/T	DO/E/T	DO/E/T
Temperature, ℃	350	400	400	400	400	400	400	400
Anthracene conv.,%	80.1	70.9	90.1	78.9	77.8	88.3	50.2	65.6
Benzothiophene conv.,%	4.1	11.7	90.4	67.6	66.6	100	28.3	22.6
Conversion of tetralin,%	15.4	4.0	11.3	6.6	11.4	22.1	2.6	23.2
CO conversion,%	2.0	7.7	15.3	10.4	15.9	18.3	16.4	2.8
Decalin remained				102.4	102.4			
cis				33.4	30.8			
trans				69.0	71.6			
trans/cis ratio				2.1	2.32			

ᵃ Catalyst impregnated with K₂CO₃ solution   ᵇ Equal wt% of each component
D:n-Decane, E:Ethylcyclohexane, T:Tetralin, DO:n-Dodecane, DL:Decalin, TD:n-Tridecane

Table 4 Coprocessing of Bituminous Coal with Petroleum Solvents(425℃,45min)
  (Solvent:n-Dodecane/Decalin/Tetralin, Solvent:Coal=4:1)

	H₂				Syngas(H₂:CO=1:1)		
Catalyst	FeSₓ	NiMo	NiMoᵃ	CoMo	FeSₓᵇ	NiMoᵇ	NiMoᵃ·ᵇ
Coal conversion,%	89.3	87.6	84.9	83.7	63.7	79.8	62.6
H₂ consumption,wt% of maf coal	3.1	3.1	3.9	5.3	0.8	-0.3	-0.2
CO conversion,%	-	-	-	-	6.2	22.1	19.3
Conversion of tetralin,%	17.3	10.1	-	12.9	14.1	8.2	-
Conversion of 1-methylnaphthalene,%	-	-	17.4	-	-	-	1.2
Decalin remained,%	98.6	90.7	88.6	95.8	95.7	87.2	94.5
cis	16.8	27.4	25.3	27.3	22.2	30.3	32.4
trans	81.8	63.3	63.3	68.5	73.5	56.9	62.1
trans/cis ratio	4.9	2.3	2.5	2.5	3.3	1.9	1.9

ᵃ Solvent:n-Dodecane/Decalin/1-Methylnaphthalene   ᵇ Impregnated with 10%k₂CO₃

CATALYSIS OF METAL-ION EXCHANGED Y-ZEOLITES AND MODIFIED Ni-Mo/Al$_2$O$_3$ FOR HYDROCRACKING OF PHENANTHRENE AND COAL-DERIVED DISTILLATES

Chunshan SONG*, Harold H. SCHOBERT*, and Hisaji MATSUI†

*Fuel Science Program, Department of Materials Science and Engineering
The Pennsylvania State University, University Park, PA 16802, USA
†Research and Development Center, Osaka Gas Co., Ltd., Osaka 554, Japan

INTRODUCTION

The liquids derived from liquefaction, pyrolysis and gasification of coals have high contents of condensed polyaromatic compounds and polar compounds. Even in the middle distillate fraction (MD) produced from the advanced two-stage coal liquefaction plant at Wilsonville, Alabama, there are considerable amounts of polyaromatics such as pyrene [1]. These liquids require catalytic hydroprocessing before they can be used as clean transportation fuels such as gasoline and jet fuels. During the last two decades, emphasis in selecting catalysts for coal liquids upgrading has always been given to the Ni-Mo and Co-Mo combinations, which are used extensively in the petroleum industry. Research has focused mainly on catalyst screening and evaluation, and little attention has been given to investigating novel formulations [2].

In regard to catalytic materials, the use of zeolites is of both fundamental and practical importance because of their higher surface area and unique catalytic property as compared to conventional catalysts supported on alumina or silica-alumina. There are numerous reports on the application of various zeolites in the catalytic reaction processes related to petroleum industry [3-4]. Introducing transition metals into zeolites by appropriate methods could make the zeolite suitable for hydrocracking, and the metals can also serve to hydrogenate the coke precursors rapidly and to prevent their conversion to coke deposit on the zeolite [3]. There are also commercial hydrocracking processes using zeolite-based catalysts for converting petroleum distillates [3], and more recently, for converting residues [5-6]. However, the research work on zeolite catalysts in hydrocracking of polyaromatics and coal liquids is still very limited. Haynes et al. [7] studied hydrocracking of prehydrogenated polycyclic hydrocarbons over Ni-W impregnated on a Y-zeolite. They showed that mixtures of hydrogenated pyrenes can be hydrocracked over Ni-W/Y catalyst. Kikuchi et al. [8] studied hydrocracking of phenanthrene using LaY catalyst in the presence of H-donor tetralin solvent. They showed that this catalyst can significantly promote phenanthrene conversion if tetralin was present, otherwise Ni-Mo/Al$_2$O$_3$ was much more active than LaY. Our preliminary work has shown that some transition metal-ion exchanged Y-zeolites show some unique catalytic activity for hydrocracking of polyaromatics [9-10] as compared to other catalysts [10-12]. The work reported here is aimed at clarifying the effects of loading small amounts of metals on the catalytic activity of Y-zeolite. In this work, we prepared several metal-loaded Y-zeolites by ion-exchange and evaluated the effects of these zeolite catalysts and of two third-generation commercial Ni-Mo catalysts in hydrocracking of phenanthrene, which is a typical polyaromatic component in liquids from pyrolysis and liquefaction of coals. Some of the catalysts were further examined in hydrocracking of a coal-derived middle distillate fraction which is rich in polyaromatics.

EXPERIMENTAL

The metal-ion exchanged Y-zeolites were prepared by mixing ammonium-exchanged Y-zeolite, NH$_4$-Y (SiO$_2$/Al$_2$O$_3$ mol ratio: 4.6) and 0.25 M aqueous solutions of Ni(NO$_3$)$_2$·6H$_2$O, Fe(NO$_3$)$_3$·9H$_2$O, or La(NO$_3$)$_3$·6H$_2$O. The mixtures were agitated at 85°C for 2 h and then filtered. The ion-exchanged zeolites were washed with distilled water, dried at 120°C for 2 h and then calcined in air at 500°C for 4 h. Two commercial Ni-Mo catalysts were sulfided with 6% CS$_2$ in n-dodecane at 250°C for 2 h and 300°C for 3 h under 100 psi H$_2$, and used in phenanthrene hydrocracking. The chemical composition of both the metal-ion exchanged zeolites and supported Ni-Mo or Co-Mo catalysts was determined by inductively coupled plasma - atomic emission spectrometry (ICP-AES, Seiko Denshi Kogyo, JY-48P-SPS1100). The surface analyses of the zeolite catalysts, unsulfided and sulfided Ni-Mo catalysts were also conducted by X-ray photoelectron spectroscopy (XPS; Shimadzu ESCA-850, MgKα) and scanning electron microscope - electron probe microanalysis (SEM-EPMA; Nihon Denshi, JXA-733).

Hydrocracking of phenanthrene was carried out at 400°C for 1 h with 1000 psi H_2 (cold) in a 100 ml autoclave with phenanthrene (4 g), n-heptane solvent (10 ml) and a catalyst (2 g). The gaseous products were analyzed by GC. The liquid and solid products were analyzed by capillary GC-MS (Shimazu QP-1000) and capillary GC (Shimazu 9A). The used catalysts were washed by methylene chloride solvent, dried in vacuum oven at 100°C, and analyzed for carbonaceous deposits by combustion method.

We also used a coal-derived distillate sample (b.p. 204-343°C), which was produced from two-stage liquefaction of Ireland Mine coal at Wilsonville two-stage liquefaction plant using Shell 324 Ni-Mo catalyst [1]. Hydrocracking of Wilsonville middle distillates (Wl-MD) was carried out at 400°C for 1 h with 1500 psi H_2 (cold) in 20 ml microautocalves with 2 g feedstock and 0.4 g catalyst. The zeolite catalysts (NiH-Y, FeH-Y) were exposed to the feedstock in the microautoclave for about 20 hours before the reaction. The gas products were analyzed by GC. The liquid products were characterized by capillary GC-MS using a Kratos MS80 GC-MS system.

RESULTS AND DISCUSSION

Catalyst Characterization

In general, the extent of metal-ion exchange depends on the conditions and the samples used. In this work, the contents of metals of the prepared catalysts, and the change in chemical composition of the Y-zeolite framework before and after the metal-ion exchange were determined by using the ICP-AES technique. As shown in Table 1, the introduction of Ni, Fe and La into the NH_4-Y zeolite by ion-exchange was successful and the contents of these three metals in the finished catalysts are 3.6 (NiO), 4.4 (Fe_2O_3) and 8.4 (La_2O_3) wt%, respectively. For NiH-Y and LaH-Y catalysts, the SiO_2/Al_2O_3 ratios of the zeolites are similar to the original NH_4-Y or H-Y. However, in the case of FeH-Y, the content of Al_2O_3 is significantly less and the SiO_2/Al_2O_3 ratio is substantially higher than the other two catalysts. This indicates that the preparation of FeH-Y was accompanied by remarkable dealumination from zeolite framework, probably due to the higher acidity of the aqueous solution with $Fe(NO_3)_3 \cdot 9H_2O$ and NH_4-Y. In fact, we measured the pH of the aqueous solutions of the Fe, Ni and La salts before ion exchange, which were 1.1, 3.5, and 4.2, respectively. It is known that steam or acid treatment can cause dealumination of Y-zeolite [13].

SEM indicated that the size and shape of the three metal-ion exchanged zeolites are very similar to that of H-Y (un-exchanged). XPS spectra of NiH-Y and FeH-Y clearly showed a strong signal of Ni and Fe on the zeolite surface. The binding energies for Al 2p or Si 2p of NiH-Y and LaH-Y are similar, while the intensity of Al 2p for FeH-Y is very low (with high noise signals), 72 cps as compared to 730 cps for Al in NiH-Y and 636 cps for Al in LaH-Y. This is considered to be due to the very low content of Al in FeH-Y, being consistent with the finding from ICP-AES. Surprisingly, ICP-AES indicated that LaH-Y contains 8.4 wt% La_2O_3, but XPS showed that the intensity of La on the surface is very low. However, it was found that when the etching technique was applied in XPS (for the depth distribution from surface to the bulk), the intensity of the peak of La increased remarkably with increasing etching time from 0.4 to 1.2 min, whereas there was little change in the relative intensity of peaks for Al and Si in LaH-Y with etching from 0 to1.2 min. These results clearly indicate that the concentration of La in the bulk or framework is higher than that on the zeolite surface. We also examined two alumina-supported NiMo catalysts obtained from two catalyst companies, which are currently being used in many commercial plants for hydroprocessing of petroleum feedstocks. Detailed analyses by ICP-AES, SEM-EPMA and other techniques revealed that one of the third-generation NiMo catalysts contains P, and the other contains B. It is clear from the figures in Table 1 that B or P was intensionally added to improve the catalyst property or performance. XPS analysis showed that spectra pattern of the Mo 3d doublets of the two catalysts is similar to each other, but the Ni 2p peak for the P-modified NiMo is relatively sharper, suggesting a better dispersion of Ni.

Phenanthrene Hydrocracking

In this work, we examined the catalytic effects of the metal-ion modified Y-zeolites (NiH-Y, FeH-Y, LaH-Y) and H-Y for hydrocracking of phenanthrene. The catalytic activity of these zeolites was also evaluated by comparing with two commercial Ni-Mo catalysts. Numerous products were formed during the catalytic hydrocracking of phenanthrene. These products can be classified into the following groups: 1) C_1-C_4

1893

gases; 2) C_5-C_7 aliphatics; 3) alkylbenzenes; 4) alkyltetralins and alkylindans; 5) alkylnaphthalenes; 6) alkylbiphenyls; 7) unsym-octahydrophenanthrene and octahydrophenanthrene isomers; 8) sym-octahydrophenanthrene; 9) methylbenzoindanes; 10) tetrahydrophenanthrene; 11) dihydro-phenanthrene; 12) phenanthrene; 13) alkylphenanthrenes; 14) carbonaceous deposits; and the others. Figure 1 shows some typical results of GC-MS and GC analysis of products from hydrocracking of phenanthrene with different catalysts. Table 2 is a summary of the results with all the catalysts. As can be seen from Figure 1 and Table 2, the product distribution and phenanthrene conversion strongly depend on the metal introduced into the Y-zeolites. When H-Y is used, alkylbenzenes and alkylnaphthalenes were obtained as major hydrocracked products together with C_1-C_4 gases. The La-exchanged zeolite, LaH-Y (Figure 1B), gave similar results to those with H-Y. Yields of alkyltetralins were very low but more than 10wt% of methyl and dimethylphenanthrene were formed with LaH-Y and H-Y, probably due to transalkylation between alkylnaphthalenes or alkylbenzenes and phenanthrene. Interestingly, introducing Ni to Y-zeolite significantly promoted the hydrocracking activity, as can be seen from comparison of Figures 1A with 1B. In fact, NiH-Y afforded much higher conversion and higher yields of BTX, especially toluene. Moreover, not only alkylnaphthalene but also tetralin and methylindanes were obtained as two-ring hydrocracked products with NiH-Y. On the other hand, FeH-Y showed quite a different catalytic behavior as compared to H-Y, NiH-Y and LaH-Y. While naphthalene was also produced with FeH-Y, the major products are dihydro- and tetrahydro-phenanthrene. The formation of alkylphenanthrenes and carbonaceous deposits was suppressed significantly with FeH-Y. These results indicate that FeH-Y has a very low acidity as compared to the other zeolites, probably due mainly to the dealumination as revealed by ICP-AES. The runs over supported Ni-Mo catalysts afforded partially hydrogenated phenanthrene as main products (Figure 1 and Table 2), and the major cracking products are alkyltetralins, cyclohexylphenylethane, cyclohexylbenzene, and alkylbiphenyls together with small amounts of alkylnaphthalenes. While the two catalysts from different sources have different metal contents, it appears that the P-modified catalyst shows higher hydrogenation activity than the B-modified one but the latter has a relatively higher cracking ability than the former (Table 2). We have observed a similar trend for P- and B-modified Co-Mo/Al_2O_3 catalysts [9-10]. Comparison of Figure 1A with Figure 1C reveals that NiH-Y has much higher hydrocracking activity than the industrial Ni-Mo hydroprocessing catalyst.

The differences in product distribution also reflect the occurence of different reaction paths. It is worthwhile noting from Figure 1 and Table 2 that yields of alkylbiphenyls are considerably lower with the Y-zeolite catalysts, probably because the ring-openning cracking of dihydrophenanthrene is difficult with the catalysts having strong acidity, such as H-Y, NiH-Y and LaH-Y. This consideration is also supported by the fact that considerable amounts of biphenyl and cyclohexylbenzene were formed with the relatively less acidic Ni-Mo/Al_2O_3 (Figure 1, Table 2), probably via the hydrocracking of the central ring in 9,10-dihydrophenanthrene. The relatively higher yields of alkylnaphthalenes with LaH-Y and H-Y suggests a major hydrocracking path via tetrahydrophenanthrene, whereas the higher yields of alkyltetralins and cyclohexylphenylethane (Figure 1) with the Ni-Mo catalysts implicate the paths of hydrocracking via sym- and unsym-octahydrophenanthrene. It seems that both these two paths exist for the hydrocracking with NiH-Y catalyst, probably because it has both high acidic cracking ability and high hydrogenation activity. Since the critical diameter of phenanthrene is 7.9 Å [7] which is similar to the diameter of Y-zeolite (about 8 Å), the hydrocracking reactions with H-Y may have been associated mainly with the external surface of the zeolite. The metal-ion exchange may induce some dealumination, which could generate some mesopores in the zeolite [6]. ICP-AES clearly indicated the dealumination during the preparation of FeH-Y. At the present stage, it is not clear wheather this occured during the preparation of NiH-Y and LaH-Y, but the "apparent" SiO$_2$/Al$_2$O$_3$ ratios of these two zeolites are similar to that of H-Y.

Hydrocracking of Wilsonville Middle Distillates

From the above results, it is clear that the zeolite ion-exchanged with Ni or Fe exhibits distinctly different catalytic activity as compared to LaH-Y and H-Y. We further examined NiH-Y and FeH-Y for hydrocracking of WI-MD, which has a boiling range of 204-343°C. Because it was produced from direct liquefaction of coal and because of the co-boiling phenomena, it has high contents of polyaromatic materials [1]. The hydrocracking of WI-MD was conducted at 400°C with 1500 psi H$_2$. In order to derive useful data on the applicability of the zeolitic catalysts for converting WI-MD, the FeH-Y and NiH-Y were immersed in the WI-

MD for over 20 hours before the reaction. This was intended to deactivate the active sites in the zeolite catalysts which would be poisoned upon contact with coal-derived distillates in a continous reactor. In this way we might be able to see the activity level of the active sites which are not poisoned by the adsorption of polar and polyaromatic materials. Figure 2 shows the GC-MS total ion chromatograms of the liquids from a non-catalytic run and catalytic runs. The GC-MS profile of the liquids from a noncatalytic run of WI-MD (Figure 2A) is very similar to the original sample [1]. Both samples contain very limited amounts of aliphatics, and are rich in polyaromatics. The most predominant peak appeared in GC-MS total ion chromatogram in Figure 2A (scan No. 3683, retention time: 59:31 min) is pyrene. The use of FeH-Y, after its 20 h exposure to WI-MD prior to reaction, did not alter the liquid composition to any significant extent. On the other hand, using NiH-Y catalyst significantly promoted the hydrocracking reactions, and resulted in a dramatical change in the composition of liquid products. The major products identified by GC-MS include alkylcyclohexanes, alkylbenzenes, tetralin and naphthalene and their homologues.

CONCLUSIONS

In summary, it has been found that NiH-Y, the proton form Y-zeolite loaded with Ni by ion exchange, shows much higher activity for phenanthrene hydrocracking than LaH-Y, H-Y, FeH-Y and commercial, B- or P-modified NiMo/Al$_2$O$_3$ hydroprocessing catalysts. The test with WI-MD also revealed that NiH-Y has high hydrocracking activity for converting the middle distillates derived from direct coal liquefaction. While some problems such as coking and pore size limitations remain to be solved, the preliminary results showed that some metal-ion exchanged zeolites can be promising hydrocracking catalysts. In future we hope to explore novel zeolitic catalysts with desired activity and performance for converting coal-derived distillates into transportation fuels.

ACKNOWLEDGEMENTS
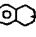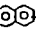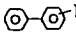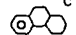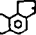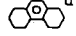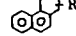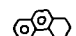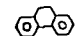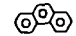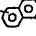
REFERENCES

1. Song, C.; Eser, S.; Schobert, H.H.; Hatcher, P.G. et al., *Technical Progress Report 42-3462-TPR-2*, DOE/Sandia National Laboratory, February 1991, 96 pp.
2. Derbyshire F. J., *Energy and Fuels*, 1989, 3, 273.
3. Bolton A. P., "*Hydrocracking, Isomerization, and Other Industrial Processes*", in "*Zeolite Chemistry and Catalysis*" (Ed. J. A. Rabo), ACS Monograph 171, Washington D.C., 1976, pp.714-780
4. Karge, H.G.; Weitkamp, J. (Eds), "*Zeolites as Catalysts, Sorbents and Detergent Builders*", Elsevier, Amsterdam, 1989, Part I, pp. 1-428.
5. Sue, H.; Fujita, M.; *Oil and Gas J.* 1986, 51
6. Yamamoto T., *Petrotech*, 1989, 12, 621
7. Haynes Jr. H. W., Parcher J. F. and Helmer N. E., *Ind. Eng. Chem. Process Des. Dev.*, 1983, 22, 401
8. Kikuchi E., Tsunoda A., Katsumata H. and Morita Y., *J. Japan Petrol. Inst.*, 1984, 27, 296
9. Song, C. "Catalytic Hydrogenation and Cracking of Phenanthrene over Y-Zeolite Catalysts", Final Report , The Research Center of Osaka Gas Co., October 1989.
10. Ueda, K.; Matsui, H.; Song, C.; Xu, W. *J. Japan Petrol. Inst.*, 1990, 33, 413.
11. Song, C.; Hanoka, K. ; Ono, T.; Nomura, M. *Bull. Chem. Soc. Japan* 1988, 61, 3788.
12. Song, C.; Nomura, M.; Ono, T.; *ACS Fuel Chem. Prepr.* 1991, 36(2), 586.
13. Humphries, A.; Yanik, S.J.; Gerritsen, L.A.; Desai, P.H. *Hydrocarbon Processing.* 1991, 70, 69.

Table 1. Chemical Composition of the Metal-Ion Exchanged Y-zeolites and Supported Ni-Mo/Al$_2$O$_3$ Catalysts Determined by ICP-AES

wt%, dry	NH$_4$-Y	H-Y	NiH-Y	FeH-Y	LaH-Y	P-Modified NiMo/Al$_2$O$_3$	B-Modified NiMo/Al$_2$O$_3$
NiO			3.6			3.7	2.4
Fe$_2$O$_3$				4.4			
La$_2$O$_3$					8.4		
MoO$_3$						18.5	9.2
SiO$_2$	71.6	73.3	70.6	91.5	66.5		
Al$_2$O$_3$	26.7	26.2	25.5	2.2	24.7	68.2	71.8
Na$_2$O	0.9	0.4	0.3	0.1	0.3		
P$_2$O$_5$						7.8	
B$_2$O$_3$							12.2
SiO$_2$/Al$_2$O$_3$	4.55	4.76	4.70	69.46	4.56		
SA, m^2/g	719	646	665	342	662	162	268

Table 2. Results of Catalytic Hydrocracking of Phenanthrene at 400°C with 6.9 MPa H_2

Catalyst	H-Y	NiH-Y	FeH-Y	LaH-Y	S-NiMo/ Al_2O_3-B_2O_3	S-NiMo/ Al_2O_3-P_2O_5
Products[a] (wt%)						
C_1-C_4	2.4	8.5	0.2	2.2	0.5	0.4
C_5-C_7	0.4	0.4	tr.	0.6	0.2	tr.
R_1⟨◯⟩R_2 [b]	1.0	6.9	0.1	1.4	1.5	1.7
R_1⟨◯⟩R_2	0.7	4.4	0.2	0.7	4.4	3.3
R_1⟨◯◯⟩R_2	4.4	6.3	1.0	3.8	1.8	0.8
◯–◯–R	0.2	0.4	0.1	0.1	1.3	1.8
(◯◯) [c] + (◯◯)–R	0.7	2.9	0.2	1.4	8.1	9.0
(◯◯◯) [d]	0.5	2.4	tr.	0.5	6.2	11.8
(◯◯)–R [e]	2.0	3.6	0.7	1.9	1.9	1.0
(◯◯)	1.3	2.7	4.6	1.2	16.7	17.0
(◯◯)	1.8	2.4	6.2	1.9	7.6	10.1
(◯◯◯)	53.3	19.3	80.4	54.0	31.6	30.5
R_1(◯◯◯)R_2	11.2	8.7	1.1	10.3	1.0	0.4
C deposits [f]	11.5	11.3	2.5	11.3	3.6	3.2
Conversion (wt%)	46.7	80.7	19.6	46.0	68.4	69.5

a) R, R_1 and R_2 mean alkyl groups or hydrogen. b) Including cyclohexyl
phenylethane and cyclohexylbenzene. c) Unsym-octahydrophenanthrene.
d) Sym-octahydrophenanthrene. e) Including some unknown components with
molecular weight (by GC-MS) of 182. f) Amount of carbonaceous deposits
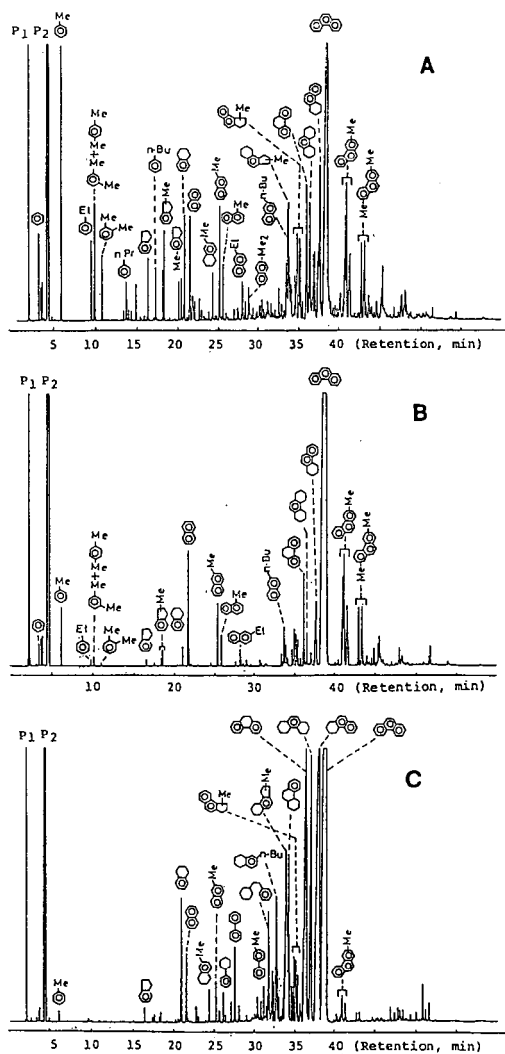on catalyst as determined by combustion method.

Figure 1. Composition of products from hydrocracking of phenanthrene over NiH-Y (A), LaH-Y (B) and commercial, B-modified NiMo/Al2O3 (C) catalysts (P$_1$: CH$_2$Cl$_2$ solvent; P$_2$: n-heptane solvent)
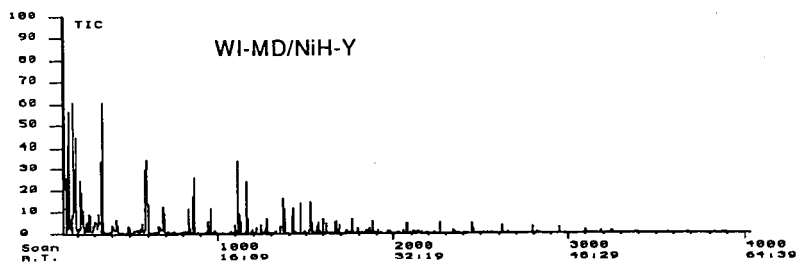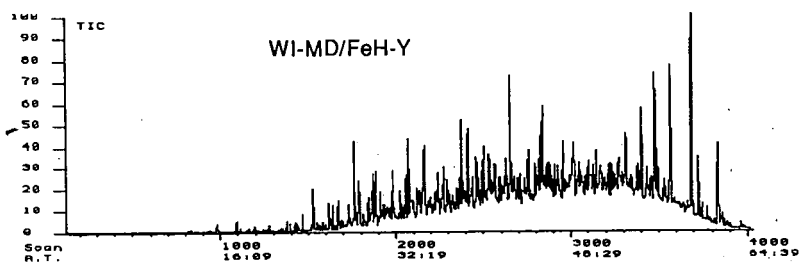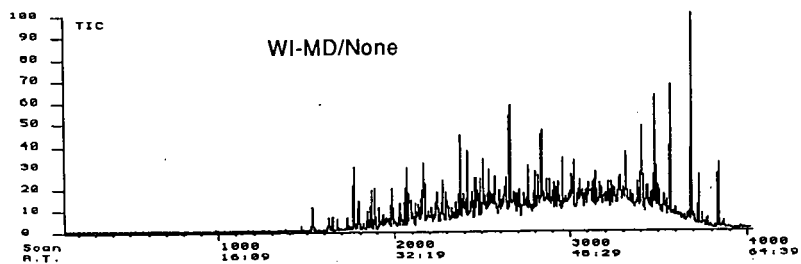
Figure 2. GC-MS TIC of liquid products from hydrocracking of Wilsonville middle distillates

ULTRAFINE IRON CARBIDE AS LIQUEFACTION CATALYST PRECURSOR

G T Hager, X-X Bi*, F J Derbyshire, P C Eklund*, and J M Stencel
University of Kentucky
Center for Applied Energy Research
3572 Iron Works Pike, Lexington, KY 40511-8433
*Department of Physics and Astromony

KEYWORDS: Ultrafine Particles, Coal Dissolution, Iron Carbide

ABSTRACT

Novel ultrafine particles (UFPs) of iron carbide have been synthesized and evaluated for their catalytic activity in coal liquefaction. The particles, with average diameters of 5 - 10 nm, were prepared by the laser driven pyrolysis reactions of ethylene and iron pentacarbonyl. Two different crystalline phases, Fe_7C_3 and Fe_3C, have been prepared and these unsupported catalysts have been characterized using a range of analytical techniques. Results of microautoclave studies indicate the high catalytic activity of these UFPs for coal liquefaction compared to iron added as iron pentacarbonyl, and to a thermal baseline. The transformation of the catalyst under liquefaction conditions in the presence of sulfur is reported. The presence and catalytic role of monolayer pyrolytic carbon coatings formed on the catalyst surface during laser synthesis will also be addressed.

INTRODUCTION

The primary use of highly dispersed slurry phase catalysts is in the first stage of a two stage liquefaction process. The preferred catalyst is one that will aid in the conversion of the coal to soluble products which may then be further upgraded in the second stage to more useful products using conventional supported catalysts. A successful slurry phase catalyst should improve product selectivity, allow increased throughput, and yield a first stage product which will reduce the rate of catalyst deactivation in the second stage. The effective use of a slurry phase catalyst may also offer an efficient means of liquefying low rank western U. S. coals which can produce more desirable products [1,2] and reduce second stage catalyst deactivation [3]. Subbituminous coals are generally found,

however, to convert at a lower rate and to a lesser extent than higher rank coals. This is purported to be caused by an imbalance in the rates of bond cleavage and hydrogenation. Dissolution promoted by an effective slurry phase catalyst may be able to correct this imbalance.

Historically, the oxides and sulfides of molybdenum, tungsten and the iron group metals were among the first catalysts used in coal liquefaction. Molybdenum compounds are generally considered to exhibit higher activity in dissolution and hydrogenation than iron compounds. However, due to the higher cost of the molybdenum and the fact that dissolution catalysts are not easily recovered, iron based catalysts are usually preferred for industrial operations.

Since the catalytic process takes place at the surface-liquid interphase, the amount of surface area available for reaction is critical. By increasing the surface area per unit volume the relative activity of a catalyst may be increased. In supported catalysts this is often done by depositing the catalyst over a high surface area porous substrate such as alumina or a zeolite. Unsupported catalysts, on the other hand, can present a high surface area by maintaining a high dispersion. The majority of the active catalyst surface is on the outside of the particles and therefore is not subject to pore diffusion limitations. Further, ultrafine particles, measuring only a few nanometers in diameter, may exhibit markedly different properties than bulk particles of the same composition and may therefore present a means to improve the activity.

The current research program is concerned with the production of ultrafine iron carbide particles by laser pyrolysis and their catalytic behavior as related to composition, structure, size, and other properties.

EXPERIMENTAL

PARTICLE SYNTHESIS

The use of laser pyrolysis for ultrafine particle synthesis was first performed by Haggerty and co-workers [4] for the production of silicon-containing ceramics. The technique was later adopted by researchers at Exxon who used it to produce transition metal carbide particles for use as catalysts in synthesis gas reactions [5,6]. One such carbide described in an Exxon patent was Fe_3C. To produce this carbide a stream of the

reactant gases, ethylene and iron pentacarbonyl ($Fe(CO)_5$), was intersected with a tunable cw CO_2 laser. The same method was used in the present research. Approximately 5% of the incident energy from the laser is adsorbed by the ethylene. The added heat causes the thermal decomposition of the iron pentacarbonyl which leads to the formation of ultrafine (2-20 nm) spherical iron carbide particles. The exact mechanism of the particle formation is still under investigation.

The apparatus used for the synthesis of these particles has been described previously [7]. The reaction cell is shown in Figure 1. Particles generated in the reaction volume were originally collected on a teflon membrane filter. In this system the production limiting factor was the pressure drop across the filter.

The collection mechanism has since been improved to allow for production of large (>1g) batches of particles. A large magnet, placed upstream of the previously used teflon membrane filter, effectively traps most of the particles in a sample chamber. This sample chamber may be sealed and removed from the system when full and the particles may then be passivated (see Results and Discussion). The use of the magnetic trap is possible due to the ferromagnetic properties of the particles. However, this ferromagnetism leads to particle agglomeration which may adversely affect dispersion in liquefaction experiments.

LIQUEFACTION

Since it has been reported that some transition metal carbide catalysts resist sulfiding under liquefaction conditions [8,9], coal-free experiments were conducted to determine the catalyst behavior under both sulfiding and nonsulfiding conditions. These experiments were carried out in 18 mL batch microautoclaves, in the absence of coal, with 4 wt% Fe_7C_3 in 5 g of tetralin, with and without sulfur added as dimethyldisulfide (DMDS) at twice the stoichiometric ratio required for formation of FeS_2. The reaction conditions used in this study were 385 °C with 800 psig (cold) hydrogen pressure and the reaction time was 30 minutes.

The liquefaction experiments were conducted in the same batch microautoclaves using 3 g of a subbituminous Wyodak coal and 5 g of tetralin. The reaction conditions were the same as the coal-free runs and

the reaction time was 15 minutes. Two passivated iron carbide catalysts, Fe_7C_3 and Fe_3C, were used in the study. A thermal run and a catalytic run using $Fe(CO)_5$ were also made for comparison. The catalyst loading was 1 wt % Fe, as determined from precursor stoichiometry, and dimethyldisulfide (DMDS) was added in 20 % excess for the formation of FeS_2. The addition of DMDS was based on the results of the previous coal-free experiments with added sulfur. The conversions (daf) of the coal liquefaction runs were determined using solubility in pyridine (preasphaltenes), benzene (asphaltenes), and pentane (oils). Gas yields were determined by gas chromatography.

RESULTS AND DISCUSSION

Two distinct phases of iron carbide particles, orthorhombic Fe_3C and metastable hexagonal Fe_7C_3, have been synthesized. These particles have been characterized by XRD, transmission electron microscopy, electron diffraction, and Mössbauer spectroscopy. The phase and size of the particles is controlled by the gas flow rate, pressure and laser intensity. Adjustment of these parameters allows the control and reproducible production of different size ranges and both phases.

The particles are formed with a thin layer of pyrolytic carbon coating the surfaces of the particles. The particles are also pyrophoric which necessitates their passivation prior to exposure to air. The passivation process involves the gradual introduction of 10% O_2 in helium with constant temperature monitoring to prevent runaway reaction. While the effect of the process on the carbon coating is unclear, X-ray photoelectron spectroscopy (XPS) has shown that the passivated particles possess a surface layer of Fe_3O_4.

The results of the coal-free experiments showed that the iron carbide particles will sulfide under liquefaction conditions in the presence of added sulfur to form pyrrhotite. While it is believed that the addition of coal will not prevent this transformation from occurring, Mössbauer spectroscopy of the liquefaction residues are being done to provide evidence of the final state of the catalyst after reaction. Particle growth, as shown by SEM micrographs and the narrowing of X-ray diffraction lines (Figure 2), is seen in both the coal-free runs. TEM micrographs of the particles formed in the absence of sulfur confirm the increase in size due to the agglomeration of the smaller particles. The

1903

larger particles have a relatively narrow size distribution and appear to be made up of the small particles which have agglomerated to form spheres around a hollow or carbon center. The XRD analysis indicates that in the absence of added sulfur the catalyst undergoes a phase change to an iron carbide, or mixture of carbides, and some Fe_3O_4. It seems unlikely that this oxide phase could have been produced in the reducing atmosphere present in the reactor. Its presence may be due to the fact that the surface oxide layer on the passivated particles was not effectively reduced or it may be an artefact of sample handling. In the presence of added sulfur the Fe_7C_3 is converted to pyrrhotite and sintering is again observed by SEM and XRD. TEM micrographs show that the sulfided catalyst exists as both small particles and as larger agglomerated crystals. Energy dispersive X-ray analysis indicates an approximate stoichiometry of $Fe_{0.85}S$, or approximately Fe_7S_8, for the pyrrhotite. The rate of the conversion to pyrrhotite is not known. The effect of coal on this transformation is under investigation.

Based on the results from the coal-free experiments with sulfur, excess sulfur was added in the liquefaction experiments to allow for the catalyst transformation to pyrrhotite, since pyrrhotite has widely been reported to be the active form of iron catalysts. Table 1 shows the results of the liquefaction experiments. When compared to the thermal run and a run using iron carbonyl as the catalyst precursor, both carbide forms showed enhanced total conversion. This increase in conversion may be more significant than these results indicate since the pyrolytic carbon coating has been suggested by the results of thermogravimetric analysis (TGA) to account for approximately 30 % of the particle weight. The exact quantity of carbon in the coating is being determined by current experiments. The corrected iron loading for the catalytic runs with iron carbide precursors was then approximately 0.75 wt. %. This shows higher conversion at lower iron loading for the heterogeneous iron carbide precursors compared to the homogeneous iron pentacarbonyl precursor. The result corresponds with other research [10-12] which has shown that aerosol iron oxide precursors produce higher activity than organometallic or salt precursors. This may be due to the unexpectedly large (70 -110 nm) crystallites which are reportedly formed by the soluble precursors and the relative stable size of the particle precursor. The reason for the larger crystallite formation by the soluble precursors is not understood at present. In addition to the higher overall conversion, there are also some differences in the product selectivity. The catalytic effect, if any,

of the carbon coating has not been determined.

Comparing the data from these experiments to the work of Keogh and Davis [13] plotted on a Wei-Prater diagram (Figure 3), a similar, but slightly different, pathway from the subbituminous pathway seems to be shown. The reason for this deviation is unclear at present. Since the deviation in the trend is present in the thermal baseline as well as the catalytic runs, it is expected that a difference in the coal and/or reactor, rather than the catalyst, is the cause. However, it is clearly seen in this plot that the addition of the iron carbide catalyst precursors increase the rate of progress along the proposed pathway with Fe_7C_3 progressing furthest in the 15 minute runs. The high conversion is particularly promising since no efforts have been made to maximize or stabilize the precursor dispersion in the slurry.

REFERENCES

1. Wu, W.R.K., Storch, H.H., 1968, Hydrogenation of Coal and Tar. Bulletin 633, Washington, DC, USA, US Department of the Interior, Bureau of Mines, 195pp.

2. Derbyshire, F.J., Stansberry, P.G., Fuel, 1987, 66, 1741-2

3. El Sawy, A., Gray, D., Talib, A., Tomlinson, G., 1986, Report SAND86-7103, Albuquerque, NM, USA, Sandia National Laboratories, 198pp.

4. Haggerty, J.S., Cannon, W.R., 1981, in Laser-Induced Chemical Processes (Ed. J I Steinfeld), Plenum Press, New York, NY, USA

5. Fiato, R.A. et al, 1987, US pat. 4,637,753

6. Rice, G.W. et al, 1987, US pat. 4,659, 681

7. Eklund, P.C., Stencel, J.M., Bi, X.X., Keogh, R.A., and Derbyshire, F.J., American Chemical Society. Div. of Fuel Chemistry. Preprints, 1991, 36(2) 551-60

8. Lee, J.S., Boudart, M., Applied Catalysis, 1985, 19, 207-210

9. Markel, E.J., Van Zee, J.W. Journal of Catalysis, 1990, 126, 643-657

10. Andres, M., Charcosset, H., Chiche, P., Davignon, L., Djega-Mariadasson, G., Joly, J-P., Peregermain, S. Fuel, 1983, **62**, 69-72

11. Andres, M., Charcosset, H., Chiche, P., Djega-Mariadasson, G., Joly, J-P., Peregermain, S. Preparation of Catalysts III (Eds. G. Poncelet and P. Grange) Elsevier 1983, 67 -682

12. Vergon, P.G., Landonisi, H.B., Industrial and Engineering Chemistry, 1980, **19**, 147-151

13. Keogh, R.A., Davis, B.H., American Chemical Society, Div. of Fuel Chemistry, Preprints, 1991, **36**(2) 438-444

Table 1   Conversion Analysis of Liquefaction Experiments

	IOM	Pre-asphaltenes	Asphaltenes	Oil & Gas	Total Conversion
Thermal	58.13	15.02	15.14	11.71	41.87
Fe(CO)$_5$	53.15	9.34	23.43	14.08	46.85
Fe$_3$C	48.88	18.74	21.07	11.32	51.12
Fe$_7$C$_3$	43.74	22.29	18.01	15.96	56.26

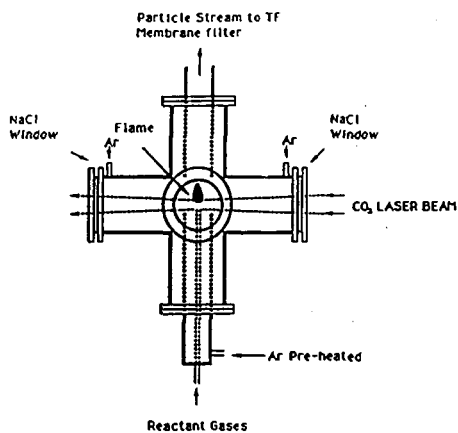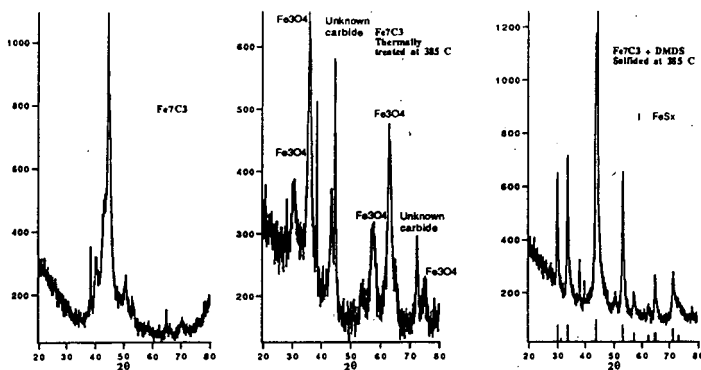

Fig. 1. Schematic Laser Pyrolysis Cell.

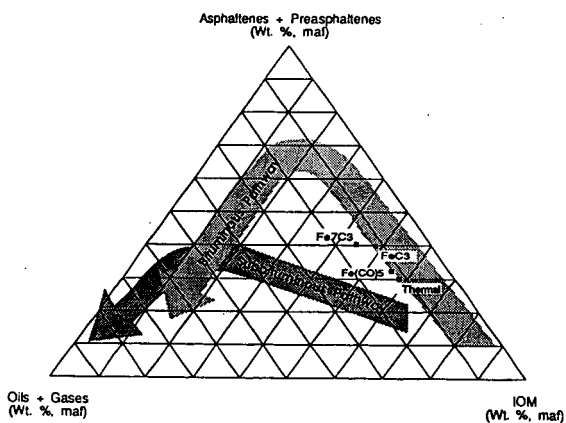Figure 2.   X-Ray Diffraction of Iron Carbide

Figure 3. Liquefaction Data Compared to Reported Pathways

1908

CATALYTIC HYDROTREATMENT OF
COAL-DERIVED NAPHTHA

Liguang Xu, Robert A. Keogh, Chen-Shi Huang,
Robert L. Spicer, Dennis E. Sparks, Scott Lambert,
Gerald A. Thomas and Burtron H. Davis

Center for Applied Energy Research
University of Kentucky
3572 Iron Works Pike
Lexington, KY 40511

ABSTRACT

A naphtha derived from the liquefaction of a subbituminous (Black Thunder) and a bituminous coal (Ill. #6) was hydrotreated on a pilot plant scale, to provide a feedstock sufficiently low in heteroatoms for further studies in reforming. Two commercial catalysts, a Ni/Mo and Co/Mo on alumina, were employed in the processing of the naphtha samples. The Black Thunder naphtha was processed for over 120 hours for two passes using a Co/Mo catalyst and once using a Ni/Mo catalyst. For this naphtha, the nitrogen removal was extremely difficult using the catalysts and conditions employed in this study. An average of 51.6% of the nitrogen was removed for the three passes. The oxygen compounds in this naphtha were relatively easily removed. During the first pass over the Co/Mo catalyst, 94.0% of the oxygen was removed. Further processing during the next two passes using a Co/Mo and a Ni/Mo catalyst further reduced the oxygen content by 54% and 40% respectively.

INTRODUCTION

The dominance of gasoline as a transportation fuel in the United States dictate that any viable coal liquefaction technology must produce a naphtha feedstock that can be upgraded for gasoline production. The concept of what a "good" gasoline is has changed over the decades depending on availability of crudes, environmental concerns, etc. One of the major problems associated with a naphtha derived from processing coal is the high heteroatom content. In order to reform a coal-derived naphtha, the heteroatom content must be further reduced by hydrotreating.

HDN and HDO has been studied extensively using model compounds to determine the mechanism (1-3) and for evaluation of catalysts (4). However, few studies have addressed the upgrading of coal-derived naphtha on a pilot plant scale (5). In the present study, the hydrotreatment of a subituminous coal-derived naphtha was catalytically hydrotreated in the CAER pilot plant. Two commercial hydrotreating catalysts (Ni/Mo and Co/Mo on alumina) were employed in this study.

EXPERIMENTAL

Naphtha Feedstock

Three, 55 gallon drums of the naphtha were obtained from the Wilsonville, Alabama Advanced Integrated Two Stage Liquefaction pilot plant. The naphtha hydrotreated was obtained from processing a Black Thunder coal (subbituminous).

Pilot Plant Operations

The naphtha was hydrotreated in the reconfigured CAER 1/8 tpd liquefaction pilot plant. The process diagram is shown in Figure 1. The plant consists of the following sections: (a) feed delivery (naphtha, H_2), (b) reactor, and (c) high and low pressure separators. The reactor was charged with 2 kg of catalyst and operated in a fixed bed down-flow configuration for the hydrotreating operations.

The first catalyst employed was a commercial Co/Mo on alumina catalyst (American Cyanamid HDS-1442A, 1/16" x 1/4" pellets). The second catalyst studied was a commercial Ni/Mo on alumina catalyst (Akzo KF-840 1.3Q).

Both catalysts were presulfided using a mixture of 3% H_2S in hydrogen prior to the beginning of hydrotreating operations. During the presulfiding operation, a flowrate 30 ft.^{3}/h of the H_2S/H_2 mixture was used. The reactor temperature was rapidly increased to 175°C followed by a 25°C/h ramp. During these operations, the composition of the gas stream exiting the plant was continuously monitored for the H_2S breakthrough by an on-line gas chromatograph. During the ramping of the reactor temperature, the data obtained from the GC indicated that no additional H_2S was being absorbed by the catalyst. At this point, the temperature was increased to 375°C and held at this temperature for 90 minutes. The reactor temperature was then cooled to 300°C and the inlet gas stream was switched to hydrogen using a flowrate 5 ft.^{3}/h prior to the start of naphtha processing. The same presulfiding procedure was used for operations with the Ni/Mo catalyst.

The processing conditions for the three pilot runs are given in Table 1. During naphtha processing, daily samples from the low pressure separator (V-451) were obtained for analysis. The pilot plant was placed under nitrogen at a system pressure of 360 psig prior to the beginning of the second hydrotreating run. Prior to the third pilot plant run, the Co/Mo catalyst was replaced by the Ni/Mo catalyst.

During the hydrotreating operations, two barrels of the Black Thunder naphtha was processed. Collection of the hydrotreated naphtha from each pass into the product barrel was initiated upon the attainment of steady state conditions as indicated by the process variables and the nitrogen content of the daily samples. The feedstock for the second pass using the Black Thunder naphtha was the product barrels obtained during the first pass. The feedstock for the third pass using the Ni/Mo catalyst was the hydrotreated product from the second pass.

Oxygen analyses were performed using the FNAA method and were provided by the University of Kentucky Radioanalytical Services. Trace level nitrogen was analyzed using a Xertex DN-10 total nitrogen analyzer equipped with a chemiluminescence detector.

RESULTS AND DISCUSSION

Black Thunder Hydrotreatment

The nitrogen content of the hydrotreated naphtha (daily samples) obtained during the three passes are shown in Figure 2. The data clearly show the difficulty in removing the nitrogen from the naphtha using either the Co/Mo or Ni/Mo catalysts using these process conditions. During the initial pass, only 43% of the nitrogen was removed from the naphtha. The amount of nitrogen during the second pass was only marginally better (51%). Switching to a Ni/Mo catalyst and using the same process conditions did increase the nitrogen removal to 61%. However, after three passes, the nitrogen content of the hydrotreated naphtha remained at an average level of 383 ppm. The average nitrogen removal was only 52% for all three passes. Based on these data, it was projected that to obtain a hydrotreated product containing 2 ppm nitrogen, the naphtha would have to be processed 10 times (Figure 3). Clearly, hydrotreatment of the Black Thunder naphtha will require more severe conditions than are normally employed in petroleum refining to obtain a final product in which the nitrogen content is sufficiently low for further upgrading by reforming.

The amount of oxygen in the hydrotreated Black Thunder naphtha is shown in Figure 4. Although the oxygen content of the original naphtha is high (2.01%), 94% of the oxygen was removed during the first pass to yield a product containing .11% oxygen. The second and third pass (Mi/Mo) removed an additional 54% and 40% of the oxygen to produce a final hydrotreated naphtha containing .03% oxygen. The results indicate that the majority of the oxygen was easily removed during the first pass using the Co/Mo catalyst and low oxygen content of naphtha feedstock not substantially improve the amount of nitrogen removed during the second pass.

It is apparent from these data, that oxygen is easily removed from the Black Thunder (subbituminous coal) naphtha. The nitrogen compounds found in this naphtha are more difficult to remove during hydrotreating using a WHSV of 1 and a reaction temperature of 403°C. The data also suggests that the HDN process did not substantially inhibit the HDO process using either the Co/Mo or Ni/Mo catalysts under these conditions.

CONCLUSIONS

The resulting data from the hydrotreatment of a Black Thunder naphtha indicate that the removal of nitrogen is difficult. To obtain a nitrogen content of less than 10 ppm require process conditions which are more severe than normally associated with petroleum hydrotreating. In contrast to the difficulty in obtaining a low nitrogen product, oxygen is relatively easy to remove from the Black Thunder naphtha. It is apparent from these data that new catalysts will have to be developed for the processing of coal-derived

naphtha to obtain a sufficiently heteroatom free product using common industrial process conditions.

ACKNOWLEDGMENT

REFERENCES

1.   McIlvried, H. G., Ind. Eng. Chem. Process Des. Dev., 10, 125 (1971).
2.   Furinsky, E., Appl. Catal., 6, 159 (1983).
3.   Ledoux, M. J., Appl. Catal., 9, 31 (1984).
4.   Furinsky, E., I & EC, Prod. Res. & Dev., 22, 34 (1983).
5.   Fischer, R. H. and Hildebrand, R. E., ACS Symp. Series, No. 156 (1981).

TABLE 1

Process Summary

Black Thunder
Hydrotreatment

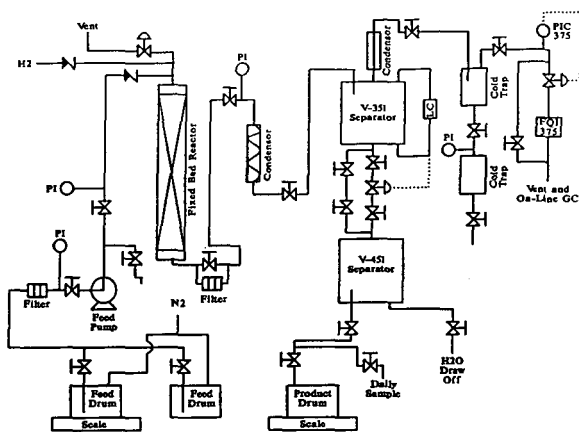| Pass # (Run Hours)	Catalyst	Feed Rate (#/hr)	WHSV # feed/# catalyst/hr	Temp (°C)	Pressure (psig)
1 (0-165)	CoMo	4.0, 4.5	.9, 1.0	418	2010
2 (0-143)	CoMo	4.0, 4.5	.9, 1.0	418	2010
3 (0-127)	NiMo	4.5	.8	403	2000

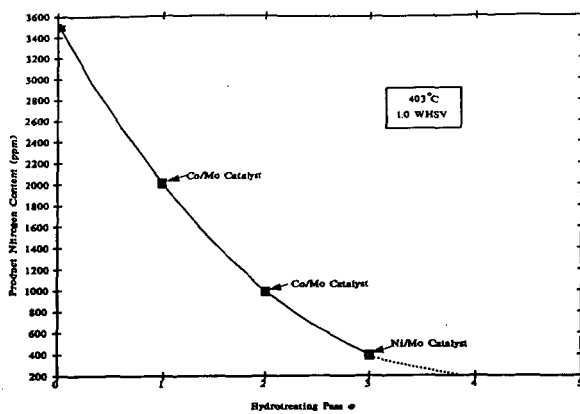Figure 1. CAER Pilot Plant configuration for naphtha hydrotreating.

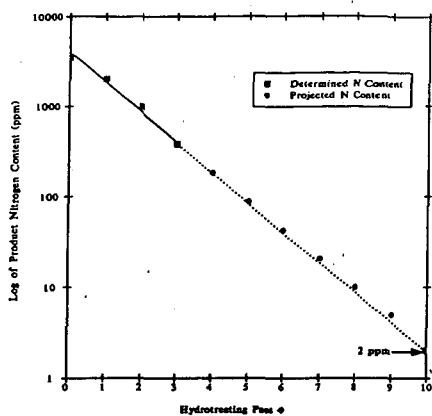Figure 2. Summary of HDN for Black Thunder hydrotreatment.

Figure 3. The projected number of passes to obtain a Black
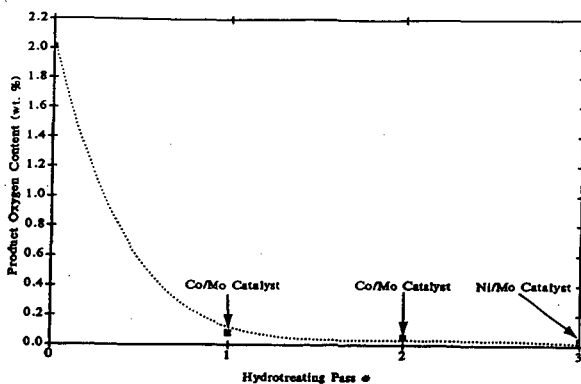Thunder product containing 2 ppm nitrogen.

Figure 4. Summary of HDO for Black Thunder hydrotreatment.

DISTILLATE SELECTIVITY AND QUALITY OF BITUMINOUS COALS IN THE CATALYTIC TWO-STAGE LIQUEFACTION PROCESS

J. M. Lee, C. E. Cantrell, S. V. Gollakota
O. L. Davies, M. M. Corser, and P. Vimalchand
Southern Electric International, Inc.
P. O. Box 1069, Wilsonville, Alabama 35186

Keywords: catalytic liquefaction, distillate selectivity

INTRODUCTION

The Clean Coal Research Center at Wilsonville, Alabama, has been operating for over 17 years to develop alternate technologies for producing low cost fuels from coal. Process developments of close-coupled integrated (CC-ITSL) configurations using the thermal/catalytic or catalytic/catalytic mode of operation were discussed in an earlier article[1].

This paper is primarily focused on the high-volatile bituminous coal performance at steady-state operation with catalyst replacement in the catalytic/catalytic mode. Process developments results from eight runs are discussed: Runs 251-I, 252, 253, 254, 256, 257, 259 and 261. Runs 251-I, 252, 253, 257 and 261 processed a normally mine-washed high-ash Illinois No. 6 coal with four bimodal and one unimodal catalysts (Amocat 1A, Amocat 1C, Shell 317, EXP-AO-60 and Shell 324). Runs 254 and 256 processed an additionally cleaned Ohio No. 6 coal with Shell 317 and 324. Run 259 processed an additionally cleaned low-ash Pittsburgh No.8 coal with Shell 324 and Amocat 1C.

The primary objective of this study is to maximize the distillate production with good quality in order to improve the process economics. The distillate production can be enhanced by improving coal reactivity, catalyst conversion activity, and distillate selectivity. Typical analyses of feed coals processed for this study are summarized in Table 1. The coal cleaning procedure was reported elsewhere[2]. Properties of EXP-AO-60, Amocat and Shell Ni-Mo catalysts tested are shown in Table 2.

PROCESS DESCRIPTION

The current catalytic close-coupled integrated two-stage liquefaction (CC-ITSL) process consists of two H-OIL® ebullated-bed reactors and a Residuum Oil Supercritical Extraction-Solids Rejection (ROSE-SR℠) unit[3]. Both the reactor designs utilize "H-OIL®" technology supplied by Hydrocarbon Research, Inc. The ebullated-bed design helps to maintain a uniform temperature distribution in the reactor. The ROSE-SR℠ is a proprietary extraction process at conditions close to the critical point of the deashing solvent. It was developed and licensed by the Kerr-McGee Corporation.

RUN EXPERIMENTS

Key process variables studied are listed below to maximize the distillate yield and production.

(1) Combined activity of coal and catalyst
-    Illinois, Ohio, Pittsburgh

```
                -    unimodal Shell 324
                     bimodal EXP-AO-60, Amocat 1C(/1A), Shell 317
                -    additionally cleaned low-ash coal
     (2)   Steady-state operation with catalyst replacement
                -    1.5 to 4 lb/ton MF coal per stage
     (3)   Recycle resid concentration in the process solvent
                -    40-50 wt %
     (4)   Low/high and high/low thermal severity modes
     (5)   Vacuum gas oil recycle
     (6)   Coal space velocity
                -    28-76 lb MF coal/hr/cuft-cat per stage
     (7)   Reaction temperature
                -    760-835°F in the first stage
                -    750-825°F in the second stage
     (8)   Inlet hydrogen partial pressure
                -    2500-2700 psia in the first stage
                -    2400-2600 psia in the second stage
                -    2100 psia in the first stage in 253H
     (9)   Slurry composition
                -    29-34 wt % coal (40 wt % in 253C)
                -    12 wt % CI (9 in 251-IA-IB, 4 wt % in 253C)
    (10)   No interstage separation
    (11)   Catalyst cascading in Run 252
    (12)   Reactor operation parameters
                -    temperature profiles, exotherms
                -    ebullation rate, gas flow, slurry flow
                -    slurry viscosity, etc.
```

Several steady-state operation periods were selected for
comparisons of the distillate production, the effect of recycle
resid concentration, and the effect of catalyst replacement rate,
and are summarized below along with the distillate production
projected for the "all-distillate" product slate with resid
extinction[c].

run	catalyst	tempera. (°F) 1st/2nd	cat. rep. (lb/t MF) 1st/2nd	recycle resid (wt %)	projected distillate product.[d]
(1) distillate production					
w/ Illinois coal					
257DE	Amo 1C	790/760	3/1.5	50	28.8
257H	Amo 1C	760/810	1.5/3	40	24.8
257J[a]	Amo 1C	810/760	3/1.5	50	42.2
251-IE	Amo 1A/1C	810/760	2[b]/1C[b]	40	23.6
261B	EXP-AO-60	790/810	3/3	40	37.1
261D	EXP-AO-60	790/810	1.5/1.5	50	29.8
w/ Ohio coal					
254B	She 317	810/760	4[b]/4[b]	40	25.3
254G[c]	She 317	810/790	3/3[b]	50	33.3
w/ Pittsburgh coal					
259H	She 324	825/790	3.6/3.6	50	28.6
259DE[c]	She 324	825/790	4/4	50	23.8
(2) effect of recycle resid concentration					
w/ Illinois coal					
257DE				50	28.8
257F				40	22.3
w/ Pittsburgh coal[c]					
259DE				50	23.8
259F				40	19.3

(3) effect of catalyst replacement
        w/ Illinois coal
261B   3/3   40.   37.1
261D   1.5/1.5 50   29.8
        w/ Ohio coal[c]
254G   3/3[b]   50   33.3
254H   3/2.1[b]   28.8
254I   3/1.5[b]   26.8
254J   3/1.3[b]   30.4
        w/ Pittsburgh coal[c]
259DE   4/4   50   23.8
259I   3[b]/3[b]   19.4
259J   2.5[b]/2.5[b]   15.8
        [a] Half-volume reactors operation.
        [b] Estimated at steady-state operation from batch aging.
        [c] Additionally cleaned low-ash coal.
        [d] Unit: lb/hr/cuft-cat per stage.
        [e] Runs 254 and 257 operated without interstage separation.

RESULTS AND DISCUSSION

DISTILILATE PRODUCTION COMPARISON

Combined Activity of Coal and Catalyst

The distillate production was significantly improved in period
261B processing Illinois with EXP-AO-60 (37.1 lb/hr/cuft-cat per
stage); 29-57% increases compared to 257DE, 257H and 251-IE.
However, the distillate production was 12% lower than 257J. With
additional coal cleaning with heavy media the distillate
production significantly improved processing Ohio with Shell 317,
by 16% in comparison of periods 254G and 257DE, while in contrast
lowered 17% processing Pittsburgh with Shell 324 in comparison of
periods 259DE, 259H and 257DE.

Effect of Recycle Resid Concentration

The effect of recycle resid concentration on distillate
production was projected in both Runs 257D-F and 259D-F. Results
are illustrated in Figure 1. The recycle resid level increase
from 40 to 50 wt % improved 29% distillate production in 257D-F
and improved 23% in 259D-F. 257D-F was with Illinois and Amocat
1C and 259D-F was with Pittsburgh and Shell 324. Both runs were
in the high/low severity.

Effect of Catalyst Replacement Rate

The effect of catalyst replacement rate on distillate production
was projected in Runs 261BD, 254G-J, and 259DEIJ. Results are
illustrated in Figure 2. If the effect of resid recycle increase
from 40 to 50 wt % observed in 257D-F with Illinois and Amocat 1C
is considered in comparison of 261B and 261D (29% increase in the
distillate production), then the catalyst replacement effect
becomes more significant, approximately 61% increase in coal
throughput by 3 lb/ton MF coal total replacement increase in 261B
compared to 261D with Illinois and EXP-AO-60. The distillate
production becomes 48 lb/hr/cuft-cat per stage, higher than that
in 257J (42.2). The effect of catalyst replacement increase on
coal throughput and distillate production was also significant in
254G-J with Ohio and Shell 317, and in 259DEIJ with Pittsburgh

and Shell 324. Both coals were cleaned with heavy media to lower
the ash content and operated at 50 wt % resid recycle level.
254G-J with 1-1.5 lb/ton MF coal total catalyst replacement
increase showed 16-24% increase in the distillate production;
259DEIJ with 2-3 lb/ton MF coal total catalyst replacement
increase showed 23-51% increase in the distillate production.

Data for 251-IE and 257DEJ in the high/low mode were also
included for comparison in Figure 2. Recycle resid concentration
was 40 wt % in 251-IE and 50 wt % in 257DEJ. Operating
conditions for these runs are listed in the previous section.
257J had the highest distillate production, primarily due to
half-volume reactors operation resulting in more isothermal
temperature distribution and better mixing, and a higher resid
recycle level at 50 wt %, while 251-IE and 257DE with full-volume
reactors operation had lower distillate production, because 251-
IE operated at a lower resid recycle level, 40 wt % and 257DE
operated at a lower first stage reaction temperature, 790°F.

259H with high-ash Pittsburgh and Shell 324 had a similar
distillate production to that in 257DE with high-ash Illinois and
Amocat 1C (28-29 lb/hr/cuft-cat per stage); 17% higher production
than 259DE with low-ash Pittsburgh and Shell 324 (Figure 2).
259H operated at 33°F higher reaction temperature and 60% higher
total catalyst replacement than 257DE in the high/low mode.
Recycle resid concentration for these periods was same at 50 wt
%.

EFFECT OF COAL CLEANING ON MAXIMUM DISTILLATE YIELD

Ohio coal was cleaned with heavy media to reduce the ash content
from 10 to 6 wt % and Pittsburgh coal was cleaned from 15 to 4-5
wt %. Coal cleaning significantly improved the coal conversion
for both Pittsburgh and Ohio coals. As a result, the organic
rejection significantly reduced and the C4+ distillate yield
significantly increased. Process performance improvements by the
coal cleaning are summarized below.

run	254		259	
coal	Ohio		Pittsburgh	
base period(s)	B	GI	AH[a]	E
cleaning	normal	addit.	normal	addit.
ash in coal (wt%)	10	6	15	5
pyritic sulfur (wt% MF)	1.9	1.5	1.6	0.6
reactives (petrograp.)	94	97	92	93
potential liquid yield C4+ resid (wt% MAF)	70	78	69-70	78
coal conversion (wt % MAF coal)	94	97	92-93	96
organics rejected to solids prod. (wt% MAF)	16	8	19-20	9
C4+ distillate yield (projected)(wt% MAF)	68	78	67-70	78
C4+ dist. selectivity to resid+UC conv.	0.81	0.84	0.83-0.88	0.85

[a] 259A was unstable.

The coal conversion improvement was probably due to removal of less reactive coal components such as inertinites by cleaning with heavy media[5]. As reported earlier[6], the linear regression analyses for bituminous coals projected that fully cleaned coals with zero ash content could achieve 100 wt % MAF coal conversion; could produce 83 wt % MAF coal C4+ distillate. The distillate yield higher than 83 wt % is possible, if the distillate selectivity further increases to higher than 0.85, which was observed with the cleaned low-ash coals (4-6 wt % ash content) with heavy media. The effect of coal conversion on organic rejection appeared to be very similar for the three coals. A good linear correlation between organic rejection (Y) and coal conversion (X) was derived for these coals by a linear regression analysis and is shown below.

$$Y = 265.7 - 2.67 X$$
$$r^2 = 0.94 \text{ (determination coefficient)}$$

DISTILLATE SELECTIVITY COMPARISON

Distillate Selectivity vs Yield

Figure 3 shows that the C4+ distillate selectivity to resid + UC conversion increases, as the distillate yield increases. High-ash Illinois, low-ash Ohio and low-ash Pittsburgh coals are compared. Processing Illinois in Runs 251-I, 252, 253, 257 and 261, the distillate selectivity was not significantly affected by four different catalysts tested (EXP-AO-60, Amocat 1C, Amocat 1A and Shell 317). The variation was 4%. For simplicity of the illustration the linear regression line with Illinois is included without showing the actual data points. Although two different thermal severity modes of low/high and high/low were investigated in runs with Illinois, it seemed that the selectivity was slightly increased by 1-3%, when operated at 790/760°F in the high/low mode (257A-FIK), 760/790-810°F in the low/high mode (257GH) and 790/810°F in the low/high mode with 3 lb/ton MF coal catalyst replacement per stage (261AB). The lower first stage reaction temperature improved the selectivity with less gas make.

Processing additionally cleaned low-ash Ohio and Pittsburgh in Runs 254 and 259, Pittsburgh and Shell 324 had 2% higher selectivity than that with the combination of Illinois and bimodal catalysts, and 4-5% higher than that with Ohio and Shell 317, although operated higher reaction temperatures, 810-825/790°F (Figure 4). Runs 254 with Ohio and Shell 317 and 257 with Illinois and Amocat 1C operated without interstage separation, which might have affected the selectivity. Coal cleaning appeared to improve the selectivity to 0.85-0.86 by producing more distillate about 78 wt % MAF coal (highest). Normally mine-washed high-ash Illinois with bimodal catalysts had a lower selectivity, 0.82-0.83 by producing less distillate about 68-70 wt % (highest). Inconsistent selectivity data were obtained with high-ash Ohio (■) and Pittsburgh (⊕), that is, 0.86 in 254A, 0.81 in 254B, 0.83 in 259A and 0.88 in 259H.

Distillate Yield vs Hydrogen Consumption

Figure 4 shows with the three coals that the C4+ distillate yield increases, as the hydrogen consumption increases. The effects of catalyst type and reaction temperature were not apparent

1919

processing Illinois. A linear correlation was observed with 4 wt % variation upto 70 wt % MAF coal distillate yield, which is the highest achieved so far with high-ash Illinois at Wilsonville. Required coal conversion and organic rejection to achieve this yield were 94 and 15 wt %, respectively. Processing low-ash Ohio and Pittsburgh, the distillate yield increased to 78 wt % MAF coal due to higher coal conversion (96-97 wt %) and lower organic rejection (7-9 wt %). Hydrogen efficiency (lb distillate/lb hydrogen consumed) in 254 with low-ash Ohio and Shell 317 increased at higher distillate yields above 70 wt %, compared to that with high-ash Illinois at lower distillate yields below 70 wt %. This trend indicated a possibility of two different hydrogenation routes with different reactants and products. Data from low-ash Pittsburgh showed a high scattering, inconclusive trend. Data from high-ash Ohio (■) and Pittsburgh (⊚) are also included in the figure for comparison.

Hydrogen Efficiency vs Reaction Temperature

Figure 5 compares hydrogen efficiencies from Runs 251-I with high-ash Illinois and Amocat 1A/1C (a regression curve without showing the actual data points), 257 with high-ash Illinois and Amocat 1C, 259 with low-ash Pittsburgh and Shell 324, and 261 with high-ash Illinois and EXP-AO-60. Reaction temperature in the high severity stage was selected as x-coordinate variable. The hydrogen efficiencies for Runs 257, 259 and 261 were significantly higher than that obtained in Run 251-I with high-ash Illinois and Amocat 1A/1C; were similar to that with low-ash Ohio and Shell 317 at 810/790°F (Run 254 data are not included in the figure). Although two different thermal severity modes of low/high and high/low were investigated in these runs, it seemed that the efficiency was increased by 10% processing Illinois coal, when operated at 790/760°F in the high/low mode (257A-FIK), 760/790-810°F in the low/high mode (257GH (●)), and 790/810°F in the low/high mode (261A-D). The lower first stage reaction temperature improved the selectivity with less gas make. Low-ash Pittsburgh and Shell 324 in Run 259 had a higher hydrogen efficiency with wide variation from 10 to 12 compared to Run 251-I, although operated higher reaction temperatures, 810-825/790°F. Coal cleaning with heavy media might be partially contributed to this efficiency improvement by producing more distillate with comparable gas make. Runs 254 with Ohio and Shell 317 and 257 with Illinois and Amocat 1C operated without interstage separation, which might have affected the hydrogen efficiency. Coal cleaning appeared to improve the efficiency by producing more distillate to 78 wt % MAF coal (highest). Two data obtained with high-ash Pittsburgh (⊚) showed an inconsitent trend, that is, a higher efficiency was observed at a higher temperature operation (12 vs 10.5 lb distillate/lb hydrogen consumed).

C_1-C_3 Gas Selectivity vs Reaction Temperature

Figure 6 compares gas selectivities from Runs 251-I (a regression curve without showing the actual data points), 257, 259, and 261. Reaction temperature in the high severity stage was selected as x-coordinate variable. The gas selectivities for Runs 257 and 261 with high-ash Illinois were significantly lower than those obtained in Run 251-I with high-ash Illinois and Amocat 1A/1C and Run 254 with low-ash Ohio and Shell 317 at 810/790°F (Run 254 data are not included in the figure). The selectivity for Run

259 with low-ash Pittsburgh and Shell 324 was similar to that for
Run 254 with low-ash Ohio and Shell 317, although operated at
higher reaction temperatures, 810-825/790°F. It seemed that the
gas selectivity was decreased with Illinois coal, when operated
at 790/760°F in the high/low mode (257A-FIK), 760/790-810°F in
the low/high mode (257GH (•)), and 790/810°F in the low/high mode
(261A-D). The lower first stage reaction temperature reduced the
gas selectivity with less gas make. Low-ash Pittsburgh and Shell
324 in Run 259 had a higher gas selectivity with wide variation
from 11 to 15, when operated at a higher first stage reaction
temperature, 825°F. Coal cleaning with heavy media seemed no
significant impact on the gas selectivity. Runs 254 with Ohio
and Shell 317, and 257 with Illinois and Amocat 1C operated
without interstage separation, which might have affected the gas
selectivity. Two data with high-ash Pittsburgh (⊙) showed an
inconsistent trend having a similar gas selctivity observed at a
higher temperature operation.

CATALYST ACTIVITY IN RESID + UC CONVERSION

Catalyst activities were calculated assuming that the resid + UC
conversion reaction follows first-order kinetics for a continuous
stirred tank reactor[3]. Cracking activity (resid conversion) is
not the only function of the catalyst. Hydrogenation activity of
the catalyst was not considered in these catalyst activity
analyses. Catalyst activity analysis should be considered as the
overall activity of combined catalytic and thermal conversion.

Figure 7 compares first stage activities in Runs 261, 257 and
259. Runs 261 and 257 processed Illinois with two different
catalysts, EXP-AO-60 and Amocat 1C. The calculated rate constant
value at 790°F for 261 with EXP-AO-60 was much higher than that
for 257 with Amocat 1C. The rate constant values at 810 and
825°F for 259 processing Pittsburgh with Shell 324 were much
lower than those at 790°F for 261 and 257 processing Illinois
with EXP-AO-60 and Amocat 1C, respectively. The rate constant
value at 810°F for 254 processing Ohio with Shell 317 was higher
than those at 810 and 825°F for 259 processing Pittsburgh with
Shell 324; lower than those at 790°F for 261 and 257 processing
Illinois with EXP-AO-60 and Amocat 1C[2].

Figure 8 compares second stage activities in Runs 261, 257 and
259. The calculated rate constant value at 810°F for 261 with
EXP-AO-60 was higher than those at 760 and 790°F for 257 with
Amocat 1C in the high/low mode; similar to that at 810°F for 257H
with Amocat 1C in the low/high mode. However, the deactivation
rate at 810°F was higher than that at 760°F. The rate constant
values became similar for these temperatures at high catalyst
ages above 50,000 lb MF coal/cuft-cat. The rate constant values
at 760 and 790°F for 259 processing Pittsburgh with Shell 324
were much lower than those at 810°F for 261 and 257H processing
Illinois with EXP-AO-60 and Amocat 1C, respectively; similar to
those at 760 and 790°F for 257 processing Illinois with Amocat
1C. The rate constant values at 760 and 790°F for 254 processing
Ohio with Shell 317 were lower than those at 760 and 790°F for
259 processing Pittsburgh with Shell 324; lower than that at
760°F for 257 processing Illinois with Amocat 1C[2]. The value at
810°F for 254 processing Ohio with Shell 317 appeared to be
similar to that at 810°F for 261 processing Illinois with EXP-AO-
60, when the deactivation curves were extrapolated for comparison

at similar catalyst ages.

COAL REACTIVITY COMPARISON IN RESID + UC CONVERSION

High-ash coal reactivity in the resid + UC conversion reaction was compared and reported in an earlier article[2], by adjusting the responses measured in Runs 253, 254, 257 and 259. Results are summarized below.

coal	run	C4+dist	resid w/OR=20%	resid+UC conv.
Illinois	257J	66	0	80
Pitts.	259A	50	19	61
Ohio	254B/253D	59	7	73

DISTILLATE PRODUCT QUALITY

Table 3 summarizes distillate product qualities in Runs 251-IE, 257FGI, 261BD, 254G and 259DH. During Run 259 with Pittsburgh and Shell 324 which was the first run tested with a better distillation separation system, the distillate product quality improved by reducing the boiling end point of the distillate product (715°F in 259D and 760°F in 259H)[7]. In Run 261BD with Illinois and EXP-AO-60, the boiling end point was 772°F in 261B and 780°F in 261D. 257FGI end point data were estimated by assuming steady recycle of heavy distillate as in Runs 259 and 261. In many respects, the properties of distillates from Illinois, Ohio and Pittsburgh with different Ni-Mo catalysts are similar. This is not unexpected, since they were converted to liquids under similar operating conditions. Hydrogen content was high, 11.3-12.2 wt %. Heteroatom contents were low, 0.1-0.3 wt % nitrogen and <0.1 wt % sulfur. Oxygen content varied 0-2.5 wt %, since it was calculated by the difference. °API gravity was 19-28. Improvements in product quality were recognized by upgrading studies performed with coal-derived liquids by Chevron Oil Company[8]. Reduced boiling end point, lower nitrogen and sulfur contents and increased hydrogen content wolud make the upgrading task easier for the usage of commercial-type transportation fuels. Some improvements have been made during the past several years and efforts continue at Wilsonville to improve the product quality for the better process economics.

CONCLUSIONS

- Processing high-ash Illinois, the distillate production improved by 30-50%. The low/high severity mode with EXP-AO-60, increased catalyst replacement, increased resid recycle, and half-volume reactors operation significantly improved the distillate production.
- Processing low-ash Ohio and Pittsburgh, the distillate yield improved to 78 wt % MAF coal by coal cleaning with heavy media, primarily due to increased coal conversion to 97 wt % and reduced organic rejection to 8 wt %. The distillate production was improved with Ohio and Shell 317 by 16%; was reduced with Pittsburgh and Shell 324 by 17%. The reduction of distillate production with the cleaned Pittsburgh and Shell 324 seemed partly due to a lower pyrite content of the cleaned coal and/or a lower resid conversion activity of the cleaned coal and catalyst.
- The increased gas oil recycle improved the distillate

product quality by reducing the boiling end point of the
distillate product. The boiling end point was 715-760°F
with Pittsburgh and Shell 324; 770-780°F with Illinois and
EXP-AO-60.
- The low/high severity operation seemed improving the
  distillate selectivity and hydrogen efficiency with less gas
  make.
- The additional coal cleaning with heavy media seemed
  improving the distillate selectivity and hydrogen efficiency
  by increasing the distillate yield to 78 wt % MAF coal.
- The theoretical maximum distillate yield of fully cleaned
  coals with zero ash content was projected to be 83 wt % MAF
  coal for high-volatile bituminous coals. The distillate
  yield higher than 83 wt % is possible, if the distillate
  selectivity further increases to higher than 0.85, which was
  observed with the cleaned coals (4-6 wt % ash content) with
  heavy media.
- Resid derived from Illinois was easier to convert to
  distillate than from Ohio and Pittsburgh; resid from
  Pittsburgh was harder to convert than Ohio. Higher reaction
  temperatures were required to achieve the "all-distillate"
  product slate with combinations of low-ash Ohio-Shell 317
  and Pittsburgh-Shell 324; hydrogen efficiencies were similar
  with higher gas selectivities due to higher distillate
  yields.

ACKNOWLEDGEMENTS

REFERENCES

1. R. V. Nalitham, J. M. Lee, C. W. Lamb, and T. W. Johnson.
   Fuel Processing Technology, Vol. 17, 1987, pp. 13-27.
2. J. M. Lee, S.V. Gollakota and O.L. Davies.Proceedings of the
   Fifteenth Annual EPRI Conference on Fuel Science, June 1990.
3. Catalytic, Inc., Topical Report. DOE Contract No. DE-AC22-
   82PC50041, EPRI Contract No. RP1234-1-2, Document No.
   DOE/PC/50041-82.
4. J. M. Lee, C. E. Cantrell, S. V. Gollakota, O. L. Davies, M.
   M. Corser, and P. Vimalchand. Proceedings of the Sixteenth
   Annual EPRI Conference on Fuel Science, June 1991.
5. R. P. Anderson, B. F. Alexander, C. H. Wright, and J. Freel.
   Fuel, Vol. 64, November, 1985, pp. 1558-1563.
6. J. M. Lee and C. E. Cantrell. Proceedings of the Fourteenth
   Annual EPRI Conference on Fuel Science, May 1989.
7. Southern Electric International, Inc., Technical Progress
   Report. DOE Contract No. DE-AC22-82PC50041, EPRI Contract
   No. RP1234-1-2, Document No. DOE/PC/50041-. (Not published)
8. R. F. Sullivan and H. A. Frumkin. ACS National Meeting, Div.
   Fuel Chem., New York, NY, April, 1986.

TABLE 1

FEED COAL ANALYSIS

Coal	Illinois No.8	Ohio No.8	Pittsburgh No.8
Mine	Burning Star	Crooksville (cleaned)	Ireland (cleaned)
Runs	251-I,252,253 257,261	254,256	259
Rank (ASTM)	hvbB	hvbB	hvaB
FC (mf wt %)	51	53	54
HV (Btu/lb mf)	12,600	13,300	14,200
Ultimate (mf wt %)			
Carbon	70.8	75.3	78.8
Hydrogen	4.8	5.3	5.7
Nitrogen	1.5	1.4	1.4
Sulfur	3.4	2.8	3.2
Ash	11.5	6.6	4.5
Oxygen (dif.)	8.2	8.8	5.8
Petrographic (mmf vol %)			
Reactives	94	97	93
Pyritic Sulfur	1.1	1.5	0.8

TABLE 2

WILSONVILLE NI-MO CATALYST PROPERTIES

Catalyst	Shell 324	Amocat 1C	EXP-AO-60	Shell 317
Run	256,259 261	251-253 257,259	261	253,254 256
Shape	<--------Cylindrical---------->			Trilobe
Size (in)	1/16	1/16,1/12	1/16	1/20
NI (wt%)	2.7	2.3	2.5	2.7
Mo	13.2	10.4	10.7	11.8
Surface Area (sqm/g)	165	190,185	241	235
Pore Volume (cc/g)	0.48	0.85,0.88	0.78	0.75
Pore Size Dist.	Unimodal	<---------Bimodal---------->		
Comp. B. Density (lb/cuft)	54	42,35	33	38

TABLE 3. TOTAL DISTILLATE PRODUCT QUALITY COMPARISON

Run	257F	257G	257I	251-IE	261B	261D	254G	259D	259H
Coal	----------		Illinois	-----------			Ohio	Pitts.	
Wt % C	87.5	87.8	87.4	87.2	87.3	87.5	88.3	86.7	87.0
H	12.2	12.1	12.1	11.6	11.4	11.3	11.3	12.0	11.7
N	0.2	0.1	0.1	0.2	0.2	0.3	0.3	0.2	0.2
S	0.0	0.0	0.0	0.0	0.0	0.0	0.0	0.0	0.0
O	0.1	0.0	0.4	1.0	1.1	0.9	0.1	1.1	1.1
									(2.5)
°API	21	21	21	26	23	22	19	28	25
Wt % Naphtha	22	21	18	26	19	14	25	20	19
Mid.D1	11	10	11	12	11	16	9	18	13
Mid.D2	50	53	64	32	40	40	35	43	43
Gas Oil	17	16	7	30	30	30	32	19	25
End point °F (D1160)	680	700	665	-	772	780	-	715	760
	- estimated -								

FIGURE 1

EFFECT OF RECYCLE RESID CONCENTRATION
ON DISTILLATE PRODUCTION

(Illinois : 257   Pittsburgh : 259)

period	catalyst	$T_{1st/2nd}(°F)$
+ 259DEF	Shell 324	825/790
o 2570EF	Amocat 1C	790/760

dist.pr.lb/hr/cuft-cat-eq

Recycle Resid Level
(wt % in process solvent)
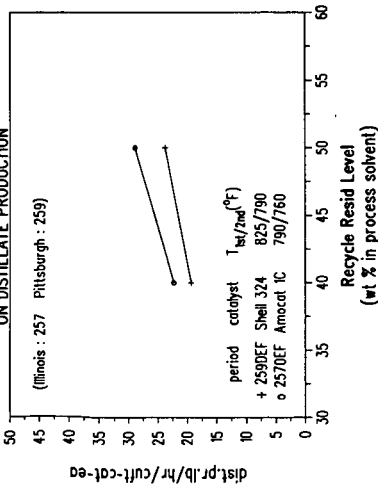
FIGURE 2

EFFECT OF CATALYST REPLACEMENT
ON DISTILLATE PRODUCTION

(Illinois : 261,257,251   Ohio:254   Pittsburgh : 259)

t (26 B wt. for 50% resid)

+ (26 B w/ 40% resid)

(261D w/ 50% resid)

period	catalyst	$T_{1st/2nd}(°F)$
□ 261D	EXP-AO-60	790/810
■ 259DEFHJ	Shell 324	825/790
+ 25418C-J	Shell 317	810/790
o 2570EJ	Amocat 1C	790-810/760
◇ 251E	Amocat IA/1C	810/760

dist.pr.lb/hr/cuft-cat-eq

Total Catalyst Replace.
(lb/ton mf coal)
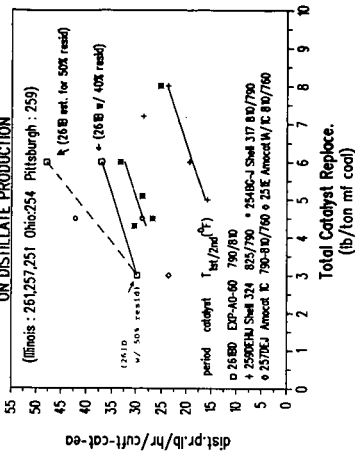
FIGURE 3

DISTILLATE SELECTIVITY VS YIELD
(Ohio and Pittsburgh Coals - Low Ash)

+ : Pitt. & She 324 (259B-J:810/790°F) (0->825/790°F)
Amo 1C (A:810/760°F) (Alt high ash)

(Illinois - high ash)

□ : Ohio & She 317 (254A-CEF:810/760°F) (no int. sep.) (Alt high ash)
(KL:810/800°F) (no int. sep.) (Alt high ash)

dist. sel. to conversion

Distillate Yield
(wt % maf coal)
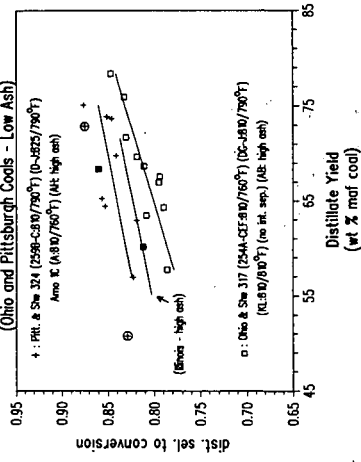
FIGURE 4

DISTILLATE YIELD VS H2 CONSUMPTION
(Ohio and Pittsburgh Coals - Low Ash)

+ : Pitt. & She 324 (259B-J:810-825/790°F) (Alt high ash)
Amo 1C (A:810/760°F) (Alt high ash)

(Illinois - high ash)

□ : Ohio & She 317 (254A-L:810/760-810°F) (Alt high ash) (no int. sep.)
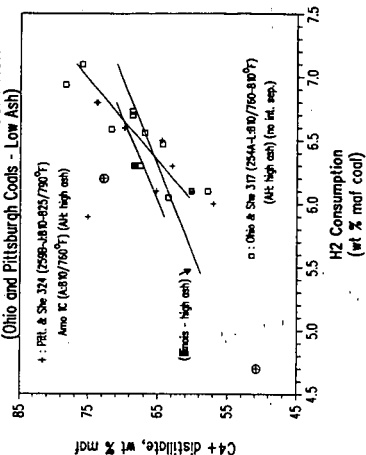
C4+ distillate, wt % maf

H2 Consumption
(wt % maf coal)

FIGURE 5 — HYDROGEN EFFICIENCY VS TEMPERATURE
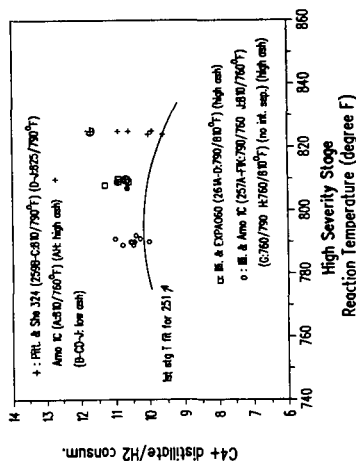
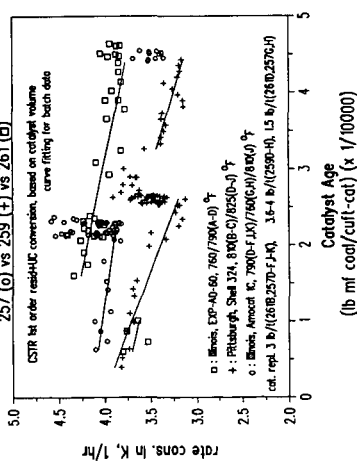FIGURE 6 — C1-C3 GAS SELECTIVITY VS TEMPERATURE
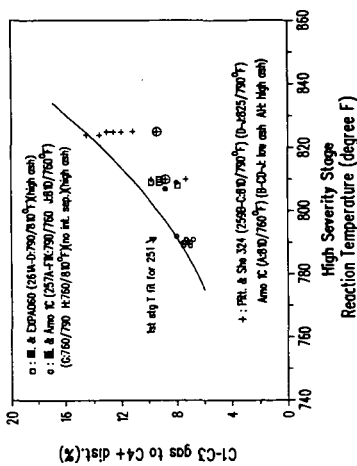
FIGURE 7 — 1ST STAGE CATALYST ACTIVITY COMPARISON
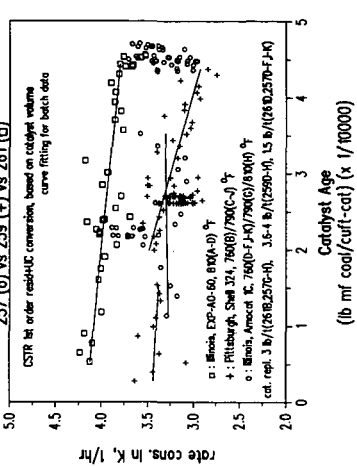
FIGURE 8 — 2ND STAGE CATALYST ACTIVITY COMPARISON

1926

TWO STAGE GASIFICATION : EFFECT OF HYDROPYROLYSIS CONDITIONS

G. Skodras and G.P. Sakellaropoulos
Departement of Chemical Engineering and
Chemical Process Engineering Research Institute
Aristotle University of Thessaloniki
Thessaloniki, Greece 54006

SUMMARY

Two-stage hydropyrolysis and CO_2 gasification has been inves-
tigated with Greek lignite at various temperatures and residence
times in order to indentify optimal conditions for switching between
the two steps. Optimality was based on carbon conversion and product
formation. Such optimum conditions are obtained for hydrocharing at
900°C for 2 to 5 min and subsequent CO_2 gasification of the resulting
chars at 900°C and 10 min.

INTRODUCTION

Hydrogasification is a relatively slow process [1,2], with most
hydrocarbons formed in the ealry hydropyrolysis step [2,3]. Carbon
dioxide gasification of chars is faster than hydrogasification and
can improve conversion and carbon atom utilization. Char gasification
in CO_2 has been investigated with respect to carbon reactivity [4,5],
kinetic behavior [6], and promotion by catalysis[7]. However, most
chars used in CO_2 gasification have been prepared, almost ex-
clusively, in non-reactive atmospheres, such as N_2 or He [4-6]. Little
is known about the effect of the initial charring step (pyrolysis or
hydropyrolysis) on the reactivity in the second stage and on total
carbon conversion and gaseous product formation.

In this work Greek lignite was gasified in a reactive hydrogen at-
mosphere and subsequently in CO_2, to explore lignite behavior under
two stage, ambient pressure gasification. The effect of temperature
and solids residence time in each stage on total carbon conversion
and on gaseous product yields and selectivity was studied.

EXPERIMENTAL

Greek lignite from the Ptolemais reserve ($4 \ 10^9$ t) was used,
with particles in the range of 150 to 250 µ. This lignite is high in
calcium carbonate ash and humidity and has a volatiles content of
47.16% (on dry basis).

The gasification test reactor was equipped with gas and solids
feeding controls and with product collection and analysis devices,
Fig. 1. The U-shape reactor design permitted rapid quenching of the
reactor, thus, hydropyrolysis or CO_2 gasification reactions could be
interrupted at any desirable time.

Lignite samples were initially hydropyrolyzed (800°C or 900°C, at
2, 5 or 10 min) and the produced chars were gasified under a CO_2 at-
mosphere (800°C or 900°C, at up to 15 min). Gaseous products were col-
lected in both stages, and were analyzed mainly for CH_4 and CO by
G.C. (Varian Vista 6000). Chars obtained in the hydropyrolysis and the
CO_2 gasification step were analyzed by a LECO C-H-N 800 analyzer, in
order to determine elemental compositions and conversions in each
step.

RESULTS AND DISCUSSION

During the first stage (hydropyrolysis), the devolatilization and
hydrocracking reactions which take place [3,8] cause significant

1927

weight loss.On a dry and ash free basis, weight losses are of the order of 62% at 800°C, reaching about 67% at 900°C and long residence times.Since the initial volatile matter of lignite is 47% w/w on a dry basis, devolatilization appears to be the main reaction during this first stage [3,8,9].The heterogeneous carbon-hydrogen gas-solid reaction becomes significant only at longer solid residence times (>10 min).

Methane, CO and CO_2 are the main gaseous products during this first stage. Tables 1 and 2.Maximum CH_4 formation is observed at 900°C and 10 min, via the heterogeneous hydrogen-carbon gas-solid reaction. In contrast, $CO+CO_2$ yields are less affected by the hydropyrolysis residence time, since these are products of hydropyrolysis and hydrocracking reactions during the initial 2 min of pyrolysis.The yield of CO, however, increases appreciably (about 60%) with temperature, from 800°C to 900°C, while that of CO_2 drops to about one third, due to enhacement of the CO_2 reduction to CO in a H_2 atmosphere [3].Other hydrocarbons (C_2H_4,C_2H_6 etc) are also produced in small quantities (1 to 12 cc/g lign. daf), Table 1 and 2.

In order to evaluate the significance of each product at the various conditions tested a "selectivity index" has been used, shown in Table 1 and 2.To calculate the selectivity of the gaseous products, other higher molecular weight products have been assumed to be insignificant compared to CO,CO_2,CH_4,C_2H_4 and C_2H_6.Increase of solid residence time at low hydropyrolysis temperature (800°C) almost doubles the CH_4 "selectivity index" (8.15% at 2 min, and 15.7% at 10 min), Table 1.Similar behavior is also exhibited by CO selectivity for both hydropyrolysis temperatures.In contrast, CO_2 selectivity decreases with an increase of hydropyrolysis time and temperature. This is particularly evident by the relative selectivity of CO and CO_2 expressed as the ratio CO/CO_2, Tables 1 and 2.Thus, high T and long times minimize CO_2 formation while total ($CO+CO_2$) selectivity decreases somewhat.

The elemental analyses of chars prepared at 800°C and 2.5 or 10 min show that elemental carbon conversion is rather low in this stage, Table 3.Increase of hydropyrolysis temperature to 900°C improves the elemental carbon conversion, which reaches 51.5% for 10 min solid residence time, Table 3.This improvement results from enhacement of the devolatilization and hydrocracking reactions with temperature. Elemental H and O conversions, are in all cases high (84-96% w/w), Table 3.Thus, during hydropyrolysis, cleavage of oxygen containing groups occurs.In the same period, cleavage and release of aliphatic and aromatic groups take place [8], resulting in high hydrogen conversion (84-96% w/w).The chars formed are, hence, rich in carbon and ash.

In the second stage, the carbon-carbon dioxide gas-solid reaction is practically the only one taking place, since the volatile matter has been almost completely removed during hydropyrolysis [8,9]. Traces of hydrocarbons detected in this stage, come from residual volatiles of the original lignite.

Conversion of organic matter (essentially C-conversion) in the second stage depends on the history of the char and on the conditions of CO_2 gasification, ie temparature and residence time.Increase of the solids residence time at low temperature (800°C) hydropyrolysis, increases conversion in the second stage, Fig 2.In contrast, at high

hydropyrolysis temperature (900°C) and solid residence time, conversion in CO_2 gasification decreases, Figs 2 and 3.Thus, chars prepared by hydropyrolysis at low T and residence time (800°C/2-5 min) yield 29% C-conversion when gasified in CO_2 at 800°C and 5 min, Fig 2.As the residence time in hydropyrolysis stage increases, more active sites are formed in the char, capable of further reaction with CO_2, thereby increasing C-conversion, Fig 2,3.For the same hydropyrolysis char, conversion increases by 20 to 30% with increasing residence time in CO_2 gasification.

Similar behavior is also exhibited by hydrochars prepared at 900°C However, CO_2-gasification of these chars yields lower conversions in the second stage, as compared with chars prepared at 800°C and 10 min, Fig 2,3.Conversion in CO_2 gasification decreases further with an increase in hydropyrolysis solid residence time, for chars prepared at 900°C, Fig 2.This is probably due to active site deactivation, occuring at high hydropyrolysis temperatures (900°C) and long residence times,[10-12] cf Fig 2,3 .

Formation of CH_4 and other hydrocarbons practically stops during CO_2 gasification of the chars.Hydropyrolysis chars react in the second stage according to the Boudouard reaction, and produce CO which is the main gaseous product, Figs 4 and 5.We should note here that second-stage product yields are presented per gram of initial lignite (daf), permiting direct comparison of yields between the two stages. Carbon monoxide formation in the second stage, improves with hydrochars obtained at 800°C and long residence time, Fig 4 and 5. However, chars prepared at 900°C and long residence times yield low CO product by CO_2 gasification, Fig 4 and 5, due to active site deactivation under such conditions.These results are in good agreement with the observed C-conversions discussed previously.Such agreement should be anticipated since CO is formed by char reaction with CO_2 in the second stage.

Elemental carbon conversion of CO_2 gasification chars at 800°C or 900°C and 5 min residence time, is rather low and incomplete (29 -46% w/w), Fig 6.The increase of second stage solid residence time improves elemental C-conversion for both CO_2-gasification temperatures (800°C & 900°C), Fig 6.It should be noted here that second stage elemental C-conversion values at 900°C are higher than at 800°C, Fig 6, due to enhacement of the Boudouard reaction rate with increasing temperature.

Similar to weight loss, elemental C-conversion in the second stage depends on the history of the char, ie hydropyrolysis temperature and residence time.Increase of the solid residence time at low temperature (800°C) hydropyrolysis, increases elemental carbon conversion in the second stage, Fig 6.In contrast, at high hydropyrolysis temperature (900°C), and long solid residence time, second stage elemental C-conversion decreases, Fig 6.This behavior is in agreement with the previously discussed active carbon deactivation at high hydropyrolysis temperatures and times.

From Figs 2-5 it is apparent that an optimum hydropyrolysis temperature and residence time should exist, which, combined with CO_2 gasification, leads to maximum carbon conversion.The optimum corresponds to hydrogasification at 900°C and 2 to 5 min.Thus, a hydropyrolysis char, obtained at 900°C/2 min, reacted with CO_2 at 800°C and 10 min, gives a maximum total carbon conversion of about

88%.For CO_2 gasification at 900°C and 10 min total C-conversion reaches 98%.At other temperatures and residene times, overall conversions are somewhat lower (84-95%), at longer times (15-20 min).

These results suggest that hydropyrolysis at 900°C and 2 to 5 min generates more active sites in the lignite matrix than hydropyrolysis at 800°C at the same residence time, resulting in higher second-stage char conversions.However, prolongation of the residence time (10 min) at lower hydropyrolysis temperature (800°C) improves C-conversion in the second stage, Fig 2.Thus, total C-conversion of hydrochars prepared at 800°C/10 min is comparable to that of chars obtained at 900°C/2 min.This indicates that similar amounts of active sites exist in the lignite matrix of these two chars, further supporting the notion of deactivation at high hydropyrolysis temperature and long time.

The above comments on optimality are based solely on total carbon conversion.However, selection of optimum operating conditions should also take into account the yields of gaseous products.Thus, maximum CH_4 production is observed for samples hydropyrolyzed at 900°C and 10 min. This maximum should be anticipated, since CH_4 formation via the heterogeneous carbon-hydrogen gas-solid reaction becomes significant for long hydropyrolysis times.Maximum CO production is observed for chars hydropyrolyzed at 900°C and 2 min and subsequently gasified in CO_2 at 900°C and 10 min (about 1700 cm^3 CO/g lignite daf).Maximum total carbon conversion (97.8% w/w) is also observed at these conditions.Thus, optimum conditions for carbon conversion coincide with these for CO formation.However, maximum CH_4 production appears at somewhat different conditions.

ACKNOWLEDGEMENT

REFERENCES

1. Kokorotsikos,P.S.,Stavropoulos,G.G.,Sakellaropoulos,G.P, Proc. 1985 Int. Conf. Coal Science, Sydney, Oct. 1985,253.

2. Kokorotsikos,P.S.,Stavropoulos,G.G.,Sakellaropoulos,G.P., Proc. Int. Symp. on "Fundamentals of Catalytic Carbon and Coal Gasification", FUNCAT COGAS 86, Rolduc, The Netherlands, May 1986,327.

3. Sakellaropoulos,G.P., Kokorotsikos,P., Korili,S., Stavropoulos, G.,"Catalytic Gasification of Lignites for Synthetic Fuels", Final Report, Contr. No 7220,EC/701, Thes/niki, October 1987.

4. Adanez, J., Miranda, J.L. and Gavilan, J.M., Fuel, 1985, 64, 801.

5. Koening,P.C.,Squires,R.G. and Laurendeau,N.M., Fuel,1986,65, 412.

6. E. Hippo and D.L. Walker, Jr., Fuel, 1975, 54, 245.

7. Sams, D.A. and Shadman, F., AIChE J., 1986, 32, 1132.

8. Anthony, D. and Howard, J.B., AIChE J., 1976, 22, 625.

9. Gavalas, G.R., "Coal Pyrolysis", Elsevier, NY 1982.

10. Johnson,J.L.,"Kinetics of Coal Gasification",J.Wiley & Sons Inc, NY 1979.

11. P. Ehrburger, F. Louys and J. Lahaye, Carbon, 1989, 27, 389.

12. Elliot, M.A. "Chemistry of Coal Utilization", Second Supplementary Volume, J Wiley and Sons, NY 1981.

Table 1 : Total gaseous products during hydropyrolysis at 800°C

Product	cm³ /g lignite d.a.f. ¹					
	800°C/2 min		800°C/5 min		800°C/10 min	
	Yield	Selectivity(%)	Yield	Selectivity(%)	Yield	Selectivity(%)
CH₄	26.6	8.2	42.5	11.8	68.4	15.7
C₂H₄	6.5	2.0	8.0	2.2	14.0	3.3
C₂H₆	1.5	0.5	2.0	0.6	2.3	0.5
CO	128.0	39.1	139.0	38.4	236.0	54.3
CO₂	164.0	50.3	170.0	47.1	114.0	26.2
CO+CO₂	292.0	89.4	309.0	85.5	350.0	80.5
CO/CO₂		0.8		0.8		2.1

Table 2 : Total gaseous products during hydropyrolysis at 900°C

Product	cm³ /g lignite d.a.f. ¹					
	900°C/2 min		900°C/5 min		900°C/10 min	
	Yield	Selectivity(%)	Yield	Selectivity(%)	Yield	Selectivity(%)
CH₄	52.3	11.6	72.2	14.4	77.1	14.8
C₂H₄	11.8	2.6	12.0	2.4	12.7	2.4
C₂H₆	0.8	0.2	1.0	0.2	1.2	0.2
CO	306.0	67.7	337.0	67.2	378.0	72.4
CO₂	81.0	17.9	80.0	15.9	53.0	10.2
CO+CO₂	387.0	85.6	41.7	83.0	431.0	82.8
CO/CO₂		3.8		4.2		7.1

Table 3 : Composition and conversion of hydropyrolysis chars

Sample Code	Temp/Time (°C,min)	Weight loss (% w/w)	Char Composition (% w/w)					Elemental conversion (Ci)% w/w			
			C	H	N	ASH	O	C_c	C_H	C_N	C_O
TS1a	800/2	48.10	55.74	1.21	1.18	31.97	9.30	38.60	86.60	51.80	83.50
TS2a	800/5	49.20	57.80	0.93	1.19	32.69	8.92	37.90	89.90	52.40	88.00
TS3a	800/10	51.70	55.04	1.22	0.66	34.35	8.13	43.60	87.40	74.90	86.60
TS4a	900/2	54.10	54.21	0.42	1.27	36.15	7.35	47.20	95.90	54.10	88.50
TS5a	900/5	55.00	54.72	0.51	1.01	36.92	6.24	48.80	95.10	64.20	90.40
TS6a	900/10	56.70	52.84	0.44	1.15	38.33	6.24	51.50	95.90	60.80	90.20
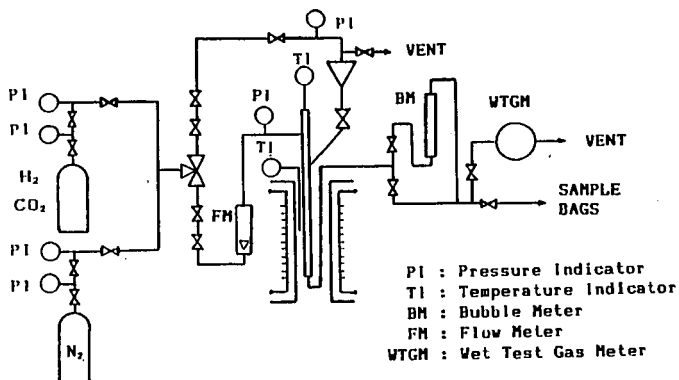
Figure 1 :   Flow diagram of a rapid quenching gasification system.
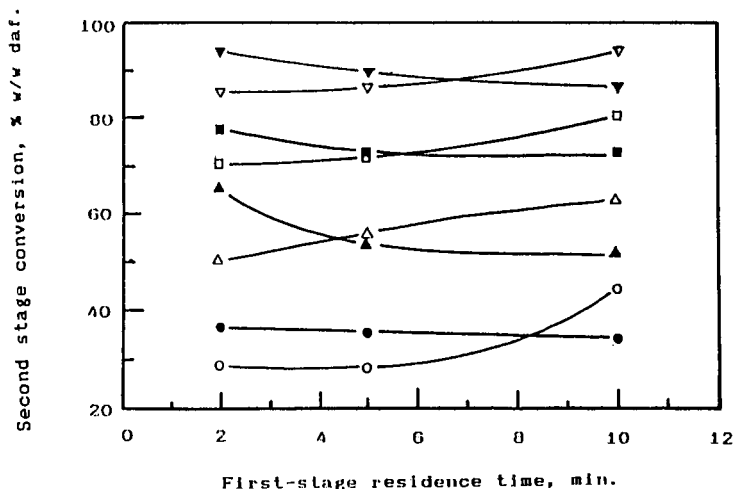

First-stage residence time, min.

Figure 2 : Effect of hydropyrolysis temperature and residence time on weight loss during CO₂ gasification. Open points: hydropyrolysis at 800°C; closed points: hydropyrolysis at 900°C. CO₂ gasification: ○ ● : 800°C/5 min, △ ▲ :800°C/10 min, ▢ ■ : 900°C/5 min, ▽ ▼ : 900°C/10 min.
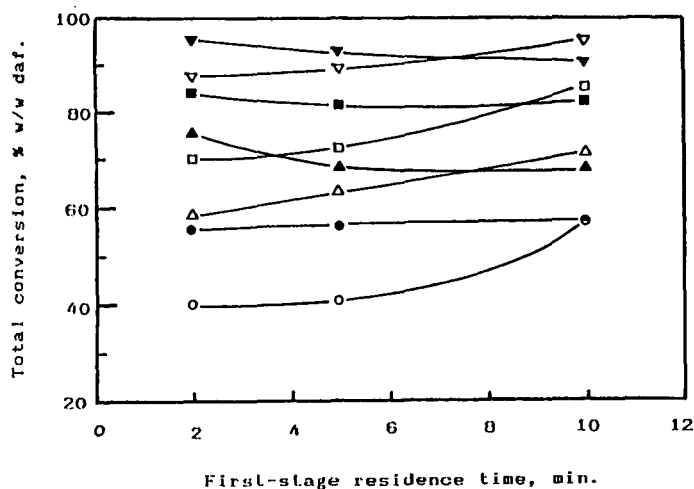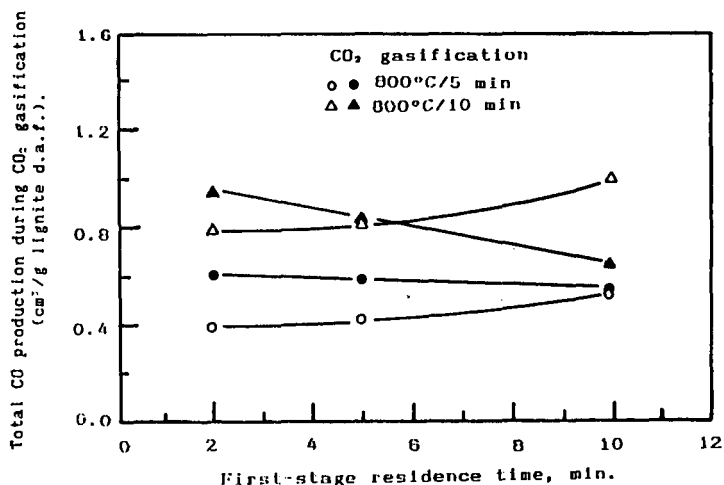
Figure 3 : Effect of hydropyrolysis temperature and residence
time on total weight loss. Open points: hydropyrolysis at
800°C; closed points: hydropyrolysis at 900°C. CO_2
gasification:o ● : 800°C/5 min, △ ▲ :800°C/10 min, ▢ ▮ : 900°C/5
min, ▽ ▼ : 900°C/10 min.

Figure 4 : Effect of hydropyrolysis temperature and residence
time on total CO production, during CO_2 gasification at 800°C.
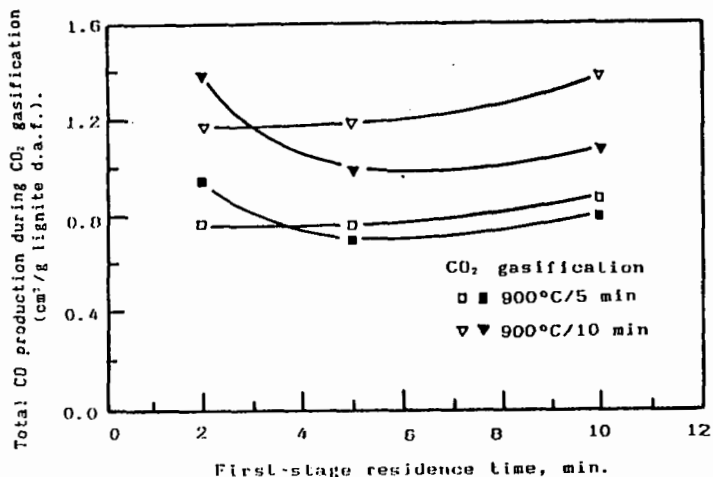Open points: hydropyrolysis at 800°C; closed points:
hydropyrolysis at 900°C.

1933

Figure 5 : Effect of hydropyrolysis temperature and residence time on total CO production, during CO_2 gasification at 900°C. Open points: hydropyrolysis at 800°C; closed points: hydropyrolysis at 900°C.
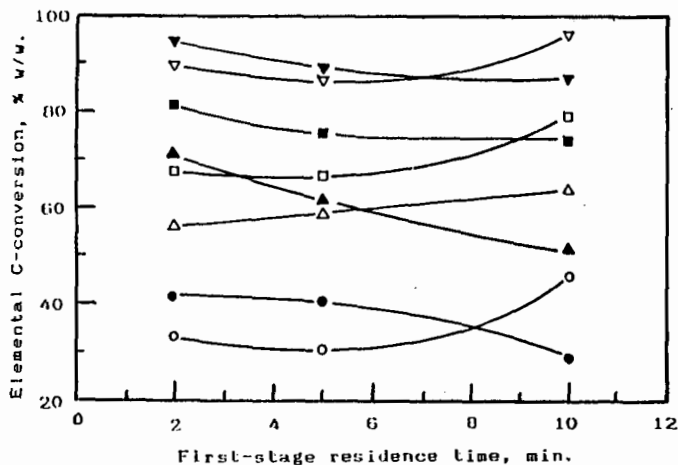

Figure 6 : Effect of hydropyrolysis temperature and residence time on elemental C-conversion during CO_2 gasification. Open points: hydropyrolysis at 800°C; closed points: hydropyrolysis at 900°C. CO_2 gasification: ○ ● : 800°C/5 min, △ ▲ :800°C/10 min, □ ■ : 900°C/5 min, ▽ ▼ : 900°C/10 min.